Research@ARL

Volume 2, Issue 2, July 2013

Autonomous Systems

$$J_{tot}\ddot{\theta}_{tot} + b_{tot}\dot{\theta}_{tot} + k_{tot}\theta = Gu(t)$$

$$J_{tot} \approx \sum_{i=1}^{N-1} m_L L_{L,i}^2 + J_N + m_N L_N^2.$$

$$\dot{\mathbf{X}}_1(t) = \tilde{A}_1\mathbf{X}_1(t) + \tilde{A}_2\mathbf{X}_2(t). \quad \mathbf{X}_1(t_0) = \mathbf{X}_{1_0}.$$
$$\dot{\mathbf{X}}_2(t) = A_3\mathbf{X}_1(t) + A_4\mathbf{X}_2(t) + B\mathbf{u}(t) + \mathbf{W}(t).$$
$$\mathbf{X}_2(t_0) = \mathbf{X}_{2_0}.$$

$$E_{C_m} = 2C_m U_{low}^2$$

$$E_A = \frac{(C_l + C_m)(U_{max} - V_{tp} - V_{tp}}{K_g}$$

$$+ \frac{(U_{max} - V_{tp})R_1 C_m V_{tn}}{K R_2 V_{tn}}$$

$$E_B = \frac{C_m (U_{max} - V_{tp} - V_{tp}}{K_g}$$

$$+ \frac{(u_{max} - V_{tp})R_1 C_m V}{K R_2 V_{tn}}$$

$$J_C + J_R$$

$$\sum_{k=1}^{n} \frac{1}{2} C U_{max}^2 ((u_k - u_{k-1})^2 + u_0^2) + \sum_{k=0}^{n} \frac{U_{max}^2}{R} T_s u_k.$$

(20)

$$\frac{1}{2} C U_{max}^2 ((u_k - u_{k-1})^2 + u_0^2)$$

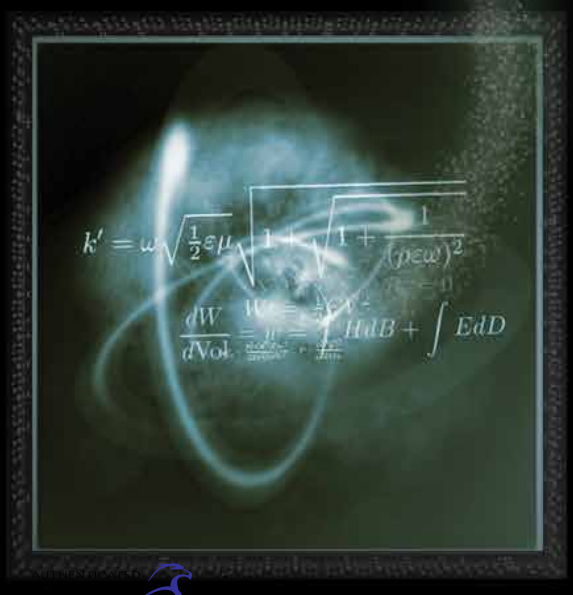

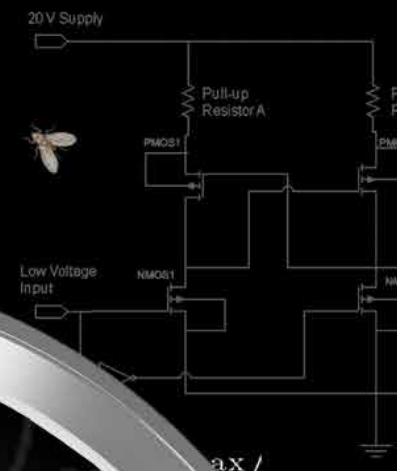

Parameters	Simulation Model	Macro System	MEM Leg Join
R (Ω)	$3 * 10^9$	$3 * 10^9$	$3 * 10^9$
C (F)	$1 * 10^{-9}$	$1 * 10^{-9}$	$1 * 10^{-9}$
$U_{max}(V)$	20	20	20
J $(kg.m2)$	$1.4 * 10^{-12}$	1	1.4×10^{-12}
b $(N.m.s/rad)$	$3.4 * 10{-}11$	14	2.7×10^{-10}
k $(N.m/rad)$	$3.2 * 10{-}6$	40350	4.4×10^{-6}
G $(N.m/V)$	$8 * 10^{-8}$	64151	2.8×10^{-8}
Sampling time (T_s)(sec)	0.0001	0.001	0.0001

Dr. Joseph N. Mait and Dr. Brian M. Sadler

Editors-in-Chief

U.S. Army Research Laboratory

Report Documentation Page

Form Approved
OMB No. 0704-0188

1. REPORT DATE	2. REPORT TYPE	3. DATES COVERED
JUL 2013		**00-00-2013 to 00-00-2013**

4. TITLE AND SUBTITLE	5a. CONTRACT NUMBER
Autonomous Systems	5b. GRANT NUMBER
	5c. PROGRAM ELEMENT NUMBER
6. AUTHOR(S)	5d. PROJECT NUMBER
	5e. TASK NUMBER
	5f. WORK UNIT NUMBER
7. PERFORMING ORGANIZATION NAME(S) AND ADDRESS(ES) **U. S. Army Research Laboratory,Aberdeen Proving Ground,MD,21005**	8. PERFORMING ORGANIZATION REPORT NUMBER
9. SPONSORING/MONITORING AGENCY NAME(S) AND ADDRESS(ES)	10. SPONSOR/MONITOR'S ACRONYM(S)
	11. SPONSOR/MONITOR'S REPORT NUMBER(S)

12. DISTRIBUTION/AVAILABILITY STATEMENT
Approved for public release; distribution unlimited

13. SUPPLEMENTARY NOTES
Research@ARL, Vol 2, Issue 2, July 2013

14. ABSTRACT

15. SUBJECT TERMS

16. SECURITY CLASSIFICATION OF:			17. LIMITATION OF ABSTRACT	18. NUMBER OF PAGES	19a. NAME OF RESPONSIBLE PERSON
a. REPORT **unclassified**	b. ABSTRACT **unclassified**	c. THIS PAGE **unclassified**	**Same as Report (SAR)**	**197**	

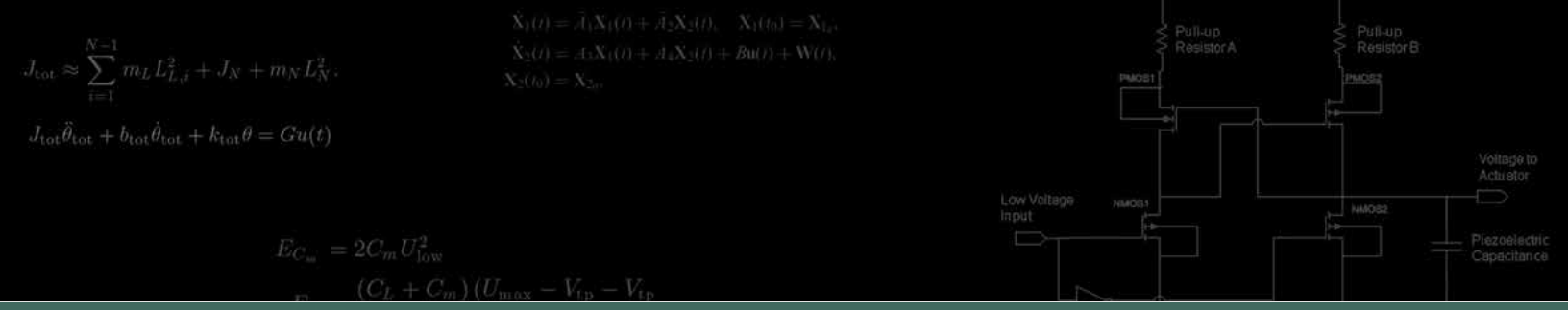

Editorial Board

Dr. Joseph N. Mait
Editor-in-Chief

Dr. Brian M. Sadler
Editor-in-Chief

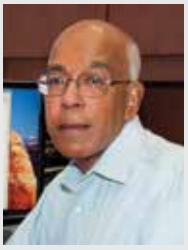

Dr. Ananthram Swami

Dr. Bruce J. West

Advisory Board

Dr. Kwong K. Choi
Dr. Brad E. Forch
Dr. Piotr J. Franaszczuk
Dr. Shashi P. Karna
Dr. Stephen J. Lee
Dr. Joseph N. Mait
Dr. Nasser M. Nasrabadi
Dr. Peter J. Reynolds
Dr. Paul H. Shen
Dr. Ananthram Swami
Dr. Bruce J. West

Research@ARL can be accessed electronically at **www.arl.army.mil/ResearchARL**

Research@ARL

Autonomous Systems • 2013

contents

b $(N.m.s/rad)$	$3.4 * 10-11$	14	2.7×10^{-10}
k $(N.m/rad)$	$3.2 * 10-6$	40350	4.4×10^{-6}
G $(N.m/V)$	$8 * 10^{-8}$	64151	2.8×10^{-8}
Sampling time (T_s)(sec)	0.0001	0.001	0.0001

Introduction to ARL

The Army Research Laboratory of the U.S. Army Research, Development and Engineering Command (RDECOM) is the Army's corporate laboratory. ARL's research continuum focuses on basic and applied research (6.1 and 6.2) and survivability/lethality and human factors analysis (6.6). ARL also applies the extensive research and analysis tools developed in its direct mission program to support ongoing development and acquisition programs in the Army Research, Development and Engineering Centers (RDECs), Program Executive Offices (PEOs)/Program Manager (PM) Offices, and Industry. ARL has consistently provided the enabling technologies in many of the Army's most important weapons systems.

The Soldiers of today and tomorrow depend on us to deliver the scientific discoveries, technological advances, and the analyses that provide Warfighters with the capabilities to execute full-spectrum operations. ARL has Collaborative Technology Alliances in Micro Autonomous Systems and Technology, Robotics, Cognition and Neuroergonomics, and Network Science, an International Technology Alliance, and new Collaborative Research Alliances in Multiscale Multidisciplinary Modeling of Electronic Materials and Materials in Extreme Dynamic Environments. ARL's diverse assortment of unique facilities and dedicated workforce of government and private sector partners make up the largest source of world class integrated research and analysis in the Army.

ARL Mission

The mission of ARL is to provide innovative science, technology, and analyses to enable full spectrum operations.

Our Vision

America's Laboratory for the Army: Many Minds, Many Capabilities, Single Focus on the Soldier

ARL's Organization

- Army Research Office (ARO) - Initiates the scientific and far reaching technological discoveries in extramural organizations: educational institutions, nonprofit organizations, and private industry.
- Computational and Information Sciences Directorate - Scientific research and technology focused on information processing, network and communication sciences, information assurance, battlespace environments, and advanced computing that create, exploit, and harvest innovative technologies to enable knowledge superiority for the Warfighter.
- Human Research and Engineering Directorate - Scientific research and technology directed toward optimizing Soldier performance and Soldier-machine interactions to maximize battlefield effectiveness and to ensure that Soldier performance requirements are adequately considered in technology development and system design.
- Sensors and Electron Devices Directorate - Scientific research and technology in electro-optic smart sensors, multifunction radio frequency (RF), autonomous sensing, power and energy, and signature management for reconnaissance, intelligence, surveillance, target acquisition (RISTA), fire control, guidance, fuzing, survivability, mobility, and lethality.
- Survivability/Lethality Analysis Directorate - Integrated survivability and lethality analysis of Army systems and technologies across the full spectrum of battlefield threats and environments as well as analysis tools, techniques, and methodologies.
- Vehicle Technology Directorate - Scientific research and technology addressing propulsion, transmission, aeromechanics, structural engineering, and robotics technologies for both air and ground vehicles.
- Weapons and Materials Research Directorate - Scientific research and technology in the areas of weapons, protection, and materials to enhance the lethality and survivability of the Nation's ground forces.

ARL Workforce in 2013

- 1,980 Civilians - 38 Military
- 1080 Contractors (1027 full-time/53 part-time)
- 1,379 Research Performing Workforce
- 552 (40%) hold PhDs
- 11 STs / 23 ARL Fellows

ARL's Primary Sites

- Aberdeen Proving Ground, MD
- Adelphi Laboratory Center, MD
- White Sands Missile Range, NM
- Raleigh-Durham, NC
- Orlando, FL

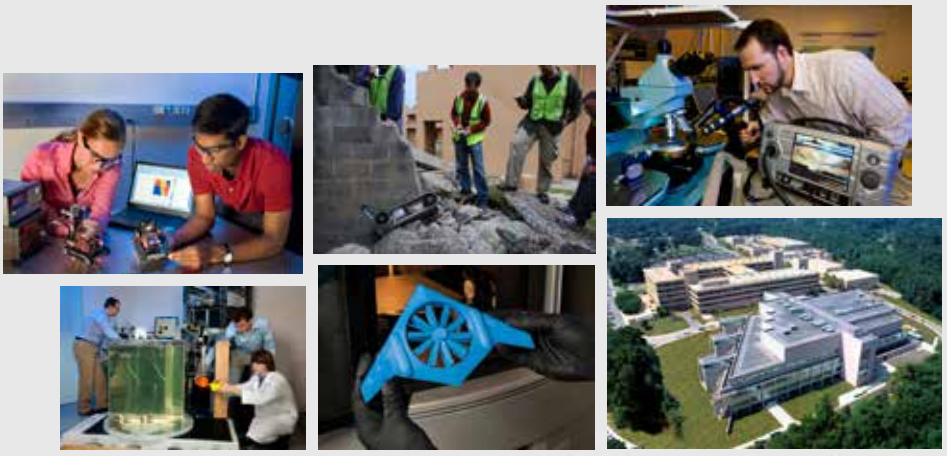

Unique ARL laboratory facilities and modeling capabilities provide our scientists and engineers with a world-class research environment.

Visit ARL's web site at **www.arl.army.mil**

ARL
U.S. ARMY RESEARCH LABORATORY

FOREWORD

Welcome to our most recent edition of the Research@ARL monograph series, a compilation of recently published journal articles highlighting the US Army Research Laboratory (ARL) research programs in autonomous systems. ARL is a robust research laboratory with a staff committed to promoting diversity of opinion, strategy, and problem solving among a variety of specialized disciplines. ARL capitalizes on our expertise in basic and applied research across multiple science and engineering disciplines, while simultaneously drawing upon the talents of others, nationally and internationally, through collaborative alliances with industry, laboratories, and academia.

ARL has a broad interest in the basic and applied research associated with the understanding, creation and development of intelligent systems to assist and augment the Army's current and future mission. Our long-term commitment to interdisciplinary scientific research for intelligent systems strongly positions our staff to discover, innovate, and transition knowledge and technology for the nation's benefit. Our discoveries enhance our country's technology base, our national security, and, ultimately, the effectiveness and safety of our Soldiers.

Current robotics capabilities are primarily controlled by remote operators, and have been showcased in recent military conflicts for applications such as aerial reconnaissance, searching caves, and disposing of unexploded ordinance. The increased use of autonomous platforms was recommended to the Department of Defense in a 2012 Defense Science Board report. We understand significant advances will be required to enable controlled movement with apparent intent. This volume of Research@ARL highlights our advances in mobility of millimeter-scale robotic platforms, intelligent robotic control, and supervisory control of robotic systems with enhanced human-machine collaboration. ARL is actively expanding the level of autonomous intent in engineered robotic systems through the combined investigation of materials, mechanics, electronics, signal processing, and technology integration. By increasing the capability for autonomous action by a single platform, ARL seeks to create mixed teams of humans and robotic platforms through research on human behavior.

As the new director of ARL, I am pleased to share this Research@ARL volume. We are committed to discover, innovate, and transition science and engineering for the next Army and the future Army.

Dr. Thomas P. Russell
Director, U.S. Army Research Laboratory

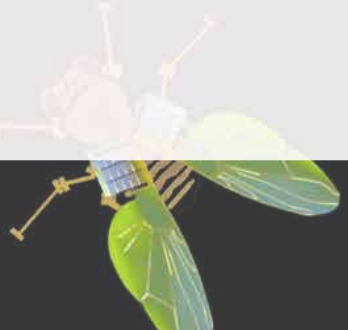

J $(kg.m2)$	$1.4*10^{-}$	1	$1.1\times10^{-}$
b $(N.m.s/rad)$	$3.1*10-11$	14	2.7×10^{-10}
k $(N.m/rad)$	$3.2*10-6$	40350	4.4×10^{-6}
G $(N.m/V)$	$8*10^{-8}$	64151	2.8×10^{-8}
Sampling time (T_s)(sec)	0.0001	0.001	0.0001

Introduction to ARL Research in Autonomous Systems and Technology Research

J. N. Mait, B. M. Sadler, A. Swami, and B. J. West

1. Introduction

Unlike the apocalyptic scenarios envisioned in the movies, autonomous systems perform critically helpful roles for today's Soldiers and first responders. Routinely aerial platforms surveil large areas of urban terrain without an on-board pilot. Ground platforms neutralize improvised explosive devices on streets in Baghdad and investigate the radiated environment of the disabled Fukushima Nuclear Plant. For over a decade, the U.S. Army Research Laboratory (ARL) has contributed significantly to the development of technologies capable of enabling autonomous behavior by mobile platforms. This volume presents some of those contributions and this introduction provides context for the research performed at ARL.

Human fascination with animating the inanimate is as old as the Golem from Jewish folklore. The Golem is a creature of mud that can be animated with magic words, but it is not intelligent — when commanded to perform a task, it performs its instructions literally, without nuance or understanding. In fact, a modern version of the Golem legend gave us the word robot. Karel Čapek, a Czech playwright, introduced and popularized the word robot (from the Czech word for labor, "robota") in his 1921 science fiction play "Rossum's Universal Robots."

Since that time, the entertainment industry has created a wide variety of robotic platforms, in various shapes and sizes with various levels of intelligence[1]. Hollywood's terrestrial robots range from R2D2 and Wall-E to the anthropomorphic C3PO and the Terminator, and provide us with a visual taxonomy for characterizing platforms. The defining features for robotic platforms are their method for mobility, their suite of sensors, the manner and degree to which they interact with and manipulate their environment, the degree to which they collaborate with humans, the degree to which they collaborate with other robotic platforms, their level of intelligence, and the degree to which humans influence or control their actions and the manner in which they do so. Although designers take considerable inspiration from biology, they produce a wide variety of platforms that differ considerably from anything found in nature. Through engineering as opposed to evolution, designers make trade-offs that nature does not.

As we discuss in Sec. 2 of this introduction, most military applications do not require anthropomorphic robots. We describe in Section 3 how ARL executes research on autonomous systems through its Robotics Enterprise. In Sec. 4, we discuss the technical issues faced by designers of autonomous systems and describe some of the work ARL researchers have performed to overcome them. We close in Sec. 5 with a discussion of nontechnical issues related to the military use of autonomous systems.

2. Army Applications

"Dirty, dangerous, and dull" is the oft-repeated description of applications best suited to robotic platforms. Inaccessible has also been added to the list, albeit without an appropriately alliterative synonym. Army applications that fall under this rubric include explosive ordinance disposal, logistics (in effect, replacing the Army mule with its robotic equivalent), and situational awareness, which includes perimeter security, building clearing, and interrogating confined spaces in buildings or rubble that are too small for humans. Further, in addition to use as remote sensing platforms, the Army has considered using robots for remote fires and for remote communications. It has also considered using robots to protect, treat, and remove the wounded from the battlefield.

However, most robots presently operating in military theaters are incapable of performing these functions autonomously. They are typically large, tele-operated platforms whose behavior is controlled remotely by a human; sometimes, as in the case of the Predator unmanned aerial vehicle, half a world away.

Communication limits the performance of tele-operated systems. For example, bandwidth constraints limited the number of unmanned aerial vehicles that could fly simultaneously in Afghanistan to no more than four. In addition, normal communication delays (latency) limit operational tempo. More limiting, tele-operation requires at least one dedicated pair of eyes and hands. In combat operations, this implies the operator requires a protector, which is a disadvantageous 2:1 ratio of humans to robots.

To overcome the limitations of tele-operation and advance capabilities beyond the current state of supervised autonomy, ARL seeks to enable the integration of robotic platforms into a team of Soldiers. To act as teammates, robotic systems need to perform their mission effectively. They must operate reliably within clearly defined operational bounds and

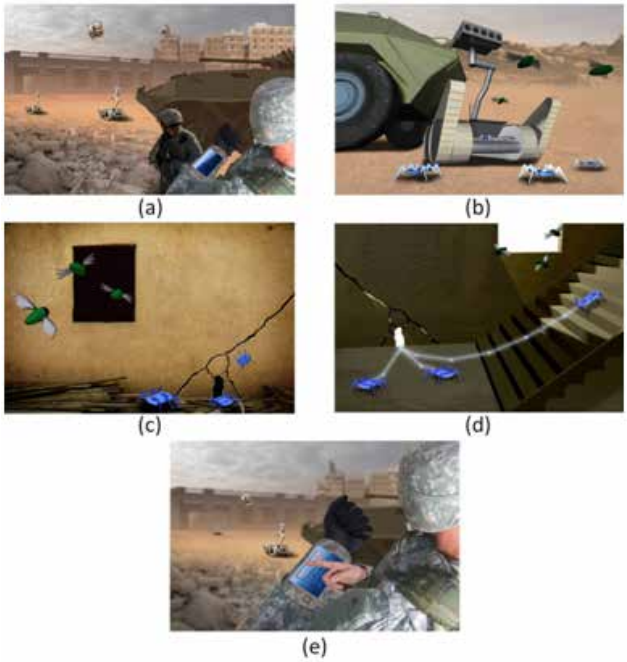

Figure 1. The Last 100 Meters. (a) Mounted and dismounted soldiers along with autonomous vehicles approach an urban structure. (b) Backpack-sized ground platforms release palm-sized ground and air platforms. Palm-sized platforms (c) approach and (d) enter the structure, and (e) relay information to dismounts.

engender the trust of their human teammates. At a technical level, they need to move in a tactically beneficial way, observe salient events in their environment, and communicate efficiently. Rather than the Army's classic dictum "move, shoot, and communicate", ARL's research focus is on autonomous capabilities to "move, sense, and communicate."

The "Last 100 Meters" vignette represented in Fig. 1 reflects some of the capabilities ARL is pursuing. In this vignette, mounted and dismounted Soldiers approach an urban objective supported by large autonomous ground and aerial platforms. Small ground and aerial platforms provide an initial assessment of the structure, e.g., they identify areas of activity and potential points of ingress. The small platforms then release even smaller platforms, which enter the building and provide more situational awareness. For example, they generate maps, identify and label potential threats, and plan paths for dismounts, all of which the network of autonomous platforms conveys to troops readying themselves to enter the structure.

3. The ARL Enterprise

To address the technical challenges presented by our vignette, ARL conducts research internally and collaboratively with industry and academia through a single investigator program supported by the Army Research Office, through two collaborative technology alliances (CTAs), the Robotics CTA[2] and the Micro-Autonomous Systems and Technology (MAST) CTA[3], through DARPA and other government agencies, and through small contracts.

ARL's internal research focuses on human-machine interaction, the development of air and ground platforms, increasing the functionality of backpack-sized ground platforms (e.g., increasing their ability to navigate and sense, and increasing their capacity for distributed networking and cognition), and developing technologies for small-scale mobility, sensors, and power. The Robotics CTA (RCTA) is concerned primarily with increasing the capacity for autonomous behavior for large platforms, e.g., unmanned vehicles and backpack-sized platforms, and the MAST CTA, with developing palm-sized autonomous platforms. An important issue addressed by all programs is enabling cooperative behavior between robots and with humans.

The RCTA focuses on five key research areas: a cognitively based world model, semantic perception, learning, meta-cognition, and adaptive behaviors. Because current world model representations are relatively shallow, metrically based, and support only brittle behaviors, the RCTA is creating a cognitive-to-metric world model that can incorporate and utilize mission context. Current perceptual capabilities for unmanned systems are generally limited to a small number of well-defined objects or behaviors. The RCTA is raising perception to a semantic level that enables understanding of relationships among objects and behaviors. To successfully team with small units, the command and control of unmanned

systems must move away from the current hardware controller paradigm to one of verbal and gestural communication, implicit cues, and transparency of action between Soldier and robot. The RCTA is also exploring adaptive behavior and mechanics that permit manipulation of arbitrarily shaped objects, animal-like mobility in complex environments, and conduct of military missions in dynamic tactical conditions.

As stated previously, scale imposes fundamental limits on system design. The MAST CTA supports and conducts research in several aforementioned critical areas. These include microsystem mechanics, microelectronics, signal processing, power and energy, and the integration of these technologies into a single platform. The development of technologies for power and energy, in particular power conditioning, is a significant internal effort at ARL. The remaining four areas are pursued both internally and externally to ARL, and jointly with ARL. Issues addressed by the Alliance include how to achieve stable aerodynamic performance in unsteady vortex-dominated flows at low Reynolds numbers; how to achieve animal-like intelligence and navigation with limited power, limited resolution sensing, limited bandwidth, and low level processing; the development of new computing architectures to insure stable and reliable processing at low power; the development of technologies capable of managing power and energy sources and loads on small-scale platforms; and understanding and exploiting intra-platform interactions and efficiencies in a collaborative ensemble of small robots.

In the next section, we consider the challenges and issues in increasing the capabilities of robotics platforms and highlight the contributions made by ARL researchers.

4. Capability Challenges and Technological Issues

4.1. Capability Challenges

Careful inspection of "The Last 100 Meters" reveals numerous fundamental challenges to enabling desired autonomous capabilities. For example, collaborative behavior across mobile air and ground platforms as well as with mounted and dismounted Soldiers requires a stable, mobile, and scalable network. Research@ARL Network Sciences discusses some of ARL's efforts in this arena[4]. However, network infrastructure and protocols must account for the limited size and power of small platforms in comparison to ones comparable in size to cars or small planes, which can port conventional network equipment.

As ground platforms transition from an exterior location to an interior one, they must alter their gait to account for the change in ground conditions from loosely packed soil to a hard surface. If the structure is partially collapsed, they must be capable of climbing over or avoiding rubble. Air platforms also must trim their control surfaces to adjust for changes in airflow as they fly through windows.

Platforms that enter the urban structure must be capable of altering their behavior from mobility between waypoints to mobility and exploration in an unmapped area. They must be able to navigate without access to GPS and to navigate and explore in low-light or no-light conditions. Recognizing these capability challenges leads to the list of technological challenges addressed in the next section.

4.2. Technological Issues

In this section, we return to the different capabilities that characterize a robot and provide more discussion.

4.2.1. Mobility

Without the ability to move, the platforms we have been discussing are simply highly capable sensing, computing, and communication platforms. The Army's primary interests are developing terrestrial and aerial platforms, and not aquatic ones. Terrestrial platforms may use wheels, tracks, or legs to provide forward motion. The choice of mechanism depends upon the size of the platform and its application. It is also possible for a platform not to have any wheels, track, or legs at all and to mimic the body undulation of a snake, which provides mechanism for both lateral motion and climbing. Other means to achieve vertical motion include jumping and hopping. For multi-legged platforms that mimic the jumping behavior of lizards, tails are also an important appendage. Aerial platforms may use fixed, flapping, or rotary wings to fly or hover, and designers may combine modalities, e.g., legs and wings, to produce hybrid platforms.

One of the primary issues associated with mobility is scale. Large, vehicle-sized autonomous platforms are simply unmanned vehicles and most backpack-sized platforms are scaled-down versions of large vehicles. This scaling is possible due to the development of small, efficient motors.

For palm-sized platforms, designers look to biology for solutions; physics and manufacturing make it difficult to scale down existing solutions further. Thankfully, nature provides a multitude of choices. For example, avian wing flapping differs considerably from that of insect wing flapping. Only at scales that are comparable, such as the humming bird and the hawk moth, is the flapping motion similar.

Further, due to the size of individual components, traditional manufacturing and assembly methods are not possible. Even if they were, since the ratio of surface area to volume increases as spatial scale decreases, friction increases and makes solutions for large-scale platforms inefficient at small scales. Thus, new designs and new fabrication techniques are necessary.

To enable small-scale mobility, ARL focuses primarily on MEMS-based technologies to actuate walking, flying, and jumping, and for navigation control of flight. ARL's expertise in thin film lead zirconate titanate (PZT), a piezoelectric material capable of generating an electric potential when a mechanical force is applied and, conversely, generating a mechanical strain when an electric field is applied, is extensively used for most mechanisms. Jumping mechanisms additionally use an energetic silicon-based actuator to generate vertical thrust. Together, this research enables mobility at the millimeter scale.

To mimic biology, actuators for small-scale mobility must achieve large force and displacement at low voltages and consume little power, a key feature of PZT. In addition, one can fabricate PZT-based actuators in series or parallel to generate large forces or wide angular ranges of motion. This is critical to realize complex mechanisms for lateral, rotational, and vertical movement.

The review article "PZT-Based Piezoelectric MEMS Technology," written by several members of ARL's MEMS team with lead author Gabriel Smith (page 13), provides an overview of PZT, the fabrication of micro-devices from PZT, and their application to enabling small-scale mobility, in addition to other applications such as mechanical logic and small motors. The paper discusses actuator design for multipedal locomotion, winged-insect flight, and an artificial haltere for measuring the rate of angular rotation on winged platforms.

Details of the actuator design for multipedal locomotion are discussed in the joint authored papers "Modeling and Optimal Low-Power On-Off Control of Thin-Film Piezoelectric Rotational Actuators," with Biju Edamana as lead author (page 31), and "Multi-Degree-of-Freedom Thin-Film PZT-Actuated Microrobotic Leg," with Choong-Ho Rhee as lead author (page 45).

To lift legs, the authors use traditional vertical unimorph actuators and out-of-plane rotational and torsional actuators. For rotational joints, the authors use lateral piezoelectric actuators. Due to inherent nonlinearities in PZT, the structures are optimal only for small displacements. Thus, flexural amplification is required to translate large forces into large displacements. The individual flexural actuators, piezoelectric actuators, and coupled flexures, can provide only ~5° of rotation and are therefore cascaded to create joints capable of larger rotations. Lithography allows one to combine thin film actuators monolithically to produce high performance flexural and structural elements.

In Smith et al. (page 13), ARL researchers discuss the design and fabrication of 2-mm long PZT-based wings that reproduce the aerodynamic forces generated by agile flying insects. The scale of the wings is comparable to that of a fruit fly. The system uses thin-film PZT actuators with two independent degrees-of-freedom to drive a micro-fabricated wing structure. A stroke actuator drives the flapping mechanism at resonance and the pitch actuator quasi-statically drives wing rotation. The coordinated motion of these two and the resulting three-dimensional wing kinematics generate the aerodynamic lift that is capable of sustaining flight. ARL has demonstrated 120° of stroke amplitude using a 10 V bias and 45° of pitch amplitude using a 20 V bias at frequencies comparable to those in nature.

The ARL team also describes in Smith et al. (page 13) the construction of an artificial haltere, a sensor that measures body rotation in some two-winged insects. The haltere consists of a pendulum-like structure that oscillates in a direction orthogonal to forward motion. When the insect turns, the resistance of the pendulum to the change in the direction of motion generates a force measured by hairs at the base of the haltere. The hairs, which are connected to the insect's neural system, provide the insect with an inertial measurement of its position in space. Inspired by the insect sensors, Smith et al. fabricated a copper pendulum that they actuated using PZT. The PZT actuator also measured the forces produced by changes in angular position. Simulation and component testing indicate the artificial haltere is sensitive to changes in angular rate on the order of 60 deg/s. Smith et al. also fabricated halteres in coupled arrays to enable triaxial measurements.

In “The First Launch of an Autonomous Thrust-Driven Microrobot Using Nanoporous Energetic Silicon,” with lead author Wayne Churaman (page 59), ARL researchers describe the fabrication of a 300-mg, 4 mm × 7 mm × 0.5 mm robotic system that reaches a vertical height of 80 mm using about 0.5 µl of nanoporous energetic silicon. Energetic silicon, which stores energy chemically, is an alternative to storing mechanical energy in a spring. This reduces system complexity by eliminating the need for an additional actuator to compress a spring. The platform uses a light-sensitive detector to initiate the reaction that converts chemical energy into mechanical. Monolithic design and fabrication enables a device with integrated control, sensing, power, and actuation, which is critical for large-scale production of small-scale robotic platforms.

4.2.2. Navigation and Control

For all platforms, developing the capacity for controlled movement without human intervention is a primary issue. The Wright Brothers receive credit for inventing flight primarily because they developed mechanisms for making a controlled turn. Presently, due to our incomplete understanding of the physics, small-scale platforms lack well-developed controls for mobility. Small-scale aeromechanics and avionics are necessary to control small platforms in wind and in gusts, and as they transition from a structure’s exterior to its interior. Similarly, as small legged-terrestrial platforms encounter different ground conditions, they must alter their gait, which requires advances in the new science of terra-mechanics and in control systems based on this new science. Once capable of controlled movement, the platforms must navigate on their own.

A fundamentally important problem in control systems is handling uncertainty, unexpected external disturbances, and system model uncertainties. Examples of disturbances include wind gusts that strongly perturb small aerial vehicles, and wheel or track slippage in rough and uneven terrain. George, Singla, and Crassidis address the problem of robust control (page 69) by expanding on a Kalman filter based adaptive disturbance accommodating stochastic control scheme. Their approach, under minimal assumptions on the disturbance, simultaneously estimates both the system states and the model-error encountered. Here the model-error dynamics are unknown, so a second Kalman filter is incorporated into the control scheme to adaptively estimate the disturbance statistics. This method is shown by the authors to be provably asymptotically optimal for linear systems with bounded external disturbance, and is readily implemented as a supplement to a conventional Kalman filter controller.

The stochastic controller idea was generalized by George (page 97) to the case of a Kalman filter operating in continuous time while under a persistent excitation. The author develops a control method that is provably convergent in the sense of estimating the unknown error statistics, even when the input excitation is unknown, and thus the method asymptotically recovers the desired optimal performance.

Many applications of autonomy are significantly complicated by the need for wireless networking. Mobile ad hoc networks without commercial infrastructure face major challenges in scalability and robustness. Radio accomplishes this but suffers from signal strength fluctuation with small movement on the order of a wavelength of the center frequency, as well as attenuation that is generally well beyond free-space loss. ARL scientists have addressed this problem by developing control strategies to measure, map, and maintain wireless connectivity while carrying out autonomous missions.

ARL researchers Twigg, Fink, Yu, and Sadler (page 105) have developed and tested sensing and control algorithms to autonomously discover the radio connectivity region of a radio base station without any a priori knowledge of the environment. The authors demonstrate a method for simultaneously exploring, developing a physical map, and overlaying a connectivity map, such that within the connectivity area communications with the base station can be accomplished with a certain quality guarantee. The method exploits the observed radio signal strength as it varies with motion, and the authors develop an efficient method that rapidly finds and explores the connectivity boundary contour using the radio signal strength gradient. The resulting control algorithms are a significant first step towards larger problems of connectivity control during autonomous operations in unknown environments, including the networking of autonomous agents and Soldiers.

4.2.3. Human-Machine Collaboration

The use of multiple autonomous platforms is inspired by bionetworks in nature such as insect swarms. Although each single entity in a swarm has limited intelligence, the swarm appears to behave with intent when the entities function in concert. Fish and birds are examples of animals whose collective behavior belies their limited intelligence.

Although the swarm analogy is intellectually appealing, differences exist between bionetworks and networks of autonomous mobile platforms. Put simply, biological swarms communicate simple messages primitively to perform primitive behaviors. Whereas some tasks performed by robots can be addressed using simple bottom-up bio-mimetic control, others that require complex messaging to achieve complex behaviors might be better suited to top-down centralized control in which a single intelligent entity controls a layered hierarchical network wherein each layer contains more entities of lesser intelligence than the layer above it. From a research perspective, we need to explore a range of possibilities and designs.

Today the joint human-robot role includes load-carrying, casualty extraction, hazardous material detection, counter explosive devices, building mapping/clearing and firefighting. Tomorrow, Soldiers may be required to navigate a robot while concurrently conducting surveillance, maintaining local security and situation awareness, and communicating with fellow team members. The ARL scientists Chen and Barnes collaborated with Haper-Sciarini on the critique "Supervisory Control of Multiple Robots: Human-Performance Issues and User-Interface Design" (page 119). This publication reviews research done on the limitations and advantages of supervisory control of unmanned air and ground vehicles.

Humans exert supervisory control of technology through the level of autonomy allowed and through interactions with the automated technology that includes planning, teaching, monitoring, intervening and learning. The Chen et al. paper examines human performance issues in supervisory control of robotic vehicles including things such as operator multitasking performance, trust in automation, situational awareness and operator workload, and reviews user-interface solutions that could potentially address these issues. The importance of understanding the interface between humans and robots in order to determine what we can and cannot control is emphasized, anticipating the increasing number of tasks that humans cannot perform alone.

Conducting large-scale experiments involving multiple people interacting with robots over various terrains is costly and the resulting vast amount of data is difficult to process and interpret. Consequently, before conducting scenarios in which robot tasks have increasing complexity it is advisable to guide their design through computer simulations with human interactions. Chen and Barnes of ARL tested some ideas concerning the management of ground robots with the assistance of an intelligent agent capable of coordinating the robots and changing their routes on the basis of battlefield developments in "Supervisory Control of Multiple Robots: Effects of Imperfect Automation and Individual Differences" (page 139). They did this using a military multitasking environment simulation of an intelligent agent, RoboLeader, assisting the performance of supervising multiple robots to complete military reconnaissance missions in a dual-task and multitasking environment.

Chen and Barnes were particularly concerned with the influence of agent imperfections, such as rates of false alarm and the propensity of the agent to miss the target, on the operator's performance of tasks, for example, on target detection, route editing and situation awareness. They found that participants' attentional control and video gaming experience significantly affected their overall multitasking performance. They determined that intelligent agents, such as RoboLeader, can benefit the overall human-robot teaming performance when perfectly reliable. On the other hand, the effects of agent imperfections can be significant and difficult to anticipate and further research needs to be done in this area.

An important factor in determining the utility of intelligent agents in supporting the dynamic robot re-tasking based on battlefield development is the level of assistance provided by the agent to the robotics operator. In "Supervisory Control of Multiple Robots in Dynamic Tasking Environments" (page 159), Chen and Barnes of ARL systematically change the level of assistance provided by RoboLeader and find that participants' primary task benefitted from all levels of assistance compared to manual performance. Here again frequent video gamers demonstrated significantly better situation awareness of the mission environment than did infrequent gamers. Moreover, the participants experienced lower workload when they were assisted by RoboLeader than when they performed the target entrapment task manually. This study increased the understanding of the interplay among the level of autonomy, multitasking performance and individual differences in military tasking environments.

The results suggest that agent/human supervision of multiple robots permits synergy without usurping the human's decision-making authority and those levels of assistance with less than full autonomy can be as effective as fully autonomous levels of assistance. Stated differently it enables the person to exceed the classical (seven ± two) finding for span of apprehension that would traditionally overwhelm cognitive resources and with the assistance of the intelligent agent successfully expand their workload.

For a team of humans and robots to complete a mission effectively, humans must trust that a robotic teammate will protect their interests and welfare. Trust directly affects the willingness of people to accept robot-produced information

and follow robot suggestions. This affects the decisions humans make in uncertain and risky environments. The less an individual trusts a robot, the sooner he or she will intervene as the robot progresses toward task completion. Most current studies on trust attempt to measure and quantify the level of trust that exists for a particular platform and human-robot team configuration. Hancock, Billings and Schaefer of the University of Central Florida, together with Chen of ARL and Visser and Parasuraman of George Mason University evaluate and quantify the effects of human, robot, and environmental factors on perceived trust in human-robot interaction in "A Meta-Analysis of Factors Affecting Trust in Human-Robot Interaction" (page 177).

Hancock et al. replace a historically qualitative and descriptive review of trust with one that is quantitative. They conclude that factors related to the robot performance had the greatest current association with trust while those related to the environment were only moderately associated with trust. Moreover, there was little evidence that trust was dependent on the human-related factors. The study provides an empirical foundation on which to advance both theory and application.

5. Other Issues

5.1. Sensors and Signal Processing

ARL, along with its partners, performs considerable work in sensors and signal processors for robotics and herein we highlight some of the important aspects that are being addressed.

With regard to sensors, it is important to distinguish between sensors for platform control, for example, using a mechanical sensor like a haltere to provide stable flight, versus sensors to complete, for example, a surveillance mission. Vision sensors, in particular, can be used either for navigation, i.e., to detect and avoid obstacles, or they can be used for situation awareness, to classify, recognize, or identify objects. For low-light or no-light navigation or situational awareness, radar is a potential solution so long as it can be made small enough to fit on a platform. The same is true of hair-like mechanical sensors. If they can be made small enough, artificial hairs are useful either for navigation or for detecting or measuring wind.

An overriding issue with regard to the development of sensors is whether they can provide the requisite accuracy and precision subject to the constraints of size, weight, and power. The accuracy and precision required depends upon the number of platforms working collaboratively. Even if a single sensor has poor resolution, by combining measurements from multiple platforms, one can improve the effective resolution.

If one needs a robot to alter and manipulate its environment, in addition to sensors, the robot requires a mechanism to do so. For example, the Mars rovers alter their environment using drills and scoops to access material below the planet's surface but they also use lasers to ablate material on its surface. Thus gripping and moving an object require tactile sensors and single or multiple arm-like appendages, multiple finger-like appendages, or both. Articulation, actuation, and control of these appendages are critical issues, as is selecting materials that are strong, compliant, and durable for repeated use.

Sensors by themselves provide only measurements pertaining to the environment. For autonomous behavior, it is necessary to process these physical measurements to give them meaning. Thus, specialized dedicated processors, for example, for vision, mapping, planning, and navigation are also required. There exists also a strong link between the requirement for integrated, low-power but high performance sensors and the photonics and electronics necessary to enable them.

Sensors impacts communications as well. What is transmitted, measurements, processed data, or commands, depends upon the processing and communications power available to a single platform. Simple messages require complex processing, whereas measurements require large bandwidths. Researchers are considering whether it is more efficient to transmit data to a single, high performance processor, or provide each platform with a moderate amount of processing to reduce the bandwidth and energy required for transmission. Latency is also an issue designers must consider in this trade-off. The amount of latency incurred and the amount of latency that can be tolerated before the distributed control of the collective becomes unstable is a critical research issue.

5.2. Non-technical Issues

ARL's purview is to solve the technical hurdles limiting the performance of autonomous platforms. However, there exist nontechnical issues that also limit the acceptance of robots in military operations. The obvious and most concerning

is their use as a remote weapon system. Government lawyers and policy makers, along with academicians, are already studying the legal and ethical issues associated with this.

As indicated in Hancock et al., trust is another significant nontechnical issue. However, trust can be expected to be gained over time as Soldiers have more interaction with robots and learn what they can and cannot do well, and when and how they should be used. Trust will also increase as scientists and engineers gain understanding and improve designs and reliability.

Army planners must consider the advantages and disadvantages of robotics, particularly as the technology changes over time. The increase in effectiveness must outweigh any changes in mission structure and logistics to support the inclusion of robotics. Is it more efficient and effective to use a robotic platform as opposed to other more conventional means? For example, is it more effective to sustain a robotic mule in the field or a real one? Ultimately, logisticians need to determine whether the gross weight of a Brigade Combat Team increases or decreases when it uses robotic platforms to provide new capabilities or enhance old ones, and planners need to assess whether the improvement in performance warrants an increase in weight.

Finally, as ARL seeks to integrate robotic platforms into teams of soldiers, others seek to integrate robotics even more intimately with biology. In DARPA's HI-MEMS program, for example, researchers implanted electronics into the larvae of a moth that the researchers used to control the moth's flight as an adult.

We are pleased to share the following collection of articles that highlight the advances ARL's researchers have made in the pursuit of enabling truly autonomous systems.

References

[1] http://www.filmsite.org/robotsinfilm.html

[2] J. A. Bornstein and R. R. Mitchell, "Foundations of Autonomy for Ground Robotics," Unmanned Systems Technology XIV, R. E. Karlsen, D. W. Gage, C. M. Shoemaker, and G. R. Gerhart, eds., Proc. SPIE 8387 (2012). (doi: 10.1117/12.919721)

[3] J. N. Mait, "The Army Research Laboratory's program on micro-autonomous systems and technology," Micro- and Nanotechnology Sensors, Systems, and Applications, T. George, M. S. Islam, and A. K. Dutta, eds., Proc. SPIE 7318 (2009). (doi: 10.1117/12.817864)

[4] This and other Research@ARL volumes may be located at http://www.arl.army.mil/www/default.cfm?page=172.

[5] http://www.time.com/time/nation/article/0,8599,1732226,00.html

PZT-Based Piezoelectric MEMS Technology

Gabriel L. Smith, Jeffrey S. Pulskamp, Luz M. Sanchez, Daniel M. Potrepka, Robert M. Proie, Tony G. Ivanov, Ryan Q. Rudy, William D. Nothwang, Sarah S. Bedair, Christopher D. Meyer, and Ronald G. Polcawich

Journal of the American Ceramic Society, 95 [6] 1777–1792 (2012)

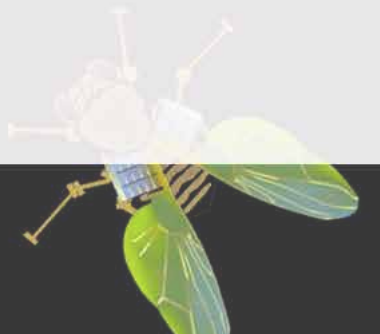

journal

J. Am. Ceram. Soc., **95** [6] 1777–1792 (2012)
DOI: 10.1111/j.1551-2916.2012.05155.x

PZT-Based Piezoelectric MEMS Technology

Gabriel L. Smith,† Jeffrey S. Pulskamp, Luz M. Sanchez, Daniel M. Potrepka, Robert M. Proie, Tony G. Ivanov, Ryan Q. Rudy, William D. Nothwang, Sarah S. Bedair, Christopher D. Meyer, and Ronald G. Polcawich

Sensors and Electron Devices Directorate, US Army Research Laboratory, Adelphi, Maryland 20783

This review article presents recent advancements in the design and fabrication of thin-film (<3 μm) lead zirconate titanate (PZT) microelectromechanical system (MEMS) devices. The article covers techniques for optimizing highly (001)/(100) oriented chemical solution deposited PZT films to achieve improved piezoelectric coefficients. These PZT films combined with surface and bulk micromachining techniques are fabricated into actuators and transducers for radio frequency (RF) switches, nanomechanical logic, resonators, and power transformers for use in communication systems and phased-array radar. In addition, the large relative displacements generated by PZT thin films have been used to demonstrate mechanical mobility in MEMS devices, including insect-inspired flight actuators and ultrasonic traveling wave motors. In conjunction with actuation, PZT films are being developed for feedback sensors for the integrated control of insect-inspired robots.

I. Introduction

The versatility of thin-film lead zirconate titanate, $PbZr_xTi_{1-x}O_3$ or PZT, as a material in microelectromechanical system (MEMS) devices has expanded greatly in the past several years.[1–4] PZT thin films, deposited by both sputtering and sol-gel, have been researched for MEMS as well as other electronic device technologies for nearly 30 years. As a result, nonvolatile ferroelectric random access memory (FRAM) is now commercially available from several vendors including Ramtron, Texas Instruments, and Fujitsu.[5–7] Although not a MEMS technology, FRAM demonstrates successful integration of high performance ferroelectric thin films with complementary metal-oxide semiconductor (CMOS) integrated circuit technology. FRAM devices are built by adding the metal-ferroelectric-metal stack on top of the CMOS circuitry in a two photomask process. This addition to CMOS creates a highly useful integrated product for embedded memory applications and provides a solid background and experience on which to base the design and fabrication of PZT-based MEMS devices.

Two PZT thin-film based MEMS technologies are starting to make their way into the commercial market. Panasonic (Kadoma, Osaka, Japan) recently developed the EWTS9T series thin-film PZT 16-mm^3 two-axis gyroscope targeted for consumer electronics applications.[8] In addition, several companies, including Epson (Suwa, Nagano, Japan) and FUJIFILM Dimatix (Santa Clara, CA) are offering inkjet print heads using thin film PZT.[9,10] The state of advanced product development of both of these devices indicates the market viability and advantages of PZT-based MEMS devices over competing technologies.

This article is intended to provide an overview, by no means all inclusive, of the types of new devices that are enabled by PZT-based MEMS with specific attention to devices targeting radio frequency (RF) and small scale robotics systems. Although most of the fabrication processes are common across the devices, the application areas are extremely diverse. The first section will cover fabrication and material processing topics. The second section of the article will focus on actuation and sensing for the use in millimeter-scale robotics. The final section of the article will outline application areas in radio frequency microelectromechanical systems (RF MEMS) devices.

II. Fabrication and Material Optimization

(1) Fabrication Overview

Before discussing specifics for any particular material, a generic piezoelectric MEMS (PiezoMEMS) fabrication process will be presented. In this general process, all materials comprising the piezoelectric composite are deposited as uniform blanket coatings onto the substrate of choice (see Figure 1). First, a substrate must be chosen specific to the targeted final device. The most common substrates are (100) silicon substrates. For RF applications, the resistivity of the substrate must be > 5000 or even as high as 10 000 Ohm·cm depending on the frequency of interest. Another option is silicon-on-insulator (SOI) substrates that are extremely attractive for resonator/filter and robotics applications. For the SOI substrates, the device layer silicon can vary between 2 and > 40 μm depending on the application requirements. Other

D. J. Green—contributing editor

Manuscript No. 30694. Received November 28, 2011; approved February 18, 2012.
†Author to whom correspondence should be addressed. e-mail: gabe.smith@us.army.mil

Feature

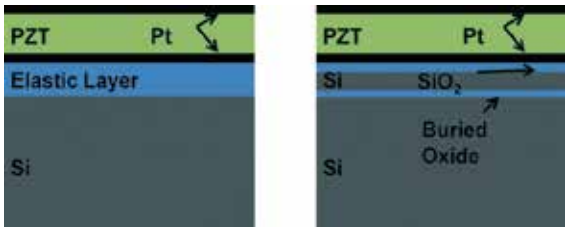

Fig. 1. Schematic cross-sections of unimorph piezoelectric composite starting wafers on both (a) Si and (b) silicon-on-insulator (SOI) substrates.

substrate choices are possible, but silicon and SOI will remain the focus of this article.

Following the substrate choice, an appropriate insulating layer is deposited to serve as a protective barrier between the subsequent metal electrode and silicon substrate. In addition, this layer can serve as a mechanical elastic layer for a unimorph piezoelectric actuator. If used as the elastic layer, proper design of the elastic layer composite will result in controlled residual stress induced deformation in the final device configuration.[11,12] As an example, see Fig. 2, in which the location of a highly stressed silicon nitride thin film is used to modify the postfabrication static deformation in a SiO_2/Si_3N_4/SiO_2/Ti/Pt/PZT/Pt piezoelectric composite. Placing the tensile silicon nitride further from the neutral axis of the structure preferentially results in curvature toward the nitride layer in the final device and can be utilized to ensure proper device operation.

The remaining steps for the piezoelectric composite are associated with the actuator and electrode materials. For a parallel plate configuration, where the PZT is sandwiched between two electrodes, the most common choice for the bottom electrode layer is sputtered Pt deposited on top of a buffer layer of titanium dioxide. Alternatively, conductive oxide electrodes, either IrO_x[13] and RuO_x,[14] can be utilized. These materials are common for FRAM where ferroelectric fatigue has a significant role in overall device performance and reliability. The PZT layer can be deposited by a variety of methods including sputtering, metal-organic chemical vapor deposition, and chemical solution deposition with thicknesses ranging from 0.5 to 2.0 μm depending on device design parameters. Finally, the top electrode is deposited, preferentially, by sputtering. Similar to the bottom electrode, Pt, IrOx, and RuOx are the most common choices. Cr/Au is also utilized, especially for experimentation or device evaluation purposes. Note, for improved ferroelectric fatigue (for FRAM and any application requiring bipolar operation of the PZT) only one of the electrodes is required to be a conductive oxide.[15]

The following description of a generic fabrication process flow is similar to that for devices fabricated at the Specialty Electronic Materials and Sensors Cleanroom Facility, U.S. Army Research Laboratory (ARL), Adelphi, MD. The general fabrication process (see schematic in Fig. 3) for PiezoMEMS devices at ARL uses the following process flow with minor variations (i.e., release process, layer thickness, and process sequence) to meet unique requirements of a particular device. For more information, specific to a particular device, see references discussed in the representative device section. The actuator is commonly patterned using four individual process steps. The first step is to pattern the top platinum electrode with the argon ion-milling in a 4Wave Ion Mill. This etch is then followed by an additional ion-milling of the PZT and bottom electrode features. To open access to the bottom electrode, a via is patterned by ion-milling using an endpoint etch to stop on the platinum layer. After ion-milling, a quick wet etch is used to clean up any remaining PZT related compounds on the bottom platinum electrode. The actuator or sensor structure is then further defined by patterning the composite elastic layer (either the dielectrics or dielectrics plus device layer Si) with a reactive ion etch to provide access to the silicon substrate for the eventual release etch. Next, Metal 2 is deposited and patterned. Metal 2 consists of a bi-layer of titanium and gold or chromium and gold deposited with electron beam evaporation and patterned via liftoff. Metal 2 commonly defines the co-planar waveguide transmission lines for RF devices, contact structures, and anchor features required for gold air bridges. In this process flow, Metal 3 is used to create air-bridge and cross-over structures. To create these structures, a photo-resist sacrificial layer is patterned and cured followed by the deposition and lift-off of 2 μm gold thin film to form Metal 3. If required, the device layer silicon or the handle wafer on silicon-on-insulator wafers are patterned and etched via silicon deep reactive ion etching. In the final process step, a XeF_2 etch is used to either etch the device layer or regions of the handle wafer to create a released PiezoMEMS device. It should be noted that in many instances, an atomic layer deposited alumina thin film is used to provide protection to the exposed PZT areas as well as provide XeF_2 etch protection of the device Si areas.[16] After processing, the devices are typically poled with a 10–20 V DC or 1 Hz AC field for a period of 3–5 min. In typical 0.5 μm PZT, reverse coercive fields can be introduced by as little as −2 V so 0–15 V unipolar positive voltage AC operation is the common actuation input. For most devices, at 0.5–2μm thickness, unipolar operation is above the coercive field and the PZT poles to an exponential limit over time.

(2) Elastic Layer and Pt Metallization

As described in the previous process flow, the elastic dielectric layer and bottom platinum electrode are the first layers deposited on the substrate and have proven to have significant impact on the properties of the subsequent PZT film. The use of epitaxial templates is critical to define well oriented PZT for improved piezoelectric coefficients.[17] The synthesis of TiO_2/Pt bottom electrodes on a well defined elastic layer of thermal SiO_2 grown on Si (100) serves as a template

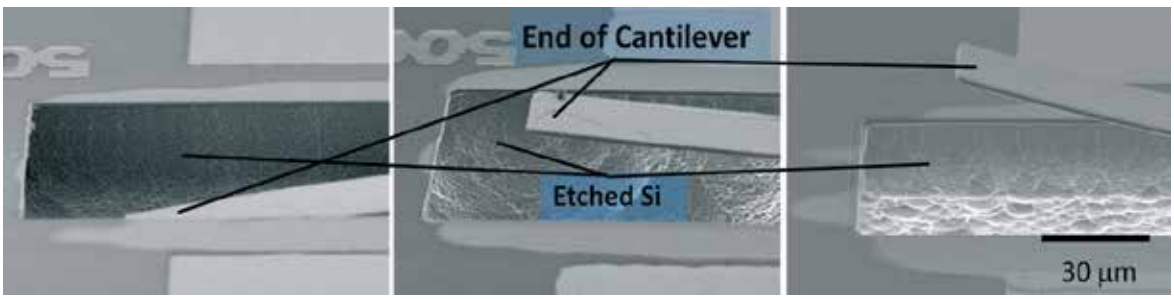

Fig. 2. Set of images of composite actuators consisting of a stack of SiO_2/Si_3N_4/SiO_2/Ti/Pt/PZT/Pt. Film thicknesses for the elastic layer are indicated on the figures while the Pt (100 nm) and PZT (500 nm) are nearly constant for each sample. Micrographs show where, (a) the Si_3N_4 is closest to the bottom interface, (b) the Si_3N_4 thin film is in the middle of the SiO_2/Si_3N_4/SiO_2 composite, (c) the Si_3N_4 is closest to the Pt bottom electrode.

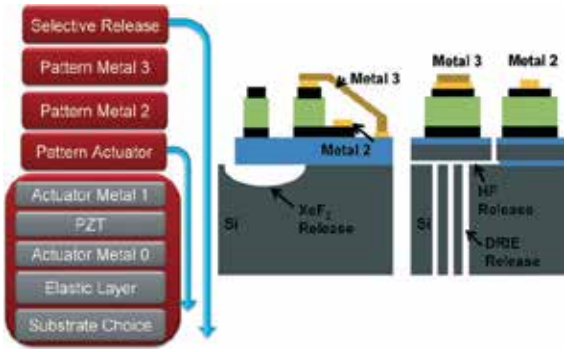

Fig. 3. Process flow schematic for PiezoMEMS devices using the substrate configurations highlighted in Fig. 1. Examples of possible XeF_2, Deep Reactive Ion Etching, Hydrofluoric Acid Released cross-sections are shown.

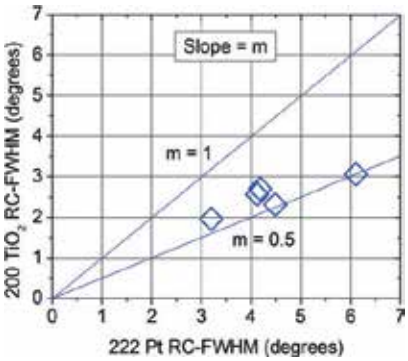

Fig. 4. Rocking Curve-Full Width Half Maximum RC-FWHM showing correlation of Pt (222) and TiO_2 (200) orientation.

for PZT growth and provides the basis of many of the devices that will be discussed in later sections.

The details regarding the TiO_2/Pt templates with an elastic layer of 500 nm SiO_2 film commercially grown by thermal oxidation on Si (100) are discussed in Ref. 17. The template begins with a well-oriented 20 nm thick Ti metal layer with a rocking curve full-width half maximum (RC-FWHM) of approximately 4.5°. Next, the Ti is converted to a well-oriented TiO_2 in the rutile phase with a RC-FWHM of 4.5 ± 1.5° degrees by a furnace anneal at 750°C in flowing oxygen. Finally, a Pt film is sputter deposited at 500°C yielding a Pt (111) film with a RC-FWHM of 2 ± 0.5°. The X-ray diffraction RC-FWHM plotted in Fig. 4 shows that the orientation of the Pt correlates well with that of the TiO_2, lower (i.e., improved) Pt RC-FWHM being obtained for lower TiO_2 RC-FWHM. This comparison demonstrates the causal impact of TiO_2 orientation improvement on that of Pt. The influence of the Pt quality on the texturing of PZT films with a Zr/Ti ratio of 52/48 is illustrated in Fig. 5. In this comparison, the PZT films were deposited via chemical solution deposition (described in greater detail in the next section) on a highly textured TiO_2/Pt template and an un-textured Ti/Pt template. The results from Fig. 5 show that a properly oriented TiO_2/Pt layer provides better PZT (111) peaks with a Lotgering Factor[18] $f_{(111)} \sim 0.95$ compared with that of Ti/Pt with a $f_{(111)} \sim 0.45$.

As mentioned in the previous section, plasma enhanced chemical vapor deposition (PECVD) Si_3N_4 and SiO_2 multilayer composites can be used to control the stress in the elastic layer for fine tuning the residual stress induced deformation in PiezoMEMS composites. However, the as-deposited surface of the PECVD films was found to have an unacceptably high surface roughness compared with the thermally grown SiO_2 elastic layer used in the work described in

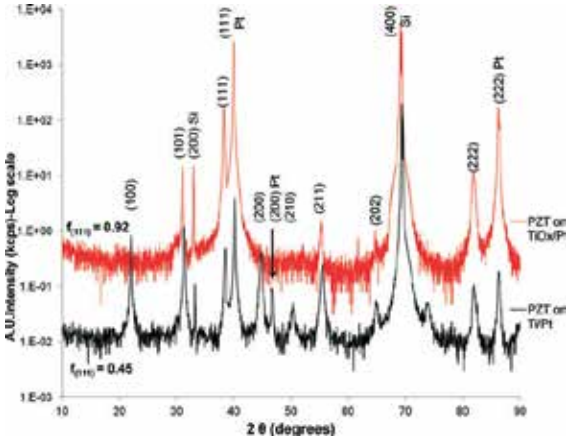

Fig. 5. X-ray diffraction scans for (a) PZT/Pt/Ti and (b) PZT/Pt/TiO_2 for Zr/Ti = 0.52/0.48. All PZT films were prepared via chemical solution deposition.

Table I. Thickness, Sheet Resistance (R_s), and Surface Roughness Calculated from AFM Measurements on Elastic Layers of Thermal SiO_2, As-deposited SiO_2, and Chemical Mechanical Polished (CMP) SiO_2. In Addition, XRD Measurement of Rocking Curve-Full Width Half Maximum (RC-FWHM) on Ti, TiO_2, and Pt Thin Films on the Various Elastic Layers is Presented

		Elastic Layer Type		
Test	Units	Thermal SiO_2	PECVD SiO_2	PECVD SiO_2 After CMP
Elastic Layer				
Surface Roughness	nm	0.211	2.8–4.2	0.30–0.38
Thickness	μm	0.5	0.7–2.2	0.5–2.0
Titanium				
R_s	Ω/sq	45	81–95	50
RC-FWHM	deg	4.5	22–27	5.7
Titanium Oxide				
Thickness	nm	33	33	33
Platinum				
R_s	Ω/sq	1.26	1.3	1.26
RC-FWHM	deg	1.7–2.3	12–14	2.25–2.35

the previous paragraph on TiO_2/Pt templates. The increased surface roughness degraded the quality of the deposited Ti as well as the resulting TiO_2 and Pt. To improve the quality of the PECVD films, chemical mechanical polishing (CMP) can be used to decrease the roughness of the as-deposited thin films to nearly that of thermally grown SiO_2. As an example, a combination of SiO_2 and $SiO_2/Si_3N_4/SiO_2$ (Oxide/Nitride/Oxide) composite films deposited by PECVD on Si(100) wafers underwent CMP performed by Axus Technology, Chandler, AZ. In each case, 200 nm of SiO_2 was removed during the polishing process. Final thicknesses based on deposition rate and spectroscopic ellipsometry measurements of the PECVD SiO_2 and oxide and nitride composites are given in Table I. Ti sputter deposition, oxidation to convert to TiO_2, and Pt sputter deposition were performed exactly as described above for the TiO_2/Pt on thermal SiO_2. Test results to characterize the elastic layer, Ti, TiO_2, and Pt for the unpolished PECVD material, CMP-processed PECVD material, and standard thermal SiO_2 are provided in Table I. The data show that polished PECVD surfaces with surface roughness comparable to that of thermal SiO_2 can be achieved, reducing the surface roughness of untreated PECVD surfaces by an order of magnitude. Pt RC-FWHM deposited on the

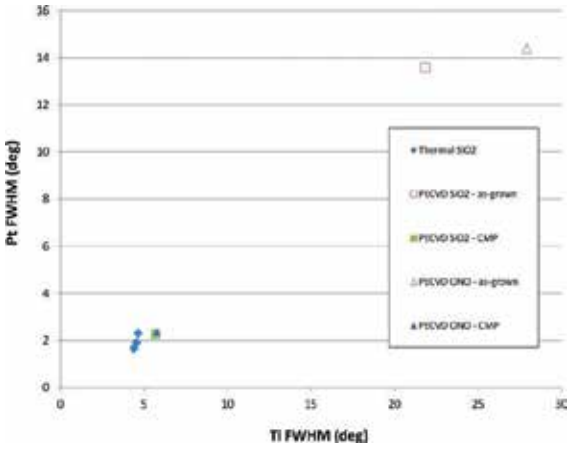

Fig. 6. Correlation of Rocking Curve Full Width Half Maximum (FWHM) of Pt (222) and Ti (001) orientation for PECVD [without and with chemical mechanical polished (CMP)] and thermal SiO_2 elastic layer.

CMP-treated PECVD is similar to that for Pt on thermal SiO_2 (~2.3°). Fig. 6 shows that the RC-FWHM of the Ti and Pt films are decreased in magnitude (improved) by the CMP compared with the case for no CMP treatment of the PECVD elastic layer. Therefore, the data show that TiO_2/Pt templates obtained on CMP PECVD exhibit satisfactory orientation for use in stress engineered PiezoMEMS composite structures.

(3) PZT Optimization

The morphotropic phase boundary (MPB) of $Pb(Zr_x\ Ti_{1-x})O_3$, PZT, exhibits exceptional piezoelectric and electrical properties that can be taken advantage of in MEMS devices. At the MPB, a mixture of rhomobohedral and tetragonal phases exists resulting in an increase in the number of equivalent poling directions (six for tetragonal and eight for rhombohedral) and exceptional dielectric and piezoelectric properties. These properties can be further improved by controlling the crystal orientation of the PZT thin films to be in the (001) direction.[19–21] For the following discussions, all of the PZT films were deposited with a Zr/Ti ratio of 52/48 using chemical solution deposition (CSD) from a solution with a 2-Methoxyethanol solvent using a process modified from that originally described by Budd, Dey, and Payne[22] and Zhou, Hong, Wolf, and Trolier-McKinstry.[23] The (001) crystal orientation in PZT (52/48) films prepared by the aforementioned CSD can be textured with proper templating, annealing procedures, and control of the excess Pb content to gain higher forces and displacements and lower power consumption in PiezoMEMS actuators. Several methods of optimization can be employed, such as the use of highly (111) oriented Pt to be used for templating, a $PbTiO_3$ seed layer deposited by CSD, and thermal treatment of PZT and Pb-excess to achieve highly (001)/(100) oriented films (for greater detail see Ref. 24).

The use of the $PbTiO_3$ seed layer is inspired by the work of Paul Muralt[21,22] who showed that the $PbTiO_3$ promoted (100) growth in PZT thin films and suppressed (111) growth. Similar results were obtained using a 17 nm thick $PbTiO_3$ seed layer deposited by CSD in conjunction with the highly textured TiO_2/Pt template (see Fig. 7). X-ray diffraction results using a Rigaku Ultima III Diffractometer (The Woodlands, TX) with Bragg-Brentano optics showed $f_{(001/100)}$ improving from 0.10 to 0.96 for films with and without the $PbTiO_3$ seed layer, respectively. Textured PZT using the PT seed layer exhibits both (001) and (100) diffraction indicating the presence of both *c*-axis and *a*-axis oriented tetragonal unit cells.

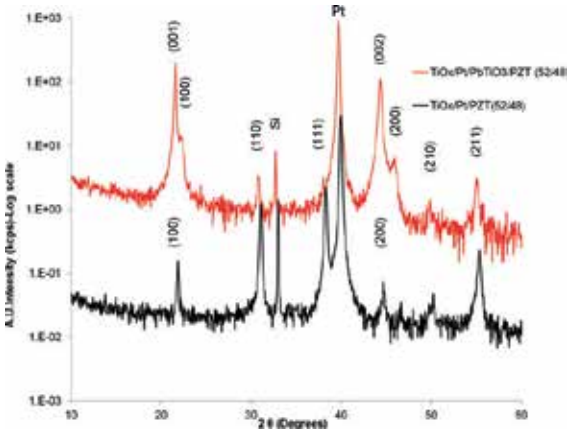

Fig. 7. XRD patterns comparing the effects of using the $PbTiO_3$ seed layer on highly textured. (111) Pt for PZT (52/48) thin films prepared by chemical solution deposition.

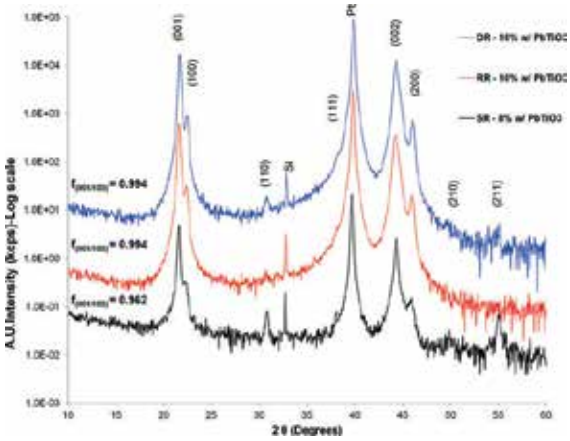

Fig. 8. Improvements of the $f_{(001/100)}$ are observed when using fast ramp techniques of $f_{(001/100)} = 0.99$ compared with the slow ramp rate with $f_{(001/100)} = 0.96$ across all Pb-excess PZT (52/48) compositions studied. The three curves represent TiO_2/Pt/$PbTiO_3$/PZT (52/48) slow ramp, rapid ramp, and double ramp data. All PZT films were prepared via chemical solution deposition.

Further improvements to the (001) orientation of PZT (52/48) can be achieved with optimization of the thermal treatment and Pb-excess processed in the films. During the crystallization anneal of the PZT, volatile PbO is lost due to high temperature processing. This PbO loss will greatly influence not only the nucleation and growth characteristic of PZT but will also lead to nonstoichiometric PZT and reduced electrical properties.[25] Traditionally, PZT (52/48) films were annealed at 700°C for 60 s in a rapid thermal anneal (RTA) with a slow ramp (SR) rate of 4°C/s. There are several theories on how "slow" or "fast" ramps generate (001) PZT films.[26–28] Examination of two alternative annealing conditions using fast ramps of 200°C/s has been compared with the slow ramp of 4°C/s. The first fast ramp condition involved a hold time of 60 s at 700°C which was referred to as rapid ramp (RR). The second condition was a double ramp (DR) technique where the temperature was ramped to 550°C to minimize Pb-loss and begin nucleation events at a lower temperature. After 60 s the temperature was ramped up to 700°C for 30 s to promote perovskite growth. The optimization of the PZT (001) texture was found to occur using either the rapid ramp or double ramp in conjunction with 10% excess lead (see Fig. 8) enabling further refinement of $f_{(001/100)}$ to 0.99.

III. Robotics MEMS Devices

The research in material optimization for higher PZT piezoelectric coefficients greatly improves performance of PZT sensors and actuators. The next three sections highlight how better piezoelectric materials have been utilized to generate larger forces, displacements and greater sensitivity for reductions in size, weight, and power (SWaP) for millimeter-scale robotic applications.

(1) PZT MEMS Actuators for Robotic Mobility

The inherent work and power densities of PZT thin films enable altogether new application spaces. One example is the emerging field of micro- and millimeter-scale robotics.[29,30] Biologically inspired autonomous millimeter-scale robots have a range of anticipated applications resulting from their unique scale, low-cost, and potential for highly integrated manufacturing. The large electromechanical coupling factors and piezoelectric coefficients of PZT thin films combined with the ability to monolithically couple thin film actuators to high performance flexural and structural elements allows PiezoMEMS devices to meet mobility and power consumption system needs for a millimeter-scale robotics platform. Flexural amplification using larger load bearing structures has demonstrated the ability of PZT thin film actuators to achieve very large forces and displacements with small footprints, low power, and low voltages.[31] Thin film PZT actuators could avoid the inefficient and bulky power conditioning circuits required for high voltage drive and permit the use of the monolithically integrated PiezoMEMS power transformers discussed in a later section.[32] Piezoelectric sensing, described in the following section, can also provide efficient and typically passive sensing capability and piezoelectric transduction may also be used for energy harvesting. The integration of the other complementary PiezoMEMS device technologies described in this article provides additional opportunities for achieving highly integrated, capable, and low cost millimeter-scale robots.

Integration will be a key element in the development of these small-scale systems by mitigating manufacturing costs and maximizing system capabilities. The batch fabrication nature of MEMS is expected to permit relatively low unit costs and limited assembly strategies amenable to modular system design. Fig. 9 depicts the kind of notional systems that PiezoMEMS technology makes possible. Everything for the mobility component of the system would be manufactured in a monolithic PZT MEMS process, described above, that would provide at a minimum, all of the necessary components like joints and actuators for a mobile millimeter-scale system. The highlighted chips represent the other requisite subsystems, like power or control that are required for a robotic platform. The entire system is expected to be comprised of five or six individual chips, manufactured in their own performance and cost optimal processes, and simply assembled with standard IC packaging techniques for a complete semi-autonomous or autonomous platform. Such an approach allows PZT MEMS device and fabrication technologies to provide the unprecedented ease of implementing large degree of freedom robotic mechanisms; the strong potential for simple and low-cost integration of actuation, sensing, and control; and the relative ease of diverse device technology integration.

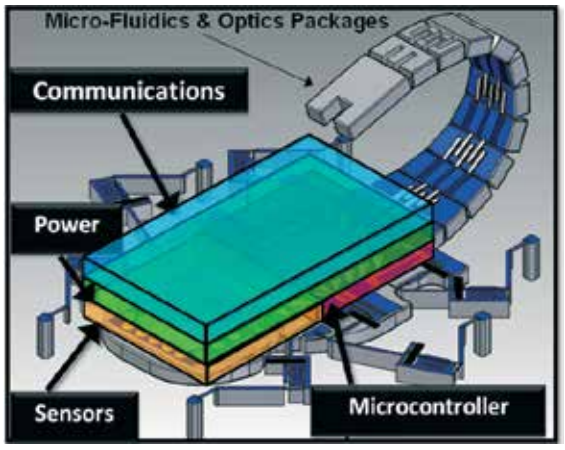

Fig. 9. Illustration of a notional PiezoMEMS enabled multi-chip millimeter-scale robot.

Actuation technologies intended to compete with their biological counterparts at this scale generally must achieve large force and displacement, extremely low-power consumption, provide system and payload enabling load bearing capacity, low voltage operation, and simplicity of design that facilitates implementation in complex robotic mechanisms. ARL has developed several integrated piezoelectric lateral, rotational, and vertical MEMS actuators that meet these requirements. Most of these designs utilize the d_{31} mode of operation and to varying degrees incorporate the unimorph bender functionality. Traditional vertical unimorph actuators and out-of-plane rotational/torsional actuators can provide leg lifting actuation, see Fig. 10. Lateral piezoelectric actuators can drive in-plane rotational joints whereas coupled high aspect ratio silicon or metal based flexures largely support the weight of the robot.[33] The lateral piezoelectric actuators demonstrated in Ref. 34 provide superior force and displacement per unit power over rival technologies, and are the basis for essential in-plane pseudo-rotational micro-robotic joints, see Fig. 10(a). Due to inherent nonlinearity, these designs produce optimal work for very small displacements (7 mN at 1 μm for 20 V in a 500 μm × 100 μm footprint at ~8 n/J per actuation) and thus require proper flexural amplification mechanism design to translate those large forces into large displacements. The individual flexural actuators, piezoelectric actuators, and coupled flexures, can provide approximately 5° of rotation and are cascaded to create individual joints capable of significantly larger rotations. Increasing load bearing capacity and hence available power is a major focus of ongoing research in actuator performance, flexure and mechanism process design, control design, and joint/robot design.

In addition to terrestrial mobility, robotics researchers are attempting to create highly maneuverable, small-scale vehicles with insect-inspired flight capabilities.[34,35] The ARL is attempting to reproduce the aerodynamic forces generated by agile insect flyers by achieving similar kinematic performance in comparable millimeter-scale wing structures. Lift production in insect flight depends upon unsteady aerodynamic effects associated with three-dimensional kinematics utilizing both stroke (i.e., flap) and pitch (i.e., wing rotation) degrees of freedom. Previous efforts demonstrated the feasibility of achieving insect-like stroke amplitudes in thin-film PZT actuated millimeter-scale wings[36] and the design and fabrication of the integrated stroke and pitch actuators and strain sensors were reported at Hilton Head 2010.[37] The 2 mm long wings are of a similar scale to that of a fruit-fly (*Drosophila*). The actuated wing design features two independent degree of freedom actuators that drive a micro-fabricated wing structure, see Fig. 11. The thin film PZT stroke actuator drives the flapping degree of freedom at resonance and the pitch actuator quasi-statically drives the wing rotation. It is the coordinated motion of these two degrees of freedom and the resulting complex three-dimensional wing kinematics that generate the aerodynamic lift that sustains flight. Such devices have successfully demonstrated 120° of stroke amplitude at 10 V and 45° of pitch amplitude at 20 V at biologically comparable frequencies.

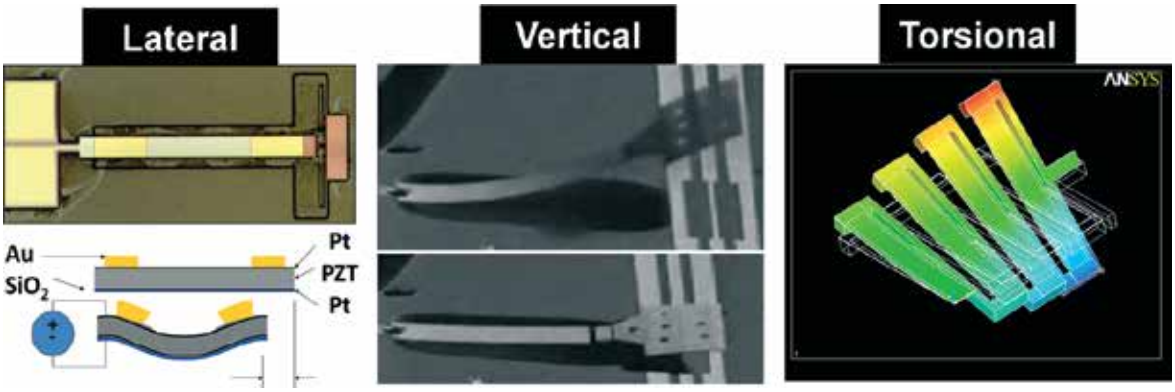

Fig. 10. Images of three examples of PiezoMEMS actuator designs applicable to millimeter-scale robotics: lateral actuator (left), traditional vertical unimorph bender (center), and in-plane torsional actuator (right).

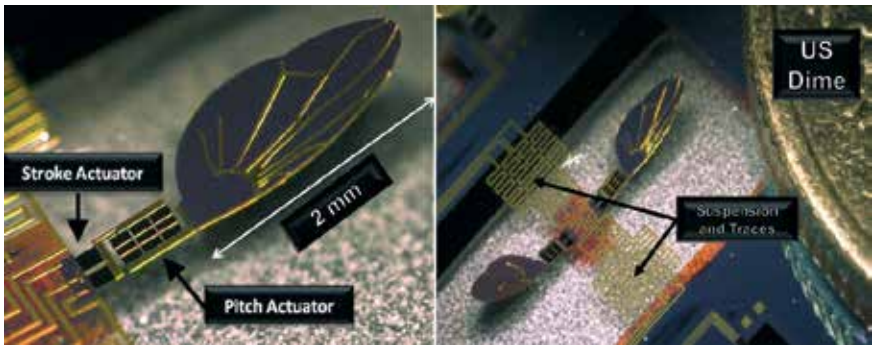

Fig. 11. (a) Image of PiezoMEMS actuated wing design, illustrating PZT stroke and pitch actuators and thin film wing structure. (b) Image of suspended platform with individually controllable wings next to a US dime.

(2) Proprioceptive Sensing with thin Film PZT

As previously described, PZT actuators can be used for mobility in small robotic systems. Alternatively, the voltage generated by applied stresses in the PZT can be utilized for inertial sensing. This section details the design, fabrication, and preliminary results of a biologically inspired, low-power, two-axis, angular rate sensor (ARS) to be integrated into micro-robotic aerial platforms. Proprioceptive sensors enable mobility control for millimeter-scale robotics and are essential to achieving stable flight in aerial autonomous systems, but they are challenging to integrate at this scale. For instance, stable hover of the aforementioned millimeter-scale flapping wing platforms requires three types of proprioceptive control.[38] These include a means of orientation control, three-axis relative velocity control, and three-axis angular rate control. Most flying insects, particularly two wing or order diptera, use both visual and inertial sensors for stable flight,[39] so mimicking biology at this scale requires inertial sensors also at a similar scale.

Traditional, packaged rate sensors do not possess compatible SWaP to be practical for millimeter-scale robotics.[8] The mass of current state of the art vibrating MEMS angular rate sensors is individually larger than the desired target mass of expected entire robotic systems, requiring alternative integration strategies. One integration option is to eliminate the lead frames and plastic encapsulation then die bond the sensor to the robot. This non-traditional packaging, sensor die integration, and sensor protection creates many difficult engineering issues at this scale. It may be possible, but entails packaging size and weight trade-offs. Ideally the rate sensors would be made monolithically in the process that makes the robotic platform and also operate effectively in air, eliminating the need for vacuum packaging. Wu *et al.* demonstrated bio-mimetic, ARS that can detect angular rates of 1 rad/s and are 5-mm in length driven by bulk PZT actuators.[38] However, these are not small enough to integrate directly with the millimeter-scale actuation platforms being developed by ARL, but they provide the basis for scaling.

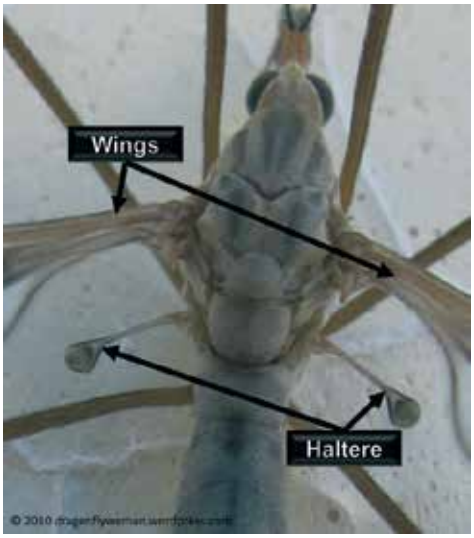

Fig. 12. Example of the club-like haltere location (circled) relative to the wings of diptera on a Giant Crane Fly. The haltere is believed to be a devolved hind wing as four wing insects do not have this structure. Two haltere can give information on all three-axes of rotation.

The haltere in insects, shown in Fig. 12, measure the resultant Coriolis forces (caused by the angular rates) and motion orthogonal to the direction of haltere oscillations. Force sensing hairs are connected to their neural system at the base of the haltere. Inspired by the insect sensors, a MEMS-based pendulum structure that is both actuated and sensed piezoelectrically has been created. The MEMS ARS are designed to be monolithically integrated with the piezoelectric mobility actuators, thus enabling direct proprioceptive control of millimeter-scale and cm-scale robotic platforms. The ARL PiezoMEMS ARS maximizes the sensitivity to rotational rate (roll-pitch or yaw) for a minimal SWaP requirement.

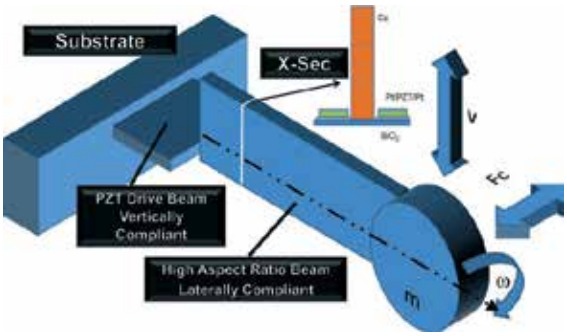

Fig. 13. Vectors show orthogonal velocity (v) and Coriolis forces (F_c) on a mass due to angular rate (ω) about the illustrated axis vectors on a notional haltere. The orthogonal aspect ratios of the beam allow for compliance in the drive and sense direction.[34]

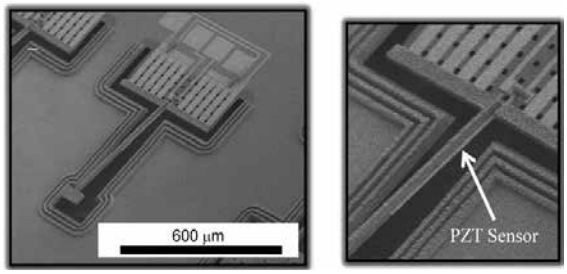

Fig. 14. SEM of a PZT-based MEMS haltere with PZT actuators to enable resonant drive and PZT sensors along the cantilever section to detect the strains generated by the Coriolis force acting upon the vibrating proof mass.

For a MEMS based haltere, Fig. 13 illustrates the general concept with the Coriolis forces (F_c) acting on the end mass due to angular rate about the illustrated axis vectors. Thin film based versions include the use of PZT actuators at the base of the structure and anchor attachment to enable resonant actuation. PZT sensing sections are patterned on the SiO_2 layer before a high aspect ratio cantilever section is added forming an inverted "T" cross-section. The PZT converts lateral Coriolis force generated strain in the film to a voltage (see Fig. 14). Electroplated metal, Cu in this case, was used to fabricate the high aspect ratio features on the cantilever section. The out-of-plane dimension was thickened to reduce the sensitivity of the sense PZT to drive motion. Figures 15,16 show an example of the ANSYS modeling used to predict and optimize the mode shape and natural frequencies of the drive and sense modes shapes, respectively. The haltere was designed so that the natural frequency of the sense mode shape is at least 2–3× higher than the drive frequency. This is to ensure that the haltere sensors can respond to the frequency of the Coriolis force. In an initial fabrication run of PZT/Cu devices, MEMS haltere has demonstrated devices vibrating at 588 Hz with tip displacements of 213 μm for a 500 μm long haltere beam.

Modeling and testing indicates the area of the PZT designated for sensing will be inherently sensitive to the Coriolis forces caused by changes in angular rate with a 1 rad/s design goal. Scale studies and modal analysis were completed to guide the MEMS-level sensor development. MEMS-based haltere have been fabricated as individual sensors and in coupled arrays in 10, 20, and 30 micrometer thick Cu. Under-

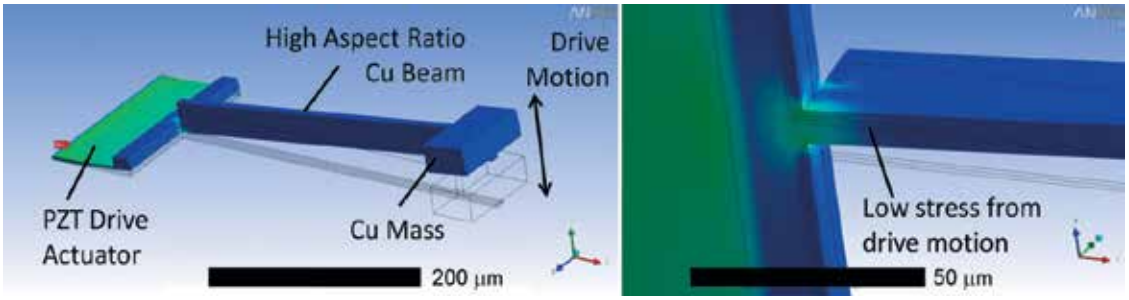

Fig. 15. ANSYS modal analysis showing drive or actuation mode shape, out of plane motion and relative strain at the root of the high aspect ratio beam due to the drive motion. (Note: the second view is rotated)

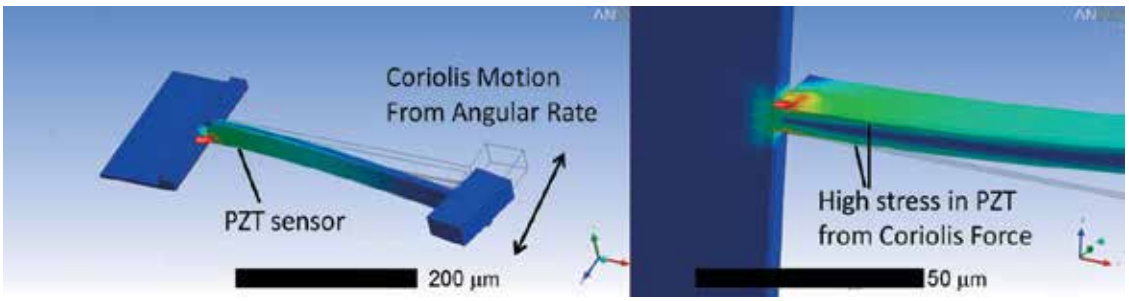

Fig. 16. ANSYS modal analysis showing the Coriolis force sensing mode shape, in-plane motion, and relative strain along the sides of the high aspect ratio beam due to the sideways motion. (Note: the second view is rotated)

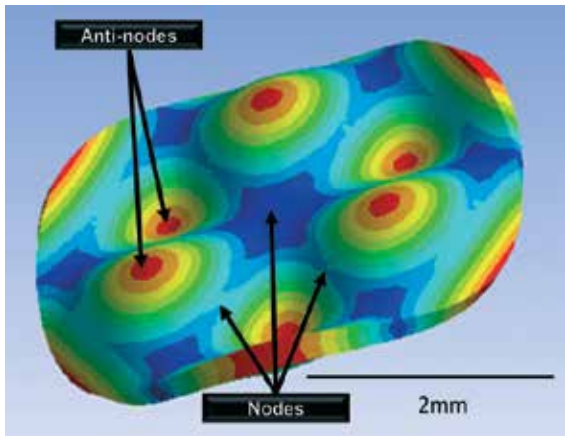

Fig. 17. ANYS modal simulation showing the B_{13} mode shape standing wave. A traveling wave results from two standing waves excited 90° in space and phase relative to each other. The patterned PZT thin film process enables a traveling wave by ensuring the antinodes and nodes of the pair of standing waves are aligned. Displacement is exaggerated in the simulations. Actual motion is <1 μm.

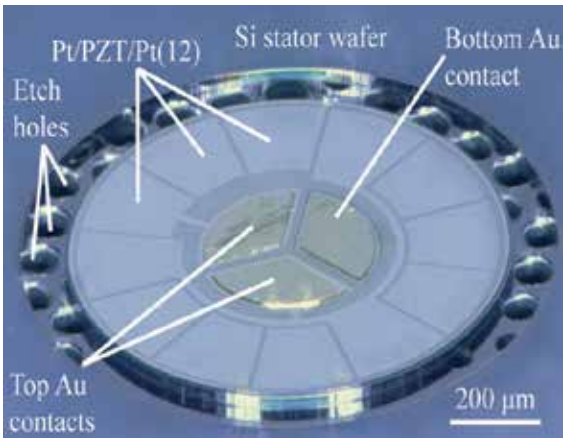

Fig. 18. This micrograph of a fabricated stator 2 mm diameter stator shows the electrode layout used to create a quarter-wavelength offset in space.

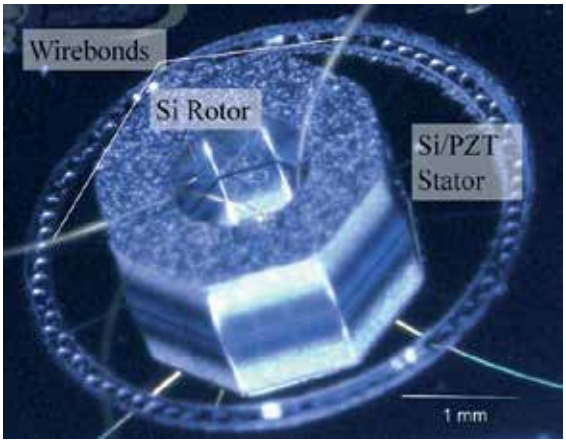

Fig. 19. Micrograph of the ultrasonic motor assembly.

standing the coupling mechanisms between multiple haltere will enable triaxial-sensitivity to angular rates resulting in reductions in size, weight, and power and enabling proprioceptive sensing on micro-air vehicles at this unprecedented scale.

(3) Traveling Wave Ultrasonic Motors

Many small scale motors have been developed over the years, however, few if any are able to produce high torques, especially at low speeds, without the use of gearing.[40,41] Traveling wave ultrasonic motors (TWUM) offer a path toward addressing this need. Advantages of TWUM include high torque-low speed performance, silent drive, zero power holding torque, compact design, and low power.[42] Macroscale, bulk PZT, TWUM have found wide application in autofocus camera lenses as well as automotive applications. Despite these many advantages, miniaturization of TWUM has stalled due to the minimum resolution of the manufacturing process. The PiezoMEMS process offers many advantages for further scaling of TWUM including high resolution (< 1 μm), batch fabrication enabling large production volumes, and zero hand assembly.

The PiezoMEMS based TWUM uses a thin film of PZT to generate standing and traveling waves within the PZT and Si stator. The stator does not rotate, but the elliptical motion of the stator surface is transferred to a rotor in contact. Teeth attached to the stator can be used to amplify the piezoelectrically induced elliptical motion in the stator resulting in increased rotation rates in the motor. ANSYS simulations were performed to optimize the performance of the stator for the desired modes. The B_{13} vibration mode is shown in Fig. 17 and described in more depth in Ref. 43. In addition, the stators were designed to allow for control of the location of the nodal diameters of the mode shape of the stator. Specifically, the top Pt electrode (Act Metal 1 from Fig. 3) layout was configured to enhance operation of the B_{13} mode and limit the number of external interconnects required for operation (see Fig. 18).

During operation, two electrical signals were used to create two standing waves apart in space and offset in phase, which add by superposition to create a traveling wave. Directional control of the traveling wave was accomplished by adjusting relative phase of the two drive signals from + 90 to − 90 thereby enabling bi-directional rotation. For a 3 mm stator using 30 μm thick Si and ~1 μm thick PZT (52/48), the resulting traveling wave propagates around the disc every 4 μs. To demonstrate motor rotation, a 2 mm wide silicon rotor, manufactured using deep silicon reactive ion etching, was placed on the stator. The stator was then wirebonded to a 24-pin dual in-line package. In this configuration, the wirebonds also served to maintain the position of the rotor on the stator. The assembled device is shown in Figure 19. Upon excitation with phase offset sine wave inputs oscillating between 0 and 10 V, the rotor spun at rates ranging from 400 to 2300 rpm depending on contact with the wirebonds. When rotational direction was changed by altering the phase offset between the two drive signals, full speed change of direction occurred within 30 ms. This assembly was used as a simple proof of concept for a PiezoMEMS enabled TWUM and significant performance enhancement is expected in future integrated designs that contain integrated confinement and positioning of the rotor relative to the stator.

IV. RF MEMS Devices

In the area of RF circuits, RF MEMS technologies, including switches and relays, phase shifters, resonators, filters, and oscillators, have been investigated. These technologies can play a significant role in reducing loss, power consumption, improving isolation and linearity, and reducing size compared with current technology solutions for tactical and com-

mercial communication systems and phased array radar systems. This section discusses several of these device technologies and how PiezoMEMS technology can be used for additional performance benefits.

(1) RF MEMS Switches

Compared with other RF MEMS technologies, PZT thin film based switches offer certain benefits. Usually, the low actuation voltage of PZT devices is pointed out as their signature advantage.[44,45] However, PZT devices are also capable of generating large contact/restoring forces and displacements. They also tend to consume less power and are typically faster than thermally[46] and magnetically[47] actuated RF MEMS devices. When compared with switches actuated by electrostatic force, an additional advantage of piezoelectric switches is the full control of their displacement when the switch is making contact. Electrostatic switches are characterized by a parameter called pull-down voltage.[48] Once the pull-down voltage is reached and the gap of the electrostatic capacitor is reduced to 2/3 of the gap at 0 V, a positive feedback is created in the device. A smaller gap creates larger closing force, which in turn moves the switch in the direction of even smaller gaps. This process of constant acceleration ends when the RF contact is closed against a typically immovable RF line. In contrast, PZT RF MEMS switches move only in response to the magnitude of the DC actuation voltage. They do not exhibit positive feedback and their dynamic behavior is well controlled. As a result, switches with piezoelectric actuation can be operated where the contacts close with only a modest acceleration resulting in minimal contact bounce thus improving switch cycle reliability.[49]

Two representative PZT based switches are shown in Fig. 20. The RF circuit is reciprocal using a co-planar waveguide (CPW) transmission line configuration with the input or output on the left or right hand side of each image. The PZT actuators reside between the center conductor and the ground plane and are mechanically coupled with the elastic layer. In addition, the mechanical link provides the location for the electrical contact, which completes the electrical circuit path between the input and output RF transmission line air bridges. At zero actuation voltage, the input and output are isolated. Upon applying voltage, the actuators move upward out of the plan of the wafer resulting in the contact pad contacting both air bridges and completing the circuit between the input and output circuit path. One significant deviation of these devices from the earlier published results in Refs. 45 and 46 is the use of a 4 μm thick Si elastic layer from a SOI wafer as opposed to a 0.5 μm thick composite silicon dioxide and silicon nitride elastic layer. The change of elastic layer was prompted in part by a desire for devices with an increase in contact force and increase restoring force for improved reliability and RF performance (for more information on switch reliability see reference 50). Devices with increasing actuator widths are shown in Fig. 20 to demonstrate the capabilities of the fabrication technology, note that release holes are required because of fabrication tolerances. It should be noted that, from an electrical perspective, these switches are four terminal devices (i.e., the two terminals for DC actuation and the two RF terminals (input/output) are decoupled from each other). Such a topology allows independent optimization of the mechanical and RF performance of the devices.

The PZT RF MEMS switches were characterized using an Agilent E8361A PNA Network Analyzer in the frequency range from 100 MHz to 40.1 GHz. In the off-state, the vertical gap between the air bridges and contact pad combined with the etch trench surrounding the contacts enables devices with isolation better than −20 dB up through 25 GHz (see Figure 21). The devices have actuation voltages as follows: single actuator –15 V; dual actuator –20 V. These voltages are 2–2.5 times higher than the previously published results as these devices have yet to be optimized for initial gap and temperature stability. Nevertheless, the contact resistances of these switches is in the range 0.5–1 Ohm with the corresponding insertion loss (see Fig. 22) better than −0.5 dB up to ~15 GHz (note, insertion loss is higher than it should be at these contact resistances. The substrate losses were substantially higher on these initial devices and will be reduced on subsequent wafers).

(2) NanoMechanical Logic

Piezoelectric RF switches have also become enabling in very low power digital logic circuits. The low leakage current observed on a PZT-based actuator has led to the development of a digital, single-pole, double-throw (SPDT) mechanical relay with zero leakage current in one state and under 30-fA of leakage current in the other state.[51] The device is shown schematically in Fig. 23 and with the two independent current paths highlighted in green in Fig. 24. In addition to low leakage currents, the structure's material composition provides innate radiation hardening[52–54] and the SPDT configuration of this device, highlighted in Fig. 24, makes it optimally suited for complimentary logic circuits.

Due to PZT's large d_{31} coefficient, large deflections, several hundred nanometers for the previously mentioned nanomechanical logic relay, can be achieved at modest voltages. This enables the relay to have an open-state contact gap sufficient to support up to 40 V hot switched across its contacts, whereas still allowing for fully functional Boolean logic operations at fewer than 2 V (see Table II). In addition, due to the ambipo-

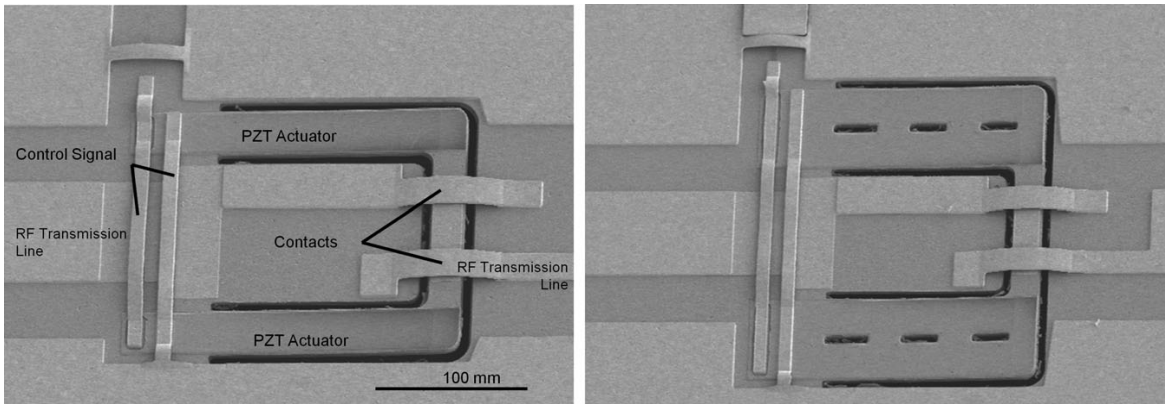

Fig. 20. SEM images of PZT-based RF MEMS switches with actuators of different width (a) single actuator and (b) dual actuator.

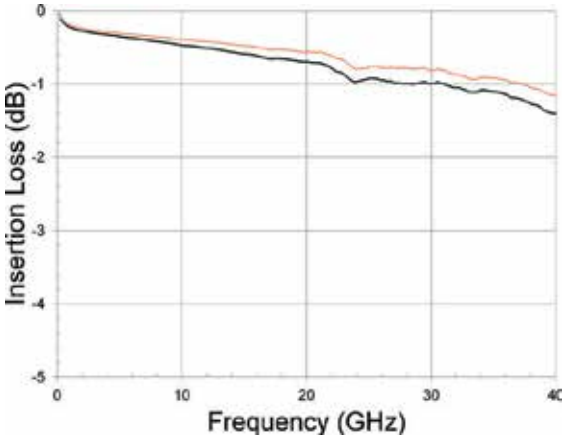

Fig. 21. Insertion loss in the on-state (voltage applied) with the single actuator in red and dual actuator in black.

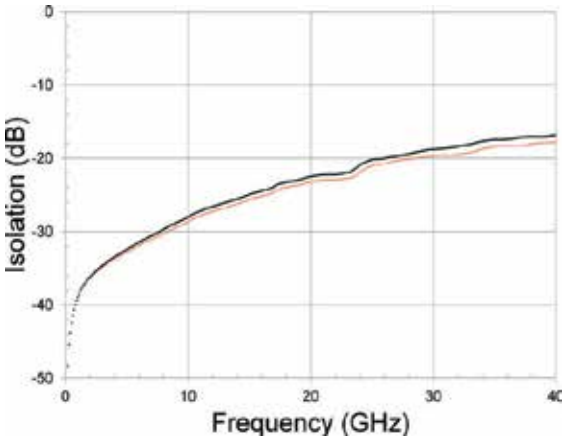

Fig. 22. Isolation in the off-state (0 V) with the single actuator in red and dual actuator in black.

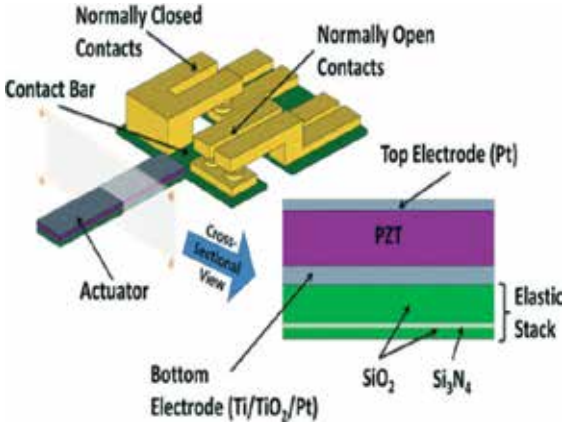

Fig. 23. Single-pole double-throw relay schematic.

lar nature of metal-to-metal contacts, the device is well suited to functioning in a pass-gate logic configuration, allowing for a reduction in gate count without harming the signal integrity. Fig. 25 demonstrates this behavior with a Boolean AND operation. Here, the top electrode of Fig. 24 is grounded, the bottom electrode is connected to "Input A," the normally closed (NC) input is grounded, the normally open (NO) input is connected to "Input B" and both the NC and NO outputs are connected together. In this configuration, when "Input A" is false, ground is shorted to the output and when "Input A" is true, "Input B" is passed to the output.

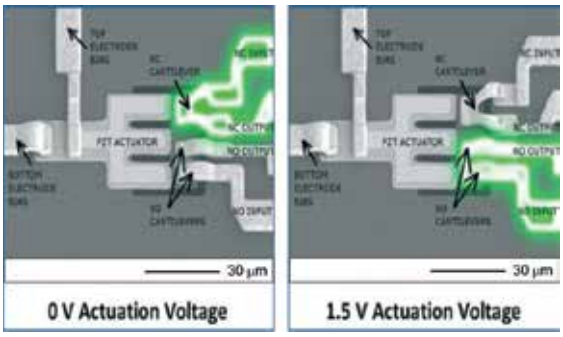

Fig. 24. Electron micrograph of a fabricated relay highlighting the two paths of current flow.

The device can also operate as either of the two classes of digital memory: dynamic and static.[55] The low leakage of the PZT dielectric makes dynamic memory especially attractive for low power operation, as the data can be preserved for long periods without any external power. Fig. 26 shows one relay, one capacitor implementation of a dynamic flip-flop. This device operates by propagating "D" to the storage capacitor when "PHI" is high and then transporting that charge to "Q" as soon as "PHI" goes low. Measured results of this operation are shown in Fig. 27. Note that the rapid decay shown in those results is due to the 1 M·Ω terminating resistance of the measurement equipment, which is approximately six orders of magnitude lower than the parasitic resistance of the MEMS relay, the component this circuit is intended to drive.

(3) RF MEMS Resonators

The PZT RF MEMS resonators provide a potential solution for bandpass and bandstop filters in communication systems in addition to high quality factor, low phase noise oscillators for timing references utilized in electronic systems. The key advantage for contour-mode, piezoelectric MEMS resonators is the multi-frequency integration on a single chip. These resonators also show promise as resonant power transformers for single chip power supplies.[33] The PZT is an attractive choice for RF MEMS acoustic resonators/transformers due to its large electromechanical coupling factors and stress constants. The high electric field PZT nonlinearity also allows for electric field tuning of the dielectric, elastic, piezoelectric constants, and coupling factors; enabling resonant frequency tuning, which is an attractive feature for RF systems. The approach with the most promise to date is to combine the high electromechanical coupling of the PZT material with the high mechanical quality factor of single crystal Si.[56–58] The silicon layer provides a means for higher quality factor, lower loss resonators.[57] PiezoMEMS resonators of this design have recently demonstrated an insertion loss as low as 2.1 dB at ~15 MHz (see Fig. 28), a loss competitive with Film Bulk Acoustic Resonator (FBAR) technology.[59] Additional research activities in thin film PZT resonators that will be discussed include unique tether designs that minimize anchor loss, ultimately improving the mechanical quality factor,[57] tunable parallel resonance with > 110 dB of rejection for notch filter applications and a numerical electrode shaping design technique permitting the excitation and detection of arbitrary modes in arbitrary geometries.[60] In addition, these PZT resonators have also been integrated with PZT switches, enabling a monolithic switchable filter approach.[61] The fol-

Table II. All 16 Boolean Logic Functions Possible with PiezoMEMS SPDT Relay

Boolean Function	Top Pt	Bottom Pt	NC Input	NC Output	NO Output	NO Input
Always 0	X	X	GROUND	OUTPUT		INPUT B
A NOR B	VDD	INPUT A	GROUND	OUTPUT		NOT INPUT B
(NOT A) AND B	GROUND	INPUT A	INPUT B	OUTPUT		GROUND
NOT A	GROUND	INPUT A	VDD	OUTPUT		GROUND
A AND (NOT B)	GROUND	INPUT B	INPUT A	OUTPUT		GROUND
NOT B	GROUND	INPUT B	VDD	OUTPUT		GROUND
A XOR B	INPUT A	INPUT B	GROUND	OUTPUT		VDD
A NAND B	GROUND	INPUT A	VDD	OUTPUT		NOT INPUT B
A AND B	GROUND	INPUT A	GROUND	OUTPUT		INPUT B
A XNOR B	INPUT A	INPUT B	VDD	OUTPUT		GROUND
B	X	X	INPUT B	OUTPUT		INPUT B
(NOT A) OR B	GROUND	INPUT A	VDD	OUTPUT		INPUT B
A	X	X	INPUT A	OUTPUT		INPUT A
A OR (NOT B)	GROUND	INPUT B	VDD	OUTPUT		INPUT A
A OR B	GROUND	INPUT A	INPUT B	OUTPUT		VDD
Always 1	X	X	VDD	OUTPUT		VDD

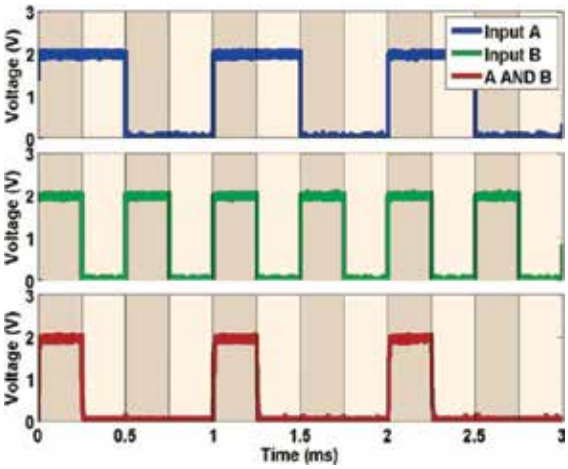

Fig. 25. Measured results of Boolean AND function being performed via a PiezoMEMS relay.

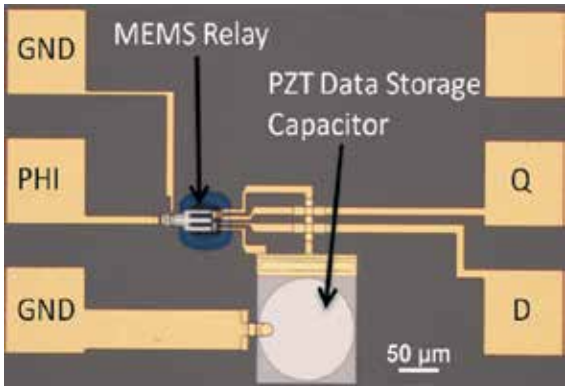

Fig. 26. Optical micrograph of a dynamic flip-flop.

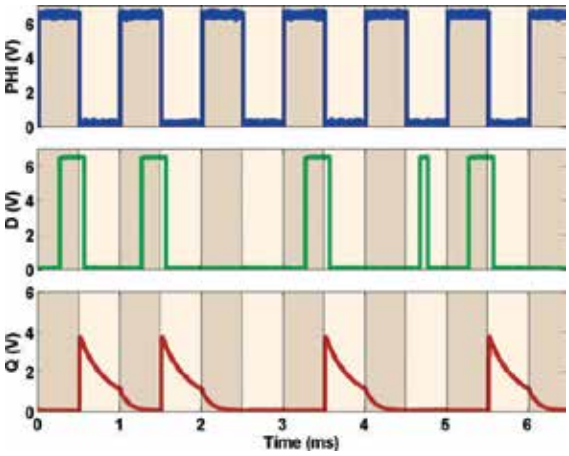

Fig. 27. Measured results of the dynamic flip-flop created from two MEMS relays. Note that glitches introduced between 4.5 and 5 m\s do not propagate to the output.

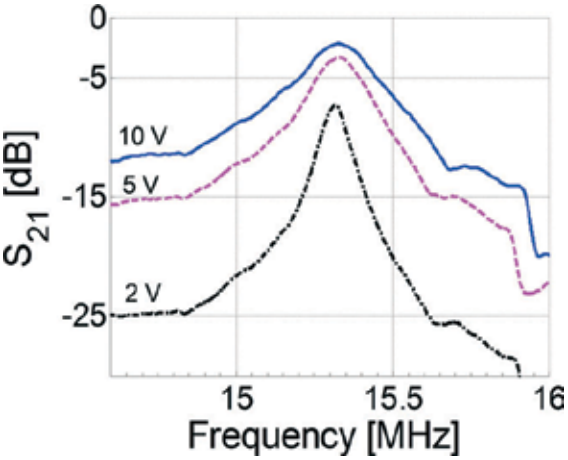

Fig. 28. Insertion loss versus frequency for a PiezoMEMS contour-mode resonator at various DC bias voltages. At 10 V bias a low-loss of 2.1 dB resulted.

lowing section briefly highlights a handful of current efforts to improve performance in PiezoMEMS resonator devices.

(A) Anchor Loss Mitigation: Anchor loss is an important research topic for resonators as it can ultimately limit the mechanical quality factor and limit device performance. Quarter-wave support design for acoustic matching has been a common MEMS-based approach for anchor loss mitigation. In general, the support should accommodate large resonator motion and velocity at the attachment point while

simultaneously providing a large mechanical impedance at the substrate attachment; ultimately, an efficient impedance transformer is desired where acoustic energy radiating into the substrate is minimized. An alternative design involves determining the desired resonator geometric and resonant mode and then subsequently designing a tether that tends to accommodate the general resonator motion. Modal analysis was used to consider dissimilar anchor support designs to gain an understanding of the tether response (which can be considered a resonator in itself) at a desired resonant frequency. The Von Mises stresses at the surface between the tether and the substrate is then used to assess the relative energy that would be radiated when comparing two variant tether designs. For example, two tether supports are considered using ANSYS 12.0 FEA (Pittsburgh, PA) modal analysis for disc resonator geometries as shown in Fig. 29. The tether displacements are assessed and compared (see inset images for each design in Fig. 29. The response is the vector sum of the unity normalized displacements, where the blue represents near zero relative displacements. It is evident that the alternative tether design [Fig. 29(b)] will present the resonator with reduced energy transfer into the substrate resulting in a larger resonator mechanical quality factor and improved device performance.

(B) Electrode Shaping: Another area of study is electrode shaping, which is motivated by designing for the most optimal electrode patterns for a particular resonant mode to both minimize insertion loss for a particular resonant mode and improve the suppression of spurious vibrational modes. The proper design of the resonator electrodes to selectively excite and detect desired modes, or "electrode-shaping," can provide improvements in these performance metrics. Optimal excitation and detection electrodes may be analytically derived for simple one-dimensional modes by utilizing the orthogonality property of the vibrational mode-shapes. However, extending this technique to more complicated modes is difficult, but extending the theory to higher dimensional modes, such as those existing in discs, poses considerable complications. An alternative approach has been developed that determines the local suitability of placing an electrode on the resonator.[60] The local suitability is accomplished by considering strain compatibility between the excited piezoelectric material and the desired mode at each location on the resonator. The electrode shapes are ascertained from maps of this local determination of electrode placement. For excitation, maximizing the local strain leads to maximizing the local contribution to the lumped equivalent excitation force, or modal force. This technique does not necessarily maximally excite the desired mode or maximally suppress unwanted modes, but rather determines electrode shapes that ensure the desired mode is excited and detected. Figure 30 displays the results of the current technique for the detection electrode for the two-port devices.

(C) PZT Resonant Power Transformers: An alternate application of thin-film PZT resonators includes piezoelectric power transformers for power supplies in on-chip applications.[35] The large size of the passive components limits the size of the switched mode power supply (SMPS), thus creating the need for a high frequency SMPS to reduce the size of the passives. Low frequency bulk resonant piezoelectric transformers (<5 MHz) have been implemented in the past in power conditioning units for advantages including high voltage isolation, small size, and the absence of induced electromagnetic noise.[62] Thin film PZT resonant transformers offer an elegant solution for on-chip high frequency power passives integration.

To realize either a voltage buck or voltage boost configuration an approximate analysis can be followed. Assuming a low loss, contour mode, two port piezoelectric resonant transformer as depicted in Fig. 31, the input power, P_{in}, is approximately equal to the output power. Based on this approximation,

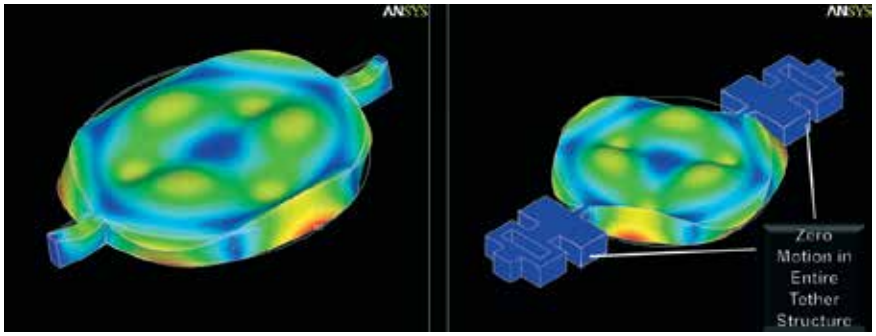

Fig. 29. Modal analysis of 100 μm diameter PZT-on-Si disc resonator operating at 60 MHz high order disc flexure mode. The plotted response is the vector-sum of unity normalized displacements (blue identifies near zero relative displacements). (left) 20 μm long × 5 μm wide straight tether design and (right) new transformer design.

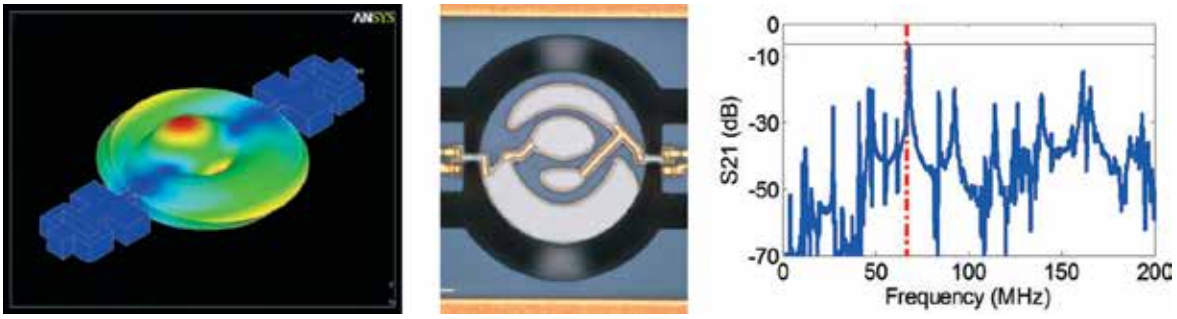

Fig. 30. (Left) FEA modal analysis a high order flexure disc mode with 100 μm diameter. (Center) Micrograph of the fabricated two-port PZT-on-Si disc resonator electrode-shaped for the mode illustrated in (left) and (right) it's corresponding frequency response. The dashed red line identifies the design frequency.

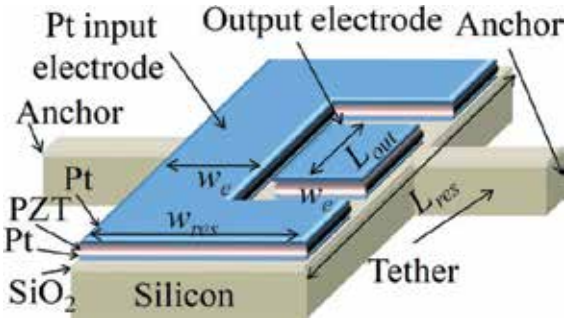

Fig. 31. Illustration of extensional mode resonator where the output electrode is designed based on the resistive load to which power will be delivered. The output electrode area is traded for the input transducer area for voltage boosting.

$$I_{in}V_{in} \cong I_{out}V_{out} \quad (1)$$

$$V_{out}/V_{in} \cong I_{in}/I_{out} \cong (A_{in}N_{in})/(A_{out}N_{out}) \quad (2)$$

where V_{in} is the input voltage amplitude, V_{out} is the output amplitude, I_{in} is the input current, I_{out} the output current, A_{in} and A_{out} the area of the input and output electrodes, respectively, and N_{in} and N_{out} are the number of input and output electrodes, respectively. Therefore, voltage bucking or voltage boosting occurs with mismatched input and output electrode areas. A detailed analysis of electrode area trade-offs for the fundamental length extensional modes can be found in[35] for a thin film PZT resonator (single PZT stack). The trade for input area versus output area is considered for a device illustrated in Fig. 31 with a 190 μm × 40 μm × 11 μm volume. The voltage gain, efficiency, and power delivery are all a function of the input and output transducer design areas and the resistive load value. With a contour mode resonator of Q ~2000, voltage boosts as high as 8, with 29% efficiency, are predicted. In addition, efficiencies as high as 80% are predicted for 1:1 transformers depicted in Fig. 31.

As previously mentioned, the PZT based PiezoMEMS resonators utilize a single crystal silicon elastic layer which serves as a high quality factor resonator material. In addition to higher quality factor devices, the implement of silicon significantly improves the device power handling,[63] which is essential for high power density SMPS. There is, however, a fundamental trade with improved quality factor and power handling with electromechanical coupling factor, k_{eff}^2. Therefore, the $k_{eff}^2 \times Q$ metric is an important design parameter as it directly impacts the open circuit voltage gain and efficiency.

V. Conclusion

Over the last decade, the potential of nano to millimeter scale PZT thin-film devices is finally being realized across a breath of commercial and military areas. Material, design, and fabrication optimization are all areas that have fueled this growth. In many areas, like FRAM, ink-jet printing, RF MEMS, and millimeter-scale actuation, thin-film PZT transduction has proven itself as a truly enabling solution to engineering challenges that have been studied for decades. Compatible processes and integration of these individual PZT solutions will only enhance system performance while reducing components to size, weight, and power scales never thought possible.

Acknowledgments

The authors thank their many collaborators over the years of development on PiezoMEMS technology at the US Army Research Laboratory including the vision of Madan Dubey and Robert Zeto in initiating the PZT MEMS research effort. Specifically, Joel Martin and Brian Power are acknowledged for their contributions to device fabrication. In addition, the roles of Fox Materials Consulting, Pennsylvania State University, Cornell University, and the University of Maryland are acknowledged for their contributions to the fabrication, design, and evaluation of PiezoMEMS devices.

References

[1]R. G. Polcawich and J. S. Pulskamp, "Chapter 5: Additive Processes for Piezoelectric Materials:Piezoelectric MEMS;" pp. 273–355 in *MEMS Materials and Processes Handbook*, Edited by R. Ghodssi and P. Lin. Springer, NY, 2011.

[2]P. Muralt, R. G. Polcawich, and S. Trolier-McKinstry, "Piezoelectric Thin Films for Sensors, Actuators, and Energy Harvesting," *MRS Bull.*, **34**, 658–64 (2009).

[3]S. Tadigadapa and K. Mateti, "Piezoelectric MEMS Sensors: State-of-the-Art and Perspectives," *Meas. Sci. Technol.*, **20**, 092001 (2009).

[4]P. Muralt, "Recent Progress in Materials Issues for Piezoelectric MEMS," *J. Am. Ceram. Soc.*, **91** [5] 1385–96 (2008).

[5]http://www.ramtron.com/products/nonvolatile-memory/

[6]http://www.ti.com/product/msp430fr5728

[7]http://www.fujitsu.com/us/services/edevices/microelectronics/memory/fram/

[8]http://industrial.panasonic.com/www-data/pdf/ARC0000/ARC0000CE13.pdf

[9]http://www.epson.com/cgi-bin/Store/Landing/InkTechPrinter.jsp

[10]http://www.dimatix.com/files/SAMBA-Technology-Backgrounder.pdf

[11]J. S. Pulskamp, A. Wickenden, R. Polcawich, B. Piekarski, M. Dubey, and G. Smith, "Mitigation of Residual Film Stress Deformation in Multilayer Microelectromechanical Systems Cantilever Devices," *J. Vac. Sci. Technol. B, Microelectron. Process. Phenom.*, **21** [6] 2482–6 (2003).

[12]E. Zakar, R. Polcawich, M. Dubey, J. Pulskamp, B. Piekarski, J. Conrad, and R. Piekarz, "Stress Analysis of SiO_2/Ta/Pt/PZT/Pt Stack for MEMS Application," *Proc. 12th IEEE Int. Symp. Appl. Ferroelectr.*, 194–7 (2000).

[13]J. S. Cross, K. Kurihara, and H. Haneda, "Diffusion of Oxygen Tracer Into Deuterium-Gas-Baked IrO_x/Pb(Zr,TiO_3)Pt Capacitors and Pb(Zr,Ti)O_3Pt Films," *J. of Appl. Phys.*, **98** [9] 094107, 5pp (2005).

[14]L. A. Bursill, I. M. Reaney, D. P. Vijay, and S. B. Desu, "Comparison of Lead Zirconate Titanate Thin Films on Ruthenium Oxide and Platinum Electrodes," *J. of Appl. Phys.*, **75** [3] 1521–5 (1994).

[15]T. S. Moise, S. R. Summerfelt, and K. R. Udayakumar, "Method of Forming PZT Ferroelectric Capacitors for Integrated Circuits"; US Patent 7,935,543, 2011.

[16]G. L. Smith, R. G. Polcawich, J. S. Pulskamp, T. Waggoner, and J. Conley, "Atomic Layer Deposited Alumina for use as an Etch Barrier Against Xenon Difluoride Etching"; pp. 194–7 in *Proceeding of 2010 Solid State Sensor, Actuator and Microsystems Workshop*, Transducers Research Foundation, Hilton Head, 2010.

[17]D. M. Potrepka, G. R. Fox, L. M. Sanchez, and R. G. Polcawich, "Pt/TiO_2 Growth Templates for Enhanced PZT Films and MEMS Devices," *MRS Online Proc. Library*, Material Research Society, **1299**, mrsf10-1299–s04-02 (2011).

[18]F. K. Lotgering, "Topotactical Reactions with Ferrimagnetic Oxides Having Hexagonal Crystal Structures," *J. Inorg. Nucl. Chem.*, **9** [2] 113 (1959).

[19]B. Jaffe, R. S. Roth, and S. Marzullo, "Piezoelectric Properties of Lead Zirconate- Lead Titanate Solid Solution Ceramics," *J. of Appl. Phys.*, **25** [6] 809–10 (1954).

[20]P. Muralt, T. Maeder, L. Sagalowicz, S. Hiboux, S. Scalese, D. Naumovic, R. G. Agostino, N. Xanthopoulos, H. J. Mathieu, L. Patthey, and E. L. Bullock, "Texture Control of $PbTiO_3$ and Pb(Zr,Ti)O_2 Thin Films With TiO_2 Seeding," *J. of Appl. Phys.*, **83**, 3835 (1998).

[21]S. Hiboux, P. Muralt, and N. Setter, "Orientation and Compostition Dependence of Piezoelectric-Dielectric Properties of Sputtered Pb(Zr_x,Ti_{1-x})O_3Thin Films," *Proc. MRS*, **596**, 499–504 (1999).

[22]K. D. Budd, S. K. Dey, and D. A. Payne, "Sol-gel Processing of $PbTiO_3$, $PbZrO_3$, PZT, and PLZT Thin Films," *Br. Ceram. Proc.*, **36**, 107–21 (1985).

[23]Q. F. Zhou, E. Hong, R. Wolf, and S. Trolier-McKinstry, "Dielectric and Piezoelectric Properties of PZT 52/48 Thick Films With (100) and Random Crystallorgraphic Orientation," *Mat. Res. Soc. Symp.*, **655**, 1171–6 (2001).

[24]L. M. Sanchez, D. M. Potrepka, G. R. Fox, I. Takeuchi, and R. G. Polcawich, "Improving PZT Thin Film Texture Through Pt Metallization and Seed Layers," *MRS Online Proc. Library*, **1299**, mrsf10-1299-s04-09 (2011).

[25]N. Ledermann, P. Muralt, J. Baborowski, S. Gentil, K. Mukati, M. Cantoni, A. Seifert, and N. Setter, "Textured, Piezoelectric Pb(Zr_x, Ti_{1-x})O_3 Thin Films for MEMS: Integration, Deposition, and Properties," *Sens. Actuators A: Phys.*, **105** [2] 162–70 (2003).

[26]J. Chen, K. R. Udayakumar, K. G. Brooks, and L. E. Cross, "Rapid Thermal Annealing of Sol-gel Derived Lead Zirconate Titanate Thin Films," *J. of Appl. Phys.*, **71** [9] 4465 (1992).

[27]H. N. Al-Shareef, K. R. Bellur, O. Auciello, X. Chen, and A. I. Kingon, "Effect of Composition and Annealing Conditions on the Electrical Properties of Pb(Zr_xTi_{1-x})O_3 Thin Films Deposited by the Sol-gel Process," *Thin Solid Films*, **252** [1] 38 (1994).

[28]C.-R. Cho, W.-J. Lee, B.-G. Yu, and B.-W. Kim, "Dielectric and Ferroelectric Response as a Function of Annealing Temperature and Film Thickness of Sol-gel Deposited Pb($Zr_{0.52}Ti_{0.48}$)O_3 Thin Film," *J. of Appl. Phys.*, **86**, 2700–12 (1999).

[29]S. Hollar, A. Flynn, S. Bergbreiter, and K. S. J. Pister, "Robot Leg Motion in a Planarized-SOI, Two-Layer Poly-Si Process," *J. Microelectromech. Syst.*, **14**, 725–40 (2005).
[30]J. S. Pulskamp, R. G. Polcawich, and K. Oldham, "Highly Integrated Piezo-MEMS Enabled Millimeter-Scale Robotics"; Vol. 6, pp. 797–805 in *Proceedings of ASME IDETC/MNS*, ASME, San Diego, CA, 2009.
[31]K. Oldham, J. Pulskamp, R. Polcawich, and M. Dubey, "Thin-Film PZT Actuators With Extended Stroke," *J. Microelectromech. Syst.*, **17** [4] 890–9 (2008).
[32]S. S. Bedair, J. Pulskamp, B. Morgan, and R. Polcawich, "Performance Model of Electrode Tailored Thin Film Piezoelectric Transformers for High Frequency Switched Mode Power Supplies"; pp. 436–8 in *Proceedings of PowerMEMS*, Transducers Research Foundation, Washington, DC, 2009.
[33]K. Oldham, J. Pulskamp, and R. Polcawich, "Thin-Film Piezoelectric Actuators for Bio-Inspired Micro-Robotic Applications"; *Integr. Ferroelectr.*, **95** [1] 54–65 2007.
[34]R. S. Fearing, K.H. Chiang, M.H. Dickinson, D.L. Pick, M. Sitti, and J. Yan, "Wing Transmission for a Micromechanical Flying Insect"; Vol. 2, pp. 1509–16 in *Proceedings of IEEE Int. Conference on Robotics and Automation*, IEEE, San Fransisco, CA, 2000.
[35]R. J. Wood, "The First Takeoff of a Biologically Inspired At-Scale Robotic Insect," *IEEE Trans. on Robotics*, **24** [2] 341–7 (2008).
[36]J. R. Bronson, J.S. Pulskamp, R.G. Polcawich, C.M. Kroninger, and E.D. Wetzel, "PZT MEMS Actuated Flapping Wings for Insect-Inspired Robotics"; pp. 1047–1050, *Proceedings of IEEE Conference on MEMS*, IEEE, Sorrento, Italy, 2009.
[37]J. S. Pulskamp, G. L. Smith, R. G. Polcawich, C. M. Kroninger, and E. D. Wetzel, "Two Degree of Freedom PZT MEMS Actuated Flapping Wings With Integrated Force Sensing"; pp. 390–391 *Proceedings of Solid State Sensor, Actuator and Microsystems Workshop*, TRF, Hilton Head Island, SC, 2010.
[38]W. Wu, R. Wood, and R. Fearing, "Halteres for the Micromechanical Flying Insect," *Proc. IEEE Int. Conf. Robot. Autom.* p. **60**, 2002.
[39]G. Frankel and J. W. S. Pringle, "Halteres of Flies as Gyroscopic Organs of Equilibrium," *Nature*, **141**, 919–21 (1938).
[40]L. F. Fan, Y. C. Tai, and R. S. Muller, "IC-Processed Electrostatic Micromotors," *Sens. Actuators*, **20**, 41–7 (1990).
[41]R. Legtenberg, E. Berenschot, J. Van Baar, and M. Elwenspoek, "An Electrostatic Lower Stator Axial-Gap Polysilicon Wobble Motor Part I: Design and Modeling," *J. Microelectromech. Syst.*, **7** [1] 87–93 (1998).
[42]K. Uchino, "Piezoelectric Ultrasonic Motors: Overview," *Smart Mater. Struct.*, **7**, 273–85 (1998).
[43]G. L. Smith, R. Q. Rudy, R. G. Polcawich, and D. L. Devoe, "Integrated Thin Film Piezoelectric Traveling Wave Ultrasonic Motor," *Sens. Actuators A: Phys.*, in press (2011).
[44]R. G. Polcawich, J. S. Pulskamp, D. Judy, P. Ranade, S. Trolier-Mc-Kinstry, and M. Dubay, "Surface Micromachined Microelectromechanical Ohmic Series Switch Using Thin-Film Piezoelectric Actuators," *Microwave Theory and Techniques, IEEE Transactions*, **55** [12] 2642–54 (2007).
[45]R. G. Polcawich, D. Judy, J. S. Pulskamp, S. T. McKinstry, and M. Dubey, "Advances in Piezoelectrically Actuated RF MEMS Switches and Phase Shifters," *IEEE MTT-S Microwave Symposium*, 2083–6 (2007).
[46]M. Daneshmand, S. Fouladi, R. R. Mansour, M. Lisi, and T. Stajcer, "Thermally Actuated Latching RF MEMS Switch and Its Characteristics," *Microwave Theory and Techniques, IEEE Transactions*, **57** [12] 3229–38 (2009).
[47]M. Glickman, P. Tseng, P. Harison, J. Niblock, T. Goldberg, I. B. Judy, and J. W. Judy, "High Performance Lateral Actuating Magnetic MEMS Switch," *J. Microelectromechanical Systems.*, **20** [4] 842–51 (2011).
[48]G. M. Rebeiz and J. B. Muldavin, "RF MEMS Switches and Switch Circuits," *Microwave Magazine, IEEE.*, **2** [4] 59–71 (2001).
[49]B. McCarthy, G. G. Adams, and N. E. McGruer, "A Dynamic Model, Including Contact Bounce, of an Electrostatically Actuated Microswitch," *J. MEMS*, **11**, [3] 276–83 (2002).
[50]J. L. Ebel, D. J. Hyman, and H. S. Newman, "RF MEMS Testing – Beyond the S-Parameters," *IEEE Microwave Mag.*, **8**, 76–88 (2007).
[51]R. M. Proie Jr, R. G. Polcawich, J. S. Pulskamp, T. Ivanov, and M. Zaghloul, "Development of a PZT MEMS Switch Architecture for Low-Power Digital Applications," *J. Microelectromech. Syst.*, **20** [4] 1032–42 (2011).
[52]F. Wang, and V. D. Agrawal, "Single Event Upset: An Embedded Tutorial"; pp. 429–34, *VLSI Design, 21st International Conference on*, IEEE, Hyderabad, India, 2008.
[53]J. M. Benedetto, R. A. Moore, F. B. McLean, P. S. Brody, and S. K. Dey, "The Effect of Ionizing Radiation on sol-gel Ferroelectric PZT Capacitors," *Nuclear Science, IEEE Transactions on*, **37** [6] 1713–7 (1990).
[54]S. C. Lee, G. Teowee, R. D. Schrimpf, D. P. I. Birnie, D. R. Uhlmann, and K. F. Galloway, "Total-Dose Radiation Effects on sol-gel Derived PZT Thin Films," *Nuclear Science, IEEE Transactions on*, **39** [6] 2036–43 (1992).
[55]J. M. Rabaey, A. Chandrakasan, and B. Nikolic, in *Digital Integrated Circuits: A Design Perspective*, 2nd ed., Edited by C. S. Sodini. United States of America: Pearson Education, Inc., Upper Saddle River, 2003.
[56]H. Chandrahalim, S. A. Bhave, R. Polcawich, J. Pulskamp, D. Judy, R. Kaul, and M. Dubey, "Influence of Silicon on Quality Factor, Motional Impedance and Tuning Range of PZT-Transduced Resonators"; pp. 360–3 in *Proceedings of 2008 Solid State Sensors, Actuators & Microsystems Workshop*, Transducers Research Foundation, Hilton Head, SC, 2008.
[57]J. S. Pulskamp, S. S. Bedair, R. G. Polcawich, D. Judy, and S. Bhave, "Ferroelectric PZT RF MEMS Resonators"; pp. 1–6 in *IEEE Frequency Control Symposium 2011 Proceedings*, IEEE, San Francisco, CA, 2011.
[58]S. S. Bedair, J. S. Pulskamp, R. G. Polcawich, D. Judy, A. Gillon, S. Bhave, and B. Morgan, "Low Loss Micromachined Lead Zirconate Titanate, Contour Mode Resonator With 50 Ω Termination," pp. 708–12 IEEE International Conference on Micro Electro Mechanical Systems Proc, Paris, France, 2012.
[59]S. S. Bedair, D. Judy, J. Pulskamp, R. G. Polcawich, A. Gillon, E. Hwang, and S. Bhave, "High Rejection, Tunable Parallel Resonance in Micromachined Lead Zirconate Titanate on Silicon Resonators," *Appl. Phys. Lett.*, **99** [10] 103509, 3pp (2011).
[60]J. S. Pulskamp, S. S. Bedair, R. G. Polcawich, G. L. Smith, J. Martin, B. Power, and S. A. Bhave, "Electrode-Shaping for the Excitation and Detection of Arbitrary Modes in Arbitrary Geometries in Piezoelectric Resonators," *IEEE Transactions Ultrasonics Ferroelectrics & Frequency Control*, (in press) (2012).
[61]J. S. Pulskamp, D. C. Judy, R. G. Polcawich, R. Kaul, H. Chandrahalim, and S. A. Bhave, "Monolithically Integrated PiezoMEMS SP2T Switch and Contour-Mode Filters"; pp. 900–3 in *IEEE International Conference on Micro Electro Mechanical Systems Proc.*, IEEE, Sorrento, Italy, 2009.
[62]A. V. Carazo, "50 Years of Piezoelectric Transformers. Trends in the Technology"; pp. 33–44 in *Proceedings of Materials Research Society Symposium*, Material Research Society, Boston, MA, 2003.
[63]R. Polcawich, J. S. Pulskamp, S. S. Bedair, G. Smith, R. Kaul, C. Kroninger, E. Wetzel, H. Chandrahalim, and S. A. Bhave, "Integrated PiezoMEMS Actuators and Sensors," in *IEEE Sensors* 2193–96 2010. □

Gabriel L. Smith received B.S. and M.S. degrees in mechanical engineering from the University of Maryland, College Park, in 1999 and 2002, respectively. He has worked in MEMS Design for the past 15 years with the U.S. Naval Surface Warfare Systems, U.S. Army Armaments Research Dev. Eng Center, and U.S. Army Research Laboratory. He has developed MEMS devices for safe and arm devices for torpedoes and gun-launched munitions, piezoelectric sensors, and actuators for millimeter-scale robotic systems, and piezoelectric traveling wave ultrasonic motors. He has also fielded inertial sensors in Army systems for target and launch detection. He currently holds six US patents with three patents pending and has authored seven journal and conference papers on MEMS devices.

Jeffrey S. Pulskamp received the B. S. degree in mechanical engineering from the University of Maryland, College Park, in 2000. He is currently a MEMS Design and Mechanical Engineer with the Micro and Nano Materials and Devices Branch, U.S. Army Research Laboratory, Adelphi, MD. His current research interests include RF MEMS devices, electromechanical design and modeling of MEMS, and millimeter-scale robotics. He is currently the holder of eight patents related to piezoelectric MEMS devices and has an additional five patents pending.

Luz M. Sanchez received her B.A. degree in Physics from Hunter College -City University of New York (CUNY), New York, N.Y. in January 2008. As of 2008, she is pursuing her Ph.D. in Materials Science and Engineering at the University of Maryland College Park under the mentorship of Dr. IchiroTakeuchi. She is also working as a student intern at the U.S. Army Research Laboratory in the Micro and Nano Materials and Electronic Devices Branch. Her current research interests are in the optimization of sol-gel deposited PZT and highly oriented PZT in multilayer structures.

Daniel M. Potrepka is a Senior Research Electronics Engineer at the U.S. Army Research Laboratory in Adelphi, Maryland. He received his Ph.D. in Physics in 1998 from the University of Connecticut. Dr. Potrepka was a Process Engineer at Mostek Corporation, an Associate Member of the Technical Staff at RCA Laboratories, and an Associate Research Scientist at United Technologies Research Center between 1979 and 1993. As a National Research Council postdoctoral fellow he studied perovskite materials and their ferroelectric behavior and is currently involved in PiezoMEMS process and materials research. His current research is focused on a crystoallographic study of PiezoMEMS response in PZT for both sputtered and atomic layer deposited thin films and on packaging applications for MEMS. He has authored or coauthored more than 40 technical papers and has five patents.

Robert M. Proie Jr. received the B. S. degree in electrical engineering from the University of Pittsburgh, Pittsburgh, PA, in 2007, the M.S. degree and the Ph.D. degree in computer engineering from The George Washington University (GWU), Washington, DC, in 2010 and 2011, respectively. He is currently an electronics engineer at the U.S. Army Research Laboratory, Adelphi, MD. His research interests are in the areas of low-power electronics and MEMS device design. His current focus is on piezoelectric MEMS design and verification for both RF and digital applications.

Tony G. Ivanov received the M.S. and Ph.D. degrees in electrical engineering from the University of Central Florida, Orlando, in 1994 and 1997, respectively. From 1997 to 2003, he was with Bell Laboratories (AT&T, Lucent Technologies, Agere Systems Holmdel, NJ), where he worked on SiGe and BiCMOS technology development. Starting and Development organization, and he was involved with CMOS silicon-on-insulator and RF microelectromechanical systems (MEMS) technologies for wireless products. He is currently with the Sensors and Electron Devices Directorate, U.S. Army Research Laboratory, Adelphi, MD. His research interests cover technologies and circuits for RF/millimeter-wave applications, with emphasis on MEMS. He has authored or coauthored more than 40 journal and conference papers and is the holder of 13 U.S. patents. Dr. Ivanov is a founder of the IEEE Central North Carolina Chapter of ED/MTT/SSC. He has been a member of the Technical Program Committees for the IEEE MTT-S International Microwave Symposium and IEEE Antennas and Propagation Society International Symposiums, and he has been involved in IEEE in various capacities.

Ryan Q. Rudy received the B.S. degree and the M.S.E. degree in mechanical engineering from the University of Michigan, Ann Arbor, MI, in 2009 and 2010, respectively. Since 2010 he has been part of the MEMS and Microfluidics Laboratory at the University of Maryland, College Park, where he is pursuing the Ph.D. degree. His current research interests include millimeter-scale robotic actuators with a specific focus on rotary traveling wave ultrasonic motors.

William D. Nothwang joined the Army Research Laboratory from Clemson University in the Fall of 2001 as a ASEE Research Fellow. In the Spring of 2003, he became a Distinguished Army Scholar within the Army Research Laboratory. Dr. Nothwang's past research experience has focused on ultra-thin film hetero-structures, residual stress, thin film deposition, and integration, and specifically on the role of residual stress on complex nanostructures composed of many layers of dissimilar materials. For research in these areas, he was one of the recipients on both the 2005 Army R&D Award and the 2007 Army R&D Award. In 2009, he transferred to the RF Division of the Sensors and Electron Devices Directorate of ARL to take on a leadership role within the MAST program and to start his new research program. Dr. Nothwang's current research endeavors focus on cyber-physical sensing and control, including bio-mimetic sensors for low power, small size applications.

Sarah S. Bedair received the B.S. degree in Applied Sciences & Computer Engineering from the University of North Carolina - Chapel Hill (2002, Magna Cum Laude with Highest Distinction). She also received her Ph.D. and M. S. degrees in Electrical & Computer Engineering from the Carnegie Mellon University (2004 and 2008, respectively) where her thesis work focused on CMOS MEMS based chemical gravimetric sensors and mechanical oscillators. Dr. Bedair spent one year (August 2008-June 2009) as an Oak Ridge Associated University Postdoctoral Fellow at the U.S Army Research Laboratory (ARL) in Adelphi, Maryland. She has been a staff researcher in the Power Components Branch at ARL since June 2009. Her research is on the modeling and fabrication of MEMS based power devices,

specifically for single chip scale power conversion and RF electronics. She has contributed to over 30 research publications and is co-inventor on 4 patent applications or invention disclosures awaiting patent submission. She is also a member of IEEE. Dr. Bedair has received fellowships and awards for excellence in academics and research. These include the Phillip and Marsha Dowd-Institute for Complex Engineered Systems Fellowship and the James D. Crawford Award at UNC-Chapel Hill. She also received the 2010 Excellence in Federal Career -Technical & Scientific Rookie of the Year Award and the 2009 ARL Research and Development Achievement Award.

Christopher D. Meyer received the B.S. and M.S. degrees in electrical engineering from the University of Florida, Gainesville, FL, in 2006 and 2009, respectively. Since 2006 he has been part of the Interdisciplinary Microsystems Group at the University of Florida while pursuing the Ph.D. degree. His current research interests include three-dimensional microfabrication technologies, hybrid integration, and magnetic power systems.

Ronald G. Polcawich received the B.S. degree in materials science and engineering from Carnegie Mellon University, Pittsburgh, PA, in 1997, and the M.S. degree in materials and the Ph.D. degree in materials science and engineering from Pennsylvania State University, University Park, in 1999 and 2007, respectively. He is currently a Staff Researcher with the Micro and Nano Materials and Devices Branch, U.S. Army Research Laboratory, Adelphi, MD, where he is also currently the Team Lead for the RF MEMS and Millimeter-Scale Robotics programs. The current research programs include switches and phase shifters for phased array antennas, tunable MEMS resonators/filters for secure communication, and mobile unattended sensor platforms. His research activities include materials processing of lead zirconatetitanate thin films, MEMS fabrication, piezoelectric MEMS, RF components, MEMS actuators, and millimeter-scale robotics. He is currently the holder of four patents and has authored over 30 journal articles and one book chapter on fabrication and design of piezoelectric MEMS devices. Dr. Polcawich is a member of IEEE.

Modeling and Optimal Low-Power On-Off Control of Thin-Film Piezoelectric Rotational Actuators

Biji Edamana, Bongsu Hahn, Jeffery S. Pulskamp, Ronald G. Polcawich and Kenn Oldham

IEEE/ASME Transactions on Mechatronics, 16(5) (2011)

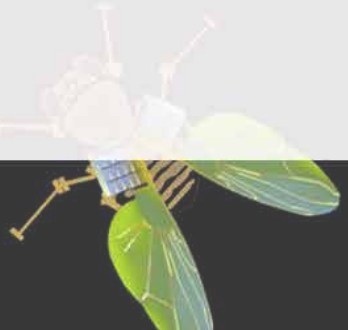

Modeling and Optimal Low-Power On–Off Control of Thin-Film Piezoelectric Rotational Actuators

Biju Edamana, Bongsu Hahn, Jeffrey S. Pulskamp, Ronald G. Polcawich, and Kenn Oldham, *Member, IEEE*

***Abstract*—A novel open-loop minimal energy on–off servo system and control strategy are described for ensuring specified displacements from new microscale piezoelectric rotational joints under extremely strict power budgets. The rotational joints are driven by thin-film lead–zirconate–titanate actuators and are targeted for use in autonomous terrestrial microrobots. A lumped-parameter, second-order model of anticipated joint behavior is utilized to estimate the natural frequency and damping ratio of the robot joints, which, in turn, are used to identify necessary sampling rates and switching drive circuit parameters for implementation of on–off control. An identified model of leg joint behavior is then used to both verify lumped-parameter modeling and to optimize on–off input sequences to the rotary joint. The optimization procedure incorporates energy costs from both switching and holding an input voltage on microactuators that behave as a capacitive load, while ensuring that specified final states of a dynamic system are achieved at a specified point in time. Optimization is done via a new application of binary programming. In addition, modest robustness of the system response to parameter variation can be produced during control sequence generation. Optimized input sequences are applied to both macroscale piezoelectric actuators and to prototype thin-film piezoelectric leg joints, and show that specified actuator motions can be achieved with energy consumption of less than 5 μJ per movement.**

***Index Terms*—Integer programming, microactuators, microelectromechanical devices, on–off control, piezoelectric devices, switched systems.**

I. Introduction

THE OPPORTUNITY to dramatically reduce the size of actuators and sensors through microelectromechanical system (MEMS) technology makes possible a variety of miniature autonomous devices, such as unattended sensor nodes or mobile microrobots. However, in autonomous operation, taking full advantage of the small size of MEMS mechanisms requires that one also ensure small size of power sources, circuitry, and other subsystems required to operate the central MEMS component.

Manuscript received December 11, 2009; revised April 7, 2010; accepted May 8, 2010. Date of publication July 23, 2010; date of current version August 30, 2011. Recommended by Technical Editor G. Alici. This work was supported in part by the U.S. Defense Advanced Research Projects Agency under Grant HR0011-08-1-0040 and in part by the U.S. Army Research Office under Grant W911QX-07-C-0072.

B. Edamana, B. Hahn, and K. Oldham are with the Department of Mechanical Engineering, University of Michigan, Ann Arbor, MI 48109 USA (e-mail: bij@umich.edu; suhahn@umich.edu; oldham@umich.edu).

J. S. Pulskamp and R. G. Polcawich are with the Sensors and Electron Devices Directorate, U.S. Army Research Laboratory, Adelphi, MD 20783 USA (e-mail: jeffrey.pulskamp@arl.army.mil; ronald.polcawich@arl.army.mil).

Color versions of one or more of the figures in this paper are available online at http://ieeexplore.ieee.org.

Digital Object Identifier 10.1109/TMECH.2010.2053041

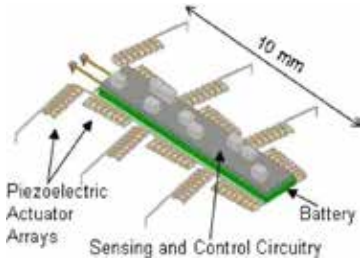

Fig. 1. Concept drawing of an autonomous microrobot based on thin-film piezoelectric actuator joint arrays.

One opportunity for reducing power needs of MEMS microactuators is aggressive reduction in power needed to perform controlled actuator movements. A new optimal on–off switching controller, as described in this paper, is a promising method for meeting especially strict constraints on power consumption. This method accommodates both efficient actuator drive circuitry and minimizes servo system energy usage to accomplish prescribed movements.

Especially severe power constraints are faced when MEMS actuators are intended to actuate autonomous microrobots, on the scale of one centimeter or smaller, as in the concept drawing shown in Fig. 1. While a few microrobots at this scale have been demonstrated in autonomous or tethered operation, their mobility has been limited by the need to either carry a large-power supply, by limited actuation force at low power, or by the need to operate on a dedicated substrate. Several previous robots have been based on thermal actuation, but the large-power consumption of thermal actuators permits only single degree of freedom, short-displacement leg joints in order to carry large-battery mass [1]–[3]. In contrast, microrobots based on electrostatic actuation can be powered with much smaller power supplies, but electrostatic actuators require very large areas to produce significant force, permitting only a few limbs or degrees of freedom per robot; alternatively, electrostatic microrobots may depend on a specialized substrate to deliver power, limiting autonomy to small areas [4]–[6].

Thin-film piezoelectric actuators, in contrast, are capable of delivering much larger forces than electrostatic actuators with much smaller power requirements than thermal actuators, or other potential robotic actuators, such as electromagnetic actuators or shape-memory alloys. A thin-film lateral actuator has been previously demonstrated capable of generating up to 3×10^{-9} N·m of work in a 500 μm $\times$ 100 μm area, and this paper may be leveraged using silicon microstructures to generate rotational motion of 3° or more from a single such actuator at 20 V [7]. Operated in multiactuator arrays, these actuators can

generate large-angle rotations of microrobotic leg joints. A typical array, as discussed in this paper, would have a capacitance of less than 1 nF, corresponding to intrinsic energy consumption of less than 1 μJ each time an actuator is charged to an operating voltage on the order of 20 to 30 V. Furthermore, integrated with silicon structures, they could potentially carry between 5 and 50 mg payloads per leg [8], [9]. However, even with state-of-the-art thin-film battery or solar power sources [10], [11], the power budget per leg at that payload capacity is on the order of a few hundred microwatts to a few milliwatts, making extremely low-power servo systems a necessity for microrobots based on these actuators. In addition, reduction in power requirements to control piezoelectric actuators could be useful to slightly larger miniature robots [12], [13], where energy constraints are not as severe, but servo power reduction still allows for larger payloads.

Unfortunately, controlling the motion of a robotic appendage, as to move a leg to a specified angle in a given step, introduces significant additional power consumption beyond that of the actuator itself. Existing operational amplifiers operating in the range of 20 to 30 V consume at least 400 μW in quiescent power, and in a typical analog amplifier circuit for piezoelectric actuators, as much as 95% of the power used by the actuator may be wasted [14]. As a result, switching interface circuits between a high-voltage supply and the piezoelectric actuator are desirable, with motion control typically applied using pulsewidth modulation (PWM). However, PWM requires very high switching frequencies, which dramatically increases power consumption when driving a capacitive load. Charge recovery, such as that developed by Campolo *et al.* [15], is one method for reducing this energy, use is through, but inductor sizes necessary for effective charge recovery can be excessively large and energy losses are still most prevalent during switching, although these losses are reduced.Another way of rotating through fixed angles is to make use of mechanical stops [16], [17]; the drawback in this method is that there is only one possible angle of rotation. Meanwhile, power consumption of sensor circuitry required for feedback also greatly exceeds power consumption of thin-film piezoelectric actuators, such that open-loop control may be necessary to meet especially strict power limits.

Open-loop on–off control, using a limited number of switching transitions per actuator movement, can produce regulated movements with extremely small energy usage, provided that on–off switching times are chosen carefully and a reasonable model of the system is available. Previous optimization techniques for on–off control schemes have minimized the time to reach a desired set of system states [18], or the amount of time spent with an "on" input to reach a desired set of states at a specified time [19], [20], but these approaches do not account for switching costs, such as energy usage to charge a capacitive actuator. Alternatively, full-fledged hybrid system models can be used to approach on–off control design [21], [22], but this may be an unnecessarily complex approach when only two input selections are available.

This paper presents a model for a piezoelectric microrobotic leg joint, a low-power switching circuit for control of the joint, and an optimization procedure for generating minimum energy on–off input sequences to direct the resulting motion. The open-loop optimal on–off switching sequences drive a set of initial states to a desired set of output states, while minimizing total energy usage. The optimization procedure is based on binary programming, which permits a simpler optimization procedure than that of full-fledged hybrid systems approaches, but allows switching costs to be incorporated into the optimization cost, unlike previous controllers designed specifically for on–off sequence optimization. Applied to the piezoelectric microactuator arrays in a novel rotational joint configuration, the controller can drive comparatively large displacements to specified angles with just a few on–off switching transitions and extremely low-power consumption. The control inputs are applied to the piezoelectric actuators through a low-power switching drive circuit, to further reduce system power consumption.

Following this introduction, Section II introduces the thin-film piezoelectric actuator and leg joint models. Section III describes the design of a low-power switching circuit for interfacing. Section IV describes the on–off input sequence optimization procedure and a simulational study. Section VI provides experimental results from the on–off controller using a low-power switching drive circuit. Section VII discusses implications for future low-power microrobot operation and concludes the paper.

II. Actuator Design and Modeling

A. Individual Flexure and Actuators

The large-angle, rotational joint to be controlled consists of a series of eight elastic silicon flexures between rigid silicon links developed at the U.S. Army Research Laboratory, as shown in Fig. 2. Each link contains a thin-film piezoelectric actuator that applies a bending moment to one of the silicon flexures via a thin silicon tether. Net rotation at the tip of the joint is the sum of the rotation angles of each flexure–actuator pair.

Each flexure in the array is a thin silicon beam that experiences elastic deflection due to the moment generated by the actuator force offset from the tip of the actuator by distance $L_{\rm act}$, as shown in Fig. 2(c2) and (c3). The rotational stiffness of each link is given by the equation

$$k_\theta = \frac{Etw_f^3}{12L_f} \tag{1}$$

where E is the elastic modulus of silicon, t is the thickness of the silicon flexures, w_f is the flexure width, and L_f is the flexure length. Flexure parameters as described and fabricated are shown in Table I. While the nominal flexure thickness was to be 10 μm in the legs tested, excessive undercut of the silicon structures during deep reactive ion etching resulted in thin silicon structures (flexures and tethers) having a thickness of only approximately 6 μm, leading to a somewhat less stiff joint structure than anticipated.

The piezoelectric actuators consist of bend-up and bend-down unimorph segments connected in series to produce net in-plane displacement at the actuator tip, as shown in Fig. 3. The bend-up unimorph segments consist of a silicon dioxide base layer that sets the height of the neutral bending axis below the pizezoelectric film, a bottom platinum electrode, a lead–zirconate–titanate (PZT) piezoelectric thin film, and a top platinum electrode. The

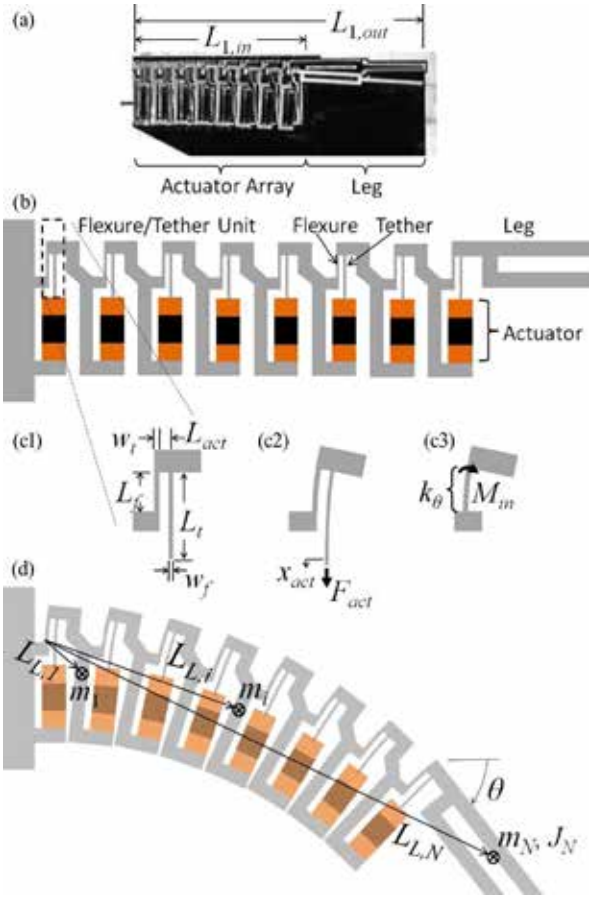

Fig. 2. Multiactuator leg joint. (a) Optical photograph. (b) Schematic drawing of components. (c1) Link dimensions. (c2) Force and displacement at actuator tip. (c3) Equivalent bending moment model. (d) Mass and inertia definitions in deflected state.

TABLE I
FLEXURE AND ACTUATOR PARAMETERS

Parameter	Label	Units	Nominal Value	Fabricated Value
Elastic Modulus (Si)	E	GPa	170	170
Device Thickness	t	μm	10	6
Flexure Width	w_f	μm	7	6.7
Flexure Length	L_f	μm	120	120
Spring Constant	k_θ	μN/rad/s	0.38	0.23
Actuator Offset	L_{act}	μm	12	12
Tether Width	w_t	μm	5	4.7
Tether Length	L_t	μm	292	292

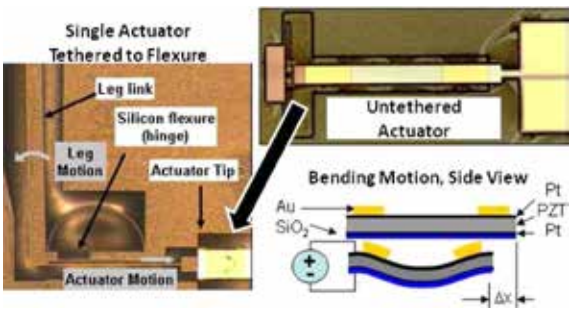

Fig. 3. Schematic diagram and optical images of an individual thin-film piezoelectric lateral actuator, alone and tethered to single flexure.

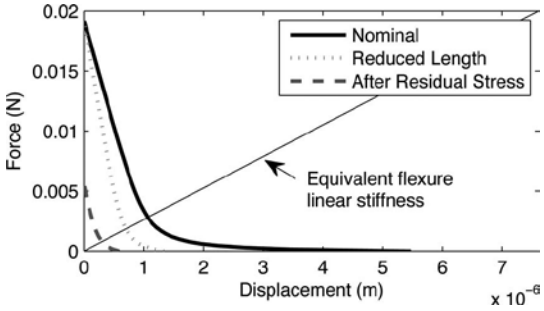

Fig. 4. Force versus displacement curve of thin-film piezoelectric actuators at 20 V, nominal model from [7] and with effects of fabrication limitations.

bend-down unimorph segments have an additional gold film added, to raise the neutral bending axis of the structure above the midline of the PZT film in that segment. The net effect is to produce in-plane lateral actuators with the large-force capacity of piezoelectric actuation and increased stroke length due to nonlinearity of the bend-up and bend-down structure. A full force–displacement model of these actuators was previously described in [7], and the resulting force–displacement curve for a nominal 500-μm-long, 100-μm-wide actuator at 20 V is shown in Fig. 4. The effective electroactive piezoelectric strain coefficient ($d_{31,\text{eff}}$) for these actuators at 20 V was approximately -60 pm/V, while the dielectric coefficient was approximately 230.

Unfortunately, while the nominal force–displacement of the actuators, as designed and tested in the previous work, would generate greater than 3° of rotation at each link, flaws during the microfabrication process greatly reduced the force–displacement capabilities of the actuators tested here. Namely, insufficient undercut of the silicon layer beneath the actuators reduced their length to only about 440 μm, and residual stress in the thin film layers, particularly the gold films used to generate bend-down motion at the outer segments of the actuator, has the effect of shifting the force–displacement curve away from its nominal position. When the observed length of the actuators following fabrication and estimated residual stress levels are incorporated in the actuator models, the expected force–displacement curve diminishes, as shown in the additional curves in Fig. 4. While this decrease in performance is not a significant factor in verifying controller performance and power consumption, reducing negative effects of residual stress and better regulating actuator length and stiffness will be necessary to achieve truly large range-of-motion microrobotic joints.

Conversion of the actuator force as a function of displacement to the moment on the flexures as a function of flexure rotation depends, first, on the offset between the actuator tether and the elastic flexure in each link, and second, on the stiffness of the tether itself. For a given offset L_{act}, the resulting moment due to the actuation force F_{act} is given by

$$M_{\text{in}} = F_{\text{act}} L_{\text{act}}. \tag{2}$$

The static lateral displacement at the tip of each actuator x_{act} is dependent on the force F_{act} that the actuator is applying, and is given by the force–displacement curve for the thin-film

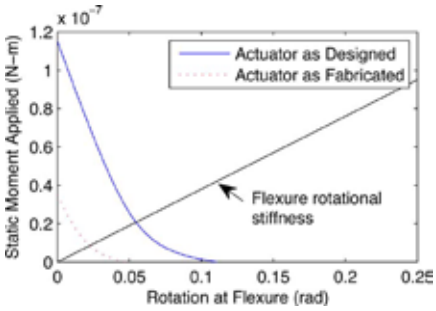

Fig. 5. Static applied actuator moment at 20 V versus rotation angle at silicon flexures, based on nominal actuator design and taking into account all fabrication limitations.

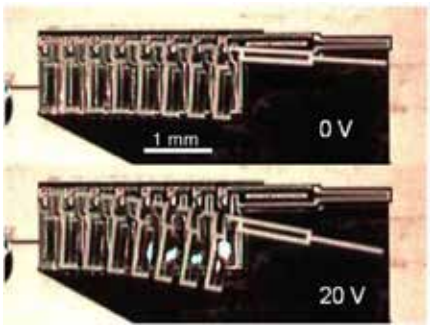

Fig. 6. Sample image of leg joint at 0 and 20 V.

piezoelectric actuators. The actuator tip displacement is also equal to displacement due to rotation of the leg link ($L_{\rm act}$ times rotation angle for the link to which it attached) plus any axial stretching in the tether x_t. A corresponding static rotation $\theta_{\max}(M)$ for each leg link can then be estimated from

$$\theta_{\max}(M_{\rm in}) = \frac{x_{\rm act}(F_{\rm act}) - x_t}{L_{\rm act}} \tag{3}$$

where x_t is given by

$$x_t = \frac{F_{\rm act} L_t}{E w_t t} \tag{4}$$

with L_t being the length of the tether and w_t is the tether width.

This rotation must match that of the flexures, such that the actual static rotation of each link occurs at the point, where the actuation moment as a function of rotation intersects the rotary stiffness curve of the flexures, as shown in Fig. 5. Had the actuators been functioning at full-nominal performance as discussed with respect to the force–displacement curve in Fig. 4, anticipated rotation angle of each link for a 20 V input was to be approximately 3° or 0.052 rad. At the reduced actuation capacity of the actuators as formed, we find rotation angles of approximately 1° or 0.021 rad per link, and 8° per leg joint. Experimentally, a rotation of 7.5° from the entire joint is observed at 20 V, with a sample rotary leg joint at 0 and 20 V shown in Fig. 6. Again, this reduction in displacement is primarily a result of underetching of silicon along the actuator length, and residual stress prestressing the actuator against the direction of desired motion.

B. Lumped-Parameter Dynamics

Although on–off input sequence optimization is ultimately performed using an identified model of system dynamics, an analytical model for joint dynamics is useful for both designing leg joint design and specifying reasonable sampling times and switching circuit parameters when implementing the on–off controller. While the large deflection leg joints consist of several flexures and rigid links in series, the small mass of the intermediate links allows actuator dynamics to be described with reasonable accuracy using a lumped-parameter second-order model, particularly for small displacement of approximately 10° or less, where small angle sine and cosine approximations are effective. The resulting second-order model has the form as follows:

$$J_{\rm tot}\ddot{\theta}_{\rm tot} + b_{\rm tot}\dot{\theta}_{\rm tot} + k_{\rm tot}\theta = Gu(t) \tag{5}$$

where $J_{\rm tot}$ is the total rotary inertia of the system, $b_{\rm tot}$ is a rotational damping coefficient, $k_{\rm tot}$ is the equivalent total spring stiffness, G is the equivalent actuation moment per volt, and $u(t)$ is the applied input voltage.

The input to the system is treated as constant when voltage is applied, taken as the moment applied by the actuator when the moment is zero, while the shape of the moment–rotation curve is accounted for in an equivalent stiffness of the actuator. As a result, $k_{\rm tot}$ is estimated from

$$k_{\rm tot} \approx \frac{k_\theta + k_{\rm act}}{N} \tag{6}$$

where N is the number of links in the joint, and $k_{\rm act}$ is an equivalent stiffness of a single actuator, taken from a linear fit of the moment–rotation curve shown in Fig. 5 over the range of anticipated link rotation.

The total inertia $J_{\rm tot}$ is calculated by treating the intermediate links as point masses m_L with the distance from the center of mass of ith link to the first flexure being $L_{L,i}$, and the total inertia of the final leg structure, incorporating both leg inertia $J_{\rm leg} = J_N$ and mass $m_{\rm leg} = m_N$

$$J_{\rm tot} \approx \sum_{i=1}^{N-1} m_L L_{L,i}^2 + J_N + m_N L_N^2 . \tag{7}$$

Damping coefficients in micromechanical systems are typically quite difficult to estimate. In the case of the piezoelectric leg joints modeled here, the leg and joint move just a few micrometers above the surface of the surrounding silicon wafer, or substrate, which would typically result in viscous drag being a significant source of damping. In addition, experimental system identification, described in following section, suggested that viscous drag might be a likely source of damping due to the similarity of experimental response to that of a second-order linear system. As a result, a basic estimate of damping coefficient was obtained by integrating the moment due to viscous drag between the underside of the joint and the wafer surface M_b, and equating it to an effective total damping coefficient $b_{\rm tot}$, using the integral

$$M_b = \int_0^{L_{N,\rm out}} \frac{\mu w(r) r}{g} (r\dot{\theta}) dr = b_{\rm tot}\dot{\theta} \tag{8}$$

TABLE II
VARIABLES FOR LUMPED-PARAMETER MODEL

Parameter	Label	Units	Value
Number of Links	N		8
Actuator Stiffness	k_{act}	μN/rad/s	0.55
Predicted Stiffness	k_{tot}	μN/rad/s	0.097
Link Mass	m_1-m_7	μg	1.1
Leg Mass	m_N	μg	1.7
Leg Inertia	J_N	μg-mm^2	15
Link 1 Distance	$L_{L,1}$	μm	220
Link 2 Distance	$L_{L,2}$	μm	440
⋮			⋮
Link 7 Distance	$L_{L,7}$	μm	1540
Link 8 (leg) Inner Radius	$L_{N,in}$	μm	1760
Link 8 (leg) CoM Distance	L_N	μm	2700
Link 8 (leg) Outer Radius	$L_{N,out}$	μm	4300
Predicted Inertia	J_{tot}	μg-mm^2	49
Viscosity	μ	mN-s/m^2	0.02
Leg width	w_{leg}	μm	90
Joint Gap to Substrate	g_i	μm	2-40
Predicted Damping	b_{tot}	μN-μm/rad/s	2-4

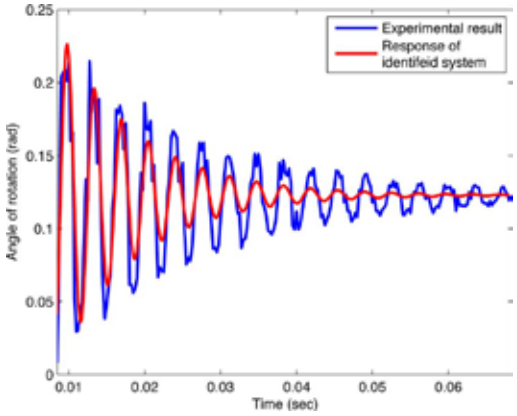

Fig. 7. Step response of the MEMS actuator, which was used for system identification.

where r is the radius from the base of the joint, $L_{N,\text{out}}$ is the outermost point on the joint and leg structure, μ is the dynamic viscosity of air, $w(r)$ is the width of the joint as a function of radius from the base, g is the gap between the underside of the leg and the ground, and $r\dot{\theta}$ is the approximate linear velocity of points along the leg. This type of drag depends heavily on the precise gap between each link in the joint and the substrate, and for a system of smaller links and one long leg link at the end is approximately equal to

$$b_{\text{tot}} \approx \sum_{i=1}^{N-1} \frac{\mu A_{L,i} L_{L,i}^2}{g_i} + \int_{L_{N,\text{in}}}^{L_{N,\text{out}}} \mu \frac{w_{\text{leg}} r^3}{3 g_N} \qquad (9)$$

where $A_{L,i}$ is the planar area of the ith link, g_i is the gap between the ith link and the ground, $L_{N,\text{in}}$ and $L_{N,\text{out}}$ are the distance from the first flexure to the inner and outer dimensions of the leg (the final, Nth link), and w_{leg} is the width of the leg. Unfortunately, the gaps g_i are difficult to predict, being dependent on residual stress in the completed legs, although it can be taken as having an approximately linear increase along the links, from approximately 0.5 μm at the first link to gaps between 0.5 and 40 μm at the leg link itself.

Values of the parameters used to predict system dynamics are shown in Table II. The estimated total spring stiffness and moment of inertia correspond to a natural frequency ω_n of approximately 1880 rad/s, and damping ratio between 2% and 20% depending on specific gap widths due to residual stress. These estimates are useful for both refining the design of future leg joints, and anticipating sampling and response time need for driving circuitry and controllers, in this case indicating sampling time for discretization on the order of 100 μs or less, and ideal switching-circuit response time, an order of magnitude or more smaller than that. Note also that sampling rate refers to the rate at which inputs may be changed, not any sensing measurements, as the system is run in open loop under the following control scheme in order to conserve energy. In practice, a 100 μs sampling rate was used for microscale actuator experiments, with the switching circuit described in the following having a response time of less than 2 μs.

C. Experimental System Identification

Exact system dynamics were measured experimentally using the step response of the completed leg joints. Joint motion was measured by filming the microscale leg joints through a stereoscope using a high-speed camera system. Images were collected at 4000 frames per second, and angle measurements in each frame were extracted using the MATLAB Image Processing Toolbox. The measured response and an identified second-order model response are shown in Fig. 7. The identified natural frequency was 1770 rad/s, while the identified damping ratio was 5.7%.

These identified parameters fit in well with the estimated response of the system, given uncertainties in MEMS processing accuracy, and indicate the utility of approximated lump-parameter modeling of the piezoelectric leg joints, although some nonlinearity in the system step response appears to be present, which is likely a result of nonlinear piezoelectric behavior (discussed in the following) and unmodeled damping effects, such as variation in gap between the joint and the substrate as the joint rotates; there is a slight upward deflection of the actuator (approximately 1–2°) due to residual stress in the thin films on the surface of the actuator. This, and etch holes remaining from the actuator fabrication process mean that the gap between the underside of the actuators and the substrate surface is not entirely constant, as is assumed to estimate the approximate linear damping coefficient. In particular, the gap between joint and substrate is larger at the deflected position, leading to a lower effective damping coefficient near the final position than the initial position during a step displacement.

In addition, changes in system parameters with environmental conditions, and hysteresis of piezoelectric materials can cause the real system to deviate from models used for controller development. For example, the deflection of the piezoelectric actuators is sensitive to temperature, and there is also a modest hysteresis in the piezoelectric actuators, as shown in Fig. 16. We will discuss methods of improving robustness of the actuator response under open loop on–off control when uncertainty is present in controller design. Namely, we treat the stiffness and damping of the system as having approximately 10% uncertainty

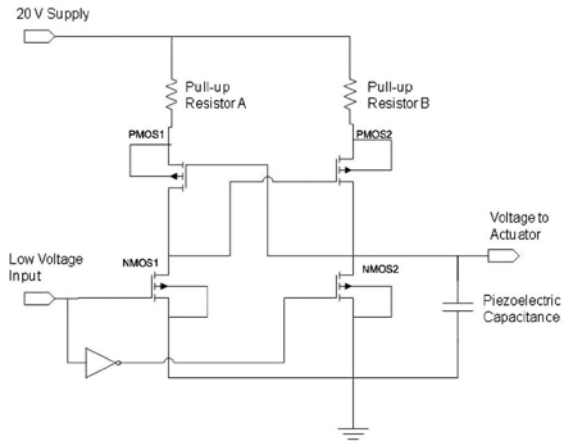

Fig. 8. Switching drive circuit with pull-up resistors to limit leakage current.

due to nonlinearities, hysteresis, or environmental changes and attempt to minimize worst-case error in final position under this uncertainty. These uncertainty bounds may be increased if larger variation is anticipated, but with corresponding reduction in accuracy; systems subject to large parameter variation would require some use of feedback if improved accuracy is required, although this would increase total actuator power consumption.

III. Drive Circuit Design and Testing

A. Circuit Design

To limit switching losses in the interface between a low-voltage controller and the comparatively high-voltage actuators, a low power on–off switching circuit was designed to interface the two elements. As this interface can cause a significant portion of the switching energy losses for microscale actuators, it is important to be able to predict and measure these losses for incorporation into controller design, as well as to improve performance of the overall system.

The on–off switching circuit designed for the thin-film piezoelectric actuators consists of a CMOS inverter with a level shifter. CMOS inverters are a commonly used switching circuit configuration in the integrated circuit design area for reducing power consumption because in the ideal case, there is no static current and power is consumed only at the "on" or "off" transition time. However, a CMOS inverter alone cannot be used directly for driving piezoelectric actuators. While a piezoelectric actuator should be driven at 20 to 30 V or more, most IC circuits, as are typically used to implement a control law, operate at 5, 3.3 V, or less. Therefore, a level shifter based on the CMOS inverter was designed to interface between a high voltage and a conventional IC process [23]. In order to reduce the power consumption of the circuit, two resistors are added to the basic-level shifter. The conceptual circuit is shown in Fig. 8.

The novel addition of these resistors to the inverter helps to reduce peak leakage current during the switching transitions. While this loss is typically of little consequence when using larger actuators, it can be a substantial portion of energy consumption when working with microscale piezoelectric actuators having comparatively small capacitance. The total energy consumption $E_{\rm tot}$ due to the circuit alone for a single cycle (charging and discharging of the actuator) can be derived from the energy consumed by transistor capacitance E_{C_m} and the energy consumed in leakage through the right and left sides of the bridge upon switching E_A and E_B

$$E_{\rm tot} = E_{C_m} + E_A + E_B \tag{10}$$

with the respective powers being calculated from

$$E_{C_m} = 2C_m U_{\rm low}^2 \tag{11}$$

$$E_A = \frac{(C_L + C_m)\,(U_{\max} - V_{\rm tp} - V_{\rm tp}\log(U_{\max}/V_{\rm tp}))}{K_g} U_{\max} + \frac{(U_{\max} - V_{\rm tp}) R_1 C_m V_{\rm tn}}{K R_2 V_{\rm tn}} \tag{12}$$

$$E_B = \frac{C_m\,(U_{\max} - V_{\rm tp} - V_{\rm tp}\log\,(U_{\max}/V_{\rm tp}))}{K_g} U_{\max} + \frac{(u_{\max} - V_{\rm tp}) R_1 C_m V_{\rm tn}}{K R_2 V_{\rm tn}} \tag{13}$$

assuming that the low voltage achieved by the switching circuit is zero, and where C_m is the capacitance of the MOSFET transistors, $U_{\rm low}$ is the low-voltage input level of the controller, $U_{\max}$ is the high-voltage "on" voltage to the actuators, $V_{\rm tp}$ is the threshold voltage of the PMOS transistor in the circuit, $V_{\rm tn}$ is the threshold voltage of the NMOS transistor in the circuit, R_1 is the pull-up resistor resistance on the low-voltage CMOS inverter, R_2 is the pull-up resistor resistance of the high-voltage CMOS inverter, C_L is the load capacitance of the piezoelectric actuators, and K_g is the gain coefficient of the transistors.

The piezoelectric joints have a total capacitance of approximately 1.1 nF, while the transistors utilized had threshold voltages of 1 V, capacitance of 0.23 nF, and gain coefficient of 1.99. Pull-up resistors of 100 and 1000 Ω, respectively, were used to balance response time of the circuit with low-power consumption, while using readily available surface mount resistors. These parameters correspond to a projected energy consumption of the circuit alone of 1.02 μJ per charge and discharge cycle, with 0.84 μJ lost due to leakage current and the remainder due to capacitive loading of the CMOS transistors' gate capacitance.

IV. Controller Design

A. System Dynamics and Constraints

As described earlier, the dynamics of the single leg are modeled as a second-order linear system, which can be discretized and represented in state space form as follows:

$$x\left((k+1)T_s\right) = A_d x(kT_s) + B_d u_k \tag{14}$$

$$y(kT_s) = C_d x(kT_s) \tag{15}$$

where the states of the system are the angle of rotation ($\theta_{\rm tot}$) and the angular velocity ($\dot{\theta}_{\rm tot}$) of the leg. The discrete time state matrix is A_d, input matrix is B_d, and output matrix is C_d. There are two important constraints on the system when using on–off control. The first is that the inputs $u_k, k = 1, 2, \ldots, n$

can take only two values, namely $\{0, 1\}$. Second, the transitions between input values can take place only at the sampling instants, meaning u_k can change its value only at these times. These constraints limit the reachable subspace of the system in a given time duration.

B. Problem Statement and Optimization Procedure

The unavailability of feedback and aforementioned input constraints limits the capabilities of this system. So, the limited objective of a controller is to make the leg joint rotate to a desired angle and stay stationary at least instantaneously at the end of a desired time, which will enable the robot to walk in a quasi-static manner.

Mathematically, then, the aim here is to find a sequence of inputs $u_k, k = 1, 2, \ldots, n$, which, if a solution exists, will move the states of the system from a specified set of initial states to an ϵ ball containing a set of desired final states x_d in a given time $t_f = nT_s$ (which limits the possible number of transitions between the input states), using minimum energy. The final-state constraints can be written mathematically as $x_d - \epsilon \leq x(t_f) \leq x_d + \epsilon$.

Our objective function is then to minimize energy consumption, while satisfying the aforementioned constraints. Energy consumption consists of two parts J_C and J_R, corresponding to capacitive and resistive energy losses in the system, respectively. The piezoelectric actuator acts as a capacitor in an electric circuit. Hence, the major part of the energy loss happens when actuators are charged or discharged. This corresponds to a transition of u_k from 0 to 1 or *vice versa*. This energy loss is termed as capacitative loss or J_C. In a general on–off control case, the quantity $CU_{\max}^2/2$ can be replaced by an arbitrary "cost-to-switch"

$$J_C = \sum_{k=1}^{n} \frac{1}{2} C U_{\max}^2 ((u_k - u_{k-1})^2 + u_0^2) \tag{16}$$

where C is the capacitance of the piezoelectric actuator and $U_{\max}$ is the 'on' voltage applied to the actuators.

The second part of the objective function J_R includes energy lost to resistive dissipation due to leakage current in the on–off drive circuit or through the piezoelectric actuator, and is given by

$$J_R = \sum_{k=0}^{n} \frac{U_{\max}^2}{R} T_s u_k \tag{17}$$

where R is the resistance of the system. In other words, this is the energy required for keeping u_k at 1. Again, here the quantity $U_{\max}^2/R$ can be generalized to an arbitrary "cost-to-hold."

The optimization problem is to minimize the total energy cost $J = J_C + J_R$ subjected to state-dynamics constraints (n constraints), binary constraints, and final-state constraints given earlier. Since the final state is the only point of interest here, the state dynamics can be calculated outside the optimization (18) and can be combined to the final-state constraints

$$x(t_f) = x(nt_s) = \sum_{i=0}^{n-1} A_d^{n-i-1} B_d u_i. \tag{18}$$

TABLE III
NOMINAL VALUES FOR THE PARAMETERS USED FOR THE DESIGN OF OPTIMAL SEQUENCES FOR THE SYSTEMS

Parameters	Simulation Model	Macro System	MEMS Leg Joint
R (Ω)	$3 * 10^9$	$3 * 10^9$	$3 * 10^9$
C (F)	$1 * 10^{-9}$	$1 * 10^{-9}$	$1 * 10^{-9}$
$U_{max}(V)$	20	20	20
J ($kg.m2$)	$1.4 * 10^{-12}$	1	1.4×10^{-12}
b ($N.m.s/rad$)	$3.4 * 10{-}11$	14	2.7×10^{-10}
k ($N.m/rad$)	$3.2 * 10{-}6$	40350	4.4×10^{-6}
G ($N.m/V$)	$8 * 10^{-8}$	64151	2.8×10^{-8}
Sampling time (T_s)(sec)	0.0001	0.001	0.0001

Now, the final-state constraints take the form

$$x_d - \epsilon \leq \sum_{i=0}^{n-1} K_i u_i \leq x_d + \epsilon \tag{19}$$

where

$$K_i = A_d^{n-i-1} B_d.$$

The total energy consumption can be rewritten as follows:

$$\begin{aligned} J &= J_C + J_R \\ &= \sum_{k=1}^{n} \frac{1}{2} C U_{\max}^2 ((u_k - u_{k-1})^2 + u_0^2) + \sum_{k=0}^{n} \frac{U_{\max}^2}{R} T_s u_k. \end{aligned} \tag{20}$$

Now, this problem is a binary programming problem with a quadratic objective function (20) and a system of linear constraints (19). Hence, it can be modeled directly in dynamic programming software such as A Mathematical Programming Language (AMPL) and solved using the integer-programming solver CPLEX, which uses the branch and bound technique to integer programming.The parameter values used for optimization are given in Table III.

C. Modification to Find a Robust Sequence

Uncertainty in the inertia, damping and stiffness estimates (either from analytical or experimental methods) affects the performance of the system, as does variation in actuator behavior due to environmental changes. It is useful to minimize the error for the worst-case system with a bounded uncertainty Δ_{bound}. This is a minimax problem, which can be represented as the following:

$$\min_u \{\max_{\Delta} \|x_1 - x_{1n}\|\}, \ \|\Delta\| \leq \Delta_{\text{bound}}. \tag{21}$$

Since the direct solution of this is numerically infeasible, the algorithm given in Fig. 9 and described in the following was developed to find an input sequence that gives a satisfactory performance.

Two optimization techniques are employed here. Continuous nonlinear optimization for determining the worst-case systems (Δ values) and binary programming for finding the best robust input sequence. In this particular problem, three parameter uncertainties are considered, namely Δ_m, Δ_b, and Δ_k

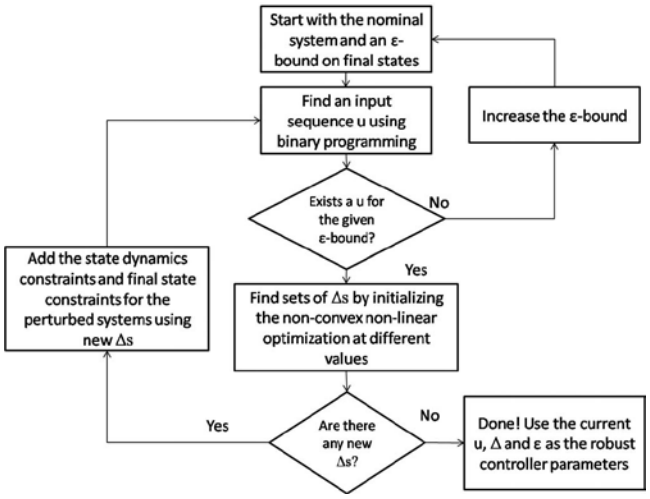

Fig. 9. Robust sequence algorithm.

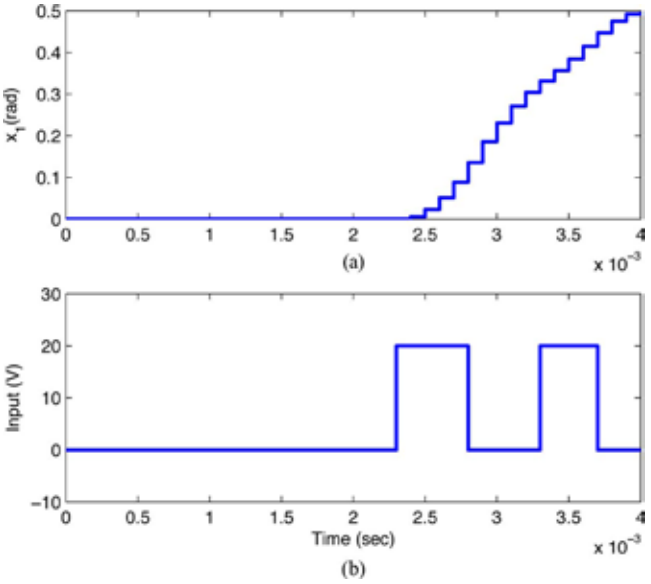

Fig. 10. Sample simulated system output using optimal on–off controller with loose positioning constraint, showing (a) output angle and (b) system input u.

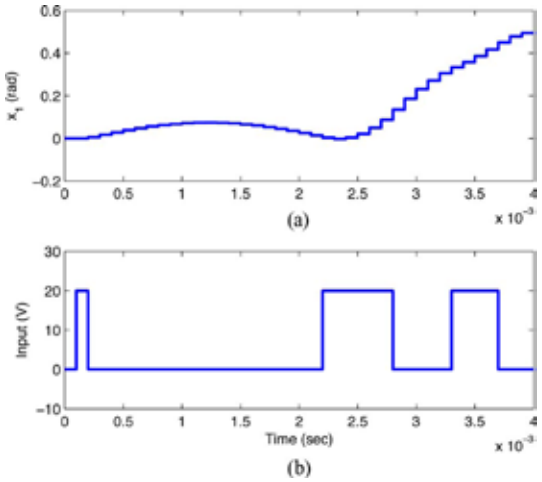

Fig. 11. Sample system output using optimal on–off controller with strict positioning constraint, showing (a) output angle and (b) system input u.

corresponding to uncertainties in inertia, damping, and stiffness. It is assumed that these uncertainties are bounded on either sides. But, the maximization of error with respect to the Δs is not a convex optimization. Hence, the optimization was initialized at a number of values and the corresponding worst-case system for each was found. For the procedure, let $(A_1, B_1), (A_2, B_2), \ldots, (A_m, B_m)$ be the dynamics of each of the worst-case systems obtained by the maximization. Then, the final-state constraints for all m systems are added to the binary programming to find the robust u as follows:

$$x_d - \epsilon \leq \sum_{i=0}^{n-1} A_1^{n-i-1} B_1 u_i \leq x_d + \epsilon$$

$$x_d - \epsilon \leq \sum_{i=0}^{n-1} A_2^{n-i-1} B_2 u_i \leq x_d + \epsilon$$

$$\vdots$$

$$x_d - \epsilon \leq \sum_{i=0}^{n-1} A_m^{n-i-1} B_m u_i \leq x_d + \epsilon. \qquad (22)$$

These constraint equations help the designer to identify a specific input sequence u such that if it exists, it will keep the final states of all the aforementioned systems within some ϵ neighborhood of the desired final state.

V. Simulation Results

$$J\ddot{\theta} + b\dot{\theta} + k\theta = Gu. \qquad (23)$$

The system given in (23) and the corresponding parameters are given in Table III was used for initial simulational study. A couple of sample system responses using the minimal energy open-loop on–off optimal controller is given in Figs. 10 and 11. In these examples, a single leg link is driven to a desired final angle. When only a single leg link is to be controlled, the control input can be quite simple, as in the example shown. In Fig. 10, the input switches twice and when the constraints on states are stringent the controller needed three switches, as shown in Fig. 11, which corresponds to a cheaper controller or higher state cost as in linear-quadratic Gaussian (LQG) controller terminology. To explore controller behavior, this on–off controller was compared to the LQG controller for the system, had feedback and analog rather than on–off inputs been available. Two LQG responses corresponding to cheap and expensive controllers are given in Figs. 12 and 13. Both the on/off and LQG controllers produce qualitatively similar trajectories from the initial to the final value. In addition, the capacitative portion of the cost functions from the respective controllers is found to be less for the optimal on–off controller, due to the minimal number of transitions that it dictates. The PZT actuators used in the prototype system have very large resistance, such that over 99% of energy

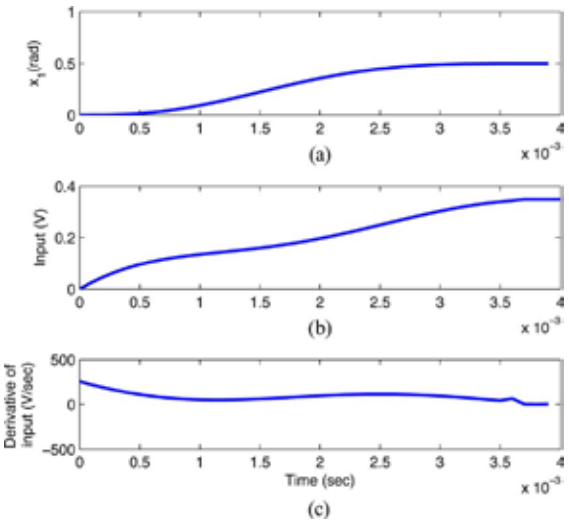

Fig. 12. Simulated LQG response with a cheap controller, analogous to strict positioning constraint, showing (a) output angle, (b) system input u, and (c) derivative of input.

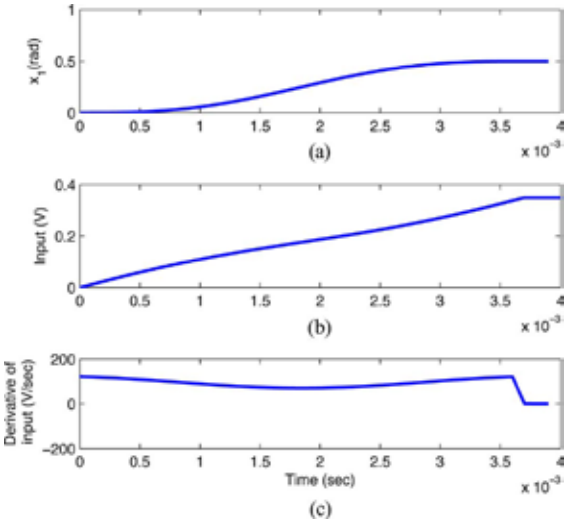

Fig. 13. Simulated LQG response with an expensive controller, analogous to a loose positioning constraint, showing (a) output angle, (b) system input u, and (c) derivative of input.

use is due to capacitive switching losses, as opposed to resistive holding losses.

The following studies are done to make sure that the optimization is indeed optimal and it can perform effectively in the presence of uncertainty in the system parameters or disturbances.

A. Comparison to Brute Force Methods

To ensure that the optimization method is working properly, the result of the efficient optimization method was compared with that of brute force optimization for a shorter time period. In the brute force method, all possible combinations of $u_i's$ were checked for feasibility and that with lowest cost, measured by the on–off cost function, was selected. This approach is, of course, numerically inefficient, as one must check the cost for

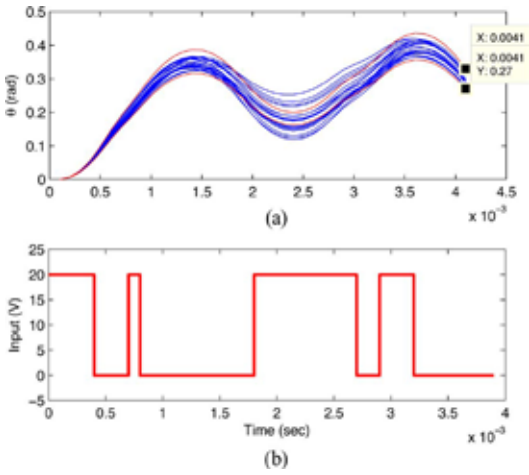

Fig. 14. (a) Response of the perturbed systems when a robust sequence is applied; the red lines show the worst case systems. (b) Corresponding robust on–off sequence.

2^n combinations of input, making it impractical for a larger time period. However, it is possible to verify that for our sample system, the result of the brute force method matches the result obtained by the branch and bound optimization method, which is computationally much more efficient. Over the shorter time period analyzed, the optimal control sequence identified by integer programming exactly matched the best of all possible control sequences tested through the brute force method.

B. Robustness Analysis Results

From the simulations, it was found that if the parameter variation (in all parameters) is within 10% of the nominal value for the sample system, then it was possible to find an on–off sequence, which keeps the final state within 10% of the desired final state. This range of parameter uncertainty is sufficient to account for hysteresis in the piezoelectric response, variation in the damping coefficient during leg motion, and potential change in piezoelectric properties over an approximately 10°C range. Examples of perturbed systems are shown in Fig. 14. When the parameter variations are kept within $\pm 10\%$ of nominal values, the final states of the randomly perturbed system are within $\pm 10\%$ of the nominal value, 0.3 ± 0.03, and this was consistent over the situations we examined.

C. Behavior of the System in the Presence of Disturbance

A natural limitation of open-loop control is its inability to reject disturbances. Additional simulation studies were performed to explore the sensitivity of the leg joint under open-loop on–off control to disturbances. While an external force is difficult to apply to the experimental system due to its small size, simulated behavior of the system in the presence of various disturbance, such as due to gravity when the system is tilted, friction forces or electrostatic forces, can be examined. In the sample simulation result shown, ideal dynamic friction between the leg and the ground was considered as a disturbance. A normal force between leg and ground of 5 mN and coefficient of dynamic

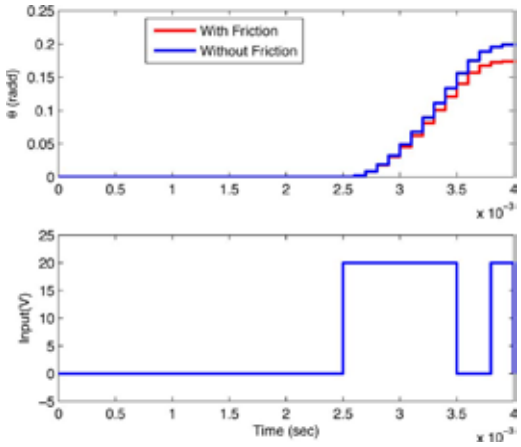

Fig. 15. Comparison between the nominal response and response in the presence of ideal friction.

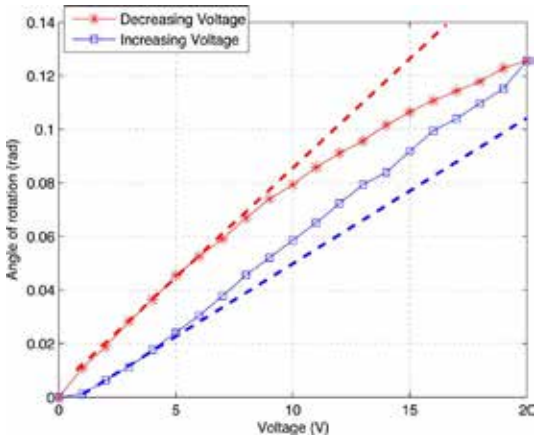

Fig. 16. Hysteresis curve for the MEMS actuator with the dotted lines showing the variation in slope.

friction of 0.3 were assumed to be present. The deviation in response from the nominal response of the simulated system is shown in Fig. 15, with an approximately 15% reduction in displacement. As this normal force is much larger than the payload capacity of the leg (5–50 mg, corresponding to approximately 0.5 mN) and much larger than electrostatic forces operating over the displacement range of the leg, there is reason to believe that disturbance forces that would not cause damage to the leg joint result in comparatively small errors. This is primarily a consequence of the large forces for this scale generated by the thin-film piezoelectric actuators. On the other hand, because there is no feedback available, the system has limited capacity to perform a disturbance rejection to reduce this positioning error. When energy constraints are so strict as to preclude sensor use, as may be the case for a microrobot, the additional positioning error must be accepted. However, if occasional sensor measurements can be made, it may be possible to adapt the input on–off sequence over multiple movements, or to switch between optimized on–off sequences if a disturbance is detected, in order to respond to disturbances or environmental changes.

VI. Experimental Results

A. Experimental System Description

Experimental testing of the on–off control algorithm was tested on both a macroscale piezoelectric test actuator and the prototype MEMS leg joint. Before conducting the experiments on the MEMS actuator, the control scheme was tested on a macroscale piezoelectric actuator to verify the controller design procedure. The macroscale actuator was a 40-mm-long, 10-mm-wide Ceratec, Inc. bimorph actuator with a strain gauge attached to it for measuring the deflection in terms of the voltage through its sensing circuitry. The on–off switching sequence was loaded into a TMS320F28335 microprocessor, which was interfaced to the bimorph actuator through the fast-switching circuit explained in the previous section. The output voltage was measured using a Tektronix TDS2024B oscilloscope and data was captured using National Instruments Signal Express Tektronix Edition Software. From the step response of the system, the following second-order system given was identified between input voltage and strain gauge voltage:

$$\frac{y(s)}{u(s)} = \frac{64151}{s^2 + 14s + 40350}. \tag{24}$$

The MEMS actuator was also operated using the microprocessor and the switching circuit. Prototype joint arrays were connected to the switching circuit using ultrasonic wire bonding to bond pads at the base of the actuator, on the fixed portion of the substrate. The switching circuit was driven by the microprocessor or a function generator, as appropriate. The motion of the leg was captured using a high-speed camera at 4000 frames per second and the angle of rotation was measured using the MATLAB Image Processing Toolbox. Using the step response given in Fig. 7, a second-order system was identified between the input voltage and the angle of rotation (radians)

$$\frac{y(s)}{u(s)} = \frac{1.9656 \times 10^4}{s^2 + 2 \times 0.0547 \times 1766.4s + 1766.4^2}. \tag{25}$$

To measure hysteresis, a static input voltage was varied from 0 to 20 V and back, giving the hysteresis plot in Fig. 16. This hysteresis effect is included as an uncertainty in stiffness for designing a robust sequence, which is used in the experimental result discussed in the next section.

B. Comparison of Experimental and Simulation Results

A comparison of the responses from the macro system is shown in Fig. 17. The optimization constraint on final output in this example was to reach 0.5 ± 0.1 V in strain gage output at 20 ms. A binary optimization was done on the identified macro system given in (24) to obtain the input sequence shown in Fig. 17(b) and the constraints are verified using the MATLAB simulation shown. The same input sequence was applied on the macro system and is shown in Fig. 17(a). The experimental response follows very closely with the simulation and reaches 0.58 V at the desired time.

A similar approach with additional robustness constraints to account for hysteresis effects was applied to the MEMS actuator given in (25). In the optimization, the constraints were

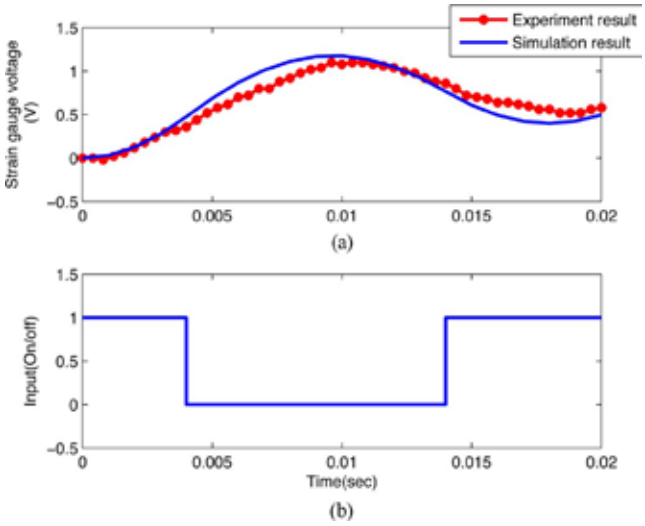

Fig. 17. Comparison of results obtained by experiment and simulation for the macroscale system and the corresponding switching sequence.

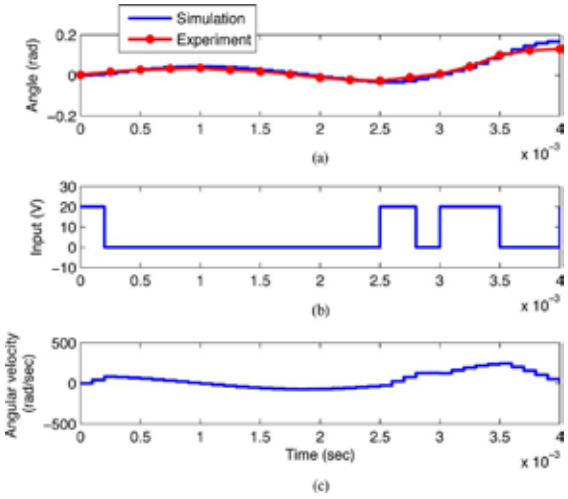

Fig. 18. (a) Comparison of displacement results obtained by experiment and simulation for the MEMS system when under an optimal on–off sequence for 0.15 rad final displacement. (b) On–off voltage input applied. (c) Angular velocity observed in the simulation, showing successful return to 0 rad/s at final time.

applied on both angle of rotation as well as angular velocity at 4 ms for all the perturbed systems with stiffness varying between $k_{\min} = 127.906$ V/rad to $k_{\max} = 190.476$ V/rad, which is about $\pm 20\%$ of the nominal value $k_{\text{nominal}} = 158.73$ V/rad. The requirement was to make the angle of rotation reach 0.15 ± 0.03 rad and angular velocity reach 0 ± 1 rad/s. From the optimization, it was found out that the minimum possible tolerance on angle is ± 0.03 rad because of the 20% uncertainty in the stiffness value. The input sequence and simulation responses shown in Fig. 18 were obtained as a result, which satisfies all the constraints in the simulation. When the same sequence was applied on the physical system, the response shown with a red line was obtained. The experimental result follows the simulation result closely and reaches about 0.1115 rad at the stipulated time, which is very close to the expectation from the simulation (misses the constraint by 0.0085 rad). Also, the direction of rotation reverses in the same video frame, indicating that the angular velocity goes through zero verifying the final-velocity constraint. The discrepancies between the experimental and desired motions are a result of nonlinearity of the actual system, particularly hysteresis in the piezoelectric film. The robust design approach aids in ensuring states are near desired final values even in the presence of model error, but does not ensure any particular accuracy at intermediate times.

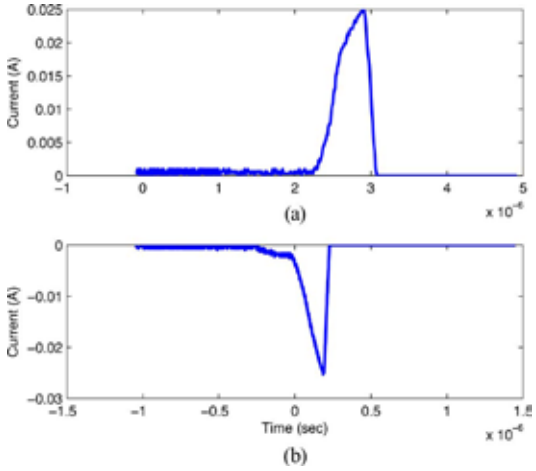

Fig. 19. Current consumption of switching circuitry and the MEMS actuator while the switch is (a) turned on and (b) turned off.

During this experiment, the cumulative energy consumption of the microrobotic leg together with the switching circuitry was also measured. The current profiles, while the switch was turned "on" and "off" were measured using a current probe and oscilloscope and are shown in Fig. 19. The power supply was kept constant at 20 V during the entire experiment and each turning "on" cost 4.6×10^{-7} J and each turning "off" consumed 1.4×10^{-7} J. Of this quantity, 2.2×10^{-7} J is attributed to charging at the microactuator, resulting in total energy loss in the circuit alone of just 3.8×10^{-7} J per cycle (the difference between total "on" and "off" energy usage and the energy required to charge the piezoelectric capacitance). This is smaller than the predicted energy usage, which appears to be due to additional resistance within the leg between electrodes for the leg and the piezoelectric actuators; the extra resistance further increases the effect of the pull-up resistors included in the circuit design. Total power consumption of a robot using this controller would depend on step frequency, but for walking gates of 20 Hz or lower, power consumption would be in the tens of microwatts or smaller. This is within the power availability we predict for a microrobot based on piezoelectric actuators, and much smaller than power consumption of an analog controller or PWM controller with much higher switching frequencies.

VII. Discussion

Although the optimal control method discussed earlier can be extended to include feedback by using a model predictive control approach, the use of open-loop on–off control to

regulate the motion of a piezoelectric actuator is driven entirely by the need to ensure extremely low-power consumption from the entirety of a servo control system. This results in significant tradeoffs in performance for the sake of power reduction. The simple switching interface between controller and actuators, and small number of transitions utilized, allows for control of microactuators that act primarily as a capacitive load with very little energy consumption, less than a microjoule per leg motion. However, such a controller explicitly forgoes the use of feedback to improve response time, robustness, or other closed-loop controller benefits due to power limitations, and the relatively low-switching frequency results in oscillatory output motions with specific desired output states being achieved only at a specific time. In addition, switching controllers may often excite high-frequency dynamics, though this is not a large effect in the experimental test actuators examined here. If present, higher order dynamics may be incorporated into the optimization procedure described here by expanding the system order, but the controller will only act to ensure that these dynamics do not influence behavior at the final time, not to avoid vibration or oscillation at intermediate transitions.

The open-loop, on–off control strategy presented here functions best when the system model is well known, and disturbances or uncertainty in modeling have known and bounded magnitudes. For example, in the MEMS application discussed here, analytical modeling of the piezoelectric rotational joint being controlled is useful in initial actuator design and setting up controller parameters. It may be used to identify necessary sampling periods and on–off drive circuit response times as well as ranges of probable system parameters (such as spring stiffness or damping). However, the accuracy of analytical models is limited by variation in fabrication processes that is difficult to predict before the actuator is completed. For instance, underetching of the silicon layer beneath individual actuators and residual stress in the thin-film piezoelectric and gold layers forming the actuators results in a significant reduction in joint displacement from its ideal performance. In addition, uncertainty in exact etch progress and light upward tilt of the entire joint causes viscous drag on the leg joints to vary over the course of motion, with resulting nonlinear deviations in damping coefficient. Once a leg joint is in use, an experimentally identified model is best used for final controller design. Even so, the on–off controller has no direct ability to adjust to variations in the plant due to environmental changes or external disturbances. It may only be designed, as described in this paper, to minimize error over a range of potential variations and disturbances.

Nonetheless, on–off switching control has a tremendous advantage in terms of power consumption, as switching an on–off signal at select time points requires much less power than analog drive circuitry or high-frequency PWM inputs. Because of its very small energy usage, this controller could provide useful baseline control for autonomous microrobotics. On–off control with a desired final time is especially well suited to quasi-static walking, with multiple legs driven through coordinated motions over a specified time, at which legs in contact with the ground are raised and raised legs lowered for the next step, and absolute precision of an individual leg is not as important as assured forward progress. In such an application, total inertia of the system would be much larger than that of the leg alone, while damping in the system will depend on the geometry of the body and feet as well as legs. In practice, the environment and loads on the robot may change dramatically, requiring some level of adaptation or feedback. A variety of optimized on–off sequences under different load conditions may be stored for use, or the optimal on–off sequence may serve to initiate adaptive control using only occasional or very low frequency sensor feedback to make modest adjustments to the input sequence, while keeping power consumption low.

VIII. Conclusion

The chief conclusions of this paper, then, are based on the idea that while thin-film piezoelectric actuation may one day enable unique mobility capabilities from microscale autonomous robots, achieving directed appendage movements will require aggressive reduction in power consumption throughout the servo control system. In this paper, we focus on modeling leg dynamics and reducing power consumption by the actuators and in the drive circuit interfacing low-voltage control electronics with a high-voltage actuator supply. In particular, we introduce a simple optimization method for achieving minimum energy on–off control when switching costs are substantial. We have applied the control algorithm to both a macroscale piezoelectric test bed and to prototype microrobotic leg joints, successfully directing the states of the systems to desired target values. In addition, with use of an inverter circuit specifically designed for low-power operation, we can limit leakage current while driving the actuators and obtain our desired motions with just a few microjoules per leg step, within the predicted energy and power limitations of future microrobotic platforms, and well below more conventional control implementations. Controlled motions are completed successfully with better than 10% positioning accuracy given a linear model, and better than 15% in simulation against a disturbance forces greater than 1 mN, and thus, larger than we would expect the actuator to face. However, further improvements in accuracy are difficult given the ultralow power open-loop strategy, such that further robustness to parameter variation or disturbances would require a true feedback implementation, and thus, increased servo system power.

Acknowledgment

The authors would like to thank R. Piekarz, J. Martin, B. Power, and R. Rudy at the U.S. Army Research Laboratory for their expertise in fabrication of the MEMS actuators.

References

[1] T. M. Ebefors, U. Johan, E. Kälvesten, and G. Stemme, "A walking silicon micro-robot," in *Proc. 10th Int. Conf. Solid-State Sens. Actuators*, Sendai, Japan, 1999, pp. 1202–1205.

[2] A. Bonvilain and N. Chaillet, "Microfabricated thermally actuated microrobots," in *Proc. IEEE Int. Conf. Robot. Autom.*, Taipei, Taiwan, 2003, pp. 2960–2965.

[3] M. H. Mohhebi, M. L. Terry, K. F. Böhringer, G. T. A. Kovacs, and J. W. Suh, "Omnidirectional walking microrobot realized by thermal microactuator arrays," in *Proc. ASME Int. Mech. Eng. Congr.*, New York, NY, 2001, pp. 1–7.

[4] S. Hollar, A. Flynn, C. Bellow, and K. S. J. Pister, "Solar powered 10 mg silicon robot," in *Proc. MEMS 2003*, Kyoto, Japan, pp. 706–711.
[5] B. R. Donald, G. G. Levy, C. D. McGray, I. Papotry, and D. Rus, "An untethered electrostatic, globally controllable MEMS micro-robot," *J. Microelectromech. Syst.*, vol. 15, no. 1, pp. 1–15, Feb. 2006.
[6] R. J. Linderman and V. M. Bright, "Nanometer precision positioning robots utilizing optimized scratch drive actuators," *Sens. Actuators A, Phys.*, vol. A91, no. 3, pp. 292–300, Jul. 2001.
[7] K. Oldham, J. Pulskamp, R. Polcawich, and M. Dubey, "Thin-film PZT actuators with extended stroke," *J. Microelectromech. Syst.*, vol. 17, no. 4, pp. 890–899, Aug. 2008.
[8] K. Oldham, J. Pulskamp, R. Polcawich, P. Ranade, and M. Dubey, "Thin-film piezoelectric actuators for bio-inspired micro-robotic applications," *Integr. Ferroelectr.*, vol. 95, no. 1, pp. 54–65, 2007.
[9] J. S. Pulskamp, R. G. Polcawich, and K. Oldham, "Millimeter-scale robotics research at the Army Research Laboratory," presented at the ASME Int. Des. Eng. Tech. Conf. Micro- Nano-Syst., San Diego, CA, Sep. 2009.
[10] W. C. West, J. F. Whitacre, E. J. Brandon, and B. V. Ratnakuma, "Lithium micro-battery development at the Jet Propulsion Laboratory," *IEEE Aerosp. Electron. Syst. Mag.*, vol. 16, no. 8, pp. 31–33, Aug. 2001.
[11] J. B. Lee, Z. Chen, M. G. Allen, A. Rohatci, and R. Arya, "A miniaturized high-voltage solar cell array as an electrostatic MEMS power supply," *J. Microelectromech. Syst.*, vol. 4, no. 3, pp. 102–108, Sep. 1995.
[12] M. Sitti, "Piezoelectrically actuated four-bar mechanism with two flexible links for micromechanical insect thorax," *IEEE/ASME Trans. Mechatronics*, vol. 8, no. 1, pp. 26–36, Mar. 2003.
[13] E. Steltz and R. S. Fearing, "Dynamometer power output measurements of miniature piezoelectric actuators," *IEEE/ASME Trans. Mechatronics*, vol. 14, no. 1, pp. 21–31, Feb. 2009.
[14] J. A. Main, D. V. Newton, L. Massengill, and E. Garcia, "Efficient power amplifiers for piezoelectric applications," *Smart Mater. Struct.*, vol. 5, no. 3, pp. 766–775, 1996.
[15] D. Campolo, M. Sitti, and R. S. Fearing, "Efficient charge recovery method for driving piezoelectric actuators with quasi-square waves," *IEEE Trans. Ultrason., Ferroelectr., Frequecy Control*, vol. 50, no. 3, pp. 237–244, Mar. 2003.
[16] P. Galambos, D. Czaplewski, R. Givler, K. Pohl, D. L. Luck, G. Benavides, and B. Jokiel, "Drop ejection utilizing sideways actuation of a mems piston," *Sens. Actuators A*, vol. 141, pp. 182–191, 2008.
[17] D. A. Horsley, W. O. Davis, K. J. Hogan, M. R. Hart, E. C. Ying, M. Chaparala, B. Behin, M. J. Daneman, and M. H. Kiang, "Optical and mechanical performance of a novel magnetically actuated MEMS-based optical switch," *J. Microelectromech. Syst.*, vol. 14, no. 2, pp. 274–284, Apr. 2005.
[18] C. Y. Kaya and J. L. Noakes, "Computational method for time-optimal switching control," *J. Optim. Theory Appl.*, vol. 117, no. 1, pp. 69–92, Apr. 2003.
[19] W. Singhose, T. Singh, and T. W. Seering, "On-Off control of flexible spacecraft with specified fuel usage," in *Proc. Amer. Control Conf.*, 1997, pp. 2308–2312.
[20] B. J. Driessen, "On-off minimum-time control with limited fuel usage: Near global optima via linear programming," in *Proc. Amer. Control Conf.*, 2000, pp. 3875–3877.
[21] A. Bemporad and N. Girogetti, "A SAT-based hybrid solver for optimal control of hybrid systems," *Lect. Notes Comput. Sci.*, vol. 2993, pp. 126–141, 2004.
[22] M. S. Branicky, V. S. Borkar, and S. K. Mitter, "A unified framework for hybrid control: Model and optimal control theory," *IEEE Trans. Autom. Control*, vol. 43, no. 1, pp. 31–45, Jan. 1998.
[23] P. H. Saul, K. M. Brunson, and R. J. T. Brunyan, "Versatile high voltage level shift and driver for MEMS applications," *Electron. Lett.*, vol. 39, no. 2, pp. 185–186, 2003.

Biju Edamana received the B.Tech. degree in mechanical engineering from the National Institute of Technology, Calicut, India, in 2004, and the M.S. degree in mechanical engineering from the University of Michigan, Ann Arbor, MI, in 2008, where he is currently working toward the Ph.D. degree.

His current research interests include developing low-energy control strategies for microrobotics, under development in the Vibrations and Acoustics Laboratory, University of Michigan.

Bongsu Hahn received the B.S. degree in mechanical engineering from Yeungnam University, Gyeongsan, Korea, in 1999, and the M.S. degree in mechatronics engineering from Gwangju Institute of Science and Technology, Gwangju, Korea, in 2002.

From 2002 to 2007, he was a Researcher with the Actuation and Control Team for Missile Guidance, Agency for Defense Development, Korea. Since 2007, he has been with the Vibration and Acoustic Laboratory: Microsystems, University of Michigan, Ann Arbor. His current research interests include low-power switching control for microdevices, coordinating highly efficient voltage conversion, and adaptive control.

Jeffrey S. Pulskamp received the B.S. degree in mechanical engineering from the University of Maryland, College Park, in 2000.

He is currently MEMS Design and Mechanical Engineer with the Micro and Nanomaterials and Devices Branch, U.S. Army Research Laboratory, Adelphi, MD. He holds six patents related to piezoelectric MEMS devices. His current research interests include tunable MEMS resonators/filters for secure communication, switches and phase shifters for phased-array antennas, millimeter-scale robotics, device design and modeling of piezoelectric MEMS, RF devices, and MEMS actuators.

Ronald G. Polcawich received the B.S. degree in materials science and engineering from Carnegie Mellon University, Pittsburgh, PA, in 1997, and the M.S. degree in materials and the Ph.D. degree in materials science and engineering from the Pennsylvania State University, University Park, in 1999 and 2007, respectively.

He is a Staff Researcher with the Micro and Nanomaterials and Devices Branch, U.S. Army Research Laboratory, Adelphi, MD, where he is currently the Team Leader for the RF MEMS and mm-scale robotics programs. He holds three patents, two of which are related to piezoelectric switches using PZT thin films. He has authored or coauthored more than 30 journal articles and one book chapter on fabrication and design of piezoelectric MEMS devices. His current research interests include switches and phase shifters for phased-array antennas, tunable MEMS resonators/filters for secure communication, mobile unattended sensor platforms, materials processing of PZT thin films, MEMS fabrication, piezoelectric MEMS, RF components, MEMS actuators, and mm-scale robotics.

Kenn R. Oldham (M'09) received the B.S. degree in mechanical engineering from Carnegie Mellon University, Pittsburgh, PA, in 2000, and the Ph.D. degree in mechanical engineering from the University of California, Berkeley, in 2006.

He is currently an Assistant Professor in the Department of Mechanical Engineering, University of Michigan, Ann Arbor, MI. His research interests include microactuator design and applications, optimal design and control, design for controllability, and efficient sensing and power strategies for microelectromechanical system devices.

Prof. Oldham is a member of the American Society of Mechanical Engineers.

Multi-Degree-of-Freedom Thin-Film PZT-Actuated Microrobotic Leg

Choong-Ho Rhee, Jeffrey S. Pulskamp, Ronald G. Polcawich, and Kenn R. Oldham

J. Microelectromechanical Systems, 21(6) (2012)

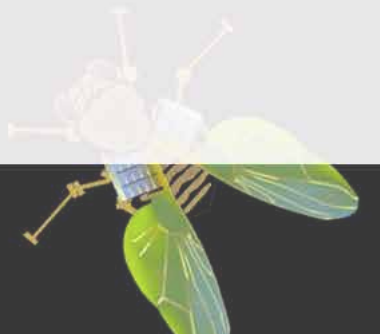

Multi-Degree-of-Freedom Thin-Film PZT-Actuated Microrobotic Leg

Choong-Ho Rhee, *Member, IEEE*, *Member, ASME*, Jeffrey S. Pulskamp,
Ronald G. Polcawich, *Member, IEEE*, and Kenn R. Oldham, *Member, IEEE*, *Member, ASME*

***Abstract*—As a novel approach to future microrobotic locomotion, a multi-degree-of-freedom (m-DoF) microrobotic appendage is presented that generates large range of motion (5°–40°) in multiple axes using thin-film lead zirconate titanate (PZT) actuators. Due to the high driving force of PZT thin films and a robust fabrication process, m-DoF legs that retain acceptable payload capacity (∼2 mg per leg) are achieved. The fabrication process permits thin-film PZT actuator integration with more complex higher aspect ratio silicon structures than previous related processes, using vertical silicon dioxide barrier trenches formed before PZT deposition to provide robust encapsulation of the silicon during later XeF_2 release. Planarization of the barrier trenches avoids detrimental effects on piezoelectric performance from the substrate alteration. Once fabricated, kinematic modeling of compact PZT actuator arrays in prototype leg joints is compared to experimental displacement measurements, demonstrating that piezoelectric actuator and assembled robot leg joint performance can be accurately predicted given certain knowledge of PZT properties and residual stress. Resonant frequencies, associated weight bearing, and power consumption are also obtained. [2012-0041]**

***Index Terms*—Actuators, lead zirconate titanate (PZT), piezoelectric devices, robots.**

I. Introduction

MICROROBOTS are a frequently discussed potential application of the ability to create highly engineered microdevices synthesizing microactuators, sensors, and processing circuitry [1]. Various microactuation mechanisms developed for walking microrobotic locomotion have been reported in the literature, but existing approaches typically feature limited mobility, large power requirements, or low speed. Thin-film piezoelectric actuation, integrated into multi-degree-of-freedom (m-DoF) robot legs may be able to overcome some of these limitations on autonomous microrobots.

Several previous researchers have demonstrated microelectromechanical-systems (MEMS)-based microrobots of less than 1 cm in length using various actuation mechanisms. For example, Ebefors *et al.* built a silicon walking robot with single-degree-of-freedom thermally actuated polyimide leg joints [2]. Although the polyimide joint structures provided large weight-bearing capacity, large power consumption and low speed were a result of thermal actuation. This tradeoff was also demonstrated by Murthy *et al.* [3] and Mohebbi *et al.* [7]. In [4], Hollar *et al.* built the electrostatic inch-worm motors in a two-legged microrobot. However, the pin-joint hinge mechanism provided a single-degree-of-freedom motion, although power consumption was very small. In [5], Bergbreiter and Pister integrated electrostatic inchworm motors with molded elastomers to generate a rapid jumping motion from a similar power source and actuation mechanism as in [4]. In [6], Donald *et al.* used electrostatic scratch drives that were actuated by electric potential difference between the actuator and the substrate, but this type of actuation limits the mobility of the microrobot to a certain operating environment.

Piezoelectric actuation is a desirable candidate technology for microrobotics because it may dramatically increase appendage speed and has large force capacity, modest voltage requirements [16], and ability to recover much stored electrical energy using charge recovery techniques [19]. Recently, lateral thin-film lead zirconate titanate (PZT) actuators were developed in [8] that demonstrated very large work densities and could be connected in parallel or series to provide large force capacities or range of motion, depending on application. Lateral thin-film PZT actuator arrays generating series rotation between 5° and 20° at 20 V potentially enable comparatively large range of motion for autonomous microrobotic appendages [9], [10], while vertical bending piezoelectric actuators can achieve even larger angles.

A first topic of this paper is to introduce basic models of out-of-plane and in-plane piezoelectric actuator arrays for microrobotic leg joints, to illustrate the critical properties of actuator design. The strength of thin-film PZT actuation for microrobotic applications is the combination of high speed, relatively large angle, and low-power operation in multiple axes, as compared to previous technologies in Table I. The cost for this improvement on the various prior robotic leg technologies is a reduction in payload capacity, at least for the type of leg configurations to be discussed in this paper.

The second topic of this paper is a robust fabrication process of the microrobotic leg joints based on thin-film PZT actuator arrays. Integrating large numbers of thin-film piezoelectric actuators into high-performance legs with multiple degrees of freedom requires high-yield fabrication of both vertical and lateral actuators and appropriate connecting structures. Preferably, associated structures should be composed of

Manuscript received February 22, 2012; revised July 3, 2012; accepted July 16, 2012. Date of publication August 27, 2012; date of current version November 27, 2012. This work was supported in part by the U.S. Army Research Laboratory under Award W911QX-07-C-0072 and in part by the National Science Foundation under Award CMMI 0954422. Subject Editor G. Stemme.

C.-H. Rhee and K. R. Oldham are with the Department of Mechanical Engineering, University of Michigan, Ann Arbor, MI 48109 USA (e-mail: chrhee@umich.edu; oldham@umich.edu).

J. S. Pulskamp and R. G. Polcawich are with the Micro and Nano Electronic and Materials Branch, U.S. Army Research Laboratory, Adelphi Laboratory Center, Adelphi, MD 20783 USA (e-mail: jeffrey.s.pulskamp.civ@mail.mil; ronald.g.polcawich.civ@mail.mil).

Digital Object Identifier 10.1109/JMEMS.2012.2211573

TABLE I
COMPARISON OF MICROROBOTIC DEVICES

	Weight Bearing	Speed [mm/s]	DoF	Maximum Angle	Volt	Power Consumption
Ebefors (Thermal)	312.5 mg/leg	6	1	~18.7°	18V	1.1W
Hollar (Electrostatic)	5.1 mg/leg	4	1	35°	50V	100nW
Murthy (Thermal)	667 mg/leg	1.55	1	~2.9°	10V	750mW
Mohebbi (Thermal)	1448 mg	0.64	3	N.A.	60V	Not specified
Current Work (Piezoelectric)	2.1 mg/leg	27 (est. max.)	3	5°, 40°	18V	60μW

high-aspect-ratio silicon or other hard materials to maintain weight-bearing capacity.

Previous processing techniques for integrating thin-film PZT unimorph benders with high-aspect-ratio structures have limited the complexity of potential microactuator joint arrays. Conway and Kim demonstrated an SU-8 integrated amplifying mechanism in [17]. Although SU-8 could be chosen for potential microactuator joint arrays, it is limited to single-level processing above the piezoelectric film. In another work, Aktakka *et al.* developed a multilayer PZT stacking process over high-aspect-ratio structures in [18]. Although the thickness of a thinning-stop layer could be chosen for various target thicknesses of the resulting PZT layer, this PZT remains thick compared to chemical-solution-deposited thin-film PZT and thus requires large voltages for equivalent strains. For several energy-harvesting devices, such as that in [20], silicon is left underneath the thin-film PZT layer; this can be acceptable for energy harvesting from vibration at such devices' natural frequency, even under the environmental vibration at low frequency. However, timed wet etching used to obtain the silicon cantilever is not desirable for undercutting the PZT layer itself, which limits displacement as an actuator.

To overcome previous processing limitations for producing complex microrobotic joint structures, low-pressure chemical vapor deposition (LPCVD) of silicon oxide vertical barrier trenches prior to thin-film PZT deposition was performed in this paper. Compared to a previous photoresist encapsulation technique in [11], consistent undercut length of thin-film PZT actuator array was realized that is essential for producing the proposed microrobotic platforms with complex joint configurations. An effective piezoelectric strain coefficient is obtained with minimal change in magnitude from PZT structures without the barrier trenches.

The final topic of this paper is then a description of experimental testing procedures and measured robot leg behavior, as related to range of motion, response speed, and power consumption. After fabrication, a prototype leg joint is characterized experimentally to validate the in-plane and out-of-plane joint models. Important nonidealities of the fabrication process as they influence robot leg joint performance and appropriate adjustments to displacement models described are noted.

To summarize paper organization, Section II introduces the analytical models for piezoelectric vertical and lateral actuators and applies them to the actuator arrays produced in this paper. Section III describes the fabrication process for thin-film piezoelectric layer, integrated with complex silicon microrobotic structures. Section IV presents experimental characterization of fabrication process and of the kinematics and dynamics of a sample microrobotic leg. Section V concludes this paper.

II. SYSTEM DESCRIPTION

A. Thin-Film PZT Actuator Basics

Two types of thin-film piezoelectric actuators are used to create M-DoF appendages such as that shown in Fig. 1: lateral (or in-plane) rotational actuators and vertical (or out-of-plane) unimorph bending actuators [15]. Individual thin-film PZT actuators consist of unimorph bending segments, as in [8]: a single bend-down uniform segment for the vertical actuators and a combination of two bend-down and two bend-up segments for the lateral actuators. Each segment contains a material stack of a base silicon dioxide layer, a bottom Ti/Pt electrode, the PZT thin film, and a top Pt electrode. For bend-down segments, an additional gold film is deposited to move the neutral axis of the unimorph above the centerline of the PZT film, as shown in Fig. 2. In the material stack, the PZT thin film both imposes a contractive force $F_{\rm act}$ and a bend-down or bend-up moment $M_{\rm act,1}$ or $M_{\rm act,2}$, under an applied voltage according to

$$F_{\rm act} = e_{31,\rm eff}\frac{V}{t_{\rm PZT}}A_{\rm PZT} \tag{1}$$

$$M_{\rm act,i} = e_{31,\rm eff}\frac{V}{t_{\rm PZT}}A_{\rm PZT}(\overline{y}_{\rm PZT} - \overline{y}_i) \tag{2}$$

where $e_{31,\rm eff}$ is the effective field-dependent electroactive stress coefficient, which is a measured ratio of stress to electric field rather than the exact linear piezoelectric coefficient of the material [8]. The coefficient is approximated by the nominal (short circuit) axial elastic modulus $E_{\rm PZT}$ of the PZT film in a free beam and by the effective field-dependent electroactive strain coefficient $d_{31,\rm eff}$ or $e_{31,\rm eff} = E_{\rm PZT}d_{31,\rm eff}$. The empirical values of $e_{31,\rm eff}$ and $d_{31,\rm eff}$ include a number of effects associated with the effective piezoelectric coefficient $d_{31,f}$ or effective piezoelectric stress coefficient $e_{31,f}$ but also nonlinear piezoelectric/ferroelectric and electroactive material responses [11]. For other nomenclature, V is the applied voltage, $t_{\rm pzt}$ and $A_{\rm pzt}$ are the thickness and the cross-sectional area of PZT, $\overline{y}_{\rm PZT}$ is the position of the PZT film midline in the unimorph material stack, and $\overline{y}_1$ and $\overline{y}_2$ are neutral axes of segments with (bend down) and without (bend up) a gold layer. The composite rigidity of respective thin-film PZT unimorphs is referred to as $(EI)_1$ or $(EI)_2$. The aforementioned parameters associated with thin-film PZT actuator structure are shown in Table II.

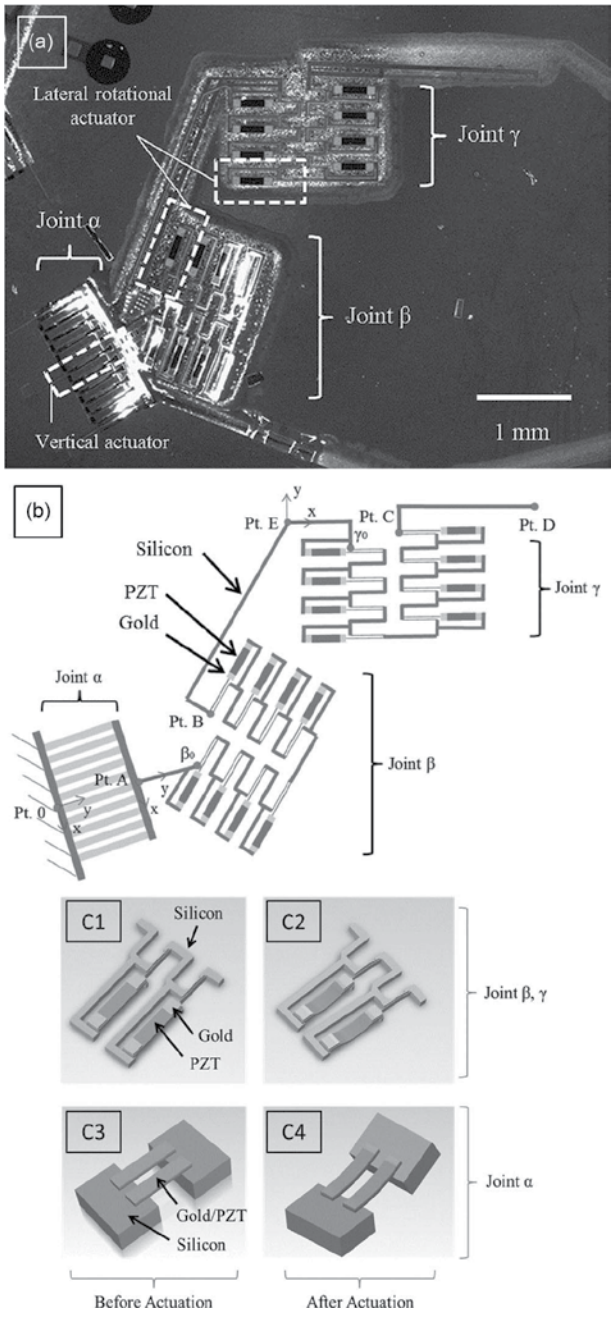

Fig. 1. Fully released m-DoF leg. (a) Optical image. (b) Schematic drawing. (c) Schematic drawing of actuation substructures [(left) before actuation, (bottom left) before actuation of PZT film, and (bottom right) after actuation of PZT film].

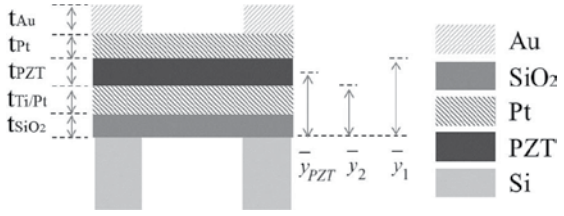

Fig. 2. Cross-sectional view of a lateral rotational actuator.

TABLE II
PROPERTIES OF THIN-FILM PZT LATERAL ROTATIONAL AND VERTICAL ACTUATORS

Parameter	Value	Parameter	Value
t_{Au}	1 (μm)	L_{PZT}	480 (μm)
t_{Pt}	0.105 (μm)	L_v	536 (μm)
t_{PZT}	0.8 (μm)	$w_{flexure}$	13 (μm)
$t_{Ti/Pt}$	0.08 (μm)	w_{tether}	10 (μm)
t_{SiO2}	0.17 (μm)	$(EI)_{\text{flex}}$	$1.693{\cdot}10^{2}$ (N·μm^2)
$\bar{y}_{PZT}$	0.62 (μm)	$(EA)_{\text{t}}$	11.20 (N)
$\bar{y}_1$	1.05 (μm)	$(EI)_1$	6.909 (N·μm^2)
$\bar{y}_2$	0.32 (μm)	$(EI)_2$	1.986 (N·μm^2)
L_{flex}	118 (μm)	F_{act} (at 20V)	$1.17{\cdot}10^{-2}$ (N)
L_{tether}	284 (μm)	$M_{act,1}$(at 20V)	$5.3{\cdot}10^{-2}$ (N·μm)
L_{act}	15.5 (μm)	$M_{act,2}$ (at 20V)	$3.7{\cdot}10^{-2}$ (N·μm)

B. Thin-Film PZT Vertical Actuator Array

Out-of-plane motion is generated by simple unimorph bending in the first joint (joint α) of the m-DoF appendages shown in Fig. 1(a) and (b). Displacements of any actuator array can be expressed using six coordinates, $d = [x\ y\ z\ \theta_x\ \theta_y\ \theta_z]^{\mathrm{T}}$, although only specific coordinates of significant motion are shown in each respective joint analysis. Since all out-of-plane or vertical actuators are composed of identical silicon dioxide, PZT thin film, and metal layers, a multilayer composite cantilever is an appropriate model to estimate the displacement of vertical actuator $d_{(\alpha)}$

$$d_{(\alpha)} = \begin{bmatrix} z_{(\alpha)} \\ \theta_{x,(\alpha)} \end{bmatrix} = \begin{bmatrix} \frac{L_v^2}{2(EI)_1} \\ \frac{L_v}{(EI)_1} \end{bmatrix} M_{\text{act},1} + \begin{bmatrix} \frac{L_v^3}{3(EI)_1} & \frac{L_v^2}{2(EI)_1} \\ \frac{L_v^2}{2(EI)_1} & \frac{L_v}{(EI)_1} \end{bmatrix} \begin{bmatrix} \frac{F_v}{N} \\ \frac{M_v}{N} \end{bmatrix} \quad (3)$$

where $z_{(\alpha)}$ and $\theta_{x,(\alpha)}$ are the vertical displacement and the rotational angle at the tip of joint α, L_v is the length of a vertical actuator, F_v and M_v are external force and moment, if present, due to the external loads applied at the tip of vertical actuators, and N is the number of vertical actuators connected in parallel. A schematic view of this motion is shown at the bottom of Fig. 1(c). If desired, a lateral displacement at the tip of the joint $y_{(\alpha)}$ component may also be estimated through numerical integration along the small angle displacement of $\theta_{x,(\alpha)}$. In prototype leg joints, ten vertical actuators are connected in parallel such that large weight-bearing capability can be maintained by joint α.

As implied by (2) and (3), vertical actuator joint angles can be very large when using thin-film PZT unsupported by silicon because the effective piezoelectric coefficient is relatively large, electric fields are high, and composite stiffness is low. Downward bending motion is used, with the added gold layer of bend-down unimorphs both increasing offset from the PZT layer to the neutral axis and preventing composite stiffness of the beams from becoming too low in resisting external loads.

C. Thin-Film PZT Lateral Rotational Actuators

In-plane motion is driven by individual lateral PZT actuators [21], [22] integrated with silicon flexural structures. The

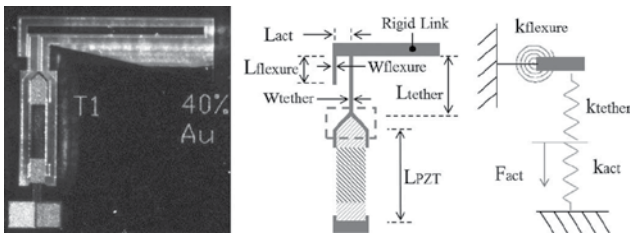

Fig. 3. Single thin-film PZT lateral rotational actuator connected to a high-aspect-ratio silicon flexural structure. (Left) Optical image. (Center) Schematic drawing. (Right) Equivalent spring structure. (Dashed-line box) Outline of the detailed view given in Fig. 6.

net motion at the tip of individual lateral actuators is ideally horizontal, as two bend-down and two bend-up segments are located symmetrically on either side of the actuator midpoint. However, due to residual stress in the thin films, unconstrained in-plane motion is not generally obtained. Thus, the end of the actuator is connected to a high-aspect-ratio silicon flexural structure that prevents out-of-plane bending under most circumstances. The flexure structure also converts small translational piezoelectric displacements into rotational displacements, as shown in Fig. 3.

Force–displacement curves for such lateral actuators have been previously described in [8]. For microrobotic leg design, a region of small displacement and large force is chosen to increase the weight-bearing capacity and locomotion speed of joint structures. In that region of behavior, the axial contraction in (1) dominates actuator motion, while the bending motion of beams that can lead to larger displacements against small forces has negligible influence on the present leg joint designs. Equation (4) shows the in-plane small displacement of a single actuator rotary joint that consists of high-aspect-ratio elastic flexure and tether, a PZT actuator, and a rigid link. The relation of the force generated by a single actuator and the displacement at the tip of the flexure in the rotary motion is as follows:

$$\left(\frac{k_{f,\theta}k_{t,\theta}}{k_{f,\theta}+k_{t,\theta}}+k_{\mathrm{act},\theta}\right)\theta = F_{\mathrm{act}}L_{\mathrm{act}} \tag{4}$$

where $k_{f,\theta}$, $k_{t,\theta}$, and $k_{\mathrm{act},\theta}$ are the equivalent rotational spring stiffness values of the flexure, tether, and actuator, which are given in the Appendix. L_{act} is the distance between the tether and the flexure joint. Because the actuator itself and the silicon tether experience the axial force generated by piezoelectric film, the maximum rotary angle θ is represented in terms of the combined spring stiffness of the joint structure.

D. Thin-Film PZT Lateral Actuator Arrays

For intended in-plane actuation in microrobotic legs, multiple lateral actuators are connected in series arrays so that large rotational displacement can be produced. In the prototype legs, this occurs in joints β and γ. In these joints, lateral actuators are arranged in two sets of four with flexural mechanisms facing each other, as shown in Fig. 1(b). A schematic view of this motion is shown in Fig. 1(c). By aligning the high-aspect-ratio flexures toward a microrobot's foot, such arrays are intended to reduce out-of-plane deflection due to torsion from weight bearing of future microrobotic platforms and to multiply rotational motion of individual actuators.

Within each in-plane joint array, displacement is calculated from the driving thin-film PZT actuation force and its equivalent rotary moment. Eight local coordinates, as shown in Fig. 4, are used to calculate the total displacement. The displacement of the origin of the ith coordinate with respect to the first coordinate at the start of the array (point β_0 or γ_0) is represented as the summation of projections onto previous coordinates. Then, displacement of the mth coordinate with respect to the origin of the first flexure joint is represented in

$$d^1_{m(\beta,\gamma)}=\sum_{n=1}^{m}\prod_{k=1}^{n} R^{k-1}_{k\ (\beta,\gamma)}\left(p^n+T\cdot f^n_{(\beta,\gamma)}+R^n_{n+1(\beta,\gamma)}q^{n+1}\right) \tag{5}$$

where $d^1_{8\ (\beta,\gamma)}$ is the total local displacement of the compact array in question, R^j_i is the rotational matrix of the ith coordinate with respect to jth coordinate by the angle of θ_i, and, for $i \geq 5$, R^4_i is a combined transformation of the reorientation of axis by π radians $R(\pi)$ with rotational displacement by $\theta_i R(\theta_i)$. When $i = 1$, R^0_1 is the identity matrix. T is the compliance matrix of the flexure structure, f^i is the forcing term generated by the actuator and, if present, external forces and moments, p^i is the initial position of flexure tip, and q^i is the position vector between the ith and $i-1$th coordinates. The subscript β or γ indicates whether the model is referring to the inner or outer compact array.

For in-plane actuator design, performance is best if the elastic flexure, denoted by $k_{f,\theta}$, can be fabricated with high aspect ratio, so that out-of-plane stiffness and weight bearing are increased without overly increasing resistance to in-plane motion. Likewise, small gaps between flexures and tethers L_{act} are also useful for generating large rotation angles. Significant forcing is again available through large piezoelectric coefficient and high electric field across the PZT thin film.

E. Kinematic Leg Model

In the prototype leg configuration, coordinate systems are defined at the silicon flexures of each individual in-plane actuator, in addition to the initial vertical actuator. As shown in Fig. 1, the following locations are used as reference frame of the local coordinates during kinematic analysis.

1) Point 0 represents the beginning of leg, at the fixed end of the vertical actuators, oriented along the long axis of the vertical actuators.
2) Point A represents the tip of the vertical actuators (end of joint α), where a rigid silicon connection to joint β begins.
3) Points β_0 and B represent the beginning and end of joint β, at the end of the rigid silicon connector between joints α and β.
4) Points γ_0 and C represent the beginning and end, respectively, of joint γ, at the end of the rigid silicon connector between joints β and γ.
5) Point D is the end tip of the m-DoF leg.

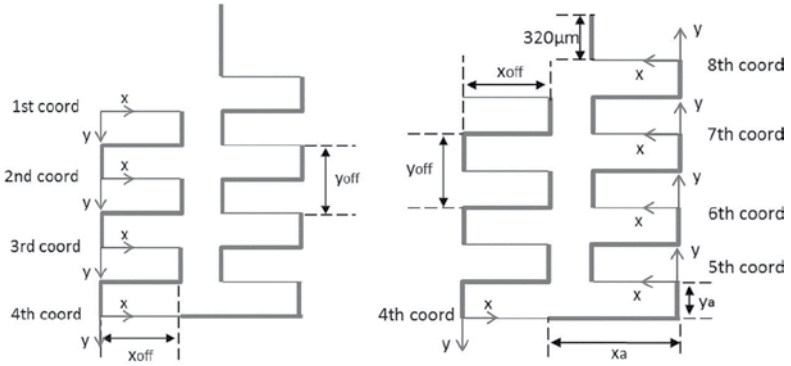

Fig. 4. Schematics of local coordinates of inner and outer actuator array in m-DoF robotic leg.

6) Point E is the corner of the rigid silicon link between joints β and γ, which is easily tracked during experimental measurements.

The local coordinate axes for each joint is chosen such that the y_0-axis is aligned along the lateral direction of the thin-film PZT actuators in the given joint. Local displacements are related to global displacements of points of interest using rotation matrices. Fixed rotation matrices are denoted by the notation $R(\theta_{i,b/a})$, where i corresponds to the local axis of rotation and b and a indicate the ending and starting points of interest, respectively, that a change in orientation is taken from. As an example, for the first rotation matrix, from the global coordinates to the base of the vertical actuators, the rotational matrix is formed from $\theta_{z,A/0}$ which is the angle between global coordinates $(x_{\text{global}}, y_{\text{global}}, z_{\text{global}})$ and the local coordinates (x_0, y_0, z_0) at point 0, the beginning of the leg. From the measured distance of point A from zero, $\theta_{z,A/0}$ is estimated at 39.5°, and coordinate transformation from the raw data to the desired coordinate (x_0, y_0, z_0) is obtained in

$$X_{\text{global}} = R(\theta_{z,A/0})X_0 \tag{6}$$

where X_{global} and X_0 are the position vectors with respect to the global and point 0 coordinates.

Rotations that may change with applied voltage are also written using standard rotation matrices, denoted by $H(\theta_{i,b/a})$, and generally, their rotation angles consist of a fixed component, due to residual stress, and a changing component due to applied voltage. For example, the rotation matrix used to transform coordinates about point A with respect to coordinates about point 0 is written $H(\theta_{x,A/0})$, with $\theta_{x,A/0}$ being the sum of vertical rotations at the tip joint α due to residual stress and due to an applied input voltage. Use of these rotations to evaluate leg joint performance will be discussed in more detail in Section IV.

III. Fabrication

A. Robust Encapsulation and Multilevel Fabrication Integrated With Thin-Film PZT Layer

A previous microfabrication process for components of thin-film PZT-actuated microrobotic leg joints has been reported in [8]. Individual actuators were released from underlying silicon with a timed XeF_2 etch when a photoresist encapsulation layer protects silicon anchor points. However, this resulted in obstacles to releasing the undercut PZT actuator layer across large devices, such as inconsistent actuator undercut length and occasional crack and failure of photoresist encapsulation layer.

A robust fabrication process used to produce the current m-DoF appendages is as follows. Fabrication begins with a silicon-on-insulator (SOI) wafer with a 10-μm-thick device layer, 0.1-μm-thick buried oxide layer, and 500-μm-thick handle wafer (thicker device layers may also be used, with legs from 30-μm device layers also fabricated). Narrow (3 μm wide) trenches are etched to the buried silicon dioxide layer (step A) in Fig. 5) along the sidewalls of bulk-micromachined silicon structures, such as flexural springs and silicon connectors from the tethers to PZT unimorphs. Prefurnace-cleaned trenches are then filled with silicon dioxide by LPCVD [step B)].

It was observed that keyholes are generated in the oxide trenches due to nonuniformity in the trench sidewalls and a slightly faster deposition rate at the trench mouth than that inside the trench. Instead of annealing above 1000 °C, which has been shown to make the oxide reflow in the trench [12], the top oxide is removed by either chemical mechanical polishing or reactive ion etching (RIE), and the upper part of the trench is etched by short RIE [steps C) and D)]. Once the keyhole is opened, LPCVD process is repeated to fill the opened trenches in step E). Several iterations of steps B)–D) may be necessary to diminish the size of keyhole, but it is difficult to eliminate it entirely. Nonetheless, since the observed piezoelectric coefficients of PZT films can be very sensitive to underlying surface conditions [13], refill is continued until a standard mechanical boundary condition of the intermediate layer between PZT film and the substrate is achieved. In this case, closure of all surface trenches and a planarized surface are achieved. Planarization of the surface of refilled oxide trenches is followed by additional silicon dioxide deposition by plasma-enhanced chemical vapor deposition to reach a minimum target base oxide thickness of 2000 Å.

After SOI wafers are processed up to step E), PZT (with a Zr/Ti ratio of 52/48) and electrode layers are deposited at the U.S. Army Research Laboratory and Radiant Technologies, Inc. The resulting metal stack consists of a platinum bottom electrode, PZT film, and platinum top electrode [step F)]. Two argon milling steps for the top electrode and PZT layers and

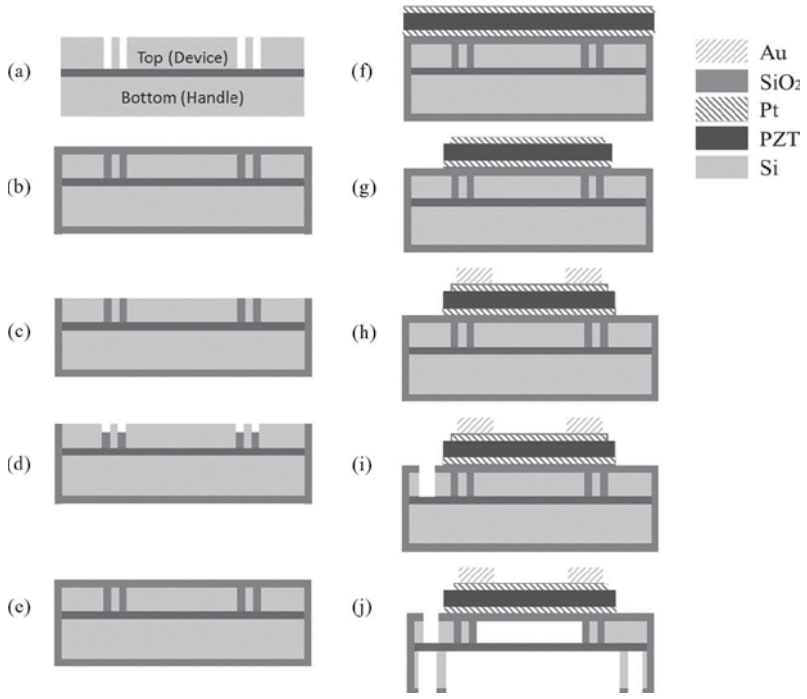

Fig. 5. Multilevel microfabrication process flow of thin-film PZT-actuated silicon structure in the microrobotic application.

a wet etch for contact vias to the bottom electrode are next performed [step G)], as in [8]. Then, a 1-μm-thick Ti/Au layer is deposited on the top of PZT actuator surface by a lift-off process [step H)], and the silicon microstructure in the top device layer is patterned and micromachined by deep RIE (DRIE) [step I)].

To perform backside etching of the SOI wafer, oven-baked photoresist is used to protect the microstructure of top device layer, and the backside of SOI wafer is patterned for other geometries such as microrobot feet. Backside patterning and etching also provide the open area for XeF_2 to etch the underneath silicon layer of actuator and other unprotected silicon structures in step J). During the XeF_2 underetching process of thin-film PZT actuator and silicon microstructure layer, a uniform undercut length of the PZT/Au unimorph actuator structure is obtained after removal of chemically inert Teflon-like passivation layer, which is deposited during DRIE process and prevents XeF_2 gas from etching the silicon underneath the material stack. Fig. 6 shows a scanning electron microscopic image of thin-film PZT actuator layer connected to silicon tether.

To summarize, in the microfabrication process described earlier, deposition of oxide trenches provides a vertical etching barrier against isotropic XeF_2 etching of the substrate silicon device layer connected to thin-film PZT actuators. This serves as a robust encapsulation structure to eliminate encapsulation failures and underetching variance of thin-film PZT actuators observed in previous integration approaches. Oxide deposited for such trenches can also be used as a hard mask on the backside of a SOI wafer permitting backside patterning and thus multilevel fabrication for complex silicon structure. Silicon structures up to 30 μm tall by 5 μm wide have been produced in this manner on other test wafers.

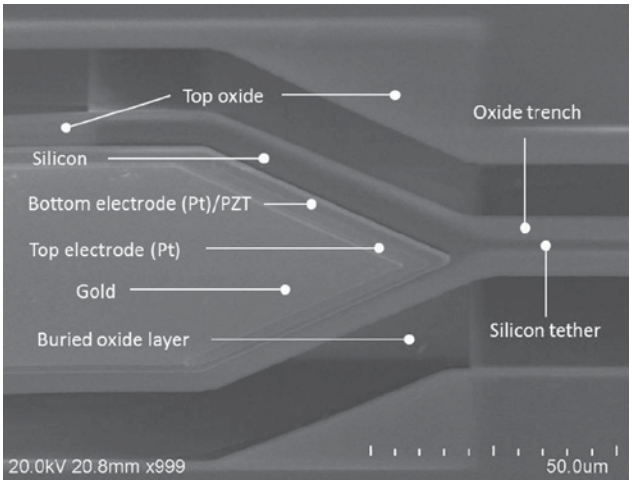

Fig. 6. Scanning electron microscopic image of thin-film PZT actuator layers connected to silicon tether, as marked in a dashed red box in Fig. 2.

One limitation of the finalized process flow is an inability to remove the oxide trenches following XeF_2 release. While the oxide trenches were originally intended to be removed via isotropic RIE, and structures were designed with the removal of silicon dioxide expected, in practice, the top platinum electrode on the PZT layer was found to be eroded in such an RIE step, causing the removal of electrical connection in most of actuators. Thus, flexible structures in the device layer are wider than originally designed by the oxide trench width, and flexible electrical interconnects (such as that providing power to the outer in-plane actuator) are also reinforced. This reduces the range of motion of the final leg structures compared to their designed specifications, and future devices should take oxide

trench width into account in the design stage. In addition, residual stresses in the metal stack result in the vertical actuator array having a nonzero neutral position. The change of the neutral position leads to variation in vertical displacements from planar neutral position which would be expected from an initially flat structure.

IV. Experimental Results

A. Piezoelectric Coefficient Measurement

Following fabrication, simple cantilever beams were used to verify piezoelectric coefficient magnitudes. This was done to verify that the preprocessing of the SOI with barrier trenches would not have a detrimental effect on thin-film PZT quality. Since a randomly oriented polycrystalline structure is present in PZT thin film after fabrication, a poling treatment is required to align the scattered polydomain structure into a metastable alignment in the direction of an applied electric field to form a consistent remnant polarization of the layer. The poling test was performed at 250 kV/cm (i.e., 20 V) using a direct-current power supply at room temperature which was used for 45 min. After poling, the static vertical displacement of the tip of cantilever was measured by optical profilometry by stepping down to 0 V in 1-V decrements and returning back to 20 V in 1-V increments.

Due to intrinsic residual thin-film stress following fabrication, the piezoelectric coefficient is experimentally determined from radius of curvature of the beam ρ in the Bernoulli–Euler equation with the superposition of the resultant moment due to the residual stress and the moment generated by PZT thin film

$$\frac{1}{\rho} = -\frac{M_{\text{residual}} + M_{\text{PZT}}}{(EI)_{\text{comp,no Au}}} \tag{7}$$

$$M_{\text{PZT}} = e_{31,\text{eff}} \frac{V}{t_{\text{PZT}}} A_{\text{PZT}} (\overline{y}_{\text{PZT}} - \overline{y}_1) \tag{8}$$

where M_{residual} is the moment due to residual stress of the films, M_{PZT} is the moment generated by PZT actuator, which corresponds to $M_{\text{act},2}$ in (2), and $(EI)_{\text{comp,no Au}}$ is the vertical composite rigidity of the material stack without Au deposition. Fig. 7 shows the estimated field-dependent effective electroactive strain coefficient $d_{31,\text{eff}}$ of the piezoelectric cantilevers with and without oxide barrier trenches. Multiple measurements have been performed at each applied electric field and represented as error bars, and the electroactive $-d_{31,\text{eff}}$ values for both test cantilevers at higher voltages are determined in the range of 60–80 pm/V. The variation of measured $d_{31,\text{eff}}$ with respect to electric field is observed inversely proportional to the applied electric field as deflection due to intrinsic residual stress is predominant at low voltage and the piezoelectric coefficient is inversely proportional to electric field. The empirical $d_{31,\text{eff}}$ coefficients in Fig. 7 show that the performance of fabricated actuators could be preserved in the proposed microfabrication process, particularly at high voltages where typical operation occurs.

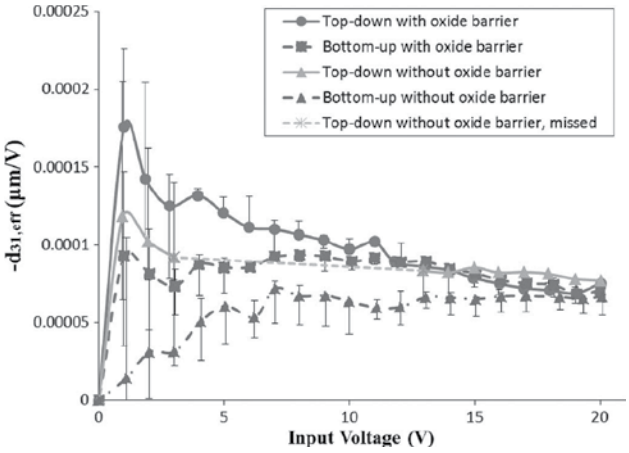

Fig. 7. Empirical effective electroactive piezoelectric strain coefficient curve at applied voltages.

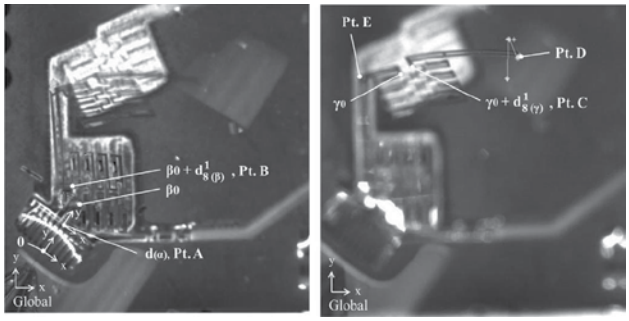

Fig. 8. Trajectory of point E (knee) between joints β and γ and point D (foot) as the vertical actuators are activated by 15-V dc. The left images are at 0 V, and the right images are at 15 V.

B. Range-of-Motion Analysis

Completed m-DoF leg joints were characterized experimentally to verify functionality and vertical and lateral joint design performance. This experimental verification is based on kinematic descriptions of joint motion, with deformation of continuous beams (vertical unimorph actuators and elastic rotational flexures, for out-of-plane and in-plane motions, respectively) converted to motion of specified points on a prototype actuator in global coordinates [14]. This motion was captured by a high-speed camera above the device, and the global coordinate $(x_{\text{global}}, y_{\text{global}})$ data are obtained from the optical images.

As discussed in (6) in Section II-E, displacements of any point of interest, as measured in global coordinates, can likewise be related to rotations and displacements of proceeding links in the robotic leg. For example, the displacement of the tip in terms of global coordinates X_D depends on all relevant rotations and displacements, as

$$\begin{aligned} X_D = {} & H(\theta_{x,A/0}) R\left(\theta_{z,\beta_0/A}\right) H\left(\theta_{x,B/\beta_0}\right) H\left(\theta_{z,C/\gamma_0}\right) X_{\frac{D}{C}} \\ & + H(\theta_{x,A/0}) R\left(\theta_{z,\beta_0/A}\right) H\left(\theta_{x,B/\beta_0}\right) s_{\text{trans}} \\ & + H(\theta_{x,A/0}) R\left(\theta_{z,\beta_0/A}\right) w_{\text{trans}} + H(\theta_{x,A/0}) u_{\text{trans}} \\ & + v_{\text{trans}} \end{aligned} \tag{9}$$

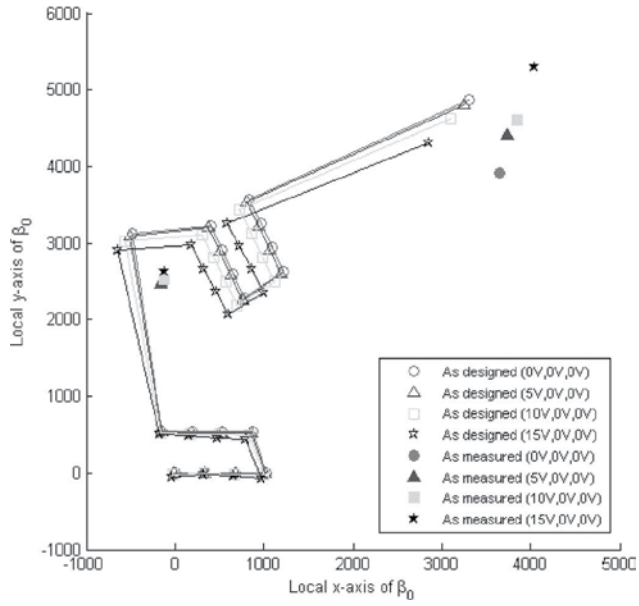

Fig. 9. Trajectory of two in-plane compact arrays with points D (foot) and E (knee) represented with hollow markers, as designed, and represented with solid markers, as measured, with respect to point β_0 when joint α is activated.

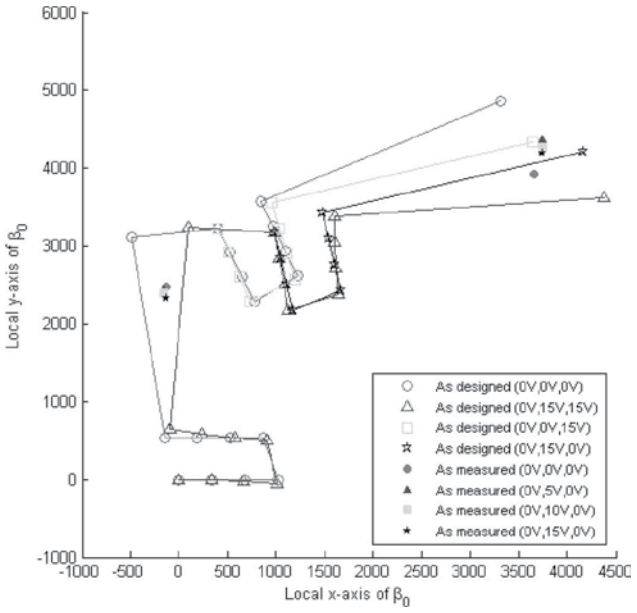

Fig. 10. Trajectory of two in-plane compact arrays with points D (foot) and E (knee) represented with hollow markers, as designed, when joints β and γ are activated separately, and represented with solid markers, as measured, with respect to point β_0 when joint β is activated.

where $H(\theta_{x,A/0})$, $H(\theta_{x,B/\beta 0})$, and $H(\theta_{z,C/\gamma 0})$ are the local coordinate transformations due to rotations at joints α, β, and γ, respectively, and $R(\theta_{z,\beta 0/A})$ is a fixed rotation representing the difference in orientation between joint α and joint β. $X_{D/C}$ is fixed translational offset of the tip of the leg from the end of joint γ, s_{trans} is the nominal offset from the beginning of joint γ to the end of joint γ plus any displacement of joint γ (i.e., $d^1_{8\ (\gamma)}$) due to an applied voltage, w_{trans} is the nominal offset from the beginning of joint β to the end of joint γ plus any displacement exerted by joint β (i.e., $d^1_{8\ (\beta)}$), due to applied voltage, u_{trans} is the nominal offset of joint β from joint α, and v_{trans} is the nominal offset from the beginning to the end of joint α plus any displacement of joint α due to an applied voltage.

Fig. 8 shows the top view of the device and the trajectory of E (knee) and point D (foot) taken by stereoscope and high-speed camera when the vertical actuators are activated by various input voltages. In Fig. 9, the direction of motion of points D and E exerted by joint α is opposite to the intended direction. This is because residual stress causes the leg to start in an upward deflected position, such that downward rotation of the vertical actuator under an applied voltage causes the tip of the leg to move away from the base (in global (x, y) coordinates), rather than closer to the base if the leg had started in a flat fully extended position. Furthermore, residual stress leading to the deformation of joint β causes significant out-of-plane bending.

Fig. 10 shows the measured trajectories of points D and E under various combinations of applied voltage to joints β and γ. Differences between the designed and the measured trajectories of the leg also arise from nonidealities in the fabrication process, particularly the following: 1) excess silicon dioxide that increases the stiffness of flexures and, particularly, the interconnect across the inner lateral actuator and 2) residual stress in the actuator arrays.

TABLE III
DISPLACEMENT OF POINT A BY VERTICAL ACTUATORS

Degree of Freedom	As designed	As fabricated (from model)	As fabricated (from experiment)
x (μm)	0	0	1.86
y (μm)	-43	10.6	19.4
z (μm)	-189	-189	-148
θ_x(°)	-40	-40	-37
θ_y(°)	0	0	0
θ_z(°)	0	0	0

C. Comparison to Actuator Models

Mapping back observed motion at the points of interest along the leg to displacements at the actuator arrays allows the actuator array performance to be measured. Since the motion of m-DoF microrobotic legs is generated by combinations of two in-plane compact actuators and vertical actuators, different sets of actuators were independently activated to verify actuator models. Three sets of displacements are shown in Tables III–V, for the three actuators. The first set of results shows the displacement of an ideal leg design, which assumes a planar neutral position (no residual stress), no excess silicon dioxide, and negligible interconnect stiffness across the inner lateral actuator; this set of results is intended to demonstrate the ideal capabilities of the device. The second set of results shows the predicted displacements when residual stress effects are included, with extra oxide and with full interconnect modeling. The third set of results is from the experimentally extracted actuator array displacements and rotations, when measurable.

TABLE IV
DISPLACEMENT OF POINT E WITH RESPECT TO POINT A BY INNER COMPACT ACTUATORS

Degree of Freedom	As designed	As fabricated (from model)	As fabricated (from experiment)
x (μm)	230	4.9	3.8
y (μm)	65	-133	-143
z (μm)	0	843	798
θ_x(°)	0	18.9	18.1
θ_y(°)	0	0	Unable to measure
θ_z(°)	-4.7	-0.1	-0.1

TABLE V
DISPLACEMENT OF POINT C WITH RESPECT TO POINT E BY OUTER COMPACT ACTUATORS

Degree of Freedom	As designed	As fabricated (from model)	As fabricated (from experiment)
x (μm)	149	144	114
y (μm)	-208	-201	-186
z (μm)	0	0	108
θ_x(°)	0	0	17.7
θ_y(°)	0	0	Unable to measure
θ_z(°)	-4.7	-4.5	-3.85

Based on experimental observations of fabrication limitations, various adjustments were made to the actuator models. First, it should be noted that, even with high-aspect-ratio flexure and tether structures, residual stress in the experimentally released prototype devices described in Section III still led to out-of-plane bending from the in-plane actuators. Thus, an addition to the lateral actuator model to account for out-of-plane deformation was obtained. This was particularly significant when the elastic interconnect is present, as a deformation similar to buckling is observed.

To account for the stiffness of the PZT interconnect to joint γ across joint β, which impeded lateral rotation in joint β and contributed to out-of-plane bending moment about the x-axis, an expanded model of the lateral actuator array with interconnect was created. Details of the augmented model are included in the Appendix, but in brief, this effect can be estimated by the average offset distance $\varepsilon_{\text{dist}}$ of the beginning of the rigid silicon links between joints β and γ along the local z-direction with respect to point A during the motion. This offset distance and in-plane actuation moment result in out-of-plane deflection and, thus, the resulting angle $\theta_{ic,y}$ of the thin-film PZT interconnect about point A. A lumped spring model is used to estimate the displacement of the parallel structure of the elastic interconnect and joint β, which is represented by the displacement of joint $\beta d^1_{8\ (\beta)}$

$$d^1_{8(\beta)} \approx (K_{\text{ic,eq}} G_{\text{ic}} + K_{\text{array,eq}})^{-1} F_{\text{act}} \tag{10}$$

where $K_{\text{ic,eq}}$ and $K_{\text{array,eq}}$ are the lumped spring stiffness values of the thin-film interconnect and inner in-plane actuator array and G_{ic} is a matrix projecting the additional spring force at the tip of the interconnect back to actuator locations.

In general, there is a good agreement between experimental and model results when nonidealities are taken into account. Angular rotation of the vertical actuator tip is closely matched to the model, although the initial curvature due to residual stress changes the associated tip displacements from the ideal case. Similarly, in-plane motions of the two lateral actuator arrays (x, y, and θ_z displacements) are very similar to experimental results, so long as the interconnect stiffness is accounted for in the design as fabricated. With the existing robot leg configuration, this means that substantial in-plane rotations can only be generated by one joint at a time, although both joints were shown to function. The total in-plane displacement of the foot was approximately 900 μm for a 4.5-mm-long leg.

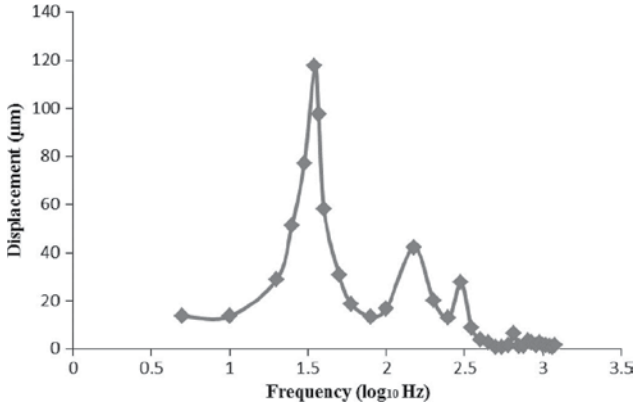

Fig. 11. Frequency response of point C (foot) measured with respect to global coordinates when the vertical actuator array is activated with driving sinusoidal input.

TABLE VI
RESONANT FREQUENCIES

Actuator	Measurement	1st and higher resonant frequency
Vertical actuator	Point A (hip)	300, 1500, 1810 Hz
	Point B (knee)	37, 300, 800 Hz
	Point C (foot)	35, 150, 300, 650 Hz
Compact actuator	Point A (hip)	1510, 1810 Hz
	Point B (knee)	800 Hz
	Point C (foot)	30, 150, 250, 650, 1150, 1450 Hz

D. Frequency Response

Resonance analysis of the fabricated m-DoF microrobotic legs indicates that such a robotic appendage is capable of moving under high bandwidth. Fig. 11 shows the frequency response of point C measured with respect to the global coordinate of high-speed camera under stereoscope when the vertical actuator array is activated with the driving sinusoidal input voltage where the offset and peak-to-peak voltages are chosen to 3 V and 2 Vpp, respectively. Q factor along the vertical motion is approximately obtained as 8.58 at the first resonant frequency of 34.7 Hz in a ten-base logarithm scale. Table VI shows resonant frequencies of other points when vertical actuator and compact actuator sets are independently activated. When the vertical actuator is activated, a 280-ms settling step time was observed at the foot.

E. Weight and Power Considerations

For use in producing terrestrial microrobot locomotion, weight bearing and energy use of a given robot leg design are critical. As fabricated, the primary source of out-of-plane

compliance to load at the leg tip is the vertical actuators. This compliance can be estimated from (3), using an external moment on the vertical actuator equal to the weight load times the leg length. Estimated compliance is 3080 rad/N. For the actuated motion of the foot to be greater than any bending of the vertical actuators during load bearing, this produces an absolute maximum weight capacity of 2.1 mg per foot, which is somewhat further reduced by out-of-plane compliance of the lateral actuator arrays. Fortunately, each actuator array has a capacitance of only 1.2 nF, such that power consumption of three actuators at 15 V with a 15-Hz step frequency is only 12 μW. This would correspond to an approximate speed of 27 mm/s for the observed 0.9-mm step lengths of 15 steps/s from each leg. This translates to an ability to operate with battery power densities as low as 5.7 W/kg, well below that of current battery technologies. In practice, the ability to successfully operate a robot leg of this type with a power supply that it can carry is more dependent on the efficient use of energy in any control and energy conversion circuitry, than on its own fundamental power consumption [15].

Still, for the immediate development of microrobotic prototypes, the current work's primary benefits are the increased reliability of thin-film PZT actuator arrays and verification of actuator array modeling techniques. This process has produced a prototype hexapod using the leg design analyzed that has been produced with five out of six legs that are intact (one leg failing due to fracture of a flexure/tether unit during fabrication). Moving forward, however, more feasible robot prototypes for the next phase of further robot development will utilize millipede-style layouts, with larger numbers of legs, fewer actuators per leg, and shorter distances to leg tips to be explored. These prototypes thus trade reduced mobility for larger weight-bearing capacity (up to approximately 200 mg for an entire chassis) to allow greater flexibility in control and power systems. Nonetheless, the ability to create as complex leg geometries as described here while meeting fundamental needs for energy use versus weight-bearing capacity and the ability to predict leg behavior given fabrication constraints appear encouraging for a long-term goal of highly mobile bioinspired microscale robots.

V. Conclusion

Prototype microrobotic leg joint arrays based on thin-film piezoelectric actuation are described, fabricated, and characterized in this paper. These leg joints take advantage of high electric fields and good piezoelectric coefficients for thin-film PZT to generate large forces and/or joint angles from in-plane or out-of-plane motion. They are coupled with a robust fabrication process that allows multiple joints to be incorporated into full high-mobility legs. Modeling of thin-film PZT lateral and vertical actuator arrays is described, noting the benefits of having both free PZT unimorphs and thicker silicon structures in a combined structure. This integration is done with complex high-aspect-ratio silicon structures encapsulated by silicon dioxide vertical barrier trenches. Consistent undercut length of thin-film PZT actuator array is obtained with minimal effect on the piezoelectric performance of the actuators.

In experimental validation, both types of joint are shown to function in the integrated structure, with angular displacements varying from joint to joint. The in-plane motion generated by the final leg structure is smaller than the intended motion generated by the proposed m-DoF microrobotic leg due to the remaining silicon dioxide vertical barrier trenches. Nonetheless, performance is well predicted by microrobotic joint modeling that includes the following: 1) compensation for intrinsic residual stress of thin-film stacks that changes the initial deflection of the actuator arrays; 2) behavior of in-plane flexure joint array structures when the width of oxide trench barrier is taken into consideration; and 3) design of an electrical interconnect structure connected with the outer compact actuator array with less impact on the final device motion. Vertical actuation performed near-original design expectations ($\sim 40^\circ$) with only the neutral position changed by residual stress.

The completed leg structures permit faster leg movement with more degrees of freedom than previous walking microrobot actuators. Weight bearing is small but sufficient for the power demands of the piezoelectric actuators. Further improvement to the current design and fabrication of thin-film PZT devices will support continued microrobotic chassis development. This includes the parametric design of the stiffness of silicon flexure and tether in which the oxide vertical barrier trenches are taken into account, and the run-to-run stress analysis and process control of metal stack layers by which the initial out-of-plane bending of the appendage is minimized.

Appendix

Lateral Actuator Array Spring Definitions

From (4), the rotational spring stiffness values of the flexure, tether, and actuator are $k_{f,\theta}$, $k_{t,\theta}$, and $k_{\mathrm{act},\theta}$, respectively

$$k_{f,\theta} = \frac{(EI)_{\mathrm{flex}}}{L_{\mathrm{flex}}} \tag{11}$$

$$k_{t,\theta} = \frac{L_{\mathrm{act}}^2 (EA)_t}{L_t} \tag{12}$$

$$k_{\mathrm{act},\theta} = k_{\mathrm{act}}(F_{\mathrm{act}}) L_{\mathrm{act}}^2 \tag{13}$$

where k_{act} is the axial spring stiffness of the actuator dependent on the actuation force, $(EI)_{\mathrm{flex}}$ and $(EA)_t$ are the composite flexural rigidity values of the silicon and silicon dioxide flexure and tether along transverse and axial directions, respectively, L_{act} is the distance between the tether and the flexure joint, and L_{flex} and L_t are the lengths of the flexure joint and tether as shown in Fig. 1 and Table I. Because the actuator itself and the silicon tether experience the axial force generated by piezoelectric film, the maximum rotary angle is represented in terms of the combined spring stiffness of the joint structure in (11)–(13) as shown in Fig. 3.

Lateral Array Modifications for Interconnect Stiffness

When combining lateral actuator models, such as that defined by (4) and (11)–(13), basic equation (4) can be applied to the

outer in-plane actuator array (joint γ), but in the m-DoF device fabricated, the motion of the inner lateral actuation array (joint β) is limited by the need to deliver an electrical signal to joint γ. This signal is transferred via an elastic interconnect created from the PZT–metal stack. As the inner compact array and the interconnect are mechanically connected in parallel, the following relation is used to predict in-plane motion of the resulting combination, based on the assumption that only small angular displacements contribute nonnegligible stiffness to the elastic interconnect:

$$M_{\mathrm{ic},z} = \frac{(EI)_{\mathrm{ic},z}}{L_{\mathrm{ic}}} \sum_{i=1}^{8} \left(\theta_{z,(\beta)}\right)_i \tag{14}$$

where $(EI)_{\mathrm{ic},z}$ and L_{ic} are the composite in-plane rigidity and effective length of the material stacked PZT thin-film interconnect and $M_{\mathrm{ic},z}$ is the moment applied at the interconnect by the inner compact actuators. The displacement of the tip of the elastic interconnect from the center of in-plane compact array δ_c is estimated from the length of the PZT interconnect and the sum of rotational displacements of each link $\Sigma(\theta_{z,(\beta)})_i$. Since the inner compact array and the PZT thin film are connected in parallel, the radius of rotation exerted by inner compact array is close to δ_c for the small displacement exerted by the parallel structure of the interconnect and inner compact array. The moment is equivalent to the force, which is the ratio of $M_{ic,z}$ to δ_c from the center of rotation, applied at the tip of eighth link of inner compact array. This force applied at eighth link f_{ic}^8 is then projected onto each flexure by f_{ic}^i at ith link in addition to the forcing component by individual actuators to form new forcing terms within the array

$$f_{\mathrm{ic}}^8 \approx \frac{M_{\mathrm{ic},z}}{\delta_c} \begin{bmatrix} \sin\left(\theta_{z,(\beta)}\right)_8 \\ \cos\left(\theta_{z,(\beta)}\right)_8 \\ 0 \end{bmatrix} \quad f_{\mathrm{ic}}^i \approx \frac{M_{\mathrm{ic},z}}{\delta_c} \begin{bmatrix} \sin\left(\theta_{z,(\beta)}\right)_{i,8} \\ \cos\left(\theta_{z,(\beta)}\right)_{i,8} \\ 0 \end{bmatrix} \tag{15}$$

where $(\theta_{z,(\beta)})_{i,8}$ is the sum of rotational displacements from ith link to eighth link. Then, the forcing term $f_{(\beta)}^n$ in (5) consists of $[F_{\mathrm{act}}, 0, F_{\mathrm{act}}]^{\mathrm{T}}$ and f_{ic}^i, and the nonlinear system of equations from (5), (14), and (15) is solved numerically for $(\theta_{z,(\beta)})_i$ [9].

From (10), the stiffness matrix $K_{\mathrm{ic,eq}}$ for PZT interconnect is modeled as

$$\begin{aligned} d_{\mathrm{ic}} &= \begin{bmatrix} x_{\mathrm{ic}} \\ y_{\mathrm{ic}} \\ z_{\mathrm{ic}} \\ \theta_{\mathrm{ic},y} \\ \theta_{\mathrm{ic},z} \end{bmatrix} = K_{\mathrm{ic.eq}}^{-1} F_{\mathrm{ic}} \\ &= \begin{bmatrix} L_{\mathrm{ic}}(EA)_{\mathrm{ic}}^{-1} & 0 & 0 \\ 0 & 0 & L_{\mathrm{ic}}^2 \left(2(EI)_{\mathrm{ic},z}\right)^{-1} \\ 0 & -L_{\mathrm{ic}}^2 \left(2(EI)_{\mathrm{ic},y}\right)^{-1} & 0 \\ 0 & L_{\mathrm{ic}}(EI)_{\mathrm{ic},y}^{-1} & 0 \\ 0 & 0 & L_{\mathrm{ic}}(EI)_{\mathrm{ic},z}^{-1} \end{bmatrix} \\ &\quad \times \begin{bmatrix} F_{\mathrm{ic},x} \\ M_{\mathrm{ic},y} \\ M_{\mathrm{ic},z} \end{bmatrix} \end{aligned} \tag{16}$$

where F_{ic} is the forcing term applied at the tip of the interconnect with the axial force $F_{\mathrm{ic},x}$, out-of-plane moment $M_{\mathrm{ic},y}$, and rotational moment $M_{\mathrm{ic},z}$, respectively. Then, the relation of the forcing term F_{ic} to the lateral actuation force F_{act} within joint β is obtained

$$\begin{aligned} F_{\mathrm{ic}} &= \begin{bmatrix} L_{\mathrm{act}}\delta_c^{-1} \cos\left(\sum_{i=1}^{8} \left(\theta_{z,(\beta)}\right)_i\right) \\ L_{\mathrm{act}}\varepsilon_{\mathrm{dist}} L_{\mathrm{ic}}^{-1} \delta_c^{-1} \cos\left(\sum_{i=1}^{8} \left(\theta_{z,(\beta)}\right)_i\right) \\ L_{\mathrm{act}} \end{bmatrix} N \cdot F_{\mathrm{act}} \\ &= G_{\mathrm{ic}} F_{\mathrm{act}}. \end{aligned} \tag{17}$$

A lumped compliance matrix for the joint β is derived for the case when only very small displacements of point B are observed and joint displacement is assumed to be exerted equally by each actuator. This model, combining the motions at the eight individual actuators into an approximate lumped model, becomes (18), shown at the bottom of the page.

ACKNOWLEDGMENT

The authors would like to thank Dr. P. Herrera-Fierro and T. Latowski for the assistance in chemical–mechanical polishing at Lurie Nanofabrication Facility of the University of Michigan, J. Martin and B. Power for metallization and milling at the U.S. Army Research Laboratories, and L. Sanchez for PZT deposition at Radiant Technologies, Inc.

$$\begin{aligned} d_{8(\beta)}^1 &= \begin{bmatrix} x_{(\beta)} \\ y_{(\beta)} \\ z_{(\beta)} \\ \theta_{y,(\beta)} \\ \theta_{z,(\beta)} \end{bmatrix} \approx K_{\mathrm{array,eq}}^{-1} F_{\mathrm{act}} \\ &= \begin{bmatrix} L_{\mathrm{flex}}(EA)_{\mathrm{flex}}^{-1} & 0 & 0 \\ 0 & 0 & L_{\mathrm{flex}}^2 L_{\mathrm{act}} \left(2(EI)_{\mathrm{flex,z}}\right)^{-1} \\ 0 & -L_{\mathrm{flex}}^2 \left(2(EI)_{\mathrm{flex,y}}\right)^{-1} & 0 \\ 0 & L_{\mathrm{flex}}(EI)_{\mathrm{flex,y}}^{-1} & 0 \\ 0 & 0 & k_{\theta,\mathrm{tot}}^{-1} L_{\mathrm{act}} \end{bmatrix} N \cdot F_{\mathrm{act}} \end{aligned} \tag{18}$$

REFERENCES

[1] P. Dario, R. Valleggi, M. C. Carrozza, M. C. Montesi, and M. Cocco, "Microactuators for microrobots: A critical survey," *J. Micromech. Microeng.*, vol. 2, no. 3, pp. 141–157, Sep. 1992.

[2] T. Ebefors, J. U. Mattsson, E. Kälvesten, and G. Stemme, "A walking silicon micro-robot," in *Proc. TRANSDUCERS*, 1999, pp. 1202–1205.

[3] R. Murthy, A. Das, and D. O. Popa, "ARRIpede: An assembled micro crawler," in *Proc. IEEE Conf. Nanotechnol.*, 2008, pp. 833–836.

[4] S. Hollar, A. Flynn, C. Bellew, and K. S. J. Pister, "Solar powered 10 mg silicon robot," in *Proc. IEEE Int. Conf. MEMS*, 2003, pp. 706–711.

[5] S. Bergbreiter and K. S. J. Pister, "Design of an autonomous jumping microrobot," in *Proc. IEEE Int. Conf. Robot. Autom.*, 2007, pp. 447–453.

[6] B. R. Donald, C. G. Levey, and I. Paprotny, "Planar microassembly by parallel actuation of MEMS microrobots," *J. Microelectromech. Syst.*, vol. 17, no. 4, pp. 789–808, Aug. 2008.

[7] M. H. Mohebbi, M. L. Terry, K. F. Bohringer, G. T. A. Kovacs, and J. W. Suh, "Omni directional walking microrobot realized by thermal microactuator arrays," in *Proc. ASME Int. Mech. Eng. Congr. Expo.*, 2001, pp. 167–173.

[8] K. R. Oldham, J. S. Pulskamp, R. G. Polcawich, and M. Dubey, "Thin-film PZT lateral actuators with extended stroke," *J. Microelectromech. Syst.*, vol. 17, no. 4, pp. 890–899, Aug. 2008.

[9] K. R. Oldham, C. Rhee, J. Ryou, R. Polcawich, and J. Pulskamp, "Lateral thin-film piezoelectric actuators for bio-inspired micro-robotic locomotion," in *Proc. ASME Int. Conf. DETC*, 2009, vol. 6, pp. 759–768.

[10] B. Edamana, B. Hahn, J. S. Pulskamp, R. G. Polcawich, and K. R. Oldham, "Modeling and optimal low-power on-off control of thin-film piezoelectric rotational actuators," *IEEE/ASME Trans. Mechatronics*, vol. 16, no. 5, pp. 884–896, Oct. 2011.

[11] Z. Qiu, J. S. Pulskamp, X. Lin, C. Rhee, T. Wang, R. G. Polcawich, and K. R. Oldham, "Large displacement vertical translational actuator based on piezoelectric thin films," *J. Micromech. Microeng.*, vol. 20, no. 7, pp. 075016-1–075016-10, Jul. 2010.

[12] R. T. Howe and R. S. Muller, "Polycrystalline and amorphous silicon micromechanical beams: Annealing and mechanical properties," *Sens. Actuators*, vol. 4, no. 3, pp. 447–454, 1983.

[13] S. Trolier-Mckinstry and P. Muralt, "Thin film piezoelectrics for MEMS," *J. Electroceram.*, vol. 12, no. 1/2, pp. 7–17, 2004.

[14] R. Murthy and D. O. Popa, "A four degree of freedom microrobot with large work volume," in *Proc. IEEE Int. Conf. Robot. Autom.*, 2009, pp. 1028–1033.

[15] K. R. Oldham, B. Hahn, and P. Park, "On-off control for low-power servo control in piezoelectricmicro-robotics," in *Proc. ASME Dyn. Syst. Control Conf.*, 2008, pp. 1269–1276.

[16] P. Muralt, R. Polcawich, and S. Trolier-McKinstry, "Piezoelectric thin films for sensors, actuators, and energy harvesting," *MRS Bull.*, vol. 34, no. 9, pp. 658–664, Sep. 2009.

[17] N. J. Conway and S.-G. Kim, "Large-strain, piezoelectric, in-plane microactuator," in *Proc. IEEE Int. Conf. MEMS*, 2004, pp. 454–457.

[18] E. E. Aktakka, R. L. Peterson, and K. Najafi, "Multi-layer PZT stacking process for piezoelectric bimorph energy harvesters," in *Proc. Int. Workshop Micro Nanotechnol. Power Gener. Energy Convers. Appl.*, 2011, pp. 139–142.

[19] D. Campolo, M. Sitti, and R. S. Fearing, "Efficient charge recovery method for driving piezoelectric actuators with quasi-square waves," *IEEE Trans. Ultrason., Ferroelect., Freq. Control*, vol. 50, no. 3, pp. 237–244, Mar. 2003.

[20] H.-B. Fang, J.-Q. Liu, Z.-Y. Xu, L. Dong, L. Wang, D. Chen, B.-C. Cai, and Y. Liu, "Fabrication and performance of MEMS-based piezoelectric power generator for vibration energy harvesting," *Microelectron. J.*, vol. 37, no. 11, pp. 1280–1284, Nov. 2006.

[21] J. P. Pulskamp and R. G. Polcawich, "Negative vertical deflection piezoelectric MEMS actuators method of fabrication," U.S. Patent 7 944 121, May 17, 2011.

[22] J. P. Pulskamp and R. G. Polcawich, "Large force and displaement piezoelectric MEMS lateral actuator," U.S. Patent 7 876 026, Jan. 25, 2011.

Choong-Ho Rhee (S'10–M'11) received the B.S. degree in mechanical engineering from the University of California, Los Angeles, in 2005, and the M.S. and Ph.D. degrees in mechanical engineering from the University of Michigan, Ann Arbor, in 2009 and 2012, respectively.

He is currently a Postdoctoral Research Fellow with the Vibration and Acoustics Laboratory: Microsystems, University of Michigan. His research interests include robust parametric design, modeling, and microfabrication of MEMS devices, and bioinspired microrobotics.

Dr. Rhee is a member of the American Society of Mechanical Engineers (ASME).

Jeffrey S. Pulskamp received the B.S. degree in mechanical engineering from the University of Maryland, College Park, in 2000.

He is currently a MEMS Design and Mechanical Engineer with the Micro and Nano Materials and Devices Branch, U.S. Army Research Laboratory, Adelphi Laboratory Center, Adelphi, MD. His current research interests include RF MEMS devices, electromechanical design and modeling of MEMS, and millimeter-scale robotics. He is currently the holder of eight patents related to piezoelectric MEMS devices and has an additional five patents pending.

Ronald G. Polcawich (M'07) received the B.S. degree in materials science and engineering from Carnegie Mellon University, Pittsburgh, PA, in 1997, and the M.S. degree in materials and the Ph.D. degree in materials science and engineering from The Pennsylvania State University, University Park, in 1999 and 2007, respectively.

He is currently a Staff Researcher with the Micro and Nano Materials and Devices Branch, U.S. Army Research Laboratory, Adelphi Laboratory Center, Adelphi, MD, where he is also currently the Team Lead for the RF MEMS and millimeter-scale robotics programs. The current research programs include switches and phase shifters for phased array antennas, tunable MEMS resonators/filters for secure communication, and mobile unattended sensor platforms. His research activities include materials processing of lead zirconate titanate thin films, MEMS fabrication, piezoelectric MEMS, RF components, MEMS actuators, and millimeter-scale robotics. He is currently the holder of four patents and has authored over 30 journal articles, one book chapter on the fabrication and design of piezoelectric MEMS devices, and one book chapter on piezoelectric MEMS switches.

Dr. Polcawich is a member of the Ferroelectrics Committee of the IEEE Ultrasonics, Ferroelectrics, and Frequency Control Society. Additionally, he is a member of the American Ceramics Society.

Kenn R. Oldham (M'10) received the B.S. degree in mechanical engineering from Carnegie Mellon University, Pittsburgh, PA, in 2000, and the Ph.D. degree in mechanical engineering from the University of California, Berkeley, in 2006.

He is currently an Assistant Professor of mechanical engineering at the University of Michigan, Ann Arbor. His research interests include microsystem design and modeling, optimal design and control, and efficient sensing and power circuitry for MEMS devices.

Dr. Oldham is a member of the American Society of Mechanical Engineers (ASME) and the American Society for Engineering Education (ASEE).

The First Launch of an Autonomous Thrust-Driven Microrobot Using Nanoporous Energetic Silicon

Wayne A. Churaman, Luke J. Currano, Christopher J. Morris
Jessica E. Rajkowski and Sarah Bergbreiter

J. Microelectromechanical Systems, 21(1), (2012)

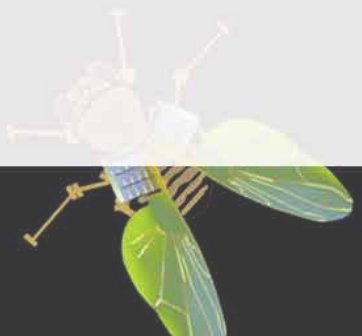

The First Launch of an Autonomous Thrust-Driven Microrobot Using Nanoporous Energetic Silicon

Wayne A. Churaman, Luke J. Currano, *Member, IEEE*, Christopher J. Morris, *Member, IEEE*, Jessica E. Rajkowski, and Sarah Bergbreiter, *Member, IEEE*

***Abstract*—As the capability and complexity of robotic platforms continue to evolve from the macro to the micron scale, the challenge of achieving autonomy requires the development of robust, lightweight architectures. These architectures must provide a platform upon which actuators, control, sensing, power, and communication modules are integrated for optimal performance. In this paper, the first autonomous jumping microrobotic platform is demonstrated using a hybrid integration approach to assemble on-board control, sensing, power, and actuation directly onto a polymer chassis. For the purposes of this paper, jumping is defined as brief parabolic motion achieved via an actuation pulse at takeoff. In this paper, the actuation pulse comes from the rapid release of chemical energy to create propulsion. The actuation pulse lasts several microseconds and is achieved using a novel high-force/low-power thrust actuator, nanoporous energetic silicon, resulting in 250 μJ of kinetic energy delivered to the robot and a vertical height of approximately 8 cm. [2011-0030]**

***Index Terms*—Autonomy, microrobot, porous silicon.**

I. Introduction

SMALL autonomous robotic platforms hold the potential to help target the efforts of first responders, provide stealthy surveillance, or add mobility to sensor networks. However, existing microrobot platforms have limited autonomy [1]–[11]. Autonomous microrobot platforms require essential components including sensors, actuators, electronic circuits, and a power supply. These components must further be integrated to provide certain essential functions including conversion of sensor data to actionable information, intelligence to make decisions based on the information, and mobility to take action on the decisions. Integration of sensing, control, power, and actuation on a single chassis increases the utility of robots, allowing them to be placed in environments where they can sense, think, and act with limited or no human intervention [1]–[5]. These enabling features of autonomy lead to robots that will eventually traverse environments unreachable by humans, while providing critical data, and the ability to adapt to ever changing surroundings.

As robot length scales decrease below the centimeter scale, it becomes an increasing challenge to integrate systems to deliver complex functionality on a single platform. Larger robots like RoACH [6] or Alice [7] are assembled using commercial off-the-shelf (COTS) components including motors, sensors, and electronics with little difficulty. Application-specific integrated circuits (ASICs) provide a unique approach to developing control architectures for millimeter scale platforms by reducing the chip area [5]. This paper will take a new hybrid integration approach that includes both custom fabrication (similar to the bottom-up design of ASICs) and COTS components (similar to simple assembly available to larger robots).

Recent work in microrobotics has made progress toward achieving autonomous functionality, which the authors define as the integration of sensing, actuation, power, and control on a single chassis. These characteristics are available to the robot independent of the operating environment. A number of the published microrobots can be characterized as "actuator only" platforms because they rely on a controlled operating environment to function, cannot make decisions based on the environment, and cannot carry their power supply. The microrobot in [8] maneuvers using an integrated scratch drive actuator and a cantilever steering arm, allowing it to achieve speeds greater than 200 μm/sec. The operation of the microrobot depends on an underlying electrical grid, which provides power and control. The "walking chip" in [9], designed to carry a maximum external load of 2.5 g on its back, relies on external power in the form of tethered wires that measure up to 10 cm in length and lacks sensing and on-board control. The bio-inspired fly in [10] demonstrates insect-like wing trajectories with integrated actuation and mechanics, but does not yet possess integrated on-board sensing, power, or control.

The complexity of the design and integration increases as more functionality is incorporated directly onto the chassis. The microrobot in [11] appears to come close to our definition of autonomy using solar cells for power, electrostatic motors for actuation, and a CMOS finite state machine for control. These components are fabricated individually and integrated using a hybrid approach involving wirebonding to electrically connect each component. However, the robot does not have integrated sensors to allow it to observe and react to changes in the environment. The only robots that appear to include all components necessary for individual autonomy are several centimeters in size or larger [6], [12].

Manuscript received January 28, 2011; revised September 23, 2011; accepted September 28, 2011. Date of publication December 5, 2011; date of current version February 3, 2012. This work was supported by the U.S. Army Research Laboratory. This work was also supported in part by the National Science Foundation under Award CNS0931878. Subject Editor C. Mastrangelo.

W. A. Churaman, L. J. Currano, and C. J. Morris are with the U.S. Army Research Laboratory, Adelphi, MD 20783 USA (e-mail: wayne.a.churaman.civ@mail.mil; luke.j.currano.civ@mail.mil; christopher.j.morris58.civ@mail.mil).

J. E. Rajkowski was with the University of Maryland, College Park, MD 20783 USA. She is now with The Mitre Corporation, McLean, VA 22102 USA (e-mail: jrajkowski@mitre.org).

S. Bergbreiter is with the Mechanical Engineering Department, University of Maryland, College Park, MD 20783 USA (e-mail: sarahb@umd.edu).

Color versions of one or more of the figures in this paper are available online at http://ieeexplore.ieee.org.

Digital Object Identifier 10.1109/JMEMS.2011.2174414

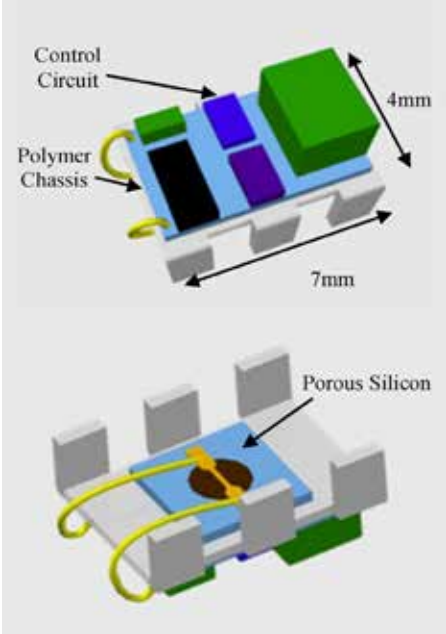

Fig. 1. Computer model of jumping microrobot showing the polymer chassis and control circuit. The energetic thrust actuator is underneath, on the "belly" of the robot.

While these microrobots have demonstrated ingenious functionality, the goal remains to develop a platform that is truly autonomous, where all required functionality is provided on-board the microrobotic platform. To overcome the challenges associated with implementation and integration on a sub-centimeter scale, the authors have developed a novel hybrid integration approach to fabricate a microrobotic platform, conceptually shown in Fig. 1. The microrobotic platform is designed with a polymer chassis, upon which micron-scale electrical traces are lithographically defined and patterned to integrate power (capacitors), sensing (a phototransistor), and the most rudimentary form of decision making (a single transistor). Nanoporous energetic silicon, a solid energetic formulation that produces gas when ignited [13], [14], functions as a thruster to provide mobility. The nanoporous energetic silicon is mounted underneath the polymer chassis. The microrobotic platform can detect a change in the ambient light and respond to the change by triggering ignition of the energetic material. This produces an upward thrust.

This work offers two key contributions toward greater autonomy in microrobotics along with a demonstration of this autonomy. First, a novel energetic silicon-based actuator is proposed to enhance mobility (Section II). Mobility is demonstrated in the form of vertical thrust as stored chemical energy is rapidly converted to mechanical energy. While only a single propulsion event is demonstrated, the nanoporous energetic silicon can be arrayed on-chip to provide multiple propulsion events in different directions. The second contribution develops a hybrid integration approach used to mechanically and electrically integrate this actuator with sensing and control elements (Section III). The integration of on-chip, chemical-based actuation with electronic controls results in sufficient autonomy for applications ranging from mobile sensor networks to dynamically controlled microthrusters. These two contributions are combined to demonstrate the first robot at this size scale with the ability to sense, think, and act (Section IV).

TABLE I
PHYSICAL DIMENSIONS OF SYSTEM COMPONENTS USED TO DESIGN THE HEXAPOD

Component	Mass (mg)	Footprint Dimensions
10uF cap	9	0.8 x 1.6 mm^2
100uF cap	133	2.6 x 3.4 mm^2
FET	8	2.9 x 1.3 mm^2
Phototransistor	3	1.2 x 2.0 mm^2
10k resistor	5	1.5 x 0.8 mm^2
Chassis w/ alloy	62-69	4.0 x 7.0 mm^2
Silicon chip	22-28	4.0 x 4.0 mm^2
Metal pads	14-18	n/a
Wires	11-15	n/a
Extra polymer	13-36	n/a

II. SYSTEM ARCHITECTURE

The goal for the microrobot system architecture was to develop a robotic platform that could sense a change in light intensity and respond by jumping. To simplify matters, the microrobot would jump vertically with a takeoff angle of 90° rather than follow a particular direction. To accomplish this goal, the system architecture required a sensor, control circuit, actuator, and power, each of which needed to be integrated on a polymer chassis. The electronics were designed and fabricated with COTS parts to provide both on-board power and logic to sense a change in light intensity and to provide an electrical stimulus to trigger the energetic material. Table I summarizes the size and weight of each of the components of the system, and the following subsections describe in detail the function of each part. The total mass of the assembled system was approximately 300 mg. In our experiments, three hexapods were assembled and tested. The overall mass of the hexapod varied from 280 mg to 318 mg across the platforms that were assembled. The largest contributor to this variation in mass was an additional layer of polymer that was applied to the hexapod once it was assembled to encapsulate the IC components and increase the robustness of the robot.

A. Actuation

Instead of using a mechanical spring to store energy as seen in [15], nanoporous energetic silicon was chosen to store and release energy chemically. The primary benefit to this approach is reduced complexity and lower part count due to eliminating the need for a separate electrically controlled actuator to compress a spring. Nanoporous energetic silicon is formed in an electrochemical etch process as outlined in [13]. It is initially inert, and only becomes energetic when infused with an oxidizer such as sodium perchlorate. The exothermic reaction can be triggered with heat, friction, or focused light. Multiple actuators can be integrated onto the chassis of a microrobot, allowing it to achieve multiple jumps in different directions. For this work, actuation was demonstrated using a single, 2 mm diameter region of nanoporous energetic silicon.

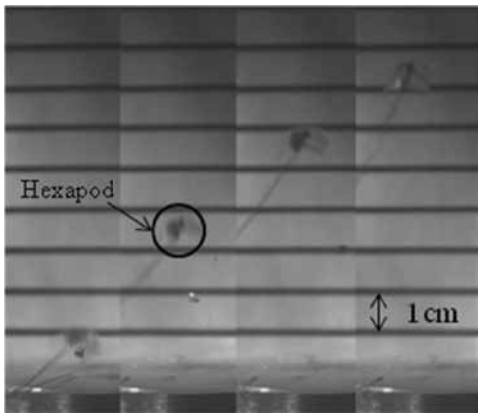

Fig. 2. Tethered jump of 100-mg hexapod platform, tethered by 12-mil wire. The images are spaced 10 frames (10 ms) apart. In frames 1–3, a portion of the silicon chip detached from the hexapod.

Propulsion of a hexapod platform was demonstrated using the nanoporous energetic silicon. Fig. 2 shows an initial (tethered) experiment with a 2 mm diameter, 40 μm thick volume of nanoporous energetic silicon incorporated on the polymer hexapod chassis [16]. The nanoporous silicon was attached to the underside of the hexapod, and connected via wires to an external DC power supply. The components of the control circuit were not attached to the hexapod in this experiment, resulting in a significantly lower system mass. Including the wire leads and the energetic silicon chip, the hexapod weighed 100 mg in this configuration. The hexapod travelled up out of the $\sim$11 cm field of view. The takeoff velocity was measured at 2.8 m/s from high-speed video frames captured at 1000 frames/s. Based on this, the projected jump height was 40 cm. This experiment showed that nanoporous energetic silicon is a viable actuator for a jumping robot, so the authors proceeded to integrate sensing, control, and power functions onto the chassis.

B. Sensing and Control

The microrobotic platform is designed to jump in response to "seeing" a change in light level, as an insect which may jump in response to sensing the shadow of a predator. Sensing is achieved using a light-sensitive phototransistor (SFH3710) shown in Fig. 3. The space available to integrate electronic control, sensing, and actuation is limited to the top and bottom of the chassis, approximately 56 mm^2 total area. The top of the chassis is used to integrate a circuit composed of five discrete surface-mount components (shown in Fig. 3), while the underside of the chassis houses the energetic material used for actuation. The control circuit itself consists of a 2N7002, single n-channel enhancement MOSFET, and a 10 kΩ resistor used to bias the gate of the MOSFET.

The spectral sensitivity of the NPN phototransistor chosen is 350 nm to 950 nm with a maximum sensitivity at 570 nm. When the lighting condition is varied from an illuminance of $\sim$0.3 lux, which is comparable to a full moon on a clear night [17], to approximately 26 lux, somewhat less than the illuminance of a family room [18], the voltage at the gate of the MOSFET rises to 5 V. This closes the MOSFET transistor.

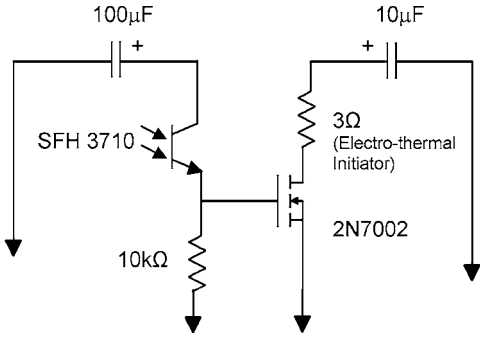

Fig. 3. Circuit designed to provide sensing and actuation. The 3 Ω resistor represents the hotwire used to ignite the energetic material.

A series connection of a 10 μF capacitor and 3 Ω resistor with the MOSFET is shown in Fig. 3. The 3 Ω resistor is used to model the electrical characteristics of an electrothermal initiator used to ignite the energetic material. Details about the electrical initiator design and performance are discussed in [13]. The 10 μF capacitor is precharged to 6 V for the experiments discussed here. As the MOSFET closes, it provides a path for current to flow through the electrical initiator, producing heat to ignite the energetic material. The electrothermal initiator requires at least 150 mA to ignite the energetic material. However, it should be noted that this current is only required for at most 100 μs. In this system, the capacitor discharges directly through the electrothermal initiator wire, without voltage or current regulation. This arrangement simplifies the circuit, reduces the part count, and is sufficient to ignite the energetic silicon.

C. Power

The two capacitors shown in Fig. 3 provide power to the phototransistor and the initiator on the nanoporous energetic silicon. The 100 μF capacitor provides power to bias the phototransistor. The 10 μF capacitor is used to provide power to ignite the nanoporous energetic silicon once the phototransistor detects the increase in light intensity. Both the 100 μF and 10 μF capacitors in Fig. 3 are precharged to 6 V. Both power sources are isolated until an event is detected, triggering the actuation response. A larger capacitor is chosen to power the phototransistor to increase the time constant and supply a larger amount of energy to accommodate leakage. While the longevity of the capacitors as power sources is not investigated in detail, the 100 μF capacitor is able to retain sufficient charge to power the phototransistor for up to 8 min in a dimly lit room ($\sim$0.3 lux). While the expected discharge time, based on the off-state resistance, for the phototransistor and the FET is approximately 40 min, a significant amount of leakage current across the phototransistor results from exposure to the low-level ambient light. It should be noted that the 100 μF capacitor used to bias the phototransistor is the heaviest single part of the robot (Table I), with the much smaller capacitor only acting to initiate the energetic material. In the future, the requirement for this larger capacitor may be removed through better sensors or through the use of a low-volume, high-capacity thin film battery. The energy associated with the capacitors and the nanoporous energetic silicon is summarized in Table II.

TABLE II
SUMMARY OF ENERGY SUPPLIED BY THE CAPACITORS AND ENERGY SUPPLIED TO AND GENERATED BY THE NANOPOROUS ENERGETIC SILICON

Component	Type of Energy	Energy
10 μF Capacitor	Electrical	0.18 mJ
100 μF Capacitor	Electrical	1.8 mJ
Energetic Porous Si	Electrical (ignition)	0.18 mJ
Energetic Porous Si	Chemical	1.9 J

III. HYBRID INTEGRATION

To electrically and mechanically integrate the sensing, power, and control components with the actuator and robot chassis with minimal added mass, a new hybrid integration process was designed. This approach used a polymer chassis for structural support to carry a payload as well as a substrate for electrical traces for the integration of the control circuit.

A. Polymer Chassis

The hexapod style chassis was chosen to enable walking in future iterations of the platform, and the polymer was chosen for robustness, durability, light weight, and ease of fabrication. The chassis provided the robot's functional skeleton as well as a point of assembly on which to integrate all other components in this hybrid integration approach (Fig. 1). It is 4 mm by 7 mm by 0.5 mm in dimensions and was fabricated using a rapid prototyping process [19]. A photodefinable polymer (Loctite3525 modified acrylic) was first spread evenly on a transparent plastic sheet, and another transparent sheet was placed on top of the polymer film. Glass slides were placed between the two sheets to define the thickness. A photolithographic mask, with the hexapod features defined as clear windows in an opaque field, was then placed on top, and UV light was used to expose the hexapod features through the mask. The exposed polymer was hardened, and the unexposed polymer could then be removed with a methanol rinse. The metal traces for assembly of the control circuit were deposited and patterned (described in the following section), then the legs were bent out of plane, and an additional layer of polymer, [shown in Fig. 4(c)], was applied to the inside corner between the legs and the body and cured. This resulted in the 3-D hexapod structure similar to that in Fig. 4(d), which allows for future integration of leg actuators for bimodal (walking/jumping) mobility or to orient the robot for a jump in a particular direction.

B. Metallization

A copper film was deposited on top of the polymer chassis using metal evaporation at room temperature. Once deposited, the electrical traces were lithographically patterned on the copper film. With photoresist protecting the underlying copper metal traces, the exposed copper was etched using a 2 : 1 mixture of water to nitric acid. To facilitate attaching the circuit elements to a flexible substrate, the copper traces were then coated with a low melting temperature solder (Indalloy 117 from Indium Corporation) using a dipping process discussed

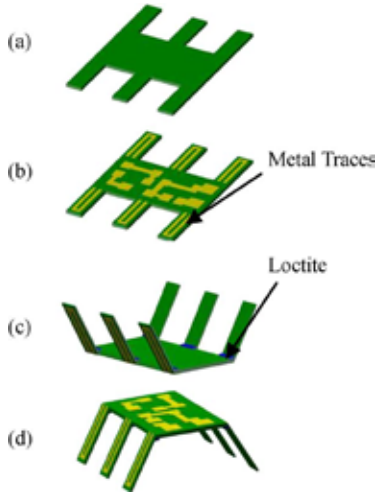

Fig. 4. Process flow to fabricate 3-D hexapod structure. This process flow shows metal patterned on the legs. For the purpose of our experiment, metal was only patterned on the body.

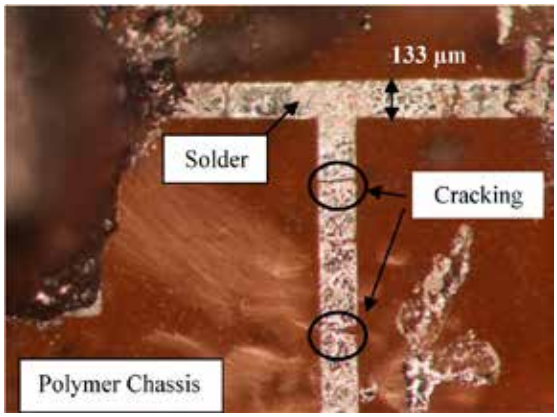

Fig. 5. Metalized layer begins to crack when submerged in low-temperature solder. Copper traces were subsequently widened to 472 μm to allow enough solder to heal the cracks.

in [20]. Indalloy 117 melts at 47 °C, and was chosen because the Loctite polymer softens above 100 °C and using a solder iron to heat the solder would result in damage to the polymer substrate. The circuit components can be attached by reflowing the low-temperature solder without damaging the substrate. For this process, the solder was kept at 65 °C to ensure the robustness of the polymer chassis. A mixture of ethylene glycol and hydrochloric acid was added to the solder dipping crucible to remove any surface oxides on the copper traces and on the solder. The polymer chassis was slowly submerged into the molten alloy, and retracted after 10 s. About 50% of the time, a visual inspection revealed incomplete coating, and the chassis was submerged again to coat all copper traces. Initial results indicated a tendency for the copper layer to crack when cooling after removal from the solution, as shown in Fig. 5. Therefore, the minimum copper feature size was increased from 133 μm to 472 μm, providing greater surface area to capture enough solder to "heal" any cracks that form.

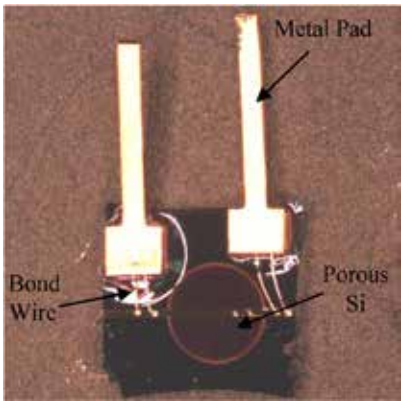

Fig. 6. Metal bond pads fixed to Si allow the energetic to be connected to the control circuit.

C. Assembly

A serial process was used to assemble each of the components. The hexapod and circuit components were separately coated with the low melting temperature alloy. A solder iron was used to manually solder external wires to the capacitors and the MOSFET before the components were assembled onto the hexapod chassis. This allowed electrical leads to be easily attached to charge the capacitor power sources after assembly. The polymer hexapod was then placed on a hotplate at 65 °C to melt the Indalloy, and the circuit components were positioned using tweezers. Moderate pressure was applied manually between the component and the binding site to ensure a robust connection. The hexapod was then removed from the hotplate and allowed to cool. As the polymer substrate cooled, the circuit components were fused to the binding sites.

Attempts to solder directly to the energetic porous silicon chip were unsuccessful because the thin-film initiator was not robust enough to withstand the heat of a soldering iron. The low melting temperature alloy was not attempted because of concern that the dipping process might contaminate the nanoporous silicon. Although it was possible to wirebond to the silicon chip, wirebonding to the polymer chassis was not successful because the polymer was too soft. Therefore, gold-plated metal pads shown in Fig. 6 were glued to the silicon chip, and wirebonds were made between the integrated initiator and the metal pads. Wires were then soldered between the control circuit and these metal pads, and the nanoporous energetic silicon was attached to the underside of the hexapod using a double-adhesive tape. In future iterations, the pads could be eliminated by creating vias in the polymer chassis and the nanoporous silicon substrate and filling them with metal for direct connection using the low-temperature solder.

Once the hexapod was assembled, the circuit and underlying electrical traces were coated with an additional layer of Loctite to prevent delamination of the rigid circuit elements from the flexible polymer skeleton. This robust integration allowed the hexapod legs to be flexed and potentially actuated out of plane, without disturbing the functionality of the circuit. This unique process therefore uses one material as the mechanical structure, electrical substrate, and packaging material for the microrobotic platform. Fig. 7 shows a circuit that has been fully assembled onto the polymer chassis.

Fig. 7. Metal bond pads soldered to wires coming off of the capacitor and MOSFET.

D. Packaging

The sodium perchlorate oxidizer used to make the nanoporous silicon into an energetic material is strongly hygroscopic, and the absorption of water by the oxidizer degrades the efficiency of the energetic reaction and produces stress within the porous layer. The induced stress can also cause the porous material to crack and the hotwire initiator to subsequently break. For this reason, the jumping experiments were all conducted in a dry box plumbed with nitrogen. Even so, the process of opening the door of the enclosure to charge the capacitors prior to ignition allowed enough time for the oxidized sample to absorb water and degrade the efficiency of the reaction.

Three techniques were employed to limit the rate at which moisture was absorbed by the oxidizer. The first technique involved applying one drop of oxidizer solution (3.2 M $NaClO_4$ in methanol) using a syringe in a dry room controlled to $< 1\%$ relative humidity and allowing the sample to dry for 20 min. After the sample was dried, a thin layer of Loctite ($\sim$500 μm thick) was carefully applied on top of the porous silicon and UV cured for 5 min. The second technique was to apply the oxidizer and dry in a nitrogen dry box, then seal the porous silicon with an evaporated parylene layer ($\sim$12 μm thick). While loading the samples into the parylene system, there was some exposure to environmental moisture. An alternative approach which has not been attempted yet would be to dry the sample under the dry nitrogen inside the parylene coating chamber to avoid transport.

The final (and simplest) humidity exposure minimization approach was to connect leads to the hexapod prior to application of the oxidizer and run these leads outside of the controlled environment chamber. The oxidizer was allowed to dry for 15 min. The door to the chamber was then opened very briefly (less than 30 s) to disconnect the leads and then closed for the experiment.

IV. Results

Experiments were performed in a laboratory, and a moderately dark environment was simulated by turning off all

overhead fluorescent lights, and turning on a small 12-W lamp in the corner of the room to allow some visibility for positioning the device and connecting and disconnecting electrical leads. The resulting ambient light level at the photodetector was ∼0.3 lux, as mentioned above. Oxidizer was applied to the nanoporous energetic silicon using one of the three different techniques discussed above to minimize moisture exposure. The 100 μF and 10 μF capacitors were charged to 6 V, and the hexapod was positioned approximately 12 inches under a high intensity 3 LED array light source. The light source was turned on, triggering the phototransistor, which closed the MOSFET switch, which in turn triggered ignition of the energetic nanoporous silicon. Each jump was captured by a high-speed camera recording at 1000 frames per second.

The first untethered experiment was performed with the Loctite moisture seal encapsulating the porous silicon. The experiment was done in ambient air; therefore an encapsulation layer was needed to prevent moisture uptake and subsequent degradation of the porous silicon and oxidizer mixture. This hexapod had a total weight of 280 mg, and achieved a vertical height of 1 cm when the light was turned on. The limited height may have been due to packaging the sample with Loctite. Deposition of the Loctite directly on the porous silicon resulted in a thick layer ($\sim$500 μm) of the Loctite remaining on the surface. A portion of the output energy being converted into thrust for movement would therefore be lost in breaking the seal created by the Loctite. It was also possible that the Loctite coating may have affected the oxidized porous silicon surface, causing it to be less reactive. Similar results were achieved with the parylene-coated samples. Further work must be done to explore other alternatives to encapsulate the energetic without degrading the performance.

The best jump heights were achieved with the simplest humidity exposure minimization approach, which involved pre-connecting the electrical leads to charge the capacitors before applying and drying the oxidizer, and running the experiment in a nitrogen-filled box. The box was only very briefly opened (less than 30 s) to disconnect the leads. In this case, a 314-mg hexapod jumped approximately 8 cm vertically (Fig. 8).

The authors analyzed approximately 200 frames of the jump trajectory to determine if any significant acceleration sources other than gravity affected the microrobotic platform during flight. Several frames at the end of the trajectory were not captured in the high-speed video, so the landing portion of the trajectory was not shown. The center of the hexapod chassis was chosen as the center of mass, and the height was measured as the center of mass crossed each half centimeter marker on the height scale. The resulting position versus time data is shown in Fig. 9. Given the resolution of the camera, the accuracy with which we were able to pinpoint the robot's center of mass in each frame, and parallax errors involved observation from a fixed viewpoint, we estimated the uncertainly for each data point as approximately 0.25 cm. Using this uncertainty, the potential energy based on the maximum observed height was between 246 μJ and 262 μJ.

The data points were then fitted to the parabolic curve describing the motion of a projectile under constant free-fall acceleration g and negligible air resistance. The parabolic curve

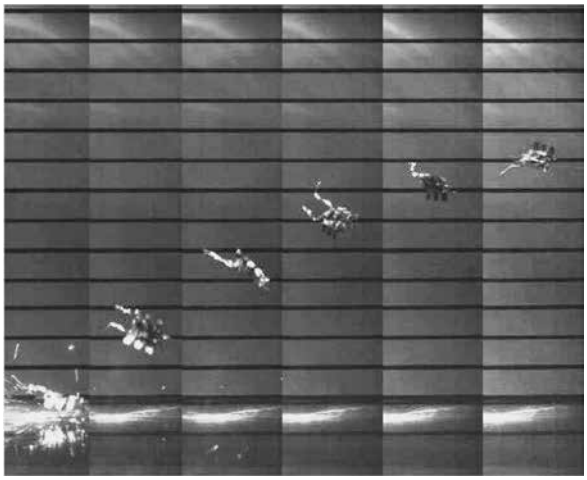

Fig. 8. Propelled hexapod when actuator triggered by light captured at 1000 frames per second. Frames shown above are 20 ms apart. The vertical scale bar shown is spaced 1 cm per division.

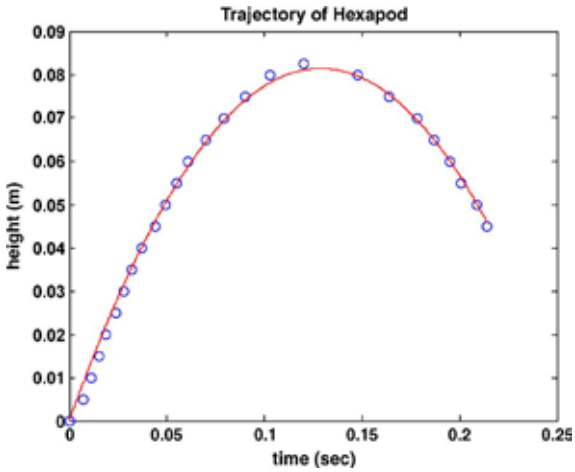

Fig. 9. Trajectory of the hexapod jump. Experimentally determined height shown as blue circles. The parabolic curve fit describes projectile motion under acceleration due to gravity and negligible air resistance.

was then fitted to the data to determine the initial velocity v_i, as shown in Fig. 9. This fit resulted in a calculated take-off velocity of 1.263 m/s. The associated kinetic energy is 250 μJ, which is within the potential energy uncertainty bounds calculated based on measured maximum height. The quality of the fit to the experimental data also demonstrates that the microrobotic platform followed a drag-free parabolic trajectory under acceleration due to gravity and negligible air resistance.

Although the overall mass of the energetic chip as given in Table I was approximately 25 mg, the mass of the reactive region was estimated at only 0.21 mg. The 2 mm diameter energetic region was able to propel the robot approximately 8 cm into the air, even though the robot was more than 1000 times the mass of the energetic material.

As a point of comparison, to achieve the same height with a conventional actuator would require an actuator stiffness of 2.4 kN/m and a force of at least 9.6 N (assuming the

leg length of 4 mm is the actuator throw). This would be very difficult if not impossible to achieve at this size scale. To ignite the nanoporous energetic silicon, a maximum of 180 μJ of electrical energy was consumed (assuming that the 10 μF capacitor discharged entirely from 6 V to 0 V). Defining an "effective actuation efficiency" as the ratio of mechanical energy produced to electrical energy consumed, the 8 cm jump here represented an effective efficiency of 137%. Based on past measurements of the energy density of the nanoporous energetic silicon reaction, approximately 1.9 J of chemical energy was released [21]. Therefore, the chemical to kinetic conversion efficiency was actually extremely low (0.0127%), indicating that the vast majority of the available energy was wasted.

There is consequently room for improvement, and the authors believe implementation of a nozzle in future designs will increase this efficiency by directing gases in a more effective manner to produce maximum thrust. However, the fact that a respectable height of over 11$\times$ the body length was achieved despite the abysmal conversion efficiency underscores the tremendous amount of energy available in the nanoporous energetic silicon. The authors believe that this technology will have many applications in future MEMS systems if the energy can be more efficiently captured and put to use.

V. Conclusion

An autonomous jumping microrobot has been demonstrated, achieving a vertical jump of 8 cm, which was over 11 times its longest physical dimension. Autonomy was achieved through on-board integration of a simple circuit constructed of discrete surface mount components. The resulting system has optical sensing, control, power, and mobility. The rudimentary sensing and intelligence allow the hexapod to detect an increase in light intensity and respond by jumping. In addition, the novel use of an energetic material for actuation was shown, allowing significantly more mechanical energy to be produced than the electrical energy needed to initiate the reaction.

A hybrid integration approach has also been presented, which uses a low-temperature solder and metal interconnects patterned directly on the robot's polymer chassis to integrate various discrete electrical components. One of the unique aspects to the integration approach is that a single UV-curable polymer material was used for the robot chassis, as a substrate for the assembly of the circuit components, and as a packaging material. The authors expect improvements in direction control and development of an array of energetic actuators to allow multiple jumps, leading to future technological leaps for autonomous microrobots.

Acknowledgment

The authors would like to thank the Micro Robotics Laboratory at the University of Maryland for assistance in fabricating the robotic polymer chassis.

References

[1] P. Verschure, B. Krose, and R. Pfeifer, "Distributed adaptive control: The self-organization of structured behavior," *Robot. Autonom. Syst.*, vol. 9, no. 3, pp. 181–196, 1992.

[2] R. Pfeifer, "Robots as cognitive tools," *Int. J. Cognit. Technol.*, vol. 1, no. 1, pp. 125–143, 2002.

[3] C. Bartneck and J. Forlizzi, "A design-centred framework for social human-robot interaction," in *Proc. 13th IEEE Int. Workshop Robot Human Interact. Commun. ROMAN*, Sep. 20–22, 2004, pp. 591–594.

[4] G. Bekey, "Software architectures for autonomous robots," in *Autonomous Robots: From Biological Inspiration to Implementation and Control*. Cambridge, MA: MIT Press, 2005, pp. 104–107.

[5] R. Casanova, A. Dieguez, A. Arbat, O. Alonso, A. Sanuy, J. Canals, J. Colomer, and J. Samitier, "Integration of the control electronics for a mm^3-sized autonomous microrobot into a single chip," in *Proc. IEEE ICRA*, May 12–17, 2009, pp. 3007–3012.

[6] A. M. Hoover, E. Steltz, and R. S. Fearing, "RoACH: An autonomous 2.4g crawling hexapod robot," in *Proc. IEEE/RSJ IROS*, 2008, pp. 26–33.

[7] G. Caprari and R. Siegwart, "Mobile micro-robots ready to use: Alice," in *Proc. IEEE/RSJ Int. Conf. IROS*, Aug. 2–6, 2005, pp. 3295–3300.

[8] B. R. Donald, C. G. Levey, C. D. McGray, I. Paprotny, and D. Rus, "An untethered, electrostatic, globally controllable MEMS micro-robot," *J. Microelectromech. Syst.*, vol. 15, no. 1, pp. 1–15, Feb. 2006.

[9] T. Ebefors, T. Mattsson, E. Kalvesten, and G. Stemme, "A walking silicon micro-robot," in *Proc. 10th Int. Conf. Solid-State Sens. Actuators (Transducers'99)*, Sendai, Japan, Jun. 7–10, 1999, pp. 1202–1205.

[10] R. J. Wood, "The first takeoff of a biologically inspired at-scale robotic insect," *IEEE Trans. Robot.*, vol. 24, no. 2, pp. 341–347, Apr. 2008.

[11] S. Hollar, A. Flynn, C. Bellew, and K. S. J. Pister, "Solar powered 10 mg silicon robot," in *Proc. IEEE 16th Annu. Int. Conf. MEMS*, Kyoto, Japan, Jan. 19–23, 2003, pp. 706–711.

[12] H. Masato and T. Tooru, "Development of a humanoid robot ASIMO," *Honda R&D Tech. Rev.*, vol. 13, no. 1, pp. 1–6, 2001.

[13] L. J. Currano and W. A. Churaman, "Energetic nanoporous silicon devices," *J. Microelectromech. Syst.*, vol. v18, no. v4, pp. 799–807, Aug. 2009.

[14] D. Kovalev, V. Y. Timoshenko, N. Kunzner, E. Gross, and F. Koch, "Strong explosive interaction of hydrogenated porous silicon with oxygen at cryogenic temperatures," *Phys. Rev. Lett.*, vol. 87, no. 6, p. 068 301, Aug. 2001.

[15] M. Kovac, M. Fuchs, A. Guignard, J.-C. Zufferey, and D. Floreano, "A miniature 7g jumping robot," in *Proc. IEEE ICRA*, Pasadena, CA, May 19–23, 2008, pp. 373–378.

[16] L. J. Currano, W. A. Churaman, J. Rajkowski, C. J. Morris, and S. Bergbreiter, "Nanoenergetic silicon as a thrust actuator for jumping microrobots," in *Proc. Hilton Head Workshop: A Solid-Sate Sens., Actuators Microsyst. Workshop*, Hilton Head Island, SC, Jun. 6–10, 2010, pp. 126–129.

[17] P. Schlyter, Radiometry and Photometry in Astronomy. [Jan. 3, 2011], Mar. 18, 2009. [Online]. Available: http://stjarnhimlen.se/comp/radfaq.html#10

[18] A. Pears, "Chapter 7: Appliance technologies and scope for emission reduction," in *Strategic Study of Household Energy and Greenhouse Issues*, Australian Greenhouse Office, Australia, Jun. 1998, pp. 61.

[19] J. Rajkowski, "Rapid polymer prototyping for applications in low cost and robust microrobots," M.S. thesis, Dept. Mech. Eng., Univ. Maryland, College Park, MD, 2010.

[20] C. Morris and B. Parviz, "Micro-scale metal contacts for capillary force-driven self-assembly," *J. Micromech. Microeng.*, vol. 18, no. 1, p. 015 022, Jan. 2008.

[21] L. J. Currano, W. Churaman, and C. Becker, "Nanoporous silicon as a bulk energetic material," in *Proc. Int. Solid-State Sens., Actuators Microsyst. Conf. (TRANSDUCERS)*, Denver, CO, Jun. 21–25, 2009, pp. 2172–2175.

Wayne A. Churaman received the B.S. and M.S. degrees in electrical engineering from the University of Maryland, College Park, in 2005 and 2010, respectively, with a specific focus on microelectronics and microrobotic platforms.

He currently works as a MEMS Engineer for the U.S. Army Research Laboratory, Adelphi, MD. His interests include experimental analysis of nanoenergetic materials, integration of nanoenergetic materials with MEMS, and MEMS sensor design and fabrication. He is currently developing novel actuators using nanoenergetic porous silicon.

Luke J. Currano (M'09) received the B.S., M.S., and Ph.D. degrees in mechanical engineering from the University of Maryland, College Park, in 2000, 2002, and 2010, respectively.

He has worked as a MEMS Engineer for the U.S. Army Research Laboratory (ARL), Adelphi, MD, since 2001. He is currently Team Leader of the MEMS and Nanoenergetic Devices team at ARL. His research interests include integration of energetic materials with MEMS, high force/displacement MEMS actuators, acceleration switches, no-power sensors, and biologically inspired MEMS devices.

Christopher J. Morris (S'04–M'07) received the M.S. degree in mechanical engineering and the Ph.D. degree in electrical engineering from the University of Washington, Seattle, in 2000 and 2007, respectively.

Between his graduate studies, he was with Micronics, Inc., developing microfluidic devices. He is currently with the U.S. Army Research Laboratory in the Sensors and Electron Devices Directorate, Adelphi, MD. His current research interests lie in the integration of new materials and technologies with microelectronics and MEMS, including on-chip energetic materials, electronics packaging, and fluidic self-assembly.

Jessica E. Rajkowski received the B.S. and M.S. degrees in mechanical engineering from the University of Maryland, College Park, in 2009 and 2010, respectively, with a focus on microrobotics.

She is currently a Senior Systems Engineer at The MITRE Corporation, McLean, VA, where she works in the Nanosystems Group. Her research interests include the design and fabrication of millimeter-scale robotics and thermal micro-actuators.

Sarah Bergbreiter (S'03–M'07) received the B.S.E. degree in electrical engineering from Princeton University, Princeton, NJ, in 1999, and the M.S. and Ph.D. degrees from the University of California, Berkeley, in 2004 and 2007, respectively.

She is currently an Assistant Professor of Mechanical Engineering, with a joint appointment in the Institute for Systems Research at the University of Maryland, College Park. Her research addresses the challenges necessary to make robotic bugs move, including effective locomotion, efficient actuation, micromechanism design and fabrication, power systems, sensing, and integration.

Dr. Bergbreiter received a DARPA Young Faculty Award for her work toward autonomous millimeter-scale robots in 2008.

Adaptive Stochastic Disturbance Accommodating Control

Jemin George , Puneet Singla and John L. Crassidis

International Journal of Control, 84:2, 310-335 (2011)

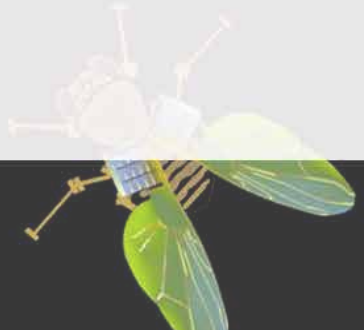

International Journal of Control
Vol. 84, No. 2, February 2011, 310–335

Taylor & Francis
Taylor & Francis Group

Adaptive stochastic disturbance accommodating control

Jemin George[a]*, Puneet Singla[b] and John L. Crassidis[b]

[a]*US Army Research Laboratory, Adelphi, MD 20783, USA;* [b]*Department of Mechanical and Aerospace Engineering, University at Buffalo, State University of New York, Amherst, NY 14260, USA*

(*Received 11 May 2010; final version received 23 December 2010*)

This article presents a Kalman filter based adaptive disturbance accommodating stochastic control scheme for linear uncertain systems to minimise the adverse effects of both model uncertainties and external disturbances. Instead of dealing with system uncertainties and external disturbances separately, the disturbance accommodating control scheme lumps the overall effects of these errors in a to-be-determined model-error vector and then utilises a Kalman filter in the feedback loop for simultaneously estimating the system states and the model-error vector from noisy measurements. Since the model-error dynamics is unknown, the process noise covariance associated with the model-error dynamics is used to empirically tune the Kalman filter to yield accurate estimates. A rigorous stochastic stability analysis reveals a lower bound requirement on the assumed system process noise covariance to ensure the stability of the controlled system when the nominal control action on the true plant is unstable. An adaptive law is synthesised for the selection of stabilising system process noise covariance. Simulation results are presented where the proposed control scheme is implemented on a two degree-of-freedom helicopter.

Keywords: disturbance accommodating control; stochastic adaptive control; Kalman filter; stochastic stability

1. Introduction

Uncertainty in dynamic systems may take numerous forms, but among them the most significant are noise/disturbance uncertainty and model/parameter uncertainty. External disturbances and system uncertainties can obscure the development of a viable control law. This article presents the formulation and analysis of a stochastic robust control scheme known as the Disturbance Accommodating Control (DAC). The main objective of DAC is to make necessary corrections to the nominal control input to accommodate for external disturbances and system uncertainties. Instead of dealing with system uncertainties and disturbances separately, DAC lumps the overall effects of these errors in a to-be-determined term that is used to directly update a nominal control input.

DAC was first proposed by Johnson in 1971 (Johnson 1971). Though the traditional DAC approach only considers disturbance functions which exhibit waveform patterns over short intervals of time (Johnson and Kelly 1981), a more general formulation of DAC can accommodate the simultaneous presence of both 'noise' type disturbances and 'waveform structured' disturbances (Johnson 1984, 1985). The disturbance accommodating observer approach has been shown to be extremely effective for disturbance attenuation (Profeta, Vogt, and Mickle 1990; Kim and Oh 1998; Biglari and Mobasher 2000); however, the performance of the observer can significantly vary for different types of exogenous disturbances, which is due to observer gain sensitivity.

This article presents a robust control approach based on a significant extension of the conventional observer-based DAC concept, which compensates for both unknown model parameter uncertainties and external disturbances by estimating a model-error vector (throughout this article the phrase 'disturbance term' will be used to refer to this quantity) in real time. The estimated model-error vector is further used as a signal synthesis adaptive correction to the nominal control input to achieve maximum performance. This control approach utilises a Kalman filter in the feedback loop for simultaneously estimating the system states and the disturbance term from measurements (Sorrells 1982, 1989; Davari and Chandramohan 2003). The estimated states are then used to develop a nominal control law while the estimated disturbance term is used to make necessary corrections to the nominal control input to minimise the effects of both system uncertainties and the external disturbance. There are several advantages of implementing the Kalman filter in the DAC approach: (i) tuning of the

*Corresponding author. Email: jemin.george@arl.army.mil

ISSN 0020–7179 print/ISSN 1366–5820 online

DOI: 10.1080/00207179.2010.551142
http://www.informaworld.com

estimator parameters, such as the process noise matrix, can be done easily unlike conventional DAC approaches in which the adaptation involves the entire feedback gain; (ii) the estimated disturbance term is a natural byproduct of state estimation and (iii) the Kalman filter can be used to filter noisy measurements.

It is a well-known fact that the closed-loop performance and the stability of the Kalman filter-based DAC approach depends on the accuracy of the estimated disturbance term. Since the dynamics of the disturbance term is unknown, the process noise covariance associated with the disturbance term is used to empirically tune the Kalman filter to yield accurate estimates. Although the Kalman filter-based DAC approach has been successfully utilised for practical applications, there has not been any rigorous stochastic stability analysis to reveal the interdependency between the estimator process noise covariance and controlled system stability. The first main contribution of this article is a detailed stability analysis, which examines the explicit dependency of the controlled system's closed-loop stability on the disturbance term process noise covariance and the measurement noise covariance. Since the system under consideration is stochastic in nature, the notion of stability is depicted in two separate fashions. The first method deals with moment stability and the second technique considers stability in a probabilistic sense.

Stochastic stability analysis on the Kalman filter-based DAC approach indicates that the effectiveness of the proposed control scheme depends on the estimator parameters such as the process noise covariance matrix. The stability analysis also indicates that the DAC scheme is most effective when the assumed process noise covariance satisfies a lower bound requirement which depends on the system uncertainties. In general, it is difficult to select a stabilising process noise covariance for the broad type of uncertain systems considered here. One could always try to select an extremely large value of process noise covariance that might stabilise the system or even monotonically increase the process noise covariance matrix in an ad-hoc manner until the system stabilises. However, it is important to keep in mind that selecting a large process noise covariance matrix would result in noisy control signal which could lead to problems such as chattering. The second main contribution of this article is the formulation of a stochastic adaptive scheme for selecting the appropriate process noise covariance that would guarantee closed-loop stability of the controlled system.

The structure of this article is as follows. A detailed formulation of the stochastic DAC approach for multi-input multi-output (MIMO) systems, followed by a stochastic stability analysis, is first given. Next, an adaptive scheme is developed for the selection of stabilising the disturbance term process noise covariance. Simulation results are then presented where the proposed control scheme is implemented on a two degree-of-freedom helicopter.

2. DAC formulation

Let $(\Omega, \mathcal{F}, \mathbb{P})$ denote a probability space, where Ω is the sample space, $\mathcal{F}$ is a σ-field and $\mathbb{P}$ is a probability measure on the measurable space $(\Omega, \mathcal{F})$. Additionally, the elements of Ω are denoted by ω and the members of $\mathcal{F}$ are called events. Now consider a linear time-invariant stochastic system of the following form:

$$\begin{aligned} \dot{\mathbf{X}}_1(t) &= \bar{A}_1\mathbf{X}_1(t) + \bar{A}_2\mathbf{X}_2(t), \quad \mathbf{X}_1(t_0) = \mathbf{X}_{1_0}, \\ \dot{\mathbf{X}}_2(t) &= A_3\mathbf{X}_1(t) + A_4\mathbf{X}_2(t) + B\mathbf{u}(t) + \mathbf{W}(t), \\ \mathbf{X}_2(t_0) &= \mathbf{X}_{2_0}. \end{aligned} \tag{1}$$

Here, the stochastic state vector, $\left[\mathbf{X}_1^T(t)\ \mathbf{X}_2^T(t)\right]^T = \mathbf{X}(t) \triangleq \mathbf{X}(t,\omega) : [t_0, t_f] \times \Omega \mapsto \Re^n$, is an n-dimensional random variable for fixed t. The state vectors, $\mathbf{X}_1(t)$ and $\mathbf{X}_2(t)$ are of dimensions $\mathbf{X}_1(t) \triangleq \mathbf{X}_1(t,\omega) : [t_0, t_f] \times \Omega \mapsto \Re^{n-r}$ and $\mathbf{X}_2(t) \triangleq \mathbf{X}_2(t,\omega) : [t_0, t_f] \times \Omega \mapsto \Re^r$, respectively. The system given in (1) is in the typical kinematics-dynamics form, where the kinematics is assumed to be fully known, i.e. the state matrices $\bar{A}_1 \in \Re^{(n-r)\times(n-r)}$ and $\bar{A}_2 \in \Re^{(n-r)\times r}$ are precisely known. Uncertainty is only associated with the dynamics, i.e. the state and control distribution matrices, $A_3 \in \Re^{r\times(n-r)}$, $A_4 \in \Re^{r\times r}$, $B \in \Re^{r\times r}$, are assumed to be unknown. Also, the input matrix B is assumed to be non-singular. Finally, the stochastic external disturbance $\mathbf{W}(t) \triangleq \mathbf{W}(t,\omega) : [t_0, t_f] \times \Omega \mapsto \Re^r$ is modelled as a linear time-invariant system driven by a Gaussian white noise process, i.e.

$$\dot{\mathbf{W}}(t) = \mathbb{L}(\mathbf{X}(t), \mathbf{W}(t)) + \boldsymbol{\mathcal{V}}(t), \quad \mathbf{W}(t_0) = \mathbf{0}_{r\times 1}, \tag{2}$$

where $\mathbb{L}(\cdot)$ is an unknown linear operator and $\boldsymbol{\mathcal{V}}(t) \triangleq \boldsymbol{\mathcal{V}}(t,\omega) : [t_0, t_f] \times \Omega \mapsto \Re^r$, is assumed to be zero-mean Gaussian white noise process, i.e. $\boldsymbol{\mathcal{V}}(t) \sim \mathcal{N}(\mathbf{0}, \mathcal{Q}\delta(\tau))$. It is important to note that the linear operator $\mathbb{L}(\cdot)$ and the covariance of the white noise process $\boldsymbol{\mathcal{V}}(t)$, are unknown. The measurement equation is given as

$$\mathbf{Y}(t) = C\mathbf{X}(t) + \mathbf{V}(t), \tag{3}$$

where $\mathbf{Y}(t) \triangleq \mathbf{Y}(t,\omega) : [t_0, t_f] \times \Omega \mapsto \Re^m$ is the measurement vector and $C \in \Re^{m\times n}$ denotes the known output matrix. The measurement noise, $\mathbf{V}(t) \triangleq \mathbf{V}(t,\omega) : [t_0, t_f] \times \Omega \mapsto \Re^m$, is assumed to be zero-mean Gaussian white noise with known covariance, i.e. $\mathbf{V}(t) \sim \mathcal{N}(\mathbf{0}, R\delta(\tau))$.

The assumed (known) system matrices are given as A_{3_m}, A_{4_m} and B_m. Now the external disturbance and the model uncertainties can be lumped into a disturbance term, $\mathcal{D}(t) \in \Re^r$, through

$$\mathcal{D}(t) = \Delta A_1 \mathbf{X}_1(t) + \Delta A_2 \mathbf{X}_2(t) + \Delta B \mathbf{u}(t) + \mathbf{W}(t), \quad (4)$$

where $\Delta A_1 = (A_3 - A_{3_m})$, $\Delta A_2 = (A_4 - A_{4_m})$ and $\Delta B = (B - B_m)$. Using this disturbance term the true model can be written in terms of the known system matrices as follows:

$$\begin{aligned} \dot{\mathbf{X}}_1(t) &= \bar{A}_1 \mathbf{X}_1(t) + \bar{A}_2 \mathbf{X}_2(t), \\ \dot{\mathbf{X}}_2(t) &= A_{3_m} \mathbf{X}_1(t) + A_{4_m} \mathbf{X}_2(t) + B_m \mathbf{u}(t) + \mathcal{D}(t). \end{aligned} \quad (5)$$

The control law, $\mathbf{u}(t)$, consists of a nominal control and a control correction term to minimise the adverse effect of the disturbance term, $\mathcal{D}(t)$, i.e.

$$\mathbf{u}(t) = \bar{\mathbf{u}}(t) + \tilde{\mathbf{u}}(t). \quad (6)$$

Here $\bar{\mathbf{u}}(t)$ is the nominal control and $\tilde{\mathbf{u}}(t)$ is the control correction term. For the purpose of analysis, the control correction term is selected to ensure the complete cancellation of the disturbance term. Thus the DAC law can be written as

$$\mathbf{u}(t) = \bar{\mathbf{u}}(t) - B_m^{-1} \mathcal{D}(t). \quad (7)$$

The disturbance term is not known, but an estimator can be implemented in the feedback loop to estimate the disturbance term online. Estimating the disturbance term requires knowledge of its dynamic model. Since the dynamics of the disturbance term is not precisely known, the disturbance term dynamics is modelled as

$$\dot{\mathcal{D}}_m(t) = \mathrm{A}_{\mathcal{D}_m} \mathcal{D}_m(t) + \mathcal{W}(t), \quad \mathcal{D}_m(t_0) = \mathbf{0}, \quad (8)$$

where $\mathrm{A}_{\mathcal{D}_m}$ is Hurwitz and $\mathcal{W}(t) \triangleq \mathcal{W}(t, \omega) : [t_0, t_f] \times \Omega \mapsto \Re^r$ is zero-mean Gaussian white noise process, i.e. $\mathcal{W}(t) \sim \mathcal{N}(\mathbf{0}, Q\delta(\tau))$. Equation (8) is used solely in the estimator design to estimate the true disturbance term. After constructing the assumed augmented state vector as $\mathbf{Z}_m(t) = \left[\mathbf{X}_{1_m}^T(t) \;\; \mathbf{X}_{2_m}^T(t) \;\; \mathcal{D}_m^T(t)\right]^T$, the assumed extended model of the system can be written as

$$\begin{bmatrix} \dot{\mathbf{X}}_{1_m}(t) \\ \dot{\mathbf{X}}_{2_m}(t) \\ \dot{\mathcal{D}}_m(t) \end{bmatrix} = \begin{bmatrix} \bar{A}_1 & \bar{A}_2 & 0_{(n-r)\times r} \\ A_{3_m} & A_{4_m} & I_{r\times r} \\ 0_{r\times(n-r)} & 0_{r\times r} & \mathrm{A}_{\mathcal{D}_m} \end{bmatrix} \begin{bmatrix} \mathbf{X}_{1_m}(t) \\ \mathbf{X}_{2_m}(t) \\ \mathcal{D}_m(t) \end{bmatrix} + \begin{bmatrix} 0_{(n-r)\times r} \\ B_m \\ 0_{r\times r} \end{bmatrix} \mathbf{u}(t) + \begin{bmatrix} \mathbf{0}_{(n-r)\times 1} \\ \mathbf{0}_{r\times 1} \\ \mathcal{W}(t) \end{bmatrix}. \quad (9)$$

The zero elements in the disturbance term dynamics are assumed for the sake of simplicity; however, the control formulation given here is also valid if non-zero elements are assumed. Equation (9) can be written in terms of the appended state vector, $\mathbf{Z}_m$, as

$$\begin{aligned} \dot{\mathbf{Z}}_m(t) &= F_m \mathbf{Z}_m(t) + D_m \mathbf{u}(t) + G\mathcal{W}(t), \\ \mathbf{Z}_m(t_0) &= [\mathbf{X}_{1_0}^T \quad \mathbf{X}_{2_0}^T \quad \mathbf{0}^T]^T, \end{aligned} \quad (10)$$

where

$$F_m = \begin{bmatrix} \bar{A}_1 & \bar{A}_2 & 0_{(n-r)\times r} \\ A_{3_m} & A_{4_m} & I_{r\times r} \\ 0_{r\times(n-r)} & 0_{r\times r} & \mathrm{A}_{\mathcal{D}_m} \end{bmatrix}, \quad D_m = \begin{bmatrix} 0_{(n-r)\times r} \\ B_m \\ 0_{r\times r} \end{bmatrix}, \quad G = \begin{bmatrix} 0_{n\times r} \\ I_{r\times r} \end{bmatrix}.$$

Note that the uncertainty is only associated with the dynamics of the disturbance term. Let $\mathbf{Z}(t) = \left[\mathbf{X}_1^T(t) \;\; \mathbf{X}_2^T(t) \;\; \mathcal{D}^T(t)\right]^T$ and $H = [C \quad 0_{m\times r}]$. Now the measured output equation can be written as

$$\mathbf{Y}(t) = H\mathbf{Z}(t) + \mathbf{V}(t). \quad (11)$$

Though the disturbance term is unknown, an estimator such as a Kalman filter can be implemented in the feedback loop to estimate the unmeasured system states and the disturbance term from the noisy measurements. Let $\hat{\mathbf{Z}}(t) = \left[\hat{\mathbf{X}}_1^T(t) \;\; \hat{\mathbf{X}}_2^T(t) \;\; \hat{\mathcal{D}}^T(t)\right]^T$, now the estimator dynamics can be written as

$$\begin{aligned} \dot{\hat{\mathbf{Z}}}(t) &= F_m \hat{\mathbf{Z}}(t) + D_m \mathbf{u}(t) + K(t)[\mathbf{Y}(t) - \hat{\mathbf{Y}}(t)], \\ \hat{\mathbf{Z}}(t_0) &= \mathbf{Z}_m(t_0), \end{aligned} \quad (12)$$

where $K(t)$ is the Kalman gain and $\hat{\mathbf{Y}}(t) = H\hat{\mathbf{Z}}(t)$. The Kalman gain can be calculated as $K(t) = P(t)H^T R^{-1}$, where $P(t)$ is obtained by solving the continuous-time matrix differential Riccati equation (Crassidis and Junkins 2004):

$$\dot{P}(t) = F_m P(t) + P(t) F_m^T - P(t) H^T R^{-1} H P(t) + GQG^T, \quad P(t_0). \quad (13)$$

Let $\mathbf{Z}(t) = \left[\mathbf{X}_1^T(t) \;\; \mathbf{X}_2^T(t) \;\; \mathcal{D}^T(t)\right]^T$, now the estimator dynamics can be rewritten as

$$\dot{\hat{\mathbf{Z}}}(t) = F_m \hat{\mathbf{Z}}(t) + D_m \mathbf{u}(t) + K(t) H [\mathbf{Z}(t) - \hat{\mathbf{Z}}(t)] + K(t)\mathbf{V}(t). \quad (14)$$

The estimator uses the assumed system model given in (10) for the propagation stage and the actual measurements for the update stage, i.e. $\hat{\mathbf{Z}}(t) = E[\mathbf{Z}_m(t) | \{\mathbf{Y}(t_0) \ldots \mathbf{Y}(t)\}]$. Due to system uncertainties, the estimator in (14) is sub-optimal and the estimates $\hat{\mathbf{Z}}(t)$ may be biased.

Remark 1: Accuracy of the estimates depends on Q which indicates how well the disturbance term dynamics is modelled via (8). *A* large Q indicates

that (8) is a poor model of the true disturbance term dynamics and a small Q indicates that (8) is an accurate model of the true disturbance term dynamics. Note that selecting a small Q, while having a poor model, would result in inaccurate estimates.

The total control law, $\mathbf{u}(t)$, consists of a nominal control and necessary corrections to the nominal control to compensate for the disturbance term as shown in (7). The nominal control is assumed to be a state feedback control, where the feedback gain, $K_m \triangleq [K_{m_1} \;\; K_{m_2}]$, is selected so that $(\mathcal{A}_m - \mathcal{B}_m K_m)$ is Hurwitz, where

$$\mathcal{A}_m = \begin{bmatrix} \bar{A}_1 & \bar{A}_2 \\ A_{3_m} & A_{4_m} \end{bmatrix} \quad \text{and} \quad \mathcal{B}_m = \begin{bmatrix} 0_{(n-r)\times r} \\ B_m \end{bmatrix}.$$

While the nominal controller guarantees the desired performance of the assumed model, the second term, $-\boldsymbol{\mathcal{D}}(t)$, in (7) ensures the complete cancellation of the disturbance term which is compensating for the external disturbance and model uncertainties. Now the DAC law can be written in terms of the estimated system states and the estimated disturbance term as

$$\mathbf{u}(t) = -\begin{bmatrix} K_m & B_m^{-1} \end{bmatrix} \begin{bmatrix} \hat{\mathbf{X}}(t) \\ \hat{\boldsymbol{\mathcal{D}}}(t) \end{bmatrix} = S\hat{\mathbf{Z}}(t), \qquad (15)$$

where $S \triangleq -[K_m \;\; B_m^{-1}]$. Note that B_m is assumed to be a non-singular matrix. A summary of the proposed control scheme is given in Table 1.

Remark 2: It is important to note that if $Q \approx 0$, then $\boldsymbol{\mathcal{D}}_m(t) \approx \boldsymbol{\mathcal{D}}_m(t_0) = \mathbf{0}$ and the total control law given in (15) becomes just the nominal control. If the nominal control, $\bar{\mathbf{u}}(t)$, on the true plant would result in an unstable system, i.e. the matrix $(\mathcal{A} - \mathcal{B}K_m)$ is unstable, where

$$\mathcal{A} = \begin{bmatrix} \bar{A}_1 & \bar{A}_2 \\ A_3 & A_4 \end{bmatrix} \quad \text{and} \quad \mathcal{B} = \begin{bmatrix} 0_{(n-r)\times r} \\ B \end{bmatrix},$$

then selecting a small Q would also result in an unstable system. On the other hand, selecting a large Q value would compel the estimator to completely rely upon the measurement signal and therefore the noise associated with the measurement signal is directly transmitted into the estimates. This could result in a noisy control signal which could lead to problems such as chattering. Also note that as R, the measurement noise covariance, increases, the estimator gain decreases and thus the estimator fails to update the propagated disturbance term based on measurements. Thus, for a highly uncertain system, if the nominal control action on the true plant results in an unstable system, then selecting a small Q or a large R would also result in an unstable closed-loop system.

If the estimator in (14) is able to obtain accurate estimates of the system states and the disturbance term, then the control law in (15) guarantees the desired closed-loop performance. The accuracy of the estimated system states and the disturbance term depends on the estimator parameters such as the process noise covariance, Q, and the measurement noise covariance, R. Thus the performance of the DAC approach presented here depends on the estimator design parameters. A schematic representation of the proposed controller is given in Figure 1.

3. Stochastic stability analysis

Without the loss of generality, the following assumption can be made about the external disturbance model.

Assumption 3.1: *The linear operator,* $\mathbb{L}(\cdot)$, *in the external disturbance term model in* (2) *is assumed to be*

$$\mathbb{L}(\mathbf{X}(t), \mathbf{W}(t)) = A_{\mathbf{w}_1}\mathbf{X}_1(t) + A_{\mathbf{w}_2}\mathbf{X}_2(t) + A_{\mathbf{w}_3}\mathbf{W}(t), \qquad (16)$$

where $A_{\mathbf{w}_1}$, $A_{\mathbf{w}_2}$ *and* $A_{\mathbf{w}_3}$ *are unknown matrices.*

Table 1. Summary of DAC control process.

Plant	$\dot{\mathbf{X}}_1(t) = \bar{A}_1\mathbf{X}_1(t) + \bar{A}_2\mathbf{X}_2(t)$
	$\dot{\mathbf{X}}_2(t) = A_{3_m}\mathbf{X}_1(t) + A_{4_m}\mathbf{X}_2(t) + B_m\mathbf{u}(t) + \boldsymbol{\mathcal{D}}(t)$
	$\mathbf{Y}(t) = C\mathbf{X}(t) + \mathbf{V}(t)$
Initialise	$\hat{\mathbf{Z}}(t_0),\ P(t_0)$
Estimator gain	$\dot{P}(t) = F_m P(t) + P(t)F_m^T - P(t)H^T R^{-1} HP(t) + GQG^T$
	$K(t) = P(t)H^T R^{-1}$
Estimate	$\dot{\hat{\mathbf{Z}}}(t) = F_m\hat{\mathbf{Z}}(t) + D_m\mathbf{u}(t) + K(t)[\mathbf{Y}(t) - \hat{\mathbf{Y}}(t)]$
Control synthesis	$\mathbf{u}(t) = -[K_m \;\; B_m^{-1}]\hat{\mathbf{Z}}(t)$

Based on Equation (4), the true disturbance term dynamics can now be written as

$$\dot{\boldsymbol{\mathcal{D}}}(t) = \Delta A_1 \dot{\mathbf{X}}_1(t) + \Delta A_2 \dot{\mathbf{X}}_2(t) + \Delta B \dot{\mathbf{u}}(t) + \mathbb{L}(\mathbf{X}(t), \mathbf{W}(t)) + \boldsymbol{\mathcal{V}}(t). \tag{17}$$

Substituting the control law (15) the above equation can be written as

$$\begin{aligned}\dot{\boldsymbol{\mathcal{D}}}(t) &= \Delta A_1 \dot{\mathbf{X}}_1(t) + \Delta A_2 \dot{\mathbf{X}}_2(t) + \Delta BS\dot{\hat{\mathbf{Z}}}(t) \\ &\quad + \mathbb{L}(\mathbf{X}(t), \mathbf{W}(t)) + \boldsymbol{\mathcal{V}}(t) \\ &= \Delta A_1 \{\bar{A}_1 \mathbf{X}_1(t) + \bar{A}_2 \mathbf{X}_2(t)\} \\ &\quad + \Delta A_2 \{A_{3_m} \mathbf{X}_1(t) + A_{4_m} \mathbf{X}_2(t) + B_m S \hat{\mathbf{Z}}(t) + \boldsymbol{\mathcal{D}}(t)\} \\ &\quad + \Delta BS\{[F_m + D_m S - K(t)H] \\ &\quad \times \hat{\mathbf{Z}}(t) + K(t)H\mathbf{Z}(t) + K(t)\mathbf{V}(t)\} \\ &\quad + A_{\mathbf{w}_1} \mathbf{X}_1(t) + A_{\mathbf{w}_2} \mathbf{X}_2(t) + A_{\mathbf{w}_3} \mathbf{W}(t) + \boldsymbol{\mathcal{V}}(t).\end{aligned}$$

Assume that the output matrix can be partitioned as $C \triangleq [C_1 \; C_2]$, and H can be written as $H \triangleq [C_1 \; C_2 \; 0_{m\times r}]$. Thus $K(t)H\mathbf{Z}(t) = K(t)C_1\mathbf{X}_1(t) + K(t)C_2\mathbf{X}_2(t)$. Also note that $\mathbf{W}(t)$ can be written as $\mathbf{W}(t) = \boldsymbol{\mathcal{D}}(t) - \Delta A_1 \mathbf{X}_1(t) - \Delta A_2 \mathbf{X}_2(t) - \Delta B\mathbf{u}(t)$. Now the true disturbance term dynamics can be written as

$$\begin{aligned}\dot{\boldsymbol{\mathcal{D}}}(t) &= \{\Delta A_1 \bar{A}_1 + \Delta A_2 A_{3_m} + \Delta BSK(t)C_1 \\ &\quad + A_{\mathbf{w}_1} - A_{\mathbf{w}_3}\Delta A_1\}\mathbf{X}_1(t) \\ &\quad + \{\Delta A_1 \bar{A}_2 + \Delta A_2 A_{4_m} + \Delta BSK(t)C_2 \\ &\quad + A_{\mathbf{w}_2} - A_{\mathbf{w}_3}\Delta A_2\}\mathbf{X}_2(t) \\ &\quad + \{\Delta BS[F_m + D_m S - K(t)H] \\ &\quad + \Delta A_2 B_m S - A_{\mathbf{w}_3}\Delta BS\}\hat{\mathbf{Z}}(t) \\ &\quad + \{\Delta A_2 + A_{\mathbf{w}_3}\}\boldsymbol{\mathcal{D}}(t) + \Delta BSK(t)\mathbf{V}(t) + \boldsymbol{\mathcal{V}}(t).\end{aligned}$$

Let $\Delta BSK(t)\mathbf{V}(t) + \boldsymbol{\mathcal{V}}(t) = \boldsymbol{\mathcal{W}}_a(t)$, thus $\boldsymbol{\mathcal{W}}_a(t)$ is also a zero-mean stochastic process with

$$\begin{aligned}E[\boldsymbol{\mathcal{W}}_a(t)\boldsymbol{\mathcal{W}}_a^T(t+\tau)] &= \{\Delta BSK(t)RK^T(t)S^T\Delta B^T + \mathcal{Q}\}\delta(\tau) \\ &= Q_a(t)\delta(\tau).\end{aligned}$$

Note that $\dot{\boldsymbol{\mathcal{D}}}(t)$ is a linear function of the true extended system state, $\mathbf{Z}(t)$, the estimated states, $\hat{\mathbf{Z}}(t)$, and the noise term, $\boldsymbol{\mathcal{W}}_a(t)$. Thus the system in (1) is rewritten as the following extended dynamically equivalent system:

$$\begin{aligned}\begin{bmatrix}\dot{\mathbf{X}}_1(t)\\ \dot{\mathbf{X}}_2(t)\\ \dot{\boldsymbol{\mathcal{D}}}(t)\end{bmatrix} &= \begin{bmatrix}\bar{A}_1 & \bar{A}_2 & 0_{(n-r)\times r}\\ A_{3_m} & A_{4_m} & I_{r\times r}\\ A_{\mathcal{D}_1}(t) & A_{\mathcal{D}_2}(t) & A_{\mathcal{D}_3}(t)\end{bmatrix}\begin{bmatrix}\mathbf{X}_1(t)\\ \mathbf{X}_2(t)\\ \boldsymbol{\mathcal{D}}(t)\end{bmatrix} \\ &\quad + \begin{bmatrix}0_{(n-r)\times(n+r)}\\ B_m S\\ B_{\mathcal{D}}(t)\end{bmatrix}\hat{\mathbf{Z}}(t) + \begin{bmatrix}\mathbf{0}_{(n-r)\times 1}\\ \mathbf{0}_{r\times 1}\\ \boldsymbol{\mathcal{W}}_a(t)\end{bmatrix},\end{aligned} \tag{18}$$

where

$$\begin{aligned}A_{\mathcal{D}_1}(t) &= \{\Delta A_1 \bar{A}_1 + \Delta A_2 A_{3_m} + \Delta BSK(t)C_1 \\ &\quad + A_{\mathbf{w}_1} - A_{\mathbf{w}_3}\Delta A_1\},\end{aligned}$$

$$\begin{aligned}A_{\mathcal{D}_2}(t) &= \{\Delta A_1 \bar{A}_2 + \Delta A_2 A_{4_m} + \Delta BSK(t)C_2 \\ &\quad + A_{\mathbf{w}_2} - A_{\mathbf{w}_3}\Delta A_2\},\end{aligned}$$

$$A_{\mathcal{D}_3}(t) = \{\Delta A_2 + A_{\mathbf{w}_3}\}$$

and

$$\begin{aligned}B_{\mathcal{D}}(t) &= \{\Delta BS[F_m + D_m S - K(t)H] \\ &\quad + \Delta A_2 B_m S - A_{\mathbf{w}_3}\Delta BS\}.\end{aligned}$$

Equation (18) can be written in concise form as

$$\dot{\mathbf{Z}}(t) = F(t)\mathbf{Z}(t) + D(t)\hat{\mathbf{Z}}(t) + G\boldsymbol{\mathcal{W}}_a(t), \tag{19}$$

where

$$F(t) = \begin{bmatrix}\bar{A}_1 & \bar{A}_2 & 0_{(n-r)\times r}\\ A_{3_m} & A_{4_m} & I_{r\times r}\\ A_{\mathcal{D}_1}(t) & A_{\mathcal{D}_2}(t) & A_{\mathcal{D}_3}(t)\end{bmatrix} \quad \text{and}$$

$$D(t) = \begin{bmatrix}0_{(n-r)\times(n+r)}\\ B_m S\\ B_{\mathcal{D}}(t)\end{bmatrix}.$$

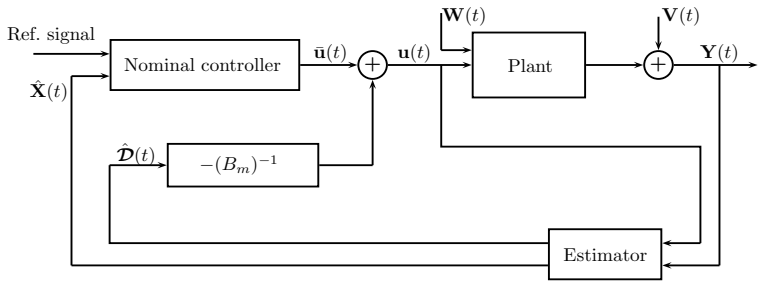

Figure 1. DAC block diagram.

After substituting the control law, the estimator dynamics can be written as

$$\dot{\hat{\mathbf{Z}}}(t) = F_m\hat{\mathbf{Z}}(t) + D_mS\hat{\mathbf{Z}}(t) + K(t)H[\mathbf{Z}(t) - \hat{\mathbf{Z}}(t)] + K(t)\mathbf{V}(t).$$

Let $\tilde{\mathbf{Z}}(t) = \mathbf{Z}(t) - \hat{\mathbf{Z}}(t)$ be the estimation error, then the error dynamics can be written as

$$\dot{\tilde{\mathbf{Z}}}(t) = [F_m - K(t)H + \Delta F(t)]\tilde{\mathbf{Z}}(t) + [\Delta F(t) + \Delta D(t)]\hat{\mathbf{Z}}(t) + G\boldsymbol{\mathcal{W}}_a(t) - K(t)\mathbf{V}(t), \tag{20}$$

where $\triangle F(t) = F(t) - F_m$ and $\triangle D(t) = D(t) - D_mS$. Combining the error dynamics and the estimator dynamics yields

$$\begin{bmatrix} \dot{\tilde{\mathbf{Z}}}(t) \\ \dot{\hat{\mathbf{Z}}}(t) \end{bmatrix} = \begin{bmatrix} (F_m - K(t)H + \Delta F(t)) & (\Delta F(t) + \Delta D(t)) \\ K(t)H & (F_m + D_mS) \end{bmatrix} \times \begin{bmatrix} \tilde{\mathbf{Z}}(t) \\ \hat{\mathbf{Z}}(t) \end{bmatrix} + \begin{bmatrix} G & -K(t) \\ 0_{(n+r)\times r} & K(t) \end{bmatrix} \begin{bmatrix} \boldsymbol{\mathcal{W}}_a(t) \\ \mathbf{V}(t) \end{bmatrix} \tag{21}$$

or in a more compact form as

$$\dot{\boldsymbol{\mathcal{Z}}}(t) = \Upsilon(t)\boldsymbol{\mathcal{Z}}(t) + \Gamma(t)\boldsymbol{\mathcal{G}}(t), \tag{22}$$

where

$$\Upsilon(t) = \begin{bmatrix} (F_m - K(t)H + \Delta F(t)) & (\Delta F(t) + \Delta D(t)) \\ K(t)H & (F_m + D_mS) \end{bmatrix},$$
$$\Gamma(t) = \begin{bmatrix} G & -K(t) \\ 0_{(n+r)\times r} & K(t) \end{bmatrix},$$
$$\boldsymbol{\mathcal{Z}}(t) = \begin{bmatrix} \tilde{\mathbf{Z}}(t) \\ \hat{\mathbf{Z}}(t) \end{bmatrix}, \quad \boldsymbol{\mathcal{G}}(t) = \begin{bmatrix} \boldsymbol{\mathcal{W}}_a(t) \\ \mathbf{V}(t) \end{bmatrix}.$$

Although the Kalman filter-based DAC approach has been successfully utilised for practical applications, there has not been any rigorous stochastic stability analysis to reveal the interdependency between the estimator process noise covariance and controlled system stability. Since the system under consideration is stochastic in nature, the notion of stability is depicted in two separate fashions. The first method deals with moment stability; for the Gaussian stochastic processes presented here, the first two moments are considered. The second technique considers stability in a probabilistic sense.

3.1 *First moment stability*

In this section a detailed stability analysis which examines the explicit dependency of the controlled system's first moment stability or the mean stability on the estimator parameters, such as the disturbance term process noise covariance Q and the measurement noise covariance R, is given. First, a few definitions regarding the closed-loop system's mean stability are given. These definitions and notations are first introduced for a system without any parameter uncertainties and are used throughout the rest of this article.

3.1.1 *System without uncertainties*

Here a system without any parameter uncertainties is considered, i.e. $F(t) = F_m$, $D(t) = D_mS$, and $\boldsymbol{\mathcal{W}}_a(t) = \boldsymbol{\mathcal{W}}(t)$. If there is no model error, then the estimator is unbiased, i.e. $E[\tilde{\mathbf{Z}}(t)] \equiv \boldsymbol{\mu}_{\bar{\tilde{\mathbf{Z}}}}(t) = \mathbf{0}$. Note that the overline is used to indicate the states of the system when there is no model uncertainties. Now (21) may be written as

$$\begin{bmatrix} \dot{\bar{\tilde{\mathbf{Z}}}}(t) \\ \dot{\bar{\hat{\mathbf{Z}}}}(t) \end{bmatrix} = \begin{bmatrix} F_m - K(t)H & 0_{(n+r)\times(n+r)} \\ K(t)H & F_m + D_mS \end{bmatrix} \begin{bmatrix} \bar{\tilde{\mathbf{Z}}}(t) \\ \bar{\hat{\mathbf{Z}}}(t) \end{bmatrix} + \begin{bmatrix} G & -K(t) \\ 0_{(n+r)\times r} & K(t) \end{bmatrix} \begin{bmatrix} \boldsymbol{\mathcal{W}}(t) \\ \mathbf{V}(t) \end{bmatrix},$$

where $\bar{\tilde{\mathbf{Z}}}(t)$ and $\bar{\hat{\mathbf{Z}}}(t)$ denote the estimation error and estimated states when there is no model error, respectively. Let $\bar{\boldsymbol{\mathcal{Z}}}(t) = \left[\bar{\tilde{\mathbf{Z}}}^T(t)\ \bar{\hat{\mathbf{Z}}}^T(t)\right]^T$ and $\bar{\boldsymbol{\mathcal{G}}}(t) = \left[\boldsymbol{\mathcal{W}}^T(t)\ \mathbf{V}^T(t)\right]^T$, now the above equation can be written in a more compact form as

$$\dot{\bar{\boldsymbol{\mathcal{Z}}}}(t) = \bar{\Upsilon}(t)\bar{\boldsymbol{\mathcal{Z}}}(t) + \Gamma(t)\bar{\boldsymbol{\mathcal{G}}}(t), \tag{23}$$

where

$$\bar{\Upsilon}(t) = \begin{bmatrix} F_m - K(t)H & 0_{(n+r)\times(n+r)} \\ K(t)H & F_m + D_mS \end{bmatrix}.$$

Note that $\bar{\boldsymbol{\mathcal{G}}}(t)$ is a zero-mean Gaussian white noise process with

$$E[\bar{\boldsymbol{\mathcal{G}}}(t)\bar{\boldsymbol{\mathcal{G}}}^T(t-\tau)] = \begin{bmatrix} Q & 0_{r\times m} \\ 0_{m\times r} & R \end{bmatrix}\delta(\tau) = \bar{\Lambda}\delta(\tau).$$

Since the first moment stability is of concern here, the first moment dynamics or the mean dynamics is written as

$$E[\dot{\bar{\boldsymbol{\mathcal{Z}}}}(t)] = \dot{\boldsymbol{\mu}}_{\bar{\boldsymbol{\mathcal{Z}}}}(t) = \bar{\Upsilon}(t)\boldsymbol{\mu}_{\bar{\boldsymbol{\mathcal{Z}}}}(t). \tag{24}$$

Definition 3.2: Given $M \geq 1$ and $\beta \in \Re$, the system in (23) is said to be (M, β)-stable in the mean if

$$|\bar{\Phi}(t, t_0)\boldsymbol{\mu}_{\bar{\boldsymbol{\mathcal{Z}}}}(t_0)| \leq Me^{\beta(t-t_0)}|\boldsymbol{\mu}_{\bar{\boldsymbol{\mathcal{Z}}}}(t_0)| \quad \forall t \geq t_0, \tag{25}$$

where $\bar{\Phi}(t, t_0)$ is the evolution operator generated by $\bar{\Upsilon}(t)$ and $|\cdot|$ indicates the Euclidean norm, i.e.

$$|\mathbf{m}| = \sqrt{m_1^2 + m_2^2 + \cdots}$$

Since most applications involve the case where $\beta \leq 0$, (M, β)-stability guarantees both a specific decay rate of the mean response (given by β) and a specific bound on the transient behaviour of the mean (given by M).

Definition 3.3: If the stochastic system in (23) is (M, β)-stable in the mean, then the transient bound of the system mean response for the exponential rate β is defined to be

$$M_\beta = \inf\left\{ M \in \Re; \forall t \geq t_0 : \|\bar{\Phi}(t, t_0)\| \leq M e^{\beta(t-t_0)} \right\}. \tag{26}$$

Here $\|\cdot\|$ indicates the matrix two-norm, i.e.

$$\|M\| = \sigma_{\max}(M),$$

where $\sigma_{\max}(\cdot)$ denotes the maximum singular value.

As shown in Theorem 3.4, the (M, β)-stability and the transient bound of the system's mean response are related to a continuous time Lyapunov matrix differential equation.

Theorem 3.4: *Assume that there exists a bounded, continuously differentiable positive definite matrix function $\bar{\mathcal{P}}(t)$ satisfying the Lyapunov matrix differential equation*

$$\dot{\bar{\mathcal{P}}}(t) = \bar{\Upsilon}(t)\bar{\mathcal{P}}(t) + \bar{\mathcal{P}}(t)\bar{\Upsilon}^T(t) + \Gamma(t)\bar{\Lambda}\Gamma^T(t), \quad \bar{\mathcal{P}}(t_0) \tag{27}$$

then the system in (23) *is (M, β)-stable in the mean and the transient bound M_β of the system mean response can be obtained as*

$$M_\beta^2 \leq \sup_{t \geq t_0} \sigma_{\max}(\bar{\mathcal{P}}(t))/\sigma_{\min}(\bar{\mathcal{P}}(t_0)), \tag{28}$$

where $\sigma_{\min}(\cdot)$ denotes the minimum singular value.

Proof: Since $\Gamma(t)\bar{\Lambda}\Gamma^T(t) \geq 0 \ \forall t \geq t_0$, the (M, β)-stability in the mean follows directly from the existence of bounded positive definite solution, $\bar{\mathcal{P}}(t)$, satisfying Equation (27). Now the solution to (27) can be written as

$$\bar{\mathcal{P}}(t) = \bar{\Phi}(t, t_0)\bar{\mathcal{P}}(t_0)\bar{\Phi}^T(t, t_0) + \int_{t_0}^{t} \bar{\Phi}(t, \tau)\Gamma(\tau)\bar{\Lambda}\Gamma^T(\tau)\bar{\Phi}^T(t, \tau)\mathrm{d}\tau$$

Note that $\forall t \geq t_0$, $\bar{\mathcal{P}}(t) \geq \bar{\Phi}(t, t_0)\bar{\mathcal{P}}(t_0)\bar{\Phi}^T(t, t_0) \geq \sigma_{\min}(\bar{\mathcal{P}}(t_0))\bar{\Phi}(t, t_0)\bar{\Phi}^T(t, t_0)$, i.e.

$$\sigma_{\max}(\bar{\mathcal{P}}(t)) \geq \|\bar{\Phi}(t, t_0)\bar{\mathcal{P}}(t_0)\bar{\Phi}^T(t, t_0)\| \geq \sigma_{\min}(\bar{\mathcal{P}}(t_0))\|\bar{\Phi}(t, t_0)\|^2, \quad t \geq t_0.$$

Now (28) follows from

$$\sigma_{\max}(\bar{\mathcal{P}}(t))/\sigma_{\min}(\bar{\mathcal{P}}(t_0)) \geq \|\bar{\Phi}(t, t_0)\|^2, \quad t \geq t_0.$$

□

Remark 3: Assume that $\bar{\mathcal{P}}(t_0)$ is selected as $\bar{\mathcal{P}}(t_0) = E[\bar{\boldsymbol{\mathcal{Z}}}(t_0)\ \bar{\boldsymbol{\mathcal{Z}}}^T(t_0)]$, then the positive definite solution, $\bar{\mathcal{P}}(t)$, satisfying Equation (27) denotes the correlation matrix, i.e.

$$\bar{\mathcal{P}}(t) = E\left[\, \bar{\boldsymbol{\mathcal{Z}}}(t) \quad \bar{\boldsymbol{\mathcal{Z}}}^T(t) \,\right].$$

Thus the transient bound of the system mean response can be obtained in terms of the bounded correlation matrix.

Note that $\Gamma(t)\bar{\Lambda}\Gamma^T(t)$ in (27) can be factored as shown below:

$$\begin{aligned}
\Gamma(t)\bar{\Lambda}\Gamma^T(t) &= \begin{bmatrix} (GQG^T + KRK^T) & -KRK^T \\ -KRK^T & KRK^T \end{bmatrix} \\
&= \begin{bmatrix} GQG^T & -0 \\ 0 & 0 \end{bmatrix} + \begin{bmatrix} KRK^T & -KRK^T \\ -KRK^T & KRK^T \end{bmatrix} \\
&= \begin{bmatrix} G \\ 0 \end{bmatrix} Q \begin{bmatrix} G^T & 0 \end{bmatrix} + \begin{bmatrix} PH^T \\ -PH^T \end{bmatrix} R^{-1} \begin{bmatrix} HP & -HP \end{bmatrix} \\
&= LQL^T + N(t)R^{-1}N^T(t),
\end{aligned}$$

where

$$L = \begin{bmatrix} G \\ 0 \end{bmatrix} \quad \text{and} \quad N(t) = \begin{bmatrix} P(t)H^T \\ -P(t)H^T \end{bmatrix}.$$

Thus (27) can be written as

$$\dot{\bar{\mathcal{P}}}(t) = \bar{\Upsilon}(t)\bar{\mathcal{P}}(t) + \bar{\mathcal{P}}(t)\bar{\Upsilon}^T(t) + LQL^T + N(t)R^{-1}N^T(t). \tag{29}$$

3.1.2 *Uncertain system*

In this section, the first moment stability of the perturbed system given in (22) is considered, i.e.

$$\dot{\boldsymbol{\mathcal{Z}}}(t) = \bar{\Upsilon}(t)\boldsymbol{\mathcal{Z}}(t) + \Delta\Upsilon(t)\boldsymbol{\mathcal{Z}}(t) + \Gamma(t)\boldsymbol{\mathcal{G}}(t), \tag{30}$$

where

$$\Delta\Upsilon(t) = \begin{bmatrix} \Delta F(t) & (\Delta F(t) + \Delta D(t)) \\ 0 & 0 \end{bmatrix}.$$

The correlation matrix $\mathcal{P}(t) = E[\boldsymbol{\mathcal{Z}}(t)\ \boldsymbol{\mathcal{Z}}^T(t)]$ satisfies the following matrix Lyapunov differential equation:

$$\dot{\mathcal{P}}(t) = \left(\bar{\Upsilon}(t) + \Delta\Upsilon(t)\right)\mathcal{P}(t) + \mathcal{P}(t)\left(\bar{\Upsilon}(t) + \Delta\Upsilon(t)\right)^T + \Gamma(t)\Lambda(t)\Gamma^T(t), \tag{31}$$

where

$$\Lambda(t)\delta(\tau) = E[\boldsymbol{\mathcal{G}}(t)\boldsymbol{\mathcal{G}}^T(t-\tau)] = \begin{bmatrix} Q_a(t) & 0_{r\times m} \\ 0_{m\times r} & R \end{bmatrix}\delta(\tau)$$

Assuming that the nominal control action on the true plant would result in an unstable system, stability of extended uncertain system given in (30) depends on the disturbance term process noise covariance, Q and the measurement noise covariance, R. Theorem 3.5 indicates that the stability of the extended uncertain system given in (30) is guaranteed if the selected Q and R satisfies a lower and an upper bound, respectively.

Theorem 3.5: *The uncertain system in* (30) *is* (M, β)*-stable in the mean if*

$$\left\{\sigma_{\min}(Q) + \sigma_{\min}(R^{-1})\|N(t)N^T(t)\| - 1\right\}\|\breve{\mathcal{P}}(t)\|^{-2} > 2\|\Delta\Upsilon(t)\|^2, \quad t \geq t_0, \tag{32}$$

where $\breve{\mathcal{P}}(t)$ *satisfies the matrix differential equation*

$$\dot{\breve{\mathcal{P}}}(t) = \bar{\Upsilon}(t)\breve{\mathcal{P}}(t) + \breve{\mathcal{P}}(t)\bar{\Upsilon}^T(t) + \|Q\|I + \|N(t)R^{-1}N(t)^T\|I - \breve{\mathcal{P}}(t)\Delta\Upsilon^T(t)\Delta\Upsilon(t)\breve{\mathcal{P}}(t). \tag{33}$$

Proof: For the linear time-varying system given in (30), uniform asymptotic stability in the mean implies (M, β)-stability in the mean. In order to show the uniform asymptotic stability of the mean, consider the mean dynamics of the system in (30):

$$\dot{\boldsymbol{\mu}}_{\mathcal{Z}}(t) = \bar{\Upsilon}(t)\boldsymbol{\mu}_{\mathcal{Z}}(t) + \Delta\Upsilon(t)\boldsymbol{\mu}_{\mathcal{Z}}(t), \tag{34}$$

where $E[\mathcal{Z}(t)] = \boldsymbol{\mu}_{\mathcal{Z}}(t)$. Construct the following Lyapunov candidate function:

$$V[\boldsymbol{\mu}_{\mathcal{Z}}(t)] = \boldsymbol{\mu}_{\mathcal{Z}}^T(t)\breve{\mathcal{P}}^{-1}(t)\boldsymbol{\mu}_{\mathcal{Z}}(t). \tag{35}$$

Note that the solution, $\breve{\mathcal{P}}(t)$, of (33) is required to be a bounded positive definite matrix as long as $\Delta\Upsilon$ is norm-bounded (Abou-Kandil, Freiling, Ionescu, and Jank 2003). Thus $\breve{\mathcal{P}}^{-1}(t)$ exists and $V[\boldsymbol{\mu}_{\mathcal{Z}}(t)] > 0$ for all $\boldsymbol{\mu}_{\mathcal{Z}}(t) \neq \mathbf{0}$. Since $\breve{\mathcal{P}}(t)\breve{\mathcal{P}}^{-1}(t) = I$, the time derivative of $\breve{\mathcal{P}}(t)\breve{\mathcal{P}}^{-1}(t)$ is 0:

$$\frac{\mathrm{d}}{\mathrm{d}t}\left[\breve{\mathcal{P}}(t)\breve{\mathcal{P}}^{-1}(t)\right] = \dot{\breve{\mathcal{P}}}(t)\breve{\mathcal{P}}^{-1}(t) + \breve{\mathcal{P}}(t)\dot{\breve{\mathcal{P}}}^{-1}(t) = 0.$$

Solving the above equation for $\dot{\breve{\mathcal{P}}}^{-1}(t)$ and substituting (33) gives

$$\begin{aligned}\dot{\breve{\mathcal{P}}}^{-1}(t) &= -\breve{\mathcal{P}}^{-1}(t)\dot{\breve{\mathcal{P}}}(t)\breve{\mathcal{P}}^{-1}(t)\\ &= -\breve{\mathcal{P}}^{-1}(t)\bar{\Upsilon}(t) - \bar{\Upsilon}^T(t)\breve{\mathcal{P}}^{-1}(t)\\ &\quad - \left\{\|Q\| + \|N(t)R^{-1}N(t)^T\|\right\}\breve{\mathcal{P}}^{-1}(t)\breve{\mathcal{P}}^{-1}(t)\\ &\quad + \Delta\Upsilon^T(t)\Delta\Upsilon(t).\end{aligned}$$

Now the time derivative of (35) can be written as

$$\begin{aligned}\dot{V}[\boldsymbol{\mu}_{\mathcal{Z}}(t)] &= \dot{\boldsymbol{\mu}}_{\mathcal{Z}}^T\breve{\mathcal{P}}^{-1}\boldsymbol{\mu}_{\mathcal{Z}} + \boldsymbol{\mu}_{\mathcal{Z}}^T\dot{\breve{\mathcal{P}}}^{-1}\boldsymbol{\mu}_{\mathcal{Z}} + \boldsymbol{\mu}_{\mathcal{Z}}^T\breve{\mathcal{P}}^{-1}\dot{\boldsymbol{\mu}}_{\mathcal{Z}}\\ &= [\bar{\Upsilon}\boldsymbol{\mu}_{\mathcal{Z}} + \Delta\Upsilon\boldsymbol{\mu}_{\mathcal{Z}}]^T\breve{\mathcal{P}}^{-1}\boldsymbol{\mu}_{\mathcal{Z}} - \boldsymbol{\mu}_{\mathcal{Z}}^T\breve{\mathcal{P}}^{-1}\bar{\Upsilon}\boldsymbol{\mu}_{\mathcal{Z}}\\ &\quad - \boldsymbol{\mu}_{\mathcal{Z}}^T\bar{\Upsilon}^T\breve{\mathcal{P}}^{-1}\boldsymbol{\mu}_{\mathcal{Z}} - \left\{\|Q\| + \|NR^{-1}N^T\|\right\}\boldsymbol{\mu}_{\mathcal{Z}}^T\\ &\quad \times \breve{\mathcal{P}}^{-2}\boldsymbol{\mu}_{\mathcal{Z}} + \boldsymbol{\mu}_{\mathcal{Z}}^T\Delta\Upsilon^T\Delta\Upsilon\boldsymbol{\mu}_{\mathcal{Z}}\\ &\quad + \boldsymbol{\mu}_{\mathcal{Z}}^T\breve{\mathcal{P}}^{-1}[\bar{\Upsilon}\boldsymbol{\mu}_{\mathcal{Z}} + \Delta\Upsilon\boldsymbol{\mu}_{\mathcal{Z}}]\\ &= \boldsymbol{\mu}_{\mathcal{Z}}^T\Delta\Upsilon^T\breve{\mathcal{P}}^{-1}\boldsymbol{\mu}_{\mathcal{Z}} + \boldsymbol{\mu}_{\mathcal{Z}}^T\breve{\mathcal{P}}^{-1}\Delta\Upsilon\boldsymbol{\mu}_{\mathcal{Z}}\\ &\quad - \left\{\|Q\| + \|NR^{-1}N^T\|\right\}\boldsymbol{\mu}_{\mathcal{Z}}^T\breve{\mathcal{P}}^{-2}\boldsymbol{\mu}_{\mathcal{Z}} + \boldsymbol{\mu}_{\mathcal{Z}}^T\Delta\Upsilon^T\Delta\Upsilon\boldsymbol{\mu}_{\mathcal{Z}}\\ &= \boldsymbol{\mu}_{\mathcal{Z}}^T\Big\{\Delta\Upsilon^T\breve{\mathcal{P}}^{-1} + \breve{\mathcal{P}}^{-1}\Delta\Upsilon\\ &\quad - \left\{\|Q\| + \|NR^{-1}N^T\|\right\}\breve{\mathcal{P}}^{-2} + \Delta\Upsilon^T\Delta\Upsilon\Big\}\boldsymbol{\mu}_{\mathcal{Z}}.\end{aligned}$$

Asymptotic stability in the first moment is guaranteed if

$$\left\{\Delta\Upsilon^T\breve{\mathcal{P}}^{-1} + \breve{\mathcal{P}}^{-1}\Delta\Upsilon - \left\{\|Q\| + \|NR^{-1}N^T\|\right\}\breve{\mathcal{P}}^{-2} + \Delta\Upsilon^T\Delta\Upsilon\right\} < 0.$$

Note that

$$\left[\Delta\Upsilon^T - \breve{\mathcal{P}}^{-1}\right]\left[\Delta\Upsilon^T - \breve{\mathcal{P}}^{-1}\right]^T \geq 0 \Rightarrow \Delta\Upsilon^T\Delta\Upsilon + \breve{\mathcal{P}}^{-2} \geq \Delta\Upsilon^T\breve{\mathcal{P}}^{-1} + \breve{\mathcal{P}}^{-1}\Delta\Upsilon.$$

Thus the above condition for asymptotic stability is satisfied as soon as

$$\left\{2\Delta\Upsilon^T\Delta\Upsilon + \breve{\mathcal{P}}^{-2} - \left\{\|Q\| + \|NR^{-1}N^T\|\right\}\breve{\mathcal{P}}^{-2}\right\} < 0$$

or

$$\left\{2\breve{\mathcal{P}}\Delta\Upsilon^T\Delta\Upsilon\breve{\mathcal{P}} + I - \left\{\|Q\| + \|NR^{-1}N^T\|\right\}I\right\} < 0.$$

Using the inequalities

$$\|\breve{\mathcal{P}}\|^2\|\Delta\Upsilon\|^2 I \geq \breve{\mathcal{P}}\Delta\Upsilon^T\Delta\Upsilon\breve{\mathcal{P}}, \quad \sigma_{\min}(Q) \leq \|Q\| \quad \text{and} \quad \sigma_{\min}(R^{-1})\|NN^T\| \leq \|NR^{-1}N^T\|$$

yields

$$2\|\breve{\mathcal{P}}\|^2\|\Delta\Upsilon\|^2 < \sigma_{\min}(Q) + \sigma_{\min}(R^{-1})\|NN^T\| - 1.$$

Hence the uniform asymptotic stability in the first moment is guaranteed if

$$2\|\Delta\Upsilon(t)\|^2 < \left\{\sigma_{\min}(Q) + \sigma_{\min}(R^{-1})\|N(t)N^T(t)\| - 1\right\} \times \|\breve{\mathcal{P}}(t)\|^{-2}, \quad t \geq t_0.$$

□

Remark 4: The uncertain system in (30) is (M, β)-stable in the mean if the selected Q and R satisfy the inequality in (32). Thus for a highly uncertain system,

if the nominal control action on the true plant would result in an unstable system, then selecting a small Q or a large R would also result in an unstable closed-loop system.

3.2 *Mean square stability*

In this section the controlled system's stability in the second moment or the mean square stability is considered. It is shown here that the (M, β)-stability in the mean implies mean square stability. More details on mean square stability can be found in Kushner (1967) and Soong (1973).

Definition 3.6: A stochastic system of the following form $\dot{\mathcal{Z}}(t) = \Upsilon(t)\mathcal{Z}(t) + \Gamma(t)\mathcal{G}(t)$ is mean square stable if

$$\lim_{t\to\infty} E[\mathcal{Z}^T(t)\mathcal{Z}(t)] < \mathrm{M}, \tag{36}$$

where M is a constant square matrix whose elements are finite.

Note that $E[\mathcal{Z}^T(t)\mathcal{Z}(t)] = \mathrm{Tr}\{\mathcal{P}(t)\}$, i.e.

$$\frac{\mathrm{d}}{\mathrm{d}t}E[\mathcal{Z}(t)\ \ \mathcal{Z}^T(t)] = \dot{\mathcal{P}}(t) = \Upsilon(t)\mathcal{P}(t) + \mathcal{P}(t)\Upsilon^T(t) + \Gamma(t)\Lambda(t)\Gamma^T(t)$$

and the solution to the above equation can be written as

$$\mathcal{P}(t) = \int_{-\infty}^{t} \Phi(t,\tau)\Gamma(\tau)\Lambda(\tau)\Gamma^T(\tau)\Phi^T(t,\tau)\mathrm{d}\tau$$

The (M, β)-stable in the mean implies that the system matrix, $\Upsilon(t) = \bar{\Upsilon}(t) + \Delta\Upsilon(t)$, generates an exponentially stable evolution operator and therefore $\mathcal{P}(t)$ has a bounded solution (Abou-Kandil et al. 2003). Therefore, for the system given in (30), (M, β)-stability in the mean implies mean square stability.

3.3 *Almost sure asymptotic stability*

The solution to the stochastic system given in (30) cannot be based on the ordinary mean square calculus because the integral involved in the solution depends on $\mathcal{G}(t)$, which is of unbounded variation (Soong and Grigoriu 1993). For the treatment of this class of problems, the stochastic differential equation may be rewritten in Itô form as

$$\mathrm{d}\mathcal{Z}(t) = \left[\bar{\Upsilon}(t)\mathcal{Z}(t) + \Delta\Upsilon(t)\mathcal{Z}(t)\right]\mathrm{d}t + \Gamma(t)\Lambda^{1/2}(t)\mathrm{d}\mathcal{B}(t)$$

or simply as

$$\mathrm{d}\mathcal{Z}(t) = \Upsilon(t)\mathcal{Z}(t)\mathrm{d}t + \Gamma(t)\Lambda^{1/2}(t)\mathrm{d}\mathcal{B}(t), \tag{37}$$

where $\mathrm{d}\mathcal{B}(t)$ is an increment of Brownian motion process with zero-mean, Gaussian distribution and

$$E[\mathrm{d}\mathcal{B}(t)\ \ \mathrm{d}\mathcal{B}^T(t)] = I\,\mathrm{d}t. \tag{38}$$

The solution $\mathcal{Z}(t)$ of (37) is a semimartingale process that is also a Markov process (Grigoriu 2002). Details on the almost sure (*a.s.*) stability for the stochastic system in (37) is presented in this section.

Definition 3.7: The linear stochastic system given in (37) is asymptotically stable with probability 1, or almost surely asymptotically stable, if

$$\mathbb{P}\left(\mathcal{Z}(t) \to \mathbf{0} \text{ as } t \to \infty\right) = 1. \tag{39}$$

(M, β)-stability in the mean response implies that $\Upsilon(t)$ generates an asymptotically stable evolution for the linear system in (37), but it does not imply almost sure asymptotic stability due to the persistently acting disturbance. In fact, given $\Upsilon(t)$ generates an asymptotically stable evolution, the necessary and sufficent condition for almost sure asymptotic stability is

$$\lim_{t\to\infty} \|\Gamma(t)\|^2 \log(t) = 0. \tag{40}$$

A detailed proof of this argument can be found in Appleby (2002). Equation (40) constitutes the sufficent condition for the almost sure asymptotic stability of a linear stochastic system given (M, β)-stability in the mean.

4. Stabilising Q and transient bound on uncertain system

The Lyapunov analysis given in Theorem 3.5 indicates a lower bound requirement on the system process noise covariance, Q, and an upper bound requirement on system measurement noise covariance, R, in order for the controlled system to be (M, β)-stable in the mean. Since the measurement noise covariance can be obtained from sensor calibration, the process noise matrix Q is usually treated as a tuning parameter. This would compel one to select an extremely large Q so that the stability is always guaranteed. Selecting a large Q value would force the estimator to completely rely upon the measurement signal and therefore the noise associated with the measurement signal is directly transmitted into the estimates. This could result in a noisy control signal which could lead to problems such as chattering. This section shows a systematic approach to select a stabilising Q using the overbounding method of Petersen and Hollot (Petersen and Hollot 1986; Douglas and Athans 1994).

Assume that the structure of the uncertainty $\Delta\Upsilon(t)$ is given as

$$\Delta\Upsilon(t) = \sum_{i=1}^{l} r_i(t)\Upsilon_i, \tag{41}$$

where Υ_i is assumed to be a rank-one matrix of the form $\Upsilon_i = \mathbf{t}_i\mathbf{e}_i^T$. In the above description, $r_i(t)$ is the ith component of the vector $\mathbf{r} \in \Re^l$ and is upper bounded by

$$\bar{r} \geq \sup_{t \geq t_0} |r_i(t)| \quad \forall i \in \{1, 2, \ldots, l\}. \tag{42}$$

Define matrices T and E as

$$T = \sum_{i=1}^{l} \mathbf{t}_i\mathbf{t}_i^T \quad \text{and} \quad E = \sum_{i=1}^{l} \mathbf{e}_i\mathbf{e}_i^T. \tag{43}$$

Lemma 4.1: *If the uncertain matrix $\Delta\Upsilon(t)$ has the structure given in* (41)*, then the following matrix inequality is valid for all matrices $\mathcal{P}^*(t)$ of appropriate dimensions*:

$$\begin{aligned}&\mathcal{P}^{*T}(t)\Delta\Upsilon^T(t) + \Delta\Upsilon(t)\mathcal{P}^*(t)\\ &\quad \leq \bar{r}^2 T + \mathcal{P}^{*T}(t)E\mathcal{P}^*(t) \quad \forall t \geq t_0,\end{aligned} \tag{44}$$

where $\bar{r}$, T and E are from (42) *and* (43).

Proof: Substituting $\Upsilon_i = \mathbf{t}_i\mathbf{e}_i^T$ into (41) yields

$$\begin{aligned}&\Delta\Upsilon(t)\mathcal{P}^*(t) + \mathcal{P}^{*T}(t)\Delta\Upsilon^T(t)\\ &\quad = \sum_{i=1}^{l}\left\{r_i(t)\mathbf{t}_i\mathbf{e}_i^T\mathcal{P}^*(t) + r_i(t)\mathcal{P}^{*T}(t)\mathbf{e}_i\mathbf{t}_i^T\right\}.\end{aligned}$$

Note that

$$\left[r_i(t)\mathbf{t}_i - \mathcal{P}^{*T}(t)\mathbf{e}_i\right]\left[r_i(t)\mathbf{t}_i - \mathcal{P}^{*T}(t)\mathbf{e}_i\right]^T \geq 0.$$

Thus

$$\begin{aligned}&r_i^2(t)\mathbf{t}_i\mathbf{t}_i^T + \mathcal{P}^{*T}(t)\mathbf{e}_i\mathbf{e}_i^T\mathcal{P}^*(t)\\ &\quad \geq r_i(t)\mathbf{t}_i\mathbf{e}_i^T\mathcal{P}^*(t) + r_i(t)\mathcal{P}^{*T}(t)\mathbf{e}_i\mathbf{t}_i^T\end{aligned}$$

and

$$\begin{aligned}&\sum_{i=1}^{l}\left\{r_i^2(t)\mathbf{t}_i\mathbf{t}_i^T + \mathcal{P}^{*T}(t)\mathbf{e}_i\mathbf{e}_i^T\mathcal{P}^*(t)\right\}\\ &\quad \geq \sum_{i=1}^{l}\left\{r_i(t)\mathbf{t}_i\mathbf{e}_i^T\mathcal{P}^*(t) + r_i(t)\mathcal{P}^{*T}(t)\mathbf{e}_i\mathbf{t}_i^T\right\}.\end{aligned}$$

Now substituting for T and E yields

$$\bar{r}^2 T + \mathcal{P}^{*T}(t)E\mathcal{P}^*(t) \geq \Delta\Upsilon(t)\mathcal{P}^*(t) + \mathcal{P}^{*T}(t)\Delta\Upsilon^T(t).$$

□

A computationally feasible procedure for the calculation of a stabilising Q is given next.

Theorem 4.2: *Assume that the uncertain matrix $\Delta\Upsilon(t)$ has the structure given in* (41) *and the process noise covariance, Q^*, is selected so that the following matrix differential Riccati equation has a bounded positive definite matrix solution, $\bar{\mathcal{P}}^*(t)$*:

$$\begin{aligned}\dot{\bar{\mathcal{P}}}^*(t) &= \bar{\Upsilon}(t)\bar{\mathcal{P}}^*(t) + \bar{\mathcal{P}}^*(t)\bar{\Upsilon}^T(t)\\ &\quad - \bar{\gamma}\bar{\mathcal{P}}^*(t)\bar{\mathcal{P}}^*(t) + \mathcal{R}\left(Q^*, R^{-1}\right)\end{aligned} \tag{45}$$

and

$$\mathcal{R}\left(Q^*, R^{-1}\right) \geq \bar{\gamma}\bar{\mathcal{P}}^*(t)\bar{\mathcal{P}}^*(t) + \bar{r}^2 T + \mathcal{P}^{*T}(t)E\mathcal{P}^*(t) \quad \forall t \geq t_0, \tag{46}$$

where $\bar{\gamma}$ is a positive constant and $\mathcal{R}(Q^*, R^{-1})$ denotes a positive definite matrix function. Then, the uncertain system in (30) *is (M, β)-stable in the mean and*

$$M_\beta^2 \leq \sup_{t \geq t_0} \sigma_{\max}\left(\bar{\mathcal{P}}^*(t)\right)/\sigma_{\min}\left(\bar{\mathcal{P}}^*(t_0)\right), \tag{47}$$

where M_β represents the transient bound of the uncertain system's mean response.

Proof: Since $\bar{\Upsilon}(t)$ is assumed to generate an exponentially stable evolution operator, there exists a bounded positive definite matrix, $\bar{\mathcal{P}}^*(t)$, that satisfies Equation (45). Note that (45) can be written as

$$\begin{aligned}\dot{\bar{\mathcal{P}}}^*(t) &= \left[\bar{\Upsilon}(t) + \Delta\Upsilon(t)\right]\bar{\mathcal{P}}^*(t) + \bar{\mathcal{P}}^*(t)\left[\bar{\Upsilon}(t) + \Delta\Upsilon(t)\right]^T\\ &\quad - \bar{\gamma}\bar{\mathcal{P}}^*(t)\bar{\mathcal{P}}^*(t) + \mathcal{R}\left(Q^*, R^{-1}\right)\\ &\quad - \Delta\Upsilon(t)\bar{\mathcal{P}}^*(t) - \bar{\mathcal{P}}^*(t)\Delta\Upsilon^T(t).\end{aligned}$$

The solution to above equation is

$$\begin{aligned}\bar{\mathcal{P}}^*(t) &= \Phi(t, t_0)\bar{\mathcal{P}}^*(t_0)\Phi^T(t, t_0)\\ &\quad + \int_{t_0}^{t}\Phi(t, \tau)\left\{\mathcal{R}\left(Q^*, R^{-1}\right) - \bar{\gamma}\bar{\mathcal{P}}^*(\tau)\bar{\mathcal{P}}^*(\tau)\right.\\ &\quad \left. - \Delta\Upsilon(\tau)\bar{\mathcal{P}}^*(\tau) - \bar{\mathcal{P}}^*(\tau)\Delta\Upsilon^T(\tau)\right\}\Phi^T(t, \tau)\mathrm{d}\tau,\end{aligned}$$

where $\Phi(t, t_0)$ is the evolution operator generated by $\Upsilon(t) = \bar{\Upsilon}(t) + \Delta\Upsilon(t)$. Based on Lemma 4.1 and the matrix inequality Equation (46)

$$\begin{aligned}&\mathcal{R}\left(Q^*, R^{-1}\right) - \bar{\gamma}\bar{\mathcal{P}}^*(t)\bar{\mathcal{P}}^*(t)\\ &\quad - \Delta\Upsilon(t)\bar{\mathcal{P}}^*(t) - \bar{\mathcal{P}}^*(t)\Delta\Upsilon^T(t) \geq 0.\end{aligned}$$

Thus

$$\begin{aligned}\bar{\mathcal{P}}^*(t) &\geq \Phi(t, t_0)\bar{\mathcal{P}}^*(t_0)\Phi^T(t, t_0)\\ &\geq \sigma_{\min}\left(\bar{\mathcal{P}}^*(t_0)\right)\Phi(t, t_0)\Phi^T(t, t_0).\end{aligned}$$

Now (47) follows from

$$\sigma_{\max}\big(\bar{\mathcal{P}}^*(t)\big)/\sigma_{\min}\big(\bar{\mathcal{P}}^*(t_0)\big) \geq \|\Phi(t,t_0)\|^2.$$

Therefore, $\Phi(t,t_0)$ generates an exponentially stable evolution. □

Assuming that the system uncertainties can be written in the form given in (41), a stabilising process noise covariance, Q^*, can be calculated. Note that bounds on the system uncertainties used here may be highly conservative and therefore it may result in an extremely large value of Q. As mentioned earlier, selecting a large Q results in a noisy control signal and it could lead to problems such as chattering. Also note that obtaining the upper bound $\bar{r}$ is rather difficult since the system uncertainties, $\Delta F(t)$ and $\Delta D(t)$, may depend on the estimator gain, $K(t)$. Thus increasing the process noise covariance would also increase the upper bound on the uncertainty, i.e. $\bar{r}$. Finally, the reader should realise that the dependency of system uncertainties on the estimator gain is eliminated if the control distribution matrix is precisely known, i.e. $\Delta B = 0$. For more details, please refer to (18).

5. Adaptive scheme

After substituting the DAC law, $\mathbf{u}(t) = S\hat{\mathbf{Z}}(t)$, the plant dynamics in (1) can be written as

$$\dot{\mathbf{X}}(t) = \mathcal{A}\mathbf{X}(t) + \mathcal{B}\Big[S\hat{\mathbf{Z}}(t) + B^{-1}\mathbf{W}(t)\Big] \tag{48}$$

and the estimator dynamics in (14) can be written as

$$\dot{\hat{\mathbf{Z}}}(t) = [F_m + D_m S]\hat{\mathbf{Z}}(t) + K(t)\tilde{\mathbf{Y}}(t), \tag{49}$$

where $\tilde{\mathbf{Y}}(t) = [\mathbf{Y}(t) - \hat{\mathbf{Y}}(t)]$. Let $\mathbf{X}_{\text{ext}}(t) = \big[\mathbf{X}_1^T(t)\ \mathbf{X}_2^T(t)\ \mathbf{W}^T(t)\big]^T$, now based on Assumption 3.1, the controlled plant in (48) can be written as

$$\dot{\mathbf{X}}_{\text{ext}}(t) = \mathcal{A}_{\text{ext}}\mathbf{X}_{\text{ext}}(t) + \mathcal{B}_{\text{ext}}S\hat{\mathbf{Z}}(t) + G\mathcal{V}(t), \tag{50}$$

where

$$\mathcal{A}_{\text{ext}} = \begin{bmatrix} \bar{A}_1 & \bar{A}_2 & 0_{(n-r)\times r} \\ A_3 & A_4 & I_{r\times r} \\ A_{\mathbf{w}_1} & A_{\mathbf{w}_2} & A_{\mathbf{w}_3} \end{bmatrix} \quad \text{and} \quad \mathcal{B}_{\text{ext}} = \begin{bmatrix} 0_{(n-r)\times r} \\ B \\ 0_{r\times r} \end{bmatrix}.$$

The following assumptions are now made.

Assumption 5.1: *The pair* $(\mathcal{A}_{\text{ext}}, \mathcal{B}_{\text{ext}})$ *is controllable and the pair* $(\mathcal{A}_{\text{ext}}, H)$ *is observable.*

Assumption 5.2: *There exist an* $r \times m$ *matrix* Π *such that* $\Pi^T\Pi \geq I_{m\times m}$, *i.e.* $m \leq r$. *If* $m > r$, *then the r-outputs considered here are selected such that the corresponding* $(\mathcal{A}_{\text{ext}}, H)$ *is observable.*

Assumption 5.3: *There exists an* $m \times m$ *matrix* $\bar{R} > 0$ *such that* $\forall t \geq t_0$, *we have*

$$E\Big[\tilde{Y}(t)\tilde{Y}^T(t)\Big] \geq \bar{R}$$

Based on Assumptions 5.1, 5.2 and 5.3, an adaptive scheme for selecting the stabilising process noise covariance matrix can be developed as shown next.

Theorem 5.4: *Given Assumptions* 5.1, 5.2, *and* 5.3, *the controlled system is mean square stable,* $E[\mathbf{X}(t)] \in L_2 \cap L_\infty$ *and* $\mathbf{X}(t)$ *is asymptotically stable in the first moment, i.e.*

$$\lim_{t\to\infty} E[\mathbf{X}(t)] = \mathbf{0}$$

if the process noise covariance is updated online using the adaptive law

$$\mathrm{d}Q(t) = \Big\{A_Q Q(t) + Q(t)A_Q^T + \gamma\Pi\tilde{\mathbf{Y}}(t)\tilde{\mathbf{Y}}^T(t)\Pi^T\Big\}\mathrm{d}t, \tag{51}$$

where A_Q *is an* $r \times r$ *negative definite matrix such that* $0 < -2\mathrm{Tr}\{A_Q\} \leq 1$ *and* γ *is the adaptive gain.*

Proof of this theorem is based on the following lemmas.

Lemma 5.5: *Consider the following linear stochastic system*

$$\dot{\mathbf{Z}}(t) = A\mathbf{Z}(t) + \mathbf{U}(t).$$

If the matrix A generates an exponentially stable evolution operator $\Phi_A(t-t_0)$ *and* $\mathbf{U}(t) \in L_2$, *i.e.*

$$E\left[\int_{t_0}^{\infty} |\mathbf{U}(\tau)|^2 \mathrm{d}\tau\right]^{1/2} < \infty,$$

where $|\cdot|$ *represents the Euclidean norm, then* $\mathbf{Z}(t) \in L_2 \cap L_\infty$ *and*

$$\lim_{t\to\infty} E[\mathbf{Z}(t)] = \mathbf{0}.$$

Proof: The solution $\mathbf{Z}(t)$ can be written as

$$\mathbf{Z}(t) = \Phi_A(t-t_0)\mathbf{Z}(t_0) + \int_{t_0}^{t} \Phi_A(t-\tau)\mathbf{U}(\tau)\mathrm{d}\tau.$$

Since $\Phi_A(t-t_0)$ is exponentially stable

$$\|\Phi_A(t-t_0)\| \leq \lambda_0 e^{-a(t-t_0)} \leq \lambda_0 \quad \forall t \geq t_0,$$

where $\|\cdot\|$ represents any induced matrix norm and λ_0 and a are two positive constants. Thus

$$|\mathbf{Z}(t)| \leq \|\Phi_A(t-t_0)\|\,|\mathbf{Z}(t_0)| + \int_{t_0}^{t} \|\Phi_A(t-\tau)\|\,|\mathbf{U}(\tau)|\mathrm{d}\tau$$

$$\leq \lambda_0 e^{-a(t-t_0)}|\mathbf{Z}(t_0)| + \int_{t_0}^{t} \lambda_0 e^{-a(t-\tau)}|\mathbf{U}(\tau)|\mathrm{d}\tau$$

$$\leq \lambda_0 e^{-a(t-t_0)}|\mathbf{Z}(t_0)| + \int_{t_0}^{t} \lambda_0 e^{-(a-a_0/2)(t-\tau)} e^{-a_0/2(t-\tau)}|\mathbf{U}(\tau)|\mathrm{d}\tau.$$

The last inequality is obtained by expressing $e^{-a(t-\tau)}$ as $e^{-(a-a_0/2)(t-\tau)}e^{-a_0/2(t-\tau)}$, where $a_0 < 2a$ is a positive constant. Applying the Schwartz inequality yields

$$|\mathbf{Z}(t)| \leq \lambda_0 e^{-a(t-t_0)}|\mathbf{Z}(t_0)| + \lambda_0 \left(\int_{t_0}^{t} e^{-(2a-a_0)(t-\tau)}\mathrm{d}\tau\right)^{1/2} \times \left(\int_{t_0}^{t} e^{-a_0(t-\tau)}|\mathbf{U}(\tau)|^2\mathrm{d}\tau\right)^{1/2}.$$

Thus

$$|\mathbf{Z}(t)| \leq \lambda_0 e^{-a(t-t_0)}|\mathbf{Z}(t_0)| + \frac{\lambda_0}{\sqrt{(2a-a_0)}}\left(\int_{t_0}^{t} e^{-a_0(t-\tau)}|\mathbf{U}(\tau)|^2\mathrm{d}\tau\right)^{1/2}$$

and

$$E[|\mathbf{Z}(t)|] \leq \lambda_0 e^{-a(t-t_0)}E[|\mathbf{Z}(t_0)|] + \frac{\lambda_0}{\sqrt{(2a-a_0)}}E\left[\left(\int_{t_0}^{t} e^{-a_0(t-\tau)}|\mathbf{U}(\tau)|^2\mathrm{d}\tau\right)^{1/2}\right].$$

Therefore

$$\lim_{t\to\infty} E[\mathbf{Z}(t)] = \mathbf{0}.$$

Also note that $E[|\mathbf{Z}(t)|]$ is bounded by

$$E[|\mathbf{Z}(t)|] \leq \lambda_0 e^{-a(t-t_0)}E[|\mathbf{Z}(t_0)|] + \frac{\lambda_0}{\sqrt{(2a-a_0)}}E\left[\left(\int_{t_0}^{t} |\mathbf{U}(\tau)|^2\mathrm{d}\tau\right)^{1/2}\right].$$

Since $\mathbf{U}(t) \in L_2$

$$E\left[\left(\int_{t_0}^{\infty} |\mathbf{U}(\tau)|^2\mathrm{d}\tau\right)^{1/2}\right] \leq E\left[\int_{t_0}^{\infty} |\mathbf{U}(\tau)|^2\mathrm{d}\tau\right]^{1/2} < \infty.$$

Note that $\mathbf{Z}(t) \in L_2$ since

$$\int_{t_0}^{\infty}\left(\int_{t_0}^{t} e^{-a_0(t-\tau)}|\mathbf{U}(\tau)|^2\mathrm{d}\tau\right)\mathrm{d}t \leq \int_{t_0}^{\infty} |\mathbf{U}(\tau)|^2\left(\int_{t_0}^{\infty} e^{-a_0(t-\tau)}\mathrm{d}t\right)\mathrm{d}\tau \leq \frac{1}{a_0}\int_{t_0}^{\infty} |\mathbf{U}(\tau)|^2\mathrm{d}\tau.$$

Finally note that

$$\mathbf{Z}(t) \in L_2 \Rightarrow E[\mathbf{Z}(t)] \in L_2.$$

□

Lemma 5.6: *Consider the following linear stochastic system*

$$\dot{\mathbf{Z}}(t) = A\mathbf{Z}(t) + \mathbf{U}(t),$$
$$\mathbf{Y}(t) = C\mathbf{Z}(t).$$

If (A, C) *is observable,* $\mathbf{Y}(t) \in L_2$ *and* $\mathbf{U}(t) \in L_2$, *then* $\mathbf{Z}(t) \in L_2 \cap L_\infty$ *and*

$$\lim_{t\to\infty} E[\mathbf{Z}(t)] = \mathbf{0}.$$

Proof: If (A, C) is observable, then there exist a matrix K such that $A_o = A - KC$ is exponentially stable. Now $\dot{\mathbf{Z}}(t)$ can be written as

$$\dot{\mathbf{Z}}(t) = A_o\mathbf{Z}(t) + \mathbf{U}(t) + K\mathbf{Y}(t).$$

Thus from Lemma 5.5 one could conclude that $\mathbf{Z}(t) \in L_2 \cap L_\infty$ and

$$\lim_{t\to\infty} E[\mathbf{Z}(t)] = \mathbf{0}.$$

□

The stability analysis given in Section 3 reveals that selecting a sufficiently large process noise covariance would guarantee asymptotic stability of the controlled system's mean response. Thus the adaptive law given in Theorem 5.4 increases the process noise covariance to ensure that $E[\tilde{\mathbf{Y}}(t)] \in L_2$. Now based on the above lemmas the proof of Theorem 5.4 can be easily obtained as shown next.

Proof: Let $\mathcal{F}_t^{\tilde{\mathbf{Y}}}$ denote a filtration generated by $\tilde{\mathbf{Y}}(t)$, i.e.

$$E\left[\tilde{\mathbf{Y}}(s)\,\middle|\,\mathcal{F}_t^{\tilde{\mathbf{Y}}}\right] = \tilde{\mathbf{Y}}(s), \quad s \leq t.$$

Now consider the following nonnegative function:

$$V(t_0, t, \hat{\mathbf{Z}}, \tilde{\mathbf{Y}}, P, Q) = \int_{t_0}^{t} E\left[\tilde{\mathbf{Y}}(\tau)\,\middle|\,\mathcal{F}_{t_0}^{\tilde{\mathbf{Y}}}\right]^T E\left[\tilde{\mathbf{Y}}(\tau)\,\middle|\,\mathcal{F}_{t_0}^{\tilde{\mathbf{Y}}}\right]\mathrm{d}\tau + E\left[\hat{\mathbf{Z}}(t)\,\middle|\,\mathcal{F}_{t_0}^{\tilde{\mathbf{Y}}}\right]^T \mathcal{X} E\left[\hat{\mathbf{Z}}(t)\,\middle|\,\mathcal{F}_{t_0}^{\tilde{\mathbf{Y}}}\right] + \mathrm{Tr}\{Q^* - Q(t)\} + \mathrm{Tr}\{P^*_{\max} - P(t)\},$$

where $Q^* \geq Q(t)\ \forall t \geq t_0$ is a stabilising process noise covariance and $P^*_{\max}$ is selected such that $P^*_{\max} \geq P^*(t)\ \forall t \geq t_0$, where $P^*(t)$ may be obtained by solving the continuous-time matrix differential Riccati equation:

$$\dot{P}^*(t) = F_m P^*(t) + P^*(t)F_m^T - P^*(t)H^T R^{-1} H P^*(t) + GQ^*G^T, \quad P^*(t_0) = P_0.$$

Note that for any $Q(t) \le Q^*$, $P(t) \le P^*_{\max}$, where $P(t)$ satisfies

$$\dot{P}(t) = F_m P(t) + P(t)F_m^T - P(t)H^T R^{-1} H P(t) + GQ(t)G^T, \quad P(t_0) = P_0. \tag{52}$$

More details on this can be found in the *comparison results* given in Abou-Kandil et al. (2003, Chapter 4). The matrix $\mathcal{X}$ is a positive definite matrix of appropriate dimensions and it is selected so that it satisfies the following matrix inequality:

$$\mathcal{X}[F_m + D_m S] + [F_m + D_m S]^T \mathcal{X} + \mathcal{X}\mathcal{X} + \mathcal{M} \le 0,$$

where $\mathcal{M} > 0$. It is important to note that the expectation given in the above non-negative function is conditioned on the filtration at the lower time limit. For example, consider a time instant s such that $t_0 \le s \le t$, now $V(s, t, \hat{\mathbf{Z}}, \tilde{\mathbf{Y}}, P, Q)$ can be written as

$$\begin{aligned} &V(s, t, \hat{\mathbf{Z}}, \tilde{\mathbf{Y}}, P, Q) \\ &\quad = \int_s^t E\left[\tilde{\mathbf{Y}}(\tau) \,\middle|\, \mathcal{F}_s^{\tilde{\mathbf{Y}}}\right]^T E\left[\tilde{\mathbf{Y}}(\tau) \,\middle|\, \mathcal{F}_s^{\tilde{\mathbf{Y}}}\right] \mathrm{d}\tau \\ &\qquad + E\left[\hat{\mathbf{Z}}(t) \,\middle|\, \mathcal{F}_s^{\tilde{\mathbf{Y}}}\right]^T \mathcal{X} E\left[\hat{\mathbf{Z}}(t) \,\middle|\, \mathcal{F}_s^{\tilde{\mathbf{Y}}}\right] \\ &\qquad + \mathrm{Tr}\{Q^* - Q(t)\} + \mathrm{Tr}\{P^*_{\max} - P(t)\}. \end{aligned}$$

Now $\mathrm{d}V(s, t, \hat{\mathbf{Z}}, \tilde{\mathbf{Y}}, P, Q)$ can be calculated as

$$\begin{aligned} &\mathrm{d}V(s, t, \hat{\mathbf{Z}}, \tilde{\mathbf{Y}}, P, Q) \\ &\quad = E\left[\tilde{\mathbf{Y}}(t) \,\middle|\, \mathcal{F}_s^{\tilde{\mathbf{Y}}}\right]^T E\left[\tilde{\mathbf{Y}}(t) \,\middle|\, \mathcal{F}_s^{\tilde{\mathbf{Y}}}\right] \mathrm{d}t \\ &\qquad + E\left[\mathrm{d}\hat{\mathbf{Z}}(t) \,\middle|\, \mathcal{F}_s^{\tilde{\mathbf{Y}}}\right]^T \mathcal{X} E\left[\hat{\mathbf{Z}}(t) \,\middle|\, \mathcal{F}_s^{\tilde{\mathbf{Y}}}\right] + E\left[\hat{\mathbf{Z}}(t) \,\middle|\, \mathcal{F}_s^{\tilde{\mathbf{Y}}}\right]^T \\ &\qquad \times \mathcal{X} E\left[\mathrm{d}\hat{\mathbf{Z}}(t) \,\middle|\, \mathcal{F}_s^{\tilde{\mathbf{Y}}}\right] - \mathrm{Tr}\{\mathrm{d}Q(t)\} - \mathrm{Tr}\{\mathrm{d}P(t)\}. \end{aligned}$$

Note that

$$\begin{aligned} E\left[\mathrm{d}\hat{\mathbf{Z}}(t) \,\middle|\, \mathcal{F}_s^{\tilde{\mathbf{Y}}}\right] &= [F_m + D_m S] E\left[\hat{\mathbf{Z}}(t) \,\middle|\, \mathcal{F}_s^{\tilde{\mathbf{Y}}}\right] \mathrm{d}t \\ &\quad + E\left[K(t)\tilde{\mathbf{Y}}(t) \,\middle|\, \mathcal{F}_s^{\tilde{\mathbf{Y}}}\right] \mathrm{d}t. \end{aligned}$$

Thus

$$\begin{aligned} &\mathrm{d}V(s, t, \hat{\mathbf{Z}}, \tilde{\mathbf{Y}}, P, Q) \\ &\quad = E\left[\tilde{\mathbf{Y}}(t) \,\middle|\, \mathcal{F}_s^{\tilde{\mathbf{Y}}}\right]^T E\left[\tilde{\mathbf{Y}}(t) \,\middle|\, \mathcal{F}_s^{\tilde{\mathbf{Y}}}\right] \mathrm{d}t \\ &\qquad - \mathrm{Tr}\{\mathrm{d}Q(t)\} - \mathrm{Tr}\{\mathrm{d}P(t)\} + E\left[\hat{\mathbf{Z}}(t) \,\middle|\, \mathcal{F}_s^{\tilde{\mathbf{Y}}}\right]^T \\ &\qquad \times [F_m + D_m S]^T \mathcal{X} E\left[\hat{\mathbf{Z}}(t) \,\middle|\, \mathcal{F}_s^{\tilde{\mathbf{Y}}}\right] \mathrm{d}t \\ &\qquad + E\left[K(t)\tilde{\mathbf{Y}}(t) \,\middle|\, \mathcal{F}_s^{\tilde{\mathbf{Y}}}\right]^T \mathcal{X} E\left[\hat{\mathbf{Z}}(t) \,\middle|\, \mathcal{F}_s^{\tilde{\mathbf{Y}}}\right] \mathrm{d}t \\ &\qquad + E\left[\hat{\mathbf{Z}}(t) \,\middle|\, \mathcal{F}_s^{\tilde{\mathbf{Y}}}\right]^T \mathcal{X}[F_m + D_m S] E\left[\hat{\mathbf{Z}}(t) \,\middle|\, \mathcal{F}_s^{\tilde{\mathbf{Y}}}\right] \mathrm{d}t \\ &\qquad + E\left[\hat{\mathbf{Z}}(t) \,\middle|\, \mathcal{F}_s^{\tilde{\mathbf{Y}}}\right]^T \mathcal{X} E\left[K(t)\tilde{\mathbf{Y}}(t) \,\middle|\, \mathcal{F}_s^{\tilde{\mathbf{Y}}}\right] \mathrm{d}t. \end{aligned}$$

Note that for any two vectors $\mathbf{a}$ and $\mathbf{b}$ of same dimensions, the following inequality holds:

$$\mathbf{a}^T\mathbf{a} + \mathbf{b}^T\mathbf{b} \ge \mathbf{a}^T\mathbf{b} + \mathbf{b}^T\mathbf{a}$$

i.e.

$$\begin{aligned} &E\left[\hat{\mathbf{Z}}(t) \,\middle|\, \mathcal{F}_s^{\tilde{\mathbf{Y}}}\right]^T \mathcal{X}\mathcal{X} E\left[\hat{\mathbf{Z}}(t) \,\middle|\, \mathcal{F}_s^{\tilde{\mathbf{Y}}}\right] + E\left[K(t)\tilde{\mathbf{Y}}(t) \,\middle|\, \mathcal{F}_s^{\tilde{\mathbf{Y}}}\right]^T \\ &\quad \times E\left[K(t)\tilde{\mathbf{Y}}(t) \,\middle|\, \mathcal{F}_s^{\tilde{\mathbf{Y}}}\right] \\ &\qquad \ge E\left[K(t)\tilde{\mathbf{Y}}(t) \,\middle|\, \mathcal{F}_s^{\tilde{\mathbf{Y}}}\right]^T \mathcal{X} E\left[\hat{\mathbf{Z}}(t) \,\middle|\, \mathcal{F}_s^{\tilde{\mathbf{Y}}}\right] \\ &\quad + E\left[\hat{\mathbf{Z}}(t) \,\middle|\, \mathcal{F}_s^{\tilde{\mathbf{Y}}}\right]^T \mathcal{X} E\left[K(t)\tilde{\mathbf{Y}}(t) \,\middle|\, \mathcal{F}_s^{\tilde{\mathbf{Y}}}\right]. \end{aligned}$$

Therefore

$$\begin{aligned} &\mathrm{d}V(s, t, \hat{\mathbf{Z}}, \tilde{\mathbf{Y}}, P, Q) \\ &\quad \le E\left[\tilde{\mathbf{Y}}(t) \,\middle|\, \mathcal{F}_s^{\tilde{\mathbf{Y}}}\right]^T E\left[\tilde{\mathbf{Y}}(t) \,\middle|\, \mathcal{F}_s^{\tilde{\mathbf{Y}}}\right] \mathrm{d}t - \mathrm{Tr}\{\mathrm{d}Q(t)\} \\ &\qquad - \mathrm{Tr}\{\mathrm{d}P(t)\} + E\left[\hat{\mathbf{Z}}(t) \,\middle|\, \mathcal{F}_s^{\tilde{\mathbf{Y}}}\right]^T \\ &\qquad \times \{\mathcal{X}[F_m + D_m S] + [F_m + D_m S]^T \mathcal{X} + \mathcal{X}\mathcal{X}\} \\ &\qquad \times E\left[\hat{\mathbf{Z}}(t) \,\middle|\, \mathcal{F}_s^{\tilde{\mathbf{Y}}}\right] \mathrm{d}t + E\left[K(t)\tilde{\mathbf{Y}}(t) \,\middle|\, \mathcal{F}_s^{\tilde{\mathbf{Y}}}\right]^T \\ &\qquad \times E\left[K(t)\tilde{\mathbf{Y}}(t) \,\middle|\, \mathcal{F}_s^{\tilde{\mathbf{Y}}}\right] \mathrm{d}t. \end{aligned}$$

Now employing the Cauchy–Schwarz's inequality gives

$$\begin{aligned} &\mathrm{d}V(s, t, \hat{\mathbf{Z}}, \tilde{\mathbf{Y}}, P, Q) \\ &\quad \le E\left[\tilde{\mathbf{Y}}^T(t)\tilde{\mathbf{Y}}(t) \,\middle|\, \mathcal{F}_s^{\tilde{\mathbf{Y}}}\right] \mathrm{d}t + E\left[\tilde{\mathbf{Y}}^T(t)K^T(t)K(t)\tilde{\mathbf{Y}}(t) \,\middle|\, \mathcal{F}_s^{\tilde{\mathbf{Y}}}\right] \mathrm{d}t \\ &\qquad - \mathrm{Tr}\{\mathrm{d}Q(t)\} + E\left[\hat{\mathbf{Z}}(t) \,\middle|\, \mathcal{F}_s^{\tilde{\mathbf{Y}}}\right]^T \\ &\qquad \times \{\mathcal{X}[F_m + D_m S] + [F_m + D_m S]^T \mathcal{X} + \mathcal{X}\mathcal{X}\} \\ &\qquad \times E\left[\hat{\mathbf{Z}}(t) \,\middle|\, \mathcal{F}_s^{\tilde{\mathbf{Y}}}\right] \mathrm{d}t - \mathrm{Tr}\{\mathrm{d}P(t)\}. \end{aligned}$$

Substituting (51) and (52) yields

$$\begin{aligned} &\mathrm{d}V(s, t, \hat{\mathbf{Z}}, \tilde{\mathbf{Y}}, P, Q) \\ &\quad \le E\left[\tilde{\mathbf{Y}}^T(t)\tilde{\mathbf{Y}}(t) \,\middle|\, \mathcal{F}_s^{\tilde{\mathbf{Y}}}\right] \mathrm{d}t + E\left[\tilde{\mathbf{Y}}^T(t)K^T(t)K(t)\tilde{\mathbf{Y}}(t) \,\middle|\, \mathcal{F}_s^{\tilde{\mathbf{Y}}}\right] \mathrm{d}t \\ &\qquad - E\left[\hat{\mathbf{Z}}(t) \,\middle|\, \mathcal{F}_s^{\tilde{\mathbf{Y}}}\right]^T \mathcal{M} E\left[\hat{\mathbf{Z}}(t) \,\middle|\, \mathcal{F}_s^{\tilde{\mathbf{Y}}}\right] \mathrm{d}t \\ &\qquad - \mathrm{Tr}\left\{A_Q Q(t) + Q(t)A_Q^T + \gamma \Pi \tilde{\mathbf{Y}}(t)\tilde{\mathbf{Y}}^T(t)\Pi^T\right\} \mathrm{d}t \\ &\qquad - \mathrm{Tr}\{F_m P(t) + P(t)F_m^T \\ &\qquad - P(t)H^T R^{-1} H P(t) + GQ(t)G^T\} \mathrm{d}t. \end{aligned}$$

Note that

$$\begin{aligned} -\mathrm{Tr}\left\{A_Q Q(t) + Q(t)A_Q^T\right\} &= -2\mathrm{Tr}\{A_Q Q(t)\} \\ &\le -2\mathrm{Tr}\{A_Q\}\mathrm{Tr}\{Q(t)\} \\ &\le \mathrm{Tr}\{Q(t)\}. \end{aligned}$$

The first inequality is valid because $-A_Q$ is positive definite and the process noise covariance $Q(t)$ is positive semi-definite (Yang 2000). The last inequality holds since $0<-2\mathrm{Tr}\{A_Q\}\leq 1$. Also note that due to the nature of matrix G, we have

$$\mathrm{Tr}\{GQ(t)G^T\}=\mathrm{Tr}\{Q(t)\}.$$

Thus

$$\begin{aligned}
&\mathrm{d}V(s,t,\hat{\mathbf{Z}},\tilde{\mathbf{Y}},P,Q)\\
&\quad\leq \mathrm{Tr}\Big\{E\Big[\tilde{\mathbf{Y}}(t)\tilde{\mathbf{Y}}^T(t)\,\Big|\,\mathcal{F}_s^{\tilde{\mathbf{Y}}}\Big]\Big\}\mathrm{d}t\\
&\qquad+\mathrm{Tr}\Big\{E\Big[K^T(t)K(t)\tilde{\mathbf{Y}}(t)\tilde{\mathbf{Y}}^T(t)\,\Big|\,\mathcal{F}_s^{\tilde{\mathbf{Y}}}\Big]\Big\}\mathrm{d}t\\
&\qquad-E\Big[\hat{\mathbf{Z}}(t)\,\Big|\,\mathcal{F}_s^{\tilde{\mathbf{Y}}}\Big]^T\mathcal{M}E\Big[\hat{\mathbf{Z}}(t)\,\Big|\,\mathcal{F}_s^{\tilde{\mathbf{Y}}}\Big]\mathrm{d}t\\
&\qquad-\gamma\mathrm{Tr}\Big\{\tilde{\mathbf{Y}}(t)\tilde{\mathbf{Y}}^T(t)\Pi^T\Pi\Big\}\mathrm{d}t+\mathrm{Tr}\{P(t)H^TR^{-1}HP(t)\}\mathrm{d}t\\
&\qquad-2\mathrm{Tr}\{F_mP(t)\}\mathrm{d}t\\
&\quad\leq E\Big[\big(1+\|K(t)K^T(t)\|\big)\mathrm{Tr}\Big\{\tilde{\mathbf{Y}}(t)\tilde{\mathbf{Y}}^T(t)\Big\}\,\Big|\,\mathcal{F}_s^{\tilde{\mathbf{Y}}}\Big]\mathrm{d}t\\
&\qquad-E\Big[\hat{\mathbf{Z}}(t)\,\Big|\,\mathcal{F}_s^{\tilde{\mathbf{Y}}}\Big]^T\mathcal{M}E\Big[\hat{\mathbf{Z}}(t)\,\Big|\,\mathcal{F}_s^{\tilde{\mathbf{Y}}}\Big]\mathrm{d}t\\
&\qquad-\gamma\mathrm{Tr}\Big\{\tilde{\mathbf{Y}}(t)\tilde{\mathbf{Y}}^T(t)\Big\}\mathrm{d}t+\mathrm{Tr}\{P(t)H^TR^{-1}HP(t)\}\mathrm{d}t\\
&\qquad-2\mathrm{Tr}\{F_mP(t)\}\mathrm{d}t.
\end{aligned}$$

The second inequality holds since

$$|\tilde{\mathbf{Y}}(t)|^2+|K(t)\tilde{\mathbf{Y}}(t)|^2\leq\big(1+\|K(t)K^T(t)\|\big)|\tilde{\mathbf{Y}}(t)|^2.$$

Therefore $E\big[\mathrm{d}V(s,t,\hat{\mathbf{Z}},\tilde{\mathbf{Y}},P,Q)\,|\,\mathcal{F}_s^{\tilde{\mathbf{Y}}}\big]$ can be written as

$$\begin{aligned}
&E\Big[\mathrm{d}V(s,t,\hat{\mathbf{Z}},\tilde{\mathbf{Y}},P,Q)\,\Big|\,\mathcal{F}_s^{\tilde{\mathbf{Y}}}\Big]\\
&\quad\leq E\Big[\big(1+\|K(t)K^T(t)\|\big)|\tilde{\mathbf{Y}}(t)|^2\,\Big|\,\mathcal{F}_s^{\tilde{\mathbf{Y}}}\Big]\mathrm{d}t\\
&\qquad-E\Big[\hat{\mathbf{Z}}(t)\,\Big|\,\mathcal{F}_s^{\tilde{\mathbf{Y}}}\Big]^T\mathcal{M}E\Big[\hat{\mathbf{Z}}(t)\,\Big|\,\mathcal{F}_s^{\tilde{\mathbf{Y}}}\Big]\mathrm{d}t\\
&\qquad-\gamma E\Big[|\tilde{\mathbf{Y}}(t)|^2\,\Big|\,\mathcal{F}_s^{\tilde{\mathbf{Y}}}\Big]\mathrm{d}t\\
&\qquad+E\Big[\mathrm{Tr}\{P(t)H^TR^{-1}HP(t)-2F_mP(t)\}\,\Big|\,\mathcal{F}_s^{\tilde{\mathbf{Y}}}\Big]\mathrm{d}t.
\end{aligned}$$

Combining the similar terms yields

$$\begin{aligned}
&E\Big[\mathrm{d}V(s,t,\hat{\mathbf{Z}},\tilde{\mathbf{Y}},P,Q)\,\Big|\,\mathcal{F}_s^{\tilde{\mathbf{Y}}}\Big]\\
&\quad\leq E\Big[\big(1+\|K(t)K^T(t)\|-\gamma\big)|\tilde{\mathbf{Y}}(t)|^2\,\Big|\,\mathcal{F}_s^{\tilde{\mathbf{Y}}}\Big]\mathrm{d}t\\
&\qquad-E\Big[\hat{\mathbf{Z}}(t)\,\Big|\,\mathcal{F}_s^{\tilde{\mathbf{Y}}}\Big]^T\mathcal{M}E\Big[\hat{\mathbf{Z}}(t)\,\Big|\,\mathcal{F}_s^{\tilde{\mathbf{Y}}}\Big]\mathrm{d}t\\
&\qquad+E\Big[\mathrm{Tr}\{P(t)H^TR^{-1}HP(t)-2F_mP(t)\}\,\Big|\,\mathcal{F}_s^{\tilde{\mathbf{Y}}}\Big]\mathrm{d}t.
\end{aligned}$$

Let $\gamma=\gamma_1+\gamma_2$, where γ_1 is selected such that

$$\gamma_1\geq 1+\|K(t)K^T(t)\|. \tag{53}$$

Thus

$$\begin{aligned}
&E\Big[\mathrm{d}V(s,t,\hat{\mathbf{Z}},\tilde{\mathbf{Y}},P,Q)\,\Big|\,\mathcal{F}_s^{\tilde{\mathbf{Y}}}\Big]\\
&\quad\leq-\gamma_2\mathrm{Tr}\Big\{E\Big[\tilde{\mathbf{Y}}(t)\tilde{\mathbf{Y}}^T(t)\,\Big|\,\mathcal{F}_s^{\tilde{\mathbf{Y}}}\Big]\Big\}\mathrm{d}t\\
&\qquad-E\Big[\hat{\mathbf{Z}}(t)\,\Big|\,\mathcal{F}_s^{\tilde{\mathbf{Y}}}\Big]^T\mathcal{M}E\Big[\hat{\mathbf{Z}}(t)\,\Big|\,\mathcal{F}_s^{\tilde{\mathbf{Y}}}\Big]\mathrm{d}t\\
&\qquad+E\Big[\mathrm{Tr}\{P(t)H^TR^{-1}HP(t)-2F_mP(t)\}\,\Big|\,\mathcal{F}_s^{\tilde{\mathbf{Y}}}\Big]\mathrm{d}t.
\end{aligned}$$

Now based on Assumption 5.3, we have

$$\begin{aligned}
&E\Big[\mathrm{d}V(s,t,\hat{\mathbf{Z}},\tilde{\mathbf{Y}},P,Q)\,\Big|\,\mathcal{F}_s^{\tilde{\mathbf{Y}}}\Big]\\
&\quad\leq-E\Big[\hat{\mathbf{Z}}(t)\,\Big|\,\mathcal{F}_s^{\tilde{\mathbf{Y}}}\Big]^T\mathcal{M}E\Big[\hat{\mathbf{Z}}(t)\,\Big|\,\mathcal{F}_s^{\tilde{\mathbf{Y}}}\Big]\mathrm{d}t\\
&\qquad+E\big[\mathrm{Tr}\{P(t)H^TR^{-1}HP(t)-2F_mP(t)\}\\
&\qquad-\gamma_2\mathrm{Tr}\{\bar{R}\}\,\Big|\,\mathcal{F}_s^{\tilde{\mathbf{Y}}}\big]\mathrm{d}t.
\end{aligned}$$

Finally note that $E\big[\mathrm{d}V(s,t,\hat{\mathbf{Z}},\tilde{\mathbf{Y}},P,Q)\,|\,\mathcal{F}_s^{\tilde{\mathbf{Y}}}\big]\leq 0$ if

$$\gamma_2\geq\mathrm{Tr}\{P(t)H^TR^{-1}HP(t)-2F_mP(t)\}\mathrm{Tr}\{\bar{R}\}^{-1}. \tag{54}$$

Assuming that $\tilde{\mathbf{Y}}(t_0)$ is precisely known yields

$$E\Big[\tilde{\mathbf{Y}}(t)\,\Big|\,\mathcal{F}_{t_0}^{\tilde{\mathbf{Y}}}\Big]=E\Big[\tilde{\mathbf{Y}}(t)\Big].$$

Thus selecting γ_1 and γ_2 according to Equations (53) and (54) yields

$$\begin{aligned}
&E\Big[V(t_0,t,\hat{\mathbf{Z}},\tilde{\mathbf{Y}},P,Q)\Big]-V(t_0,t_0,\hat{\mathbf{Z}},\tilde{\mathbf{Y}},P,Q)\\
&\quad=\int_{t_0}^{t}E\Big[\mathrm{d}V(t_0,\tau,\hat{\mathbf{Z}},\tilde{\mathbf{Y}},P,Q)\Big]\leq 0.
\end{aligned}$$

Therefore

$$\begin{aligned}
E\Big[V(t_0,t,\hat{\mathbf{Z}},\tilde{\mathbf{Y}},P,Q)\Big]\leq\hat{\mathbf{z}}^T(t_0)\mathcal{X}\hat{\mathbf{z}}(t_0)+\mathrm{Tr}\{Q^*-Q(t_0)\}\\
+\mathrm{Tr}\{P^*_{\max}-P(t_0)\}.
\end{aligned}$$

Also note that

$$\begin{aligned}
&E\Big[V(s,t,\hat{\mathbf{Z}},\tilde{\mathbf{Y}},P,Q)\,\Big|\,\mathcal{F}_s^{\tilde{\mathbf{Y}}}\Big]-V(t_0,s,\hat{\mathbf{Z}},\tilde{\mathbf{Y}},P,Q)\\
&\quad=\int_{s}^{t}E\Big[\mathrm{d}V(s,\tau,\hat{\mathbf{Z}},\tilde{\mathbf{Y}},P,Q)\,\Big|\,\mathcal{F}_s^{\tilde{\mathbf{Y}}}\Big]\leq 0.
\end{aligned}$$

Thus

$$E\Big[V(s,t,\hat{\mathbf{Z}},\tilde{\mathbf{Y}},P,Q)\,\Big|\,\mathcal{F}_s^{\tilde{\mathbf{Y}}}\Big]\leq V(t_0,s,\hat{\mathbf{Z}},\tilde{\mathbf{Y}},P,Q).$$

Now the properties of $V(t_0,t,\hat{\mathbf{Z}},\tilde{\mathbf{Y}},P,Q)$ may be summarised as

(i) $V(t_0,t,\hat{\mathbf{Z}},\tilde{\mathbf{Y}},P,Q)\geq 0$;
(ii) $E\big[V(t_0,t,\hat{\mathbf{Z}},\tilde{\mathbf{Y}},P,Q)\big]<\infty$;
(iii) $E\big[V(t_0,t,\hat{\mathbf{Z}},\tilde{\mathbf{Y}},P,Q)\,|\,\mathcal{F}_s^{\tilde{\mathbf{Y}}}\big]\leq V(t_0,s,\hat{\mathbf{Z}},\tilde{\mathbf{Y}},P,Q)$, $s\leq t$;
(iv) $V(t_0,t,\hat{\mathbf{Z}},\tilde{\mathbf{Y}},P,Q)$ is adapted to $\mathcal{F}_t^{\tilde{\mathbf{Y}}}$.

These properties imply that $V(t_0, t, \hat{\mathbf{Z}}, \widetilde{\mathbf{Y}}, P, Q)$ is a non-negative $\mathcal{F}_s^{\widetilde{\mathbf{Y}}}$-supermartingale (Kushner 1967; Liptser and Shiryayev 1989) and the non-negative supermartingale probability inequality yields (Doob 1953)

$$\mathbb{P}\left(\sup_{t\geq t_0} V(t_0, t, \hat{\mathbf{Z}}, \widetilde{\mathbf{Y}}, P, Q) \geq \lambda\right) \leq \frac{\hat{\mathbf{z}}^T(t_0)\mathcal{X}\hat{\mathbf{z}}(t_0) + \mathrm{Tr}\{Q^* - Q(t_0)\} + \mathrm{Tr}\{P^*_{\max} - P(t_0)\}}{\lambda},$$

where $\lambda > 0$ is any positive constant. Thus selecting sufficiently large λ yields

$$\mathbb{P}\left(\sup_{t\geq t_0} V(t_0, t, \hat{\mathbf{Z}}, \widetilde{\mathbf{Y}}, P, Q) < \infty\right) = 1.$$

That is, $V(t_0, t, \hat{\mathbf{Z}}, \widetilde{\mathbf{Y}}, P, Q)$ is almost surely bounded. Note that $V(t_0, t, \hat{\mathbf{Z}}, \widetilde{\mathbf{Y}}, P, Q)$ is defined as

$$\begin{aligned} &V(t_0, t, \hat{\mathbf{Z}}, \widetilde{\mathbf{Y}}, P, Q) \\ &\quad = \int_{t_0}^{t} E\left[\widetilde{\mathbf{Y}}(\tau)\right]^T E\left[\widetilde{\mathbf{Y}}(\tau)\right] \mathrm{d}\tau + E\left[\hat{\mathbf{Z}}(t)\right]^T \mathcal{X} E\left[\hat{\mathbf{Z}}(t)\right] \\ &\qquad + \mathrm{Tr}\{Q^* - Q(t)\} + \mathrm{Tr}\{P^*_{\max} - P(t)\}. \end{aligned}$$

Therefore

$$\begin{aligned} &V(t_0, t, \hat{\mathbf{Z}}, \widetilde{\mathbf{Y}}, P, Q) \in L_\infty \quad \text{a.s.} \\ &\quad \Longrightarrow E\left[\widetilde{\mathbf{Y}}(t)\right] \in L_2, \quad Q(t) \in L_\infty \quad \text{and} \quad P(t) \in L_\infty \text{ a.s.} \end{aligned}$$

Since $P(t)$ is a.s. bounded, the estimator gain, $K(t) = P(t)H^T R^{-1}$, is also a.s. bounded. Thus there exists a k^* such that

$$\mathbb{P}\left(\sup_{t\geq t_0} \|K(t)\| > k^*\right) = 0.$$

The estimator dynamics is given as

$$\dot{\hat{\mathbf{Z}}}(t) = [F_m + D_m S]\hat{\mathbf{Z}}(t) + K(t)\widetilde{\mathbf{Y}}(t).$$

Since $[F_m + D_m S]$ generates an exponentially stable evolution operator, and since $E[\widetilde{\mathbf{Y}}(t)] \in L_2$, based on Lemma 5.5, it can be shown that $E[\hat{\mathbf{Z}}(t)] \in L_2 \cap L_\infty$, and

$$\lim_{t\to\infty} E\left[\hat{\mathbf{Z}}(t)\right] = \mathbf{0}.$$

Since $E[\widetilde{\mathbf{Y}}(t)] \in L_2$,

$$E[\hat{\mathbf{Z}}(t)] \in L_2 \Longrightarrow E[\mathbf{Y}(t)] \in L_2.$$

Now given the observability assumption, based on Lemma 5.6, it can be shown that $E[\mathbf{X}(t)] \in L_2 \cap L_\infty$, and

$$\lim_{t\to\infty} E[\mathbf{X}(t)] = \mathbf{0}.$$

Finally note that the controlled closed-loop system can be written as

$$\begin{bmatrix} \dot{\mathbf{X}}_{\text{ext}}(t) \\ \dot{\hat{\mathbf{Z}}}(t) \end{bmatrix} = \begin{bmatrix} \mathcal{A}_{\text{ext}} & \mathcal{B}_{\text{ext}} S \\ K(t)H & \{F_m + D_m S - K(t)H\} \end{bmatrix} \begin{bmatrix} \mathbf{X}_{\text{ext}}(t) \\ \hat{\mathbf{Z}}(t) \end{bmatrix} + \begin{bmatrix} G\mathcal{V}(t) \\ K(t)\mathbf{V}(t) \end{bmatrix}. \tag{55}$$

Note that the closed-loop state matrix

$$F_{\text{CL}}(t) = \begin{bmatrix} \mathcal{A}_{\text{ext}} & \mathcal{B}_{\text{ext}} S \\ K(t)H & \{F_m + D_m S - K(t)H\} \end{bmatrix}$$

is bounded. Also, the asymptotic stability of $E[\mathbf{X}_{\text{ext}}(t)]$ and $E[\hat{\mathbf{Z}}(t)]$ implies that the matrix, $F_{\text{CL}}(t)$, generates an asymptotically stable evolution operator, $\Phi_{\text{CL}}(t, t_0)$, i.e.

$$\lim_{t\to\infty} \|\Phi_{\text{CL}}(t, t_0)\| = 0.$$

Equation (55) can be written in Itô form as

$$\mathrm{d}\mathbf{X}_{\text{CL}}(t) = F_{\text{CL}}(t)\mathbf{X}_{\text{CL}}(t)\mathrm{d}t + \Gamma_{\text{CL}}(t)\mathrm{d}\boldsymbol{\mathcal{B}}_{\text{CL}}(t), \tag{56}$$

where

$$\Gamma_{\text{CL}}(t) = \begin{bmatrix} G & 0 \\ 0 & K(t) \end{bmatrix} \quad \text{and}$$

$$E\left[\mathrm{d}\boldsymbol{\mathcal{B}}_{\text{CL}}(t)\mathrm{d}\boldsymbol{\mathcal{B}}_{\text{CL}}^T(t)\right] = \begin{bmatrix} \mathcal{Q} & 0 \\ 0 & R \end{bmatrix}\mathrm{d}t = Q_{\text{CL}}\mathrm{d}t.$$

Remark 5: It is important to note that if one wishes to express (55) in Stratonovich form, the results given here hold since we are considering linear stochastic differential equations with state free diffusion term and the solution obtained from the Stratonovich integral equation converges a.s. and uniformly to that obtained from the Itô integral equation. For more details please refer to the Wong-Zakai theorem (Grigoriu 2002).

Now using Itô formula $\mathrm{d}\left(\mathbf{X}_{\text{CL}}(t)\mathbf{X}_{\text{CL}}^T(t)\right)$ can be written as

$$\begin{aligned} &\mathrm{d}\left(\mathbf{X}_{\text{CL}}(t)\mathbf{X}_{\text{CL}}^T(t)\right) \\ &\quad = \mathbf{X}_{\text{CL}}(t)\mathrm{d}(\mathbf{X}_{\text{CL}}(t))^T + \mathrm{d}(\mathbf{X}_{\text{CL}}(t))\mathbf{X}_{\text{CL}}^T(t) \\ &\qquad + \Gamma_{\text{CL}}(t)Q_{\text{CL}}\Gamma_{\text{CL}}(t)\mathrm{d}t \\ &\quad = \left\{\mathbf{X}_{\text{CL}}(t)\mathbf{X}_{\text{CL}}^T(t)F_{\text{CL}}^T(t) + F_{\text{CL}}(t)\mathbf{X}_{\text{CL}}(t)\mathbf{X}_{\text{CL}}^T(t)\right. \\ &\qquad \left. + \Gamma_{\text{CL}}(t)Q_{\text{CL}}\Gamma_{\text{CL}}(t)\right\}\mathrm{d}t \\ &\qquad + \Gamma_{\text{CL}}(t)\mathrm{d}\boldsymbol{\mathcal{B}}_{\text{CL}}(t)\mathbf{X}_{\text{CL}}^T(t) + \mathbf{X}_{\text{CL}}(t)\mathrm{d}\boldsymbol{\mathcal{B}}_{\text{CL}}^T(t)\Gamma_{\text{CL}}^T(t). \end{aligned}$$

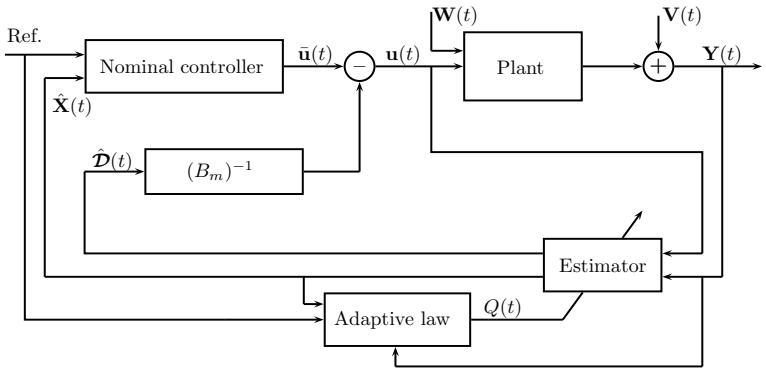

Figure 2. Adaptive DAC block diagram.

Thus

$$\begin{aligned}
&\mathbf{X}_{\mathrm{CL}}(t)\mathbf{X}_{\mathrm{CL}}^T(t)\\
&\quad = \Phi_{\mathrm{CL}}(t,t_0)\mathbf{X}_{\mathrm{CL}}(t_0)\mathbf{X}_{\mathrm{CL}}^T(t_0)\Phi_{\mathrm{CL}}^T(t,t_0)\\
&\qquad + \int_{t_0}^{t}\Big[\mathbf{X}_{\mathrm{CL}}(\tau)\big[\Gamma_{\mathrm{CL}}(\tau)\mathrm{d}\boldsymbol{\mathcal{B}}_{\mathrm{CL}}(\tau)\big]^T\Big]^T\\
&\qquad + \int_{t_0}^{t}\mathbf{X}_{\mathrm{CL}}(\tau)\big[\Gamma_{\mathrm{CL}}(\tau)\mathrm{d}\boldsymbol{\mathcal{B}}_{\mathrm{CL}}(\tau)\big]^T\\
&\qquad + \int_{t_0}^{t}\Phi_{\mathrm{CL}}(t,\tau)\Gamma_{\mathrm{CL}}(\tau)Q_{\mathrm{CL}}\Gamma_{\mathrm{CL}}^T(\tau)\Phi_{\mathrm{CL}}^T(t,\tau)\mathrm{d}\tau.
\end{aligned}$$

Therefore

$$\begin{aligned}
&E\Big[\mathbf{X}_{\mathrm{CL}}(t)\mathbf{X}_{\mathrm{CL}}^T(t)\Big]\\
&\quad = E\Big[\Phi_{\mathrm{CL}}(t,t_0)\mathbf{X}_{\mathrm{CL}}(t_0)\mathbf{X}_{\mathrm{CL}}^T(t_0)\Phi_{\mathrm{CL}}^T(t,t_0)\\
&\qquad + \int_{t_0}^{t}\Phi_{\mathrm{CL}}(t,\tau)\Gamma_{\mathrm{CL}}(\tau)Q_{\mathrm{CL}}\Gamma_{\mathrm{CL}}^T(\tau)\Phi_{\mathrm{CL}}^T(t,\tau)\mathrm{d}\tau\Big].
\end{aligned}$$

Since $\Phi_{\mathrm{CL}}(t,t_0)$ is an asymptotically stable evolution operator and $\Gamma_{\mathrm{CL}}(t)$ is bounded, it can be easily shown that the closed-loop system is mean square stable, i.e.

$$\lim_{t\to\infty} E[\mathbf{X}_{\mathrm{CL}}(t)\mathbf{X}_{\mathrm{CL}}^T(t)] < \mathrm{M},$$

where M is a constant square matrix whose elements are finite (Soong 1973). □

Even though the initial process noise covariance, $Q(t_0)$, may not be the stabilising Q, the adaptive law given in (51) can be used to update the process noise covariance online so that the controlled system is asymptotically stable. A schematic representation of the proposed adaptive controller is given in Figure 2.

6. Simulation results

For simulation purposes, consider a two degree-of-freedom helicopter that pivots about the pitch axis by angle θ and about the yaw axis by angle ψ. As shown in Figure 3, pitch is defined positive when the nose of the helicopter goes up and yaw is defined positive for a counterclockwise rotation. Also in Figure 3, there is a thrust force F_p acting on the pitch axis that is normal to the plane of the front propeller and a thrust force F_y acting on the yaw axis that is normal to the rear propeller. Therefore a pitch torque is being applied at a distance r_p from the pitch axis and a yaw torque is applied at a distance r_y from the yaw axis. The gravitational force, F_g, generates a torque at the helicopter centre of mass that pulls down on the helicopter nose. As shown in Figure 3, the centre of mass is a distance of l_{cm} from the pitch axis along the helicopter body length.

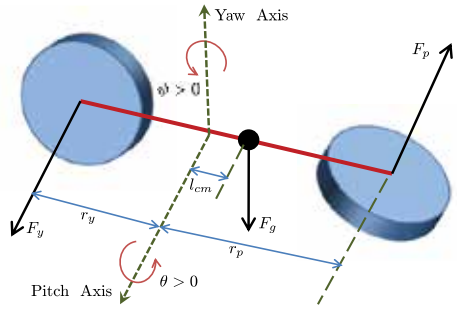

Figure 3. Two degree-of-freedom helicopter.

After linearising about $\theta(t_0) = \psi(t_0) = \dot{\theta}(t_0) = \dot{\psi}(t_0) = 0$, the helicopter equations of motion can be written as

$$\begin{aligned}
&(J_{\mathrm{eq},p} + m_{\mathrm{heli}}l_{\mathrm{cm}}^2)\ddot{\theta}(t)\\
&\quad = K_{pp}V_{m,p}(t) + K_{py}V_{m,y}(t) - B_p\dot{\theta}(t) + W_1(t) \qquad (57a)\\
&(J_{\mathrm{eq},y} + m_{\mathrm{heli}}l_{\mathrm{cm}}^2)\ddot{\psi}(t)\\
&\quad = K_{yy}V_{m,y}(t) + K_{yp}V_{m,p}(t) - B_y\dot{\psi}(t) + W_2(t). \qquad (57b)
\end{aligned}$$

Table 2. Two degree-of-freedom helicopter model parameters.

System parameter	Description	Assumed values	True values	Unit
B_p	Equivalent viscous damping about pitch axis	0.8000	1	N/V
B_y	Equivalent viscous damping about yaw axis	0.3180	−0.3021	N/V
$J_{\text{eq},p}$	Total moment of inertia about yaw pivot	0.0384	0.0288	Kg m^2
$J_{\text{eq},y}$	Total moment of inertia about pitch pivot	0.0432	0.0496	Kg m^2
K_{pp}	Trust torque constant acting on pitch axis from pitch motor/propeller	0.2041	0.2552	N m/V
K_{py}	Trust torque constant acting on pitch axis from yaw motor/propeller	0.0068	0.0051	N m/V
K_{yp}	Trust torque constant acting on yaw axis from pitch motor/propeller	0.0219	0.0252	N m/V
K_{yy}	Trust torque constant acting on yaw axis from yaw motor/propeller	0.0720	0.0684	N m/V
m_{heli}	Total mass of the helicopter	1.3872	1.3872	Kg
l_{cm}	Location of centre-of-mass	0.1857	0.1764	m

A detailed description of system parameters and assumed values is given in Table 2. The system states are the pitch and yaw angles and their corresponding rates, i.e. $\theta(t)$, $\psi(t)$, $\dot{\theta}(t)$ and $\dot{\psi}(t)$. The control input to the system are the input voltages of the pitch and yaw motors, $V_{m,p}$ and $V_{m,y}$, respectively. The external disturbances are denoted as $W_1(t)$ and $W_2(t)$. Let $\mathbf{X}_1(t)=[\theta(t)\ \ \psi(t)]^T$, $\mathbf{X}_2(t)=\left[\dot{\theta}(t)\ \ \dot{\psi}(t)\right]^T$, $\mathbf{u}(t)=[V_{m,p}(t)\ \ V_{m,y}(t)]^T$ and $\mathbf{W}(t)=[W_1(t)\ \ W_2(t)]^T$. For simulation purposes, the external disturbance $\mathbf{W}(t)$ is selected to be

$$\begin{aligned}\dot{W}_1(t) &= 2.43\dot{\theta}(t) - 1.3\dot{\psi}(t) - W_1(t) + 2W_2(t) + \mathcal{V}_1(t),\\ \dot{W}_2(t) &= -0.34\dot{\theta}(t) + 1.92\dot{\psi}(t) + W_1(t) - 3W_2(t) + \mathcal{V}_2(t)\end{aligned} \tag{58}$$

and

$$\begin{bmatrix}\mathcal{V}_1(t)\\ \mathcal{V}_2(t)\end{bmatrix} = \boldsymbol{\mathcal{V}}(t) \sim \mathcal{N}\big(\mathbf{0}, 1\times 10^{-2} I_{2\times 2}\delta(\tau)\big).$$

Now the state-space representation of the plant can be written as

$$\begin{aligned}\dot{\mathbf{X}}_1(t) &= \mathbf{X}_2(t),\\ \dot{\mathbf{X}}_2(t) &= A_4\mathbf{X}_2(t) + B\mathbf{u}(t) + \mathbf{W}(t),\\ \dot{\mathbf{W}}(t) &= A_{\mathbf{w}_2}\mathbf{X}_2(t) + A_{\mathbf{w}_3}\mathbf{W}(t) + \boldsymbol{\mathcal{V}}(t),\end{aligned} \tag{59}$$

where

$$A_{\mathbf{w}_2} = \begin{bmatrix}2.43 & -1.3\\ -0.34 & 1.92\end{bmatrix},\quad A_{\mathbf{w}_3} = \begin{bmatrix}-1 & 2\\ 1 & -3\end{bmatrix},$$
$$A_4 = \begin{bmatrix}a_1 & 0\\ 0 & a_2\end{bmatrix},\quad B = \begin{bmatrix}b_1 & b_2\\ b_3 & b_4\end{bmatrix}$$

and the system parameters are given as

$$a_1 = \frac{-B_p}{(J_{\text{eq},p} + m_{\text{heli}}l_{\text{cm}}^2)},\quad a_2 = \frac{-B_y}{(J_{\text{eq},y} + m_{\text{heli}}l_{\text{cm}}^2)},$$
$$b_1 = \frac{K_{pp}}{(J_{\text{eq},p} + m_{\text{heli}}l_{\text{cm}}^2)},\quad b_2 = \frac{K_{py}}{(J_{\text{eq},p} + m_{\text{heli}}l_{\text{cm}}^2)},$$
$$b_3 = \frac{K_{yp}}{(J_{\text{eq},y} + m_{\text{heli}}l_{\text{cm}}^2)},\quad b_4 = \frac{K_{yy}}{(J_{\text{eq},y} + m_{\text{heli}}l_{\text{cm}}^2)}.$$

The state-space representation of the assumed system model is

$$\begin{aligned}\dot{\mathbf{X}}_{1_m}(t) &= \mathbf{X}_{2_m}(t),\\ \dot{\mathbf{X}}_{2_m}(t) &= A_{4_m}\mathbf{X}_{2_m}(t) + B_m\mathbf{u}(t),\end{aligned}$$

where

$$A_{4_m} = \begin{bmatrix}a_{1_m} & 0\\ 0 & a_{2_m}\end{bmatrix},\quad B_m = \begin{bmatrix}b_{1_m} & b_{2_m}\\ b_{3_m} & b_{4_m}\end{bmatrix}.$$

The measured output equations are given as

$$\mathbf{Y}(t) = C\mathbf{X}(t) + \mathbf{V}(t),$$

where $\mathbf{X}(t) = \left[\mathbf{X}_1^T(t)\ \ \mathbf{X}_2^T(t)\right]^T$ and $C=[I_{2\times 2}\ \ 0_{2\times 2}]$. Note that the disturbance term, $\boldsymbol{\mathcal{D}}(t) = [\mathcal{D}_{\dot{\theta}}(t)\ \ \mathcal{D}_{\dot{\psi}}(t)]^T$, can be written as

$$\begin{aligned}\mathcal{D}_{\dot{\theta}}(t) &= \triangle a_1\dot{\theta}(t) + \triangle b_1u_1(t) + \triangle b_2u_2(t) + W_1(t)\\ \mathcal{D}_{\dot{\psi}}(t) &= \triangle a_2\dot{\psi}(t) + \triangle b_3u_1(t) + \triangle b_4u_2(t) + W_2(t).\end{aligned}$$

The assumed disturbance term dynamics is modelled as

$$\begin{aligned}\dot{\mathcal{D}}_{\dot{\theta}_m}(t) &= -\mathcal{D}_{\dot{\theta}_m}(t) + \mathcal{W}_1(t),\\ \dot{\mathcal{D}}_{\dot{\psi}_m}(t) &= -3\mathcal{D}_{\dot{\psi}_m}(t) + \mathcal{W}_2(t).\end{aligned}$$

Let the extended assumed state vector be $\mathbf{Z}_m(t) = \left[\mathbf{X}_m^T(t)\ \ \mathcal{D}_{\dot{\theta}_m}(t)\ \ \mathcal{D}_{\dot{\psi}_m}(t)\right]^T$. Now the assumed extended state-space equation can be written as

$$\dot{\mathbf{Z}}_m(t) = F_m\mathbf{Z}_m(t) + D_m\mathbf{u}(t) + G\boldsymbol{\mathcal{W}}(t),$$

where

$$F_m = \begin{bmatrix}0_{2\times 2} & I_{2\times 2} & 0_{2\times 2}\\ 0_{2\times 2} & A_{4_m} & I_{2\times 2}\\ 0_{2\times 2} & 0_{2\times 2} & A_{\mathcal{D}_m}\end{bmatrix},\quad D_m = \begin{bmatrix}0_{2\times 2}\\ B_m\\ 0_{2\times 2}\end{bmatrix}\quad \text{and}$$
$$G = \begin{bmatrix}0_{4\times 2}\\ I_{2\times 2}\end{bmatrix}.$$

The estimator dynamics can be written as

$$\dot{\hat{\mathbf{Z}}}(t) = F_m\hat{\mathbf{Z}}(t) + D_m\mathbf{u}(t) + K(t)[C\mathbf{X}(t) - H\hat{\mathbf{Z}}(t)] + K(t)\mathbf{V}(t), \quad (60)$$

where $H = [C\ 0_{2\times 2}]$. The nominal controller is a linear quadratic regulator which minimises the cost function

$$J = \frac{1}{2}E\left[\int_0^\infty \left((\mathbf{X}_m(t) - \mathbf{x}_d)^T\mathcal{Q}_{\mathbf{X}}(\mathbf{X}_m(t) - \mathbf{x}_d) + \mathbf{u}^T(t)\mathcal{R}_{\mathbf{u}}\mathbf{u}(t)\right)\mathrm{d}t\right], \quad (61)$$

where $\mathbf{x}_d^T = [\theta_d \quad \psi_d \quad 0 \quad 0]$, θ_d and ψ_d are some desired final values of θ and ψ, respectively, and $\mathcal{Q}_{\mathbf{X}}$ and $\mathcal{R}_{\mathbf{u}}$ are two symmetric positive definite matrices. The nominal control that minimises the above cost function is

$$\bar{\mathbf{u}}(t) = -K_m(\mathbf{X}_m(t) - \mathbf{x}_d),$$

where K_m is the feedback gain. Now the DAC law can be written in terms of the estimated states and the estimated disturbance term as

$$\mathbf{u}(t) = [-K_m \quad -(B_m)^{-1}]\begin{bmatrix}\hat{\mathbf{X}}(t) - \mathbf{x}_d \\ \hat{\mathcal{D}}_{\dot{\theta}}(t) \\ \hat{\mathcal{D}}_{\dot{\psi}}(t)\end{bmatrix} = S\hat{\mathbf{Z}}(t) + K_m\mathbf{x}_d.$$

After substituting the above control law, the true extended system dynamics can be written as

$$\begin{bmatrix}\dot{\mathbf{X}}_1(t) \\ \dot{\mathbf{X}}_2(t) \\ \dot{\boldsymbol{\mathcal{D}}}(t)\end{bmatrix} = \begin{bmatrix}0_{2\times 2} & I_{2\times 2} & 0_{2\times 2} \\ 0_{2\times 2} & A_{4_m} & I_{2\times 2} \\ A_{\mathcal{D}_1}(t) & A_{\mathcal{D}_2}(t) & A_{\mathcal{D}_3}(t)\end{bmatrix}\begin{bmatrix}\mathbf{X}_1(t) \\ \mathbf{X}_2(t) \\ \boldsymbol{\mathcal{D}}(t)\end{bmatrix} + \begin{bmatrix}0_{2\times 6} \\ B_mS \\ B_{\mathcal{D}_1}(t)\end{bmatrix}\hat{\mathbf{Z}}(t) + \begin{bmatrix}0_{2\times 4} \\ B_mK_m \\ B_{\mathcal{D}_2}\end{bmatrix}\mathbf{x}_d + \begin{bmatrix}\mathbf{0}_{2\times 1} \\ \mathbf{0}_{2\times 1} \\ \boldsymbol{\mathcal{W}}_a(t)\end{bmatrix}, \quad (62)$$

where

$$A_{\mathcal{D}_1}(t) = \Delta BSK(t), \quad A_{\mathcal{D}_2}(t) = \Delta A_2A_{4_m} + A_{\mathbf{w}_2} - A_{\mathbf{w}_3}\Delta A_2,$$
$$A_{\mathcal{D}_3}(t) = \Delta A_2 + A_{\mathbf{w}_3}$$

$$B_{\mathcal{D}_1}(t) = \left\{\Delta BS[F_m + D_mS - K(t)H] + \Delta A_2B_mS - A_{\mathbf{w}_3}\Delta BS\right\}$$

and

$$B_{\mathcal{D}_2}(t) = \Delta A_2B_mK_m - A_{\mathbf{w}_3}\Delta BK_m.$$

Here $\Delta B = B - B_m$ and $\Delta A_2 = A_4 - A_{4_m}$.

Table 3 shows the nominal controller and estimator matrices. Since the measurement noise covariance, R, can be obtained from sensor calibration, the process noise matrix, Q, is treated as a tuning parameter. Based on the weighting matrices given in Table 3, the feedback gain is calculated to be

$$K_m = \begin{bmatrix}7.0229 & 0.8239 & 1.6691 & 0.3310 \\ -0.8239 & 7.0229 & -0.0830 & 2.4486\end{bmatrix}.$$

For simulation purposes the initial states are selected to be $[\theta_0 \quad \psi_0 \quad \dot{\theta}_0 \quad \dot{\psi}_0]^T = [-45^\circ \quad 0 \quad 0 \quad 0]^T$ and the desired states θ_d and ψ_d are selected to be 45° and 30°, respectively.

The desired response given in Figure 4 is the system response to the nominal control when there is no model error and external disturbance. For illustrative purposes, simulations are conducted using the traditional DAC as well as the proposed adaptive DAC. Results obtained using the traditional DAC is given first.

6.1 *DAC results*

Figure 5(a) shows the unstable system response obtained for the first simulation where the disturbance term process noise covariance is selected to be $Q = 10^3 \times I_{2\times 2}$. Figure 5(b) shows the input corresponding to the first simulation scenario. Figure 6(a) and (b) contains the estimated disturbance term and the error between the desired states and the true states corresponding to the first simulation. Note that the first simulation results given in Figures 5 and 6 are unstable due to the low value of Q selected.

A second simulation is conducted using $Q = 10^5 \times I_{2\times 2}$. The system response obtained for the

Table 3. Nominal controller/estimator matrices.

LQR weighting matrices	Covariance matrices
$\mathcal{R}_{\mathbf{u}} = 10 \times I_{2\times 2}$	$Q = \begin{bmatrix}q_1 & q_2 \\ q_3 & q_4\end{bmatrix}$, $R = 10^{-3} \times I_{2\times 2}$,
$\mathcal{Q}_{\mathbf{x}} = \begin{bmatrix}500 \times I_{2\times 2} & 0_{2\times 2} \\ 0_{2\times 2} & 100 \times I_{2\times 2}\end{bmatrix}$	$P(t_0) = \begin{bmatrix}10^{-1} \times I_{2\times 2} & 0_{2\times 2} & 0_{2\times 2} \\ 0_{2\times 2} & I_{2\times 2} & 0_{2\times 2} \\ 0_{2\times 2} & 0_{2\times 2} & 10^2 \times I_{2\times 2}\end{bmatrix}$

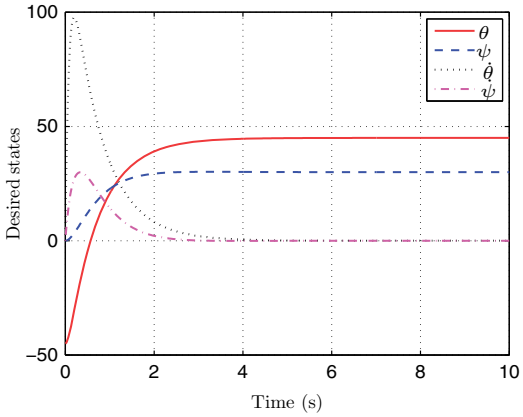

Figure 4. Desired system response.

second simulation is given in Figure 7. Figure 8 shows the estimated disturbance term and state error obtained for the second simulation. Note that the estimated system rates, estimated disturbance term and the control input are highly noisy because of the large Q selected.

The results shown here indicate that for a small value of process noise covariance, the controlled system is unstable. Though a large value of process noise covariance stabilises the controlled system, it also results in highly noisy estimates. The direct dependency of the controlled system's stability on the process noise covariance is more evident in the simulation results given next.

Combining the plant dynamics in (59) and the estimator dynamics in (60), the closed-loop system

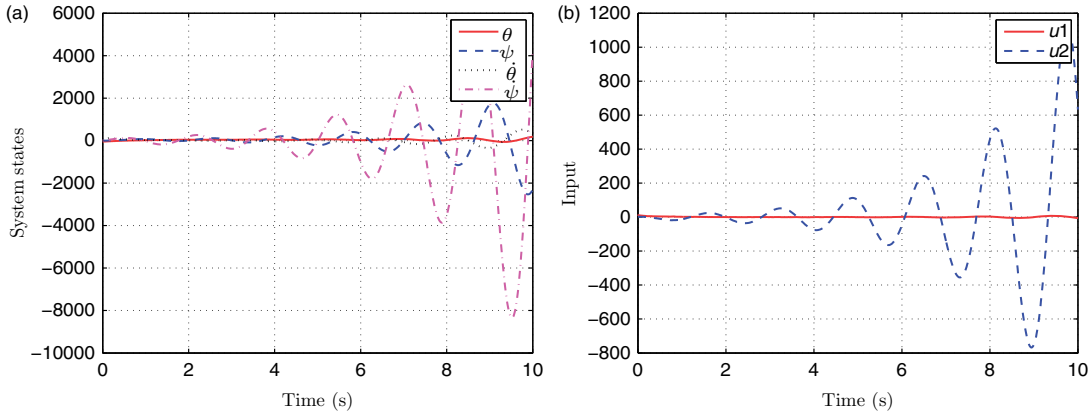

Figure 5. (a) Actual states and (b) input: $Q = 10^3 \times I_{2\times 2}$.

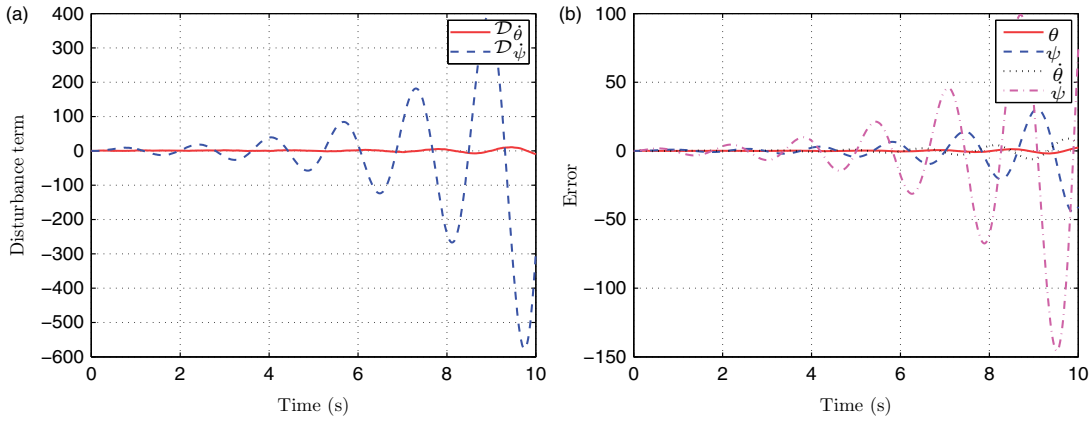

Figure 6. (a) Disturbance term and (b) state error: $Q = 10^3 \times I_{2\times 2}$.

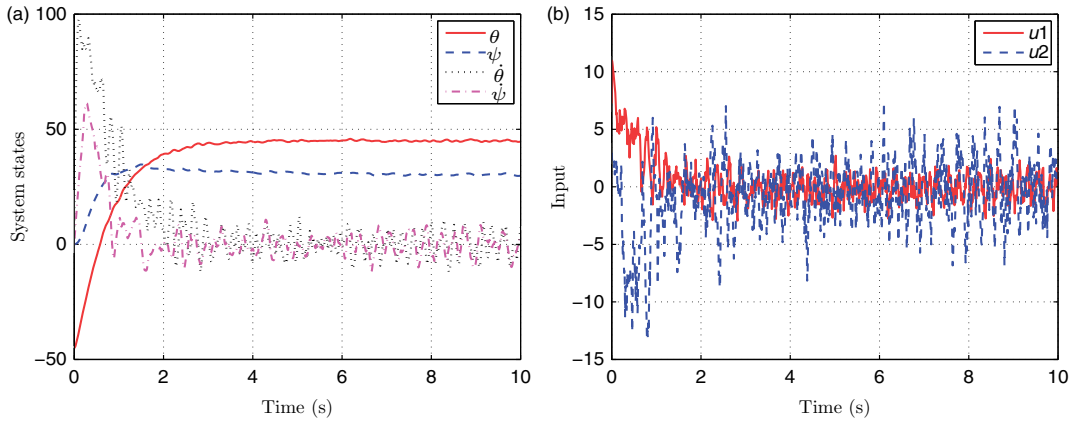

Figure 7. (a) Actual states and (b) input: $Q = 10^5 \times I_{2\times 2}$.

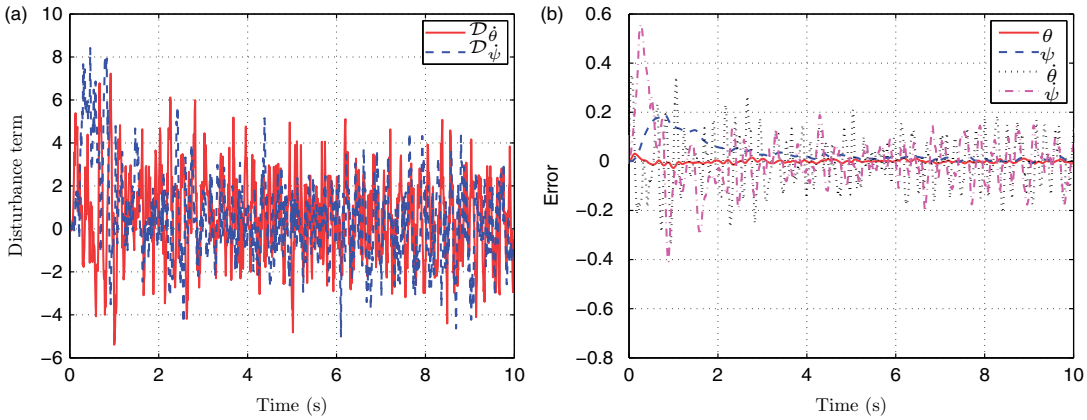

Figure 8. (a) Disturbance term and (b) state error: $Q = 10^5 \times I_{2\times 2}$.

dynamics can be written as

$$\begin{bmatrix} \dot{\mathbf{X}}_1(t) \\ \dot{\mathbf{X}}_2(t) \\ \dot{\mathbf{W}}(t) \\ \dot{\hat{\mathbf{Z}}}(t) \end{bmatrix} = \begin{bmatrix} 0_{2\times 2} & I_{2\times 2} & 0_{2\times 2} & 0_{2\times 6} \\ 0_{2\times 2} & A_4 & I_{2\times 2} & BS \\ 0_{2\times 2} & A_{\mathbf{w}_2} & A_{\mathbf{w}_3} & 0_{2\times 6} \\ K(t) & 0_{2\times 2} & 0_{2\times 2} & (F_m + D_m S - K(t)H) \end{bmatrix} \times \begin{bmatrix} \mathbf{X}_1(t) \\ \mathbf{X}_2(t) \\ \mathbf{W}(t) \\ \hat{\mathbf{Z}}(t) \end{bmatrix} + \begin{bmatrix} \mathbf{0}_{2\times 1} \\ BK_m\mathbf{x}_d \\ \boldsymbol{\mathcal{V}}(t) \\ D_m K_m \mathbf{x}_d + K(t)\mathbf{V}(t) \end{bmatrix}. \quad (63)$$

Since we are considering a time-invariant system here, the Kalman gain $K(t)$ converges to its steady-state value fairly quickly. Using the steady-state Kalman gain, the stability of the closed-loop system can be easily verified. Figure 9 shows the closed-loop poles of the system for different values of Q ranging from $1 \times 10^2 \times I_{2\times 2}$ to $1 \times 10^5 \times I_{2\times 2}$. Figure 9 indicates that the controlled system is unstable for the initial small values of Q and the closed-loop poles migrate into the stable region as Q increases.

6.2 *Adaptive DAC results*

Results obtained by implementing the proposed adaptive disturbance accommodating scheme is presented in this section. Based on the assumed system parameters and controller design matrices given in Tables 2 and 3, the assumed state matrix, $\mathcal{A}_m$, the assumed input matrix, $\mathcal{B}_m$ and the DAC matrix,

S, can be calculated as

$$\mathcal{A}_m = \begin{bmatrix} 0 & 0 & 1.00 & 0 \\ 0 & 0 & 0 & 1.00 \\ 0 & 0 & -9.28 & 0 \\ 0 & 0 & 0 & -3.50 \end{bmatrix}, \quad \mathcal{B}_m = \begin{bmatrix} 0 & 0 \\ 0 & 0 \\ 2.37 & 0.08 \\ 0.24 & 0.79 \end{bmatrix} \text{ and}$$

$$S = \begin{bmatrix} -7.02 & -0.82 & -1.67 & -0.33 & -0.42 & 0.04 \\ 0.82 & -7.02 & 0.08 & -2.45 & 0.13 & -1.28 \end{bmatrix}.$$

As shown in Section 6, matrix $\mathrm{A}_{\mathcal{D}_m}$ is given as

$$\mathrm{A}_{\mathcal{D}_m} = \begin{bmatrix} -1 & 0 \\ 0 & -3 \end{bmatrix}.$$

Now the matrix $[F_m + D_m S]$ can be calculated as

$$[F_m + D_m S] = \begin{bmatrix} 0 & 0 & 1.00 & 0 & 0 & 0 \\ 0 & 0 & 0 & 1.00 & 0 & 0 \\ -16.56 & -2.50 & -13.22 & -0.98 & 0 & 0 \\ -1.04 & -5.756 & -0.34 & -5.51 & -0 & 0 \\ 0 & 0 & 0 & 0 & -1.00 & 0 \\ 0 & 0 & 0 & 0 & 0 & -3.00 \end{bmatrix}.$$

Let $\mathcal{M} = 10^{-1} \times I_6$, now the positive definite symmetric matrix $\mathcal{X}$ that satisfies the following matrix inequality:

$$\mathcal{X}[F_m + D_m S] + [F_m + D_m S]^T \mathcal{X} + \mathcal{X}\mathcal{X} + \mathcal{M} \leq 0$$

can be calculated as

$$\mathcal{X} = \begin{bmatrix} 0.1117 & 0.0005 & 0.0035 & -0.0011 & -0.0000 & -0.0000 \\ 0.0005 & 0.1165 & -0.0008 & 0.0102 & -0.0000 & -0.0000 \\ 0.0035 & -0.0008 & 0.0041 & -0.0005 & -0.0000 & -0.0000 \\ -0.0011 & 0.0102 & -0.0005 & 0.0110 & 0.0000 & -0.0000 \\ -0.0000 & -0.0000 & -0.0000 & 0.0000 & 0.0513 & -0.0000 \\ -0.0000 & -0.0000 & -0.0000 & -0.0000 & -0.0000 & 0.0167 \end{bmatrix}.$$

Since the number of inputs and the number of outputs are the same here, the matrix Π is selected as the identity matrix $I_{2\times 2}$. For the implementation of the adaptive law, the following parameters are selected:

$$A_Q = -0.25 \times I_{2\times 2} \quad \text{and}$$
$$\gamma = \big(\|K(t)\| + \mathrm{Tr}\{P(t)H^T R^{-1} H P(t) - 2F_m P(t)\}\mathrm{Tr}\{R\}^{-1} + 10^3\big).$$

Three different simulation scenarios are considered here.

6.2.1 *Simulation I*

For the first simulation, the initial process noise covariance is selected to be $Q(t_0) = 10^{-5} \times I_{2\times 2}$.

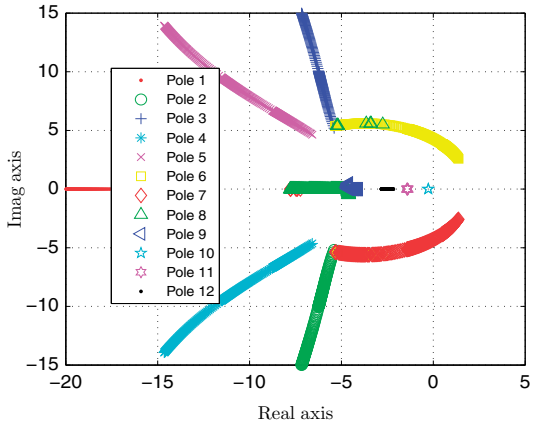

Figure 9. System closed-loop poles for Q varying from 1×10^2 to 1×10^5.

Figure 10(a) and (b) shows the system response and the DAC input obtained for the first simulation. Figure 11(a) and (b) contains the estimated disturbance term and the error between the desired states and the true states corresponding to the first simulation. Note that the first simulation results given in Figures 10 and 11 indicate that the adaptive scheme is able to stabilise and recover the desired performance despite the initial unstable process noise covariance selected. The time varying process noise covariance obtained for the first simulation is given in Figure 12.

6.2.2 *Simulation II*

For the second simulation, the initial process noise covariance is selected to be $Q(t_0) = I_{2\times 2}$. Figure 13(a) and (b) shows the system response and the DAC input obtained for the second simulation. Figure 14(a) and (b) contains the estimated disturbance term and the error between the desired states and the true states corresponding to the second simulation. The simulation results given in Figures 13 and 14 indicate that the adaptive scheme is able to stabilise and recover the desired performance despite the initial unstable process

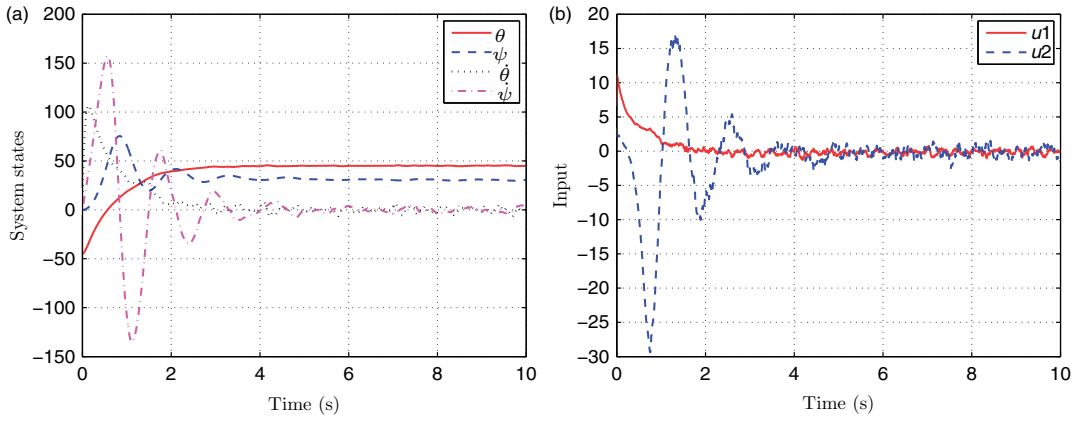

Figure 10. (a) Actual states and (b) input: $Q(t_0) = 10^{-5} \times I_{2\times 2}$.

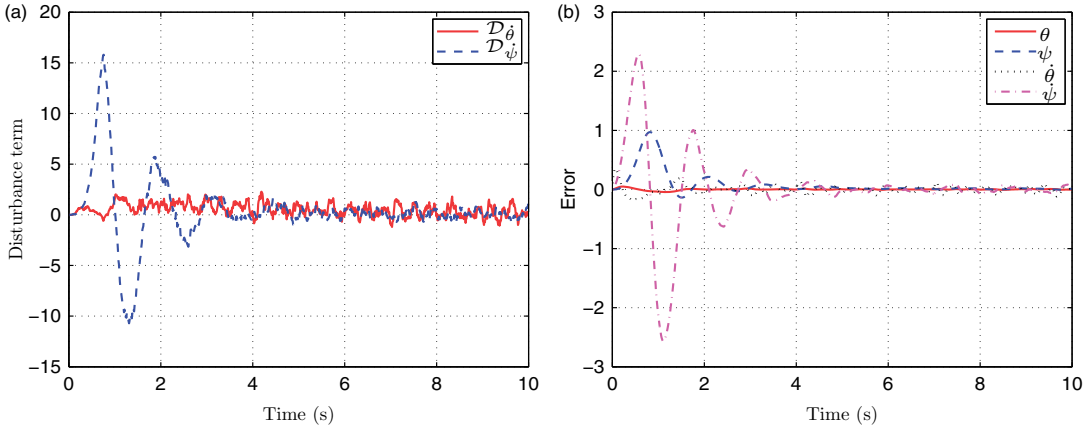

Figure 11. (a) Disturbance term and (b) state error: $Q(t_0) = 10^{-5} \times I_{2\times 2}$.

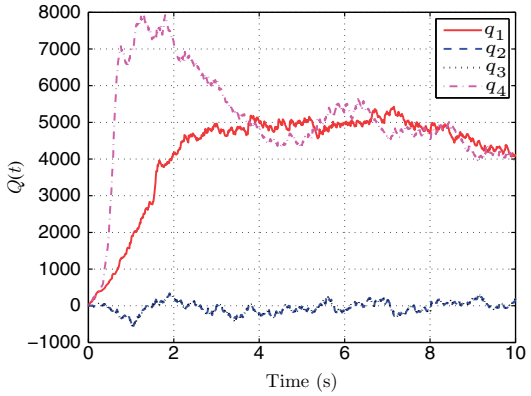

Figure 12. Adaptive process noise covariance: $Q(t_0) = 10^{-5} \times I_{2\times 2}$.

noise covariance selected. The time varying process noise covariance obtained for the second simulation is given in Figure 15.

6.2.3 *Simulation III*

For the third simulation, the initial process noise covariance is selected to be $Q(t_0) = 10^5 \times I_{2\times 2}$. Figure 16(a) and (b) shows the system response and the DAC input obtained for the third simulation. Figure 17(a) and (b) contains the estimated disturbance term and the error between the desired states and the true states corresponding to the third simulation. Figure 18 shows the time varying process noise covariance obtained for the third simulation.

Figure 19 shows the time varying process noise covariance obtained for the three simulations. Figure 19 indicates that, regardless of the initial

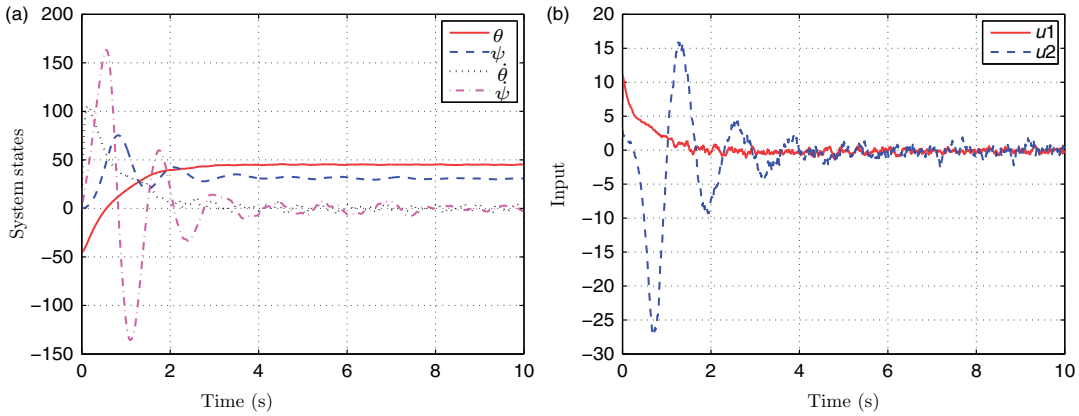

Figure 13. (a) Actual states and (b) input: $Q(t_0) = I_{2\times 2}$.

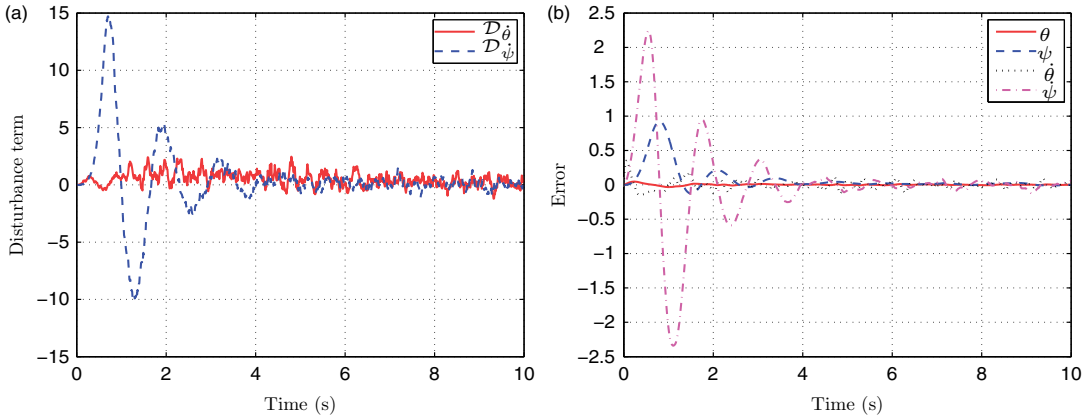

Figure 14. (a) Disturbance term and (b) state error: $Q(t_0) = I_{2\times 2}$.

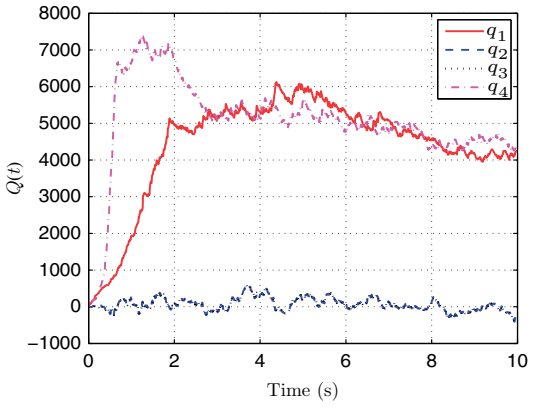

Figure 15. Adaptive process noise covariance: $Q(t_0) = I_{2\times 2}$.

matrix selected, the process noise covariance settles down at its steady-state value, which is around $4 \sim 5 \times 10^3$ for the present scenario.

7. Conclusion

This article presents the formulation of an observer-based stochastic DAC approach for linear time-invariant MIMO systems which automatically detects and minimises the adverse effects of both model uncertainties and external disturbances. Assuming that all system uncertainties and external disturbances can be lumped in a disturbance term, this control approach utilises a Kalman estimator in the feedback loop for simultaneously estimating the system states and the disturbance term from measurements. The estimated states are then used to develop a

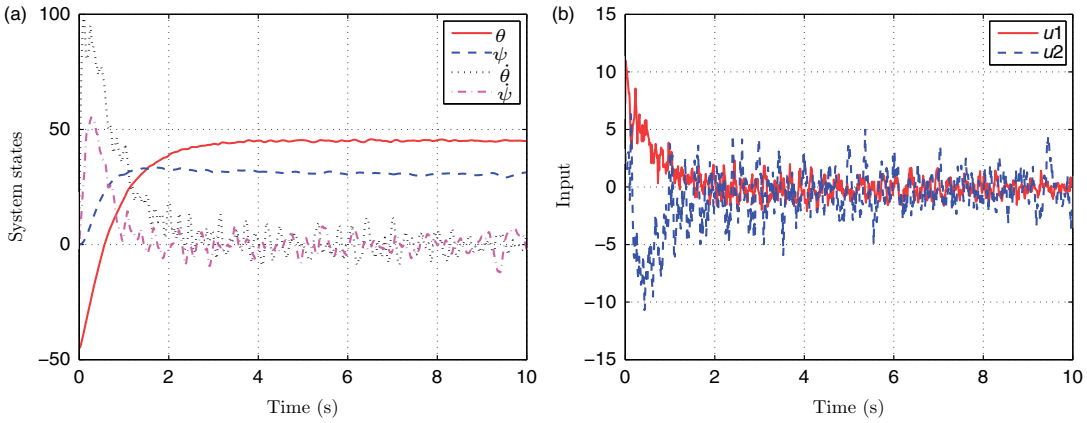

Figure 16. (a) Actual states and (b) input: $Q(t_0) = 10^5 \times I_{2\times 2}$.

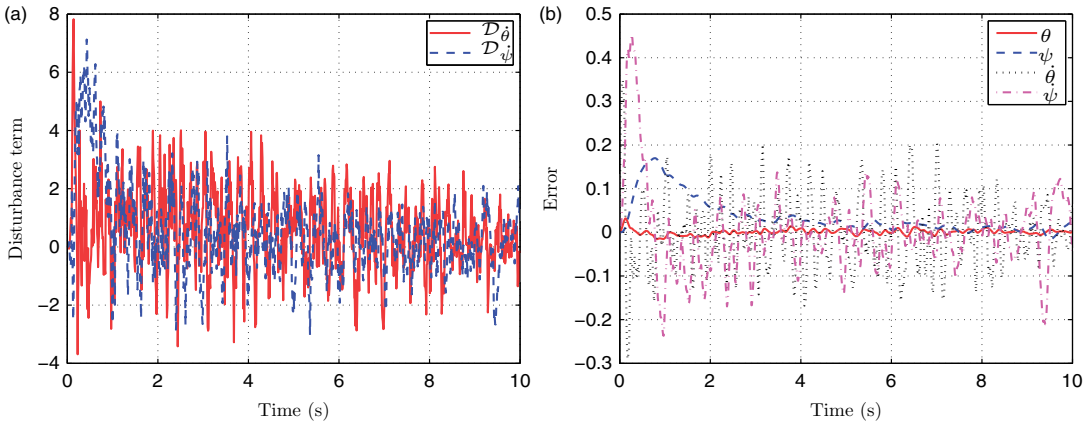

Figure 17. (a) Disturbance term and (b) state error: $Q(t_0) = 10^5 \times I_{2\times 2}$.

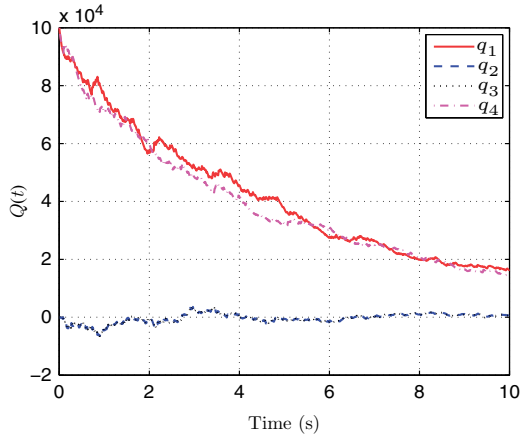

Figure 18. Adaptive process noise covariance: $Q(t_0) = 10^5 \times I_{2\times 2}$.

nominal control law while the estimated disturbance term is used to make necessary corrections to the nominal control input to minimise the effect of system uncertainties and the external disturbances. The stochastic stability analysis conducted on the controlled system reveals a lower bound requirement on the estimator design parameters, such as the process noise covariance matrix and the measurement noise covariance matrix, in order to ensure the controlled system stability. Since the measurement noise covariance can be obtained from sensor calibration, the process noise matrix is treated as a tuning parameter. Based on the stochastic Lyapunov analysis, an adaptive law is developed for updating the selected process noise covariance online so that the controlled system is stable. The adaptive scheme introduced here guarantees asymptotic stability in the mean and the mean square stability of the controlled system.

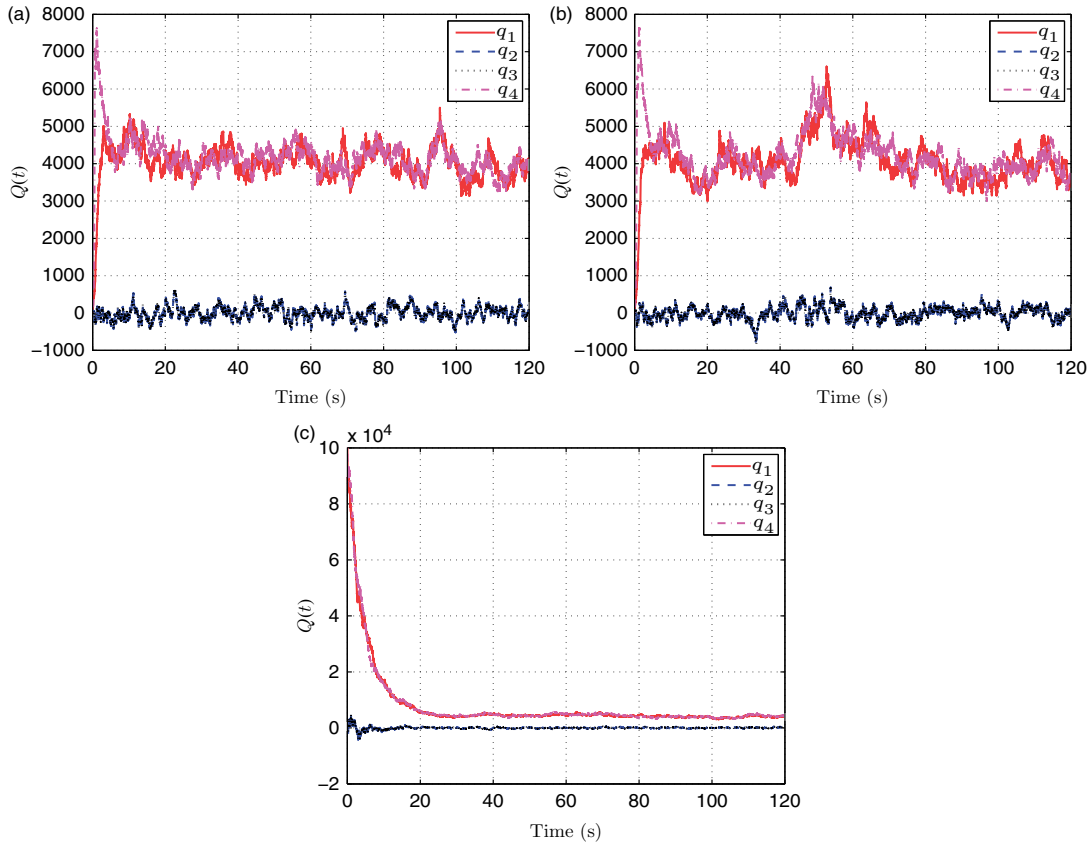

Figure 19. Adaptive process noise covariance matrices: (a) $Q(t_0) = 10^{-5} \times I_{2\times 2}$; (b) $Q(t_0) = I_{2\times 2}$; and (c) $Q(t_0) = 10^{5} \times I_{2\times 2}$.

The simulation results given here explicitly reveal the direct dependency of the proposed control scheme on the process noise covariance matrix. Since the nominal control action on the true plant is unstable, selecting a very low process noise covariance resulted in an unstable system. On the other hand, selecting a large value stabilised the system but resulted in a highly noisy control input. The numerical simulations indicate that the adaptive scheme is able to stabilise and recover the desired performance despite selecting an initial unstable process noise covariance. The results also indicate that regardless of the initial matrix selected, the process noise covariance settles down to its steady-state value.

References

Abou-Kandil, H., Freiling, G., Ionescu, V., and Jank, G. (2003), 'Matrix Riccati Equations in Control and Systems Theory', *Systems and Control: Foundations and Applications* (1st ed.), Basel, Switzerland: Birkhäuser.

Appleby, J.A.D. (2002), 'Almost Sure Stability of Linear Itô-volterra Equations with Damped Stochastic Perturbations', *Electronic Communications in Probability*, 7, 223–234.

Biglari, H., and Mobasher, A. (2000), 'Design of Adaptive Disturbance Accommodating Controller with Matlab and Simulink', in *NAECON, Proceedings of the IEEE National Aerospace and Electronics Conference (NAECON)*, Dayton, OH, pp. 208–211.

Crassidis, J.L., and Junkins, J.L. (2004), *Optimal Estimation of Dynamic System*, Boca Raton, FL: Chapman & Hall/CRC.

Davari, A., and Chandramohan, R. (2003), 'Design of Linear Adaptive Controller for Nonlinear Systems', in *Proceedings of the 35th Southeastern Symposium on System Theory*, pp. 222–226.

Doob, J.L. (1953), *Stochastic Processes*, New York, NY: Wiley.

Douglas, J., and Athans, M. (1994), 'Robust Linear Quadratic Designs with Real Parameter Uncertainty', *IEEE Transactions on Automatic Control*, 39, 107–111.

Grigoriu, M. (2002), *Stochastic Calculus*, Boston, MA: Birkhäuser.

Johnson, C. (1971), 'Accommodation of External Disturbances in Linear Regulator and Servomechanism Problems', *IEEE Transactions on Automatic Control*, AC-16, 635–644.

Johnson, C. (1984), 'Disturbance-utilising Controllers for Noisy Measurements and Disturbances', *International Journal of Control*, 39, 859–862.

Johnson, C. (1985), 'Adaptive Controller Design using Disturbance Accommodation Techniques', *International Journal of Control*, 42, 193–210.

Johnson, C., and Kelly, W. (1981), 'Theory of Disturbance-utilising Control: Some Recent Developments', in *Proceedings of IEEE Southeast Conference*, Huntsville, AL, pp. 614–620.

Kim, J.-H., and Oh, J.-H. (1998), 'Disturbance Estimation using Sliding Mode for Discrete Kalman Filter', in *Proceedings of the 37th IEEE Conference on Decision and Control*, Tampa, FL, pp. 1918–1919.

Kushner, H.J. (1967), *Stochastic Stability and Control*, New York, NY: Academic Press.

Liptser, R.S., and Shiryayev, A. (1989), *Theory of Martingales*, Dordrecht: Kluwer Academic.

Petersen, I.R., and Hollot, C.V. (1986), 'A Riccati Equation Approach to the Stabilisation of Uncertain Linear Systems', *Automatica*, 22, 397–411.

Profeta, J.A., Vogt, W.G., and Mickle, M.H. (1990), 'Disturbance Estimation and Compensation in Linear Systems', *IEEE Transactions on Aerospace and Electronic Systems*, 26, 225–231.

Soong, T.T. (1973), *Random Differential Equations in Science and Engineering*, New York, NY: Academic Press.

Soong, T.T., and Grigoriu, M. (1993), *Random Vibration of Mechanical and Structural Systems*, Englewood Cliffs, NJ: Prentice Hall.

Sorrells, J.E. (1982), 'Design of Disturbance Accommodating Controllers for Stochastic Environments', in *Proceedings of the 1982 American Control Conference*, Arlington, VA, pp. 2603–2608.

Sorrells, J. (1989), 'Comparison of Contemporary Adaptive Control Design Techniques', in *Proceedings of the Twenty-First Southeastern Symposium on System Theory*, pp. 636–640.

Yang, X. (2000), 'A Matrix Trace Inequality', *Journal of Mathematical Analysis and Applications*, 250, 372–374.

Robust Kalman-Bucy Filter

Jemin George

IEEE Transactions on Automatic Control, 58(1), (2013)

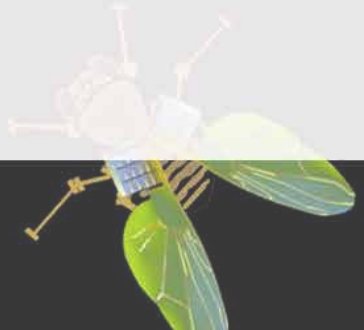

Robust Kalman-Bucy Filter

Jemin George

***Abstract*—Development of a robust estimator for uncertain stochastic systems under persistent excitation is presented. The given continuous-time stochastic formulation assumes norm bounded parametric uncertainties and excitations. When there are no system uncertainties, the performance of the proposed robust estimator is similar to that of the Kalman-Bucy filter and the proposed approach asymptotically recovers the desired optimal performance in the presence of uncertainties and or persistent excitation.**

***Index Terms*—H_∞ filtering, Kalman–Bucy filter.**

I. Introduction

Even though the Kalman-Bucy filter possesses some innate robust characteristics, the estimator performance degradation in the presence of system uncertainties may not be tolerable. The robust estimation problem addressed here involves recovering unmeasured state variables when the available plant model and the noise statistics are uncertain. There exist several literature on the design of robust estimators based on H_∞ filtering [1]–[6], where the estimators are designed to minimize the worst case H_∞ norm of the transfer function from the noise inputs to the estimation error output. Since H_∞ filtering is a worst-case design method, while guaranteeing the worst-case performance, it generally sacrifices the average filter performance. While the H_∞ formulation involves deregularization, a robust estimator design based on the regularized least-squares approach is presented in [7]. Extension of the regularized least squares approach to time-delay systems and time varying system are presented in [8] and [9], respectively.

Robust estimation approach known as the guaranteed cost filtering is presented in [10]–[12]. Here, estimators are designed to guarantee that the steady-state variance of the state estimation error is upper bounded by a certain constant value for all admissible model uncertainties. Design of robust estimators that ensure minimum filtering error variance bounds for systems with parametric uncertainty residing in a polytope are given in [13] and [14]. A robust state estimator for a class of uncertain systems where the noise and uncertainty are modeled deterministically via an integral quadratic constraint is presented in [15]. This approach, known as the set-valued state estimation, involves finding the set of all states consistent with given output measurements for a system with norm bounded noise input [16]. Petersen and Savkin [17] provides a comprehensive research monograph on robust filtering for both discrete and continuous time systems from a deterministic as well as H_∞ point of view. More recently, [18] and [19] proposes a robust filtering approach based on penalizing the sensitivity of estimation errors to parameter variations.

Presented here is the formulation of a robust estimator for uncertain linear stochastic systems under persistent excitation. The proposed estimator guarantees asymptotic convergence of the estimation error even in the presence of persistent excitation. In contrast to the existing approaches, the main contributions of this manuscript are given below:

Manuscript received May 24, 2011; revised October 26, 2011; accepted May 04, 2012. Date of publication June 06, 2012; date of current version December 17, 2012. Recommended by Associate Editor M. Lops.

The author is with the U.S. Army Research Laboratory, Adelphi, MD 20783 USA (e-mail: jemin.george.civ@mail.mil).

Color versions of one or more of the figures in this technical note are available online at http://ieeexplore.ieee.org.

Digital Object Identifier 10.1109/TAC.2012.2203052

- Most of the existing robust estimator schemes are in discrete-time or assumes deterministic noise scenario. Therefore, a complete stochastic formulation of a continuous time robust estimator is presented here.
- Present formulation considers uncertainties in both system and output matrices as well as an unknown persistently exciting signal.
- Proposed approach asymptotically recovers the desired optimal performance.

The structure of this technical note is as follows. A detailed problem formulation and the development of the robust estimator are first given in Sections II and III, respectively. Afterwards, numerical simulations are presented in Section IV to further illustrate the performance of the proposed robust estimator. Finally concluding remarks are given in Section V.

II. Problem Formulation

Consider the following linear time-invariant stochastic process defined on the filtered probability space $(\Omega, \mathcal{F}, \{\mathcal{F}_t\}, \mathbb{P})$:

$$d\mathbf{X}_t = \{A\mathbf{X}_t + \mathbf{W}_t\}\, dt + d\boldsymbol{\mathcal{B}}_t, \qquad t \in [t_0,\, \infty) \tag{1}$$

with initial condition $\mathbf{X}_{t_0} = \mathbf{X}_0$. Here, $\mathbf{X}_t : [t_0, \infty) \times \Omega \mapsto \Re^n$ is the state vector, $\mathbf{W}_t : [t_0, \infty) \times \Omega \mapsto \Re^n$ is an unknown persistent excitation, and $\boldsymbol{\mathcal{B}}_t : [t_0, \infty) \times \Omega \mapsto \Re^n$ is an n-dimensional $\mathcal{F}_t$-Wiener process with zero mean and the correlation of increments

$$E\left[\{\boldsymbol{\mathcal{B}}(\tau) - \boldsymbol{\mathcal{B}}(\zeta)\}\,\{\boldsymbol{\mathcal{B}}(\tau) - \boldsymbol{\mathcal{B}}(\zeta)\}^T\right] = \mathcal{Q}|\tau - \zeta|.$$

Elements of the system matrix $A \in \Re^{n\times n}$, and the noise intensity matrix $\mathcal{Q} \in \Re^{n\times n}$, are assumed to be unknown. The measurement process is given as

$$d\mathbf{Y}_t = C\mathbf{X}_t dt + d\boldsymbol{\mathcal{V}}_t \tag{2}$$

where $\mathbf{Y}_t : [t_0, \infty) \times \Omega \mapsto \Re^m$ is the output vector, and $\boldsymbol{\mathcal{V}}_t : [t_0, \infty) \times \Omega \mapsto \Re^m$, is assumed to be an $\mathcal{F}_t$-Wiener process with zero mean and the correlation of increments

$$E\left[\{\boldsymbol{\mathcal{V}}(\tau) - \boldsymbol{\mathcal{V}}(\zeta)\}\,\{\boldsymbol{\mathcal{V}}(\tau) - \boldsymbol{\mathcal{V}}(\zeta)\}^T\right] = R|\tau - \zeta|.$$

The output matrix $C \in \Re^{m\times n}$ is assumed to be unknown and the measurement covariance $R \in \Re^{m\times m}$ is assumed to be known.

Definition 1: The stochastic process $\mathbf{W}_t$ is persistently exciting with level α[20] if

$$\mathbb{P}\left(\int_t^{t+T} \mathbf{W}_\tau \mathbf{W}_\tau^T d\tau \geq \alpha T I_{n\times n}\right) = 1 \tag{3}$$

for some $\alpha > 0$, $T > 0$, and $\forall t > t_0$.

Since the true system state matrix, A, and the output matrix, C, are unknown, the assumed (known) system matrix and output matrix are given as A_m and C_m, respectively. Define

$$\boldsymbol{M}_t = \{A - A_m\}\,\mathbf{X}_t + \mathbf{W}_t, \quad \text{and} \tag{4}$$

$$\boldsymbol{N}_t = \{C - C_m\}\,\mathbf{X}_t. \tag{5}$$

Now the system equation and the output equation may be rewritten in terms of the assumed system matrix, A_m, and the assumed output matrix, C_m, as

$$d\mathbf{X}_t = \{A_m\mathbf{X}_t + \boldsymbol{M}_t\}\, dt + d\boldsymbol{\mathcal{B}}_t, \tag{6}$$

$$d\mathbf{Y}_t = \{C_m\mathbf{X}_t + \boldsymbol{N}_t\}\, dt + d\boldsymbol{\mathcal{V}}_t. \tag{7}$$

Assumption 1: The persistent disturbance, $\mathbf{W}_t$, is an $\mathcal{F}_t$-adapted process and is almost surely (a.s.) upper bounded as follows

$$\mathbb{P}\left(\sup_{t\geq t_0} |\mathbf{W}_t| < \infty\right) = 1 \tag{8}$$

where $|\cdot|$ is the one-norm, i.e., $|\mathbf{x}| = \sum_i |x_i|$

Assumption 2: The matrices, A and A_m are Hurwitz. The assumption of the stability of the uncertain system is a weak one, as it is rare that an estimator be applied 'open-loop' to an unstable system [10]. Furthermore, if A is only marginally stable, and the the persistent excitation is such that the system states are bounded, then an equivalent representation of system (1) similar to the one in(6) can be selected such that the state matrix is Hurwitz.

Lemma 1: Given assumptions 1 and 2, the process, $\mathbf{X}_t$, is a.s. upper bounded as follows:

$$\mathbb{P}\left(\sup_{t\geq t_0} |\mathbf{X}_t| < c\right) = 1$$

where $c < \infty$ is a constant.

Proof: Matrix A generates an exponentially stable evolution operator $\Phi_A(t - t_0)$ and the solution of (1), $\mathbf{X}(t)$, can be written as [21]

$$\mathbf{X}(t) = \Phi_A(t - t_0)\mathbf{X}(t_0) + \int_{t_0}^t \Phi_A(t-\tau)\mathbf{W}(\tau)d\tau + \int_{t_0}^t \Phi_A(t-\tau)d\boldsymbol{\mathcal{B}}(\tau).$$

Since $\Phi_A(t - t_0)$ is exponentially stable

$$\|\,\Phi_A(t - t_0)\,\| \leq \lambda_0 e^{-a(t-t_0)} \leq \lambda_0, \quad \forall t \geq t_0$$

where $\|\cdot\|$ represents induced matrix norm and λ_0 and a are two positive constants. Now define

$$\boldsymbol{\mathcal{M}}_t = \int_{t_0}^t \Phi_A(t-\tau)d\boldsymbol{\mathcal{B}}(\tau).$$

Note that $\boldsymbol{\mathcal{M}}_t$ is a *supermartingale* and based on Doob's martingale inequality [22] it is a.s. bounded. Thus

$$\begin{aligned}
|\mathbf{X}(t)| &\leq \|\,\Phi_A(t - t_0)\,\|\,|\mathbf{X}(t_0)| \\
&\quad + \int_{t_0}^t \|\,\Phi_A(t-\tau)\,\|\,|\mathbf{W}(\tau)|d\tau + |\boldsymbol{\mathcal{M}}_t|, \\
&\leq \lambda_0 e^{-a(t-t_0)}|\mathbf{X}(t_0)| \\
&\quad + \int_{t_0}^t \lambda_0 e^{-a(t-\tau)}|\mathbf{W}(\tau)|d\tau + |\boldsymbol{\mathcal{M}}_t|, \\
&\leq \lambda_0 e^{-a(t-t_0)}|\mathbf{X}(t_0)| \\
&\quad + \int_{t_0}^t \lambda_0 e^{-(a-a_0/2)(t-\tau)} e^{-a_0/2(t-\tau)}|\mathbf{W}(\tau)|d\tau \\
&\quad + |\boldsymbol{\mathcal{M}}_t|.
\end{aligned}$$

The last inequality is obtained by expressing $e^{-a(t-\tau)}$ as $e^{-(a-a_0/2)(t-\tau)}e^{-a_0/2(t-\tau)}$, where $a_0 < 2a$ is a positive constant. Applying the Schwartz inequality yields

$$\begin{aligned}
|\mathbf{X}(t)| &\leq \lambda_0 e^{-a(t-t_0)}|\mathbf{X}(t_0)| \\
&\quad + \lambda_0 \left(\int_{t_0}^t e^{-(2a-a_0)(t-\tau)}d\tau\right)^{1/2} \\
&\quad \times \left(\int_{t_0}^t e^{-a_0(t-\tau)}|\mathbf{W}(\tau)|^2 d\tau\right)^{1/2} + |\boldsymbol{\mathcal{M}}_t|.
\end{aligned}$$

Thus

$$|\mathbf{X}(t)| \leq \lambda_0 e^{-a(t-t_0)}|\mathbf{X}(t_0)| + \frac{\lambda_0}{\sqrt{(2a-a_0)}}\left(\int_{t_0}^{t} e^{-a_0(t-\tau)}|\mathbf{W}(\tau)|^2 d\tau\right)^{1/2} + |\boldsymbol{\mathcal{M}}_t|.$$

Given $|\mathbf{X}_0|$ is a.s. bonded, based on assumption 1, it can be shown that there exist a positive constant $c < \infty$ such that

$$\mathbb{P}\left(\sup_{t\geq t_0}|\mathbf{X}_t| < c\right) = 1.$$

■

Given the system parameter uncertainties are bounded and the system states are a.s. bounded, an upper bound on $\boldsymbol{M}_t$ can be obtained as

$$\mathbb{P}\left(|\boldsymbol{M}_t| \leq \bar{\mu}(t)\right) = 1, \quad \forall t \geq t_0. \tag{9}$$

Consider the process $\boldsymbol{N}_t$ defined in (5), now the trivial application of Ito formula [23] on $\boldsymbol{N}_t$ yields

$$d\boldsymbol{N}_t = \{C - C_m\}\{A_m\mathbf{X}_t + \boldsymbol{M}_t\}dt + \{C - C_m\}d\boldsymbol{\mathcal{B}}_t. \tag{10}$$

Define

$$\boldsymbol{U}_t = \{C - C_m\}\{[A_m + I_{n\times n}]\mathbf{X}_t + \boldsymbol{M}_t\}. \tag{11}$$

Since the system parametric uncertainties, system states, and $\boldsymbol{M}_t$ are assumed to be upper bounded, a conservative upper bound on the stochastic process $\boldsymbol{U}_t$ can easily be obtained, i.e.

$$\mathbb{P}\left(|\boldsymbol{U}_t| \leq \bar{\upsilon}(t)\right) = 1, \quad \forall t \geq t_0. \tag{12}$$

After appending $d\boldsymbol{N}_t$ to the system equation the extended system may be written as

$$d\begin{bmatrix}\mathbf{X}_t\\ \boldsymbol{N}_t\end{bmatrix} = \left\{\begin{bmatrix}A_m & 0\\ 0 & -I\end{bmatrix}\begin{bmatrix}\mathbf{X}_t\\ \boldsymbol{N}_t\end{bmatrix}\begin{bmatrix}\boldsymbol{M}_t\\ \boldsymbol{U}_t\end{bmatrix}\right\}dt + \begin{bmatrix}I\\ \Delta C\end{bmatrix}d\boldsymbol{\mathcal{B}}_t \tag{13}$$

where $\Delta C = \{C - C_m\}$. Define $\mathbf{Z}_t = [\mathbf{X}_t^T \quad \boldsymbol{N}_t^T]^T$, $F = \begin{bmatrix}A_m & 0\\ 0 & -I_{m\times m}\end{bmatrix}$, $G = \begin{bmatrix}I_{n\times n}\\ \Delta C\end{bmatrix}$ and $\boldsymbol{\Gamma}_t = [\boldsymbol{M}_t^T \quad \boldsymbol{U}_t^T]^T$. Now (13) may be written as

$$d\mathbf{Z}_t = \{F\mathbf{Z}_t + \boldsymbol{\Gamma}_t\}dt + Gd\boldsymbol{\mathcal{B}}_t \tag{14}$$

and the output equation may be written as

$$d\mathbf{Y}_t = H\mathbf{Z}_t dt + d\boldsymbol{\mathcal{V}}_t \tag{15}$$

where $H = [C_m \quad I_{m\times m}]$. Note that the process $\boldsymbol{\Gamma}_t = [\boldsymbol{M}_t^T \quad \boldsymbol{U}_t^T]^T$ may be upper bounded by $\gamma(t)$, where

$$\gamma(t) = \max\{\bar{\mu}(t), \quad \bar{\upsilon}(t)\}. \tag{16}$$

Remark 1: In practice, an upper bound on the system states and the disturbance can be obtained from knowing the regime and the environment in which the system is operating. An upper bound on parameter uncertainties can be obtained from system identification/calibration [24], [25]. After substituting these bounds into (4) and(11), an upper bound on $\boldsymbol{\Gamma}_t$ can be obtained from (16).

Now assume for a minute that there are no uncertainties, i.e., $A_m = A$, $C_m = C$, $\mathbf{W}_t = \mathbf{0}$, and $\boldsymbol{\mathcal{B}}_t = \bar{\boldsymbol{\mathcal{B}}}_t$, where $\bar{\boldsymbol{\mathcal{B}}}_t$ is an $\mathcal{F}_t$-Wiener process with zero mean and known correlation of increments Q

$$E\left[\{\bar{\boldsymbol{\mathcal{B}}}(\tau) - \bar{\boldsymbol{\mathcal{B}}}(\zeta)\}\{\bar{\boldsymbol{\mathcal{B}}}(\tau) - \bar{\boldsymbol{\mathcal{B}}}(\zeta)\}^T\right] = Q|\tau - \zeta|.$$

Then, $\boldsymbol{\Gamma}_t$ is identically zero for all time and the system in (14) can be written as

$$d\mathbf{Z}_{m_t} = F\mathbf{Z}_{m_t}dt + G_m d\bar{\boldsymbol{\mathcal{B}}}_t \tag{17}$$

where $G_m = [I_{n\times n} \quad 0_{n\times m}]^T$. The corresponding measurement process is given as

$$d\mathbf{Y}_{m_t} = H\mathbf{Z}_{m_t}dt + d\boldsymbol{\mathcal{V}}_t. \tag{18}$$

For the system in (17), an optimal estimator, such as a Kalman-Bucy filter [26], of the following form can be designed:

$$d\hat{\mathbf{Z}}_{m_t} = F\hat{\mathbf{Z}}_{m_t}dt + K\left[d\mathbf{Y}_{m_t} - H\hat{\mathbf{Z}}_{m_t}dt\right] \tag{19}$$

where $K \in \Re^{(n+m)\times m}$ is the steady-state Kalman gain and is calculated as

$$K = PH^T R^{-1} \tag{20}$$

where $P \in \Re^{(n+m)\times(n+m)}$ can be obtained by solving the algebraic Riccati equation [27]:

$$FP + PF^T - PH^T R^{-1}HP + G_m Q G_m^T = 0. \tag{21}$$

Now subtracting (19) from(17), the estimator error dynamics corresponding to the optimal estimator in(19) may be written as

$$d\tilde{\mathbf{Z}}_{m_t} = [F - KH]\tilde{\mathbf{Z}}_{m_t}dt - Kd\boldsymbol{\mathcal{V}}_t + G_m d\bar{\boldsymbol{\mathcal{B}}}_t \tag{22}$$

where $\tilde{\mathbf{Z}}_{m_t} = \mathbf{Z}_{m_t} - \hat{\mathbf{Z}}_{m_t}$. Note that the estimation error is unbiased, i.e., $E\left[\tilde{\mathbf{Z}}_{m_t}\right] = \mathbf{0}$, and the steady-state value of the error covariance is given as [26]

$$\lim_{t\to\infty} E\left[\tilde{\mathbf{Z}}_{m_t}\tilde{\mathbf{Z}}_{m_t}^T\right] = P. \tag{23}$$

Given next is the formulation of a robust estimator which guarantees the asymptotic convergence of the true state estimation error to the desired optimal error $\tilde{\mathbf{Z}}_{m_t}$.

III. Robust Estimator

In this section, a robust estimator of the following form is proposed:

$$d\hat{\mathbf{Z}}_t = \left\{F\hat{\mathbf{Z}}_t + \boldsymbol{\eta}(t)\right\}dt + K\left[d\mathbf{Y}_t - H\hat{\mathbf{Z}}_t dt\right] \tag{24}$$

where $\boldsymbol{\eta}(t)$ is a signal whose details would be explained shortly. The robust estimator formulation presented here follows the typical robust controller formulation [20] in that the estimator "input," $\boldsymbol{\eta}(t)$, is selected such that the true estimator error dynamics given in (25) asymptotically tracks the desired error dynamics given in (22). A systematic approach for the selection of $\boldsymbol{\eta}(t)$ constitutes the main result of this section and is presented in Theorem 1.

Define $\tilde{\mathbf{Z}}_t = \mathbf{Z}_t - \hat{\mathbf{Z}}_t$, now subtracting (24) from(14), the estimator error dynamics, i.e., $d\tilde{\mathbf{Z}}_t$, may be written as

$$d\tilde{\mathbf{Z}}_t = \left\{[F - KH]\tilde{\mathbf{Z}}_t + \boldsymbol{\Gamma}_t - \boldsymbol{\eta}(t)\right\}dt - Kd\boldsymbol{\mathcal{V}}_t + Gd\boldsymbol{\mathcal{B}}_t. \tag{25}$$

Define $\boldsymbol{\mathcal{Z}}_t$ as the difference between the desired estimation error in (22) and the true estimation error in (25), i.e., $\boldsymbol{\mathcal{Z}}_t = \tilde{\mathbf{Z}}_t - \tilde{\mathbf{Z}}_{m_t}$. After subtracting (22) from (25), $d\boldsymbol{\mathcal{Z}}_t$ can be written as

$$d\boldsymbol{\mathcal{Z}}_t = \{[F-KH]\,\boldsymbol{\mathcal{Z}}_t + \boldsymbol{\Gamma}_t - \boldsymbol{\eta}(t)\}\,dt + Gd\boldsymbol{\mathcal{B}}_t - G_m d\bar{\boldsymbol{\mathcal{B}}}_t. \quad (26)$$

The solution $\boldsymbol{\mathcal{Z}}_t$ of (26) can be written as

$$\boldsymbol{\mathcal{Z}}_t = \boldsymbol{\mathcal{Z}}_0 + \int_{t_0}^{t} \{[F-KH]\,\boldsymbol{\mathcal{Z}}_s + \boldsymbol{\Gamma}_s - \boldsymbol{\eta}(s)\}\,ds + \int_{t_0}^{t} Gd\boldsymbol{\mathcal{B}}_s - \int_{t_0}^{t} G_m d\bar{\boldsymbol{\mathcal{B}}}_s. \quad (27)$$

Let $\tilde{\mathbf{Y}}_t$ denotes the innovations process, i.e.

$$d\tilde{\mathbf{Y}}_t = \left[d\mathbf{Y}_t - H\hat{\mathbf{Z}}_t dt\right].$$

Now define $\hat{\boldsymbol{\mathcal{Z}}}_t = E\left[\boldsymbol{\mathcal{Z}}_t \middle| \mathcal{F}_t^{\tilde{\mathbf{Y}}}\right]$, where $\mathcal{F}_t^{\tilde{\mathbf{Y}}}$ is the filtration generated by $\tilde{\mathbf{Y}}_t$[28]. Note $E\left[d\boldsymbol{\mathcal{B}}_t \middle| \mathcal{F}_t^{\tilde{\mathbf{Y}}}\right] = 0$ and $E\left[d\bar{\boldsymbol{\mathcal{B}}}_t \middle| \mathcal{F}_t^{\tilde{\mathbf{Y}}}\right] = 0$, thus $\hat{\boldsymbol{\mathcal{Z}}}_t$ can be written as

$$\hat{\boldsymbol{\mathcal{Z}}}_t = \hat{\boldsymbol{\mathcal{Z}}}_0 + E\left[\int_{t_0}^{t} \left\{[F-KH]\,\hat{\boldsymbol{\mathcal{Z}}}_s + \boldsymbol{\Gamma}_s - \boldsymbol{\eta}(s)\right\} ds \middle| \mathcal{F}_t^{\tilde{\mathbf{Y}}}\right]. \quad (28)$$

Based on previously stated assumptions, we could presume that $\boldsymbol{\mathcal{Z}}_t$ is mean square Riemann integrable[1] and therefore, $\hat{\boldsymbol{\mathcal{Z}}}_t$ can be written as

$$\hat{\boldsymbol{\mathcal{Z}}}_t = \hat{\boldsymbol{\mathcal{Z}}}_0 + \int_{t_0}^{t} [F-KH]\,\hat{\boldsymbol{\mathcal{Z}}}_s ds + \int_{t_0}^{t} E\left[\boldsymbol{\Gamma}_s \middle| \mathcal{F}_t^{\tilde{\mathbf{Y}}}\right] ds - \int_{t_0}^{t} E\left[\boldsymbol{\eta}(s) \middle| \mathcal{F}_t^{\tilde{\mathbf{Y}}}\right] ds.$$

Thus, $d\hat{\boldsymbol{\mathcal{Z}}}_t$ can be written as

$$\hat{\boldsymbol{\mathcal{Z}}}_t = [F-KH]\,\hat{\boldsymbol{\mathcal{Z}}}_t dt + E\left[\boldsymbol{\Gamma}_t \middle| \mathcal{F}_t^{\tilde{\mathbf{Y}}}\right] dt - E\left[\boldsymbol{\eta}(t) \middle| \mathcal{F}_t^{\tilde{\mathbf{Y}}}\right] dt. \quad (29)$$

Theorem 1: Assume there exist a positive definite symmetric matrix $\mathcal{X} \in \Re^{(n+m)\times(n+m)}$ such that

$$[F-KH]^T\,\mathcal{X} + \mathcal{X}\,[F-KH] + S \leq \mathbf{0} \quad (30)$$

and

$$\mathcal{X} = H^T \Lambda^T \quad (31)$$

where $S \in \Re^{(n+m)\times(n+m)}$ is a positive definite matrix and $\Lambda \in \Re^{(n+m)\times m}$. Then the robust estimator error dynamics in (25) is globally asymptotically stable in the first moment, i.e.

$$\lim_{t\longrightarrow\infty} E\left[\tilde{\mathbf{Z}}_t\right] = \mathbf{0}$$

and we have mean square convergence of the true conditional error to the desired conditional error, i.e.

$$\lim_{t\longrightarrow\infty} E\left[\left|\hat{\boldsymbol{\mathcal{Z}}}_t\right|^2\right] = 0$$

if the estimator inputs, $\boldsymbol{\eta}(t)$, are selected as

$$\boldsymbol{\eta}(t) = \operatorname{sgn}\left\{\Lambda d\tilde{\mathbf{Y}}_t\right\}\gamma(t) \quad (32)$$

[1]See [26, Theorem 3.8]

where $\operatorname{sgn}\{\cdot\}$ denotes the signum function or the sign function and $\gamma(t)$ is an upper bound on the process $\boldsymbol{\Gamma}_t$.

Proof: Proof of this theorem is based on the stochastic Lyapunov stability analysis. Consider a stochastic Lyapunov function

$$V(\hat{\boldsymbol{\mathcal{Z}}}_t) = \hat{\boldsymbol{\mathcal{Z}}}_t^T\,\mathcal{X}\,\hat{\boldsymbol{\mathcal{Z}}}_t.$$

Now $dV(\hat{\boldsymbol{\mathcal{Z}}}_t)$ can be calculated as

$$dV(\hat{\boldsymbol{\mathcal{Z}}}_t) = \hat{\boldsymbol{\mathcal{Z}}}_t^T \left\{[F-KH]^T\,\mathcal{X} + \mathcal{X}\,[F-KH]\right\}\hat{\boldsymbol{\mathcal{Z}}}_t dt + 2E\left[\hat{\boldsymbol{\mathcal{Z}}}_t^T\,\mathcal{X}\boldsymbol{\Gamma}_t \middle| \mathcal{F}_t^{\tilde{\mathbf{Y}}}\right] dt - 2E\left[\hat{\boldsymbol{\mathcal{Z}}}_t^T\,\mathcal{X}\boldsymbol{\eta}(t) \middle| \mathcal{F}_t^{\tilde{\mathbf{Y}}}\right] dt.$$

Substituting (30) and (31) yields

$$dV(\hat{\boldsymbol{\mathcal{Z}}}_t) \leq -\hat{\boldsymbol{\mathcal{Z}}}_t^T S\,\hat{\boldsymbol{\mathcal{Z}}}_t dt + 2E\left[\hat{\boldsymbol{\mathcal{Z}}}_t^T H^T\Lambda^T\boldsymbol{\Gamma}_t \middle| \mathcal{F}_t^{\tilde{\mathbf{Y}}}\right] dt - 2E\left[\hat{\boldsymbol{\mathcal{Z}}}_t^T H^T\Lambda^T\boldsymbol{\eta}(t) \middle| \mathcal{F}_t^{\tilde{\mathbf{Y}}}\right] dt.$$

Note

$$\begin{aligned} H\hat{\boldsymbol{\mathcal{Z}}}_t dt &= E\left[H\boldsymbol{\mathcal{Z}}_t \middle| \mathcal{F}_t^{\tilde{\mathbf{Y}}}\right] dt \\ &= E\left[\left(H\tilde{\mathbf{Z}}_t dt - H\tilde{\mathbf{Z}}_{m_t} dt\right) \middle| \mathcal{F}_t^{\tilde{\mathbf{Y}}}\right] \\ &= E\left[\left(d\tilde{\mathbf{Y}}_t - d\tilde{\mathbf{Y}}_{m_t}\right) \middle| \mathcal{F}_t^{\tilde{\mathbf{Y}}}\right] \\ &= d\tilde{\mathbf{Y}}_t - E\left[d\tilde{\mathbf{Y}}_{m_t} \middle| \mathcal{F}_t^{\tilde{\mathbf{Y}}}\right] \end{aligned}$$

where $d\tilde{\mathbf{Y}}_{m_t} = \left[d\mathbf{Y}_{m_t} - H\hat{\mathbf{Z}}_{m_t} dt\right]$. Given $\hat{\mathbf{Z}}_m(t_0) = \mathbf{Z}_m(t_0)$, one could conclude that $\tilde{\mathbf{Y}}_{m_t}$ is a zero mean processes and

$$E\left[d\tilde{\mathbf{Y}}_{m_t} \middle| \mathcal{F}_t^{\tilde{\mathbf{Y}}}\right] = E\left[d\tilde{\mathbf{Y}}_{m_t}\right] = 0.$$

Therefore $dV(\hat{\boldsymbol{\mathcal{Z}}}_t)$ can be bounded as

$$dV(\hat{\boldsymbol{\mathcal{Z}}}_t) \leq -\hat{\boldsymbol{\mathcal{Z}}}_t^T S\,\hat{\boldsymbol{\mathcal{Z}}}_t dt + 2E\left[\left\{d\tilde{\mathbf{Y}}_t^T\Lambda^T\boldsymbol{\Gamma}_t - d\tilde{\mathbf{Y}}_t^T\Lambda^T\boldsymbol{\eta}(t)\right\} \middle| \mathcal{F}_t^{\tilde{\mathbf{Y}}}\right].$$

After substituting (32), an upper bound on $dV(\hat{\boldsymbol{\mathcal{Z}}}_t)$ can be obtained as

$$dV(\hat{\boldsymbol{\mathcal{Z}}}_t) \leq -\hat{\boldsymbol{\mathcal{Z}}}_t^T S\,\hat{\boldsymbol{\mathcal{Z}}}_t dt + 2E\left[\left\{d\tilde{\mathbf{Y}}_t^T\Lambda^T\boldsymbol{\Gamma}_t - d\tilde{\mathbf{Y}}_t^T\Lambda^T\operatorname{sgn}\left\{\Lambda d\tilde{\mathbf{Y}}_t\right\}\gamma(t)\right\} \middle| \mathcal{F}_t^{\tilde{\mathbf{Y}}}\right].$$

Note

$$d\tilde{\mathbf{Y}}_t^T\Lambda^T\operatorname{sgn}\left\{\Lambda d\tilde{\mathbf{Y}}_t\right\} = \left|\Lambda d\tilde{\mathbf{Y}}_t\right|$$

and $d\tilde{\mathbf{Y}}_t^T\Lambda^T\boldsymbol{\Gamma}_t \leq |d\tilde{\mathbf{Y}}_t^T\Lambda^T||\boldsymbol{\Gamma}_t| \leq |d\tilde{\mathbf{Y}}_t^T\Lambda^T|\gamma(t)$. Thus

$$dV(\hat{\boldsymbol{\mathcal{Z}}}_t) \leq -\hat{\boldsymbol{\mathcal{Z}}}_t^T S\,\hat{\boldsymbol{\mathcal{Z}}}_t dt.$$

Now it can be concluded that for every initial value $\hat{\boldsymbol{\mathcal{Z}}}(t_0)$, the solution, $\hat{\boldsymbol{\mathcal{Z}}}_t$, of (29) has the property that $\hat{\boldsymbol{\mathcal{Z}}}_t \longrightarrow \mathbf{0}$ almost surely as $t \longrightarrow \infty$[29], i.e.

$$\mathbb{P}\left(\lim_{t\longrightarrow\infty} |\hat{\boldsymbol{\mathcal{Z}}}_t| = 0\right) = 1.$$

Also note that, $\forall t \geq t_0$, we have

$$V(\hat{\boldsymbol{\mathcal{Z}}}_t) \leq V(\hat{\boldsymbol{\mathcal{Z}}}_0) \Rightarrow E\left[V(\hat{\boldsymbol{\mathcal{Z}}}_t)\right] \leq E\left[V(\hat{\boldsymbol{\mathcal{Z}}}_0)\right] < \infty.$$

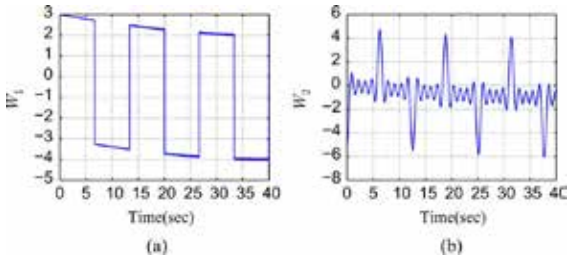

Fig. 1. Persistently exciting disturbances. (a) $\boldsymbol{W}_{1_t}$. (b) $\boldsymbol{W}_{2_t}$.

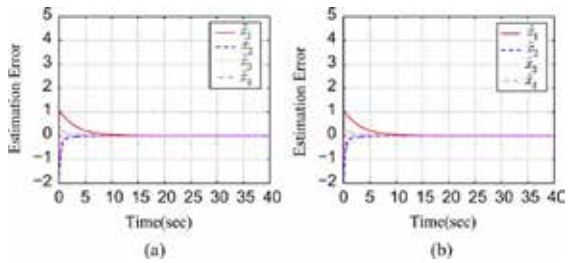

Fig. 2. Simulation I: State estimation error. (a) Kalman-Bucy Filter. (b) Robust Kalman-Bucy Filter.

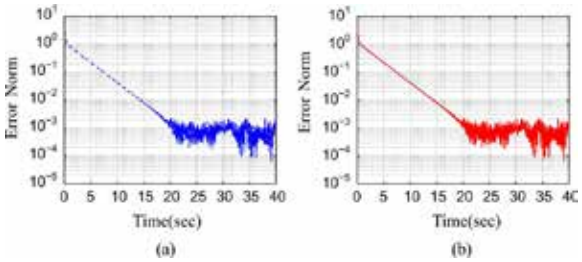

Fig. 3. Simulation I: State Estimation Error Norm. (a) Kalman-Bucy Filter. (b) Robust Kalman-Bucy Filter.

Thus $\forall t \geq t_0$, $\hat{\boldsymbol{\mathcal{Z}}}_t \in \mathcal{L}^2$, i.e., $E\left[\left|\hat{\boldsymbol{\mathcal{Z}}}_t\right|^2\right] < \infty$. Therefore, we could conclude that

$$E\left[\sup_{t\geq t_0}\left|\hat{\boldsymbol{\mathcal{Z}}}_t\right|^2\right] < \infty.$$

Now based on the Lebesgue's dominated convergence theorem, a.s. convergence of $\hat{\boldsymbol{\mathcal{Z}}}_t$ implies [30]

$$\lim_{t\longrightarrow\infty} E\left[|\hat{\boldsymbol{\mathcal{Z}}}_t|^2\right] = 0.$$

Moreover, $\hat{\boldsymbol{\mathcal{Z}}}_t \in \mathcal{L}^2$ implies $\hat{\boldsymbol{\mathcal{Z}}}_t \in \mathcal{L}^1$ and

$$\lim_{t\longrightarrow\infty} E\left[|\hat{\boldsymbol{\mathcal{Z}}}_t|\right] = 0.$$

Note

$$E\left[|\hat{\boldsymbol{\mathcal{Z}}}_t|\right] \geq \left|E\left[\hat{\boldsymbol{\mathcal{Z}}}_t\right]\right| = \left|E\left[\tilde{\mathbf{Z}}_t\right] - E\left[\tilde{\mathbf{Z}}_{m_t}\right]\right|.$$

Thus, the asymptotic convergence in the mean follows from the fact that $\tilde{\mathbf{Z}}_{m_t}$ is a zero mean process. ■

The design of proposed robust estimator requires the calculation of matrices $\mathcal{X}$ and Λ that satisfies the conditions given in (30) and(31). As shown in [31], matrices $\mathcal{X}$ and Λ that satisfies the conditions (30) and(31) can be obtained by solving the following linear matrix inequality:

$$\begin{bmatrix} \{F-KH\}^T\mathcal{X} + \mathcal{X}\{F-KH\} + S & \mathcal{X} - H^T\Lambda^T \\ \mathcal{X}^T - \Lambda H & \mathbf{0}_{(n+m)\times(n+m)} \end{bmatrix} \leq \mathbf{0}. \quad (33)$$

Matrices that satisfy the above LMI can be obtained by using the MATLAB LMI toolbox [31], [32].

IV. Numerical Simulations

Performance of the proposed estimator is evaluated here though numerical simulations. For simulation purposes consider a stochastic system of following form:

$$d\begin{bmatrix} X_{1_t} \\ X_{2_t} \\ X_{3_t} \\ X_{4_t} \end{bmatrix} = \begin{bmatrix} 0 & 0 & -1.000 & 0 \\ 0 & 0 & 0 & -2.000 \\ 2.300 & 1.330 & -8.500 & -1.620 \\ 1.780 & 2.030 & -1.020 & -9.500 \end{bmatrix} \begin{bmatrix} X_{1_t} \\ X_{2_t} \\ X_{3_t} \\ X_{4_t} \end{bmatrix} dt + [\mathbf{0}_{1\times 2} \quad W_{1_t} \quad W_{2_t}]^T dt + [\mathbf{0}_{1\times 2} \quad d\mathcal{B}_{1_t} \quad d\mathcal{B}_{2_t}]^T.$$

The measurement equation is of the following form:

$$d\begin{bmatrix} Y_{1_t} \\ Y_{2_t} \\ Y_{3_t} \\ Y_{4_t} \end{bmatrix} = \begin{bmatrix} 0.4300 & 0 & -2.310 & 0 \\ 0 & -2.400 & 0 & 1.540 \\ 3.640 & 2.740 & 0 & 0 \\ 0 & 2.420 & 1.120 & 4.340 \end{bmatrix} \begin{bmatrix} Y_{1_t} \\ Y_{2_t} \\ Y_{3_t} \\ Y_{4_t} \end{bmatrix} dt + [d\mathcal{V}_{1_t} \quad d\mathcal{V}_{2_t} \quad d\mathcal{V}_{3_t} \quad d\mathcal{V}_{4_t}]^T.$$

The assumed matrices are selected as

$$A_m = \begin{bmatrix} 0 & 0 & -1.000 & 0 \\ 0 & 0 & 0 & -2.000 \\ 0.300 & 0.130 & -4.240 & 0.200 \\ -0.400 & 0.530 & 0.420 & -5.430 \end{bmatrix}$$

and

$$C_m = \begin{bmatrix} 0.430 & 0 & -2.310 & 0 \\ 0 & -2.400 & 0 & 1.540 \\ 0.950 & 1.700 & 0 & 0 \\ 0 & 0 & 1.300 & 0.430 \end{bmatrix}.$$

The processes W_{1_t} and W_{2_t} are given in Fig. 1. Note that the system uncertainty is only associated with the dynamics of the last two states and the output matrix error is only associated with the last two outputs. Since the two measurement uncertainties are only associated with the last two outputs, $\mathbf{N}_t \in \Re^2$ and thus the matrices F and H are defined as $F = \begin{bmatrix} A_m & 0_{4\times 2} \\ 0_{2\times 4} & -I_{2\times 2} \end{bmatrix}$ and $H = [C_m \quad [0_{2\times 2} \quad I_{2\times 2}]^T]$, respectively. After defining $G_m = [I_{2\times 2} \quad 0_{2\times 4}]^T$, the steady-state Kalman gain can be calculated.

Since there is no uncertainties or external disturbances acting on the first two states $\boldsymbol{\Gamma}_t$ is defined as $\boldsymbol{\Gamma}_t = \Xi[M_{1_t}^T \quad M_{2_t}^T \quad U_{1_t}^T \quad U_{2_t}^T]^T$, where $\Xi = [0_{4\times 2} \quad I_{4\times 4}]^T$. Now the robust estimator may be designed based on the premises of Theorem 1 after replacing the condition $\mathcal{X} = H^T\Lambda^T$ with $\mathcal{X}\Xi = H^T\Lambda^T$. System process noise covariance and the measurement noise covariance matrices are selected as $R = 10^{-2} \times I_{4\times 4}$ and $Q = \begin{bmatrix} 0.25 & 0 \\ 0 & 0.35 \end{bmatrix}$. Two different simulations are considered here. The first simulation scenario considers the case where there is no system uncertainties. For the second scenario, aforementioned uncertainties as assumed. True initial states are

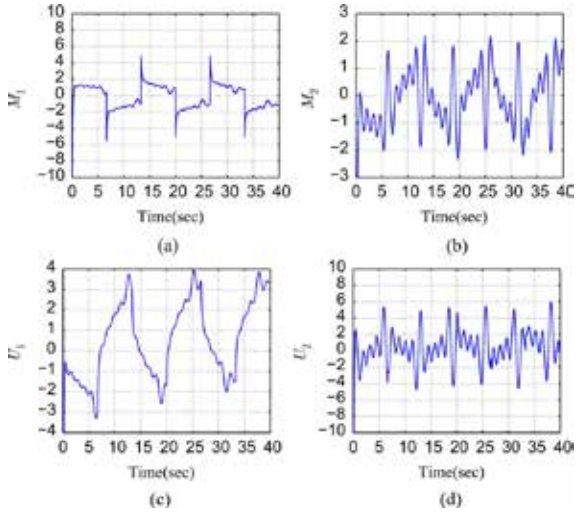

Fig. 4. Simulation II: Model-error vector $\mathbf{\Gamma}_t = \begin{bmatrix} \boldsymbol{M}_{1_t} & \boldsymbol{M}_{2_t} & \boldsymbol{U}_{1_t} & \boldsymbol{U}_{2_t} \end{bmatrix}^T$. (a) $\boldsymbol{M}_{1_t}$. (b) $\boldsymbol{M}_{2_t}$. (c) $\boldsymbol{U}_{1_t}$. (d) $\boldsymbol{U}_{2_t}$.

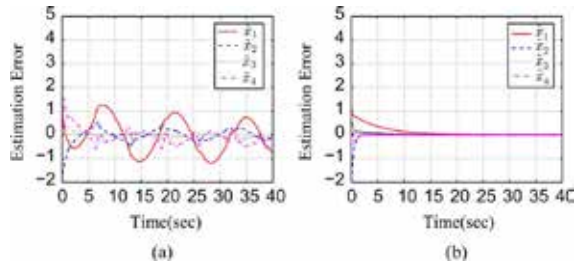

Fig. 5. Simulation II: State estimation error. (a) Kalman-Bucy Filter. (b) Robust Kalman-Bucy Filter.

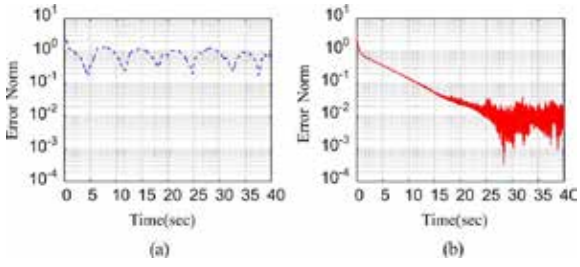

Fig. 6. Simulation II: State estimation error norm. (a) Kalman-Bucy Filter. (b) Robust Kalman-Bucy Filter .

selected to be $\mathbf{X}_0 = \begin{bmatrix} 1 & -2 & 5 & 0 \end{bmatrix}^T$ and the assumed initial states are $\mathbf{X}_{m_0} = \mathbf{0}_{4\times 1}$.

A. Simulation I

For the first simulation, consider a scenario where there is no model uncertainties and external disturbances, i.e., $A = A_m$, $C = C_m$ and $\mathbf{W}_t = \mathbf{0}$. For the first simulation, the state estimation error obtained using the Kalman-Bucy filter is given in Fig. 2(a) and the estimation error obtained from the proposed robust estimator is presented in Fig. 2(b). Fig. 3 shows the estimation error norm obtained for both estimators. Results shown in Figs. 2 and 3 indicate that the performance of the proposed robust estimator is identical to that of the Kalman-Bucy filter when there is no system uncertainties.

B. Simulation II

The uncertain system is considered for the second simulation. Fig. 4 contains the model-error vector, $\mathbf{\Gamma}_t$, corresponding to the aforementioned uncertainties. Note that at any time, $|\mathbf{\Gamma}_t|$ is upper bounded by $\gamma = 8$. The state estimation error obtained using the Kalman-Bucy filter is given in Fig. 5(a) and the estimation error obtained from the robust estimator is presented in Fig. 5(b). Fig. 6 shows the estimation error norm obtained for both estimators. Results shown in Figs. 5 and 6 indicate that the performance of the proposed robust estimator is superior to that of the Kalman-Bucy filter when there is system uncertainties. Finally note that the performance of the robust estimator given in Figs. 5(b) and 6(b) are similar to the ones given in Figs. 2(b) and 3(b).

V. Conclusion

This technical note presents the formulation of a robust estimator for uncertain stochastic systems under persistent excitation. The continuous-time stochastic formulation given here assumes norm bounded parametric uncertainties and excitations. Proposed robust estimator guarantees the asymptotic convergence of the state estimation error. Simulation results given here indicate that the performance of the proposed robust estimator is similar to that of the Kalman-Bucy filter when there are no system uncertainties and excitations. As shown by the numerical simulation results, the approach asymptotically recovers the desired optimal performance in the presence of system uncertainties and persistent excitation. Potential future work include extending the proposed approach to the nonlinear estimation problem by introducing constrains on the drift and diffusion terms of the nonlinear stochastic differential equation.

References

[1] C. E. de Souza, M. Fu, and L. Xie, "$\mathbf{H}_\infty$ estimation for discrete-time linear uncertain systems," *Int. J. Robust Nonlin. Control*, vol. 1, pp. 11–23, 1991.

[2] L. Xie, C. E. de Souza, and M. D. Fragoso, "$\mathbf{H}_\infty$ filtering for linear periodic systems with parameter uncertainty," *Syst. Control Lett.*, vol. 17, pp. 343–350, 1991.

[3] K. Nagpal and P. Khargonekar, "Filtering and smoothing in an $\mathbf{H}_\infty$ setting," *IEEE Trans. Autom. Control*, vol. 36, no. 2, pp. 152–166, Feb. 1991.

[4] M. Fu, C. E. de Souza, and L. Xie, "$\mathbf{H}_\infty$ estimation for uncertain systems," *Int. J. Robust Nonlin. Control*, vol. 2, pp. 87–105, 1992.

[5] D. S. Bernstein, W. M. Haddad, and D. Mustafa, "Mixed-norm $\mathbf{H}_2/\mathbf{H}_\infty$, regulation and estimation: The discrete-time case," *Syst. Control Lett.*, vol. 16, pp. 235–248, 1991.

[6] Z. Wang and H. Unbehauen, "Robust $\mathbf{H}_2/\mathbf{H}_\infty$-state estimation for systems with error variance constraints: the continuous-time case," *IEEE Trans. Autom. Control*, vol. 44, no. 5, pp. 1061–1065, May 1999.

[7] A. H. Sayed, "A framework for state-space estimation with uncertain models," *IEEE Trans. Autom. Control*, vol. 46, no. 7, pp. 998–1013, Jul. 2001.

[8] A. Subramanian and A. Sayed, "Multiobjective filter design for uncertain stochastic time-delay systems," *IEEE Trans. Autom. Control*, vol. 49, no. 1, pp. 149–154, Jan. 2004.

[9] A. Subramanian and A. Sayed, "Regularized robust filters for time-varying uncertain discrete-time systems," *IEEE Trans. Autom. Control*, vol. 49, no. 6, pp. 970–975, Jun. 2004.

[10] I. R. Petersen and D. C. McFarlane, "Robust state estimation for uncertain systems," in *Proc. 30th IEEE Conf. Decision Control*, Dec. 1991, vol. 3, pp. 2630–2631.

[11] L. Xie, Y. C. Soh, and C. E. de Souza, "Robust Kalman filtering for uncertain discrete-time systems," *IEEE Trans. Autom. Control*, vol. 39, pp. 1310–1314, Jun. 1994.

[12] I. Petersen and D. McFarlane, "Optimal guaranteed cost control and filtering for uncertain linear systems," *IEEE Trans. Autom. Control*, vol. 39, no. 9, pp. 1971–1977, Sep. 1994.
[13] U. Shaked, L. Xie, and Y. C. Soh, "New approaches to robust minimum variance filter design," *IEEE Trans. Signal Process.* , vol. 49, no. 11, pp. 2620–2629, Nov. 2001.
[14] C. de Souza, K. Barbosa, and A. Trofino, "Robust filtering for linear systems with convex-bounded uncertain time-varying parameters," *IEEE Trans. Autom. Control*, vol. 52, no. 6, pp. 1132–1138, Jun. 2007.
[15] A. Savkin and I. Petersen, "Recursive state estimation for uncertain systems with an integral quadratic constraint," *IEEE Trans. Autom. Control*, vol. 40, no. 6, pp. 1080–1083, Jun. 1995.
[16] M. James and I. Petersen, "Nonlinear state estimation for uncertain systems with an integral constraint," *IEEE Trans. Signal Process.*, vol. 46, no. 11, pp. 2926–2937, Nov. 1998.
[17] I. R. Petersen and A. V. Savkin, *Robust Kalman Filtering for Signals and Systems With Large Uncertainties*. Boston, MA: Birkhäuser, 1999.
[18] P. Neveux, E. Blanco, and G. Thomas, "Robust filtering for linear time-invariant continuous systems," *IEEE Trans. Signal Process.* , vol. 55, no. 10, pp. 4752–4757, Oct. 2007.
[19] T. Zhou, "Sensitivity penalization based robust state estimation for uncertain linear systems," *IEEE Trans. Autom. Control*, vol. 55, no. 4, pp. 1018–1024, Apr. 2010.
[20] J.-J. E. Slotine and W. Li, *Applied Nonlinear Control*. Englewood Cliffs, NJ: Prentice-Hall, 1991, ch. 7–8.
[21] B. Øksendal, *Stochastic Differential Equations*. New York: Springer-Verlag, 2003, ch. 5.
[22] J. L. Doob, *Stochastic Processes*. New York: Wiley, 1953, ch. 7.
[23] M. Grigoriu, *Stochastic Calculus*. Boston, MA: Birkhäuser, 2002, ch. 1–5.
[24] J. Spall and J. Garner, "Parameter identification for state-space models with nuisance parameters," *IEEE Trans. Aerosp. Electron. Syst.*, vol. 26, no. 6, pp. 992–998, Nov. 1990.
[25] J. Juang, *Applied System Identification*. Upper Saddle River, NJ: Prentice-Hall, 1994.
[26] A. H. Jazwinski, *Stochastic Processes and Filtering Theory*. Mineola, NY: Dover, 1998.
[27] J. L. Crassidis and J. L. Junkins, *Optimal Estimation of Dynamic System*. Boca Raton, FL: CRC, 2004, ch. 5.
[28] J. Jacod and P. Protter, *Probability Essentials*, 2nd ed. Berlin, Germany: Springer-Verlag, 2004.
[29] H. J. Kushner, *Stochastic Stability and Control*. New York: Academic, 1967, ch. 2.
[30] P. Billingsley, *Convergence of Probability Measures*. New York: Wiley, 1999.
[31] S. Boyd, L. E. Ghaoui, E. Feron, and V. Balakrishnan, *Linear Matrix Inequalities in System and Control Theory, ser. Studies in Applied Mathematics*. Philadelphia, PA: SIAM, 1997, vol. 15.
[32] P. Gahinet, A. Nemirovski, A. J. Laub, and M. Chilali, LMI Control Toolbox The MathWorks, Inc., Natick, MA, 1995.

Efficient Base Station Connectivity Area Discovery

Jeffrey N. Twigg, Jonathan R. Fink, Paul L. Yu, Brian M. Sadler

International Journal of Robotics Research, Special Issue on Robotic Communications and Collaboration in Complex Environments (2013)

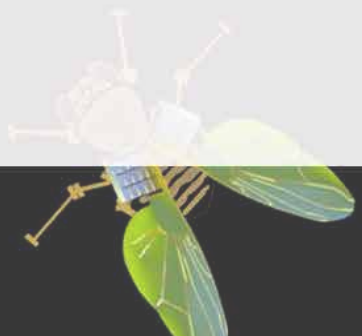

Article

The International Journal of
Robotics Research
0(0) 1–13

DOI: 10.1177/0278364913488634
ijr.sagepub.com

Efficient base station connectivity area discovery

Jeffrey N. Twigg, Jonathan R. Fink, Paul L. Yu and Brian M. Sadler

Abstract

Many applications of autonomy are significantly complicated by the need for wireless networking, with challenges including scalability and robustness. Radio accomplishes this in a complex environment, but suffers from rapid signal strength variation and attenuation typically much worse than free space loss. In this paper, we propose and test algorithms to autonomously discover the connectivity area for a base station in an unknown environment using an average of received signal strength (RSS) values and a RSS threshold to delineate the goodness of the channel. We combine region decomposition and RSS sampling to cast the problem as an efficient graph search. The nominal RSS in a sampling region is obtained by averaging local RSS samples to reduce the small-scale fading variation. The RSS gradient is exploited during exploration to develop an efficient approach for discovery of the base station connectivity boundary in an unknown environment. Indoor and outdoor experiments demonstrate the proposed techniques. The results can be used for sensing and collaborative autonomy, building base station coverage maps in unknown environments, and facilitating multi-hop relaying to a base station.

Keywords

communication maintenance, networked robotics, environment sampling, channel estimation, map decomposition

1. Introduction

The use of autonomous agents is significantly complicated by the need for wireless networking, with its challenges of maintaining scalability and robustness. Radio provides the ability to communicate around and through barriers in a complex environment, but suffers from rapid signal strength variation with relatively small movements induced by multipath propagation, as well as attenuation that is typically well beyond free space loss. To gain in robustness and maintain connectivity, we would like a map delineating the physical boundary between good and poor communications from some location, e.g. between a base station and its surrounding environment. This is much more preferable than to assume a fixed distance (disk) model, which is highly inaccurate unless the propagation is essentially free space without scattering. Knowledge of this boundary is useful in developing behaviors that maintain reliable communication among robots or between robots and a base station, including applications such as sensor data collection or collaborative control. Furthermore, when considering a variety of base stations and environments, the discovery of the boundary between good and poor communication scales in a manageable way.

Given a stationary node or base station, we can create algorithms so that platforms can maintain communication with this base station with some relatively high probability of success for each packet transmission. We assume a platform is any autonomous entity capable of relating its position to a physical map of the environment. Determining the (possibly disconnected) physical boundary between regions of good and poor communication in an environment is useful for constraining the movement of these platforms. The *connectivity boundary* is selected such that if the platform remains inside the bounded region, then communications are deemed sufficiently reliable. We refer to the area of good communication as the *connectivity area* with regard to the base station, and we propose techniques for building a 2D map of this connectivity boundary using an autonomous platform. The exploration, mapping, region segmentation, received signal strength (RSS) sampling, and connectivity area discovery are carried out autonomously and simultaneously. This requires the platform to be capable of simultaneous localization and mapping (SLAM) as well as estimating

US Army Research Laboratory, Adelphi, MD, USA

Corresponding author:
Jonathan R. Fink, US Army Research Laboratory, 2800 Powder Mill Road, Adelphi, MD 20783, USA.
Email: jonathan.r.fink3.civ@mail.mil

RSS on a transmission by transmission basis. Our experimental platform is equipped with a radio receiver, laser scanner, and inertial measurement unit (IMU) in order to accomplish these tasks.

In a complex environment with line-of-sight (LOS) and non-line-of-sight (NLOS) propagation, the problem of determining the good/poor boundary is non-trivial. Exhaustive search and sampling can be used to learn the propagation environment by estimating the parameters of fading models such as Rayleigh/Rician or Nakagami (see, e.g., Mostofi et al., 2010). If a single model is built, then it is representative of the environment on average but, due to local non-stationary variation, is not necessarily good for prediction. For example, in an indoor environment, the fading model parameters can be highly variable from room to room, and parameter estimation requires many samples in each local area. The parameters may also change with small local movement of scatterers such as doors.

The problem of how to sample and build a data-driven model of a random field such as radio signal propagation in a non-parametric way is also challenging. One approach is to employ a kernel to spatially smooth RSS samples, such as a Gaussian process. The use of a Gaussian process with a stationary non-compact kernel function (Fink and Kumar, 2010) presents two main issues. First, computational complexity of the Gaussian process is not scalable over a large number of samples. Second, the Gaussian process does not provide adequate information to guide anything more than simple exploration of the environment.

The idea of simplified models and reliance on measured data for determination of wireless connectivity has been described in the robotics literature. Zickler and Veloso (2010) presented a data-driven model that relates the distance between nodes with the RSS in a probabilistic way to enable tethering and localization of non-cooperative mobile agents. However, by relying on a distance-based abstraction, this method will reduce to the standard disk-based model for our base station connectivity area application. Our work takes more inspiration from that of Hsieh et al. (2008), where an outdoor environment is decomposed into a number of cells such that agents within the same cell can communicate with high probability.

In this paper, we propose and test algorithms to discover the connectivity area for a base station, using average RSS value and a threshold to delineate the goodness of the channel. The primary issues are how to build the RSS map with sufficient information while not over-parameterizing or over-sampling and developing exploration algorithms that efficiently discover the connectivity boundary. We show that the connectivity boundary can be discovered efficiently, while the entire connectivity area can also be mapped if desired. With the complete map, it is simple to delineate regions with different quality of connectivity (good, fair, poor, etc.).

2. Problem statement and approach

We consider the problem of autonomously exploring and mapping a connectivity area for a fixed radio transmitter (a base station). We define connectivity as the satisfaction of a minimum local average RSS threshold, which can be equivalently viewed as a bit error rate, capacity, or reliability requirement (Proakis, 1995). The agent is initially deployed within the base station connectivity area. Owing to the complex propagation, the RSS at position x is given by the random field $P(x)\colon \mathbb{R}^2 \rightarrow \mathbb{R}$. Therefore, the connectivity area can be determined with only probabilistic guarantees and we characterize this by computing a local average of the RSS within each region. With the base station at position x_0, the goal of the robot is to determine the base station's connectivity area $\mathcal{C}$ such that (1) $x_0 \in \mathcal{C}$, (2) $x \in \mathcal{C} \Rightarrow \Pr[P(x) > \tau] > 1 - \epsilon$, for $\epsilon > 0$ and some minimum RSS τ, and (3) $x, y \in \mathcal{C} \Rightarrow x \rightsquigarrow y$, where $x \rightsquigarrow y$ indicates the existence of a navigable path from position x to position y that is contained entirely in $\mathcal{C}$. Although the connectivity area of the base station may generally be disjoint due to the propagation phenomena, in this paper we consider only the region that contains the base station. This simplifies and limits the exploration required to find the boundary of $\mathcal{C}$.

Classic fading models, such as Rayleigh/Rician or Nakagami, can be employed to characterize the statistical variation averaged over an environment. However, we explicitly take a non-parametric approach with an emphasis on exploration and mapping of the base station's connectivity area. A key idea of our approach is to partition the environment in a way that enables relatively sparse sampling of the RSS, yet provides a useful RSS map and has sufficient spatial resolution to enable efficient autonomous discovery of the connectivity area. We sample locally and estimate the RSS mean, as well as the local RSS spatial gradient, and use the local gradient to inform the exploration algorithm (Section 3).

To make exploration and sampling tractable in a complex unknown environment, we leverage the fact that radio signal propagation exhibits spatial correlation (Proakis, 1995; Goldsmith, 2005) and progressively compute a decomposition of the environment to use for sampling (Section 4). The decomposition is computed such that adjacencies can be determined and used to induce a graph on the navigable space in the environment. Thus, the exploration problem can be cast as a graph traversal (Section 5).

3. RSS sampling and gradient estimation

Any propagation environment can be characterized with a statistical model, although this generally requires many samples, and in a complex environment it is challenging to account for the spatial non-stationarity in the model parameters. A key idea of our approach is to partition the environment in a way that enables relatively sparse sampling of

the RSS, yet provides a useful RSS map and has sufficient spatial resolution to enable efficient autonomous discovery of the connectivity area. In this section we consider intra-region sampling and estimation, and in Section 4 we consider partitioning the environment into regions.

In this paper we exploit the RSS estimate provided by the receiver, so we concentrate on estimation and exploitation of the RSS local spatial mean and spatial gradient. Measurement of the RSS has been analyzed elsewhere. For example, using a matched filter detector and assuming a Rayleigh/Rician fading model, we have analyzed RSS estimation as a function of the signal-to-noise ratio, the number of independent frequency bins, and LOS (Rician) or NLOS (Rayleigh) conditions (Yu and Sadler, 2010).

Here, given multiple RSS estimates, we consider spatial sampling and estimation of the average RSS within a spatial region, as well as estimation of the RSS gradient in that region. Given the fading and physical environment, we want a sufficient number of samples per region to obtain reliable estimates of the average RSS and to estimate the RSS gradient which will inform exploration in order to efficiently seek the base station connectivity boundary.

3.1. Sampling regions

Within each region we need a sufficient number of independent RSS samples for estimation. The RSS within the region in a complex environment may vary rapidly due to the small-scale (fast) fading, with spatial decorrelation affected by both fast fading and shadowing. We assume an unknown environment, and seek general guidelines for sampling.

The RSS average trend generally obeys $d^{-\alpha}$ decay with transmit to receive range d, where α varies depending on the environment with $2 \leq \alpha \leq 5$ typical. Fast fading creates rapid spatial variation around this average trend.

Consider the Rayleigh fading model for local RSS measurements, which has nominal spatial autocorrelation given by

$$R(\delta) = aJ_0^2(2\pi\delta/\lambda) \tag{1}$$

where δ is the distance between locations, a is a constant, J_0 is the zero-order Bessel function of the first kind, and λ is the carrier wavelength (Goldsmith, 2005; Proakis, 1995). This indicates that samples taken 0.38λ apart have zero correlation, and samples taken at larger distances have small correlation. This heuristic is well-supported in rich scattering environments by many measurement campaigns, especially at microwave frequencies (Lindhe et al., 2007). However, the spacing necessary for decorrelation is variable depending on the propagation environment, with generally longer correlation in line of sight conditions. In practice, NLOS indoor microwave measurements taken one or two wavelengths apart are generally viewed as experiencing independent fades. In other cases, such as hallways with LOS, the distance required for highly decorrelated RSS samples can increase by an order of magnitude (10–20 wavelengths, say), and the correlation will tend to drop off less rapidly with distance (see, e.g., Lindhe et al., 2007). As an aside, an interesting special case occurs with a fixed ground node and an elevated mobile node; here the spatial correlation varies slowly in a trajectory along the LOS direction, whereas it varies more rapidly in a trajectory orthogonal to the LOS direction (Wadhwa et al., 2011).

In addition to spatial variation, independent samples of the small-scale fading may be realized through frequency diversity, with the transmitter and receiver at fixed locations. The required frequency separation is $\Delta f > B_c$ with $B_c \approxeq 1/\sigma_{T_m}$, where B_c is the coherence bandwidth of the channel and σ_{T_m} is the root mean square (rms) delay spread (Goldsmith, 2005). In indoor channels, rms delay spread typically ranges from 10 to 1000 ns which corresponds to coherence bandwidths between 1 and 100 MHz (Rappaport, 2001). For the experimental results presented in this paper, we do not have control of center frequency and so do not explicitly average over frequency to obtain enhanced RSS estimates.

3.2. RSS gradient estimation

The RSS gradient within a region yields an estimate of the direction of greatest increase of RSS, and we exploit this as we characterize the overall connectivity boundary. Within each region, we model the RSS trend as linear. To justify this approximation, consider the curvature of the exponential path loss model for RSS, $p(d) = p_0 d^{-\alpha}$, where p_0 is a constant, d is the distance from the source and α is the path loss exponent. The curvature of a plane curve $p(d)$ is defined as $\kappa = p''/(1+p'^2)^{3/2}$ with $p' \triangleq \frac{\partial p}{\partial d}$. With the exponential path loss model, then $\kappa = \alpha(\alpha+1)p_0 d^{-\alpha-2}/(1+\alpha^2 p_0^2 d^{-2\alpha-2})^{3/2} \approxeq \alpha(\alpha+1)p_0 d^{-\alpha-2}$ for non-small d. Because κ is close to zero (note that a line has zero curvature), the linear approximation is reasonable for regions not too close to the signal source.

Beyond the path loss, which varies slowly over large distances ($100 - 1000$ meters), the RSS observed at any particular location is also affected by shadowing and multipath fading. Shadow effects are highly correlated over distances proportional to the obstructing object (10–100 m outdoors, and less indoors) (Goldsmith, 2005). Thus, path loss and shadowing are often referred to as large-scale propagation effects and the linear approximation of the gradient is reasonable when the sampling region is relatively small (e.g. confined to a region $< 10\,\mathrm{m}^2$), as is the case in our experiments.

Let $\underline{P} = \{P_1, P_2, \ldots, P_N\} \in \mathbb{R}^N$ be the nominal signal strength at N distinct locations $\mathbf{X} = \{\underline{X}_1, \underline{X}_2, \ldots, \underline{X}_N\} \in \mathbb{R}^{N\times 2}$. Without loss of generality, we shift the reference frame to align the centroid of $\mathbf{X}$ on the origin for convenience. Using the linear approximation, the nominal RSS at locations $\mathbf{X}$ is

$$\underline{P} = \mathbf{X}\underline{\beta} + c\underline{1} \tag{2}$$

where $\underline{\beta} = [\beta_1, \beta_2]^{\mathrm{T}} \in \mathbb{R}^2$ is the *RSS gradient* and c is a constant that expresses the average power in the region. As discussed in Section 3.1, we do not observe the nominal values directly due to the multipath fading, but rather make measurements $\underline{\hat{P}} = \{\hat{P}_1, \hat{P}_2, \ldots, \hat{P}_N\}$ that fluctuate around the RSS trend.

The least-squares solution for $\underline{\beta}$ given $\underline{\hat{P}}$ is

$$\underline{\hat{\beta}} = (\mathbf{X}^{\mathrm{T}}\mathbf{X})^{-1}\mathbf{X}^{\mathrm{T}}\underline{\hat{P}} = \mathbf{X}^{+}\underline{\hat{P}} \tag{3}$$

where $\mathbf{X}^{+}$ is the pseudo-inverse of $\mathbf{X}$ (Draper and Smith, 1998). Note that $\mathbf{X}^{\mathrm{T}}\mathbf{X}$ must be non-singular in order to solve for the gradient. This requires diversity in two-dimensional motion, e.g. avoiding a straight-line path. Because we assume that the centroid of $\mathbf{X}$ is on the origin, $\underline{\hat{\beta}}$ is unaffected by the value of c in (2).

It may be of interest to assess the reliability of $\underline{\hat{\beta}}$ by estimating $\mathrm{Cov}(\underline{\hat{\beta}})$. For example, this can be used to develop a hypothesis test with a statistical confidence level on whether the gradient is increasing or relatively flat, and this can be input to the control algorithm for contour following (Yu and Sadler, 2010). An approximation to the confidence level can be obtained as follows. Suppose that $\hat{\mathbf{P}}$ is unbiased. It follows that $\underline{\hat{\beta}}$ is unbiased and then using (3) we find $\mathrm{Cov}(\underline{\hat{\beta}}) = (\mathbf{X}^{+})\,\mathrm{Cov}(\underline{\hat{P}})\,(\mathbf{X}^{+})^{\mathrm{T}}$. Here $\mathrm{Cov}(\underline{\hat{P}})$ depends on the distribution of $\underline{\hat{P}}$. For example, if each $\hat{P}_i$ is independent and distributed exponentially with mean P_i, $\mathrm{Cov}(\underline{\hat{P}})$ is a diagonal matrix with $\mathrm{Cov}(\hat{P}_i, \hat{P}_i) = P_i^2$. Combining these results we obtain an estimate of $\mathrm{Cov}(\underline{\hat{\beta}})$, which can be used in an hypothesis test to determine whether $\underline{\beta}$ significantly deviates from zero.

4. Spatial decomposition and corresponding graph

In order to support the sampling described above, we develop a general method to decompose the environment into regions that balance several factors. These factors include the geometric complexity and scale of the physical environment along with the dimensions of the robot, and the desire to have larger regions and therefore limit the number of regions sampled. Making the regions small enough that they are generally convex and result in a densely packed decomposition is an additional factor. For a given decomposition, we compute an adjacency graph, and use this to formulate exploration algorithms that are encoded as graph traversals. The region decomposition and corresponding graph result in a unified approach that is applicable across many environments with a wide range of geometric complexity.

In this section, we describe our decomposition algorithm and the resulting graph. In Section 5, we couple this with autonomous exploration, map building, and RSS sampling. Consequently, region decomposition is not carried out only once for the entire mapped space. Rather, the decomposition is run repeatedly as new space is discovered, with regions that have been RSS-sampled remaining fixed while the remaining free space is decomposed. This is a key motivation for our use of clustering-based algorithms rather than more traditional Voronoi-based decomposition approaches.

Spatial decomposition is a well-studied problem in robotics and often reduces to a variant of the Voronoi diagram computation (Choset and Burdick, 1995; Thrun, 1998; Schwager et al., 2011). The Voronoi diagram can be computed efficiently in realistic settings as in Lau et al. (2010), where the authors propose an algorithm to update a Voronoi diagram based on input from a dynamic occupancy-grid representation of the environment. Owens and Fields (2010) used Voronoi information to extract higher-level semantic information about the environment in order to identify features such as hallways, doors, and rooms. Our approach draws on some elements of these, using an occupancy grid supplied by an underlying SLAM algorithm, but rather than a Voronoi partition, we employ a k-means-based clustering algorithm (Kanungo et al., 2002) to compute a decomposition of the environment where the desired cluster size is a function of the geometric complexity. This clustering is used repeatedly during exploration as new space is mapped and the occupancy grid expands. Once a region has been defined and the RSS within that region has been sampled, then that region is fixed over future map updates.

Given an occupancy grid representation of free space in the environment, the k-means clustering algorithm is used to find a decomposition of space into k regions. To determine the desired number of regions, let M be the total number of open cells in the occupancy grid $\mathcal{M}$, and δ_m be the resolution of the grid so that the total open area to be clustered is of size $M\delta_m^2$ square meters. Then, define the *characteristic length* ρ to be the approximate radius of a notional desired cell size, whose area is $\pi\rho^2$. Our target for the number of clusters is then

$$k = \frac{M\delta_m^2}{\pi\rho^2}. \tag{4}$$

For each iteration, the k-means algorithm receives the current free space occupancy grid and an initialization of the k region centers. The k-means algorithm perturbs the region centers until the cells induced by the k centers are approximately the same size, i.e. with characteristic length ρ. This roughly equates to finding the Voronoi cells that cover the free space, i.e. each region contains the set of points that are closest to its center. Choice of ρ is governed by the geometric feature size in the environment, the size of the robot, and the radio wavelength. In our experiments ρ is fixed. We discuss the choice of ρ below.

4.1. Decomposition algorithm

Our decomposition algorithm is summarized in Algorithm 1 with subroutine Algorithm 2. At any given time,

Algorithm 1 Decompose Environment

Require: Characteristic length ρ, free space cells $m_i \in \mathcal{M}$, unsampled region centers $\tilde{r}_{j_{old}}$

1: $k \leftarrow M\delta_m^2/\pi\rho^2$ {Compute number of regions}
2: $\hat{\mathcal{M}} = \mathcal{M}$ {Unassigned free cells for new regions}
3: **while** $k > \|\mathcal{R}\|$ **do**
4: $r_j \leftarrow$ UniformRandom($\hat{\mathcal{M}}$) for $j = 1 \ldots k$ {initialize new region centers}
5: $\mathcal{R}_j \leftarrow k$-means($\hat{\mathcal{M}}, r_j, r_{j_{old}}$) algorithm
6: **for all** $\mathcal{R}_j$ **do**
7: **if** $\bar{d}_{rj-m_i} \leq \rho$ **then**
8: $\mathcal{R} = \mathcal{R} \cup \mathcal{R}_j$
9: **else**
10: $m_i \in \mathcal{R}_j$ are removed from $\hat{\mathcal{M}}$
11: **end if**
12: **end for**
13: $k \leftarrow \hat{M}\delta_m^2/\pi\rho^2$
14: **end while**
15: $\mathcal{R}_j \leftarrow$ Ensure Region Continuity($\mathcal{R}_j$)
16: **return** $\mathcal{R}$ {Set of sampling regions}

Algorithm 2 Ensure Region Continuity

Require: regions $\mathcal{R}$

1: **for all** $\mathcal{R}_j \in \mathcal{R}$ **do**
2: **for all** $p_i \in \mathcal{R}_j$ **do**
3: **if** p_i has no neighbors labeled as same region **then**
4: $\mathcal{R}_j = \mathcal{R}_j \setminus p_i$ {Remove p_i from $\mathcal{R}_j$}
5: **end if**
6: **end for**
7: **end for**
8: **return** $\mathcal{R}_j$ {return the points that constitute a continuous region}

the decomposition is carried out over the currently known free space, characterized by the occupancy grid obtained from the underlying SLAM algorithm. A region is characterized by its centroid r_j, and the elements of the occupancy grid assigned to that cluster. We refer to two types of regions: sampled and unsampled. A sampled region refers to a region that the robot has entered and collected enough RSS samples. We refer to all other regions as unsampled, where the total number of samples is below the sampling threshold.

As exploration and sampling proceeds, the sampled regions are permanently fixed. Thus, the input to the decomposition algorithm includes the currently known free space occupancy grid which is not assigned to sampled regions, and an initialization of the region centers. Some of the region centers initializing the k-means algorithm are from unsampled regions created in the previous decomposition, which we refer to as $r_{j_{old}}$. After a clustering and sampling step, the robot will also have augmented the known free space. Thus, each time the clustering algorithm is executed, it is given an initial set of centers, composed of the old unsampled region centroids $r_{j_{old}}$, and a uniformly random set r_j taken over the remaining free space. We emphasize that the clustering algorithm uses $r_{j_{old}}$ for initialization, but these will generally shift as the clustering algorithm accommodates the newly discovered free space.

The k-means algorithm (line 5 of Algorithm 1) returns a candidate set of clusters, denoted by $\mathcal{R}_j$, $j = 1 \ldots k$, attempting to decompose into k regions with area roughly equal to $\pi\rho^2$. Because the clustering is carried out as exploration, mapping, and RSS-sampling proceeds, the occupancy grid may be disconnected (non-contiguous). To account for this, we then check the regions $\mathcal{R}_j$ for appropriate size and shape.

Algorithm 1, line 7, compares the average point-to-centroid distance to a threshold for each region. We reject any region whose average point-to-centroid distance is greater than ρ. This pruning strategy favors regions that are roughly circular and results in densely packed regions that are typically convex, as shown in our experiments subsequently. Once identified, grid cells that form poorly shaped regions are removed from the list of unsampled open grid cells in line 10. The loop will execute until all of the regions created by k-means meet the average centroid-to-point distance constraint.

A second check is then carried out via the call to Algorithm 2 in line 16. This simple filtering step removes single occupancy grid cells that are disconnected from their assigned region, i.e. they have no neighbors within their assigned region. We find experimentally that disconnected grid cells can occur, for example, near barriers. Any grid cells pruned from the current clustering will be retained in the free space occupancy grid for subsequent clustering as the robot continues its exploration.

At completion, Algorithm 1 returns the region decomposition in the set $\mathcal{R}$. We then analyze the region decomposition to compute the adjacency graph for this decomposition of the known environment. Adjacency between regions is based on the ability of the robot to navigate from one region to the other, where we assume regions are adjacent if the grid cells of two regions neighbor each other. This is informed by our choice of ρ. If regions are too large, then regions created near narrow spaces might not have grid cells neighboring each other. Thus, while the characteristic region length ρ should be large enough to allow independent RSS samples (i.e. sufficient spatial separation), it also needs to be small enough to allow for regions to be roughly convex.

The exploration algorithm will use the adjacency graph to inform its next mobility step, and the entire process is repeated until the base station connectivity area has been mapped.

5. Exploration algorithms

To map out the base station connectivity area $\mathcal{C}$ in an efficient way, we combine exploration, RSS sampling, RSS

gradient estimation, and the process of graph generation described in Section 4. We compare exhaustive exploration with a connectivity contour seeking approach. The exhaustive approach yields a complete decomposition of $\mathcal{C}$ with RSS measured in each region, whereas the contour seeking method yields a decomposition of $\mathcal{C}$ that ideally encompasses only the connectivity boundary. If only the boundary is desired, the contour seeking method can be much more efficient than exhaustive mapping.

Exploration proceeds by updating the environment map in the form of the occupancy grid, a decomposition is carried out over the current free space and an updated graph is computed as described in Section 4, and then the next region for RSS sampling is selected. The robot moves to this region and performs RSS sampling, and the process is repeated until the entire base station connectivity area is mapped. The decomposition occurs after the robot has finished RSS sampling a region and updating the map. Regions that have been sampled are kept because we assume that the environment is static. Thus, the robot creates new regions incrementally, with the criterion for choice of the next region to RSS sample dictated by the overall exploration goal.

5.1. Exhaustive exploration

An exhaustive exploration algorithm requires that the robot visit and sample every region in the component of the graph connected to the base station. This essentially constitutes a solution to the Traveling Salesman Problem. However, because a map of the entire environment is not available *a priori*, we instead pursue a greedy heuristic.

The algorithm is summarized in Algorithm 3. Given a partial map of the environment, a decomposition is computed to yield sample regions $\mathcal{R}$, and its adjacency graph is computed. Exploration proceeds by finding the closest unsampled region in $\mathcal{R}$ that is connected to the base station through the adjacency graph. The robot drives to this region, updates the SLAM algorithm, and makes RSS measurements. A new decomposition is computed based on the updated occupancy grid, minus the regions that are sampled which are permanently fixed for the experiment. This process continues until there are no unsampled regions connected to the base station.

5.2. Contour-seeking exploration

The goal of the contour-seeking exploration algorithm, summarized in Algorithm 4, is to efficiently drive to and sample RSS only along the outer contour of the base station's connectivity area $\mathcal{C}$. We enable this behavior by using the RSS gradient to predict RSS averages inside unsampled regions that are adjacent to the sampled region currently occupied by the robot. After sampling a region $\mathcal{R}_j$, the robot chooses the next region to sample $\mathcal{R}_{next}$ based on which of the adjacent regions has the lowest predicted RSS. The RSS prediction assumes that the negative of the gradient is the direction of steepest descent and therefore points toward the neighboring region with the lowest RSS. If all adjacent regions have been sampled already, the robot moves to the region with the lowest RSS that is still inside the connectivity area of the base station and continues.

Algorithm 3 Exhaustive Exploration

Require: Initial map $\mathcal{M}$
1: $\mathcal{R} \leftarrow$ Decompose Environment($\mathcal{M}$)
2: Compute adjacency graph
3: $\tilde{\mathcal{R}} \leftarrow$ Unsampled regions connected to base station
4: **while** $\exists\, \mathcal{R}_j \in \tilde{\mathcal{R}}$ **do**
5: Find closest unsampled region $\mathcal{R}_{closest} \in \tilde{\mathcal{R}}$
6: Drive to $\mathcal{R}_{closest}$ and collect RSS samples
7: **if** Average RSS in $\mathcal{R}_{closest} < \tau$ **then**
8: Disconnect $\mathcal{R}_{closest}$
9: **end if**
10: $\mathcal{R} \leftarrow$ DecomposeEnvironment($\mathcal{M}$)
11: Compute adjacency graph
12: $\tilde{\mathcal{R}} \leftarrow$ Unsampled regions connected to base station
13: **end while**

Upon initialization near the base station, the robot will move away from the base station along a line of estimated steepest RSS descent until it encounters a region that is below the connectivity threshold τ dB. With this crossing of the connectivity threshold, the robot has encountered the base station connectivity boundary. When the connectivity boundary is crossed, the gradient is used to predict a neighboring region whose RSS will be highest, i.e. will ideally lead to a region inside the connectivity area. Proceeding in this manner, the connectivity boundary will be discovered and regions adjacent to the connectivity boundary will be mapped as the robot zig-zags along this boundary. As the robot proceeds to discover the connectivity boundary, interior regions with RSS above the threshold τ may be pruned from the graph. The remaining leaf nodes define the connectivity boundary.

The contour seeking control strategy results in fewer total regions sampled than the exhaustive approach. As with the exhaustive search, only regions connected to the initial region are considered for sampling. With the contour seeking method some areas within the connectivity area will not be identified for sampling. We assume that the area within the boundary has good connectivity, while noting that in some complex environments this might not be strictly true.

6. Experimental configuration

Our experiments were performed using a *Packbot*, shown in Figure 1, equipped with a skid-steer drive system, and on board computation. Both IEEE 802.11 and *Zigbee* radios were on the platform, and the *Zigbee* provided the RSS measurements. The *Zigbee* operated at 2.4 GHz with corresponding wavelength of 12.5 cm. The Packbot was also

Algorithm 4 Contour Seeking Exploration

Require: Initial map $\mathcal{M}$
$\mathcal{R} \leftarrow$ Decompose Environment($\mathcal{M}$)
Compute adjacency graph
$\tilde{\mathcal{R}} \leftarrow$ Unsampled regions connected to base station
$\mathcal{R}^p \leftarrow$ Unsampled perimeter regions
while $\exists\, \mathcal{R}_j \in \mathcal{R}^p$ **do**
  if $\exists \tilde{\mathcal{R}}$ Adjacent to $\mathcal{R}_{next}$ **then**
    $\mathcal{R}_{next} \leftarrow$ lowest predicted region in Adjacent($\mathcal{R}_{last}$)
  else
    $\mathcal{R}_{next} \leftarrow$ lowest predicted region in $\tilde{\mathcal{R}}$
  end if
  Drive to $\mathcal{R}_{next}$ and collect RSS samples
  if Average RSS in $\mathcal{R}_{next} < \tau$ **then**
    Disconnect $\mathcal{R}_{next}$
  end if
  $\mathcal{R} \leftarrow$ DecomposeEnvironment($\mathcal{M}$)
  Compute adjacency graph
  $\mathcal{R}_{last} \leftarrow \mathcal{R}_{next}$
  $\tilde{\mathcal{R}} \leftarrow$ Unsampled regions connected to base station
  $\mathcal{R}^p \leftarrow$ Unsampled perimeter regions
end while

equipped with a Hokuyo UTM-30LX scanning laser range finder with 30 m range and Microstrain 3DM-GX2 IMU, utilized by the SLAM algorithm. A *Zigbee* transmitter was used as a fixed base station, periodically broadcasting a beacon at 12 Hz, so this defines the maximum RSS measurement rate. Note that at lower signal-to-noise ratio some beacon packets may be undetected and therefore some RSS measurements lost. For each successfully received beacon packet we recorded the current position (as estimated via SLAM) and the reported RSS.

Autonomous SLAM and navigation were implemented by leveraging libraries running on the open-source *Robotics Operating System* (ROS). These libraries enabled the robot to dynamically build a map and navigate throughout an initially unknown 2D environment. In each experiment the robot was initially deployed near the base station, without any prior map or knowledge of the environment (unless otherwise specified). Thus, the exploration, mapping, region segmentation, RSS sampling, and connectivity area discovery were carried out autonomously and simultaneously.

6.1. Experimental parameters

The parameters in Table 1 are consistent across all experiments. The *ZigBee* radio reported RSS measurements periodically at 12 Hz. If no measurement was available, e.g. because of dropped packets, this was also reported. At each measurement time the robot position and RSS measurement were recorded. The map resolution δ_m was determined by the choice of ROS-based SLAM algorithm.

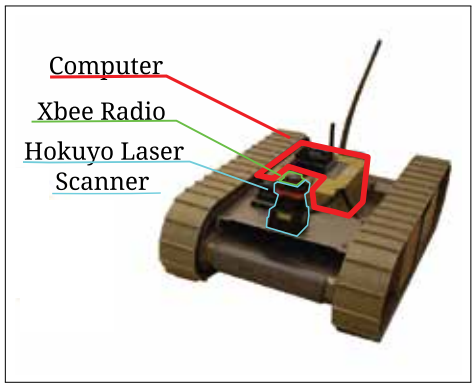

Fig. 1. The Packbot experimental platform, including laser scanner and IMU for SLAM, and *Zigbee* radio for RSS measurements.

Table 1. Table of parameters.

Parameter	Value
RSS sample rate	12 Hz
Map resolution (δ_m)	0.25 m
Characteristic region length (ρ)	0.8 m
Robot length	0.7 m
Robot width	0.4 m
Receiver placement	0.23 m off-center
Connectivity threshold (τ)	Variable (dB)
RSS sampling threshold	Variable

The characteristic length ρ is a critical parameter that specifies the desired region size for spatial decomposition. Choice of ρ is influenced by the geometric complexity of the environment, and the size and maneuverability of the platform. Experimental decompositions with different values of ρ showed that $\rho = 0.8$ m was a good choice because the resultant regions are large enough for good separation of RSS measurements while small enough to allow the robot to form regions even in confined areas. For example, if ρ is too large then, regions may take non-convex and irregular shapes; this may be acceptable in a given application, although it somewhat complicates the adjacency graph definition and trajectory planning. We chose $\rho = 0.8$ m, which resulted in region decompositions whose region shapes were generally convex despite the geometric complexity of various test environments.

The Packbot has a relatively large $0.7\,\text{m} \times 0.4\,\text{m}$ footprint. To facilitate RSS sampling in a confined space, we mounted the *Zigbee* radio antenna 0.23 m in front of the robot's center of rotation. A simple rotation in place then yielded a set of spatially diverse RSS samples, and this maneuver was executed within each region (see Figure 8).

The base station connectivity area is defined by an RSS threshold τ, that specifies the acceptable quality of a communications link, and depends on the transmit power and propagation loss. Lower τ implies that more propagation loss is acceptable, and results in a larger connectivity area

for a fixed base station transmit power. We experimented with different values for τ as described below.

7. Connectivity area mapping experiments

In this section we describe two connectivity area mapping experiments, outdoors in an uncluttered courtyard, and indoors with obstacles.

7.1. Open outdoor environment

Experiments were conducted in an open courtyard, as illustrated in Figures 2a, 2b, and 3. The black areas along the right and top are low concrete partitions (obstacles) in the courtyard of a multi-story building. Figure 2a shows the region decomposition result for one run of the exhaustive exploration algorithm. To test the decomposition algorithm in a controlled manner, the map was generated a priori for this experiment. The regions are roughly uniformly shaped in this uncluttered area. Some small spatial gaps occur that are not interior to any region and are much less than the characteristic length ρ. The corresponding adjacency graph is shown in Figure 2b. The region centroids are plotted as squares, with lines indicating adjacent regions.

The contour seeking Algorithm 4 was tested in the courtyard, with the RSS threshold τ set such that the connectivity area was confined within the size of the courtyard. An experimental run is depicted in Figure 3 where base station signal source is indicated by a dot and the resulting contour is shown as a dashed line. The average RSS per region is mapped to the gray scale shown. The robot is initially placed near the base station signal source. Once the robot has sampled a region, it follows the gradient (denoted by a outlined arrow) to the region of lowest estimated average RSS. It continues to do this until it samples a region with RSS lower than τ, which first occurs at about location $(-4, 1)$ m. Then, the robot retreats (denoted by a solid arrow) to an unexplored region which is estimated to have average RSS above τ. The robot then works its way around the environment, alternating between advance-retreat across the boundary, mapping the connectivity boundary (shown as a dashed cyan line). As shown in the figure, roughly 30% of the courtyard area remains unsampled, illustrating the efficiency gain using the contour following approach. The efficiency gain versus exhaustive exploration will grow as the overall connectivity area becomes larger, e.g. with a higher power base station.

7.2. Complex indoor environment

Experiments were carried out in several different indoor environments. A challenging example is shown in Figure 4, conducted inside a fire house. This room had concrete block walls, and four large metal garage doors. There were also obstacles including metal lockers in the center of the room (shown in black), and a large table along one wall. Thus, the environment presented both geometric challenges as well as

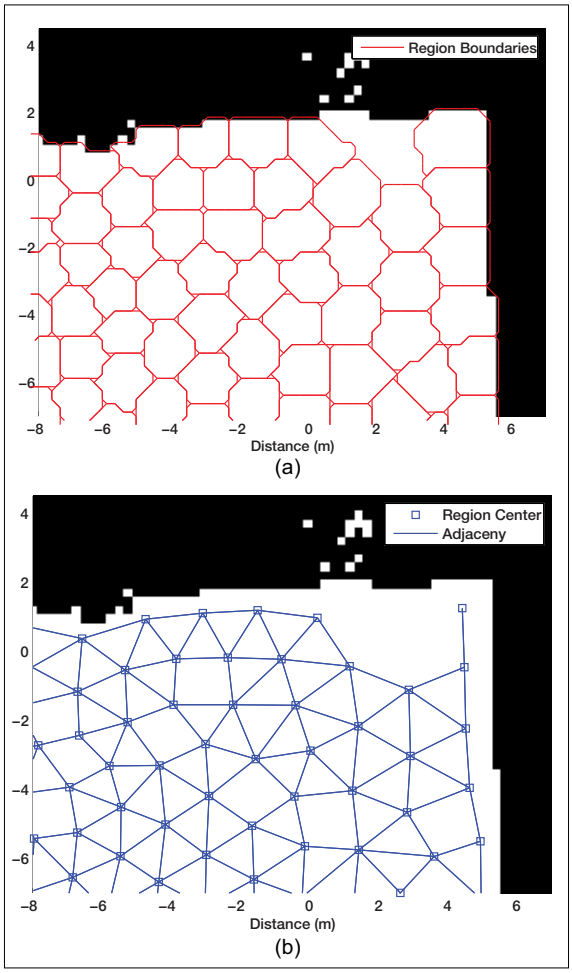

Fig. 2. Outdoor courtyard experimental decomposition results. (a) Sampling region boundaries. (b) The corresponding adjacency graph. Squares represent nodes and lines represent adjacencies.

complex radio propagation. For example, note that there is relatively high RSS even in some non-line of sight regions due to the radio reflectivity from the large amount of metal in the environment.

A example run of the contour seeking algorithm is depicted in Figure 4. Note that in this experiment, the robot does not smoothly track the trajectory near $(-6, 2)$ m. However, the algorithm is robust. The robot successfully maps out the connectivity area, despite noisy gradient estimates and obstacles intersecting the connectivity boundary.

8. Varying the RSS threshold

The connectivity area is a function of the RSS threshold τ, with lower τ resulting in an extended area. We illustrate this using two threshold values in the same environment,

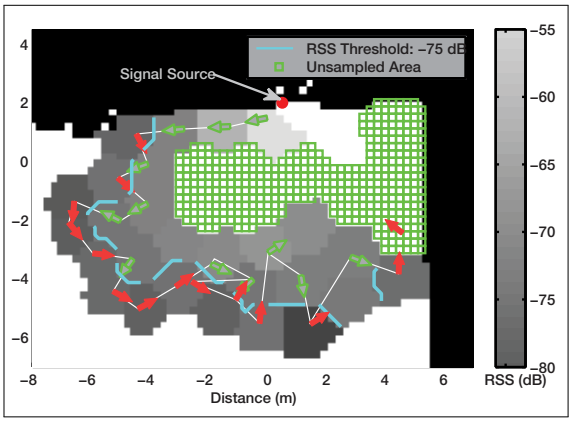

Fig. 3. Outdoor courtyard experiment using the contour seeking Algorithm 4. Obstacles are black in this overhead view of the environment. The dashed line indicates the connectivity boundary, with arrows indicating estimates of the RSS gradient as the exploration evolves. Average RSS per region is mapped to gray scale.

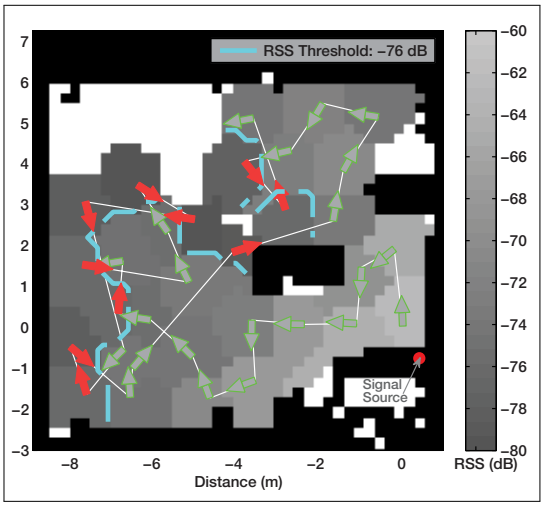

Fig. 4. Indoor fire house experiment. The contour seeking algorithm was used to find the connectivity area in this complex environment.

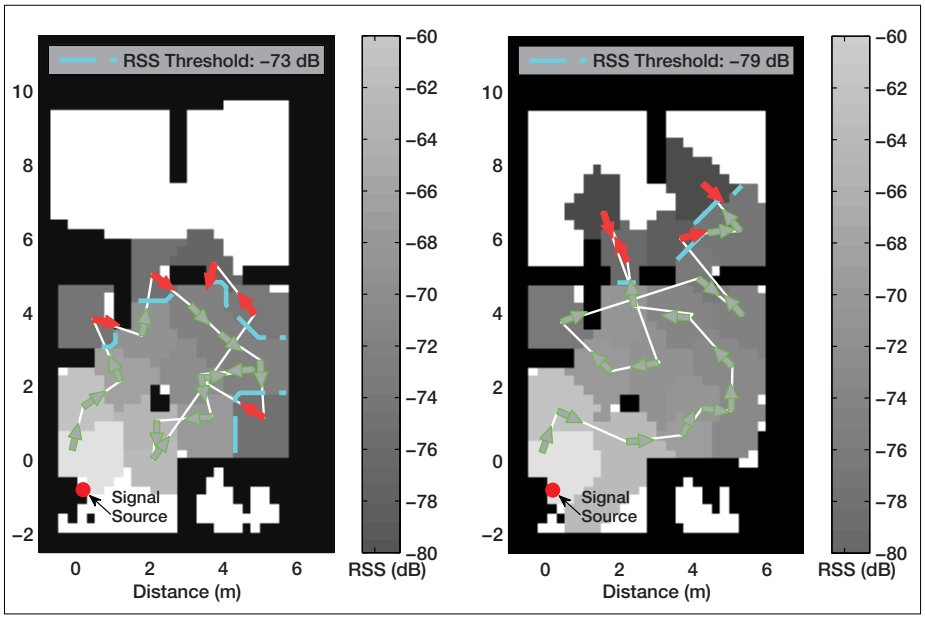

Fig. 5. Indoor connectivity areas mapped with the contour seeking algorithm, with different values for RSS threshold τ. (a) Higher RSS threshold results in a smaller connectivity area. (b) Lower RSS threshold results in a larger connectivity area, including LOS and NLOS regions.

a concrete block building with window spaces, and obstacles including wooden desks and a large PVC pipe. Two experiments are shown in Figure 5a and (b).

In Figure 5(a), $\tau = -73$ dB. Using the contour following algorithm, the robot maps a connectivity area that is almost exclusively in LOS of the base station transmitter. In Figure 5b τ is lowered to -79 dB. As a result the connectivity area is larger and encompasses line of sight and non-line of sight regions.

9. Base station siting

Exhaustive exploration provides a complete picture of the connectivity area, with each region characterized by its average RSS. Experimental results are shown in Figure 6a

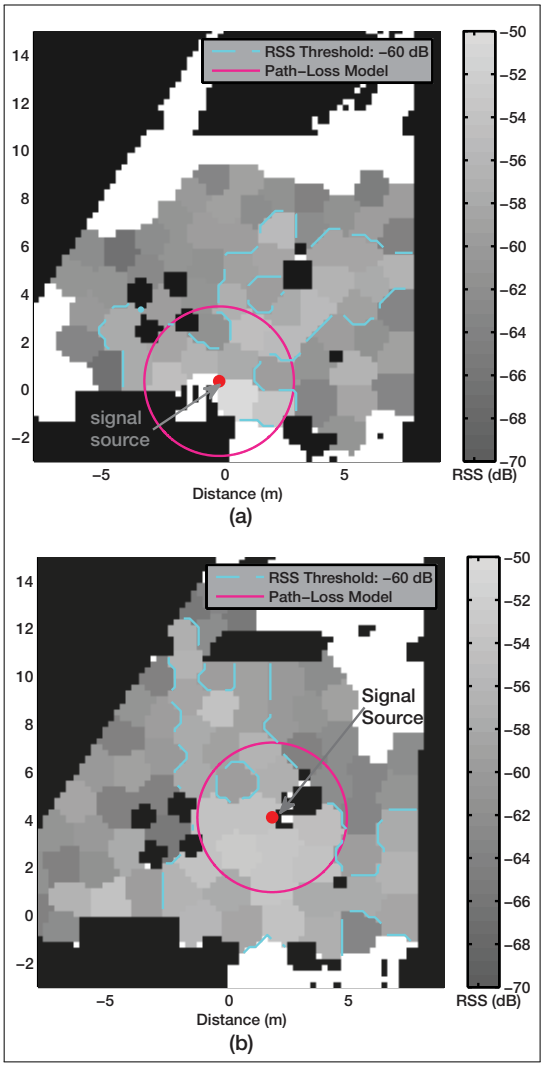

Fig. 6. Indoor connectivity area maps for two different base station sites. (a) Base station sited at $(-0.25, 0.35)$. (b) Base station sited at $(1.8, 4.1)$.

and (b) in a large office building lobby. The room shape is somewhat irregular as indicated by the white area with walls in black. There are reinforced concrete walls, exterior walls with windows, and irregular ceiling height. Chairs, tables, and structural columns serve as obstacles for the robot. Overall, this environment has very complex radio propagation.

The exhaustive exploration Algorithm 3 was used for two different base station source locations as shown in the figures. To illustrate the complexity of the environment, an RSS threshold contour is drawn with threshold τ set to -60 dB. This threshold was chosen to highlight the irregular connectivity area that results, including shadowing effects due to obstacles. The contours are not obvious from the room geometry. Note how the average estimated RSS in some regions is below the threshold, even when they are rather close to the base station and have LOS propagation.

Also shown in Figure 6a and (b) are circles showing conservative estimates of the connectivity boundary based on a simple disk model for the radio propagation. A path loss model was fitted to the data collected during the experiment shown in Figure 6a. In this figure the radius d that solves $\tau = L_0 - 10\alpha \log_{10} d$ represents a conservative estimate of the connectivity boundary, where $L_0 = -50$ dB and $\alpha = 2$. Assuming that the path loss characterizes the environment, the same disk is plotted in Figure 6b. Although these are based on averages taken within the environment, the disk represents a weak prediction of the actual connectivity area.

10. RSS sampling

To obtain a good estimate of the RSS and its gradient within a region, the robot should take sufficiently many spatially separated measurements, as discussed in Section 3.2. In practice it is not good to assume that either the samples are sufficiently spaced as to be uncorrelated or that the spatial correlation is known *a priori*. In our scenario, neither assumption would necessarily hold for many reasons including imperfect odometry (motion slippage, non-constant velocity, etc.) and insufficient sample spacing distances between consecutive samples. However, we can use the sample variance of the RSS measurements to determine when a region has been sufficiently sampled.

To study the required sample size experimentally, consider a collection of N RSS measurements $\hat{P}_j, j = 1, \ldots, N$, taken within a region. The size of N depends on the sampling rate (nominally 12 Hz in our experiments), the exploration path of the robot within the region, and the number of dropped packets. In the results we present in this section, we only use measurements that were made while the robot was moving to improve the spatial diversity of the samples. Although the spatial decomposition yields regions of roughly the same size, the robot spends varying amounts of time within each region and therefore the number of samples per region are not identical. Figure 7 shows the samples per region, and the corresponding spatial distance between consecutive samples, for the indoor experiment depicted in Figure 8. The robot makes around 50 to 200 RSS samples per region. The consecutive sample spacing is typically less than half a wavelength (6.25 cm at 2.4 GHz) because the 12 Hz RSS measurement rate is high relative to the robot speed. However, as we show below, these samples are sufficient in number and spacing for good estimation of the RSS average in each region.

Figure 8 shows the robot trajectory, where RSS sample sites within the same region are plotted with the same color. The robot rotation for spatial sampling is evident in the looping trajectory. We have previously presented this

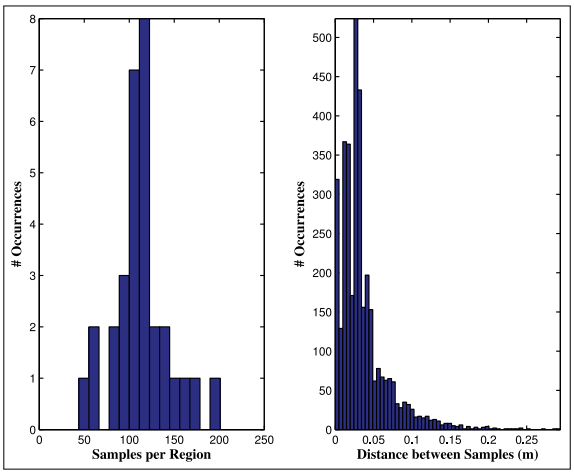

Fig. 7. Left: Histogram of the number of RSS samples taken per region in an indoor environment (cf. Figures 4 and 8). Right: Histogram of consecutive sample spacing, indicating that many samples have spacing less than one wavelength.

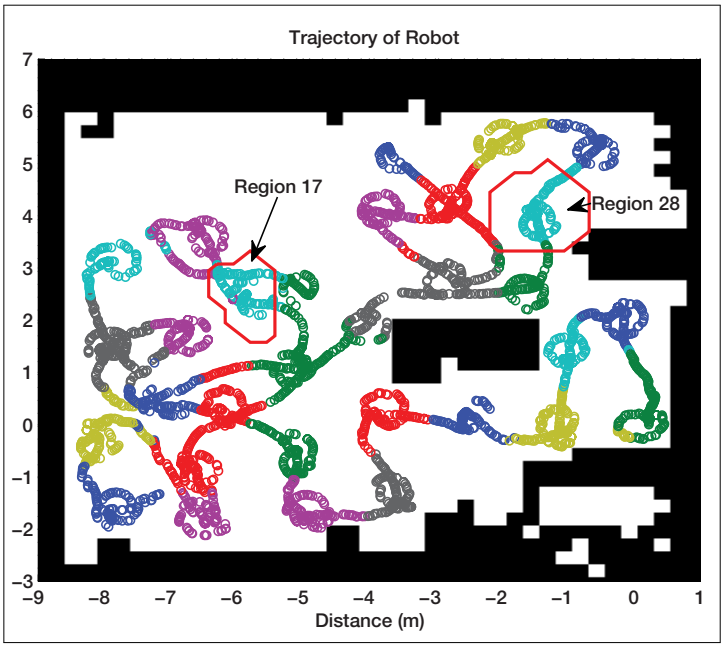

Fig. 8. Exploration path with RSS sampling locations for an indoor fire house environment (cf. Figure 4). Samples within a region have the same color. The loops are samples taken during robot rotation.

experiment in Section 7.2, Figure 4. Consider the samples taken in region 17 and region 28. The sampling of region 17 yields $N = 121$ measurements while that of region 28 yields $N = 114$. Although the values for N are close, the sampling trajectories are quite different. Recalling from Section 3.2 that $\mathbf{X}$ is the centered matrix of sampling locations, then a measure of the spread of the samples within a region is $\Delta = \frac{1}{N}\lambda_1\lambda_2$, where λ_i is the i^{th} eigenvalue of the 2×2 matrix $\mathbf{X}^T\mathbf{X}$. The greater this metric, the more spread out the RSS samples are within the region. Here, region 17 yields ($\Delta = 0.46$) whereas region 28 yields ($\Delta = 0.38$), indicating that region 17 has slightly better spatial spread in the RSS sampling locations. Increased spatial separation of the RSS samples improves the RSS and gradient estimate.

The top panels of Figure 9 depicts the sampling trajectory for regions 17 and 28. Time evolution is depicted by color transformation from dark (earlier samples) to light (later samples). The middle panels plot the RSS samples that showing the significant small scale variation in RSS with mobility. Also on the middle two panels we overlay

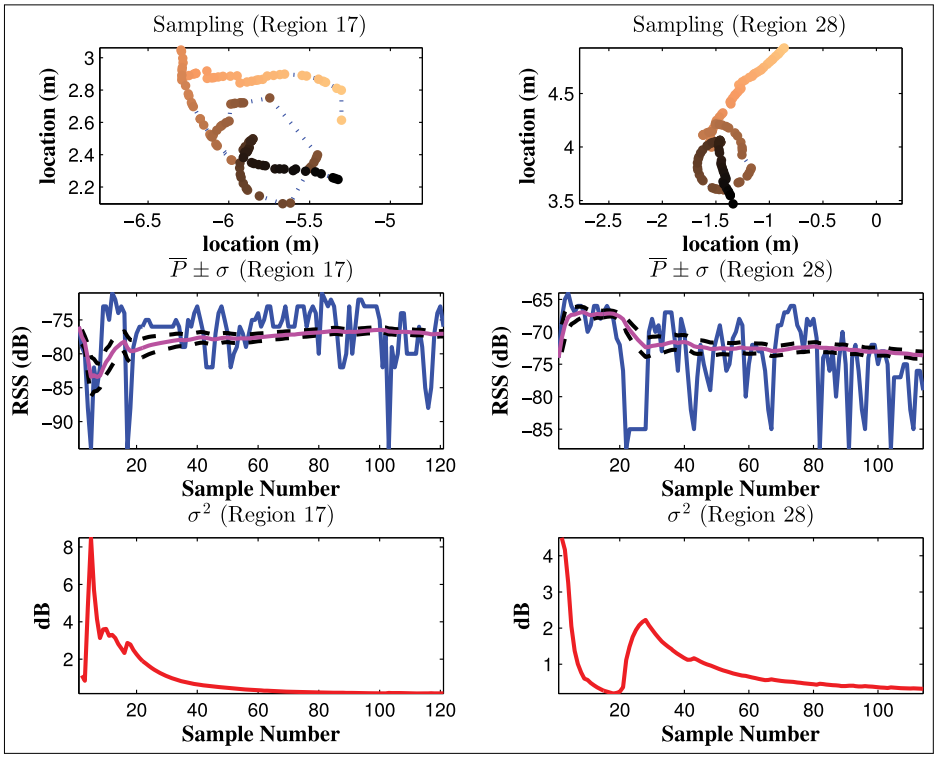

Fig. 9. Detailed look at two regions in an indoor environment (cf. Figure 4). Top row: exploration path. Middle row: RSS measurements and evolution of RSS estimate. Bottom row: Evolution of the variance of the RSS mean.

the evolution of the RSS mean (solid line) as the sample size grows, calculated by $\overline{P}_j = \frac{1}{j}\sum_{i=1}^{j}\hat{P}_i$. The evolving RSS mean estimate is bracketed by a one standard deviation interval (dashed lines) given by $\sigma_j^2 = \mathrm{Var}(\overline{P}_j) = \frac{1}{j}\mathrm{Var}_j(\hat{P})$. The unbiased sample variance is $\mathrm{Var}_j(\hat{P}) \approxeq \frac{1}{j-1}\sum_{i=1}^{j}(\hat{P}_i - \overline{P}_j)^2$. This approximation does not consider the effect of correlated samples.

The bottom two panels in Figure 9 plot the evolving sample variance of the RSS mean estimate. In region 17 the variance drops quickly, indicating high confidence in the RSS mean estimate as the sample size grows. In region 28, the variance of the RSS mean has more interesting behavior. It drops rapidly and then rises sharply again before finally decaying. Looking at the map in Figure 8, we see that the robot mobility introduces an additional barrier between it and the base station around sample number 20. The additional barrier results in a sharp drop in the RSS, with a corresponding sharp rise in the variance of the RSS mean within the region. However, as the robot continues to move and further measurements are made the variance dies down again, leading to a good estimate of the RSS mean for that region.

Figure 10 summarizes the variance of the RSS estimate $\mathrm{Var}(\overline{P}_j)$ for the entire experiment. The left panel shows the variance for each region, plotted against the above metric for spatial separation. It is clear that increased spatial spread in the data results in lower variance. The right panel depicts the variance for each region as a function of the total number of RSS samples collected, showing a clear preference for more samples. Note that the spatial spread can be calculated online, so that the exploration algorithm could be modified to continue intra-region sampling until a desired spatial spread and/or total sample size is achieved.

11. Conclusions

We have developed and demonstrated new algorithms for mapping the physical boundary of a radio connectivity area within a map. Our approach uses region decomposition and sampling to estimate the RSS average in unexplored regions. Heuristics for computing good regions and RSS sampling were postulated. These heuristics were applied to develop a region decomposition algorithm. We demonstrated contour seeking and exhaustive exploration algorithms that exhibit robustness to environmental complexity. The resulting control algorithms are applicable to a wide variety of scenarios involving a base station as they do not require knowledge of the propagation environment beyond basic fading assumptions and do not require a map *a priori*.

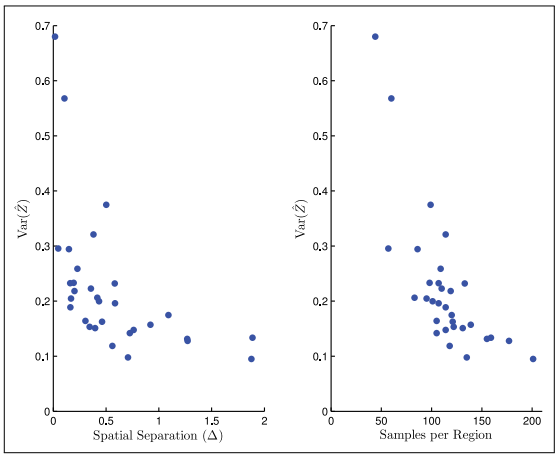

Fig. 10. Variance of RSS mean estimate decreases as spatial separation (Δ) increases (left) and as the number of samples increases (right).

Our methods naturally fit into and extend autonomous exploration and mapping to characterize network connectivity. Some avenues for further research include coupling RSS with a particular physical layer radio technology, e.g. coupling with packet loss probability or measures of quality of service. Larger-scale outdoor experiments are of interest, e.g. in establishing coverage areas for cellular telephone systems that are rapidly deployed in an emergency. Also, our method could be extended to a multiple base station system. We have assumed a constant transmit power at the base station, so an extension to incorporate power control could couple quality of service guarantees as agents move in the connectivity region, or to service agents during base station hand off as they traverse from one cell to another. More generally, base station technology such as antenna arrays and frequency diversity could also be incorporated. We have shown how the number of RSS samples needed can be estimated during collection, and this could be incorporated into the exploration and decomposition algorithms. Finally, we note that in different physical environments it could be advantageous to spatially adapt the size of sampling regions, ρ.

Funding

This research received no specific grant from any funding agency in the public, commercial, or not-for-profit sectors.

References

Choset H and Burdick J (1995) Sensor based planning - I: The generalized voronoi graph. In: *IEEE International Conference on Robotics and Automation (ICRA)*, pp. 1649–1655.

Draper N and Smith H (1998) *Applied Regression Analysis*, 3rd edn. New York: John Wiley & Sons.

Fink J and Kumar V (2010) Online methods for radio signal mapping with mobile robots. In: *IEEE International Conference on Robotics and Automation (ICRA)*, pp. 1940–1945. DOI: 10.1109/ROBOT.2010.5509574.

Goldsmith A (2005) *Wireless Communications*. New York: Cambridge University Press.

Hsieh MA, Cowley A, Kumar V and Taylor CJ (2008) Maintaining network connectivity and performance in robot teams. *Journal of Field Robotics* 25(1-2): 111–131. DOI: 10.1002/rob.20221.

Kanungo T, Mount D, Netanyahu N, Piatko C, Silverman R and Wu A (2002) An efficient *k*-means clustering algorithm: analysis and implementation. *IEEE Transactions on Pattern Analysis and Machine Intelligence* 24(7): 881–892.

Lau B, Sprunk C and Burgard W (2010) Improved updating of euclidean distance maps and voronoi diagrams. In: *IEEE/RSJ International Conference on Intelligent Robots and Systems (IROS)*, pp. 281–286. DOI: 10.1109/IROS.2010.5650794.

Lindhe M, Johansson KH and Bicchi A (2007) An experimental study of exploiting multipath fading for robot communications. In: *Proceedings of Robotics: Science and Systems*.

Mostofi Y, Malmirchegini M and Ghaffarkhah A (2010) Estimation of communication signal strength in robotic networks. In: *IEEE International Conference on Robotics and Automation (ICRA)*, pp. 1946–1951. DOI: 10.1109/ROBOT.2010.5509677.

Owens J and Fields M (2010) Incremental region segmentation for hybrid map generation. In: *Army Science Conference*, pp. 281–286.

Proakis J (1995) *Digital Communications*. Englewood Cliffs, NJ: Prentice-Hall.

Rappaport T (2001) *Wireless Communications - Principle and Practice*. Englewood Cliffs, NJ: Prentice-Hall.

Schwager M, Rus D and Slotine J (2011) Unifying geometric, probabilistic, and potential field approaches to multi-robot deployment. *The International Journal of Robotics Research* 30(3): 371–383.

Thrun S (1998) Learning metric-topological maps for indoor mobile robot navigation. *Artificial Intelligence* 99(1): 21–71.

Wadhwa A, Madhow U, Hespanha J and Sadler BM (2011) Following an RF trail to its source. In: *49th Annual Allerton Conference on Communication, Control, and Computing*, pp. 580–587.

Yu P and Sadler B (2010) Received signal strength gradient estimation for mobile networks. In: *Military Communication Conference (MILCOM)*, pp. 519–523. DOI: 10.1109/MILCOM.2010.5680357.

Zickler S and Veloso M (2010) RSS-based relative localization and tethering for moving robots in unknown environments. In: *IEEE International Conference on Robotics and Automation (ICRA)*, pp. 5466–5471. DOI: 10.1109/ROBOT.2010.5509975.

Supervisory Control of Multiple Robots: Human-Performance Issues and User-Interface Design

Jessie Y. C. Chen, Michael J. Barnes, and Michelle Harper Sciarini

IEEE Transactions on Systems, Man, and Cybernetics - Part C: Applications and Reviews, 41(4) (2011)

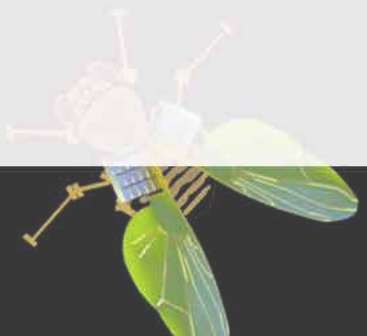

Supervisory Control of Multiple Robots: Human-Performance Issues and User-Interface Design

Jessie Y. C. Chen, Michael J. Barnes, and Michelle Harper-Sciarini

***Abstract*—The purpose of this paper is to review research pertaining to the limitations and advantages of supervisory control for unmanned systems. We identify and discuss results showing technologies that mitigate the observed problems such as specialized interfaces, and adaptive systems. In the report, we first present an overview of definitions and important terms of supervisory control and human-agent teaming. We then discuss human performance issues in supervisory control of multiple robots with regard to operator multitasking performance, trust in automation, situation awareness, and operator workload. In the following sections, we review research findings for specific areas of supervisory control of multiple ground robots, aerial robots, and heterogeneous robots (using different types of robots in the same mission). In the last section, we review innovative techniques and technologies designed to enhance operator performance and reduce potential performance degradations identified in the literature.**

***Index Terms*—Human-agent teams, human–robot interaction (HRI), levels of automation (LOAs), robotics control, supervisory control, unmanned vehicles, user-interface design.**

I. Introduction

UNMANNED vehicles (UVs), including unmanned air vehicles (UAVs) and unmanned ground vehicles (UGVs), are becoming an essential part of the battlefield. The Armed Forces have large programs for developing robotic systems [1] that encompass aerial, sea, ground, and subterranean applications. Future warfare will depend on collaboration among UVs, not only within services but also between services, and eventually, among allied partners. Battlefield collaborations will involve hundreds of UVs, as well as an equal number of manned systems requiring novel techniques such as call center approaches, to monitor the unfolding decision environment. The complexity and sheer number of mixed assets in future operations will require increased autonomy and problem-solving capabilities for unmanned systems [2]. Furthermore, to maximize human resources, it will be desirable to designate a single operator to supervise multiple UVs, adding to his or her already heavy task loading [3], [4]. However, having systems with automated behaviors introduces its own set of problems, including overreliance on the automated system, potential situation awareness (SA) degradations, and possible loss of skills to perform the tasks manually when automation fails [5]–[7].

The purpose of this paper is to review research pertaining to the limitations and advantages of supervisory control for UV systems. More importantly, we identify and discuss results showing technologies that mitigate the observed problems such as specialized interfaces and adaptive systems. In the following section, we first present an overview of definitions and important terms of supervisory control and human-agent teaming. We then discuss human performance issues in supervisory control of UVs with regard to operator multitasking performance, trust in automation, SA, and operator workload. In Sections III–V, we review research findings for specific areas of supervisory control of UAVs, UGVs, and heterogeneous UVs (using both UAVs and UGVs in the same mission). Finally, in Section VI, we review innovative techniques and technologies designed to enhance operator performance and reduce potential performance degradations identified in the literature.

A. Supervisory Control—Overview

Supervisory control of technology may be defined from the perspectives of human information processing and the operator's role in a given task, by the level of automation (LOA) employed, or by the types of operator interactions with the automated technology.

1) Operator's Role: Humans play a variety of roles in supervisory tasks including: planning, teaching, monitoring, intervening, and learning [8]. These roles typically occur in the temporal order described, and may repeat throughout a supervisory task. Sheridan [8] describes these roles in sequence as follows.

1) Planning the course of action before the automation is activated.
2) Instructing the computerized technology to perform a task in a particular manner.
3) Monitoring the instructed automation to be sure it goes as planned.
4) Intervening, when necessary, to adjust or correct the automation.

Manuscript received August 3, 2009; revised November 30, 2009 and February 24, 2010; accepted June 23, 2010. Date of publication July 29, 2010; date of current version June 17, 2011. This work was supported by the U.S. Army's Army Technology Objective (ATO): Safe Operations of Unmanned Reconnaissance in Complex Environments (SOURCE). This paper was recommended by Associate Editor P. J. Sanz.

J. Y. C. Chen and M. J. Barnes are with the U.S. Army Research Laboratory, Human Research and Engineering Directorate, Aberdeen Proving Ground, Aberdeen, MD 21005-5425 USA (e-mail: jessie.chen@us.army.mil; michael.barnes@hua.army.mil).

M. Harper-Sciarini is with the APRISE, LLC, Winter Springs, FL 32708 USA (e-mail: mharper-sciarini@knights.ucf.edu).

Color versions of one or more of the figures in this paper are available online at http://ieeexplore.ieee.org.

Digital Object Identifier 10.1109/TSMCC.2010.2056682

TABLE I
TEN LEVELS OF AUTOMATION (LOA)*

High	10	**Full Autonomy**: The computer makes all decisions, acts autonomously, and ignores the human operator.
	9	The computer informs the human operator, only if it "decides" to.
	8	The computer informs the human operator, only if asked to.
	7	The computer executes automatically, then informs the human operator as necessary.
	6	Allows the human a limited amount of time to veto an action before it is automatically executed.
	5	The computer executes the suggestion with approval from the human operator.
	4	The computer suggests one alternative.
	3	The computer narrows the decision-making to a few selections.
	2	The computer offers a complete set of decision / action alternatives.
Low	1	**Manual Operation**: The computer offers no assistance to the human operator, who must make all decisions and take all actions.

*Modified from [7, Table I].

5) Learning from the performance and outcomes of the automation in order to improve planning for future interactions.

As task complexity increases, there is greater need for planning and teaching. In addition, the need for monitoring and intervening depend on the quality of planning and instruction.

2) Level of Autonomy: When implementing a supervisory control task, the amount and types of human interaction with the automated technology must be considered in order to determine the appropriate LOA to employ. Parasuraman *et al.* have defined human interaction with automated technology in terms of ten "levels of automation of decision and action selection," that are based on four stages of human information processing.

1) Information acquisition.
2) Information analysis.
3) Decision and action selection.
4) Action implementation [7, p. 287].

The ten LOAs are defined in Table I, which has been modified from "Table I" appearing in [7]. There are risks, benefits, and consequences associated with each LOA in terms of the associated mental workload, reliance on the automation (which introduces the issues of trust and reliability of the automation), and the human operator's level of SA [7]. Therefore, it is important to plan for an LOA that provides a balance of human workload that is challenging to the operator, yet manageable, and that also provides a level of SA sufficient to meet task performance goals. For example, automation level 10 excludes the human operator from making decisions and taking actions; thus, the supervisory *monitoring* role of the human becomes a vigilance task, which can lead to operator complacency, resulting in human performance errors.

3) Human–Automation Interactions: Supervisory control may also be defined in terms of the coordinated interactions that occur between the human and the automation, referred to here as human-agent (H-A) teaming. Researchers have referred to H-A teaming as team play and argue that the interactions between the operator and the automation should be the focus of supervisory task designs [5], [9], [10]. Researchers have empirically investigated how constructs associated with team play (e.g., common ground) may be facilitated by the characteristics of the automation during an exploration task. Stubbs *et al.* [11], for example, studied how common ground could be facilitated among a (simulated) globally distributed team of operators and an exploration robot. More specifically, Stubbs *et al*. investigated how introducing a robot proxy would influence the degree of collaboration the operators perceived they were engaged in during the task. The robot proxy's role in the task was to assist the operators with planning. Results indicated that those who were assisted by the robot proxy reported higher perceptions of collaboration than those who did not use the robot proxy. Furthermore, those who used the robot proxy had improved performance, more accurate mental models of the robot's capabilities, and were more efficient at the exploration task.

Concepts such as common ground, and other human-team processes (e.g., coordination and communication) may provide a comprehensive understanding of H-A coordination [11], [12]. H-A coordination is similar to human-team coordination in that they both address interdependency and dynamic interplay among team members. Given these similarities, the processes that occur during human-team coordination may very likely emerge during H-A coordination [13]. For example, communication, a team process, emerges from the exchange of information between the operator (who may, for example, request information) and the automation (which may provide information about the state of the system and the operating environment). In sum, the team behaviors that occur during a supervisory task will illuminate relevant team processes. Knowing what team processes are necessary and understanding how they will affect the outcome of H-A coordination, can inform the design of supervisory tasks.

The following section discusses in detail some of the major human performance issues associated with supervisory control of multiple UVs. Particularly, we discuss operator multitasking performance, trust in automation, SA (issues associated with tasking switching and error diagnosis and recovery), and operator workload.

II. OPERATOR PERFORMANCE ISSUES IN SUPERVISORY CONTROL OF MULTIPLE ROBOTS

A. Operator Multitasking Performance

In the future battlefield, soldiers will very likely be expected to perform other tasks concurrently while operating a robot (or multiple robots) [14]. Researchers have studied how characteristics of the automation (e.g., reliability and autonomy) and the task (e.g., complexity) may affect performance on these concurrent tasks, and the supervisory task as a whole. Manzey *et al*. [15], for example, investigated performance consequences of automated aids (for fault identification and management) that are occasionally unreliable in a simulated multitasking supervisory control task. The results showed that automation benefits both primary (fault diagnosis) and secondary task (response to communications) performance. However, a significant automation bias effect was observed. About half of the participants

followed a wrong diagnosis generated by the automated system. Additionally, with the highest LOA, participants showed degraded "return-to-manual" performance. The authors, therefore, recommended that medium LOAs be used if manual skills need to be maintained.

Recent studies have investigated the consequence of task complexity on multitasking performance. These researchers combined navigation tasks concurrently with targeting and firing (search and destroy) tasks and intermittent communication tasks [16], [17]. Typical navigation task manipulations included perception (egocentric versus exocentric), attention (number of robots to control simultaneously), and communication with teammates. To increase task complexity, search and destroy tasks manipulated attentional resources by increasing the number of targets or gunner stations to command. The multitasking study by Chen and Joyner [16] required an operator to perform a gunner task, detecting and firing upon targets, while simultaneously either managing a semiautonomous UGV or teleoperating or monitoring a UGV. A third intermittent task required participants to simulate communication with a gunner crew. Results showed that overloading the operator's mental capacity with multiple complex tasks simultaneously led to performance decrements (decreased target detection); however when (semi-) autonomy was given to robotic entities, the operator could focus cognitive resources on complex tasks (target detection and communication/reasoning tasks) while simply monitoring (rather than controlling) the semiautonomous robots, intervening only when necessary.

The impact of task complexity was also investigated by Cummings and Guerlain [17] in terms of the number of entities one can operate under multitasking conditions. More specifically, the researchers tried to determine the approximate number of autonomous vehicles (missiles) that one operator could efficiently command and control simultaneously, under a low- or high-tempo multitask condition (performing a missile retargeting task and an intermittent communication task). Results showed that 16 missiles were the limit to control, beyond which point performance (reallocation of missiles to time-sensitive targets) began to degrade. Cummings and Guerlain cited that their findings corresponded with air traffic control (ATC) studies, where 17 managed aircraft was the limit that operators could handle well. Other studies have concluded that a much fewer number of UAVs could be controlled simultaneously [18]; however, it is important to consider the LOAs applied to the autonomous entities. In many cases, the more manual operation that was demanded, the fewer entities that could effectively be supervised [19].

These studies show that both the characteristics of the automation (e.g., reliability) and the characteristics of the task (e.g., complexity) will influence an operator's ability to multitask during a supervisory control task. Other factors, specifically related to the characteristics of the environment in which the task occurs, may impact supervisory control as a whole. One example of such factors is the degrees of coherence (comprehensiveness, consistency, and rational soundness) and correspondence (accuracy) of the information available for these tasks [20]. Since coherence is a prerequisite to correspondence, Mosier *et al.* [20] studied the effects of coherence (information congruence) in the context of time pressure and operator confidence. In their study, airplane pilots were found to make quicker, less-accurate decisions under time pressure, as they did not utilize all of the cues available to them. Instead, they tended to use cognitive heuristics such as anchoring the most salient cues to satisfice, rather than take the time necessary to make a better-informed decision. Satisficing was also observed in the supervisory command and control study by Cummings and Guerlain [17] in which participants, who were under a time constraint, had to select one of several missiles to redirect toward a target. Participants often redirected a missile that was sub-optimal, yet sufficient, to complete the mission.

B. Trust in Automation

Trust in automation is a ubiquitous construct, particularly with respect to performance during supervisory control tasks. Trust in automation, however, may be misleading because trust has the connotation of a prescribed behavior. Calibration, instead, is a more fitting term because it suggests that during a supervisory control task, operators intervene only when they have reason to believe their own decisions (od) are superior to the automated system's decisions (ad). In decision theoretic terms, operators choose to use automated systems when the probability of a correct decision, *p*(c), meets the following criterion: Intervene $if(p\_od(c)) > (p\_ad(c))$ [21].

Operators, however, have a difficult time assessing their own accuracy. In general, humans tend to be poorly calibrated—often overestimating their own abilities [22]. This implies that humans will overvalue their own decisions in comparison to automated solutions. However, the opposite tendency for humans to over rely on automated systems has been shown by a number of researchers [23]–[29].

Researchers have studied factors affecting the under or overuse of automation that encompasses both *extrinsic* factors, in that they are related to the characteristics of the environment or the automation, and *intrinsic* factors in that they are related to the characteristics of the operator.

1) Extrinsic Factors: Researchers suggest that the psychological context of the decision determines the tendency of the operator to disuse (under rely) or misuse (over rely on) automated systems [6]. In a series of experiments, Dzindolet *et al*. [30] showed that by a simple change in decision order, *disuse* of an automated target recognition device changed to *misuse*. If participants made a decision before being informed of the automated solution, they tended to rely on their own decisions even when they were suboptimal, whereas, in a related experiment using a similar paradigm, participants tended to over rely on the device whenever the automated solution was presented *at the same time* as the target scene. One explanation is that participants were attempting to reduce their cognitive load to maintain reasonable timeliness. However, such a strategy was not useful in the first experiment (automated solutions being shown *after* the participants made their decisions) because considering an alternative would increase workload by requiring operators to reconsider their original decisions [31].

The workload hypothesis is supported by complacency research that indicates operators misuse automation in a multitasking environment but not in single task environment [27].

The reliability of the automated system also impacts operator disuse or misuse. A number of researchers reported that target cueing is ineffective below a certain level of reliability (approximately 60%–70%) [32], [33]. In their metaanalytic study, Wickens and Dixon found that "a reliability of 0.70 was the 'crossover point' below which unreliable automation was worse than no automation at all" [32, p. 2]. Reliable automation enhances performance [34]; however, even reliable aids tend to be disused if the few mistakes the aid makes are obvious such as failing to detect a target when it is plainly visible [35]. However, the converse, automation *paradox* is also evident; operators tend to over rely more on highly accurate aids when advisories are incorrect, i.e., operators are more complacent when they develop trust in automation with high reliability because the possibility that the aid will mislead them is perceived as minimal [34], [36].

The type of unreliability has an important impact on the operator's perception of and response to system alerts. Cueing systems for the automated systems are often false-alarm prone (FAP) or miss-prone (MP) based on the threshold settings of the alert. Wickens *et al*. [37] showed that the operator's automated task (system-failure monitoring) performance degraded when the false alarm (FA) rate of the alerts for the automated task was high. In other words, high FA rate reduced operator's compliance with automation (compliance was defined as "the tendency to agree with an automated aid when it provides an alert" [38, p. 1941]. Conversely, when the miss rate was high, performance on a concurrent task was affected more than the automated task, because the operator had to allocate more visual attention to monitor the automated task. In other words, high miss rate reduced operator reliance on automation (reliance was defined as "the operator's assumption that a system is functioning normally while the alert is silent" [38, p. 1941]. Similarly, Dixon and Wickens [39] showed that FAs and misses affected compliance and reliance, respectively, and their effects appeared to be relatively independent of each other. In contrast, Dixon *et al*. [40] showed that FAP automation hurt "performance more on the automated task than did MP automation (e.g., the "cry wolf" effect) and hurt performance (both speed and accuracy) at least as much as MP automation on the concurrent task" (pp. 570–571). FAP automation was found to affect both operator compliance and reliance, while MP automation affected only operator reliance. The authors suggested that the FAP automation had a negative impact on reliance because of operator's overall reduced trust in the automated system. Similarly, Wickens *et al*. [41] demonstrated a greater cost associated with FAP automation (than with MP automation), which affected both the automated and concurrent tasks.

Lees and Lee [42] showed that "unnecessary alarms" (i.e., alerts that are legitimate but, due to the peculiarities of the situation, do not require operator compliance) foster the operators' trust in the automated system and actually enhance their compliance with the alerts rather than reducing it. Lees and Lee's data suggest that the three dimensions of trust (utility, predictability, and intent) need to be considered beside the traditional description of alarms according to signal detection theory (i.e., FAP versus MP).

Another distinction important to disuse or misuse of automation is the difference between evaluation errors and intent errors. For evaluation errors, the operator misperceives the optimal solution and commits a calibration error. For intent errors, the operator is aware of the aids superiority but still chooses to "disuse" automation in order to maintain control over the decision environment. For example, intent errors occurred when participants were aware of the superiority of an automated target detection aid but 84% of them still tended to disuse the aid leading to suboptimal targeting decisions [43].

Many of the above results suggest that trust (or calibration) is an extrinsic factor determined by operators' perception of the task environment. However, intent errors and FAs, indicate "trust" decisions are also based on the operators' belief in the importance of personally controlling decision outcomes [24], [43], which can be labeled as intrinsic factors.

2) Intrinsic Factors: Chen and Terrence [24] showed that there is a strong interaction between the type of automation unreliability and participants' self-assessed attentional control. Overall, it appears that for high attentional control participants, FAP alerts were more detrimental than MP alerts, due to *disuse* of automation. For low attentional control participants, conversely, MP automation was more harmful than FAP automation, due to *misuse* of (i.e., overreliance on) automation. Their results are consistent with past research that self-confidence is a critical factor in mediating the effect of trust (in automation) on reliance (on the automatic system) [44], [45]. Lee and Moray found that when self-confidence exceeded trust, operators tended to use manual control. When trust exceeded self-confidence, automation was used more.

Lee and See [45] characterize the interactions within a supervisory control task in terms of how human teams interact. They, therefore, define trust as the *attitude that an agent will help achieve an individual's goal in a situation characterized by uncertainty and vulnerability.* When humans perceive automated systems as team members, their attitudes of misuse or disuse should develop as operators become familiar with the system; therefore, implying that the "trust" decision is dependent on the attitude of humans towards automated systems. This intrinsic definition has interesting implications suggesting that humans view automated systems anthropomorphically. This begs the question whether we can design systems not only to perform human-like tasks, but to actually act like humans. For example, if robots can be made to be perceived as human, then teaming relations would not only be more natural but also instinctive and synergistic like a well-honed basketball team. Research to date is sparse but suggestive. Based on their research, Arkin [46] and his colleagues posit that, in the future, robots can be made not only to react to human cues but do so in a predictable and human-like manner—even to extent of developing ethical behaviors. This would allow humans and robots to share mental models of not only the external environment but also share each others' models [47]. However, the research in this area is not mature; humanoid robots or even robots that act like dogs can operate successfully only in constrained laboratory or

commercial environments. Currently, humans control or monitor unmanned systems as sophisticated equipment rather than as team members, showing more trust in a perceived human peer than a machine peer with the same capabilities [21].

Studying both the extrinsic and intrinsic factors affecting the use or disuse of automation is essential for developing training tools for reducing errors associated with disuse or misuse. Beck *et al.* [43] indicate that a combination of performance feedback and scenario training can reduce both appraisal and intent errors suggesting that different training regimes may be necessary for extrinsic (feedback) and intrinsic (scenario training) sources of automation usage errors.

Recently, researchers have suggested that the trust in automation research addressed above is a foundation for modeling trust in human–robot interactions (HRIs); however, a new model of trust must be developed [48]. Desai *et al.* suggested that the model account for the differences between current systems, and those used in prior research; for example, the newer systems' lack of reliability, and the more dynamic nature of the systems in terms of adjustable autonomy and their ability to carry out multiple tasks.

C. Situation Awareness

One of the most critical factors for achieving effective supervisory control of multiple UVs is maintaining adequate SA of the overall tasking environment as well as individual UVs. There are three levels of SA as defined by Endsley [49]: 1) perception of data and environmental elements; 2) comprehension of the current situation; and 3) projection of future states and events. Changes in the environment that may affect the plans for the robots need to be detected and the plans need to be modified in a timely fashion. While updates of information are needed, recent studies have also shown that interrupting a primary task (i.e., supervisory control of UVs) with an intermittent task (e.g., communication messages) can have a negative impact on SA [50], [51]. For example, Cummings [50] found that instant messages diverted participants' attention from their primary task (simulated supervisory control of Tomahawk missiles), thus reducing their SA when returning their focus to the primary task. Therefore, the challenge is to identify the means by which operators can most effectively maintain SA.

SA may also be affected perceptually as a result of the change blindness phenomenon, which is the inability to perceptually attend to a change in one's environment. Parasuraman *et al*. [52] examined change blindness in the context of a supervisory control task, in which participants were asked to monitor a UAV and a UGV video feed in a reconnaissance tasking environment. Participants performed four tasks in this experiment, including target detection and route planning (primary tasks), a communications task to evaluate SA, and a change detection task. The routes for the UAV and the UGV were preplanned, and the only time the participant controlled the UGV was when it was necessary to navigate around an obstacle in the environment. The primary tasks were interrupted by both the verbal communication task and the change detection task. The latter required participants to indicate each time they noticed that an icon of a target they had previously detected had unexpectedly changed position on a map grid. Half of these changes occurred during a "transient event," when the UGV stopped and its status bar flashed, while the remaining four changes occurred while participants were focused on the UAV monitoring task. Parasuraman *et al.* [52] found that participants' accuracy at detecting changes related to the position of the target icons was very low, especially during the transient events. Their results suggest that change blindness occurred most frequently when a distracter (a transient event) was present, but also occurred while participants shifted their attention from the UAV monitoring task to the UGV monitoring task. These results also suggest that task switching during a robot supervisory task may incur change blindness, which by its very nature affects an operator's SA (additional information on task switching is provided in the next paragraph). According to Norman's [53] seven stages of user activity, interruptions incur the greatest cognitive costs during the planning phases (intention forming and action planning) as well as the evaluation phases (outcome interpretation and assessment). Thus, interface designers should account for this, so that primary tasks are only interrupted during emergency situations or during moments of low workload (e.g., after evaluation is completed or before initiating a new plan). However, alerts should be provided to the operator indicating the changes to the interface and the degree of importance of the changes [54].

1) Task Switching: Simultaneous control of multiple UVs may require the operator to switch attention/control among the vehicles from time to time. Basic research on costs of task switching consistently shows that people's responses tend to be substantially slower and more error-prone after task switching [55], [56]. There is some evidence that this cost may be reduced if the participants have a chance to prepare for the switch or receive task switching cues [55], [56]. In the context of HRI, research has been conducted to investigate the effects of task switching on SA and operator performance [57]–[59]. Squire *et al.* [58] studied operators' response time as it related to interface type (options available to the user) and task switching, as well as strategy switching (offensive versus defensive, in the context of a RoboFlag-simulated game). Task switching was shown to slow response time by several seconds, especially when automation was involved. Likewise, Squire *et al.* found that response time increased by several seconds when participants switched between offensive and defensive strategies. When participants were provided an interface that allowed the flexibility to choose between a fixed sequence of automated actions or selectable waypoint-to-waypoint movement, mission time was reduced in spite of task or strategy switching. Crandall *et al.* [57] examined the amount of interaction time (IT) versus non-IT, or "neglect tolerance," to develop a predictive model to determine the number of robots (heterogeneous or homogeneous) that may be effectively monitored simultaneously by a single operator, given the requirements of a particular interactive task. Crandall *et al.* suggested that a predictive analysis such as theirs might be useful in the context of task switching.

2) Error Diagnosis and Recovery: Frequently, changes in the environment may require the operator to modify his/her plans for the UVs. Muthard and Wickens [60] evaluated the

effects of automation on pilot's performance in plan monitoring and revision. They found that pilots only detected about 30% of the experimenter-induced changes, which should have resulted in flight plan revisions. Mumaw *et al*. [61] showed an even more alarming inadequacy in monitoring performance. In their study, pilots only detected about 3% (1 of 32 total cases) of unexpected changes to the mode of an automation aid. Indeed, it has been well documented that operators are frequently unaware of mode changes when interacting with automation systems and, therefore, are confused about the systems' behaviors [62]. In fact, data show that even if changes in the environment are detected, operators may have difficulty interpreting the relevance of the changes and their effects on the existing plans [49]. According to the National Transportation Safety Board (1994, as cited in [60]), nearly two-thirds of aviation accidents caused by faulty human decision making can be attributed to pilots' failure to revise their flight plans. In Muthard and Wickens [60], pilots failed to modify their plans based on environmental changes on nearly one-third of the trials. Plan continuation errors were especially pronounced when there was an unreliable automation aid as compared with no aid present.

D. Operator Workload

An operator's perceived workload can impact his/her performance in an UV supervisory task relative to the LOA assigned to the robotic entities being supervised. The LOA of a robotic entity further influences operator compliance and reliance on the automated robots. Ruff *et al.* [19] examined perceived workload and found that when given complex tasks, operators tended to prefer autonomy that provided an LOA exhibiting "management-by-exception" (approximately level 6 in Table I). Although this LOA produced performance decrements, it lowered perceived workload as participants demonstrated satisficing. In contrast to "management-by-exception," Ruff *et al.* found that perceived workload increased when participants were subjected to automation that was less than perfectly accurate. Their lack of trust in the automation led participants to take extra time to double-check the system's accuracy in a "management-by-consent" condition (approximately LOA 3, 4, or 5 in Table I). There are also individual differences associated with perceived workload. For example, Mogford *et al*. [63] found that individual operator differences were a mediating factor of perceived mental workload, along with equipment quality and ATC operator strategies, in a model of ATC. More on operator workload will be discussed in Sections III and IV.

In summary, the findings in this section suggest that human operator's supervisory control task performance can be affected by factors such as the reliability of the automated systems, individual differences (e.g., operator's attentional control skills and confidence in his/her own manual control abilities), informational display (e.g., timings of information being presented and how the information is displayed), and concurrent workload (e.g., task switching, replanning, and additional tasks such as communication). The following sections review research findings in specific areas of supervisory control of UAVs, UGVs, and heterogeneous UVs (using different types of UVs in the same mission), followed by a review of user-interface designs for supervisory control of multiple robots.

III. Supervisory Control of Unmanned Aerial Vehicles

Two often used methods of supervisory control of UAVs are management by consent (MBC) and management by exception (MBE), which have been researched extensively in the manned aviation environment [64]. MBC requires the automation to ask for explicit consent from the human operator before taking any actions; MBE, on the other hand, allows the automation to initiate/perform actions unless overruled by the human operator. In their survey of airline pilots, Olson and Sarter [65] found that MBC was preferred by most pilots under normal circumstances, as it gave them more control over the automated systems. However, MBE was preferred when the pilots were under time pressure and higher workload, or when the task was highly complex or of low criticality. Olson and Sarter [64] conducted a simulation experiment to further examine pilot performance when interacting with MBC systems. The results showed that, under time constraints, pilots often had difficulties in detecting conflicts before giving consent to the automation, especially when the automation did more than expected by the pilots.

Comparisons of the effectiveness of MBC and MBE were also conducted in the unmanned aviation environment [19], [66], [67]. Ruff *et al.* [19] evaluated the effects of LOA, decision-aid reliability, and number of UAVs under control (1, 2, or 4) on the human operator's target-acquisition task performance. They found that, overall, an MBC-type decision aid provided the highest mission efficiency (total number of targets destroyed divided by the total number of missiles fired) and resulted in the best survivability performance (number of UAV hit points sustained). However, the authors reported that automation level interacted with number of UAVs controlled and reliability of decision aid for subjective measures of SA, perceived workload, and trust in the automation system. They found that SA was highest in the MBC condition, followed by manual operation, and finally, the MBE condition. As the number of controlled UAVs increased, SA degraded for all three LOA conditions, with the manual condition having the most severe degradation. Furthermore, the higher the LOA, the more benefit of vigilance (e.g., system monitoring) and workload relief it provided during complex tasks (when the number of UAVs increased and/or when reliability decreased). For example, in the MBC condition at 95% reliability, participants experienced higher workload (compared with the MBE condition) as a result of double-checking to be sure the automation was accurate. In the context of trust in the system, researchers found that it increased in both the MBC and the manual conditions as the number of UAVs increased when reliability was perfect, with the MBC providing the most trust. However, when the reliability was not perfect (i.e., 95% reliable), both MBC and MBE resulted in lower trust ratings as the number of UAVs increased.

Ruff *et al.* [66] conducted another study to compare the effectiveness of MBC and MBE systems in a UAV control setting (2 or 4 UAVs). In this study, the MBC system proposed route replans and target identifications. The MBE system, on the other

hand, automatically implemented proposed actions after a predetermined time period, unless the operator overruled. Overall, regardless of experimental condition, participants did not utilize the automation aiding system much at all. When under greater time constraints, they utilized it more often, but still rarely. As contrary to the previous study, MBC did not result in significantly better performance than MBE. However, with MBE, participants' perceived workload increased as time pressure increased. With MBC, in contrast, perceived workload remained at a similar level with an increased time constraint. In other words, although MBE was hypothesized to reduce workload under high time pressure, the opposite was found.

Cummings and Mitchell [67] investigated LOA in the context of controlling four UAVs for target acquisition tasks. The LOAs employed in the study roughly corresponded to levels 1, 2, 4, and 6 in Parasuraman *et al.* [7]. Level of replanning required in reaction to unexpected events was also manipulated (high versus low). They found that under the high replanning condition, operators performed the worst with the "active" level automation (corresponding most closely to MBC). The authors described this performance decrement as "cognitive saturation" and observed that operators were unable to correctly assimilate data from various sources, weigh uncertainty in the solution space, and prioritize their tasks. Operators had the highest level of level-1 SA (perception) and level-2 SA (comprehension) with the "superactive" level automation (MBE) but not the level-3 SA (future projection). In fact, operators exhibited automation complacency and erroneously destroyed more targets than they did when using automation with lower LOAs. This finding of complacency is consistent with what has been reported in the literature and is an important issue that user-interface designers of automation systems need to consider [16], [27]–[29].

Levinthal and Wickens [38] also investigated the effects of imperfect automation on robotics operator's target detection performance when controlling multiple (2 or 4) UAVs. This study compared Meyer's [68] independence hypothesis (which posited that FAP and MP automations have qualitatively different effects on operator dependence on the automated systems) to the model that FAP automation hurts more than MP automation. Their results were in favor of the independence hypothesis as participants in a MP condition (60% reliability with 3:1 likelihood of misses over FAs) showed an increase in compliance and a decrease in reliance whereas participants in a FAP condition (60% reliability with 3:1 likelihood of FAs over misses) showed a decrease in compliance and an increase in reliance. However, it was found that FAP aids resulted in delayed response times compared to the MP aids and 90% reliability aids. The authors, therefore, concluded that FAP aids, overall, were more disruptive to operator performance than MP aids.

Some researchers examined operator performance and workload in control of large numbers of UAVs [69]. For example, Miller [18] modeled the operator workload whose task is to authorize weapon release for targets identified by UAVs. His model shows that, under anticipated target densities, the operator would become overloaded when controlling 13 UAVs, even if the weapon release authorization is the only task the operator has to perform. In an empirical study, Galster *et al.* [69] examined operator performance in a supervisory control task of 4, 6, or 8 UAVs. Overall, participants performed well on their primary task (selecting the correct targets and the highest priority targets to process). Results suggested that although the increase in number of UAVs slightly impacted performance (negatively), the number of targets (not the number of UAVs) had a higher impact on perceived workload. Secondary (monitoring) task performance, on the other hand, was significantly worse for the 8 UAV condition than for the 4 and 6 UAV conditions.

Overall, the findings reviewed in this section suggest that the benefits of MBE versus MBC automation for supervisory control of multiple UAVs are not always consistent and they are affected by factors such as the difficulty level of the task (e.g., target density) and the type of automation unreliability (e.g., FAP or MP). Additionally, operators may exhibit complacency under high task load when using systems with higher LOAs. Studies reviewed in the "Trust in Automation" segment of the previous section suggest that factors such as individual differences also play an important role in how operators interact with highly automated systems.

IV. Supervisory Control of UGVs

Supervisory control of multiple UGVs has been examined in contexts of search and rescue tasks [70], [71] and other exploration and reconnaissance tasks [72], [73]. Olsen and Wood [74] proposed an equation to calculate fan-out (FO; the number of robots a human operator can control simultaneously [span of control]) based on activity time (AT; the time that a robot is active) and IT (the time that it takes for a human operator to interact with a robot). The authors also conducted four simulated experiments to test the equation. Results showed that, when 18 robots were available for a target search task, FO for the type of robots with the highest autonomy was as high as 9 for the less-cluttered tasking environment (compared to 5 in the more-cluttered environment). Olsen and Wood concluded that their FO equation could accurately model operator span of control in many cases; however, FO might change due to other task characteristics and complexities in the environment.

Riley and Strater [75] investigated navigating two UGVs through a maze while manipulating the control mode (serial, parallel, and two parallel conditions involving manual control of one robot and a varying LOA in the second, supervised robot). Performance measures included: SA (measure of awareness of current and future status of robotics task using the Situation Awareness Global Assessment Technique [SAGAT]), workload (NASA-TLX), and performance navigating the robots (time-to-task completion) as well as monitoring performance (detection of diagnostic failures). Monitoring performance was positively correlated with SA scores, and participants in the serial control condition exhibited slightly higher SA scores than the parallel conditions. However, the parallel control condition resulted in the best navigation performance and the lowest perceived workload.

Participants in Chadwick's [76] study were responsible for controlling 1, 2, or 4 semiautonomous UGVs simultaneously. Operators were assessed on monitoring, responding to cued

decision requests, and detecting contextual errors, the latter of which occurred when the robot was performing correctly but inappropriately, given contextual or environmental factors. In the case of a contextual error, the robot cannot recognize such a malfunction, so the operator must take notice of it; one example may be failed navigation, in which the robot would need to be redirected to a more optimal path. Participants were required to monitor and recharge robots' batteries, attend to targets, and detect and redirect navigation errors. Operator performance varied depending upon the cognitive demands of the various tasks. Degradation was found to come from "event time-line conflicts" and attentional limitations, the latter of which were most prevalent in the contextual error identification and redirecting task.

In Trouvain and Wolf [73], participants used either 2, 4, or 8 simulated UGVs to perform inspection tasks at the predesignated inspection locations. Results showed that participants' overall task performance (number of inspections completed) improved from the two-robot condition to the four-robot condition, but not from the four-robot to eight-robot condition. However, their data also showed that when the number of robots increased from 2 to 4, the average inspection delay (amount of time robots spent on waiting for human inspection after reaching the inspection locations) also more than doubled. In fact, it was found that participants had difficulties keeping more than two robots active at the same time. The subjective workload data also showed that participants experienced slightly higher workload when the number of robots increased from 2 to 4; however, they experienced significantly higher workload when the number of robots was 8.

Wang and Lewis [70] explored operator demands of autonomous robot teams versus manually controlled robot teams in a building search task. In this within-subjects experiment, three robots were controlled serially, so only the selected robot would accept commands. Participants controlled waypoint movements, manually teleoperated the robots, and operated a camera (panning and tilting it to achieve an optimal view). Waypoint and teleoperation control improved in the autonomous condition, but camera control did not differ. Participants also switched control between the three robots more frequently in the autonomous mode than in the manual control mode. Results further showed that autonomous cooperation between robots aided operator performance. Wang and Lewis believed that this was because their search task consisted of several subtasks, which participants had to interact with during the windows of their "neglect time" (see [57]). Switching control between the robots more frequently (as in the autonomous mode) gave participants more time to finish the subtasks involved [70].

In a follow-on study, Lewis and coworkers [71] investigated operators' performance when they controlled 4, 8, or 12 robots (within-subject variable) for a victim-search task. The results showed that, in the full-task control condition (participants implemented waypoints for the robots and controlled the cameras), operators performed better (found more victims) with eight robots compared with 4 and 12 robots. Operators' perceived workload, however, increased monotonically with number of robots. Wang *et al.* [71], therefore, concluded that somewhere between 8 and 12 robots seemed to be the limit for direct human control. The authors also suggested that automation of navigation-related tasks (e.g., path planning) seemed to be more important than "efforts to improve automation for target recognition and cueing" [71, p.146] in the context of controlling a large team of robots.

Overall, the findings reviewed in this section seem to support Olson and Wood's model [74] that FO can be as high as around 8–9 robots in less demanding tasking environments; however, in more challenging conditions, human operators can only supervise around 4–5 robots effectively simultaneously. Operator's performance can be enhanced by intelligent coordination among the robots and, according to Lewis and coworkers [71], automating navigation-related tasks particularly benefits operator's performance.

V. Supervisory Control of Heterogeneous Unmanned Vehicles (UAVs and UGVs)

Future warfare employing UVs may need to integrate information from multiple platforms, potentially from both aerial and ground sources. UAVs generally provide exocentric views of the problem space (i.e., the battlefield) while UGVs present viewpoints that are egocentric and immersed in the environment. The ideal view depends on the task; overall awareness and pattern recognition are optimized by exocentric views whereas the immediate environment is often viewed better egocentrically. Displays for integrating information from different frames of reference (FOR; e.g., exocentric and egocentric) present potential human performance issues that need to be carefully evaluated [28]. Research has shown that integrating information across egocentric and exocentric views can be challenging for the operator [77], [78], especially for those with poor spatial ability [79]. Essentially, dual displays with both FOR require effective scanning of the displays and integrating information from two different perspectives to form an accurate assessment of the situation. Furthermore, operators may be susceptible to a saliency effect and anchoring heuristic/bias [28]. In other words, salient information on one display may catch most of the operator's attention, and the operator may form an inaccurate judgment because information from the other sources are not properly attended to and integrated. In Thomas and Wickens [28], participants were found to tunnel their attention into the egocentric view to the exclusion of information from the exocentric view.

Chen *et al.* [4] simulated a command vehicle environment and had the participants perform a target designation task with a semiautonomous UAV, a semiautonomous UGV, teleoperating a UGV, or, in the mixed condition, controlling all three assets. They found that when the operator could use all three assets, they tended to ignore the equally efficacious UGV and relied on the UAV. This agreed with other U.S. Army sponsored research using gaming technology showing the counterintuitive result that even when participants performed better with UGVs, they still preferred UAVs [80]. This may indicate a generalized preference for the gods-eye exocentric view afforded by the UAVs in comparison to the egocentric views obtained from the UGVs.

Billman and Steinberg [81] described a set of HRI performance metrics for evaluation of mixed-initiative heterogeneous robots (i.e., 5–10 air, sea, and undersea UVs). They found that these metrics were useful in understanding collaboration between human operators and heterogeneous robots. The metrics included: planning time, task time, SA, operator workload, operator assessment of the usability of the systems, and mental model mapping (between reality and the operator's temporal and spatial mental model of the system state). Lessons learned from a series of human-in-the-loop experiments were documented and recommended modifications of the metrics were also presented.

In summary, the findings reviewed in this section suggest that the effectiveness of supervisory control of heterogeneous UVs may be affected by factors such as operator's preference of viewpoint, attentional tunneling phenomenon induced by egocentric perspective, and individual differences in spatial ability (which influences how well the information from different FORs can be integrated). In the following section, we review innovative techniques and technologies designed to enhance operator performance of supervisory control of UVs.

VI. Interface Designs for Supervisory Control of Multiple Robots

When conducting supervisory control research, the interface design must support effective interactions and provide good usability, or the design itself may affect perceived workload, and overall performance. For instance, Cummings [50] found that intermittent messages from a chat communication tool interrupted primary task performance. This finding demonstrates how the presentation of alerts and alarms can be important in both experimental and "real-world" system interfaces, as alerts and alarms may impact overall operator performance in unexpected and negative ways if they are designed as independent features of the system. Some methodologies for interface design have been investigated in the context of complex supervisory control tasks, including abstraction hierarchy and cognitive task analysis [82], [83]. For example, Linegang *et al.* [82] applied the abstraction hierarchy approach to design a novel system. This approach allows an interface designer to decompose a system into subcomponents that may each be analyzed in terms of how to best apply automation to best aid the user. Additionally, Nehme *et al.* [83] examined how cognitive task analysis could be mixed with SA criteria to determine a list of requirements for interfaces of future technologies.

Olson and Wuennenberg [84] presented a list of recommended user-interface-design guidelines for supervisory control of UAVs. The recommendations included the following.

1) Automation behavior (e.g., system status/mode, system goals, and flight control functions) should be highly visible to the operator (rationale: operators tend to be "out of the loop" when systems are highly automated and they often find it difficult to understand system behavior due to system complexity, coupling, and autonomy).
2) It should be easy for the operator to extract meaning from the display quickly—minimize information access costs by highlighting relevant information, integrating dimensions and displaying information in appropriate formats (rationale: operators often find it difficult to understand system behavior due to system complexity, coupling, and autonomy).
3) Display/highlight projected changes and predicted information based on operator inputs and direct operator attention to the relevant areas (rationale: changes to system behavior may be difficult for the operator to visualize or detect).
4) Provide a quick and easy way to reinstruct automated systems (rationale: highly automated systems tend to be difficult to reprogram and manual control may not be an option).

In a recent study, Nam *et al.* [85] applied human–computer interaction principles to the design of a multiagent system interface. Using a user-centered design approach, three types of interfaces were designed and tested. Each interface satisfied a set of design goals including:

1) one window display of relevant information;
2) user-friendly layout;
3) displaying only essential information for decision making;
4) providing rapid user interaction;
5) providing necessary and essential information for dynamic role changing;
6) providing feedback.

Nam *et al.* concluded that interfaces for multiagent systems are efficient when they are compact and when they accentuate information that aids in the decision making process. Based on the results, guidelines for multiagent interface design were proposed.

Adaptive automation can be a very useful tool to aid operators with supervisory control tasks as it can "leverage the strengths of humans and computers to improve overall system performance while mitigating the negative aspects of both" [50, p. 653]. More information on adaptive automation and other potential user-interface designs for supervisory control of unmanned vehicles will be discussed in Section F.

Finally, within the context of H-A teaming, interface design techniques should focus on supporting team processes between the human supervisor and the UVs. As mentioned previously, team processes can be supported by identifying team behaviors that will occur during the task. For interface design, the goal would be to identify characteristics of the interface that could support the team processes that emerge from the H-A team's behaviors. For example, if shared awareness emerges, then the interface should support communication methods that will facilitate a shared understanding among the team. This approach to interface design could be referred to as a *team-centered* interface design approach. Designing an interface using a team-centered approach may enhance the robustness of the interface and facilitate the management of workload through a balance between task workload and interaction workload [86].

It is important to note that designing an agent's interface that supports team processes will not alone lead to effective team interactions; both the human and the agent are jointly responsible for developing team play [49], [87]. In Fan *et al.*'s [87] collaboration model of an H-A team, agents can work autonomously

until they run into a problem, at which time they could query the human. The active role of the human within the H-A team, therefore, requires attributes that allow the human to accept/exploit an agent's capabilities. For example, an agent may support coordination among team members, yet, whether the human accepts the agent's attempt to coordinate may depend on the human's trust in the agent. Trust may be established through an understanding of the agent's abilities and reliability ([45]; also see Section II-B). Therefore, developing team play within H-A teams requires consideration of not only the agent's capabilities and attributes, but also the human's knowledge, skills, abilities, and attitudes.

This section reviews several innovative user-interface-design techniques in the following areas: multimodal displays and controls, planning tools, visualization tools, attention management tools, trust calibration tools, adaptive automation, and intelligent agent for human–robot teaming. Several design guidelines based on empirical studies to test the effectiveness of these designs are also presented.

A. Multimodal Displays/Controls

Remote perception is essential for effective teleoperation. In teleoperating environments, human perception is compromised because the natural perceptual processing is decoupled from the physical environment. This decoupling affects people's perception of affordances in the remote scene and can have a detrimental effect on SA and, therefore, the overall effectiveness of the robotics' task performance [88]. The performance degradations can be further exacerbated due to less than ideal video quality [89], [90]. Simpson *et al*. [91] proposed using a spatial audio display to augment UAV operator's SA and discussed its utility for each of the three SA levels. They recommended that both visual and spatial audio information should be presented concurrently. They also suggested that presenting the audio information spatially may enhance UAV operator's sense of presence (telepresence). However, the link between presence and task performance has yet to be established. Additionally, spatial audio displays can be ineffective in a noisy environment and the user may experience front-back confusion. Tactile displays, therefore, present a viable alternative to audio displays. Haas *et al*. [92] designed a soldier-swarm display (the swarm consisted of 40 simulated ducted fan aircraft) and compared its effectiveness when information was displayed using visual, auditory, and tactile combinations. The multimodal displays (compared with the visual display baseline) significantly improved Marine participants' detection performance (i.e., reduction in response times) and decreased their perceived workload. In another study, Gunn *et al.* [93] compared the effectiveness of a sensory display and a cognitive display for presenting warning information in a UAV control task. They found that the sensory display (which presented the information by changing the physical attributes of stimuli) resulted in more threat detections, fewer FAs, faster response time, and lower perceived workload than did the cognitive display (which required symbolic manipulations to define critical signals). Gunn *et al.* [93] also compared the utility of different types of directional cueing interfaces (visual, spatial audio, and haptic) and found no differences in their effectiveness. For a comprehensive review of multimodal displays and controls for robotics control, see [89].

B. Planning Tools

Planning (e.g., route-planning task) is a vital part of HRI. It is increasingly common for plans to be generated by automated/intelligent systems in mixed-initiative operations. However, lessons learned from a U.S. Naval Intelligent Autonomy program indicated that human operators sometimes questioned the accuracy and effectiveness of automated plans [82]. Specifically, some human operators indicated that they had difficulties understanding the rationales for some plans and how the plans were generated (as cited in [82, Billman *et al.*, 2005]). Additionally, some operators reported that they had difficulties at times when trying to specify mission parameters (e.g., goals and constraints) in the way required by the automated planning system (as cited in [82, Billman *et al.*, 2005]). Furthermore, real-time development on the battlefield may require the human operator to change the plan for the robot team and/or for the individual robots. Therefore, effective communication between the human operator and the robots is critical in ensuring planning effectiveness and mission success.

Research has been conducted on ways to enhance human–robot communication [11]. For example, Stubbs *et al.* demonstrated the effectiveness of a robot proxy to enhance shared understanding between the human operator and the robot in an exploration task. The communication mechanism was based on a common ground collaboration model and was able to improve the human operator performance in the following areas: more accurate plans, more efficient planning (fewer times of replanning), more efficient and faster task performance, and better mental model of the robots' capabilities. The U.S. Navy has also sponsored a research and development program to design a mission-planning tool for human operators controlling a heterogeneous group of robots [82]. The tool, mission displays for autonomous systems (MiDAS), uses an ecological approach to reduce conflicts between human operators and the automated planning system.

1) Schedule Management Aid: When controlling multiple semiautonomous UVs, each executing its own predetermined plan, the operator may experience high workload when more than one UV needs his/her attention at the same time. It is, therefore, beneficial to let the operator know when potential processing bottlenecks may occur so they make arrangements to mitigate the bottleneck if necessary. Cummings *et al*. [94] designed an intelligent schedule management aid and tested its effectiveness in a simulated suppression of enemy air defenses mission environment with four UAVs. The aid incorporated timeline displays that show potential bottlenecks and it also presented potential scheduling conflicts using configurable displays (see Fig. 1).

Overall, both the timeline and the configural displays were effective. However, the authors cautioned that, in order for the displays to be effective, the user-interface designers need to ensure the following.

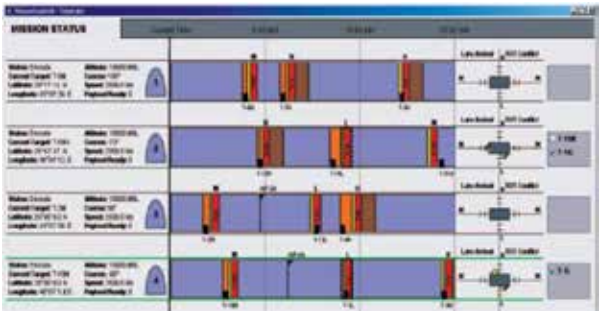

Fig. 1. Timeline display and configural display (right) (adapted from [94], with permission).

1) The information's importance matches its representation salience (rationale: overly salient representations may cause the operator to fixate on something not important while overlooking more serious issues).
2) The aid presents useful solutions to emerging problems rather than simply providing visualizations of potential problems (rationale: Cummings *et al.* showed that only presenting visualizations without solutions was not more effective than no visualizations) [94, p. 58].

Dorneich *et al.* [51] took a different approach and used neurophysiological sensors (EEG) to detect cognitive workload in a navigation task (walking along a familiar route) with an intermittent communication task and mathematical interruption task. Throughout the experiment, EEG sensors accurately evaluated cognitive workload about 70% of the time, and a Communication Scheduler adapted task scheduling information by informing the participant what to focus on next. The communication scheduler positively impacted participants' performance by rescheduling their priorities, resulting in only a temporary loss of SA for low-priority messages [51].

C. Visualization Tools

Humphrey *et al*. [95] examined the use of visualizations as an aid for operators responsible for controlling a team of robots. Previous studies examined color-coding robot status and team associations; this study added shapes to represent an individual robot (condition 1), or teams of robots (condition 2—semitransparent, and condition 3—solid) (see Fig. 2). Participants were tasked with selecting specific robots relative to other robots or environmental characteristics, and to verbally confirm or deny accuracy of statements regarding a robot's status. Investigators were interested in the level of operator engagement, as indicated by the frequency with which participants utilized the visualizations. Results indicated that the semitransparent and solid visualizations were preferred and utilized significantly more than the individual visualization. Participants slightly preferred (in a post-trial questionnaire) the presentation of both an individual and semitransparent visualization (in the same trial). The authors plan to continue this research with the hypothesis that an operator's SA will increase when visualization techniques are applied to managing teams of robots; this technique may also help an operator supervise a larger team of robots.

Fig. 2. (Left to right) Individual robots, semitransparent, and solid (adapted from [95], with permission).

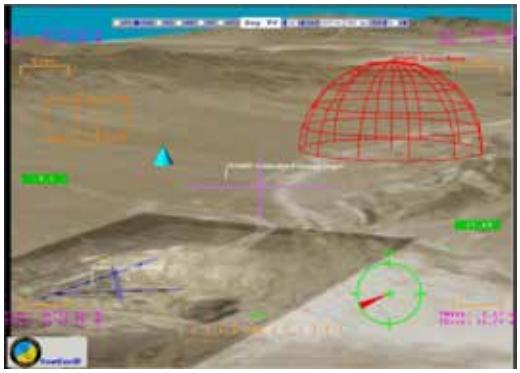

Fig. 3. Synthetic vision symbology added to simulated UAV gimbal camera video, marking threat, landmarks, areas of interest and runway (symbology generated with LandForm SmartCam3D, Rapid Imaging Software, Inc.; adapted from [96], with permission).

1) Augmented Reality: Augmented reality (AR; also known as synthetic vision) has been found to be an effective means to enhance pilot/UAV operator SA by portraying a more veridical view of the combat environment [96]–[99]. For example, the U.S. Air Force has identified several candidate synthetic vision overlay concepts for UAV applications [96] (see Fig. 3). The following information, potentially, can be overlaid graphically on the streaming video: maps and other synthetically generated symbology, photoimagery, terrain elevation, laser range scans, past and potential future robot paths, updates via networked communication with other sources, and other vital statistical data [96], [100]–[103]. However, large amounts of information, although helpful in reducing the operator's scanning effort by providing more data in a centralized area (e.g., the video), can create visual clutter and degrade operator's information processing [104]. Thus, it is important that a declutter capability be provided so the operator can customize the overlaid information presentation according to the situation and tasks.

More research is needed to determine the optimal approach to decluttering (i.e., global approach by deselecting classes of information or local approach by deselecting individual symbology; [104]). Additionally, overlaying information on a video feed can potentially lead to cognitive tunneling, as operator's attention can be captured by the overlaid data while important elements/developments in the video might be overlooked [99],

[105], [106]. However, a more recent study by Iani and Wickens [107] indicated that the attentional tunneling effect of the AR displays may not be as pronounced as previously suggested. The tradeoff between adding information to the video feed and cognitive tunneling needs to be more systematically evaluated. A list of human factors issues with UAV AR systems and their potential solutions can be found in Calhoun *et al.* [104].

2) Ecological Interface Designs: Ecological interface design (EID) is a user-interface-design technique that conveys the constraints in the tasking environment, usually visually via emergent patterns, so the operator can intuitively perceive and solve the problem [108]. Furukawa and Parasuraman [109] demonstrated that EID was beneficial for enhancing human operators' detection of automation errors as well as their comprehension of system states. In their first experiment, Furukawa and Parasuraman showed that human operators, using an EID display showing an emergent perceptual feature, were able to detect significantly more system errors than when they used a nonintegrated display (i.e., they showed significantly less automation-induced complacency). More strikingly, the operators were able to achieve better performance even though their visual attention to the EID display was significantly less, according to an eye movement analysis, indicating that their monitoring was more efficient. In the second experiment, Furukawa and Parasuraman [109] showed the effectiveness of an EID display that portrays graphically the intention of the automated system. Their results showed that this visualization tool helped the human operators to achieve a better mental model of the system, which enabled them to make better decisions. In yet another study, Furukawa *et al*. [110] integrated the intention-represented EID display in a partially automated process control simulation and compared its effectiveness with that of an EID display without intention indicators of the automated system. Results showed that the intention-represented EID display was able to enhance the operators' predictions of the actions and behaviors of the automated system and therefore, was able to improve the operator's action planning and decision making. Additionally, the benefits were demonstrated in novel scenarios, suggesting that the operators had a better mental model of the automated system with the intention-represented EID display than with the EID display without the intention indicators.

Cummings and Bruni [111] designed a user interface that supports a single operator's ability to control four UAVs simultaneously. They utilized visualization techniques in designing a tool that helps the operator replan the mission. For example, they used a configural display to depict the overall cost of the revised plan (see Fig. 4).

Furukawa [112] also incorporated an EID display into a RoboFlag simulation program. The results showed that the EID display enhanced the human operator's performance of supervising a team of robots by portraying essential functional information (graphical representations of the offensive and defensive functions for the RoboFlag-simulated game). A detailed review of the EID—the empirical evidence of the efficacy of EID, why EID improves operator performance, how EID can be leveraged, and challenges of implementing EID—can be found in Vincente [113].

Fig. 4. Supervisory control of four UAVs—configural display is the center panel with three green triangles indicating the costs of planned operations (image adapted from [111], with permission).

D. Attention Management Tools (Interruption Recovery Aid)

When controlling multiple robots at the same time, it is inevitable that the operator will tend to some aspects of the environment (e.g., one of the robots) before resuming his/her monitoring of all the robots. Techniques that facilitate task resumption have been proposed and tested in various tasking environments [114]–[116]. Some techniques focus on reminding the operator where s/he was before the interruption [114], while others present aids for the operator to quickly review what happened during the interruption [115], [116]. Ratwani *et al.* [114] demonstrated that simply by reducing the size (by about 75%) of the window for the interrupting task (i.e., reducing the occlusion of the primary task screen by the interrupting task window), participants were able to resume their primary task significantly faster. Eye-tracking data also showed that participants were more accurate at returning to where they left off. Other more sophisticated techniques to facilitate recovery from interruptions have also been developed. For example, St. John *et al.* [116] discussed the utility of a SA recovery tool (named CHEX; see Fig. 5), which displayed a textual event history list in a naval air warfare environment (monitoring a geoplot of an airspace which contained ownship and approximately 50 other aircraft).

St. John *et al.* found that CHEX was more effective in helping the operator resume their task after interruptions (blank screen lasting either 30 or 120 s) than a video replay tool, which was worse than the baseline condition (no aid). CHEX presented changes in a table and linked them to the map when the operator selected a change from the table. However, Scott *et al.* [115] argued that the ineffectiveness of the video replay tool shown in St. John *et al.* [116] might be improved if a better design had been adopted. Scott *et al.* [115] presented two types of replay tools—one replayed the events at a 10× real-time speed and the other presented bookmarks on the event timelines and the operator could view the replay by selecting the bookmarks (see Fig. 6). Results showed that both replay techniques were effective,

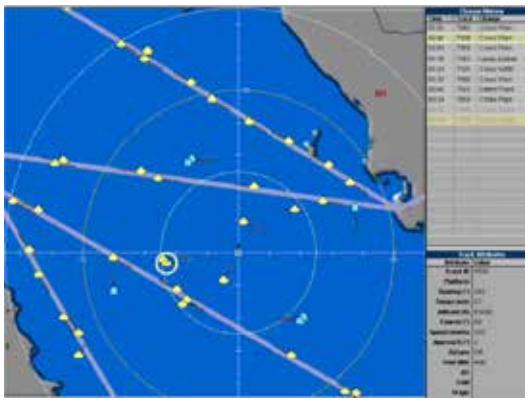

Fig. 5. Interruption recovery aid—textual event history list (CHEX—upper right) (adapted from [116], with permission).

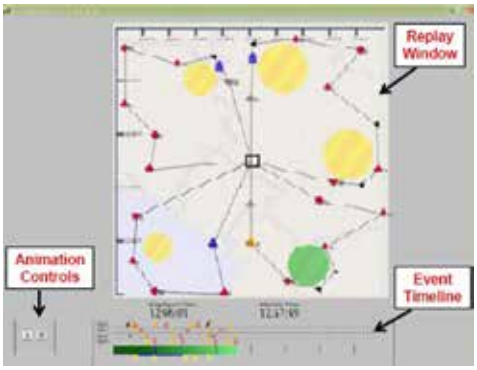

Fig. 6. Interruption assistance interface (adapted from [115], with permission).

especially when the tasking environment was challenging. Based on the results, the authors presented several recommended design guidelines for interruption assistance interfaces.

1) Enable user control of event replay.
2) Provide visual summary of critical events.
3) Limit visual summary to goal-related events.
4) Clearly indicate relationships between past and current system state [115, p. 703].

E. Trust Calibration Tools

Lee and See [45] recommended that the capabilities and limitations of the automated systems be conveyed to the operator, when feasible, in order for the operator to develop appropriate trust and reliance. Bagheri and Jamieson [117] demonstrated that when operators were aware of the context-related nature of automation reliability, their detection rate of automation failures increased significantly without affecting their concurrent tracking and system management tasks. The authors attributed this improvement in performance to a more effective attentional allocation strategy. Rovira *et al.* [34] investigated the differential effect of automation reliability and different types of automation (decision support and information support) on performance during a command and control task. Their results confirmed a differential cost of automation unreliability for three forms of decision automation, as compared with information automation when the overall automation reliability was at 80%. At 60% overall automation reliability, however, there was a reduction in performance for both information and decision automation during unreliable trials. This finding suggests that the type of automation employed is irrelevant when automation reliability is below a certain threshold. Based on their findings on the different types of automation, Rovira *et al.* suggested that decrements in decision-making performance will be lower when operators can query the automation, inspect raw information sources, and verify or negate the automated advice.

In another study, Seppelt and Lee [118] designed a display, based on EID that portrayed graphically the capabilities and limitations of the adaptive cruise control of a vehicle for a driving task in different traffic and weather conditions. They found that drivers' reliance on the automation (i.e., cruise control) was more appropriate when the display was present than when it was not. Lee and See [45] developed the following guidelines on designing systems that promote appropriate trust in the automation.

1) Design for appropriate trust, not greater trust.
2) Show the past performance of the automation.
3) Show the process and algorithms of the automation by revealing intermediate results in a way that is comprehensible to the operators.
4) Simplify the algorithms and operation of the automation to make it more understandable.
5) Show the purpose of the automation, design basis, and range of applications in a way that relates to the user's goals.
6) Train operators regarding its expected reliability, the mechanisms governing its behavior, and its intended use.
7) Carefully evaluate any anthropomorphizing of the automation, such as using speech to create a synthetic conversational partner, to ensure appropriate trust [45, p. 74].

F. Adaptive Automation

Adaptive systems were developed more than 50 years ago to aid the operator by keeping performance constant as a function of task difficulty [119]. One of the early paradigms used queuing theory as an allocation system to service aviation tasks on which the operator was performing poorly during high workload situations. More recently, adaptive automation has been proposed as a technique to keep operators engaged in a multitasking situation without overwhelming them during peak workload situations [31], [120], [121]. These systems, a middle ground between fully automated and manual control, provide a means of keeping operators in the loop. The basic concept consists of decisions rules for the computer invoking automation during high workload and for reinvoking manual control during lower workload mission segments. The purpose of the adaptive automation is to keep operator performance within acceptable levels while maintaining attentional focus on important tasks. Decision tasks, in particular, should be completely automated with extreme care

because even with perfectly automated tasks, the operator may lose SA if the environment changes or unexpected emergencies occur [31], [34], [36]. For imperfect automation the situation is worse. Even for highly accurate automated aids, operators tend to over rely on the automated solution, which can cause even obvious errors to be missed (i.e., automation paradox; [34]). Consequently, with less-accurate aids, automation itself can be a detriment [33]. Therefore, important issues with adaptive systems such as type of invocation process, switching rate, and engagement time must be taken into account in the design of these systems.

Invocation rules (when to invoke automated or manual control) can be based on models, performance levels, physiological changes, or some mixture of them [36]. A number of physiological measures have been used to covertly monitor operator's workload state: EEG, event-related potential (ERP), heart-rate variability (HRV), functional MRI (fMRI), and combinations of the measures [31], [122]. Freeman *et al*. [123] showed the potential of using an adaptive system for human tracking performance using three neurophysiological EEG indices for automation invocation. To test whether EEG was a good indicator of performance, the authors compared two methods for invoking automation: high arousal components of the EEG (high ratios of the beta wave components divided by theta and/or alpha components) and components associated with low arousal (higher ratios of alpha and theta wave components). As predicted, conditions that used EEGs with high beta ratios resulted in better tracking performance indicating that neurophysiological indices could provide a potential means of covertly measuring the operator's arousal level for adaptive processes. Milkulka *et al*. [124] showed similar patterns of performance for a vigilance task using the high beta weightings of the EEG to control adaptive event rate procedures. However, because yoked participants (adaptive processes not based on the operator's EEG) performed as well as participants in the high beta ratios conditions, it is possible that task difficulty measures may be as efficient as EEG indices for invoking automated processes. They also reported that an automation switching rate of about 15 s between conditions was sufficient for operators to be able to focus on the current task and to adjust to new adaptive conditions.

Wilson and Russell [125] developed a more sophisticated adaptive automation invocation method using multiple physiological indices that were performance weighted using a neural network based algorithm. The adaptive conditions resulted in better performance than manual conditions. More importantly, the weights based on the individual's past performance resulted in better performance than group weighted invocation methods, indicating their indices were sensitive to individual differences. All three studies [123]–[125] showed that physiological indices were potential invocation methods for adaptive processes; they also indicated that fairly short switching rates were feasible. Moreover, the Wilson and Russell study [125] indicated that the measures should be tailored to individual differences (see also [51] discussed above). However, none of these studies actually showed an advantage for adaptive processes compared to static automation nor did they compare physiological to nonphysiological indices.

Parasuraman *et al*. [126] demonstrated the efficacy of adaptive processes in a multitasking aviation environment. There were three conditions: static automation, model-based adaptive automation (mission segments with high task difficulty), and performance-based adaptive automation (operator error rate determined invocation). Manual control was invoked in the middle of the 90-min experiment for the two adaptive conditions. The adaptive system did increase the SA of the operators—showing significantly better instrument monitoring performance compared to the static automated conditions for the sessions immediately following the manual conditions. The authors interpreted this as indicating that putting operators in the loop, even briefly during a 90-min experiment, increased their awareness compared to automating a system for the entire 90 min. Also, the experiment demonstrated that either model-based or performance-based rules could be used as invocation triggers for automation.

Parasuraman *et al*. [52] compared performance-based adaptive automation, static automation, and manual target identification using an automatic target recognition (ATR) device in the automated conditions. Their study employed a multitasking environment involving targeting with UAVs and planning UGV routes. The trigger for adaptive automation was the number of missed changes in a situation map, which suggests that adaptive processes can be invoked from secondary task as well as primary task difficulties. The results were dramatic—SA, workload, and performance on the secondary task were all improved by automation, but more importantly, performance gains for the adaptive (performance-based) versus static (model-based) automation were substantial. Based on this study and a review of the literature, Parasuraman *et al.* suggested the following guidelines for adaptive automation.

1) Information displays should adapt to the changing military environment.
2) Software should be developed to allow the operator to allocate automation under specified conditions before the mission (as in the Rotorcraft Pilot's Associate; [127]).
3) At least initially, adaptive systems should be evaluated that do *not* take decision authority away from the operator. This can be accomplished in two ways:
    a) an advisory asking permission to invoke automation (i.e., MBC); or
    b) an advisory that automation will be invoked unless overridden (i.e., MBE).
4) For safety or crew-protection situations, specific tactical or safety responses can be invoked without crew permission [36, p. 61].

Steinhauser *et al*. [128] also provided several design guidelines for implementing adaptive automation based on their review of empirical research on adaptive automation and aiding in the past three decades. The guidelines are as follows.

1) Adaptive function allocation to the operator should be used intermittently. Intermittent allocation can improve performance in monitoring tasks.
2) Energetic human qualities should be considered in design. For example, degrees of challenge can be automatically adjusted with artificial tasks.

3) Emotional requirements of the human operator must be considered. The human operator should not feel unnecessary to the system as a whole.
4) The system should be calibrated to the individual operating it. Individual differences factor into the human operator portion of a human–system pairing and thus should be incorporated into the design.
5) Task transformation should be used to simplify tasks for operators. A task that is partitioned and transformed can be handled piecemeal instead of as a whole.
6) The environmental context of the system should be used to determine allocation. Environmental stressors such as heat, vibration, and gravitational force affect human performance and should be addressed.
7) Tasks should be partitioned when both the human and the system can contribute effectively. A true human–system collaboration operates as a pairing instead of a dichotomy of effort. Performance is improved when the most effective attributes of each part are employed.
8) Adaptation should be controlled by the system but be open to human intervention when the system fails to recognize new conditions or demands. In order to reduce task load on the human operator and improve general performance, the system should allocate tasks. To improve satisfaction and motivation, the human operator should retain control, or perceived control, of the system [128, p. 9].

Hou *et al*. developed an intelligent adaptive system for controlling multiple UAVs and demonstrated that the system significantly reduced operators' workload, improved their SA, and facilitated the operators' ability to work under high time pressure [129]. Hou *et al*. [130] also presented a framework, based on their review of more than 200 papers, for designing intelligent adaptive systems. A number of useful guidelines for designing intelligent adaptive systems were provided in this paper.

Adaptable systems and adjustable automation are two related schemas for combining automated and manual control. Adaptable systems allow the operator to elicit preprogrammed behaviors during system use similar to the way a coach would send in various "plays" from a playbook during a football game. The advantage of adaptable systems is the introduction of more flexible roles for supervisory control that allows the operator to command complex behaviors without requiring complicated communication protocols [131]. Adjustable automation allows operators to fix the level of system autonomy, allowing them to decide, depending on the changing situation, how much decision authority to reserve for themselves, and how much autonomy to delegate [132], [133]. The best type of adaptive system obviously depends on the task environment, the amount of complexity required, and the ability of the operator to delegate autonomy during high workload environments. However, it should be kept in mind that delegation and choosing an appropriate autonomy level can be very high-workload decisions in themselves. Hardin and Goodrich [134] demonstrated that a mixed-initiative control scheme (allowing the human operator and the intelligent robotic agents to jointly decide the appropriate level of autonomy) resulted in better overall performance than did adaptive autonomy and adjustable autonomy in a simulated target search task. The authors, however, caution that mixed-initiative control schemes should meet the following requirements in order to be effective.

1) The human operator and the agents should have complementary abilities.
2) Agents should have the capabilities to progress without waiting for commands from the human operator.
3) The human operator must be able to interact with multiple agents efficiently and simultaneously [134, p. 172].

The next section further discusses teaming between human and intelligent agents.

G. Intelligent Agent and Human–Robot Teaming

The necessity for more powerful intelligent agents that can interact with human operators in increasingly sophisticated ways will require that current performance improving techniques and technologies be augmented with techniques and technologies that facilitate effective H-A team interactions [135]–[138]. In recent years, researchers have designed agents that support team behaviors. Dias *et al.* [139], for example, presented the architecture of a dynamically formed Human–robot team that performs coordinated tasks. The architecture was developed based on the vision that H-A teams will dynamically form to solve complex tasks by coordinating their complementary capabilities. The architecture included TraderBot [140], TeamTalk [141], and Plays [142]. These components were used to support the development of coordination among both H-A teams and Agent-Agent teams.

TraderBot supports team coordination by allocating tasks to other agents using a market-based coordination approach. This approach is analogous to and is described within the context of market trading [139]. Market-based approaches can distribute much of the planning and execution of an operation over the team, gather information about the team, and distribute resources all within a *team aware* context. Within the architecture described by Dias *et al.*, each team member is assigned an interface agent, or *trader* (see [143]). This agent is the team members' interface to the *market* and simplifies the communication process among human and agent team members. The use of TeamTalk, a multiagent multimodal dialog system, further simplifies the communication between humans and agents. Finally, the architecture supports shared environment awareness by broadcasting all user input to all robots on the team. Therefore, coordination, communication, and shared awareness are all supported within the architecture.

Yen *et al*. [144], presented research on agents that can support the development of shared mental models. These researchers discussed the use of the collaborative agents for simulating teamwork (CAST) model, which enables agents and humans to anticipate potential information needs and proactively exchange information between team members. Component of the CAST model were tested in a simulated battlefield over two experiments. The ability of CAST to support communication and decision making was investigated. For the scenario used in the first study, the human was considered a virtual agent and invisible to other team agents. Human team members could affect team activities by directly adjusting their agent's behaviors and

strategies. For this team, the decision-making process was supported by the interactions (e.g., communication) between the human and the agents; the human provided domain expertise, while the agents gathered relevant information by collaborating with other agents. In experiment one, the use of a CAST-supported communication model (i.e., decision-theoretic) was compared to a non-CAST-supported communication model. Results of the simulation indicated that using the decision-theoretic approach, which analyzes the cost benefit ratio of communicating with other team members versus not communicating with other team members, produced better decision making than when team members communicated every time.

In the simulated scenario used in the second experiment, humans had an assistant agent that was invisible to the other team members. The assistant agent supported the human by fusing and filtering information received from other agents, tracking the human team member's mental model, and tracking the mental model shared among the team. Here, both the interactions between the human and the agents, and the interaction between the human- and the assistant-agent-supported decision making. For this experiment, the use of information fusion provided by the assistant agent was compared to not using information fusion (i.e., no assistant agent) by assessing the accuracy of decision making, particularly when the human's cognitive capacity was taxed. The results indicated that the simulated fusion team, in general, performed better than the nonfusion team. Furthermore, the disparity in performance between the two simulated teams increased as cognitive capacity decreased.

The results of the two experiments by Yen *et al.* [144] suggest that using Collaboration models such as CAST to form H-A teams may lead to better performance. However, future research should determine whether the increase in performance was a result of the CAST approach facilitating team cognition. For example, did the decision-theoretic approach support team-decision-making processes and/or did fusion lead to an increase in shared mental models among team members? Investigating these questions along with investigating factors that may influence an operator's decision to accept an agent's attempt to establish team cognition just begins to open the door to the design of future human–robot team systems.

The missing element in current research is the development of a true peer relationship between humans and artificially intelligent entities. Work cited suggest the underpinning of peer relationship in trust, artificial animal surrogates, advanced interfaces, collaborative behaviors, supervisory control allocated to robotic entities, and even shared ethical values. Whereas this ongoing research all contributes to a shared SA, the most important element of a shared linguistic awareness is still in a nascent state. Natural language interfaces by themselves are not sufficient for peer relationships which require more robust shared cognitive architectures that allow the artificial entity to infer intent, generalize instructions, and participate in a problem solving dialogue in novel situations. Intelligent agents in a mature state that can operate as peers in truly complex environments will most likely not be available in the short term. However, defining the characteristics of peer relationships is an important requisite for understanding the boundaries of the relationship. For example, delineating human-to-human problem solving in environments of interest will help to isolate cognitive factors necessary to communicate in novel environments. Investigating cognitive architectures in simpler environments will help measure what variables influence peer synergy for intent inferencing and two-way dialogues. There is no requirement for intellectual equality between human and artificial agents; the important issue is to understand what factors are necessary for peer problem solving in truly interesting, real-world environments.

VII. Conclusion

This paper examined human performance issues in supervisory control of robotic vehicles and reviewed user-interface solutions that could potentially address those issues. As robotics become increasingly prevalent in both military and civilian operations, it is important to understand HRI and its associated limitations as well as potentials. In the foreseeable future, it will be more common for humans to work with robots as a team to perform tasks that humans cannot realistically accomplish alone. Research programs such as the U.S. Army's SOURCE Army Technology Objective (ATO) were also initiated to explore how to enhance operator performance by employing advanced technologies and user-interface-design concepts. These solutions, and other innovative user-interface designs reviewed in this report, can hopefully improve HRI and therefore reduce the current challenges of operators' robotic control tasks.

Acknowledgment

The authors wish to thank B. Clark for his assistance. The views expressed in this work are those of the authors and do not necessarily reflect official Army policy.

References

[1] M. J. Barnes and A. W. Evans, III, "Soldier–robot teams in future battlefields: An overview," in *Human–Robot Interactions in Future Military Operations,* M. J. Barnes and F. Jentsch, Eds. Hampshire England: Ashgate Publishing, 2010, pp. 9–29.

[2] M. Lewis, J. Wang, and P. Scerri, "Teamwork coordination for realistically complex multi robot systems," presented at the NATO Symp. Human Factors Uninhabited Mil. Vehicles Force Multipliers, Biarritz, France, 2006.

[3] M. J. Barnes, J. Y. C. Chen, F. Jentsch, and E. Haas, "Soldier interactions with aerial and ground robotic systems in future military environments," presented at the NATO Conf. Human Factors Uninhabited Military Syst. (NATO Task Group HFM-135), Biarritz, France, Oct. 10–12, 2006.

[4] J. Y. C. Chen, J. P. Durlach, J. A. Sloan, and L. D. Bowens, "Human robot interaction in the context of simulated route reconnaissance missions," *Mil. Psychol.*, vol. 20, no. 3, pp. 135–149, 2008.

[5] G. Klein, D. D. Woods, J. M. Bradshaw, R. R. Hoffman, and P. J. Feltovich, "Ten challenges for making automation a "team player" in joint human-agent activity," *IEEE Intell. Syst.*, vol. 19, no. 6, pp. 91–95, Nov./Dec. 2004.

[6] R. Parasuraman and V. Riley, "Humans and automation: Use, misuse, disuse, abuse," *Human Factors*, vol. 39, pp. 230–253, 1997.

[7] R. Parasuraman, T. B. Sheridan, and C. D. Wickens, "A model for types and levels of human interaction with automation," *IEEE Trans. Syst., Man, Cybern. A, Syst. Humans.*, vol. 30, no. 3, pp. 286–297, May 2000.

[8] T. B. Sheridan, "Supervisory control," in *Humans and Automation*. Santa Monica, CA: Human Factors Ergonomics Soc., 2002, pp. 115–129.

[9] S. W. A. Dekker and D. D. Woods, "MABA–MABA or abracadabra? Progress on human-automation coordination," *Cogn., Technol., Work*, vol. 4, pp. 240–244, 2002.

[10] N. B. Sarter and D. D. Woods, "Teamplay with a powerful and independent agent: A full-mission simulation study," *Human Factors*, vol. 42, no. 3, pp. 390–402, 2000.

[11] K. Stubbs, D. Wettergreen, and I. Nourbakhsh, "Using a robot proxy to create common ground in exploration tasks," in *Proc. 3rd Int. Conf. Human–Robot Interact.*, 2008, pp. 375–382.

[12] S. M. Fiore, J. Elias, S. Gallagher, and F. Jentsch, "Cognition and coordination: Applying cognitive science to understand macrocognition in human-agent teams," presented at the 8th Annu. Symp. Human Interact. Complex Syst., Norfolk, VA, 2008.

[13] H. M. Cuevas, S. M. Fiore, B. S. Caldwell, and L. Strater, "Augmenting team cognition in human-automation teams performing in complex operational environments," *Aviat., Space, Environ. Med.*, vol. 78, pp. B63–B70, 2007.

[14] D. K. Mitchell and J. Y. C. Chen, "Impacting system design with human performance modeling and experiment: Another success story," in *Proc. Human Factors Ergon. Soc. 50th Annu. Meeting*, 2006, pp. 2477–2481.

[15] D. Manzey, J. Reichenbach, and L. Onnasch, "Performance consequences of automated aids in supervisory control: The impact of function allocation," in *Proc. Human Factors Ergon. Soc. 52nd Annu. Meeting*, 2008, pp. 297–301.

[16] J. Y. C. Chen and C. T. Joyner, "Concurrent performance of gunner's and robotic operator's tasks in a multi-tasking environment," *Mil. Psychol.*, vol. 21, no. 1, pp. 98–113, 2009.

[17] M. L. Cummings and S. Guerlain, "Developing operator capacity estimates for supervisory control of autonomous vehicles," *Human Factors*, vol. 49, no. 1, pp. 1–15, 2007.

[18] C. Miller, "Modeling human workload limitations on multiple UAV control," in *Proc. Human Factors Ergon. Soc. 48th Annu. Meeting*, 2004, pp. 526–527.

[19] H. A. Ruff, S. Narayanan, and M. H. Draper, "Human interaction with levels of automation and decision-aid fidelity in the supervisory control of multiple simulated unmanned air vehicles," *Presence*, vol. 11, no. 4, pp. 335–351, 2002.

[20] K. L. Mosier, N. Sethi, S. McCauley, L. Khoo, and J. M. Orasanu, "What you don't know can hurt you: Factors impacting diagnosis in the automated cockpit," *Human Factors*, vol. 49, no. 2, pp. 300–310, 2007.

[21] M. T. Dzindolet, L. G. Pierce, H. P. Beck, and L. A. Dawe, "A framework for automation use," U.S. Army Research Laboratory, Aberdeen Proving Ground, Aberdeen, MD, Tech Rep. ARL-TR-2412, 2001.

[22] B. Fischhoff, P. Slovic, and S. Lichtenstein, "Knowing with certainty: The appropriateness of extreme confidence," *J. Exp. Psychol.: Human Percept. Perform.*, vol. 3, pp. 552–564, 1977.

[23] J. Y. C. Chen and P. I. Terrence, "Effects of tactile cueing on concurrent performance of military and robotics tasks in a simulated multi-tasking environment," *Ergonomics*, vol. 51, no. 8, pp. 1137–1152, 2008.

[24] J. Y. C. Chen and P. I. Terrence, "Effects of imperfect automation on concurrent performance of military and robotics tasks in a simulated multi-tasking environment," *Ergonomics*, vol. 52, no. 8, pp. 907–920, 2009.

[25] M. T. Dzindolet, L. G. Pierce, H. P. Beck, L. A. Dawe, and B. W. Anderson, "Misuse of an automated decision making system," in *Proc. 5th Int. Conf. Human Interact. Complex Syst.*. Urbana, IL: Human Interact. Complex Syst. (HICS), 2000, pp. 81–85.

[26] K. L. Mosier and L. J. Skitka, "Automated decision makers and automated decision aids: Made for each other," in *Automation and Human Performance: Theory and Applications*, R. Parasuraman and M. Mouloua, Eds. Mahwah, NJ: Lawrence Erlbaum Associates, 1996.

[27] R. Parasuraman, R. Molloy, and I. Singh, "Performance consequences of automation-induced 'complacency'," *Int. J. Aviat. Psychol.*, vol. 3, pp. 1–23, 1993.

[28] L. C. Thomas and C. D. Wickens "Effects of display frames of reference on spatial judgments and change detection." University of Illinois, Urbana-Champaign, IL, Tech. Rep. ARL-00-14/FED-LAB-00-4, 2000.

[29] M. S. Young and N. A. Stanton, "Back to the future: Brake reaction times for manual and automated vehicles," *Ergonomics*, vol. 50, pp. 46–58, 2007.

[30] M. T. Dzindolet, L. G. Pierce, H. P. Beck, L. A. Dawe, and B. W. Anderson, "Predicting misuse and disuse of combat identification systems," *Mil. Psychol.*, vol. 13, pp. 147–164, 2001.

[31] M. J. Barnes, R. Parasuraman, and K. A. Cosenzo, "Adaptive automation for military robotic systems (chap.7.4)," in *Uninhabited Military Vehicles: Human Factors Issues in Augmenting the Force*. Brussels, Belgium: NATO, 2006, pp. 420–440, Tech. Rep. RTO-TR-HFM-078.

[32] C. D. Wickens and S. R. Dixon, "Is there a magic number 7 (to the minus 1)? The benefits of imperfect diagnostic automation: A synthesis of the literature." University of Illinois, Urbana-Champaign, IL, Tech. Rep. AHFD-05-01/MAAD-05-01, 2005.

[33] C. D. Wickens, S. R. Dixon, and M. Ambinder, "Workload and automation reliability in unmanned air vehicles," in *Human Factors of Remotely Operated Vehicles*, N. J. Cooke, H. L. Pringle, H. K. Pederson, and O. Connor, Eds. Amsterdam, The Netherlands: Elsevier, 2006, pp. 209–222.

[34] E. Rovira, K. McGarry, and R. Parasuraman, "Effects of imperfect automation on decision making in a simulated command and control task," *Human Factors*, vol. 49, pp. 76–87, 2007.

[35] M. T. Dzindolet, H. P. Beck, and L. G. Pierce, "Adaptive automation: Building flexibility into human-machine systems," in *Understanding Adaptability: A Prerequisite for Effective Performance within Complex Environments (Advances in Human Factors and Cognitive Engineering,* vol. 6, E. Salas, S. Burke, and L. Pierce, Eds. Boston, MA: Elsevier, 2006, pp. 213–245.

[36] R. Parasuraman, M. J. Barnes, and K. A. Cosenzo, "Adaptive automation for human–robot teaming in future command and control systems," *Int. C2 J.*, vol. 1, no. 2, pp. 43–68, 2007.

[37] C. D. Wickens, S. R. Dixon, J. Goh, and B. Hammer "Pilot dependence on imperfect diagnostic automation in simulated UAV flights: An attentional visual scanning analysis," University of Illinois, Urbana-Champaign, IL, Tech. Rep. AHFD-05-02/MAAD-05-02, 2005.

[38] B. R. Levinthal and C. D. Wickens, "Management of multiple UAVs with imperfect automation," in *Proc. Human Factors Ergon. Soc. 50th Annu. Meeting*, 2006, pp. 1941–1944.

[39] S. R. Dixon and C. D. Wickens, "Automation reliability in unmanned aerial vehicle control: A reliance-compliance model of automation dependence in high workload," *Human Factors*, vol. 48, pp. 474–486, 2006.

[40] S. R. Dixon, C. D. Wickens, and J. S. McCarley, "On the independence of compliance and reliance: Are automation false alarms worse than misses?," *Human Factors*, vol. 49, pp. 564–572, 2007.

[41] C. D. Wickens, S. R. Dixon, and N. Johnson, "UAV automation: Influence of task priorities and automation imperfection in a difficult surveillance task," University of Illinois, Urbana-Champaign, IL, Tech. Rep. AHFD-05-20/MAAD-05-6, 2005.

[42] M. N. Lees and J. D. Lee, "The influence of distraction and driving context on driver response to imperfect collision warning systems," *Ergonomics*, vol. 50, pp. 1264–1286, 2007.

[43] H. P. Beck, M. T. Dzindolet, and L. G. Pierce, "Automation usage decisions: Controlling intent and appraisal errors in a target detection task," *Human Factors*, vol. 49, pp. 429–437, 2007.

[44] J. D. Lee and N. Moray, "Trust, control strategies and allocation of function in human–machine systems," *Ergonomics*, vol. 35, pp. 1243–1270, 1992.

[45] J. D. Lee and K. A. See, "Trust in technology: Designing for appropriate reliance," *Human Factors*, vol. 46, pp. 50–80, 2004.

[46] R. C. Arkin "Governing lethal behavior: Embedded ethics in hybrid deliberative reactive robot architecture." Georgia Inst. Technol., Atlanta, GA, Tech. Rep. GIT-GVU-07-11, 2007.

[47] M. R. Endsley and J. M. Riley, "Supporting situation awareness in human operator—UAV/UGV collaboration," presented at the Presentation Army AMRDEC Sci. Technol. Workshop, Moffet Field, AFB, CA, 2004.

[48] M. Desai, K. Stubbs, A. Steinfeld, and H. Yanco, "Creating trustworthy robots: Lessons and inspirations from automated systems," presented at the AISB Conv.: New Front. Human–Robot Interact., Edinburgh, U.K., Apr. 6–9, 2009.

[49] M. R. Endsley, "Toward a theory of situation awareness in dynamic systems," *Human Factors*, vol. 37, no. 1, pp. 32–64, 1995.

[50] M. L. Cummings, "The need for command and control instant message adaptive interfaces: Lessons learned from Tactical Tomahawk human-in-the-loop simulations," *CyberPsychol. Behav.*, vol. 7, no. 6, pp. 653–661, 2004.

[51] M. C. Dorneich, P. M. Ververs, S. D. Whitlow, S. Mathan, J. Carciofini, and T. Reusser, "Neuro-physiologically-driven adaptive automation to improve decision making under stress," in *Proc. Human Factors Ergon. Society 50th Annu. Meeting*, 2006, pp. 410–414.

[52] R. Parasuraman, K. A. Cosenzo, and E. de Visser, "Adaptive automation for human supervision of multiple uninhabited vehicles: Effects on change detection, situation awareness, and mental workload," *Mil. Psychol.*, vol. 21, no. 2, pp. 270–297, 2009.

[53] D. Norman, "Cognitive engineering," in *User Centered System Design: New Perspectives on Human–Computer Interaction*, D. Norman and S. Draper, Eds. Hillsdale, NJ: Lawrence Erlbaum, 1986, pp. 31–61.

[54] N. B. Sarter, R. J. Mumaw, and C. D. Wickens, "Pilots' monitoring strategies and performance on automated flight decks: An empirical study combining behavioral and eye-tracking data," *Human Factors*, vol. 49, no. 3, pp. 347–357, 2007.

[55] S. Monsell, "Task switching," *TRENDS Cogn. Sci.*, vol. 7, no. 3, pp. 134–140, 2003.

[56] J. S. Rubinstein, D. E. Meyer, and J. E. Evans, "Executive control of cognitive processes in task switching," *J. Exp. Psychol.: Human Percept. Perform.*, vol. 27, pp. 763–797, 2001.

[57] J. W. Crandall, M. A. Goodrich, D. R. Olson, and C. W. Nielsen, "Validating human–robot systems in multi-tasking environments," *IEEE Trans. Syst., Man, Cybern. A, Syst. Humans*, vol. 35, no. 4, pp. 438–449, Jul. 2005.

[58] P. Squire, G. Trafton, and R. Parasuraman, "Human control of multiple unmanned vehicles: Effects of interface type on execution and task switching times," in *Proc. 2006 ACM Conf. Human–Robot Interact.*, Salt Lake City, UT, Mar. 2–4, 2006, pp. 26–32.

[59] J. Wang and M. Lewis (2007), "Human control for cooperating robot teams" in *Proc. 2nd ACM/IEEE Conf. Human–Robot Interact.*, [Online]. Available: http://usl.sis.pitt.edu/ulab/hri222-wang.pdf.

[60] E. K. Muthard and C. D. Wickens, "Factors that mediate flight plan monitoring and errors in plan revision: An examination of planning under automated conditions," Univ. Illinois, Urbana-Champaign, IL, Tech. Rep. AFHD-02-11/NASA-02-8, 2002.

[61] R. J. Mumaw, N. B. Sarter, and C. D. Wickens, "Analysis of pilots' monitoring and performance on an automated flight deck," in *Proc. 11th Int. Symp. Aviation Psychol.*. Columbus, OH: Ohio State Univ., 2001.

[62] N. B. Sarter and D. D. Woods, ""How in the world did we get into that mode?" Mode error and awareness in supervisory control," *Human Factors*, vol. 37, pp. 5–19, 1995.

[63] R. H. Mogford, J. A. Guttman, S. L. Morrow, and P. Kopardekar "The complexity construct in air traffic control: A review and synthesis of the literature." U.S. Dept. Transport. Federal Aviation Admin., Washington, DC, Tech. Rep. DOT/FAA/CT-TN95/22, 1995.

[64] W. A. Olson and N. B. Sarter, "Management by consent in human-machine systems: When and why it breaks down," *Human Factors*, vol. 43, pp. 255–266, 2001.

[65] W. A. Olson and N. B. Sarter, ""As long as I'm in control. . .": Pilot preferences for and experiences with different approaches to automation management," in *Proc. 4th Symp. Human Interaction Complex Syst.*. Los Alamitos, CA: IEEE Press, 1998, pp. 63–72.

[66] H. A. Ruff, G. Calhoun, M. Draper, J. Fontejon, and B. Guilfoos, "Exploring automation issues in supervisory control of multiple UAV's," in *Proc. Human Performance, Situation Awareness Automat. Conf.*. Mahwah, NJ: Lawrence Erlbaum, 2004, pp. 218–223.

[67] M. L. Cummings and P. M. Mitchell, "Managing multiple UAVs through a timeline display," *AIAA J. Aerosp. Comput., Inf., Commun.*, vol. 3, pp. 294–308, 2006.

[68] J. Meyer, "Effects of warning validity and proximity on responses to warnings," *Human Factors*, vol. 43, pp. 356–572, 2001.

[69] S. M. Galster, B. A. Knott, and R. D. Brown, "Managing multiple UAVs: Are we asking the right questions?," in *Proc. Human Factors Ergon. Soc. 50th Annu. Meeting*, 2006, pp. 545–549.

[70] J. Wang and M. Lewis, "Autonomy in human–robot team control," in *Proc. Human Factors Ergon. Soc. 50th Annu. Meeting*, 2006, pp. 525–529.

[71] H. Wang, M. Lewis, P. Velagapudi, P. Scerri, and K. Sycara, "How search and its subtasks scales in N robots," in *Proc. 4th ACM/IEEE Conf. Human–Robot Interact.*, La Jolla, CA, Mar. 11–13,2009, pp. 141–147.

[72] B. Trouvain, C. Schlick, and M. Mevert, "Comparison of a map- vs. camera-based user interface in a multi-robot navigation task," in *Proc. Int. Conf. Robot. Autom.*, 2003, pp. 3224–3231.

[73] B. Trouvain and H. Wolf, "Evaluation of multi-robot control and monitoring performance," in *Proc. IEEE Int. Workshop Robot Human Interactive Commun.*, 2002, pp. 111–116.

[74] D. R. Olsen and S. B. Wood, "Fan-out: Measuring human control of multiple robots," in *Proc. SIGCHI Conf. Human Factors Comput. Syst.*, Vienna, Austria, Apr. 24–29, 2004, pp. 231–238.

[75] J. M. Riley and L. D. Strater, "Effects of robot control mode on situation awareness and performance in a navigation task," in *Proc. Human Factors Ergon. Soc. 50th Annu. Meeting*, 2006, pp. 540–544.

[76] R. A. Chadwick, "Operating multiple semi-autonomous robots: Monitoring, responding, detecting," in *Proc. Human Factors Ergon. Soc. 50th Annu. Meeting*, 2006, pp. 329–333.

[77] O. Olmos, C. D. Wickens, and A. Chudy, "Tactical displays for combat awareness: An examination of dimensionality and frame of reference concepts and the application of cognitive engineering," *Int. J. Aviat. Psychol.*, vol. 10, no. 3, pp. 247–271, 2000.

[78] L. C. Thomas and C. D. Wickens, "Visual displays and cognitive tunneling: Frames of reference effects on spatial judgments and change detection," in *Proc. Human Factors Ergon. Soc. 45th Annu. Meeting*, 2001, pp. 336–340.

[79] J. Y. C. Chen and B. R. Clark, "UAV-guided navigation for ground robot operations," in *Proc. Human Factors Ergon. Soc. 52nd Annual Meeting*, 2008, pp. 1412–1416.

[80] J. P. Luck, P. L. McDermott, L. Allender, and A. Fisher, "Advantages of co-location for effective human to human communication of information provided by an unmanned vehicle," in *Proc. Human Factors Ergon. Soc. 50th Annu. Meeting*, 2006, pp. 550–554.

[81] L. Billman and M. Steinberg, "Human system performance metrics for evaluation of mixed-initiative heterogeneous autonomous systems," in *Proc. PerMIS*, 2007, pp. 120–126.

[82] M. P. Linegang, H. A. Stoner, M. J. Patterson, B. D. Seppelt, J. D. Hoffman, Z. B. Crittendon, and J. D. Lee, "Human-automation collaboration in dynamic mission planning: A challenge requiring an ecological approach," in *Proc. Human Factors Ergon. Soc. 50th Annu. Meeting*, 2006, pp. 2482–2486.

[83] C. E. Nehme, S. D. Scott, M. L. Cummings, and C. Y. Furusho, "Generating requirements for futuristic heterogeneous unmanned systems," in *Proc. Human Factors Ergon. Soc. 50th Annu. Meeting*, 2006, pp. 235–239.

[84] W. A. Olson and M. G. Wuennenberg, "Autonomy based human–vehicle interface standards for remotely operated aircraft," presented at the 20th Digital Avion. Syst. Conf., Daytona Beach, FL, Oct. 14–18, 2001.

[85] C. S. Nam, S. Johnson, Y. Li, and S. Seong, "Evaluation of human-agent user interfaces in multi-agent systems," *Int. J. Ind. Ergon.*, vol. 39, no. 1, pp. 192–201, 2009.

[86] S. Saget, F. Legras, and G. Coppin, "Collaborative model of interaction and unmanned vehicle systems' interface," presented at the HCP Workshop Superv. Control Crit. Syst. Manage., 3rd Int. Conf. Human Centered Process., Delft, The Netherlands, 2008.

[87] X. Fan, S. Oh, M. McNeese, J. Yen, H. Cuevas, L. Strater, and M. R. Endsley, "The influence of agent reliability on trust in human-agent collaboration," presented at the ECCE2008, Madeira, Portugal, Sep. 16–19, 2008.

[88] D. D. Woods, J. Tittle, M. Feil, and A. Roesler (2004), "Envisioning human–robot coordination in future operations," *IEEE Trans. Syst., Man, Cybern. C, Spec. Issue Human–Robot Interact.* [Online]. Available: http://csel.eng.ohio-state.edu/woods/papers/woods_hri_IEEE.pdf

[89] J. Y. C. Chen, E. C. Haas, and M. J. Barnes, "Human performance issues and user interface design for teleoperated robots," *IEEE Trans. Syst., Man, Cybern. C, Appl. Rev.*, vol. 37, no. 6, pp. 1231–1245, Nov. 2007.

[90] J. Y. C. Chen and J. E. Thropp, "Review of low frame rate effects on human performance," *IEEE Trans. Syst., Man, Cybern. A, Syst. Humans*, vol. 37, no. 6, pp. 1063–1076, Nov. 2007.

[91] B. D. Simpson, R. S. Bolia, and M. H. Draper, "Spatial auditory display concepts supporting situation awareness for operators of unmanned aerial vehicles," in *Human Performance, Situation Awareness, and Automation: Current Research and Trends*, vol. 1, D. A. Vincenzi, M. Mouloua, and P. A. Hancock, Eds. Mahwah, NJ: Erlbaum, 2004, pp. 61–65.

[92] E. Haas, S. Hill, C. Stachowiak, and M. Fields, *Extreme Scalability: Designing Interfaces and Algorithms for Soldier–Robotic Swarm Interaction*, U.S. Army Res. Lab., Aberdeen Proving Ground, Aberdeen, MD, Tech Rep. ARL-TR-4800, 2009.

[93] D. V. Gunn, J. S. Warm, W. T. Nelson, R. S. Bolia, D. A. Schumsky, and K. J. Corcoran, "Target acquisition with UAVs: Vigilance displays and advanced cuing interfaces," *Human Factors*, vol. 47, pp. 488–497, 2005.

[94] M. L. Cummings, A. S. Brzezinski, and J. D. Lee, "The impact of intelligent aiding for multiple unmanned aerial vehicle schedule management," *IEEE Intell. Syst. (Spec. Issue Interact. Autonomy)*, vol. 22, no. 2, pp. 52–59, Mar./Apr. 2007.

[95] C. M. Humphrey, S. M. Gordon, and J. A. Adams, "Visualization of multiple robots during team activities," in *Proc. Human Factors Ergon. Soc. 50th Annu. Meeting*, 2006, pp. 651–655.

[96] G. L. Calhoun and M. H. Draper, "Multi-sensory interfaces for remotely operated vehicles," in *Human Factors of Remotely Operated Vehicles*, N. J. Cooke, H. L. Pringle, H. K. Pedersen, and O. Connor, Eds. Oxford, U.K.: Elsevier, 2006, pp. 149–163.

[97] G. L. Calhoun, M. H. Draper, J. T. Nelson, and H. A. Ruff, "Advanced display concepts for UAV sensor operations: Landmark cues and picture-in-picture," in *Proc. Human Factors Ergon. Soc. 50th Annu. Meeting*, 2006, pp. 121–125.

[98] M. Draper G. Calhoun J. Nelson, and H. Ruff "Evaluation of synthetic vision overlay concepts for UAV sensor operations: Landmark cues and picture-in-picture." U.S. Air Force Res. Lab., Wright-Patterson AFB, OH, Tech. Rep. AFRL-HE-WP-TP-2006-0038, 2006.

[99] L. Kramer, L. Prinzel, J. Arthur, and R. Bailey "Advanced pathway guidance evaluations on a synthetic vision head-up display." NASA Langley, Hampton, VA. Tech. Rep. NASA/TP-2005-213782, 2005.

[100] M. Baker, R. Casey, B. Keyes, and H. A. Yanco. (2004). "Improved interfaces for human–robot interaction in urban search and rescue," in *Proc. 2004 IEEE Int. Conf. Syst., Man Cybern.* [Online]. Available: http://www.cs.uml.edu/∼holly/papers/baker-casey-keyes-yanco-smc04.pdf

[101] T. H. J. Collett and B. A. MacDonald, "Developer oriented visualisation of a robot program: An augmented reality approach," in *Proc. 2006 ACM Conf. Human–Robot Interact.*, Salt Lake City, UT, pp. 49–56.

[102] M. Daily, Y. Cho, K. Martin, and D. Payton, "World embedded interfaces for human–robot interaction," in *Proc. 36th Hawaii Int. Conf. Syst. Sci.*, 2003, pp. 125–130.

[103] H. K. Keskinpala and J. A. Adams, "Objective data analysis for a PDA-based human–robot interface," in *Proc. IEEE Int. Conf. Syst., Man, Cybern.*, Hague, The Netherlands, Oct. 10–13, 2004, pp. 2809–2814.

[104] G. L. Calhoun, M. H. Draper, M. F. Abernathy, F. Delgado, and M. Patzek, "Synthetic vision system for improving unmanned aerial vehicle operator situation awareness," in *Proc. SPIE*, 2005, vol. 5802, pp. 219–230.

[105] D. Tufano, "Automotive HUDs: The overlooked safety issues," *Human Factors*, vol. 39, pp. 303–311, 1997.

[106] C. D. Wickens, "Attentional tunneling and task management," presented at the 13th Int. Symp. Aviat. Psychol., Oklahoma City, OK, 2005.

[107] C. Iani and C. D. Wickens, "Factors affecting task management in aviation," *Human Factors*, vol. 49, pp. 16–24, 2007.

[108] K. J. Vincente and J. Rasmussen, "Ecological interface design: Theoretical foundations," *IEEE Trans. Syst., Man, Cybern.*, vol. 22, no. 4, pp. 589–606, Jul./Aug. 1992.

[109] H. Furukawa and R. Parasuraman, "Supporting system-centered view of operators through ecological interface design: Two experiments on human-centered automation," in *Proc. Human Factors Ergon. Soc. 47th Annu. Meeting*, 2003, pp. 567–571.

[110] H. Furukawa, H. Nakatani, and T. Inagaki, "Intention-represented ecological interface design for supporting collaboration with automation: Situation awareness and control in inexperienced scenarios," in *Proc. Human Perform., Situation Awareness Autom. II*, 2004, vol. I, pp. 49–55.

[111] M. L. Cummings and S. Bruni, "Replanning tools for supervisory control of multiple UAVs," to be published.

[112] H. Furukawa, "An empirical study on ecological interface design for multiple robot operations: Feasibility, efficacy, and issues," in *Recent Advances in Multi-Robot Systems*, A. Lazinica, Ed. Vienna, Austria: I-Tech Education and Publishing, 2008, pp. 15–32.

[113] K. J. Vincente, "Ecological interface design: Progress and challenges," *Human Factors*, vol. 44, pp. 62–78, 2002.

[114] R. M. Ratwani, A. E. Andrews, M. McCurry, J. G. Trafton, and M. S. Peterson, "Using peripheral processing and spatial memory to facilitate task resumption," in *Proc. Human Factors Ergon. Soc. 51st Annu. Meeting*, 2007, pp. 244–248.

[115] S. D. Scott, S. Mercier, M. L. Cummings, and E. Wang, "Assisting interruption recovery in supervisory control of multiple UAVs," in *Proc. Human Factors Ergon. Soc. 50th Annu. Meeting*, 2006, pp. 699–703.

[116] M. St. John, H. S. Smallman, and D. J. Manes, "Recovery from interruptions to a dynamic monitoring task: The beguiling utility of instant replay," in *Proc. Human Factors Ergon. Soc. 49th Annu. Meeting*, 2005, pp. 473–477.

[117] N. Bagheri and G. A. Jamieson, "The impact of context-related reliability on automation failure detection and scanning behavior," in *Proc. IEEE Int. Conf. Syst., Man, Cybern.*, 2004, pp. 212–217.

[118] B. D. Seppelt and J. D. Lee, "Making adaptive cruise control (ACC) limits visible," *Int. J. Human-Comput. Stud.*, vol. 65, pp. 192–205, 2007.

[119] C. R. Kelley, *Manual and Automatic Control*. New York: Wiley, 1968.

[120] W. B. Rouse, "Adaptive aiding for human/computer control," *Human Factors*, vol. 30, pp. 431–438, 1988.

[121] R. Parasuraman, T. Bahri, J. Deaton, J. Morrison, and M. J. Barnes, "Theory and design of adaptive automation in aviation systems." Aircraft Division, Naval Air Warfare Center, Warminster, PA, Progress Report NAWCADWAR-92033-60, 1992.

[122] M. S. Scerbo, F. G. Freeman, P. J. Milkulka, R. Parasuraman, F. Dinocera, and L. J. Prinzel, "The efficacy of psychophysiological measure for implementing adaptive technology." NASA Langley Res. Center, Hampton, VA, Tech. Paper NASA/TP-2001–211018, 2001.

[123] F. G. Freeman, P. J. Mikulka, L. J. Prinzel, and M. W. Scerbo, "Evaluation of an adaptive automation system using three EEG indices with a visual tracking task," *Biol. Psychol.*, vol. 50, pp. 61–76, 1999.

[124] P. J. Milkulka, M. W. Scerbo, and F. G. Freeman, "Effects of a biocybernetic system on vigilance performance," *Human Factors*, vol. 44, pp. 654–664, 2002.

[125] G. Wilson and C. A. Russell, "Performance enhancement in a UAV task using psychophysiologically determined adaptive aiding," *Human Factors*, vol. 50, no. 3, pp. 468–474, 2007.

[126] R. Parasuraman, M. Mouloua, and R. Molloy, "Effects of adaptive task allocation on monitoring automated systems," *Human Factors*, vol. 38, pp. 665–679, 1996.

[127] M. A. Dornheim, "Apache tests power of new cockpit tool," *Aviat. Week Space Technol.*, vol. 151, no. 16, pp. 46–49, 1999.

[128] N. B. Steinhauser, D. Pavlas, and P. A. Hancock, "Design principles for adaptive automation and aiding," *Ergon. Design*, vol. 17, no. 2, pp. 6–10, 2009.

[129] M. Hou, R. D. Kobierski, and M. Brown, "Intelligent adaptive interfaces for the control of multiple UAVs," *J. Cogn. Eng. Decis. Making*, vol. 1, no. 3, pp. 327–362, 2007.

[130] M. Hou, M. S. Gauthier, and S. Banbury, "Development of a generic design framework for intelligent adaptive systems," in *Human–computer Interaction: HCI Intelligent Multimodal Interaction Environments, Part III, HCII 2007* (LNCS 4552), J. Jacko, Ed. New York: Springer-Verlag, 2007, pp. 313–320.

[131] C. Miller and R. Parasuraman, "Designing for flexible interaction between humans and automation: Delegation interfaces for supervisory control," *Human Factors*, vol. 49, pp. 57–75, 2007.

[132] M. A. Goodrich, "On maximizing fan-out: Controlling multiple unmanned vehicles," in *Human–Robot Interaction in Future Military Applications*, M. J. Barnes and F. G. Jentsch, Eds. Hampshire, U.K.: Ashgate Publishing, 2010, pp. 375–395.

[133] B. P. Sellner, F. W. Heger, L. M. Hiatt, R. Simmons, and S. Singh, "Coordinated multi-agent teams and sliding autonomy for large-scale assembly," *Proc. IEEE*, vol. 94, no. 7, pp. 1425–1444, Jul. 2006.

[134] B. Hardin and M. A. Goodrich, "On using mixed-initiative control: A perspective for managing large-scale robotic teams," in *Proc. 4th ACM/IEEE Int. Conf. Human–Robot Interact.*, La Jolla, CA, Mar. 11–13, 2009, pp. 165–172.

[135] C. E. Billings, *Aviation Automation: The Search for a Human-Centered Approach*. Mahwah, NJ: Lawrence Erlbaum Associates, 1996.

[136] J. M. Bradshaw, A. Acquisti, J. Allen, M. R. Breedy, L. Bunch, N. Chambers *et al.*, "Teamwork-centered autonomy for extended human–agent interaction in space applications," in *Proc. AAAI 2004 Spring Symp.*, 2004, pp. 22–24.

[137] S. A. Green, M. Billinghurst, X. Chen, and J. G. Chase, "Human–robot collaboration: A literature review and augmented reality approach in design," *Int. J. Adv. Robot. Syst.*, vol. 5, no. 1, pp. 1–18, 2008.

[138] M. Lewis, "Designing for human–agent interaction," *AI Mag.*, vol. 19, no. 2, pp. 67–78, 1998.

[139] M. B. Dias, T. K. Harris, B. Browning, E. G. Jones, B. Argall, M. Veloso *et al.*, "Dynamically formed human–robot teams performing coordinated tasks," presented at the 2006 AAAI Spring Symp., Stanford, CA, 2006.

[140] B. M. Dias, M. Zinck, R. Zlot, and A. Stentz, "Robust multirobot coordination in dynamic environments," in *Proc. IEEE Int. Conf. Robot. Autom.*, 2004, vol. 4, pp. 3435–3442.

[141] T. K. Harris, S. Banerjee, A. Rudnicky, J. Sison, K. Bodine, and A. Black, "A research platform for multi-agent dialogue dynamics," in *Proc. IEEE Int. Workshop Robot. Human Interactive Commun.*, 2004, pp. 497–502.

[142] M. Bowling, B. Browning, and M. Veloso, "Plays as effective multiagent plans enabling opponent-adaptive play selection," in *Proc. Int. Conf. Automated Plann. Scheduling*, 2004, pp. 1–8.

[143] R. Zlot and A. Stentz, "Market-based multi robot coordination for complex tasks," *Int. J. Robot. Res.*, vol. 25, no. 1, pp. 73–101, 2006.

[144] J. Yen, X. Fan, S. Sun, T. Hanratty, and J. Dumer, "Agents with shared mental models for enhancing team decision-makings," *Decis. Support Syst.*, vol. 41, no. 3, pp. 634–653, 2006.

Supervisory Control of Multiple Robots: Effects of Imperfect Automation and Individual Differences

Jessie Y.C. Chen and Michael J. Barnes

Human Factors: The Journal of the Human Factors and Ergonomics Society 54:157 (2012)

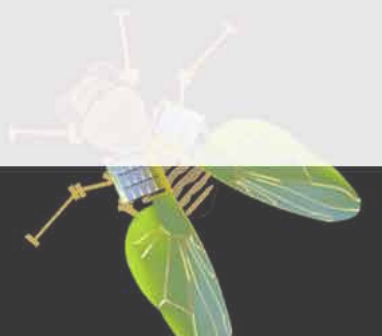

Supervisory Control of Multiple Robots: Effects of Imperfect Automation and Individual Differences

Jessie Y. C. Chen and **Michael J. Barnes,** U.S. Army Research Laboratory, Orlando, Florida

Objective: A military multitasking environment was simulated to examine the effects of an intelligent agent, RoboLeader, on the performance of robotics operators.

Background: The participants' task was to manage a team of ground robots with the assistance of RoboLeader, an intelligent agent capable of coordinating the robots and changing their routes on the basis of battlefield developments.

Method: In the first experiment, RoboLeader was perfectly reliable; in the second experiment, RoboLeader's recommendations were manipulated to be either false-alarm prone or miss prone, with a reliability level of either 60% or 90%. The visual density of the targeting environment was manipulated by the presence or absence of friendly soldiers.

Results: RoboLeader, when perfectly reliable, was helpful in reducing the overall mission times. The type of RoboLeader imperfection (false-alarm vs. miss prone) affected operators' performance of tasks involving visual scanning (target detection, route editing, and situation awareness). There was a consistent effect of visual density (clutter of the visual scene) for multiple performance measures. Participants' attentional control and video gaming experience affected their overall multitasking performance. In both experiments, participants with greater spatial ability consistently outperformed their low-spatial-ability counterparts in tasks that required effective visual scanning.

Conclusion: Intelligent agents, such as RoboLeader, can benefit the overall human-robot teaming performance. However, the effects of type of agent unreliability, tasking requirements, and individual differences have complex effects on human-agent interaction.

Application: The current results will facilitate the implementation of robots in military settings and will provide useful data to designs of systems for multirobot control.

Keywords: human-robot interaction, supervisory control, intelligent agent, military, imperfect automation, individual differences, spatial ability, attentional control, gaming experience

Address correspondence to J. Chen, U.S. Army Research Laboratory, Human Research and Engineering Directorate, Orlando, FL 32826; e-mail: jessie.chen@us.army.mil.

HUMAN FACTORS
Vol. 54, No. 2, April 2012, pp. 157-174
DOI:10.1177/0018720811435843

INTRODUCTION

Robots are being used more frequently in military operations, and the tasks they are being used for are evolving in complexity. In the future battlefield, soldiers may be given multiple tasks to perform concurrently, such as navigating a robot while conducting surveillance, maintaining local security and situation awareness (SA), and communicating with fellow team members. The possibility of a robotic battlefield creates a number of human factors as well as ethical issues related to nonhuman intelligence conducting combat missions (Barnes & Evans, 2010; Singer, 2010).

A potential issue is that the proliferation of intelligent systems could easily overwhelm the human operators' ability to adequately supervise these systems (Chen, Durlach, Sloan, & Bowens, 2008; Schurr, 2007). As the size of the robot team increases, human operators may fail to maintain adequate SA when their attention is constantly switching between the robots; cognitive resources may also be overwhelmed by the numerous intervention requests from the robots (Lewis et al., 2010). Research shows that autonomous cooperation between robots can aid the performance of the human operators and enhance the overall human-robot team performance (Lewis et al., 2010; Schurr, 2007). However, human operators' involvement in mixed-initiative teams will still be required for the foreseeable future, especially in situations involving critical decision making. Human operators' decision making may be influenced by "implicit goals" that the robots are not aware of (i.e., are not programmed into the behaviors of the robots; Linegang et al., 2006) and by real-time developments on the battlefield that may require the human operator to change plans for individual robots or the entire robotic team. Effective communication between the human operator and robots, therefore, becomes critical in ensuring mission success.

Past research has demonstrated the effectiveness of a robot proxy to enhance shared understanding between the human operator and the robot in an exploration task (Stubbs, Wettergreen, & Nourbakhsh, 2008). Other research and development efforts more related to supervisory control of military robotics include the U.S. Army's Playbook program and the U.S. Air Force's Vigilant Spirit Control Station for management of multiple unmanned aerial systems (UASes; Fern et al., 2011; Miller & Parasuraman, 2007).

Current Study

To achieve a better balance of enhancing autonomy and capability while simplifying human-robot interaction, a robotic surrogate for the human operator, RoboLeader, was developed under the U.S. Army Research Laboratory's (ARL) Director's Research Initiative Program (Snyder, Qu, Chen, & Barnes, 2010). RoboLeader is an intelligent agent that interprets an operator's intent and issues detailed command signals to a team of robots of lower capabilities. Instead of directly managing each individual robot, the human operator deals only with a single entity, RoboLeader. The operator can, therefore, better focus on other tasks requiring his or her attention.

The present research focuses on issues related to human-agent teams: the dynamics of using an agent as a subordinate supervisor to aid in multirobot control as a function of mission task load and agent reliability as well as individual differences among human operators. Specifically, we were interested in understanding the effects of using an intelligent agent as a team member in highly demanding multitasking environments when its suggestions were less than perfect and in understanding how individual differences interacted with agent unreliability. To date, there has been minimal research on supervisory control investigating all these factors in one study.

We examined the effectiveness of RoboLeader for enhancing the overall human-robot teaming performance in two experiments. In Experiment 1, we compared the operators' target detection performance in the four-robot and eight-robot conditions, with or without RoboLeader. In Experiment 2, we investigated the effects of various reliability levels for RoboLeader on operators' multitasking performance; the reliability of RoboLeader's recommendations was manipulated to be either false-alarm prone (FAP) or miss prone (MP), with a reliability level of either 60% or 90%. In both experiments, the effects of individual differences in spatial ability, attentional control, and gaming experiences were examined. In the rest of this section, we briefly review the main theoretical issues investigated in these experiments. For a detailed review on human performance issues related to supervisory control of multiple robots, see Chen, Barnes, and Harper-Sciarini (2011).

Imperfect Automation

Since it is unlikely for any automated systems to achieve 100% reliability at all times, the effects of unreliable automation on human operator performance need to be better understood before these intelligent systems can be implemented. The effects of imperfect automation are examined by Meyer (2001, 2004), who suggests that FAP and MP alerts may affect the use of an automated system in different ways. High false alarm (FA) rates were seen to reduce the operator's response to alerts (i.e., compliance), and high miss rates reduced the operator's reliance on automated systems. Similar results were reported in Dixon and Wickens (2006). They found that the operator's performance of the *automated* task degraded when the automation was FAP because of the operator's reduced compliance with the automated system; when the miss rate was high, the operator's performance of the *concurrent* task was affected more than the automated task because the operator allocated more visual attention to monitor the automated task.

McCarley (2007) showed that FAP automation hurt performance more on the automated task than did MP automation ("cry wolf" effect) and hurt performance at least as much as MP automation on the concurrent task (pp. 570–571). Finally, Wickens and Dixon (2007) demonstrated that when the reliability level is below approximately 70%, operators will often ignore the alerts. In their meta-analytic study, Wickens and Dixon found that "a reliability of 0.70 was the 'crossover point' below which unreliable

automation was worse than no automation at all" (p. 201). In our first experiment, which serves as a baseline investigation of the utility of RoboLeader, a perfect reliability level was implemented. In the second experiment, we manipulated both RoboLeader's error type and reliability level to systematically examine the effects of automation imperfections on the overall human-robot team performance.

Individual Differences

In the current study, we also sought to evaluate whether individual differences in spatial ability, attentional control, and video gaming experience might affect the operator's performance. Spatial ability (SpA) has been found to be a significant factor in certain visual display domains (Stanney & Salvendy, 1995), multitasking involving flight asset monitoring and management (Morgan et al., 2011), virtual environment navigation (Chen, Czerwinski, & Macredie, 2000), target search task (Chen, 2010; Chen et al., 2008; Chen & Joyner, 2009; Chen & Terrence, 2008, 2009), and robotics task performance (Cassenti, Kelley, Swoboda, & Patton, 2009; Lathan & Tracey, 2002). U.S. Air Force scientists (Chappelle, McMillan, Novy, & McDonald, 2010; Chappelle, Novy, Randall, & McDonald, 2010) interviewed 53 subject matter experts about abilities that were critical to effective performance of UAS control tasks in terms of piloting and sensor operations; SpA was identified as an important factor for both tasks. Our previous research showed that individuals with greater SpA exhibited more effective visual scanning and target detection performance (Chen, 2010; Chen et al., 2008; Chen & Joyner, 2009; Chen & Terrence, 2008, 2009).

In addition to spatial ability, the relationship between attentional control and multitasking performance was also examined. Attentional control is defined as one's ability to focus and shift attention in a flexible manner (Derryberry & Reed, 2002). Several studies have shown that there are individual differences in multitasking performance, and some people are less prone to performance degradation during multitasking conditions (Rubinstein, Meyer, & Evans, 2001; Schumacher et al., 2001). There is evidence that people with better attention control can allocate their attention more flexibly and effectively, and attention-switching flexibility can predict performance of such diverse tasks as flight training and driving (Bleckley, Durso, Crutchfield, Engle, & Khanna, 2003; Derryberry & Reed, 2002; Feldman Barrett, Tugade, & Engle, 2004; Kahneman, Ben-Ishai, & Lotan, 1973). According to a recent U.S. Air Force survey of subject matter experts on the performance of operators of UASes (Chapelle, McMillan et al., 2010), attentional control is one of the most important abilities that would affect an operator's performance, since the robotics control task is inherently multitasking (e.g., sensor manipulation, tracking, communication).

According to Feldman Barrett et al. (2004), those with lower attentional control tend to take the "cognitive miser" approach (i.e., conserving the amount of cognitive resources) when dealing with complex information processing to reduce the attentional control requirements. When dealing with automated systems, therefore, it is likely that operators with different levels of attention switching abilities may react differently to unreliable automated systems. In other words, operators' behaviors of compliance with, and reliance on, automation may be altered by their ability to effectively switch their attention among the systems. For example, the automation-induced complacency effect repeatedly demonstrated in previous research (Dzindolet, Pierce, Beck, Dawe, & Anderson, 2001; Parasuraman & Manzey, 2010; Thomas & Wickens, 2004; Young & Stanton, 2007) may be more severe for individuals with poor attentional control compared with those with better attentional control. This phenomenon has been demonstrated in Chen and Terrence (2009) and was further tested in the current experiment, which employed a simulation environment considerably different from that of Chen and Terrence's.

Finally, the current study sought to examine the relationship between participants' video gaming experience and their task performance as well as SA of the mission environment. According to Green and Bavelier (2006) and Hubert-Wallander, Green, and Bavelier (2010), experienced action video game players, compared with infrequent gamers and nongamers, were found to

Figure 1. RoboLeader user interface.

perform significantly better on tasks that required visuospatial selective attention, multiple object tracking, rapid process of visual information and imagery, and flexibility in attention allocation. Hambrick, Oswald, Darowski, Rench, and Brou (2010) also demonstrated the relationship between video game experience and multitasking performance. Therefore, we expected frequent gamers would outperform infrequent gamers in our visually demanding task environment in terms of target and event detection and monitoring of the mission environment.

EXPERIMENT 1

In Experiment 1, a military reconnaissance mission environment was simulated to examine the effectiveness of RoboLeader, an intelligent agent capable of coordinating a team of ground robots and changing their routes on the basis of developments in the mission environment. The participants' task was to manage either four or eight robots with or without the assistance of RoboLeader while searching for hostile targets via streaming video from the robots. The experiment is a mixed-model design, with RoboLeader (with or without RoboLeader [baseline]) as the between-subject variable and the number of robots used in the scenario (four vs. eight) as the within-subject variable.

Method

Participants. A total of 30 individuals from the Orlando, Florida, area (17 males and 13 females, mean age 24.7) participated in the study. Participants were compensated $15 per hour for their participation in the experiment.

Simulators. A modified version of the Mixed Initiative Experimental (MIX) Testbed was used as the simulator for this experiment (Barber, Davis, Nicholson, Finkelstein, & Chen, 2008). The Operator Control Unit (OCU) of the MIX Testbed (Figure 1) was modeled after the Tactical Control Unit developed under the ARL Robotics Collaborative Technology Alliance. RoboLeader has the capability of collecting information from subordinate robots with limited autonomy (e.g., collision avoidance and self-guidance to reach target locations), making tactical decisions, and coordinating the robots by issuing commands, waypoints, or motion trajectories (Snyder et al., 2010). See the Procedure

section for more details about the user interface of RoboLeader.

Surveys and tests. A demographics questionnaire was administered at the beginning of the training session. An Ishihara color vision test (with nine test plates) was administered via PowerPoint presentation. The RoboLeader user interface employed several colors to display the plans for the robots, and normal color vision was required to effectively interact with the system. A questionnaire on attentional control (Derryberry & Reed, 2002) was used to evaluate participants' perceived attentional control (PAC). The Attentional Control survey consists of 21 items and measures attention focus and shifting. The scale has been shown to have good internal reliability ($\alpha = .88$). The Cube Comparison Test (Ekstrom, French, & Harman, 1976) and the Spatial Orientation Test (Gugerty & Brooks, 2004) were used to assess participants' spatial ability. Participants' perceived workload was evaluated with use of the computer-based version of the NASA Task Load Index questionnaire (NASA-TLX; Hart & Staveland, 1988).

Procedure. Participants were randomly assigned to the RoboLeader group or the baseline (no RoboLeader) group before their sessions started. Before the training session, they completed the preliminary tests (color vision and spatial) and surveys (demographic and PAC). Training, lasting about 1 hr, was self-paced and was delivered by PowerPoint slides showing the elements of the OCU, steps for completing various tasks, several mini exercises for practicing the steps, and exercises for performing the experimental tasks. The participants had to demonstrate that they could recall all the steps for performing the tasks without any help. The experimental session immediately followed the training session and consisted of two scenarios, each lasting approximately 30 min, in which participants used their robotic assets to locate 20 targets (i.e., 10 insurgents carrying weapons and 10 improvised explosive devices [IEDs]) in the remote environment. There were four robots available in one scenario and eight robots in the other scenario. The order of scenarios was counterbalanced across participants.

When each scenario started, the robots began by following preplanned routes, at which time the operator's task of monitoring the environment and detecting insurgents or IEDs began (by clicking on one of the four video thumbnail views highlighted in the color of its route to enlarge it into the expanded view on the top of the screen). Because of the size of the thumbnails, the participants needed to enlarge them into the expanded view to identify the targets. The robots did not have aided target recognition capability; therefore, the participants had to detect the 10 insurgents (individuals dressed in Middle Eastern attire and carrying weapons) and 10 IEDs by themselves.

For the insurgents, participants used their computer mouse to click on the targets to "lase" them as soon as they were detected. The "lased" insurgents were automatically displayed on the map. For the IEDs, the participants clicked on the IED button on the interface and then marked the locations of the IEDs on the map. There were friendly dismounted soldiers (individuals dressed in military uniform) and civilians (individuals dressed in Middle Eastern attire without weapons) in the simulated environment to increase the visual noise for the target detection tasks. The participants were told that their objective was to finish reconnoitering the area using their robots in the least amount of time possible. Therefore, when replanning a route, the participant and/or RoboLeader must consider both the effectiveness and efficiency of the new route.

In each scenario, there were six "events" that required revisions to a robot's current plans or route. In some cases, robots had to be rerouted to avoid certain areas (e.g., obstructions and hostile areas); in other cases, robots were rerouted to investigate nearby high-priority areas on the basis of intelligence messages. After an event transpired (indicated by visual and/or auditory alerts), the baseline participants must notice that the event had occurred and then reroute the robot that was affected by the event. For the RoboLeader group, RoboLeader would recommend plan revisions to the operator (by presenting the new route to the operator visually on the map), who could either accept the plans (by clicking on a button) or modify them

TABLE 1: Experiment 1: Mean Operator Task Performance and Workload Assessments

	Baseline		RoboLeader		Summary of Main Effects[a]
Measure	4 Robots	8 Robots	4 Robots	8 Robots	
Targets (% detected)	75.0 (10.9)	61.3 (13.9)	77.0 (14.6)	62.7 (18.9)	4 robots > 8 robots
Situation awareness queries (% correct)	46.3 (17.2)	26.7 (25.8)	48.7 (22.6)	23.8 (20.2)	4 robots > 8 robots
Workload (NASA Task Load Index)	67.4 (16.3)	71.4 (18.1)	61.3 (14.9)	67.1 (14.7)	8 robots > 4 robots

Note. Standard deviations are presented in parentheses.
[a]Based on statistical analyses reported in the Results section

as necessary (by dragging the waypoints to the desired locations). Out of these six events, three were "bottom-up" (e.g., unanticipated obstacles detected by the robots that obstructed their navigation; indicated by flashing thumbnails) and three "top-down" (e.g., intelligence that the human operator received from the intelligence network; indicated by auditory alerts as well as appearance of icons on the map). The participants were told to do their best to perform both the rerouting and the target detection tasks instead of focusing on one at the expense of the other.

In each scenario, there were five SA queries, which were triggered on the basis of time progression (e.g., 3 min into the scenario). The SA queries included questions such as "Which areas have the robots searched?" (the participants were instructed to mark the searched areas on a blank map), "Which of your robots is the closest to [area of interest]?" and so on. The OCU screen was blank when an SA query was triggered, and only the SA query and the answer box were displayed on the screen. After each scenario, the participants assessed their workload (NASA-TLX) and then took a 2-min break. The entire experimental session lasted approximately 2 hr.

Dependent measures and data analysis. Dependent measures include number of targets located and identified, the operator's SA of the mission environment as well as awareness of the status of the individual robots, and perceived workload. Mixed-model ANCOVAs were performed with RoboLeader (with or without RoboLeader) as the between-subject factor and number of robots (four vs. eight) as the within-subject factor. Participants' SpA (composite score of the two spatial tests) and their Attentional Control survey scores were used as covariates.

Results

Target detection performance. Table 1 lists several measures relating to operator performance and perceived workload. In terms of target detection performance, the analysis revealed that participants detected significantly fewer targets (with insurgents and IEDs combined) when they had eight robots compared with the condition when four robots were available, $F(1, 26) = 25.35$, $p = .0001$, $\eta^2_p = .494$. Participants with higher SpA (those with higher composite scores of spatial tests) detected significantly more targets than did those with lower SpA, $F(1, 26) = 8.83$, $p = .02$, $\eta^2_p = .254$ (Figure 2). The effects of RoboLeader and attentional control were not statistically significant.

SA. The analysis revealed that participants' SA was significantly poorer in the eight-robot condition compared with the four-robot condition, $F(1, 26) = 13.31$, $p = .001$, $\eta^2_p = .33$ (Figure 3). Frequent video game players had significantly better SA than infrequent gamers in the RoboLeader condition, $F(1, 11) = 5.90$, $p = .02$, $\eta^2_p = .35$, but not in the baseline condition.

Perceived workload. The analysis showed that participants experienced significantly higher workload when there were eight robots ($M = 69.3$) versus four robots ($M = 64.3$),

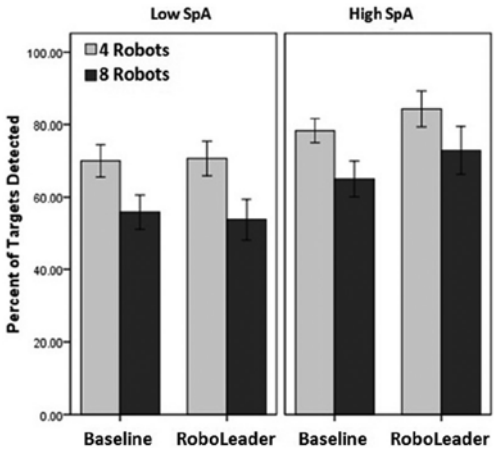

Figure 2. Target detection performance and effects of operator spatial ability (SpA).

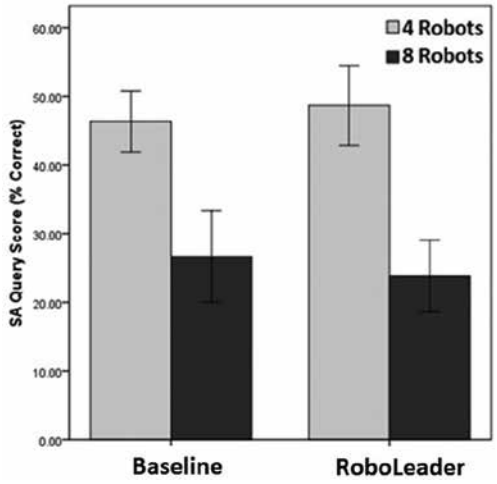

Figure 3. Situation awareness queries.

$F(1, 27) = 5.24$, $p = .023$, $\eta^2_p = .158$ (Figure 4). Participants in the RoboLeader group assessed their workload slightly lower ($M = 64.1$) than did those in the baseline group ($M = 69.4$). However, the difference failed to reach statistical significance. Participants with higher PAC rated their workload as significantly lower than did those with lower PAC; similarly, frequent video gamers' workload assessments were significantly lower than those of infrequent gamers', $p < .05$ (Figure 4).

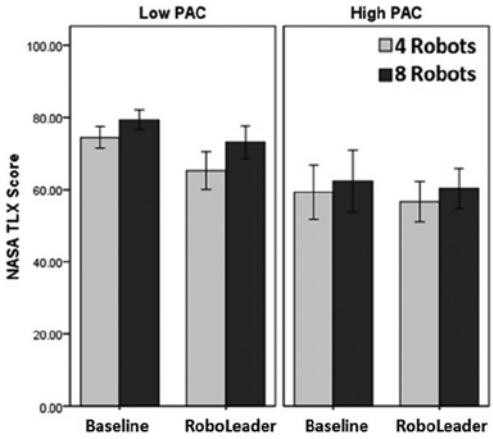

Figure 4. Perceived workload and effects of perceived attentional control (PAC).

Operator's interaction with the OCU. Participants' interaction with the OCU (e.g., clicks on the graphical control interface) was analyzed. Participants' SpA was significantly correlated with the number of thumbnail clicks (to expand the video to find targets), $r = .448$, $p = .006$. Additionally, participants in the RoboLeader group spent significantly less time completing their mission scenarios (not including the time on modifying the plans) than did those in the baseline group (20.7 vs. 23.8 min), $F(1, 27) = 7.12$, $p = .013$, $\eta^2_p = .209$. The longer completion times in the baseline condition suggest that the robots' routes were less efficient than those in the RoboLeader condition, since both groups were alerted about the events that required route revisions and the time participant spent on rerouting was excluded from the mission completion times.

EXPERIMENT 2

In Experiment 2, the effects of unreliable RoboLeader on operator performance were investigated. The participants' task, as in Experiment 1, was to manage four robots with the assistance of RoboLeader while searching for hostile targets via streaming video from the robots. The reliability of RoboLeader's solutions was manipulated to be either FAP or MP, with a reliability level of either 60% or 90%. Furthermore, Experiment 2 simulated a multitasking environment rather than a

Figure 5. RoboLeader user interface in Experiment 2.

dual-tasking environment as in Experiment 1. In addition to the target detection and route revision tasks, the participants had to simultaneously perform a gauge monitoring task and an auditory communication task. Finally, the visual density (VD) of the simulated environment (clutter of the visual scene) was manipulated; there were twice as many entities (virtual human characters) in the high-density environment as in the low-density environment. The experiment is a mixed-model design, with RoboLeader imperfection type (FAP vs. MP) and reliability level (60% vs. 90%) as the between-subject factors and VD (high vs. low) of the simulated environment as the within-subject factor.

Method

Participants. For the second experiment, 40 individuals (23 males and 17 females, mean age 23.8 years) from the Orlando, Florida, area participated. They were compensated $15 per hour for their time.

Apparatus. The simulator in the first experiment was modified so the reliability of RoboLeader was either FAP or MP, at a level of either 60% or 90% (FAP60, FAP90, MP60, and MP90, respectively; see Procedure). The number of robots was reduced to four and a gauge monitoring task and a communication task (a text input area and a submission button) were added to the user interface (Figure 5). More details about these manipulations and changes are presented in the Procedure section.

The same surveys and tests used in Experiment 1 were employed in Experiment 2. A modified version of the Usability and Trust Questionnaire used in Chen and Terrence (2009) assessed participants' perceived usability of the RoboLeader system as well their trust in the system. The items that measured participants' trust in the system were modified from the Trust Between People and Automation questionnaire (Jian, Bisantz, & Drury, 2000). The questionnaire consisted of 22 questions on a scale of 1 to 7 and included items such as "The RoboLeader display can be deceptive" and "The RoboLeader system is dependable."

Procedure. Participants were randomly assigned to the FAP60, FAP90, MP60, or MP90 group (with 10 participants per group) before their sessions started. The procedure of the preexperimental session (surveys, tests, and training) followed the procedure of Experiment 1 and lasted approximately 1 hr. The type and

reliability level of each participant's RoboLeader condition (FAP60, FAP90, MP60, or MP90) matched in the training and experimental scenarios. The participants were informed that RoboLeader was either FAP or MP and "fairly but not always reliable" (for the 90% conditions) or "not always reliable" (for the 60% conditions).

The experimental session began immediately after the training session and lasted about 1 hr. Each experimental session had two scenarios (one with high VD and one with low density), both lasting approximately 30 min. During the scenarios, participants used their four robots to locate 10 targets (insurgents carrying weapons) while rerouting their robots around events in the remote environment (described later). In the low-density scenario, there were about 600 civilians throughout the scenario, and in the high-density scenario, there were about 600 civilians and 600 friendly soldiers visible in the environment. The presence of friendly soldiers in the high-density scenario made the target detection task more difficult, as the friendly soldiers all carry weapons. The procedure of the target search task followed that of Experiment 1, and the order of scenarios was counterbalanced across participants.

During the scenarios, as in Experiment 1, several events required revisions to the robots' routes. RoboLeader and the participants needed to create new routes toward "high-priority areas" while avoiding rerouting the robots through "hostile areas" or areas already traversed. As in Experiment 1, participants were told that their objective was to finish reconnoitering the area using their robots in the least amount of time possible while keeping all route edits as close as possible to the original routes. In the FAP conditions, RoboLeader would provide rerouting recommendations that were not necessary. Participants could check the validity of RoboLeader's recommendations by reviewing their map. A true event was associated with an icon (a red square for a hostile area and a blue square for a high-priority area; see Figure 5), but FAs were not.

In the FAP60 scenario, following the signal detection theory paradigm (Green & Swets, 1988), RoboLeader provided solutions to all five events that required revisions to robots' routes, and it also provided solutions on four occasions when no events occurred and no revisions were necessary (i.e., five hits, four FAs, zero misses, and one correct rejection), making a total of 10 events, 6 of which were positive. In the FAP90 scenario, RoboLeader provided solutions to all 5 events that required revisions, and it also provided solutions on one occasion when no events occurred. In the MP scenarios, RoboLeader would fail to provide solutions when some events happened. In the MP60 scenario, 10 true events occurred that required revisions to a robot's route, although RoboLeader provided solutions for only 2 of them. In the MP90 scenario, 10 true events occurred and RoboLeader provided solutions for 8 of them.

In addition to the tasks described already, the participants simultaneously performed a gauge monitoring task and an auditory communications task. The gauge monitoring task (upper left corner of the OCU under the blue RoboLeader message box) displayed four gauges constantly in motion that entered an upper or lower limit at various prespecified times throughout the scenarios. The participants were required to monitor the gauges and press a "Reset" button when any gauge entered the upper or lower limit to put the gauges back to their normal levels. The auditory communications task presented prerecorded questions at 30-s intervals during the scenarios. Questions included simple military-related reasoning and memory (i.e., call-sign recognition) tests. Participants used a keyboard to enter their responses for the questions into the communications panel on the OCU (adjacent to the gauges; see Figure 5). As in Experiment 1, the participants were told to do their best to perform all the tasks instead of focusing on some at the expense of the others. Each scenario also contained five SA queries, which followed the same format and procedure as in Experiment 1.

A 2-min break was given between the experimental scenarios. Participants assessed their workload using an electronic NASA-TLX immediately after each scenario. Following completion of both scenarios, participants were asked to evaluate the usability of the RoboLeader

system by filling out the Usability and Trust Questionnaire.

Dependent measures and data analysis. Dependent measures include the number of targets located and identified, the number of routes edited, the operators' SA of the mission environment, concurrent task performance (gauge monitoring and auditory communications), and perceived workload. Mixed-model ANCOVAs were performed with RoboLeader imperfection type (FAP vs. MP) and reliability level (60% [low] vs. 90% [high]) as the between-subject factors and VD (high vs. low) as the within-subject factor. Participants' composite SpA test scores and their Attentional Control survey scores were used as covariates.

Results

Route editing task performance. Table 2 lists several measures relating to operator performance and perceived workload. In terms of the operator's route editing (i.e., automated) task performance, the analysis showed that both imperfection type and reliability level of RoboLeader significantly affected the percentage of routes that participants edited, $F(1, 35) = 161.7$, $p = .0001$, $\eta^2_p = .82$, and $F(1, 35) = 7.4$, $p = .01$, $\eta^2_p = .18$, respectively (Figure 6). Participants edited more routes in the FAP condition and in the high-reliability (90%) condition. There was a significant difference between those with higher SpA and lower SpA, $F(1, 35) = 7.5$, $p = .008$, $\eta^2_p = .18$. The difference between the high- and low-SpA participants was especially pronounced in the MP60 condition, with high-SpA participants editing 74% of the routes and low-SpA participants editing only 56% ($p = .024$). Participants with lower PAC performed significantly worse than their higher-PAC counterparts in the MP condition, $F(1, 18) = 6.0$, $p = .04$, $\eta^2_p = .25$, but not in the FAP condition. Further examination of the data revealed that the difference mainly came from the low-reliability condition (73% vs. 60%), whereas both groups performed at the same level in the high-reliability condition (76%).

Target detection performance. The analysis revealed that there were main effects of imperfection type and VD, $F(1, 35) = 45.7$, $p = .0001$, $\eta^2_p = .57$, and $F(1, 35) = 12.2$, $p = .001$, $\eta^2_p = .26$, respectively. Participants detected significantly fewer insurgents in the MP condition and in the high-VD environment. There was a significant difference between those with higher SpA and those with lower SpA, $F(1, 35) = 4.1$, $p = .045$, $\eta^2_p = .104$ (Figure 7). Further analysis revealed that high-SpA participants outperformed low-SpA participants to a greater extent in the high-VD condition than in the low-VD condition, $F(1, 37) = 6.09$, $p = .018$, $\eta^2_p = .141$.

SA. Participants' SA (percentage of SA queries answered correctly) was significantly better in the MP condition than in the FAP condition, $F(1, 35) = 8.5$, $p = .003$, $\eta^2_p = .20$ (Figure 8). Frequent video game players had slightly better SA than did infrequent gamers; however, the difference failed to reach statistical significance, $F(1, 38) = 3.33$, $p = .076$.

Communication task performance. There were no main effects associated with the communication task performance. There was a significant interaction between VD and participants' PAC, $F(1, 35) = 5.4$, $p = .026$, $\eta^2_p = .134$.

Gauge monitoring performance. There was a significant interaction between VD and reliability level of RoboLeader, $F(1, 35) = 4.3$, $p = .047$, $\eta^2_p = .11$. Higher-PAC participants responded faster than those with lower PAC, $F(1, 35) = 84.7$, $p = .0001$, $\eta^2_p = .31$ (Figure 9). The difference between high- and low-PAC participants was especially pronounced in low-reliability conditions than in high-reliability conditions. Frequent video game players also outperformed infrequent gamers, $F(1, 38) = 8.19$, $p = .009$, $\eta^2_p = .18$.

Individual differences in multitasking performance. To further test the effects of individual differences in operators' overall multitasking performance, multivariate ANOVAs were performed on all the task performance data. There was a main effect of PAC, $F(5, 33) = 3.60$, $p = .011$, $\eta^2_p = .35$. Further analysis revealed that high-PAC participants outperformed low-PAC participants in the MP condition, $F(5, 14) = 4.50$, $p = .012$, $\eta^2_p = .62$. In the FAP condition, however, the difference failed to reach statistical significance. There was also a main effect of participants' video gaming experience, $F(5, 34) = 2.42$, $p = .04$, $\eta^2_p = .26$. There failed to be an overall effect of operator's SpA on task performance.

TABLE 2: Experiment 2: Mean Operator Task Performance and Workload Assessments

	False Alarm Prone (FAP)				Miss Prone (MP)				Summary of Main Effects[a]
	60%		90%		60%		90%		
Measure	High VD	Low VD	High VD	Low VD	High VD	Low VD	High VD	Low VD	
Route editing (% correct)	95.6 (7.7)	97.8 (4.6)	95.0 (11.2)	98.3 (5.4)	65.0 (13.5)	67.0 (11.6)	76.0 (11.7)	76.0 (9.7)	FAP > MP 90% > 60%
Target detection (% correct)	80.0 (11.5)	96.0 (5.2)	72.0 (31.2)	86.0 (14.3)	53.0 (14.2)	57.0 (15.7)	52.0 (16.2)	73.0 (10.6)	FAP > MP Low VD > High VD
Situation awareness queries (% correct)	16.0 (12.6)	18.0 (19.9)	26.0 (9.6)	20.0 (23.1)	32.0 (19.3)	40.0 (16.3)	30.0 (19.4)	36.0 (29.5)	MP > FAP
Gauge monitoring, reaction time (seconds)	3.91 (1.49)	4.27 (1.87)	4.48 (2.22)	4.16 (3.14)	3.99 (2.27)	4.49 (1.91)	3.13 (1.53)	2.94 (1.28)	
Communication (% correct)	87.7 (4.7)	80.7 (6.0)	82.0 (8.5)	86.7 (8.3)	82.3 (6.5)	82.3 (7.4)	87.7 (5.5)	86.7 (5.9)	
Workload (NASA Task Load Index)	79.4 (10.5)	70.7 (7.3)	67.1 (13.6)	60.0 (17.4)	79.8 (14.4)	78.5 (14.0)	75.1 (14.7)	71.0 (17.8)	High VD > Low VD 60% > 90%

Note. Standard deviations are presented in parentheses. VD = visual density.
[a]Based on statistical analyses reported in the Results section.

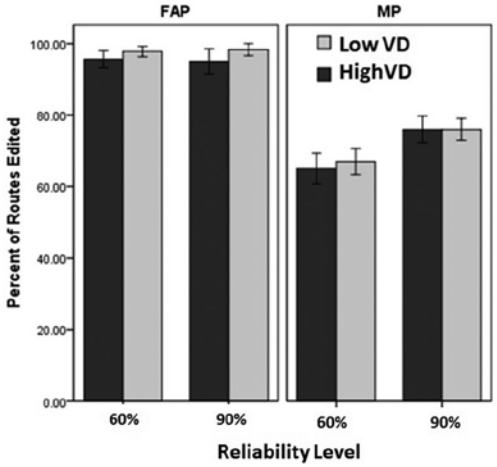

Figure 6. Route editing task performance.

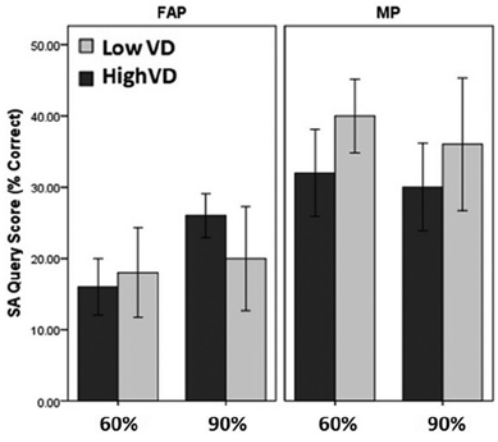

Figure 8. Percentage of situation awareness queries answered correctly.

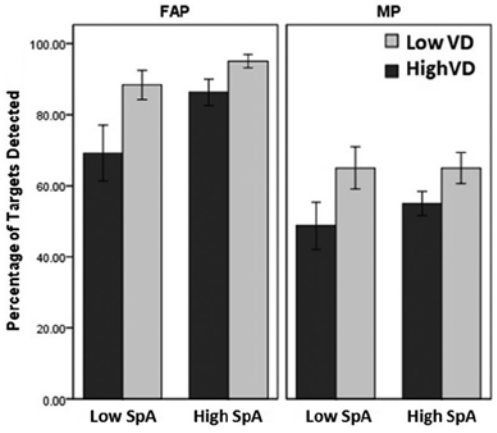

Figure 7. Target detection performance and effects of operator spatial ability (SpA).

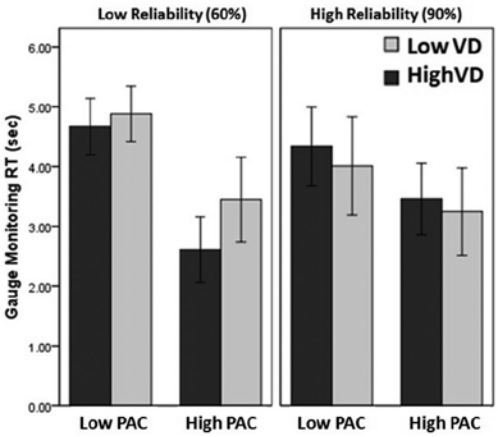

Figure 9. Gauge monitoring performance and effects of perceived attentional control (PAC).

Perceived workload. The analysis showed that both VD of the target environment and the reliability level of RoboLeader contributed significantly to the participants' perceived workload, $F(1, 36) = 7.7$, $p = .009$, $\eta^2_p = .18$, and $F(1, 36) = 4.8$, $p = .036$, $\eta^2_p = .12$, respectively (Figure 10). Participants experienced higher workload in the high-VD condition as well as when the reliability level was lower.

Operator's interaction with the OCU. Participants made significantly more thumbnail clicks in the low-VD condition than in the high-VD condition, $F(1, 35) = 6.5$, $p = .006$, $\eta^2_p = .16$. Participants' SpA was also significantly correlated with the number of thumbnail clicks, $r = .33$, $p = .019$. There was no significant difference between higher- and lower-PAC participants in the aggregate scores of the trust questionnaire.

GENERAL DISCUSSION

We investigated, in two simulation experiments, the effectiveness of human operators' performance of military tasks when interacting

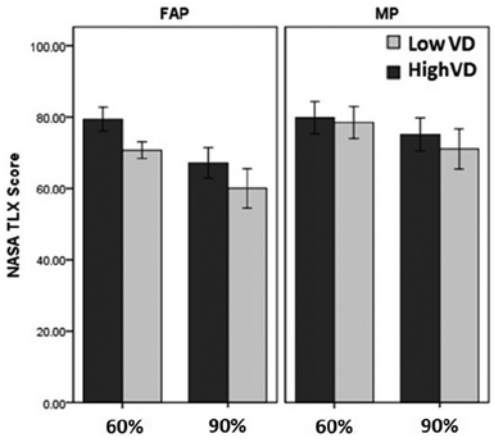

Figure 10. Perceived workload.

with an intelligent agent, RoboLeader, with perfect or less-than-perfect reliability. In both experiments, participants' main task was to supervise a team of ground robots while detecting hostile targets via streaming video from the robots. Whereas the first experiment involved only the robotic route revision task and the target detection task, the second experiment simulated a multitasking environment in which the participants had to simultaneously perform an additional gauge monitoring task and an auditory communication task.

In the first experiment, although we did not find significant differences in target detection between the two groups, the participants in the RoboLeader group completed their missions in significantly less time than did those in the baseline group. On average, RoboLeader saved the participants approximately 3 min for missions lasting 20 or more minutes (not including time on plan revisions). This suggests that the RoboLeader's plans were more efficient than the operators'. The results of Experiment 2 showed that the type of RoboLeader imperfection and its reliability level both significantly affected the participants' route editing performance. As expected, participants edited more routes in the FAP condition and when RoboLeader was highly reliable. Participants' spatial ability and attentional control both played a role in their performance of route editing, with the performance differences especially pronounced in the MP and low-reliability conditions.

In both experiments, one of participants' tasks was to find targets via streaming video from the robots. In Experiment 1, participants detected significantly fewer targets when there were eight robots compared with the four-robot condition, indicating less efficiency with more resources or assets. This result is consistent with the finding of a recent study by Squire and Parasuraman (2010), in which the participants performed worse (i.e., won fewer games) with eight robots versus four robots. The results of Experiment 2 showed that participants detected fewer targets when the RoboLeader was MP or when target VD was high. This finding is consistent with that of Dixon and Wickens (2006) that concurrent tasks (compared with automated tasks) are affected more by MP systems than by FAP systems because the operator allocates more visual attention to monitor the automated task when the automation is MP. However, the effectiveness of this elevated visual attention to the automated task was modulated by one's SpA, as we explain later.

From the performance data, it does not appear that the difference in the numbers of routes that participants had to manually edit had any noticeable effects on their performance of the concurrent tasks. For example, for the target detection tasks, there was not a significant difference between the MP60 and MP90 conditions, although participants were required to change eight routes on their own in the MP60 condition and only two routes in the MP90 condition. Similarly, in Experiment 1, when RoboLeader was perfect and the number of events was the same, there was no difference between RoboLeader and baseline-manual conditions although the manual conditions required six edits and the RoboLeader required none. Taken together, these results suggest that the number of manual route edits required was not the crucial factor. It is, therefore, more likely that the continuous visual monitoring requirement associated with the MP conditions (and factors such as VD) contributed more to the performance decrements observed for the MP condition (although the MP group did have better SA, which is discussed later).

In both experiments, those participants with higher SpA detected more targets (especially in high-VD conditions in Experiment 2) and made more thumbnail clicks than did those with lower SpA. These results are consistent with previous findings (Chen, 2010; Chen et al., 2008; Chen & Joyner, 2009; Chen & Terrence, 2008, 2009) that individuals with higher SpA tend to exhibit more effective scanning performance and, therefore, are able to detect more targets than do those with lower SpA, especially when visual processing load is heavy (high-VD conditions in Experiment 2). The fact that high-SpA participants edited more routes than did low-SpA participants in Experiment 2 also suggests more effective scanning by the high-SpA individuals. In the MP60 condition, which required the most visual monitoring by the participants, high-SpA participants were able to edit almost 20% more of the routes than were their lower-SpA counterparts.

These findings support the recommendations by Lathan and Tracey (2002) and two recent U.S. Air Force studies (Chappelle, McMillan, et al., 2010; Chappelle, Novy, et al., 2010) that military missions can benefit from selecting personnel with higher SpA to operate robotic devices. Training interventions that could enhance the spatial interpretations required to perform a mission task might also be of benefit (Rodes, Brooks, & Gugerty, 2005).

In terms of awareness of the overall mission environments, participants' SA was significantly better when there were four robots than when there were eight robots to keep track of. This result is not surprising and is consistent with previous findings (Crandall, Goodrich, Olsen, & Nielsen, 2005; Squire & Parasuraman, 2010; Trouvain & Wolf, 2002). Participants' SA was also better in the MP condition than in the FAP condition. This suggests that the participants scanned the map more frequently in the MP condition than in the FAP condition. Again, this is consistent with Dixon and Wickens's (2006) finding that MP systems drew operators' visual attention away from the concurrent tasks to focus more on the automated tasking environment. Interestingly, participants' self-assessed trust in the RoboLeader system did not differ significantly between the MP and FAP groups.

Although we did not collect eye movement data, we can infer some of the attentional processes and strategies of the participants from the performance data. In their effort to maintain optimal performance across the tasks, the participants appeared to allocate more attentional resources to the MP tasking environment than to the FAP environment, as the elevated SA performance for the MP condition suggested. However, this biased attention allocation came with a price—as the degraded target detection performance in MP conditions indicated.

There was some evidence that frequent video gamers tended to have somewhat better SA than did infrequent gamers, although the results were not always consistent (e.g., only in the RoboLeader condition but not in the baseline condition in Experiment 1; difference not reaching statistical significance in Experiment 2). In another RoboLeader study employing different dynamic replanning tasks, it was observed that frequent gamers had significantly better SA of the tasking environment than did infrequent gamers (Chen, Barnes, Quinn, & Plew, 2011). Given findings reported in Green and Bavelier (2006) that frequent gamers tend to have better visual short-term memory, it is not surprising to find them exhibiting better SA of the tasking environments. Additionally, Cummings, Clare, and Hart (2010) found that frequent gamers collaborated more with an automated UAS replanning system (higher degree of consent) than did infrequent gamers. Their finding suggests that the frequent gamers in our Experiment 1 probably worked better with the RoboLeader system than did the infrequent gamers, and this more effective collaboration might have contributed to the frequent gamers' better SA, especially when RoboLeader was reliable.

Participants experienced significantly higher workload when there were eight robots compared with the four-robot condition, but the presence of RoboLeader did not seem to have a significant effect on their perceived workload. Participants' workload assessments were also higher when the density of the visual environment was higher or when RoboLeader's reliability level was lower.

Participants' PAC was found to have a significant effect on their multitasking performance,

especially the execution of secondary tasks (communication and gauge monitoring). This finding is consistent with those of Chen and Joyner (2009) that participants performed at a similar level on the primary tasks (gunnery and robotics), but those with higher PAC performed better on the secondary communication task than did those with lower PAC. These results suggest that participants with higher PAC were more able to allocate their attentional resources effectively in the multitasking environment than those with lower PAC, especially when tasking environments became more challenging (e.g., low-reliability conditions in Experiment 2). When the automation had low reliability, low-PAC individuals did not appear to be able to allocate as much attention to parts of the tasking environment (e.g., gauges) as did high-PAC individuals (Figure 9). It was also found that participants with higher PAC consistently performed better in the MP condition across different tasks than those with lower PAC. This is consistent with Chen and Terrence's (2009) finding that MP automated systems tended to be more detrimental to lower PAC individuals than to higher PAC individuals.

An interesting difference between the current results and those of Chen and Terrence (2009) was that in the current study, participants with higher PAC did not exhibit as much undertrust (i.e., disuse) of the FAP system as those high-PAC participants did in the Chen and Terrence study. In the current study, high-PAC participants performed at similar levels as low-PAC participants in the FAP conditions but outperformed low-PAC individuals in the MP conditions. The discrepancy between these results and those of Chen and Terrence may be attributable to the different "costs" of scanning in the two simulated environments. In the Chen and Terrence study, the gunner station and the robotics OCU were displayed on two separate monitors, whereas in the current study, all tasks were performed on the same monitor. Compared with the current study, the cost of scanning in the Chen and Terrence study was greater, and those of higher PAC clearly demonstrated reduced compliance with the FAP automated system. In the current study, high-PAC participants did not show this decrement, likely because of the relative ease of verifying the RoboLeader recommendations on the map by checking the icons.

It is interesting to note that while it was considerably easier to verify the validity of the alerts in the current study, participants with low PAC performed more poorly in the MP conditions did than those with high PAC, just as the results of the Chen and Terrence (2009) study showed. A likely reason for this phenomenon is that MP scenarios required continuous scanning of the map to find new icons. This requirement made the task similar to a "change detection" task, although performed in a multitasking environment. The current results suggest that low-PAC individuals cannot detect changes as effectively as their high-PAC counterparts, likely because of their poorer attentional management abilities. The way the low-PAC participants interacted with the automated system in the current experiment was consistent with the "cognitive miser" phenomenon described in Feldman Barrett et al. (2004). The phenomenon states that low-PAC individuals, because of their limited attentional resources, tend to reduce their information processing demands by simplifying their task(s) (e.g., relying on automation to help them with their tasks). Depending on the context, this oversimplification (e.g., overreliance on automation) may have very undesirable consequences (e.g., MP condition) when the aids fail to provide anticipated assistance.

On the other hand, notably, there were no observable trade-off strategies adopted by the low-PAC participants (their performance across the different tasks was uniformly low in the MP condition). In other words, the low-PAC participants were not found to conserve cognitive resources on one task to perform better on the other tasks. This performance decrement, therefore, seems to reflect something more related to attentional abilities than to deliberate strategies. Future research should investigate factors contributing to this deficiency by low-PAC individuals (e.g., working memory capacity and cognitive flexibility; Bühner, König, Pick, & Krumm, 2006; Feldman Barrett et al., 2004; Youmans, Figueroa, & Kramarova, 2011) and possible training or interfaces design strategies to mitigate them.

Participants' video gaming experience had a significant impact on their overall multitasking performance. These results are consistent with previous findings (Green & Bavelier, 2006) suggesting that video game play is associated with greater visual short-term memory and faster information processing, which in turn may have contributed to game-playing participants' superior multitasking performance in the current study. These results are consistent with the findings of one recent U.S. Air Force study (McKinley, McIntire, & Funke, 2010) that frequent video gamers outperformed infrequent gamers on robotics (UAS) tasks and, in some cases, performed as well as experienced pilots. These results also support the conclusion of an U.S. Air Force study (Triplett, 2008) based on interviews of UAS pilots that gamers' superior visual information-processing skills may be able to translate into superior robotics management performance.

CONCLUSION

In the current study, we investigated the effects of an intelligent agent, RoboLeader, on human operators' performance of supervising multiple robots to complete military reconnaissance missions in a dual-task and a multitasking environment. Overall, it appears that RoboLeader, when perfectly reliable, was effective in reducing the operators' mission times in target search tasks, although significant benefits of RoboLeader on the operators' concurrent task performance and workload were not observed.

Results of Experiment 2 show that the type of RoboLeader imperfection affected operator's performance of tasks involving visual scanning (target detection, route editing, and SA). Furthermore, there was a consistent effect of VD for multiple performance measures. Participants' self-assessed attentional control and video gaming experience was found to affect their overall multitasking performance. Across experiments, participants with higher SpA consistently outperformed those with lower SpA in tasks that required the most visual scanning (e.g., target detection and thumbnail clicks), regardless of the experimental conditions. Future research should investigate training interventions (e.g., attention management) and/or user interface designs (e.g., multimodal cueing displays) that can mitigate performance shortfalls of those with lower SpA and attentional control (Chen, Barnes, & Harper-Sciarini, 2011; Chen, Haas, & Barnes, 2007; Dux et al., 2009).

ACKNOWLEDGMENTS

This research was supported by U.S. Army Research Laboratory's Director's Research Initiative program and SOURCE Army Technology Objective. The authors wish to thank Zhihua Qu, Mark Snyder, Caitlin Kenny, Daniel Barber, David Adams, and Michelle Harper-Sciarini for their contribution to this project.

KEY POINTS

- Intelligent agents, such as RoboLeader, can benefit the overall human-robot teaming performance. However, the effects of unreliable automation, tasking requirements, and individual differences are complex, and their interactions with one another have different ways to affect human-automation interaction in multitasking environments.
- The type of RoboLeader imperfection (false alarm vs. miss prone) affected operator's performance of tasks involving visual scanning (target detection, route editing, and situation awareness). The effectiveness of participants' elevated visual attention to the miss-prone environment was modulated by individual differences in spatial ability and attentional control.
- Participants' attentional control and video gaming experience affected their overall multitasking performance. The positive effects of higher attentional control were most evident when the automated system (RoboLeader) was miss prone.
- In both experiments, participants with higher spatial ability consistently outperformed their low-spatial-ability counterparts in tasks that required effective visual scanning: They scanned the environment faster and detected more targets. The performance differences were especially pronounced when visual processing load was heavy (high visual density and low system reliability).

REFERENCES

Barber, D., Davis, L., Nicholson, D., Finkelstein, N., & Chen, J. Y. C. (2008, December). *The Mixed Initiative Experimental (MIX) Testbed for human robot interactions with varied levels of automation*. Paper presented at the 26th Army Science Conference, Orlando, FL.

Barnes, M. J., & Evans, A. W., III. (2010). Soldier-robot teams in future battlefields: An overview. In M. Barnes & F. Jentsch (Eds.), *Human-robot interactions in future military operations* (pp. 9–29). Farnham, UK: Ashgate.

Bleckley, M., Durso, F., Crutchfield, J., Engle, R., & Khanna, M. (2003). Individual differences in working memory capacity predict visual attention allocation. *Psychonomic Bulletin & Review*, *10*, 884–889.

Bühner, M., König, C. J., Pick, M., & Krumm, S. (2006). Working memory dimensions as differential predictors of the speed and error aspect of multitasking performance. *Human Performance*, *19*, 253–275.

Cassenti, D., Kelley, T., Swoboda, J., & Patton, D. (2009). The effects of communication style on robot navigation performance. In *Proceedings of the Human Factors and Ergonomics Society 53rd Annual Meeting* (pp. 359–363). Santa Monica, CA: Human Factors and Ergonomics Society.

Chappelle, W., McMillan, K., Novy, P., & McDonald, K. (2010). Psychological profile of USAF unmanned aerial systems Predator & Reaper pilots. *Aviation, Space, and Environmental Medicine*, *81*, 339.

Chappelle, W., Novy, P., Randall, B., & McDonald, K. (2010). Critical psychological attributes of U.S. Air Force (USAF) Predator & Reaper sensor operators according to subject matter experts. *Aviation, Space, and Environmental Medicine*, *81*, 253.

Chen, C., Czerwinski, M., & Macredie, R. (2000). Individual differences in virtual environments: Introduction and overview. *Journal of the American Society for Information Science*, *51*, 499–507.

Chen, J. Y. C. (2010). UAV-guided navigation for ground robot teleoperation in a military reconnaissance environment. *Ergonomics*, *53*, 940–950.

Chen, J. Y. C., Barnes, M. J., & Harper-Sciarini, M. (2011). Supervisory control of multiple robots: Human performance issues and user interface design. *IEEE Transactions on Systems, Man, and Cybernetics–Part C: Applications and Reviews*, *41*, 435–454.

Chen, J. Y. C., Barnes, M. J., Quinn, S. A., & Plew, W. (2011). Effectiveness of RoboLeader for dynamic re-tasking in an urban environment. In *Proceedings of Human Factors and Ergonomics Society 55th Annual Meeting* (pp. 1501–1505). Santa Monica, CA: Human Factors and Ergonomics Society.

Chen, J. Y. C., Durlach, P., Sloan, J., & Bowens, L. (2008). Human robot interaction in the context of simulated route reconnaissance missions. *Military Psychology*, *20*, 135–149.

Chen, J. Y. C., Haas, E. C., & Barnes, M. J. (2007). Human performance issues and user interface design for teleoperated robots. *IEEE Transactions on Systems, Man, and Cybernetics–Part C: Applications and Reviews*, *37*, 1231–1245.

Chen, J. Y. C., & Joyner, C. T. (2009). Concurrent performance of gunner's and robotic operator's tasks in a multitasking environment. *Military Psychology*, *21*, 98–113.

Chen, J. Y.C., & Terrence, P. I. (2008). Effects of tactile cueing on concurrent performance of military and robotics tasks in a simulated multitasking environment. *Ergonomics*, *51*, 1137–1152.

Chen, J. Y. C., & Terrence, P. I. (2009). Effects of imperfect automation on concurrent performance of military and robotics tasks in a simulated multi-tasking environment. *Ergonomics*, *52*, 907–920.

Crandall, J., Goodrich, M., Olsen, D., & Nielsen, C. (2005). Validating human-robot interaction schemes in multitasking environments. *IEEE Transactions on Systems, Man, and Cybernetics, Part A*, *35*, 438–449.

Cummings, M. L., Clare, A., & Hart, C. (2010). The role of human-automation consensus in multiple unmanned vehicle scheduling. *Human Factors*, *52*, 17–27.

Derryberry, D., & Reed, M. A. (2002). Anxiety-related attentional biases and their regulation by attentional control. *Journal of Abnormal Psychology*, *111*, 225–236.

Dixon, S. R., & Wickens, C. D. (2006). Automation reliability in unmanned aerial vehicle control: A reliance-compliance model of automation dependence in high workload. *Human Factors*, *48*, 474–486.

Dixon, S. R., Wickens, C. D., & McCarley, J. (2007). On the independence of compliance and reliance: Are automation false alarms worse than misses? *Human Factors*, *49*, 564–572.

Dux, P., Tombu, M., Harrison, S., Rogers, B., Tong, F., & Marois, R. (2009). Training improves multitasking performance by increasing the speed of information processing in human prefrontal cortex. *Neuron*, *63*, 127–138.

Dzindolet, M., Pierce, L., Beck, H., Dawe, L., & Anderson, B. (2001). Predicting misuse and disuse of combat identification systems. *Military Psychology*, *13*, 147–164.

Ekstrom, R. B., French, J. W., & Harman, H. H. (1976). *Kit of factor-referenced cognitive tests.* Princeton, NJ: Educational Testing Service.

Feldman Barrett, L., Tugade, M., & Engle, R. (2004). Individual differences in working memory capacity and dual-process theories of the mind. *Psychological Bulletin*, *130*, 553–573.

Fern, L., Shively, R. J., Draper, M. H., Cooke, N. J., Oron-Gilad, T., & Miller, C. A. (2011). Human-automation challenges for the control of unmanned aerial systems. In *Proceedings of the Human Factors and Ergonomics Society 55th Annual Meeting* (pp. 424–428). Santa Monica, CA: Human Factors and Ergonomics Society.

Green, C., & Bavelier, D. (2006). Enumeration versus multiple object tracking: The case of action video game players. *Cognition*, *101*, 217–245.

Green, D., & Swets, J. (1988). *Signal detection theory and psychophysics.* New York, NY: Wiley.

Gugerty, L., & Brooks, J. (2004). Reference-frame misalignment and cardinal direction judgments: Group differences and strategies. *Journal of Experimental Psychology: Applied*, *10*, 75–88.

Hambrick, D. Z., Oswald, F. L., Darowski, E. S., Rench, T. A., & Brou, R. (2010). Predictors of multitasking performance in a synthetic work paradigm. *Applied Cognitive Psychology*, *24*, 1149–1167.

Hart, S., & Staveland, L. (1988). Development of NASA TLX (Task Load Index): Results of empirical and theoretical research. In P. Hancock & N. Meshkati (Eds.), *Human mental workload* (pp. 139–183). Amsterdam, Netherlands: Elsevier.

Hubert-Wallander, B., Green, C., & Bavelier, D. (2010). Stretching the limits of visual attention: The case of action video games. *WIREs Cognitive Science*, *2*, 222–230. doi:10.1002/wcs.116

Jian, J., Bisantz, A., & Drury, C. (2000). Foundations for an empirically determined scale of trust in automated systems. *International Journal of Cognitive Ergonomics*, *4*, 53–71.

Kahneman, D., Ben-Ishai, R., & Lotan,M. (1973). Relation of a test of attention to road accidents. *Journal of Applied Psychology*, *58*, 113–115.

Lathan, C., & Tracey, M. (2002). The effects of operator spatial perception and sensory feedback on human-robot teleoperation performance. *Presence*, *11*, 368–377.

Lewis, M., Wang, H., Chien, S. Y., Velagapudi, P., Scerri, P., & Sycara, K. (2010). Choosing autonomy modes for multirobot search. *Human Factors*, *52*, 225–233.

Linegang, M., Stoner, H., Patterson, M., Seppelt, B., Hoffman, J., Crittendon, Z., & Lee, J. (2006). Human-automation collaboration in dynamic mission planning: A challenge requiring an ecological approach. In *Proceedings of the Human Factors and Ergonomics Society 50th Annual Meeting* (pp. 2482–2486). Santa Monica, CA: Human Factors and Ergonomics Society.

McKinley, A., McIntire, L., & Funke, M. (2010). Operator selection for unmanned aerial vehicles: A comparison of video game players and manned aircraft pilots. In *Proceedings of the Aerospace Medical Association 81st Annual Scientific Meeting* (p. 336). Alexandria, VA: Aerospace Medical Association.

Meyer, J. (2001). Effects of warning validity and proximity on responses to warning. *Human Factors*, *43*, 563–572.

Meyer, J. (2004). Conceptual issues in the study of dynamic hazard warnings. *Human Factors*, *46*, 196–204.

Miller, C., & Parasuraman, R. (2007). Designing for flexible interaction between humans and automation: Delegation interfaces for supervisory control. *Human Factors*, *49*, 57–75.

Morgan, B., D'Mello, S., Fike, K., Abbott, R., Haass, M., Tamplin, A., Radvansky, G., & Forsythe, C. (2011). Individual differences in multitasking ability and adaptability. In *Proceedings of the Human Factors & Ergonomics Society 55th Annual Meeting* (pp. 919–923). Santa Monica, CA: Human Factors and Ergonomics Society.

Parasuraman, R., & Manzey, D. H. (2010). Complacency and bias in human use of automation: An attentional integration. *Human Factors*, *52*, 381–410.

Rodes, W., Brooks, J., & Gugerty, L. (2005, May). *Using verbal protocol analysis and cognitive modeling to understand strategies used for cardinal direction judgments*. Poster presented at the Human Factors of UAVs Workshop, Mesa, AZ.

Rubinstein, J., Meyer, D., & Evans, J. (2001). Executive control of cognitive processes in task switching. *Journal of Experimental Psychology: Human Perception and Performance*, *27*, 763–797.

Schumacher E., Seymour, T., Glass, J., Fencsik, D., Lauber, E., Kieras, D., & Meyer, D. (2001). Virtually perfect time sharing in dual-task performance: Uncorking the central cognitive bottleneck. *Psychological Science*, *12*, 101–108.

Schurr, N. (2007). *Toward human-multiagent teams* (Unpublished dissertation). University of Southern California, Los Angeles.

Singer, P. (2010). War of the machines. *Scientific American*, *303*, 56–63.

Snyder, M., Qu, Z., Chen, J. Y. C., & Barnes, M. (2010). RoboLeader for reconnaissance by a team of robotic vehicles. In *Proceedings of the International Symposium on Collaborative Technologies and Systems* (pp. 17–21). Los Alamitos, CA: IEEE Press.

Squire, P. N., & Parasuraman, R. (2010). Effects of automation and task load on task switching during human supervision of multiple semi-autonomous robots in a dynamic environment. *Ergonomics*, *53*, 951–961.

Stanney, K., & Salvendy, G. (1995). Information visualization: Assisting low spatial individuals with information access tasks through the use of visual mediators. *Ergonomics*, *38*, 1184–1198.

Stubbs, K., Wettergreen, D., & Nourbakhsh, I. (2008). Using a robot proxy to create common ground in exploration tasks. In *Proceedings of the 3rd ACM/IEEE International Conference on Human-Robot Interaction* (pp. 375–382). New York: Association for Computing Machinery.

Thomas, L., & Wickens, C. D. (2004). Eye-tracking and individual differences in off-normal event detection when flying with a synthetic vision system display. In *Proceedings of the Human Factors and Ergonomics Society 48th Annual Meeting* (pp. 223–227). Santa Monica, CA: Human Factors and Ergonomics Society.

Triplett, J. (2008). *The effects of commercial video game playing: A comparison of skills and abilities for the Predator UAV* (Unpublished thesis). U.S. Air Force–Air University, Montgomery, AL.

Trouvain, B., & Wolf, H. (2002). Evaluation of multi-robot control and monitoring performance. In *Proceedings of IEEE International Workshop on Robot and Human Interactive Communication* (pp. 111–116). Los Alamitos, CA: IEEE Press.

Wickens, C. D., & Dixon, S. R. (2007). The benefits of imperfect diagnostic automation: A synthesis of the literature. *Theoretical Issues in Ergonomics Science*, *8*, 201–212.

Youmans, R. J., Figueroa, I. J., & Kramarova, O. (2011). Reactive task-set switching ability, not working memory capacity, predicts change blindness sensitivity. In *Proceedings of the Human Factors and Ergonomics Society 55th Annual Meeting* (pp. 914–918). Santa Monica, CA: Human Factors and Ergonomics Society.

Young, M. S., & Stanton, N. A. (2007). Back to the future: Brake reaction times for manual and automated vehicles. *Ergonomics*, *50*, 46–58.

Jessie Y. C. Chen received her BA in linguistics from National Tsing-Hua University in Taiwan in 1987, her MA in communication studies from the University of Michigan at Ann Arbor in 1989, and her PhD in applied experimental and human factors psychology from University of Central Florida in 2000. She is a research psychologist with U.S. Army Research Laboratory, Human Research and Engineering Directorate, at the field element in Orlando, Florida. Her research interests include human-robot interaction, human-vehicle interaction, supervisory control, and individual differences.

Michael J. Barnes was educated at University of Arizona and New Mexico State University (MA, experimental psychology, 1975). Currently, he works for U.S. Army Research Laboratory (ARL) where he is the ARL lead for the human-robot interaction (HRI) portion of the Army Technology Objective: Safe Operations of Unmanned Reconnaissance in Complex Environments. He currently serves as member of a NATO committee for the HRI of autonomous systems and has coauthored more than 70 articles on the human factors of military systems. His previous human factors positions were as a researcher with the U.S. Navy and as a manager with General Electric. In his present position, he is the ARL chief of the Fort Huachuca, Arizona, field element, where he supports cognitive research in intelligence analysis, unmanned aerial systems, and visualization tools for risk management.

Date received: May 25, 2011
Date accepted: December 19, 2011

Jessie Y. C. Chen received the B.A. degree in linguistics from National Tsing-Hua University, Hsinchu, Taiwan, in 1987, the M.A. degree in communication studies from the University of Michigan at Ann Arbor, in 1989, and the Ph.D. degree in applied experimental and human factors psychology from the University of Central Florida, Orlando, in 2000.

She is currently a Research Psychologist with the U.S. Army Research Laboratory (ARL), Human Research and Engineering Directorate, Aberdeen Proving Ground, Aberdeen, MD. Her research interests include human–robot interaction, human–vehicle interaction, supervisory control, and individual differences.

Michael J. Barnes received the M.A. degree in experimental psychology in 1975 from the University of Arizona, Tucson, and the New Mexico State University, Las Cruces.

He is currently with the U.S. Army Research Laboratory (ARL), Human Research and Engineering Directorate, Aberdeen Proving Ground, Aberdeen, MD, where he is the ARL lead for the human–robot interaction (HRI) portion of the Army Technology Objective (ATO): Safe Operations of Unmanned Reconnaissance in Complex Environments. He is a member of the North Atlantic Treaty Organization (NATO) Committee for the HRI of autonomous systems. He has coauthored more than 70 articles on the human factors of military systems. He was a Researcher with the U.S. Navy and was a Manager with the General Electric Cooperation. He is the ARL Chief of the Ft. Huachuca, AZ field element, where he supports cognitive research in intelligence analysis, unmanned aerial systems, and visualization tools for risk management.

Michelle Harper-Sciarini received the B.S. degree in psychology and the Ph.D. degree in applied experimental human factors from the University of Central Florida, Orlando, in 2001 and 2009, respectively.

She is currently the President and Owner of APRISE, LLC, Winter Springs, FL, a small business dedicated to enhancing individual and team performance within complex sociotechnical systems. Her current research interests include applying psychological theory and principles to the design of training aids, evaluation methods, and human–system interaction support aids.

Supervisory Control of Multiple Robots in Dynamic Tasking Environments

Jessie Y.C. Chen and Michael J. Barnes

Ergonomics, 55:9, 1043-1058 (2012)

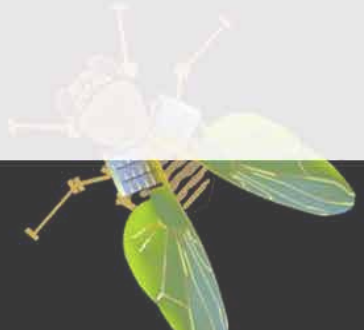

Ergonomics
Vol. 55, No. 9, September 2012, 1043–1058

Taylor & Francis
Taylor & Francis Group

Supervisory control of multiple robots in dynamic tasking environments

Jessie Y.C. Chen* and Michael J. Barnes

U.S. Army Research Laboratory – Human Research & Engineering Directorate, Aberdeen Proving Ground, MD, USA

(*Received 1 July 2011; final version received 23 April 2012*)

A military targeting environment was simulated to examine the effects of an intelligent route-planning agent RoboLeader, which could support dynamic robot re-tasking based on battlefield developments, on the performance of robotics operators. We manipulated the level of assistance (LOAs) provided by RoboLeader as well as the presence of a visualisation tool that provided feedback to the participants on their primary task (target encapsulation) performance. Results showed that the participants' primary task benefited from RoboLeader on all LOAs conditions compared to manual performance; however, visualisation had little effect. Frequent video gamers demonstrated significantly better situation awareness of the mission environment than did infrequent gamers. Those participants with higher spatial ability performed better on a secondary target detection task than did those with lower spatial ability. Finally, participants' workload assessments were significantly lower when they were assisted by RoboLeader than when they performed the target entrapment task manually.

Practitioner Summary: This study demonstrated the utility of an intelligent agent for enhancing robotics operators' supervisory control performance as well as reducing their workload during a complex urban scenario involving moving targets. The results furthered the understanding of the interplay among level-of-autonomy, multitasking performance and individual differences in military tasking environments.

Keywords: human–robot interaction; supervisory control; level of autonomy; intelligent agent; military; individual differences

1. Introduction

Robots are becoming an essential part of the battlefield (Chen *et al*. 2011a). Thousands of robots are currently working side-by-side with soldiers, and the tasks they are used for are evolving in complexity – from load-carrying, casualty extraction, hazardous material detection, counter explosive devices, building mapping/clearing, to firefighting (Purdy 2008, Greenemeier 2010, Osborn 2011). In the future battlefield, Soldiers may be given multiple tasks to perform concurrently, such as navigating a robot while conducting surveillance, maintaining local security and situation awareness (SA), and communicating with fellow team members. The possibility of a robotic battlefield creates a number of human factors as well as ethical issues related to non-human intelligence conducting combat missions (Barnes and Evans 2010, Singer 2010). One obvious issue is that the proliferation of intelligent systems could easily overwhelm the human operators' ability to adequately supervise these systems. Hundreds of robots, both aerial and ground, may share the battlefield with hundreds of manned systems and conduct numerous missions concurrently. In these situations, the military may not be able to afford the manpower to have operators control individual systems; instead, future missions will likely require single operators to supervise multiple systems simultaneously (Cummings *et al*. 2010).

Past research has shown that human operators are often unable to control multiple robots/agents simultaneously in an effective and efficient manner (Schurr 2007, Chen *et al*. 2008). As the size of the robot team increases, human operators may fail to maintain adequate SA when their attention is constantly switching between the robots. Cognitive resources may also be overwhelmed by the numerous intervention requests from the robots (Wang *et al*. 2009a, Lewis *et al*. 2010). Wang *et al*. (2009a) reviewed a number of studies on supervisory control of multiple ground robots for target detection tasks and concluded that in order to be effective, 'the Fan-out plateau lies somewhere between 4 and 9+ robots depending on the level of robot autonomy and environmental demands' (p. 143) – limits very close to the classical (seven plus or minus two) findings for span of apprehension (Miller 1956). Unfortunately, increases in autonomy often present its own set of problems, including tunnel vision, misuse and disuse of automated systems, complacency, and loss of SA (Parasuraman and Riley 1997, Chen *et al*. 2011a). For

*Corresponding author. Email: jessie.chen@us.army.mil

ISSN 0014-0139 print/ISSN 1366-5847 online

http://dx.doi.org/10.1080/00140139.2012.689013
http://www.tandfonline.com

a detailed review on human performance issues supervisory control of multiple robots and potential user interface designs, see Cummings *et al*. (2010) and Chen *et al*. (2011a).

1.1. Systems to enhance human supervisory control of multiple robots

Researchers have proposed a number of solutions to the potential issues of a robotic battlefield, such as setting up a robot call center in which robots can query the human operator only when there is a problem (Wang *et al*. 2009b). The operator can make the necessary adjustments but are not required to monitor robots continuously. A potential problem with this solution is that it assumes that the robot can reliably self-diagnose its own problems; additionally, the number of operator–robot interactions is expected to increase exponentially during the heat of combat, making the call center ineffective during the most critical time periods. As a potential safeguard, a number of researchers have suggested algorithms that share control responsibility among robots and humans as a function of either the robots' behaviour or the operator's cognitive state (Parasuraman *et al*. 2007, Miller and Parasuraman 2007, Cosenzo *et al*. 2010, Goodrich 2010). Closely aligned concepts involve play-book solutions that permit the operator to insert pre-programmed algorithmic solutions that control robots during difficult mission segments (Miller and Parasuraman 2007, Fern and Shively 2009). This generic class of adaptive systems is designed to keep operators in the decision loop while keeping the overall supervisory burden within manageable cognitive limits. However, while this approach mitigates problems during high workload segments, it does not overcome cognitive limitations when the number of human–robot interactions surpasses human cognitive capacity (Lewis *et al*. 2010).

Research shows that autonomous cooperation between robots can aid the performance of the human operators (Lewis *et al*. 2010) and enhance the overall human-robot team performance (Schurr 2007). Human operators' involvement in mixed-initiative teams will still be required for the foreseeable future, however, especially in situations involving critical decision making. Human operators' decision making may be influenced by 'implicit goals' that the robots are not aware of (i.e. are not programmed into the behaviors of the robots; Linegang *et al*. 2006) and real-time developments on the battlefield that may require the human operator to change plans for individual robots or the entire robotic team. Effective communication between the human operator and robots then becomes critical in ensuring mission success. Past research has demonstrated the effectiveness of a robot proxy to enhance shared understanding between the human operator and the robot in an exploration task (Stubbs *et al*. 2008). The communication mechanism was based on a common ground collaboration model and improved the human operator performance by assisting in the creation of more accurate plans, more efficient planning (fewer planning repetitions), faster task performance, as well as a better mental model of the capabilities of the robot (Stubbs *et al*. 2008).

1.2. RoboLeader

To achieve a better balance of enhancing autonomy and capability while simplifying human–robot interaction, an intelligent agent called RoboLeader, a robotic surrogate that could help the human operator coordinate a team of ground robots, was developed under the US Army Research Laboratory's (ARL) Director's Research Initiative Program (Chen *et al*. 2011b, Chen and Barnes 2012). In other words, instead of directly managing the robot team, the human operator only dealt with RoboLeader; consequently, the operator could better focus on the other tasks requiring attention. In Chen and Barnes (2012), RoboLeader had the capabilities of revising route plans for the robots based on *static* battlefield intelligence and developments (e.g. potential attacks, road blocks, high priority areas, etc). Chen and Barnes investigated the effectiveness of RoboLeader in a human-in-the-loop simulation experiment (in which 30 individuals participated) and compared the operators' target detection performance in a four- and eight-robot condition. The results showed that participants detected significantly fewer targets with eight robots versus four robots. Although there were no significant differences between the RoboLeader and baseline (no RoboLeader) conditions for target detection, the RoboLeader group reduced their mission completion times by approximately 13% compared to the baseline group. Additionally, those participants with higher spatial ability detected more targets than did those with lower spatial ability. Participants experienced significantly higher workload with eight robots compared to the four-robot condition, and those with better attentional control reported lower workload than did those with poorer attentional control.

1.3. Current study

The purpose of the current study was to investigate the efficacy of agent/human cooperation during more challenging mission tasking while varying the level of operator interaction with RoboLeader. In the current study,

the capabilities of RoboLeader were expanded to deal more specifically with *dynamic* re-tasking requirements for persistent surveillance of a simulated urban environment based on various battlefield developments, as well as coordination between unmanned aerial vehicles (UAVs) and unmanned ground vehicles (UGVs) in pursuit of *moving targets* in urban environments (for more information on the RoboLeader algorithm, see Chen *et al*. 2011b). More specifically, the participants used four UGVs to 'entrap' a primary moving target (a truck) via a map that displays the location of the target via a UAV link while monitoring the streaming videos from the four UGVs to look for other secondary targets (insurgents) in the remote environments. This dynamic tasking environment is significantly more challenging than what was investigated in the past RoboLeader studies and it captures the complexity inherent in future military environments requiring robot re-routing decisions in reference to mobile targets while optimising detection of targets of opportunity.

RoboLeader's role was to coordinate multiple robots in concert with the human decision maker. We manipulated the level of assistance (LOAs) provided by RoboLeader and examined its effect on the operator's performance (i.e. primary target entrapment, percentage of secondary targets detected and SA of the mission environment) and workload. The four levels of manipulation were as follows: *Manual* (without Visualisation), Semi-Autonomous without Visualisation (*Semi-Auto w/o Vis*), Semi-Autonomous with Visualisation (*Semi-Auto w/ Vis*) and Fully Automated (*Auto*; with Visualisation; see Procedure). The Semi-Autonomous condition was divided into two conditions so that the effect of the visualisation tool could be isolated and evaluated. The visualisation tool informed the participant of the synchronisation of the robots as well as overall target entrapment effectiveness based on the movement of the target (see Apparatus). The four conditions, therefore, represented four levels of assistance of RoboLeader (Figure 1), each adding more capability to the previous level – (1) manual (baseline); (2) the waypoint completion capability added to the Semi-Auto w/o Vis; (3) the visualisation tool added to the Semi-Auto w/Vis; (4) the automated encapsulation and route endpoint planning capability added to the Auto condition. In terms of level of automation, RoboLeader's route-planning capability resembles the fifth level ('execute that suggestion if the human approves') described in Parasuraman *et al*. (2000, p. 287). In the previous RoboLeader studies, RoboLeader was either fully automated (100% reliable) or imperfectly automated (miss prone or false-alarm prone); the tasking environments were also considerably more static than the current one (Chen and Barnes 2012). Thus we expanded on our previous research not only by increasing the complexity level (i.e. dynamic re-tasking) but also by varying the LOAs available to the human operators for human–agent interactions.

Finally, we investigated the effects of individual differences on the operators' robotics control as well as multitasking performance. Specifically, we investigated the effects of participants' spatial ability, attentional control and gaming experience (using the same tests and surveys as in Chen and Barnes 2012). The rest of this section briefly reviews the individual differences factors investigated in the current study.

1.4. Individual differences in spatial ability, attentional control and gaming experience

In the current study, we sought to evaluate whether individual differences in spatial ability, attentional control, and video gaming experience might impact the operator's performance. Our simulated tasking environments required the participants to process a large amount of spatial information from multiple sources (even when working with the RoboLeader agent). Past research suggests individual differences in spatial ability, attentional control and video gaming experience can play significant roles in such tasking environments where effective scanning and multitasking are critical to performance success. The current study sought to evaluate the interaction between these individual differences factors and the LOAs provided by RoboLeader. To date, there has been minimal research on human–agent interaction investigating all these factors in one single study. The rest of the section briefly reviewed each factor and its relevance to the current study.

Spatial ability has been found to be a significant factor in certain visual display domains (Stanney and Salvendy 1995), virtual environment navigation (Chen *et al*. 2000), target search task (Chen *et al*. 2008, Chen and Joyner 2009,

Figure 1. Four levels of assistance of RoboLeader (WP = waypoint; EP = endpoint).

Chen and Terrence 2008, 2009, Chen 2010, Chen and Barnes 2012) and robotics task performance (Lathan and Tracey 2002, Cassenti *et al*. 2009, Baber *et al*. 2011). For example, Stanney and Salvendy (1995) found that high spatial individuals outperformed those with low spatial ability on tasks that required visuo-spatial representations to be mentally constructed (i.e. mental model of hierarchical menu systems). Previous studies also found that spatial ability was correlated with robot teleoperation tasks such as robot navigation (Lathan and Tracey 2002, Cassenti *et al*. 2009). Lathan and Tracey (2002) showed that people with higher spatial ability (determined based on a test battery of two spatial recognition and two spatial manipulation tests) performed better in a robot teleoperation task through a maze in terms of both speed and accuracy. A recent study by Baber *et al*. (2011) showed that low spatial participants responded significantly more slowly when controlling multiple robots. Our previous research showed that individuals with higher spatial ability exhibited more effective visual scanning and target detection performance (Chen *et al*. 2008, Chen and Joyner 2009, Chen and Terrence 2008, 2009, Chen 2010, Chen and Barnes 2012). Chappelle *et al*. 2010a, 2010b interviewed 53 subject matter experts about abilities that were critical to effective performance of UAV control tasks in terms of piloting and sensor operations – spatial ability was identified as an important factor for both tasks. Based on these previous findings, therefore, we expected participants with higher spatial ability would outperform their lower spatial counterparts in tasks that required effective visual scanning and spatial reasoning.

In addition to spatial ability, the relationship between attentional control and multitasking performance was also examined. Attentional control is defined as one's ability to focus and shift attention in a flexible manner (e.g. ability to re-direct attention to certain aspect of the environment without being distracted by other elements of the environment; Derryberry and Reed 2002). Several studies have shown that there are individual differences in multitasking performance, and some people are less prone to performance degradation during multitasking conditions (Rubinstein *et al*. 2001, Schumacher *et al*. 2001). There is some evidence that attention-switching flexibility can predict performance of such diverse tasks as flight training and bus driving (Kahneman *et al*. 1973). There is also evidence that people with better attention control can allocate their attention more flexibly and effectively (Derryberry and Reed 2002), and the ability to allocate attention flexibly is related to one's working memory capacity (Bleckley *et al*. 2003, Feldman Barrett *et al*. 2004). According to a recent US Air Force's survey of subject matter experts on the performance of operators of UAVs (Chapelle *et al*. 2010a), attentional control is one of the most important abilities that would affect an operator's performance since the robotics control task is inherently multitasking (e.g. sensor manipulation, tracking, communication, etc.). According to Feldman Barrett *et al*. (2004), those with lower attentional control tend to take the 'cognitive miser' approach when dealing with complex information processing in order to reduce the attentional control requirements. When dealing with automation, therefore, it is likely that operators with different levels of attention switching abilities may react differently to automated systems. In other words, operators' behaviours of compliance with, and reliance on, automation may be altered based on their ability to effectively switch their attention among the systems. For example, the automation-induced complacency effect repeatedly demonstrated in previous research (Dzindolet *et al*. 2001, Thomas and Wickens 2004, Young and Stanton 2007, Parasuraman and Manzey 2010) may be more severe for poor attentional control individuals compared with those with better attentional control. This phenomenon has been demonstrated in Chen and Terrence (2009) and Chen and Barnes (2012) and was further tested in the current experiment, which employed a simulation environment considerably different from those of the previous experiments.

Finally, the current study sought to examine the relationship between participants' video gaming experience and their task performance as well as SA of the mission environment. Chen and Barnes (2012) demonstrated that frequent gamers (i.e. those who play video games daily or weekly) could multitask better and had better SA than did infrequent gamers (i.e. those who play monthly or less frequently than monthly). According to Green and Bavelier (2006) and Hubert-Wallander *et al*. (2010), experienced action video game players, compared to infrequent/non gamer, were found to perform significantly better on tasks that required visuo-spatial selective attention, multiple object tracking, fast process of visual information and imagery, and flexibility in attention allocation. Therefore, we expected frequent gamers would outperform infrequent gamers in our visually demanding task environment in terms of target/event detection and monitoring of the mission environment.

2. Method

2.1. Participants

Twenty-eight individuals [25 males and 3 females; mean age = 21.4 (SD = 4.3), min = 18, max = 34] from the Orlando, FL area participated in the experiment. Out of the 28 participants, none had any prior military

experiences. The majority of the participants were students from a university in the Orlando area, and six had completed four years of college. Overall, the participants were similar in age and in background to potential military operators before training. Based on their self-reported gaming experience, 20 of them played video games either daily or weekly. These individuals were classified as frequent gamers. The other eight played video games either monthly or with even less frequency. These individuals were classified as infrequent gamers. Participants received $15/hour for their time.

2.2. *Apparatus*

2.2.1. *Simulator*

A modified version of the Mixed Initiative Experimental (MIX) Testbed was used as the simulator for this experiment. The MIX Testbed is a distributed simulation environment for investigation into how robots are used and how automation affects human operator performance (Barber *et al*. 2008). The Operator Control Unit (OCU) of the MIX Testbed (Figure 2a) was modelled after the Tactical Control Unit developed under the ARL Robotics Collaborative Technology Alliance. This platform includes a camera payload and supports multiple levels of automation. Users can send mission plans or teleoperate the platform with a computer mouse while being provided video feeds from the camera payload. Typical tasks include reconnaissance and surveillance. The RoboLeader software was integrated in the MIX OCU and had the capability of collecting information from subordinate robots with limited autonomy (e.g. collision avoidance and self-guidance to reach target locations), making tactical decisions and coordinating the robots by issuing commands, waypoints, or motion trajectories (see Chen *et al*. 2011b for a detailed description of the algorithm of RoboLeader; Figure 2a). Participants entered/modified waypoints or endpoints for robots' routes by selecting the appropriate button at the top of the OCU and then click on the spot of the map where the point should be placed (see Figure 2b)

2.2.2. *RoboLeader*

The RoboLeader user interface is shown in Figure 2a. The map was located in the top left portion of the display and showed the location of the moving target (a slowly moving truck) via a link to a UAV flying over the mission area (i.e. the icon representing the truck was displayed as a red arrow to show the direction of movement and continuously moved on the map display based on the truck's actual movement, which was updated from the UAV). The right half of the screen was divided into four separate camera feeds, streaming from the four UGVs. The visualisation display (one horizontal bar and four vertical bars) was located in the lower left corner of the OCU (for design principles for information visualisation, see Robertson *et al*. 2009). The purpose of the visualisation display was to provide real-time performance feedback to the participants regarding their target encapsulation task and the scoring algorithm took into account of the moving target's heading as well as the absolute distances between the target and the UGV (Chen *et al*. 2011b). The four *vertical* bars had the words 'NEAR' and 'AWAY' at the top and bottom of each bar, respectively, and represented the scores for each robot's progress in getting closer to the moving target; the *horizontal* bar represented the aggregate entrapment score of the robots' plans (in terms of *blockage* of the target's escape routes). As the target moved, RoboLeader calculated the scores based on each robot's plan as well as the speed and movement of the target and showed the scores via the bar graphs. As a UGV approached the target, its associated green vertical bar would increase in size and move closer to the 'NEAR' end (longer green bars meaning closer distances); conversely, as a UGV moved further away from the target, its associated red vertical bar would increase in size and move closer to the 'AWAY' end (longer red bars meaning farther distances). Additionally, a red arrow was displayed to the right of each graph if a UGV was moving away from the target (see Figure 2a). The *horizontal* bar, on the other hand, indicated whether the target's escape routes were properly blocked by at least two UGVs based on the current plans (longer bar meaning better blockage). The score could be perfect if the target's escape routes were properly blocked by two robots, regardless where the other two UGVs were. In other situations, the target's escape routes might need 3 or 4 UGVs for proper blockage. The scoring algorithm only took into account whether the target's escape routes were properly blocked, not the number of robots contributing to the blockage. More specifically, the scores were based on the percentage of escape routes properly blocked by UGVs. For example, two out of two or four out of four would result in the same perfect score (i.e., 100). One out of two or two out of four would also result in the same score of 50. RoboLeader continuously updated the calculations and visualisations (bar graphs) until the target was encapsulated. The timing of the target encapsulation ($\times$ minutes into the scenario when the target was encapsulated for the first time) was logged and

(a)

(b)

Figure 2. (a) RoboLeader user interface in the MIX Testbed; (b) RoboLeader user interface for route revisions.

used in the data analysis. The scores from the horizontal bars and the vertical bars were not used in the final data analysis of this study (they were only used to provide real-time feedback to the participants during experimental scenarios).

2.2.3. *Surveys and tests*

A demographics questionnaire was administered at the beginning of the training session. An Ishihara colour vision test (with nine test plates) was administered via PowerPoint presentation using the same computer/display system for the experimental trials. The RoboLeader user interface employed several colours to display the plans for the robots and normal colour vision was required in order to effectively interact with the system. A questionnaire on Attentional Control (Derryberry and Reed 2002) was used to evaluate participants' perceived attentional control. The Attentional Control survey consists of 21 items and measures attention focus and shifting. Examples of questions include 'When I need to concentrate and solve a problem, I have trouble focusing my attention' and 'I can quickly switch from one task to another.' The scale has been shown to have good internal reliability ($\alpha = 0.88$). The Cube Comparison Test (Ekstrom *et al*. 1976) and the Spatial Orientation Test (Gugerty and Brooks 2004) were used to assess participants' spatial ability. The Cube Comparison Test required participants to compare, in three-minutes, 21 pairs of six-sided cubes and determine if the rotated cubes were the same or different. The Spatial Orientation Test was modelled after the cardinal direction test developed by Gugerty and Brooks 2004 and was a computerised test consisting of a brief training segment and 32 test questions. Both accuracy and response time were automatically captured by the programme.

A modified version of the Usability and Trust Questionnaire used in Chen and Terrence (2009) assessed participants' perceived usability of the RoboLeader system as well their trust in the system. The questionnaire consisted of 22 questions on a scale of 1 (strongly disagree) to 7 (strongly agree). Eleven of the items were intended to measure the participants' perceived utility and usability of RoboLeader. For example, participants were asked to evaluate whether they 'made use of the RoboLeader's recommendations,' 'felt ''lost'' using the RoboLeader display,' 'relied heavily on the RoboLeader for the task,' and felt 'the RoboLeader display was intuitive and made it easy to determine how to edit routes.' The other 11 items assessed participants' perceived trust in the RoboLeader system and included questions such as 'The RoboLeader system is dependable,' 'I am confident in the RoboLeader system,' and 'the RoboLeader display may have harmful effects on the task.' These trust-related items were modified from the 'Trust Between People and Automation' questionnaire (Jian *et al*. 2000). The 'Trust Between People and Automation' questionnaire has been demonstrated to have high internal reliability (Spain and Bliss 2008) and has been previously validated by Spain *et al*. (2008).

Participants' perceived workload was evaluated using the computer-based version of NASA-TLX questionnaire (Hart and Staveland 1988). The NASA-TLX is a self-reported questionnaire of perceived demands in six areas: mental, physical, temporal, effort (mental and physical), frustration and performance. Participants were asked to evaluate their perceived workload level in these areas on 10-point scales. They also assessed the contribution (i.e. weight) of each factor to the perceived workload by comparing the 15 possible pairs of the six factors. According to Noyes and Bruneau (2007), computer-based NASA-TLX tends to generate higher workload ratings compared with the traditional paper-based survey. However, since the ratings were used to compare the workload levels across the experimental conditions, the elevated ratings should not affect these comparisons.

2.3. *Procedure*

After being briefed on the purpose of the study and signing the informed consent form, participants completed the demographics questionnaire and the Attentional Control survey, and were administered a brief Ishihara Colour Vision Test to ensure they had normal colour vision. After the Colour Vision Test, the participants completed the two spatial ability tests. Participants then received training and practiced on the tasks they would need to conduct during the experimental session. Training was self-paced and was delivered by a video tutorial showing the elements of the OCU, steps for completing various tasks, several hands-on mini-exercises for practicing the steps, and exercises for performing the robotic control tasks. The training session lasted approximately one hour. The participants had to demonstrate that they could recall all the steps for performing the tasks (including interpreting the visualisation display) without any help before they started the experimental session.

The experimental session lasted about 1.5 hour and began immediately after the training session. Each experimental session had four scenarios (corresponding to the four experimental conditions; however, the pairing of scenarios and conditions was counterbalanced), each lasting approximately 20 min. During the scenarios, participants used their four ground robots (UGVs) to pursue a primary moving target (a truck traveling at about 3 MPH) while monitoring the streaming videos from the robots in order to find additional (secondary) targets (insurgents carrying weapons) in the mission environment. When the scenario for the

Manual condition started, the participants put in waypoints for each UGV manually and adjusted the waypoints based on the movement of the primary target. In the Semi-Autonomous conditions, the participant selected an end point/location for the UGV at which time RoboLeader provided an optimum solution (i.e. intermediate waypoints) with how to reach the desired destination. With the visualisation condition, in which RoboLeader provided real-time feedback to the participants, the user might consult the bar graphs as an indicator of whether their point selections were effective in terms of synchronisation of the robots and entrapment of the target or if the plans needed revisions. The scores displayed in the visualisation area (which were not included in the final data analysis of this study) were calculated based on the RoboLeader's encapsulation algorithm and were based on how many of the target's escape routes had a robot assigned to them and it was recalculated every time the endpoint of the robot path changed and when the target changed directions (for more information on the scoring algorithm, see Chen *et al*. 2011b). Without visualisation, the participant had to determine if they were properly cornering the target for capture (i.e. entrapping the target by at least two robots). In the Fully Automated condition, RoboLeader provided the recommended endpoints as well as intermediate waypoints for each robot. The participant could either accept or reject the plans. If a plan is rejected, the participants could still use the rejected plan as a basis and modify the waypoints to create a new plan. RoboLeader's revisions were not implemented until the participant accepted (i.e. management by consent) or modify them. In each scenario, there were hostile areas (indicated by red squares on the map) that the robots needed to avoid. The participants were asked to finish the scenario if the target was encapsulated within the 20-minute limit (in order for all the participants to have equal amount of experiment time). In this case, the target would move pass one of the blocking UGV and the participants would have to revise the plans to block the target. The simulator logged the amount of time the participants spent on encapsulating the target (for the first time) in each scenario. It also logged whether the participants successfully encapsulated the target by the end of the scenario (encapsulation is defined as at least two of the four robots blocking the road the target vehicle was traversing). Both of these data were analysed (see 3.1.1). The order of experimental conditions was counterbalanced across participants.

The robots did not have aided target recognition capability; therefore, the participants had to detect the insurgents (secondary targets) by themselves. For the insurgent targets, participants used a mouse to click the Insurgent button on the interface and then click on the insurgent to 'laze' them (i.e. using the simulated laser range finder) as soon as they were detected. The 'lazed' insurgent was then displayed on the map. Additionally, there were civilians as well as friendly Soldiers in the simulated environment to increase the visual noise present in the target detection tasks. If the participants accidently lazed a non-insurgent entity, the icon for lazed insurgents would not appear on the map and the scoring system would not count that as a hit.

Each scenario also contained five SA queries, which were triggered based on time progression (e.g. three minute into the scenario). The SA queries included questions such as 'Use the provided paper to identify which route(s) have encountered the most Insurgents,' etc. When an SA query was triggered, the OCU screen went blank, the simulation was paused, and the SA query was displayed on the screen. Participants then wrote their response to the query on an answer sheet. After participants responded to the SA query, it was removed from the OCU screen and the simulation resumed. During the training session, participants were told the SA queries they would encounter in the experimental scenarios and had a chance to practice answering those queries during the training exercises.

There was a two-minute break between the experimental scenarios. Participants assessed their perceived workload using the NASA-TLX as well as their perceived usability of the RoboLeader user interface using the Usability/Trust survey immediately after each experimental scenario. The entire data collection session lasted about three hours.

2.4. Dependent measures and data analysis

The study was a within-subject design with RoboLeader's LOAs as the independent variable [with four levels: Manual, Semi-Autonomous without Visualisation (Semi-Auto w/o Vis), Semi-Autonomous with Visualisation (Semi-Auto w/ Vis) and Fully Automated (Auto)]. Dependent measures included the participants' performance of encapsulating the primary target [time spent on encapsulating the target (time elapsed until the target was encapsulated for the first time in each scenario)], the percentage of secondary targets (insurgents) detected, the participants' SA of the mission environment (percentage of SA queries answered correctly), and the participants' perceived workload. A repeated-measure analysis of variance with RoboLeader as the within-subject factor was used to evaluate the operator performance differences among the four conditions.

3. Results

3.1. Operator task performance

3.1.1. Primary target encapsulation performance

Table 1 lists several measures relating to operator performance and perceived workload. The analysis revealed that the LOAs of RoboLeader significantly affected the participants' performance of primary target encapsulation (time spent on encapsulating the moving target with maximum being 20 minutes if target was not encapsulated before the end of the scenario), $F(3,24) = 4.29$, $p < 0.05$ (Figure 3). Post hoc comparisons [least significant difference (LSD)] showed that the participants spent significantly more time on encapsulating the target in the Manual condition than each of the other three RoboLeader-assisted conditions, p's < 0.05. The differences among the three RoboLeader conditions were not significant. We felt it was important to examine the latency data with the 20-minute times included because a large percentage (57%) of the infrequent gamers failed to achieve encapsulation in the Manual condition (see results in the next paragraph); latency scores would possibly be biased by their deletion. Additionally, 20 minutes seemed to be a conservative estimate of the latency since longer latencies were capped at 20 minutes. An additional analysis, however, was also performed with the 20-minute times removed from the data (i.e., only the times for successful encapsulation were included). The analysis showed that the differences among the conditions were not significant.

On average, 63% of the participants successfully encapsulated the primary target in the Manual condition; 96% of them did so in the Semi-Autonomous without Visualisation condition; 86% in the Semi-Autonomous with Visualisation condition and 86% the Fully Automated condition (Figure 4). A chi-squared test showed that the percentage of successful encapsulation in the Manual condition was significantly lower than the average of the other three conditions (i.e. RoboLeader-assisted conditions), χ^2 $(1,\ N = 27) = 11.9$, $p < 0.001$. In the Manual condition, frequent gamers successfully encapsulated the target 70% of the times and infrequent gamers did so only 43% of the times. Participants' spatial ability (composite scores of the two spatial tests) and perceived attentional control (Attentional Control Survey scores) did not have effects on their encapsulation performance.

Table 1. Mean operator task performance and workload assessments (standard deviations are presented in parentheses).

Measures	Manual	Semi-Auto w/o Visualisqation	Semi-Auto w Visualisation	Auto
Time spent on encapsulating (min)	14.19 (5.82)	8.86 (3.27)	10.65 (4.67)	9.70 (4.64)
% of secondary targets detected	46.47 (13.24)	44.51 (20.51)	47.71 (20.76)	43.64 (22.79)
SA (% correct)	76.2 (13.0)	68.7 (17.5)	69.8 (20.2)	71.8 (15.7)
WorkloadôNASATLX	63.9 (10.7)	55.5 (16.9)	59.6 (11.4)	60.2 (17.6)

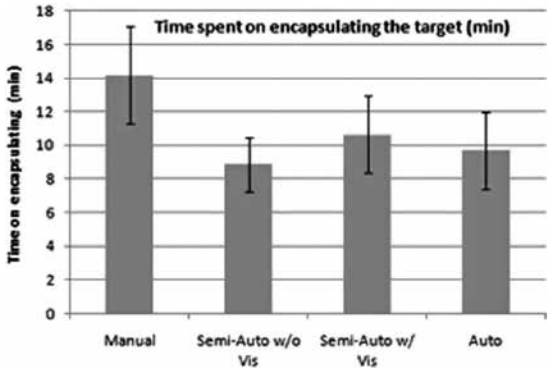

Figure 3. Time spent on encapsulating the moving target in minutes.

3.1.2. *Secondary target detection performance*

On average, the participants detected less than half (44–48%) of the insurgents in the mission environment. However, there was not a significant main effect of RoboLeader's LOAs on participants' target detection performance. Across conditions, participants with higher spatial ability (SpA) detected significantly more targets than did those with lower spatial ability, $F(1,23) = 6.42$, $p < 0.05$ (Figure 5).

3.1.3. *Situation awareness*

The participants' SA of the mission environment did not differ among the conditions. Participants' gaming experience had an effect on their SA, $F(2,24) = 3.48$, $p < 0.05$ (Figure 6). Post hoc comparisons (LSD) showed that, across conditions, the frequent (daily and weekly) gamers outperformed infrequent gamers, $p < 0.05$. There was no difference between daily and weekly gamers.

3.2. *Perceived workload*

There was not a significant main effect of RoboLeader's LOAs on participants' perceived workload (weighted NASA TLX composite scores; Figure 7). However, when the workload assessment in the Manual condition was

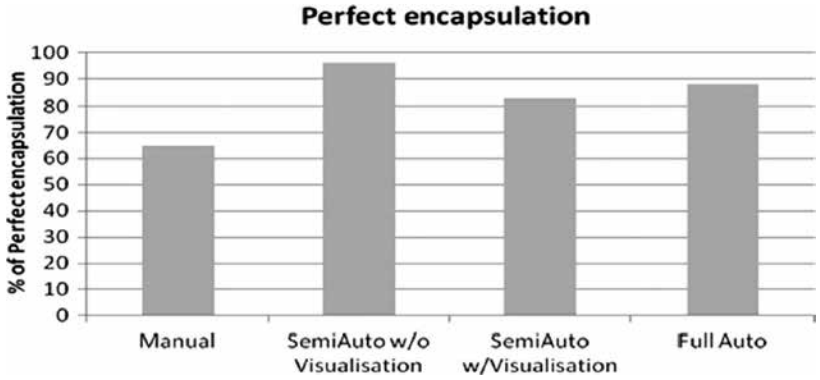

Figure 4. Percentage of participants with successful encapsulation performance.

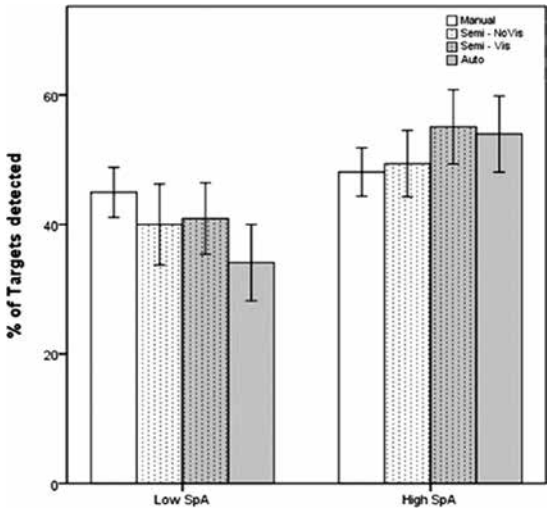

Figure 5. Secondary target detection performance and spatial ability (SpA).

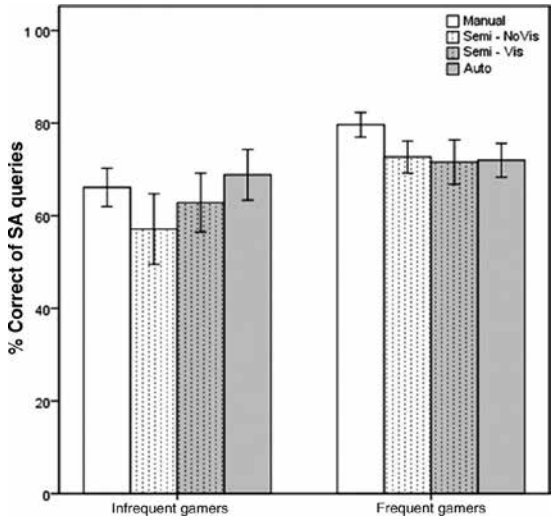

Figure 6. SA queries.

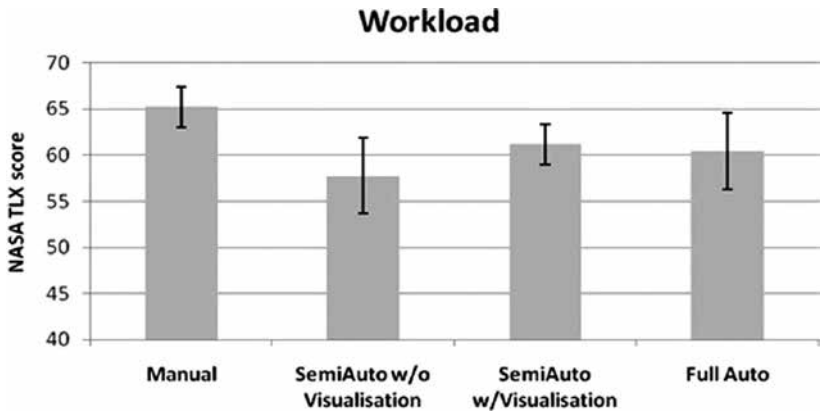

Figure 7. Perceived workload.

compared against the aggregated workload assessments of the other three conditions combined, there was a significant difference between the Manual and the RoboLeader-assisted conditions, $t(26) = 2.93$, $p < 0.01$. Participants reported significantly higher workload ratings in the Manual condition ($M = 63.9$) than they did in the other three conditions ($M = 58.4$).

3.3. Operators' interaction with the RoboLeader user interface

Participants' interaction with the RoboLeader user interface (including the visualisation display) was further analysed based on their responses in the Usability/Trust survey. The responses were aggregated into two categories: perceived utility of RoboLeader (Q1–10 & Q22) and trust in RoboLeader (Q11–21). There were no significant differences among the three RoboLeader conditions on either of the aggregate scores. In other words, there were no observable differences in participants' perceived utility of RoboLeader and their trust in RoboLeader across the three conditions. There was also no evidence from the survey data that the added visualisation displays helped participants. Based on the button presses captured from the user interface, 47% of the RoboLeader route solutions in the Full Auto condition were rejected/modified by the participants. Participants with higher spatial ability tend to

modify RoboLeader's solutions more often (54%) than did those with lower spatial ability (41%), $r = 0.464$, $p < 0.01$. However, there was no evidence of a significant relationship between participants' rejection rates and their task performance and/or workload. The rejection data were only analysed for the Full Auto condition, as the other three conditions required the participants to put in the endpoints and/or intermediate waypoints of the plans.

4. Discussion

An intelligent agent, RoboLeader, was developed to coordinate a team of ground robots and revise route plans for the robots based on battlefield intelligence (Chen and Barnes 2012). In the current study, the capabilities of RoboLeader were expanded to deal more specifically with dynamic re-tasking requirements based on battlefield developments as well as coordination between UAVs and UGVs in pursuit of moving targets. The results of our human-in-the-loop simulation experiment showed that RoboLeader (the Auto and the two Semi-Auto conditions) benefited participants' target encapsulation performance compared with the Manual condition (when they were without assistance from RoboLeader). Participants were able to encapsulate the moving target in shorter times when they were assisted by RoboLeader than when they were not, although the differences among the three RoboLeader-assisted conditions did not significantly differ from one another. Additionally, participants successfully encapsulated the moving targets only 63% of the time in the Manual condition but 89% of the time when they were assisted by RoboLeader (i.e. the other three conditions combined). Interestingly, only one participant (out of 28) in the second lowest LOAs condition (Semi-Auto w/o Vis) failed to encapsulate the target within the 20-minute time limit. This result suggests that the mixed-initiative planning where the human operator entered the end-points and RoboLeader filled in the intermediate waypoints seemed sufficiently effective in our simulated tasking environment. In the Manual condition, 70% of those participants who played video games frequently (daily or weekly) were able to encapsulate the target, while only 43% of those infrequent gamers (those who played monthly or with even less frequency) successfully encapsulated the target. These results are consistent with the findings of one recent US Air Force study (McKinley *et al*. 2010) that frequent video gamers outperformed infrequent gamers on robotics (UAV) tasks and, in some cases, even outperformed experienced pilots.

It is somewhat surprising that visualisation had little effect on the Semi-Autonomous conditions; possibly having a separate visualisation from the map may have actually made the task somewhat more difficult. Follow-on efforts should investigate effective ways to integrate the map display with the information currently displayed in the visualisation portion, in order to reduce the requirement of visual scanning and facilitate more efficient utilisation of RoboLeader's feedback (Porat *et al*. 2010). It is also interesting to note that, in the Auto condition, 47% of the RoboLeader route solutions (i.e. route endpoint placements) were modified by the participants (especially those with higher spatial ability) – although there was not a significant correlation between the participants' tendency to modify RoboLeader's solutions and their encapsulation performance. The relationship between participants' perceived attentional control ability and their tendency to modify RoboLeader's solutions was not clear. More specifically, participants with lower attentional control did not have a higher rate of accepting RoboLeader's solutions than did those with higher attentional control. In other words, those with low attentional control did not exhibit significantly higher level of complacency and trust in automation than did those with higher attentional control. The low acceptance rate of RoboLeader's solutions in the Auto condition was similar to the 'clumsy automation' described in Squire and Parasuraman (2010). The main reason for the high modification rates may be related to flaws in RoboLeader's algorithm, which should be further improved in the follow-on research. It is worth noting that in the current study, the speed of the moving target was fairly slow (nominally 3 MPH), which made the target encapsulation task relatively easy. If the moving target had traveled at a higher speed, the target encapsulation task would have been more difficult and the utility of RoboLeader and the effects of operator spatial ability might have been even more pronounced.

Unlike previous findings (Chen and Terrence 2008), the LOAs of RoboLeader failed to have any significant effects on participants' concurrent performance of detecting secondary targets. Compared with previous RoboLeader experiments, the target detection rates of the current study were considerably lower (44–48% in the current study vs. 61–77% in Chen and Barnes 2012). It is likely that the continuous tracking of the moving target drew the participants' visual attention away from the secondary target detection task. Even when the participants were assisted by RoboLeader, they continued to monitor the moving target and assessed the viability of the plans. In other words, as Parasuraman and Manzey (2010) noted, automation (in this case, RoboLeader) did not simply perform the task for the participants – it changed the nature of the task. Judging from the secondary target detection data, the visual attention required in the RoboLeader-assisted conditions was no less than in the Manual condition. It should be noted that requiring the participants' active engagement in the two Semi-Autonomous conditions did

not hurt performance – suggesting that requiring limited active engagement may be a compromise strategy for designing semi-autonomous agents in order to ameliorate automation bias and delegation authority issues (Fern and Shively 2009, Parasuraman and Manzey 2010). The dynamics of human/agent roles need to be delineated further, but assigning the human a more active role with the agent mitigating most of the high workload task components (as opposed to having the operator act as a passive yes/no supervisor) may be more effective in the long term (Cosenzo *et al* 2010).

Consistent with prior studies, we found that those participants with higher spatial ability detected more targets than did those with lower spatial ability (Chen *et al*. 2008, Chen and Joyner 2009, Chen and Terrence 2008, 2009, Chen 2010, Chen and Barnes 2012). These results suggest that individuals with higher spatial ability tend to exhibit more effective scanning performance and, therefore, are able to detect more targets than do those with lower spatial ability. Figure 5 also shows different trends of interaction between RoboLeader LOAs and operators' spatial ability. Those with lower spatial ability performed worse (detected fewer targets) as the LOAs became higher; those with high spatial ability, on the other hand, showed the opposite trend. These results suggest that if the automated system requires significant amount of visual attention, it may not benefit low spatial individuals as much as high spatial individuals or may require remedial training for low spatial operators. The findings of the current study also support the recommendations by Lathan and Tracey (2002) and two recent US Air Force studies (Chappelle *et al*. 2010a, 2010b) that military missions can benefit from selecting personnel with higher spatial ability to operate robotic devices. Training interventions that could enhance the spatial interpretations required to perform a mission task might also be of benefit (Baldwin and Reagan 2009).

Notably, frequent video gamers had significantly better SA of the mission environments than did infrequent gamers. These results are consistent with previous findings (Green and Bavelier 2006, Chen and Barnes 2012) suggesting that video game play is associated with greater visual short-term memory and faster information processing, which in turn, may have contributed to game playing participants' superior SA in the current study. These results also support the conclusion of a US Air Force study (Triplett 2008) based on interviews of UAV pilots that gamers' superior SA may be able to translate into superior robotics management performance.

The participants reported significantly higher workload when they were in the Manual condition than when they were assisted by RoboLeader. This finding is consistent with Chen and Terrence (2008) and Chen and Joyner (2009). The higher workload associated with manual controls needs to be taken into account when designing the user interfaces for the robotic management systems (Chen *et al*. 2007).

5. Conclusions

In conclusion, RoboLeader demonstrated significant utility for enhancing human operators' performance as well as reducing their workload. The results clearly demonstrated the benefits of RoboLeader's assisting the participants in their route planning. Most importantly, the results suggest that agent/human supervision of multiple robots permits synergy without usurping the human's decision authority and those LOAs with less than full autonomy can be as effective as fully autonomous LOAs. The Manual condition, compared with the other three conditions, was associated with the lowest performance in terms of speed of target encapsulation, percentages of target encapsulation, and perceived workload. The results suggest that, compared with our previous research, RoboLeader's utility increases for more difficult scenarios (e.g. estimating mobility effects of moving targets). Furthermore, it appears that semiautonomous assistance of RoboLeader was sufficiently beneficial for the encapsulation task perhaps because it permitted the operator to 'stay in the loop' while reducing task difficulty to a manageable level (Endsley and Kiris 1995). Additionally, displaying dynamic re-tasking information on a map display was sufficient to allow participants to visualise the encapsulation process without specialised displays. Finally, the current study shows that individual differences such as spatial ability and video gaming experience can have a profound impact on operator's task performance and can modulate the effectiveness of RoboLeader. Those with higher spatial ability, compared with low spatial individuals, were better able to detect secondary targets while monitoring and managing the moving target encapsulation task. Furthermore, RoboLeader with higher levels of assistance seemed to benefit the high spatial individuals in their secondary target detection task more than it helped the low spatial individuals – likely due to the amount of visual attention required for even highly automated RoboLeader. Frequent gamers, compared with infrequent gamers, had significantly better SA of the mission environments. These results may have important implications for system design and personnel selection for future military programmes (Triplett 2008, Chappelle *et al*. 2010a, 2010b, McKinley *et al*. 2010). Future research can investigate training interventions (e.g. attention management) and/or user interface designs (e.g. multimodal cueing displays) to enhance robot operator performance in challenging tasking environments (Chen *et al*. 2007, Dux *et al*.

2009, Chen *et al*. 2011a). Future efforts will also examine the feasibility of implementing RoboLeader-like agent in other military multi-robot missions such as building-mapping and clearing and swarm control.

Acknowledgements

This research was funded by the U.S. Army Research Laboratory Director's Research Initiative Program and the Safe Operations for Unmanned Reconnaissance in Complex Environments (SOURCE) Army Technology Objective (ATO). The authors would like to acknowledge the contributions of the following individuals: Zhihua Qu, Mark Snyder, Daniel Barber, David Adams, Stephanie Quinn, and William Plew.

Note on contributors

Jessie Y. C. Chen received her BA in linguistics from National Tsing-Hua University in Taiwan in 1987, her MA in communication studies from the University of Michigan at Ann Arbor in 1989, and her PhD in applied experimental and human factors psychology from University of Central Florida in 2000. She is a research psychologist with US Army Research Laboratory (ARL) – Human Research & Engineering Directorate at the field element in Orlando, Florida. Her research interests include human–robot interaction, human–vehicle interaction, supervisory control, and individual differences.

Michael J. Barnes was educated at University of Arizona and New Mexico State University (MA – Experimental Psychology, 1975). Currently, he works for US Army Research Laboratory (ARL) where he is the ARL lead for the human–robot interaction (HRI) portion of the Army Technology Objective (ATO): Safe Operations of Unmanned Reconnaissance in Complex Environments. He currently serves as member of a NATO committee for the HRI of autonomous systems and has co-authored over 70 articles on the human factors of military systems. His previous human factor's positions were as a researcher with the US Navy and as a manager with the General Electric Cooperation. In his present position, he is the ARL chief of the Ft. Huachuca, AZ field element where he supports cognitive research in intelligence analysis, unmanned aerial systems and visualisation tools for risk management.

References

Baber, C., *et al*., 2011. Multimodal control of sensors on multiple simulated unmanned vehicles. *Ergonomics*, 54, 792–805.

Baldwin, C.L. and Reagan, I., 2009. Individual differences in route-learning strategy and associated working memory resources. *Human Factors*, 51, 368–377.

Barber, D., *et al*., 2008. The Mixed Initiative Experimental (MIX) testbed for human robot interactions with varied levels of automation. *In*: *Proceedings of the 26th Army Science Conference*, 1–4 December 2008 Orlando, FL. Available from: http://www.dtic.mil/cgi-bin/GetTRDoc?Location=U2&doc=GetTRDoc.pdf&AD=ADA505701 [Accessed 24 March 2011].

Barnes, M.J. and Evans, A.W. III., 2010. Soldier-robot teams in future battlefields: an overview. *In*: M.J. Barnes and F. Jentsch, eds. *Human-robot interactions in future military operations*. Farnham Surrey, UK: Ashgate, 9–29.

Bleckley, M.K., *et al*., 2003. Individual differences in working memory capacity predict visual attention allocation. *Psychonomic Bulletin & Review*, 10, 884–889.

Cassenti, D.N., *et al*., 2009. The effects of communication style on robot navigation performance. *In*: *Proceedings of Human Factors and Ergonomics Society 53rd Annual Meeting*, 19–23 October 2009, San Antonio, TX. Santa Monica, CA: HFES, 359–363.

Chappelle, W.L., *et al*., 2010a. Psychological profile of USAF unmanned aerial systems Predator & Reaper pilots. *In*: *Proceedings of the aerospace medical association 81st annual scientific meeting*, 9–13 May 2010, Phoenix, AZ. Alexandria, VA: Aerospace Medical Association, 339.

Chappelle, W.L., *et al*., 2010b. Critical psychological attributes of U.S. Air Force (USAF) Predator & Reaper sensor operators according to subject matter experts. *In*: *Proceedings of the aerospace medical association 81st annual scientific meeting*, 9–13 May 2010, Phoenix, AZ. Alexandria, VA: Aerospace Medical Association, 253.

Chen, C., Czerwinski, M., and Macredie, R., 2000. Individual differences in virtual environments – Introduction and overview. *Journal of the American Society for Information Science*, 51, 499–507.

Chen, J.Y.C., 2010. UAV-guided navigation for ground robot teleoperation in a military reconnaissance environment. *Ergonomics*, 53, 940–950.

Chen, J.Y.C. and Barnes, M.J., 2012. Supervisory control of multiple robots: effects of imperfect automation and individual differences. *Human Factors*, 54, 157–174.

Chen, J.Y.C., Barnes, M.J., and Harper-Sciarini, M., 2011a. Supervisory control of multiple robots: human performance issues and user interface design. *IEEE Transactions on Systems, Man, and Cybernetics – Part C: Applications and Reviews*, 41, 435–454.

Chen, J.Y.C., Barnes, M.J., and Qu, Z., 2011b. *RoboLeader: dynamic re-tasking for persistence surveillance in an urban environment using robot-to-robot control*. (ARL Memorandum Report ARL-MR-0761) [online]. Aberdeen Proving Ground, MD: U.S.Army Research Laboratory. Available from: http://www.dtic.mil/cgi-bin/GetTRDoc?Location=U2&doc=GetTRDoc.pdf&AD=ADA534897 [Accessed 24 March 2011].

Chen, J.Y.C., *et al*., 2008. Human robot interaction in the context of simulated route reconnaissance missions. *Military Psychology*, 20, 135–149.
Chen, J.Y.C., Haas, E.C., and Barnes, M.J., 2007. Human performance issues and user interface design for teleoperated robots. *IEEE Transactions on Systems, Man, and Cybernetics – Part C: Applications and Reviews*, 37, 1231–1245.
Chen, J.Y.C. and Joyner, C.T., 2009. Concurrent performance of gunner's and robotic operator's tasks in a multitasking environment. *Military Psychology*, 21, 98–113.
Chen, J.Y.C. and Terrence, P.I., 2008. Effects of tactile cueing on concurrent performance of military and robotics tasks in a simulated multitasking environment. *Ergonomics*, 51, 1137–1152.
Chen, J.Y.C. and Terrence, P.I., 2009. Effects of imperfect automation on concurrent performance of military and robotics tasks in a simulated multi-tasking environment. *Ergonomics*, 52, 907–920.
Cosenzo, K.A., Parasuraman, R., and De Visser, E., 2010. Automation strategies for facilitating human interaction with military unmanned vehicles. *In*: M.J. Barnes and F. Jentsch, eds. *Human-robot interactions in future military operations*. Farnham, Surrey, UK: Ashgate, 103–123.
Cummings, M.L., Bruni, S., and Mitchell, P.J., 2010. Human supervisory control challenges in network-centric operations. *Reviews of Human Factors and Ergonomics*, 6, 34–78.
Derryberry, D. and Reed, M., 2002. Anxiety-related attentional biases and their regulation by attentional control. *Journal of Abnormal Psychology*, 111, 225–236.
Dzindolet, M., *et al*., 2001. Predicting misuse and disuse of combat identification systems. *Military Psychology*, 13, 147–164.
Dux, P.E., *et al*., 2009. Training improves multitasking performance by increasing the speed of information processing in human prefrontal cortex. *Neuron*, 63, 127–138.
Endsley, M. and Kiris, E., 1995. The out-of-the-loop performance problem and level of control in automation. *Human Factors*, 37, 381–394.
Ekstrom, R.B., French, J.W., and Harman, H.H., 1976. *Kit of factor referenced cognitive tests*. Princeton, NJ: Educational Testing Service.
Feldman Barrett, L., Tugade, M.M., and Engle, R.W., 2004. Individual differences in working memory capacity and dual-process theories of the mind. *Psychological Bulletin*, 130, 553–573.
Fern, L. and Shively, R.J., 2009. A comparison of varying levels of automation on the supervisory control of multiple UASs. *In*: *Proceedings of AUVSI's Unmanned Systems North America*, 10–13 August 2009, Washington, DC. Arlington, VA: Association for Unmanned Vehicle Systems International.
Goodrich, M.A., 2010. On maximizing fan-out: Towards controlling multiple unmanned vehicles. *In*: M.J. Barnes and F. Jentsch, eds. *Human-robot Interactions in future military operations*. Farnham, Surrey, UK: Ashgate, 375–395.
Green, C.S. and Bavelier, D., 2006. Enumeration versus multiple object tracking: The case of action video game players. *Cognition*, 101, 217–245.
Greenemeier, L., 2010. Robot pack mule to carry loads for G.I.s on the move. *Scientific American* [online]. Available from: http://www.scientificamerican.com/article.cfm?id=boston-dynamics-ls3 [Accessed 24 March 2011].
Gugerty, L. and Brooks, J., 2004. Reference-frame misalignment and cardinal direction judgments: group differences and strategies. *Journal of Experimental Psychology: Applied*, 10, 75–88.
Hart, S. and Staveland, L., 1988. Development of NASA TLX (Task Load Index): results of empirical and theoretical research. *In*: P. Hancock and N. Meshkati, eds. *Human mental workload*. Amsterdam: Elsevier, 139–183.
Hubert-Walllander, B., Green, C.S., and Bavelier, D., 2010. Stretching the limits of visual attention: the case of action video games. *WIREs Cognitive Science,* 2 (DOI: 10.1002/wcs.116) [online]. Available from: http://www.bcs.rochester.edu/people/daphne/VisionPDF/hubertwallander.pdf [Accessed 24 March 2011].
Jian, J., Bisantz, A., and Drury, C., 2000. Foundations for an empirically determined scale of trust in automated systems. *International Journal of Cognitive Ergonomics*, 4, 53–71.
Kahneman, D., Ben-Ishai, R., and Lotan, M., 1973. Relation of a test of attention to road accidents. *Journal of Applied Psychology*, 58, 113–115.
Lathan, C.E. and Tracey, M., 2002. The effects of operator spatial perception and sensory feedback on human-robot teleoperation performance. *Presence: Teleoperators and Virtual Environments*, 11, 368–377.
Lewis, M., *et al*., 2010. Choosing autonomy modes for multirobot search. *Human Factors*, 52, 225–233.
Linegang, M., *et al*., 2006. Human-automation collaboration in dynamic mission planning: a challenge requiring an ecological approach. *In*: *Proceedings of the 50th Human Factors & Ergonomics Society Annual Meeting*, 16–20 October 2006, San Francisco, Santa Monica, CA: HFES, 2482–2486.
McKinley, A., Mcintire, L., and Funke, M., 2010. Operator selection for unmanned aerial vehicles: a comparison of video game players and manned aircraft pilots. *In*: *Proceedings of the Aerospace Medical Association 81st Annual Scientific Meeting*, 9–13 May 2010, Phoenix, AZ. Alexandria, VA: Aerospace Medical Asso., 336.
Miller, G., 1956. The magical number 7 plus or minus two: some limits on our capacity for processing information. *Psychological Review*, 63, 81–97.
Miller, C. and Parasuraman, R., 2007. Designing for flexible interaction between humans and automation: delegation interfaces for supervisory control. *Human Factors*, 49, 57–75.
Noyes, J.M. and Bruneau, D.P., 2007. A self-analysis of the NASA-TLX workload measure. *Ergonomics*, 50, 514–519.
Osborn, K., 2011. Army building smarter robots. *Army AL&T Magazine* [online web-exclusive article]. Available from:http://www.usaasc.info/alt_online/article.cfm?iID=1101&aid=07.
Parasuraman, R., Barnes, M.J., and Cosenzo, K.A., 2007. Adaptive automation for human-robot teaming in future command and control systems. *The International C2 Journal*, 1, 43–68.
Parasuraman, R. and Manzey, D.H., 2010. Complacency and bias in human use of automation: an attentional integration. *Human Factors*, 52, 381–410.

Parasuraman, R. and Riley, V., 1997. Humans and automation: Use, misuse, disuse, abuse. *Human Factors*, 39, 230–253.
Parasuraman, R., Sheridan, T.B., and Wickens, C.D., 2000. A model for types and levels of human interaction with automation. *IEEE Transactions on Systems, Man, and Cybernetics – Part A: Systems and Humans*, 30, 286–297.
Porat, T., *et al*., 2010. "Castling Rays" a decision support tool for UAV-switching tasks. *In*: *Proceedings of the 28th of the International Conference on Human Factors in Computing Systems (CHI '10)*, 10–15 April, Atlanta, GA. New York: ACM, 3589–3594.
Purdy, E.M., 2008. The increasing role of robots in national security. *Defense AT&L,* 5. (May–June 2008, 26–29 [online]. Available from: http://www.dau.mil/pubscats/PubsCats/atl/new/may-june08.pdf [Accessed 24 March 2011].
Robertson, G., *et al*., 2009. Selected human factors issues in information visualization. *Reviews of Human Factors and Ergonomics*, 5, 41–81.
Rubinstein, J., Meyer, D., and Evans, J., 2001. Executive control of cognitive processes in task switching. *Journal of Experimental Psychology: Human Perception and Performance*, 27, 763–797.
Schumacher, E., *et al*., 2001. Virtually perfect time sharing in dual-task performance: uncorking the central cognitive bottleneck. *Psychological Science*, 12, 101–108.
Schurr, N., 2007. *Toward human-multiagent teams*. Unpublished Dissertation, University of Southern California.
Singer, P.W., 2010. War of the machines. *Scientific American*, 303, 56–63.
Spain, R.D. and Bliss, J.P., 2008. The effect of sonification display pulse rate and reliability on operator trust and perceived workload during a simulated patient monitoring task. *Ergonomics*, 51, 1320–1337. *In*: *Proceedings of the Human Factors and Ergonomics Society 52th Meeting*, 22–26 September 2008, New York City, Santa Monica, CA: HFES, 1335–1339.
Spain, R.D., Bustamante, E.A., and Bliss, J.P., 2008. Towards an empirically developed scale for system trust:. Take two.
Squire, P.N. and Parasuraman, R., 2010. Effects of automation and task load on task switching during human supervision of multiple semi-autonomous robots in a dynamic environment. *Ergonomics*, 53, 951–961.
Stanney, K.M. and Salvendy, G., 1995. Information visualization: assisting low spatial individuals with information access tasks through the use of visual mediators. *Ergonomics*, 38, 1184–1198.
Stubbs, K., Wettergreen, D., and Nourbakhsh, I., 2008. Using a robot proxy to create common ground in exploration tasks. *In*: *Proceedings of the 3rd ACM/IEEE International Conference on Human-Robot Interaction*, 12–15 March 2008, Amsterdam, the Netherlands New York: ACM Press, 375–382.
Thomas, L. and Wickens, C.D., 2004. Eye-tracking and individual differences in off-normal event detection when flying with a synthetic vision system display. *In*: *Proceedings of the Human Factors and Ergonomics Society 48th Meeting*, 20–24 September 2004, New Orleans, Santa Monica, CAHFES, 223–227.
Triplett, J., 2008. The effects of commercial video game playing: a comparison of skills and abilities for the Predator UAV [online]. Unpublished thesis. US Air Force: Air University. Available from: http://www.dtic.mil/cgi-bin/GetTRDoc?Location=U2&doc=GetTRDoc.pdf&AD=ADA483256 [Accessed 24 March 2011].
Wang, H., *et al*., 2009a. How search and its subtasks scale in N robots. *In*: *Proceedings of the 4th ACM/IEEE International Conference on Human-Robot Interaction*, 11–13 March 2009, La Jolla, New York: ACM Press, 141–147.
Wang, H., *et al*., 2009b. Human teams for large scale multirobot control. *In*: *Proceedings of the 2009 IEEE International Conference on Systems, Man, and Cybernetics*, 11–14 October, San Antonio, TX. Piscataway, NJ: IEEE Press, 1306–1311.
Young, M.S. and Stanton, N.A., 2007. What's skill got to do with it? Vehicle automation and driver mental workload. *Ergonomics*, 50, 1324–1339.

A Meta-Analysis of Factors Affecting Trust in Human-Robot Interaction

Peter A. Hancock, Deborah R. Billings, Kristin E. Schaefer, Jessie Y. C. Chen, Ewart J. de Visser, and Raja Parasuraman

Human Factors: The Journal of the Human Factors and Ergonomics Society 53:517 (2011)

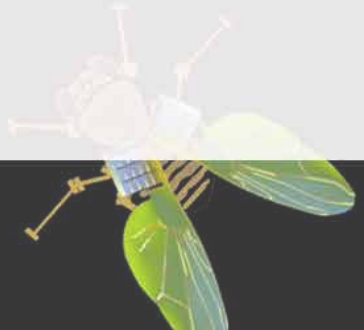

A Meta-Analysis of Factors Affecting Trust in Human-Robot Interaction

Peter A. Hancock, **Deborah R. Billings**, and **Kristin E. Schaefer**, University of Central Florida, **Jessie Y. C. Chen**, U.S. Army Research Laboratory, and **Ewart J. de Visser**, and **Raja Parasuraman**, George Mason University

Objective: We evaluate and quantify the effects of human, robot, and environmental factors on perceived trust in human-robot interaction (HRI).

Background: To date, reviews of trust in HRI have been qualitative or descriptive. Our quantitative review provides a fundamental empirical foundation to advance both theory and practice.

Method: Meta-analytic methods were applied to the available literature on trust and HRI. A total of 29 empirical studies were collected, of which 10 met the selection criteria for correlational analysis and 11 for experimental analysis. These studies provided 69 correlational and 47 experimental effect sizes.

Results: The overall correlational effect size for trust was $\bar{r} = +0.26$, with an experimental effect size of $\bar{d} = +0.71$. The effects of human, robot, and environmental characteristics were examined with an especial evaluation of the robot dimensions of performance and attribute-based factors. The robot performance and attributes were the largest contributors to the development of trust in HRI. Environmental factors played only a moderate role.

Conclusion: Factors related to the robot itself, specifically, its performance, had the greatest current association with trust, and environmental factors were moderately associated. There was little evidence for effects of human-related factors.

Application: The findings provide quantitative estimates of human, robot, and environmental factors influencing HRI trust. Specifically, the current summary provides effect size estimates that are useful in establishing design and training guidelines with reference to robot-related factors of HRI trust. Furthermore, results indicate that improper trust calibration may be mitigated by the manipulation of robot design. However, many future research needs are identified.

Keywords: trust, trust development, robotics, human-robot team

Address correspondence to D. R. Billings, Department of Psychology, University of Central Florida, Orlando, FL 32816; e-mail: dbillings@knights.ucf.edu.

HUMAN FACTORS
Vol. 53, No. 5, October 2011, pp. 517-527
DOI:10.1177/0018720811417254

INTRODUCTION

Human-Robot Partnerships

Robots are frequently used in environments that are unreachable by or are unsafe for human beings. Robotic operations include, among others, planetary exploration, search and rescue, activities that impose hazardous levels of workload on human operators, and actions requiring complex tactical skills and information integration (Hinds, Roberts, & Jones, 2004; Parasuraman, Cosenzo, & de Visser, 2009). Robotic usage is penetrating into many diverse applicational realms, especially in the advanced surgical areas and as assistive technologies for injured and disabled persons (Guizzo & Goldstein, 2005; Heerink, Krose, Evers, & Wielinga, 2010; Tsui & Yanco, 2007). When they are used in military operations, robots are often currently perceived as tools to be manipulated by humans to accomplish specific discrete functions (Chen, Barnes, & Harper-Sciarini, 2010).

Yet, as robot capabilities grow, the possibility arises that they might provide higher level functions as full-fledged team members. For this higher functioning to blossom, however, effective human-robot partnerships will need to be forged to ensure success in dangerous conflict situations, particularly because of the increased stress and cognitive workload demands placed on contemporary warfighters (Hancock & Warm, 1989).

In future military contexts, warfighters are likely to be mandated to interact with a diverse inventory of robots on a regular basis, particularly in dynamic and stressful environments (Chen & Terrence, 2009). Already, robotic systems have demonstrated their usefulness in decision making, communication, enhancement of warfighter situation awareness, combat efficiency, and reducing uncertainty in volatile situations (Adams, Bruyn, Houde, & Angelopoulos, 2003). However, the assumption that introducing robots into human teams will result in better performance, as

compared with when the team or robot operates independently, may not always be justified. Although the addition of robotic systems may lead to improved team capabilities, it may also create difficult challenges that need to be overcome before such hybrid partnerships can work more effectively (Adams et al., 2003).

Research continues to address such challenges as creating and validating metrics for the evaluation of a wide spectrum of human-robot interactions (HRI) issues (Steinfeld et al., 2006); designing human-robot interfaces to facilitate interaction, operator understanding, and situation awareness (Chen et al., 2010; Chen, Haas, & Barnes, 2007; Keyes, Micire, Drury, & Yanco, 2010); translating qualities of good human teammates into features of the robot; and encouraging human trust in robots (Groom & Nass, 2007), which is perhaps foremost among these challenges.

Human-Robot Trust

For a human-robot team to accomplish its goal, humans must trust that a robotic teammate will protect the interests and welfare of every other individual on the team. The level of trust in any robotic partner will be particularly critical in high-risk situations, such as combat missions (Groom & Nass, 2007). Trust is important in these contexts because it directly affects the willingness of people to accept robot-produced information, follow robots' suggestions, and thus benefit from the advantages inherent in robotic systems (Freedy, de Visser, Weltman, & Coeyman, 2007). Trust therefore very much affects the decisions that humans make in uncertain or risky environments (Park, Jenkins, & Jiang, 2008). For example, the less an individual trusts a robot, the sooner he or she will intervene as it progresses toward task completion (de Visser, Parasuraman, Freedy, Freedy, & Weltman, 2006; Steinfeld et al., 2006).

However, some accounts from warfighters in the field demonstrate the ease with which trust can actually develop between robots and humans in stressful operations. In fact, one Explosive Ordnance Disposal unit named its robot Sgt. Talon and gave it promotions and even Purple Hearts for its stellar bomb disposal performance (Garreau, 2007). Other accounts by soldiers, in contrast, illustrate the difficulties in trusting robots in these situations. For instance, the SWORD (Special Weapons Observation Reconnaissance Detection) system was developed and deployed in Iraq in 2007 to support combat operations (Ogreten, Lackey, & Nicholson, 2010). SWORD, although fully operational, was never used in the field because soldiers did not trust it to function appropriately and safely in dangerous situations because of unexpected movements caused by technological malfunctions (Ogreten et al., 2010).

As illustrated by these respective accounts, varying levels of trust in robots currently exist across the HRI domain. Inappropriate levels of trust may have negative consequences, such as overreliance on and misuse of the system (in cases of extremely high levels of trust) or disuse of the system entirely (in cases of very low levels of trust) (Lee & See, 2004; Parasuraman & Manzey, 2010; Parasuraman & Riley, 1997). Both distrust and overreliance can undermine the value of the HRI system. Trust also influences neglect tolerance, which is defined as the decline in semiautonomous robot performance as human attention is directed to other tasks and/or as the task complexity increases (Goodrich, Crandall, & Stimpson, 2003).

When an individual places a large amount of trust in a robot and does not feel compelled to actively manage it, he or she may ignore the robot for long periods. Consequently, neglect tolerance should be appropriately calibrated to the capabilities of the robot and the level of human-robot trust. Too much neglect can make it difficult for the individual to regain situation awareness after redirecting attention back toward the robot. Too little neglect means the human operator is not attending to his or her own personal tasks, thus resulting in suboptimal system performance overall.

Current Research

Trust in HRI is very much related to trust in automation in general, which has been studied with respect to its various performance influences (Chen et al., 2010; Lee & See, 2004; Parasuraman, Sheridan, & Wickens, 2008; Sheridan, 2002). Robots differ from most other automated systems in that they are mobile, are sometimes built in a fashion that approximates human or animal

form, and are often designed to effect action at a distance. Such differences could suggest that human trust may differ for robots versus other forms of automation, although this difference would need to be demonstrated empirically, and few if any such direct comparisons have been conducted to date.

Alternatively, one can begin with the view that human-robot trust and human-automation trust share similar fundamental characteristics but allow for the possibility for differences as new evidence is obtained. Certainly the literature on human-automation trust provides a fertile ground for understanding a number of factors influencing how humans trust other external agents. The human-robot trust literature is more restricted, but nevertheless, sufficient numbers of empirical studies have been conducted to warrant a meta-analysis to identify the major factors currently involved.

Trust can be dynamically influenced by factors (or antecedents) within the robotic system itself, the surrounding operational environment, and the nature and characteristics of the respective human team members (Park et al., 2008). Each of these factors can play an important role in trust development. To date, reviews of trust in HRI have been qualitative and descriptive, and existing experiments largely attempt to extrapolate the optimum degree of trust for a given outcome (e.g., team performance, reliance on the robot). In doing so, a degree of inappropriate trust (i.e., excessive trust or too little trust) is also identified for each potential outcome of HRI, such as over- or underreliance and poor team collaboration. The factors that affect the process by which trust develops in any HRI situation also need to be considered. However, to date, the existing body of knowledge has mostly looked at the momentary state of trust and not its process of development per se. This latter evolution clearly awaits further investigation.

Given the foregoing observations, the goal of the current research was to perform a comprehensive objective and quantitative review of identified antecedents of trust in human-robot teams. Meta-analytic methods were applied to the extant literature on trust and HRI with the aim of quantifying the effects of differing dimensions on human-robot trust. Determining their relative impact on trust will not only provide an indication of current trends in the human-robot trust research, but will also lead to the identification of areas critical for future study. Consequently, our quantitative review contributes an empirical foundation upon which to advance both theory and practice.

ANALYTICAL METHOD

Sample of Studies

A literature search was conducted using library databases (including PsycINFO, PsycARTICLES, PsycBOOKS, ACM Digital Library, Applied Science and Technology, IEEE, ScienceDirect, and ProQuest Dissertations and Theses). U.S. Army Research Laboratory technical reports were also examined for relevance. In addition, we used a number of web-based search engines, for example, Google and its derivative Google Scholar, to seek further references not discovered by the initial formal scan. The primary search terms included *human-robot interaction*, *robot*, and *trust*. After the initial listing of articles was obtained, reference lists were checked to determine whether any other related studies could be included. In a concurrent process, subject matter experts (SMEs) were consulted for reference to articles that had not been identified by the prior, formal search procedure. SMEs were drawn from military, industry, and academia on the basis of their willingness to participate and their availability.

Following this initial procedure, we examined the collected literature and identified potential factors associated with the development of trust. SMEs also provided guidance in identifying factors influencing trust in human-robot relationships. On the basis of these identified factors, we conducted specific searches in the aforementioned databases using the primary search terms *robot* and *trust* combined with these secondary terms: *prior experience*, *attentional capacity*, *expertise*, *competency*, *personality*, *attitudes*, *propensity to trust*, *self-confidence*, *false alarm*, *failure rate*, *automation*, *anthropomorphism*, *predictability*, *proximity*, *robot personality*, *multitasking*, *workload*, *task load*, *culture*, *shared mental models*, and *situation awareness*. When these elicitation processes no longer yielded

new citations, we compiled the final listing of articles. This process resulted in 29 empirical articles, reports, dissertations, and conference proceedings published between 1996 and 2010. Of these, 10 papers containing 69 correlational effect sizes and 11 papers containing 47 experimental effect sizes met selection criteria for inclusion.

Criteria for Study Inclusion

All studies were inspected to ensure that they fulfilled the following four criteria for inclusion in the meta-analysis: (a) Each study had to report an empirical examination of trust in which trust was a directly measured outcome of an experimental manipulation. Studies in which trust served as the experimental manipulation were excluded. (b) The empirical examination of trust was directed toward a robot. Thus, for instance, studies on human-automation trust focusing on a decision aid were excluded because the emphasis of such research is on the decision aid and not a robot, which as discussed earlier can differ in many ways from automated systems in terms of such factors as mobility, sensor and effector capabilities, and so on. (c) The study had to incorporate human participants who either viewed or participated directly in interactions with a robot through physical, virtual, or augmented means. (d) Each study had to include sufficient information to determine effect size estimates.

Papers and literature meeting these criteria are identified in the reference listing in the present article by an asterisk appearing in front of the first author's name (American Psychological Association, 2001). It is important to note that rejecting primary studies in a meta-analysis is a common occurrence and is necessary to ensure meaningful results when combining effect sizes across studies.

Identification of Possible Antecedents of Trust

Studies included in the meta-analysis were classified into three broad categories according to the experimental manipulation: robot-related factors (including performance-based and attribute-based factors), human-related factors (including ability-based and human characteristic factors), and environment-related factors affecting trust (including team collaboration and task-based factors). These differentiates enabled a quantitative review of the predictive strength of these respective trust factors in human-robot teams. See Figure 1 for factors identified as potential antecedents of human-robot trust on the basis of the literature review and SME guidance.

The Calculation of Effect Size

A meta-analytic approach was used to evaluate the data collected to determine the pattern of findings in the contemporary body of human-robot trust research. First, each study's effect size was calculated using standard formulas (see Hedges & Olkin, 1985; Hunter & Schmidt, 2004; Morris & Deshon, 2002). Studies included in effect size calculation contained both correlational and group design data; therefore the use of multiple meta-analytic methods (correlation and Cohen's *d*) was necessary. The correlational effects represent an association between trust and the given factor. Cohen's *d* indicates the standard difference between two means in standard deviation units. From these, we can gather correlational and causal inferences between trust and any given factor. Through both types of meta-analytic effects, the more positive the effect, the more trust. Findings were interpreted with the use of Cohen's (1988) established ranges for small ($d \leq .20$; $r \leq .10$), medium ($d = .50$; $r = .25$), and large ($d \geq .80$; $r \geq .40$) effect sizes.

Variance Estimates

Several variance estimates were calculated. First, variability of the effect sizes themselves (s_g^2) and variability attributable to sampling error (s_e^2) were estimated. Next, these two values were used to compute the residual variance ($s^2\delta$). A large ($s^2\delta$) is an indication that the effect sizes may be heterogeneous and therefore one or more variables are likely to be moderating the magnitude of that particular effect. A final check for homogeneity of variance (s_e^2 / s_g^2) was calculated (proportion of total variance accounted for by sampling error). Hunter and Schmidt (2004) suggest that an outcome of 0.75 or greater suggests that the remaining variance is attributable to a variable that could not be controlled for and represents homogeneity of variance. However, large residual variance and small homogeneity

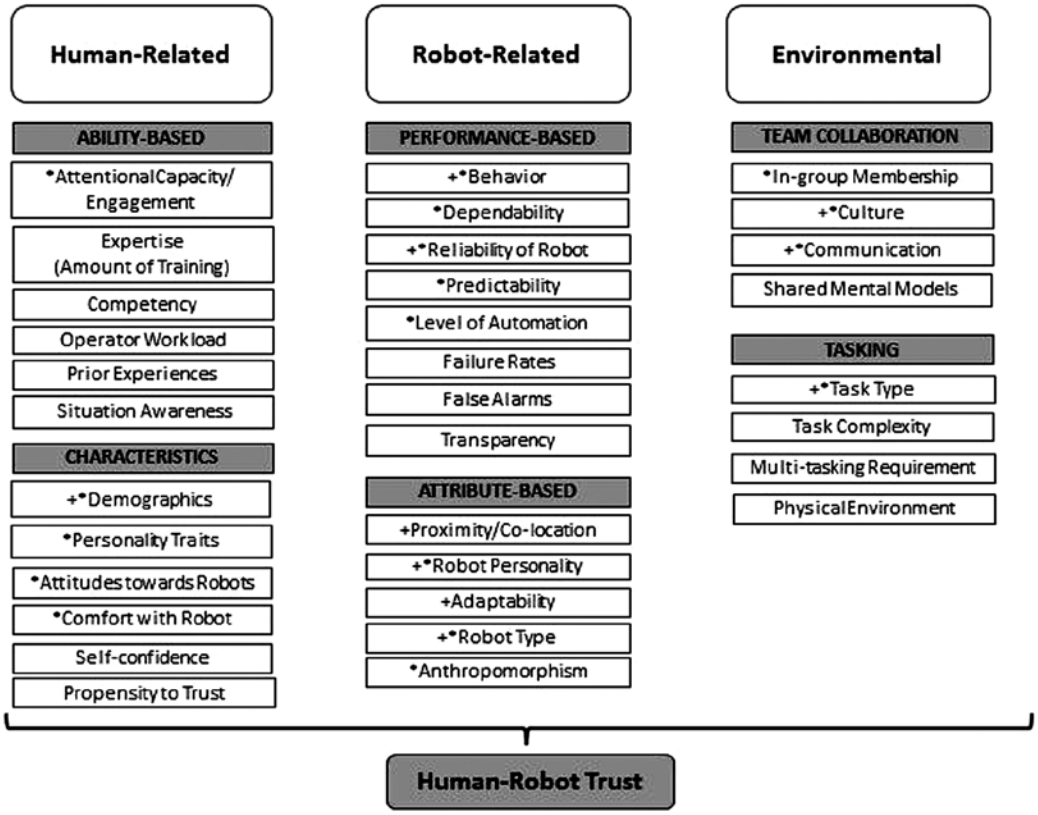

Figure 1. Factors of trust development in human-robot interaction. These factors were identified a priori via literature review and subject matter expert guidance. Factors included in the correlational analysis are starred (*). Factors included in the experimental analysis are crossed (+).

of variance may be seen because of a small number of sample studies, as is evident in some of the following results (see Lipsey & Wilson, 2001, for an in-depth examination of the various strengths and weaknesses relating to meta-analytic procedures).

RESULTS

Overall Outcome Effects

Correlational analysis. For the 10 studies reporting correlational data, the present meta-analytic results indicated that there was a moderate global effect between trust and all factors influencing HRI ($\bar{r}$ = +0.26; see Table 1). That the identified confidence interval does not include zero confirms that this identified relationship is consistent and substantive. The subsidiary analysis between trust and human, robot, and environmental factors individually indicated only small effects for the human dimensions ($\bar{r}$ = +0.09) and also the environmental characteristics ($\bar{r}$ = +0.11), and because the confidence intervals for human and environmental factors included zero, our current state of knowledge suggests that the human and the environment are not strongly associated with trust development in HRI at this point in time. We should, however, emphasize that these results derive from only a limited number of studies and thus may change with future evaluations.

Robot-related characteristics were found to be moderately associated with trust in HRI ($\bar{r}$ = +0.24), in line with the level of the global effect. Robot influences were able to be parsed into two

TABLE 1: Formal Human-Robot Trust Meta-Analysis Results With Correlational Data: Global, Trust Factors, and Robot Factors

Category	*k*	$\bar{r}$	s^2_r	s^2_e	s^2_p	s^2_e/s^2_p	95% CI	*n*
Global	10	+.26	.14	.01	.13	.05	+.21 < δ < +.31	1,228
Trust factors								
Robot	8	+.24	.21	.01	.20	.05	+.16 < δ < +.31	882
Human	7	+.09	.14	.02	.13	.11	.00 < δ < +.19	727
Environment	4	+.11	.11	.01	.10	.08	+.02 < δ < +.20	645
Robot factors								
Attribute	5	+.03	.08	.02	.07	.22	−.09 < δ < +.15	686
Performance	5	+.34	.43	.01	.42	.03	+.25 < δ < +.43	607

Note. *k* = number of studies; *n* = sample size; s^2_r estimates the variability of the effect sizes themselves; s^2_e estimates the variability attributable to sampling error; s^2_p is an estimate of the residual variance; s^2_e/s^2_p) is a calculation of homogeneity of variance; CI = confidence interval.

subcategories: robot performance-based factors (e.g., reliability, false alarm rate, failure rate) and attribute-based factors (e.g., proximity, robot personality, and anthropomorphism). With respect to the influence of the robot, it was determined that performance factors were more strongly associated ($\bar{r}$ = +0.34) with trust development and maintenance. However, in contrast, robot attributes had only a relatively small associated role ($\bar{r}$ = +0.03). Such potential influences for human- and environmental-related factors were not examined, as there were insufficient samples at the present juncture to run acceptable quantitative meta-analytic procedures.

Experimental analysis. In contrast to studies that presented correlational data, experimental studies reported group differences. Therefore, for this latter meta-analysis, we used Cohen's *d*. The results for the meta-analytic approach with the use of Cohen's *d* produced a similar pattern to that for the correlational studies. These results, shown in Table 2, indicated there was a large global effect concerning trust and HRI ($\bar{d}$ = +0.71). As the confidence interval excluded zero, we can assume this is a substantive and consistently large effect. The subdivision of this global effect into robot, human, and environmental characteristics indicated that the robot ($\bar{d}$ = +0.67) had the greatest effect. There was a moderate effect for environmental factors ($\bar{d}$ = +0.47) but only very small effects for human factors ($\bar{d}$ = –0.02). Robot factors were again parsed into the two categories of attributes and performance. Robot performance factors ($\bar{d}$ = +0.71) were the largest identifiable influences on HRI trust, whereas robot attributes ($\bar{d}$ = +0.47) had a smaller but still sizeable influence on trust development.

We should, however, point out that the performance factors are based on two studies, which may bring into question the stability of the effect. However, each study has a sizable effect supporting this found effect. The attribute factors are based on eight studies, pointing to stronger stability of the effect. Specific influential effects for human- and environment-related factors were not examined, as there were insufficient data to run the meta-analysis. In all of the aforementioned categories in which there were sufficient data to identify effects, none of the confidence intervals for the experimental work included zero. Therefore, we can have a degree of confidence that these are each consistent and real effects.

DISCUSSION

Trust is a crucial dimension in maintaining effective relationships with robots. The presence, growth, erosion, and extinction of trust have powerful and lasting effects on how each member of any shared relationship behaves and will behave in the future. Currently, we see technology (and the present panoply of robots) as largely insensate and without individual motive

TABLE 2: Formal Human-Robot Trust Meta-Analysis Results With Cohen's *d*: Global, Trust Factors, and Robot Factors

Category	*k*	$\bar{d}$	s^2_g	s^2_e	$s^2\delta$	$s^2_e/s^2\delta$	95% CI	*n*
Global	11	+.71	.26	.09	.16	.36	+.53 < δ <+.89	1,567
Trust factors								
Robot	8	+.67	.15	.07	.08	.48	+.48 < δ < +.85	1,119
Human	2	−.02	g = +.01 (Kidd, 2003); g = –.88 (Scopelliti, Giuliani, & Fornana, 2005)	202				
Environment	5	+.47	.21	.07	.13	.36	+.23 < δ < +.71	609
Robot factors								
Attribute	8	+.47	.25	.07	.19	.27	+.28 < δ < +.65	1,119
Performance	2	+.71	g = +.71 (Ross, 2008); g = +.74 (Tsui, Desai, & Yanco, 2010)	554				

Note. *k* = number of studies; *n* = sample size; s^2_g estimates the variability of the effect sizes themselves; s^2_e estimates the variability attributable to sampling error; $s^2\delta$ is an estimate of the residual variance; s^2_e/s^2_g is a calculation of homogeneity of variance; CI = confidence interval.

force. Although we are often frustrated with technological shortcomings and failures and express our frustration accordingly, at heart, we know we are dealing with the residual effects of a remote human designer. However, we stand on the verge of a sufficiently impactful change that our attribution of intentionality to all technology will soon be justified (and see Epley, Waytz, & Cacioppo, 2007; Moravec, 1988). At this juncture, the issue of trust in technological systems will be as influential on social development as it is in our own human-human relationships.

Trust is only one of a number of critical elements essential to human-robot collaboration, but it continues to be a growing concern as robots advance in their functionality. This is especially the case in military and emergency contexts in which a warfighter's or an operator's own life and the lives and safety of others depend on successful interaction. The present research represents one of the first systematic efforts to quantify effects concerning human trust in robots. Our results reveal that robot characteristics, and in particular, performance-based factors, are the largest current influence on perceived trust in HRI. These findings imply that manipulating different aspects of the robot's performance influences trust the most. This finding is central to the consideration of coming robot design. Trends in the literature indicate that higher trust is associated with higher reliability (for example, see Ross, 2008). Furthermore, the type, size, proximity, and behavior of the robot also affect trust (for examples, see Bainbridge, Hart, Kim, & Scassellati, 2008; Tsui, Desai, & Yanco, 2010). Taking such factors into consideration can have meaningful influence on future robot design and associated human-robot interaction, although further research is still needed to develop specific design heuristics.

Environmental factors were also found to be moderately influential on trust development. Team collaboration characteristics and tasking factors, as identified by SMEs and in the literature itself, were included in this analysis. However, further specification of team-related and task-related effects could not be drawn because of the insufficient number of empirically codable studies. Limited evidence for human-related factors was found. The present findings, however, should not be taken to imply that human characteristics in HRI are not necessarily important. Rather, the small number of studies found in this area suggests a strong need for future experimental efforts on human-related, as well as environment-related, factors.

Although human-automation interaction in general has been researched in more depth (Dzindolet, Peterson, Pomranky, Pierce, & Beck, 2003; Lee & See, 2004; Madhavan & Wiegmann,

2007; Sheridan, 2002; Sheridan & Parasuraman, 2006), sparse empirical research has been conducted in a number of specific and important areas associated with human-robot trust. For instance, as noted, there is a dearth of studies on the human-related characteristics, including prior level of operational experience, attentional capability, the amount of training received, self-confidence, the propensity to trust, existing attitudes toward robots, personality traits, operator workload, situation awareness, and other individual difference factors (see Hancock, Hancock, & Warm, 2009). Gaps in the understanding of the various environmental characteristics include culture (of the team, the individual, and the ambient environment), shared mental models, multitasking requirements, task complexity, and task type. We also have limited empirical evidence on the effects of robot "false" alarms. Resolution in these areas is crucial to provide an increasing depth of understanding on trust in HRI.

Our meta-analytic findings have implications for both research and practice. In terms of research, as we build functional models of HRI, we will need to understand and quantify the various influences and derive information on factors we have shown that, to date, are completely missing. Without a larger and active empirical attack, our knowledge will remain precarious and based often on either anecdotal or engineering-centered case studies. With regard to practical implications, the major lesson learned is that a robot's performance and attributes should be considered the primary drivers of trust. Understanding exactly how these factors affect the development of trust will be critical for trust calibration. For example, we are aware of, and have cited one instance of, a number of occasions in the military in which robots have looked to be deployed, but because of the intrinsic trust question, they have never been taken "out of the box" (often because of a bad reputation preceding the system or its perceived complexity of operation). Consequently, if the perceived risk of using the robot exceeds its perceived benefit, practical operators almost always eschew its use. Hence, training that encourages trust in specific robots is necessary from the point of design inception on, until its eventual field use.

The implications of this research can also be applied to trust in HRI in a number of critical areas outside of the military. These include, especially, considerations in the medical and health care arenas. Assistive robotic technologies are also being developed and tested for mobility purposes, rehabilitation, and of course, surgical aids (Tsui & Yanco, 2007). Social robots for domestic use are also being designed to help people with cognitive and physical challenges maintain a high quality of life (Heerink, et al., 2010). For example, the Care-O-Bot II is a robotic home assistant that was created to support the needs of elderly persons in private homes, allowing individuals greater independence without the necessary presence of a human caregiver (Graf, Hans, & Schraft, 2004).

Other robotic devices, such as wheelchairs (Yanco, 2001) and exoskeletons (e.g., robotic arms, legs; Guizzo & Goldstein, 2005) can benefit disabled individuals by enhancing their remaining physical capabilities. Furthermore, robots are capable of telepresence in life-threatening situations when medical professionals cannot be physically present as well as in cases involving high risk, such as search-and-rescue operations (Murphy, Riddle, & Rasmussen, 2004) and repairs in contaminated conditions, as the recent Japanese nuclear power plant experience has shown (Glionna & Nagano, 2011). Given our current meta-analytic findings, robot performance factors in these domains are also therefore most critical to consider. Regardless of context, a user must trust the robot to enable effective interaction.

Future Research

The type of trust measure used is relevant to the present conclusions. Our meta-analysis found that current trust in HRI is derived almost exclusively via subjective response, measured one time after a specific interaction. However, physiological indicators, such as oxytocin-related measures, and objective measures, such as trust games that assess actual investment behavior, are used frequently in the human-interpersonal trust literature (for examples, see Chang, Doll, van 't Wout, Frank, & Sanfey, 2010; Keri, Kiss, & Kelemen, 2009). These measures should be

explored in the context of human-robot trust to augment the present perceptual assessments and identify potential inconsistencies between such measures. Discrepancies between an individual's self-report (i.e., perception) and his or her behavior (i.e., observable reaction) is an issue that has been a topic of concern in psychology, and especially applied psychology, for a number of decades (see Hancock, 1996; Natsoulas, 1967). An individual can report that he (or she) will trust a robot, but existing research leads us to believe that this statement-action relationship is not always perfect (Chen & Terrence, 2009). Therefore, empirical research that includes both subjective and objective measurements can provide a more complete portraiture of the genesis and persistence of trust.

A comparison of perceptions and actual robot capabilities is also needed. Each person in a team can have differing perceptions of the intent, performance, and actions of a robotic entity, but indeed, these perceptions may not all match the true capabilities of the robot. These differences in perception may be mitigated to an extent by employing training methods that adequately prepare an individual for the coming interaction. In summary, numerous avenues of research need to be pursued to fully comprehend the role that trust plays in HRI as well as the factors that influence trust in robots themselves as stand-alone entities. Even so, our current findings indicate that currently, the most important element of trust is robot related. Fortunately, these factors (e.g., robot performance, robot attributes) can be directly manipulated by designers (with the constraints of technological capabilities). In this way, we are able to predict to some degree the development of trust in human-robot partnerships in existing systems.

ACKNOWLEDGMENTS

The research reported in this document was performed in connection with Contract No. W911NF-10-2-0016 with the U.S. Army Research Laboratory, under UCF Task No. 3, P. A. Hancock, Principal Investigator. The views and conclusions contained in this document are those of the authors and should not be interpreted as presenting the official policies or position, either expressed or implied, of the U.S. Army Research Laboratory or the U.S. government unless so designated by other authorized documents. Citation of manufacturer's or trade names does not constitute an official endorsement or approval of the use thereof. The U.S. government is authorized to reproduce and distribute reprints for government purposes notwithstanding any copyright notation herein. We wish to thank the associate editor and two anonymous reviewers for their most helpful comments in revising the present work.

KEY POINTS

- The meta-analytic procedures included 10 references for correlational analysis (yielding 69 correlational effect sizes) and 11 for experimental analysis (yielding 47 experimental effect sizes).
- Robot characteristics, and in particular, robot performance, were found to be the most important influences of trust development.
- Environmental factors moderately influenced trust, whereas little evidence was found for the effect of human characteristics on trust in human-robot interaction (HRI).
- Although human dimensions played a small role in trust development, the lack of findings may be attributable to insufficient empirical data (suggesting limitations in the research), which should be addressed in future experimentation.
- The current summary of findings emphasizes the importance of focusing on robot-related factors in design and training guidelines for HRI.

REFERENCES

References marked with an asterisk indicate studies included in the meta-analysis.

Adams, B. D., Bruyn, L. E., Houde, S., & Angelopoulos, P. (2003). *Trust in automated systems literature review* (DRDC Toronto No. CR-2003-096). Toronto, Canada: Defence Research and Development Canada.

American Psychological Association. (2001). *Publication manual of the American Psychological Association* (5th ed.). Washington, DC: Author.

*Bainbridge, W. A., Hart, J., Kim, E. S., & Scassellati, B. (2008). The effect of presence on human-robot interaction. In *Proceedings of the 17th IEEE Symposium on Robot and Human Interactive Community* (pp. 701–706). Munich, Germany: IEEE.

*Biros, D. P., Daly, M., & Gunsch, G. (2004). The influence of task load and automation trust on deception detection. *Group Decision and Negotiation*, *13*, 173–189.

Chang, L. J., Doll, B. B., van 't Wout, M., Frank, M. J., & Sanfey, A. G. (2010). Seeing is believing: Trustworthiness as a dynamic belief. *Cognitive Psychology*, *61*, 87–105.

Chen, J. Y. C., Barnes, M. J., & Harper-Sciarini, M. (2010). Supervisory control of multiple robots: Human-performance issues and user-interface design. *IEEE Transactions on Systems, Man, and Cybernetics–Part C: Applications and Reviews*, *41*, 435–454.

Chen, J. Y. C., Haas, E. C., & Barnes, M. J. (2007). Human performance issues and user interface design for teleoperated robots. *IEEE Transactions on Systems, Man, and Cybernetics–Part C: Applications and Reviews*, *37*, 1231–1245.

Chen, J. Y. C., & Terrence, P. I. (2009). Effects of imperfect automation and individual differences on concurrent performance of military and robotics tasks in a simulated multitasking environment. *Ergonomics*, *52*, 907–920.

Cohen, J. (1988). *Statistical power analysis for the behavioral sciences* (2nd ed.). Hillsdale, NJ: Lawrence Erlbaum.

*De Ruyter, B., Saini, P. Markopoulous, P., & van Breeman, A. (2005). Assessing the effects of building social intelligence in robotic interface in the home. *Interacting With Computers*, *17*, 522–541.

de Visser, E. J., Parasuraman, R., Freedy, A., Freedy, E., & Weltman, G. (2006). A comprehensive methodology for assessing human-robot team performance for use in training and simulation. In *Proceedings of the 50th Annual Meeting of the Human Factors and Ergonomics Society* (pp. 2639–2643). Santa Monica, CA: Human Factors and Ergonomics Society.

Dzindolet, M. T., Peterson, S. A., Pomranky, R. A., Pierce, L. G., & Beck, H. P. (2003). The role of trust in automation reliance. *International Journal of Human-Computer Studies*, *58*, 697–718.

Epley, N., Waytz, A., & Cacioppo, J. T. (2007). On seeing human: A three-factor theory of anthropomorphism. *Psychological Review*, *114*, 864–886.

*Evers, V., Maldanado, H., Brodecki, T., & Hinds, P. (2008). Relational vs. group self-construal: Untangling the role of national culture in HRI. In *Proceedings in the 3rd ACM/IEEE International Conference on Human Robot Interaction* (pp. 255–262). New York, NY: Association for Computing Machinery.

Freedy, A., de Visser, E., Weltman, G., & Coeyman, N. (2007). Measurement of trust in human-robot collaboration. In *Proceedings of the 2007 International Conference on Collaborative Technologies and Systems* (pp. 106–114). Orlando, FL: IEEE.

Garreau, J. (2007, May 6). Bots on the ground: In the field of battle (or even above it), robots are a soldier's best friend. *The Washington Post*. Retrieved from http://www.washingtonpost.com

Glionna, J. M., & Nagano, Y. (2011, May 8). Japan looks abroad for high-tech help at Fukushima plant. *Los Angeles Times*. Retrieved from http://articles.latimes.com/2011/may/08/world/la-fg-japan-robots-20110508

Goodrich, M. A., Crandall, J. W., & Stimpson, J. (2003, March). *Neglect tolerant teaming: Issues and dilemmas*. Paper presented at the 2003 AAAI Spring Symposium on Human Interaction with Autonomous Systems in Complex Environments, Palo Alto, CA.

Graf, B., Hans, M., & Schraft, R. D. (2004). Care-O-Bot II development of a next generation robotic home assistant. *Autonomous Robots*, *16*, 193–205.

Groom, V., & Nass, C. (2007). Can robots be teammates? Benchmarks in human-robot teams. *Interaction Studies*, *8*, 483–500.

Guizzo, E., & Goldstein, H. (2005). The rise of the body bots [robotic exoskeletons]. *IEEE Spectrum*, *42*(10), 50–56.

Hancock, P. A. (1996). Effects of control order, augmented feedback, input device and practice on tracking performance and perceived workload. *Ergonomics*, *39*, 1146–1162.

Hancock, P. A., Hancock, G. M., & Warm, J. S. (2009). Individuation: The *N* = 1 revolution. *Theoretical Issues in Ergonomic Science*, *10*, 481–488.

Hancock, P. A., & Warm, J. S. (1989). A dynamic model of stress and sustained attention. *Human Factors*, *31*, 519–537.

Hedges, L. V., & Olkin, I. (1985). *Statistical methods for meta-analysis*. Orlando, FL: Academic Press.

*Heerink, M., Krose, B., Evers, V., & Wielinga, B. (2010). Assessing acceptance of assistive social agent technology by older adults: The Almere model. *International Journal of Social Robots*, *2*, 361–375.

Hinds, P. J., Roberts, T. L., & Jones, H. (2004). Whose job is it anyway? A study of human-robot interaction in a collaborative task. *Human-Computer Interaction*, *19*, 151–181.

Hunter, J. E., & Schmidt, F. L. (2004). *Methods of meta-analysis: Correcting for error and bias in research findings*. Thousand Oaks, CA: Sage.

Keri, S., Kiss, I., & Kelemen, O. (2009). Sharing secrets: Oxytocin and trust in schizophrenia. *Social Neuroscience*, *4*, 287–293.

Keyes, B., Micire, M., Drury, J. L., & Yanco, H. A. (2010). Improving human-robot interaction through interface evolution. In D. Chugo (Ed.), *Human-robot interaction* (pp. 183-202). Rijeka, Croatia: InTech.

*Kidd, C. D. (2003). *Sociable robots: The role of presence and task in human-robot interaction*. (Master's thesis). Massachusetts Institute of Technology, Cambridge.

*Kidd, C. D., & Breazeal, C. (2004). Effect of a robot on user perception. In *Proceedings of the IEEE/RSJ International Conference on Intelligent Robots and Systems* (pp. 3559–3564). Sendai, Japan: IEEE.

*Kiesler, S., Powers, A., Fussell, S. R., & Torry, C. (2008). Anthropomorphic interactions with a robot and robot-like agents. *Social Cognition*, *26*, 169–181.

Lee, J. D., & See, K. A. (2004). Trust in automation: Designing for appropriate reliance. *Human Factors*, *46*, 50–80.

*Li, D., Rau, P., & Li, Y. (2010). A cross-cultural study: Effect of robot appearance and task. *International Journal of Social Robots*, *2*, 175–186.

Lipsey, M. W., & Wilson, D. B. (2001). *Practical meta-analysis*. Thousand Oaks, CA: Sage.

*Looije, R., Neerinex, M. A., & Cnossen, F. (2010). Persuasive robotic assistant for health self-management of older adults: Design and evaluation of social behaviors. *International Journal of Human-Computer Studies*, *68*, 386–397.

Madhavan, P., & Wiegmann, D. A. (2007). Similarities and differences between human-human and human-automation trust: An integrative review. *Theoretical Issues in Ergonomics Science*, *8*, 277–301.

Moravec, H. (1988). *Mind children: The future of robot and human intelligence*. Cambridge, MA: Harvard University Press.

Morris, S. B., & DeShon, R. P. (2002). Combining effect size estimates in meta-analysis with repeated measures and independent groups designs. *Psychological Methods*, *7*, 105–125.

Murphy, R. R., Riddle, D., & Rasmussen, E. (2004). Robot-assisted medical reachback: A survey of how medical personnel expect to interact with rescue robots. In *Proceedings of the 13th Annual IEEE International Workshop on Robot and Human Interactive Communication (RO-MAN 2004),* (pp. 301–306). Kurashiki, Okayama, Japan: IEEE.

*Mutlu, B., Yamaoka, F., Kanda, T., Ishiguro, H., & Hagita, N. (2009). Nonverbal leakage in robots: Communication of intentions through seemingly unintentional behavior. In *Proceedings of the 4th ACM/IEEE International Conference on Human Robot Interaction* (pp. 69–76). New York, NY: Association for Computing Machinery.

Natsoulas, T. (1967). What are perceptual reports about? *Psychological Bulletin*, *67*, 249–272.

Ogreten, S., Lackey, S., & Nicholson, D. (2010, May). *Recommended roles for uninhabited team members within*

mixed-initiative combat teams. Paper presented at the 2010 International Symposium on Collaborative Technology Systems, Chicago, IL.

Parasuraman, R., Cosenzo, K. A., & de Visser, E. (2009). Adaptive automation for human supervision of multiple uninhabited vehicles: Effects on change detection, situation awareness, and mental workload. *Military Psychology*, *21*, 270–297.

Parasuraman, R., & Manzey, D. (2010). Complacency and bias in human use of automation: An attentional integration. *Human Factors*, *52*, 381–410.

Parasuraman, R., & Riley, V. (1997). Humans and automation: Use, misuse, disuse, abuse. *Human Factors*, *39*, 230–253.

Parasuraman, R., Sheridan, T., & Wickens, C. (2008). Situation awareness, mental workload, and trust in automation: Viable, empirically supported cognitive engineering constructs. *Journal of Cognitive Engineering and Decision Making*, *2*, 140–160.

Park, E., Jenkins, Q., & Jiang, X. (2008 September). *Measuring trust of human operators in new generation rescue robots*. Paper presented at the 7th JFPS International Symposium on Fluid Power, Toyama, Japan.

*Powers, A., Kiesler, S., Fussell, S., & Torrey, C. (2007). Comparing a computer agent with a humanoid robot. In *Proceedings of the International Conference on Human Robot Interaction* (pp. 145–152). Arlington, VA: ACM.

*Rau, P. L., Li, Y., & Li, D. (2009). Effects of communication style and culture on ability to accept recommendations from robots. *Computers in Human Behavior*, *25*, 587–595.

*Ross, J. M. (2008). *Moderators of trust and reliance across multiple decision aids* (Doctoral dissertation). University of Central Florida, Orlando.

*Scopelliti, M., Giuliani, M. V., & Fornara, F. (2005). Robots in a domestic setting: A psychological approach. *Universal Access in the Information Society*, *4*, 146–155.

Sheridan, T. B. (2002). *Humans and automation: System design and research issues*. Santa Monica, CA: Wiley.

Sheridan, T. B., & Parasuraman, R. (2006). Human-automation interaction. *Reviews of Human Factors and Ergonomics*, *1*, 89–129.

Steinfeld, A., Fong, T., Kaber, D., Lewis, M., Scholtz, J., Schultz, A., & Goodrich, M. (2006). Common metrics for human-robot interaction. In *Proceedings of 2006 ACM Conference on Human-Robot Interaction,* (pp. 33–40). Salt Lake City, UT: ACM.

*Tenney, Y. J., Rogers, W. H., & Pew, R. W. (1998). Pilot opinions of cockpit automation issues. *International Journal of Aviation Psychology*, *8*, 103–120.

*Tsui, K. M., Desai, M., & Yanco, H. A. (2010). Considering the bystander's perspective for indirect human-robot interaction. In *Proceedings of the 5th ACM/IEEE International Conference on Human Robot Interaction* (pp. 129–130). New York, NY: Association for Computing Machinery.

Tsui, K. M., & Yanco, H. A. (2007). Assistive, surgical, and rehabilitation robots from the perspective of medical and healthcare professionals. In *Proceedings of the AAAI Workshop on Human Implications of Human-Robot Interaction* (pp. 34–39). Vancouver, Canada: AAAI Press.

*Wang, L., Rau, P. L., Evers, V., Robinson, B. K., & Hinds, P. (2010). When in Rome: The role of culture and context in adherence to robot recommendations. In *Proceedings of the 5th ACM/IEEE International Conference on Human Robot Interaction* (pp. 359–366). New York, NY: Association for Computing Machinery.

Yanco, H. A. (2001). Development and testing of a robotic wheelchair system for outdoor navigation. In *Proceedings of the 2001 Conference of the Rehabilitation Engineering and Assistive Technology Society of North America*. Arlington, VA: RESNA Press.

Peter A. Hancock is Provost Distinguished Research Professor and Pegasus Professor in the Department of Psychology and the Institute for Simulation and Training at the University of Central Florida. He received a PhD in motor performance from the University of Illinois, Champaign, in 1983. He is a fellow of and a past president of the Human Factors and Ergonomics Society.

Deborah R. Billings is a postdoctoral researcher with the Institute for Simulation and Training at the University of Central Florida. She received a PhD in applied experimental and human factors psychology from the University of Central Florida in 2010. She also obtained an MS in modeling and simulation from the University of Central Florida.

Kristin E. Schaefer is a doctoral student in the modeling and simulation PhD program at the University of Central Florida. She received an MS in modeling and simulation from the University of Central Florida in 2009 and a BA in the field of psychology with a minor in sociology from Susquehanna University.

Jessie Y. C. Chen is a research psychologist with the U.S. Army Research Laboratory–Human Research and Engineering Directorate (Field Element in Orlando, Florida). She received a PhD in applied experimental and human factors psychology from the University of Central Florida in 2000.

Ewart J. de Visser is pursuing a PhD degree in human factors and applied cognition at George Mason University. He received his BA in film studies from the University of North Carolina at Wilmington and an MA in human factors and applied cognition from George Mason University in 2007.

Raja Parasuraman is a university professor in the Department of Psychology at George Mason University and director of the graduate program in human factors and applied cognition. He is director of the Center of Excellence in Neuroergonomics, Technology, and Cognition and chair of the Neuroimaging Core of the Krasnow Institute. He received a PhD in psychology from Aston University, Birmingham, United Kingdom, in 1976.

Date received: February 16, 2011
Date accepted: June 10, 2011

Biographies of ARL Authors

Sarah S. Bedair received her M.S. and Ph.D. degrees in electrical and computer engineering from the Carnegie Mellon University, in 2004 and 2008, respectively; her thesis work focused on CMOS-MEMS-based chemical sensors and mechanical oscillators. She spent one year (2008-2009) as an Oak Ridge Associated University postdoctoral fellow at the U.S. Army Research Laboratory (ARL) and she has been a staff researcher in the Power Components Branch since June 2009. Her research focuses on the modeling and fabrication of MEMS-based power devices, specifically for single-chip-scale power conversion and RF electronics. Dr. Bedair has contributed to more than 40 research publications and is a co-inventor on five patents and applications. In 2009, she received the Department of the Army Research and Development Achievement Award and in 2010 she was awarded the Excellence in Federal Career-Technical & Scientific Rookie of the Year Award (Gold).

Jessie Y.C. Chen joined the U.S. Army Research Laboratory's (ARL) Human Research and Engineering Directorate in 2003 as a research psychologist, with a focus on human-robot interaction, human-vehicle interaction, supervisory control and individual differences. She received a Ph.D. in applied experimental and human factors psychology from the University of Central Florida, an M.A. in communication studies from the University of Michigan (Ann Arbor), and a B.A. in linguistics from National Tsing-Hua University in Taiwan. Due to her research on human-robot interaction in multitasking environments, she is the recipient of the 2008 Army-wide Modeling and Simulation (Individual Experimentation) Award. Dr. Chen has co-authored over 100 peer-reviewed papers and has received two best-paper awards (2010 Army Science Conference and 2006 Industrial Engineering Research Conference). She has been a reviewer for 13 scientific journals and has served on scientific review panels for the National Science Foundation National Robotics Initiative, AFOSR, and ONR. Currently, she is working on two projects under the OSD Autonomy Research Pilot Initiative.

Michael J. Barnes is a research psychologist with the Human Research and Engineering Directorate of the U.S. Army Research Laboratory (ARL). Most recently, he was the lead for the human robotic interaction (HRI) component of Safe Operations for Unmanned Systems for Reconnaissance in Complex Environments (SOURCE). Prior to joining ARL, he conducted human factors (HF) research for the U.S. Navy and served as the HF manager for the General Electric Corporation. Since coming to ARL, he has served on a number of NATO committees related to HRI and battlefield visualization. He has authored or co-authored over 80 articles and co-edited a book — Human-Robot Interactions in Future Military Operations, 2010 (ed. Barnes & Jentsch). Located at Fort Huachuca, Ariz., his research interests include investigations of risk visualization, intelligence processes and unmanned aerial vehicle crew systems. He was educated at the University of Arizona (B.A.) and New Mexico State University (M.A.).

Wayne A. Churaman received a B.S. and M.S. in electrical engineering from the University of Maryland, College Park, in 2005 and 2010, respectively, with a specific focus on microelectronics and microrobotic platforms. Since 2005, he has been working as a micro-electro-mechanical systems (MEMS) engineer for the U.S. Army Research Laboratory (ARL). His interests include experimental analysis of nanoenergetic materials, integration of nanoenergetic materials with MEMS and MEMS sensor design and fabrication. He is currently pursuing a Ph.D. – supported by ARL – in mechanical engineering at the University of Maryland, College Park, where his research involves developing nanoenergetic porous silicon as a novel actuator to enhance the mobility of microrobotic platforms.

Jonathan R. Fink is a researcher in the Asset Control and Behavior Branch, Information Sciences Division of the U.S. Army Research Laboratory's (ARL) Computational & Information Sciences Directorate. He received his Ph.D. from the University of Pennsylvania, Philadelphia, Pa., in 2011, where he worked in the GRASP Laboratory on communication-constrained planning for teams of networked robots. Since joining ARL, he has contributed to the development and experimental testing of fundamental capabilities for autonomous ground robots, including techniques for mapping and navigation in militarily relevant environments. Dr. Fink has also continued his graduate research into multi-agent planning that takes place at the intersection of networking and robotics through collaborations with the Network Sciences Division of Computational & Information Sciences. He is a member of the Institute of Electrical and Electronics Engineers (IEEE) and has published over 20 technical articles in the field of robotics and autonomous systems.

Jemin George received his B.S. (2005), M.S. (2007), and Ph.D. (2010) in aerospace engineering from the State University of New York at Buffalo. In 2008, he was a summer research scholar with the U.S. Air Force Research Laboratory's Space Vehicles Directorate at Kirtland Air Force Base, Albuquerque, N.M. He was a National Aeronautics and Space Administration Langley

Aerospace research summer scholar with the Langley Research Center in 2009. From 2009-2010, he was a research fellow with the Stochastic Research Group, Department of Mathematics, at Technische Universität Darmstadt, Darmstadt, Germany. Joining ARL in 2010 as a civilian employee, he is currently with the Networked Sensing & Fusion Branch of the Signal & Image Processing Division. He has published over 30 refereed technical articles in the areas of estimation, control and information fusion. Dr. George received the 2012 Army Research and Development Achievement Award for Outstanding Collaboration and has chaired numerous sessions at the Institute of Electrical and Electronics Engineers (IEEE) American Control Conference; the Society for Industrial and Applied Mathematics (SIAM) Conference on Uncertainty Quantification; and the American Institute of Aeronautics and Astronautics (AIAA) Guidance, Navigation, and Control Conference. His principal research interests include stochastic systems, control theory, nonlinear filtering, information fusion and target tracking.

Tony G. Ivanov has been a research scientist in the Sensors and Electronic Devices Directorate at the U.S. Army Research Laboratory (ARL) since 2009. His professional interests include the area of power-combining amplifiers and novel devices/technologies for millimeter-wave circuits. In 1987, Dr. Ivanov received his B.S. degree in electrical engineering from Baltic State Technical University, St. Petersburg, Russia. Subsequently, he received M.S. and Ph.D. degrees from the University of Central Florida, Orlando, in 1994 and 1997, respectively. Dr. Ivanov has worked for Bell Laboratories (AT&T, Lucent Technologies, Agere Systems) in Orlando, Fla., on SiGe technology development; and for RF Micro Devices, in Greensboro, N.C., on new RF/microwave semiconductor technologies and MEMS. He has authored and co-authored more than 50 publications and holds nine U.S. patents. Dr. Ivanov is Chairman of the Washington D.C./Northern Virginia Chapter of the Institute of Electrical and Electronics Engineers (IEEE) Microwave Theory and Techniques Society.

Christopher D. Meyer is an electronics engineer in the Power Components Branch, Energy & Power Division. He received his B.S. (cum laude), M.S. and Ph.D. degrees in electrical engineering in 2006, 2009, and 2012, respectively, from the University of Florida, and began working at ARL as a doctoral student in 2009. His current research interests include three-dimensional microfabrication technologies, contactless power transfer and environmental energy scavenging. Dr. Meyer has contributed to seven peer-reviewed journal articles and 17 conference presentations on topics including thermoelectric power generation, microscale magnetic passives and microelectronics-integrated magnetic materials. His awards include the University of Florida Alumni Fellowship, the National Science Foundation Graduate Research Fellowship (Honorable Mention) and he is also a member of the Eta Kappa Nu electrical engineering honor society. Dr. Meyer received the 2010 Research & Development Achievement Award for Technical Excellence for his contributions to nanoparticle self-assembly in MEMS structures using capillary wicking.

Christopher J. Morris joined the U.S. Army Research Laboratory (ARL) in 2009, after receiving a DARPA-sponsored S.M.A.R.T. graduate fellowship and working as an onsite contractor/postdoctoral fellow since 2007. Following a two-year engagement at a biotechnology startup company, he earned a Ph.D. in electrical engineering from the University of Washington in 2007 and earned an M.S. in mechanical engineering also from the University of Washington, in 2000. He has authored or co-authored over 50 peer-reviewed journal and conference papers, delivered seven invited speaker presentations and received a 2012 U.S. Army RDA award.

William D. Nothwang received a B.S. with Superior Distinction from the Worcester Polytechnic Institute in chemical engineering, an M.S. degree from Clemson University in chemical engineering and the Ph.D. from Clemson University in materials science and engineering. He joined the U.S. Army Research Laboratory (ARL) in 2001 as an ASEE postdoctoral researcher. In 2003, Dr. Nothwang permanently joined ARL as part of the Distinguished Scholar Program and is currently the team leader for the Nano and Micro Sensors Team within the Sensors and Electron Devices Directorate at ARL, where the principles of cyberphysical sensing are applied to neuroscience and autonomous control research problems. Dr. Nothwang has been a co-author on two Army R&D Awards and numerous Army commendations for his research at ARL, including the 2012 Directors Choice Award for Innovation in Research. He has over 50 publications and patents since joining ARL and routinely organizes Department of Defense (DoD) and academic conferences in the area. Dr. Nothwang is the Army Lead for the Microelectronics Research Center of the Micro and Autonomous Systems and Technology (MAST) Collaborative Technology Alliance (CTA).

Ronald G. Polcawich is a staff researcher in the Micro & Nano Materials & Devices Branch of the U.S. Army Research Laboratory (ARL). He received a B.S. in materials science and engineering from Carnegie Mellon University (1997) and M.S. and Ph.D degrees in materials science and engineering from Pennsylvania State University (1999 and 2007, respectively). He is currently the team lead for the RF MEMS and mm-scale robotics programs at ARL. His current research programs include switches and phase shifters for phased-array antennas, tunable MEMS resonators/filters for secure communication and mobile unattended sensor platforms. His research activities include materials processing of PZT thin films, MEMS fabrication, piezoelectric MEMS, RF components, MEMS actuator technologies and mm-scale robotics. Dr. Polcawich currently holds seven patents and has eight patent applications pending review. He has authored over 70 articles and two book chapters on fabrication and design of piezoelectric MEMS devices using PZT thin films. Along with his colleagues, he was a recipient of the 2006 Department of the

Army Research and Development Achievement Award for Piezoelectric RF MEMS Switch Using PZT Thin Films, and the 2009 ARL Engineering Award for groundbreaking work on Piezoelectric MEMS. Dr. Polcawich is a member of the Institute of Electrical and Electronics Engineers (IEEE) and an elected member of the IEEE Ferroelectrics Committee.

Daniel M. Potrepka joined the U.S. Army Research Laboratory (ARL) in 2002 as an electronics engineer with a focus on ferroelectric materials for microwave radar applications. Dr. Potrepka earned a Ph.D. in physics in 1998 from the University of Connecticut, with a thesis on high-temperature superconductivity. From 1979-1993, he was a process engineer at Mostek Corporation, an associate member of the technical staff at RCA Laboratories and an associate research scientist at United Technologies. As a National Research Council postdoctoral fellow at ARL (1999-2001), he studied the ferroelectric behavior of perovskite materials. In 2002, he received an RDA Award. Currently, he is involved in a crystallographic study of PiezoMEMS response in PZT for sputtered and atomic layer deposited thin films and on packaging applications for MEMS. He has published more than 40 technical articles in the areas of superconductivity, perovskites and PZT MEMS; has five patents; and is a member of the American Physical Society.

Robert M. Proie Jr. received a B.S. degree in electrical engineering from the University of Pittsburgh, Pittsburgh, Pa., in 2007, and an M.S. and Ph.D. degree in computer engineering from the George Washington University (GWU), Washington, D.C., in 2010 and 2011, respectively. He is currently an electronics engineer at the U.S. Army Research Laboratory (ARL) and an adjunct professor at GWU. His research interests are in the areas of low-power electronics and MEMS device design, with a current focus on Sub-Vt and high-voltage CMOS, GaN and Piezoelectric MEMS design and verification – for both RF and digital applications.

Jeffrey S. Pulskamp is a MEMS Design and Mechanical Engineer in the Micro & Nano Materials & Devices Branch of the U.S. Army Research Laboratory (ARL). In 2000, he received a B.S. in mechanical engineering from the University of Maryland, College Park. He is a senior research engineer in the RF MEMS and mm-scale robotics group at ARL. His research interests include RF MEMS devices, electromechanical design and modeling of MEMS and mm-scale robotics. He has authored and co-authored over 50 research publications and two book chapters on the design and fabrication of piezoelectric MEMS devices. He also currently holds eight patents related to MEMS devices and has an additional eight patents pending. He has designed and co-developed the micro-fabrication processes for numerous state-of-the-art devices; including low-insertion-loss RF-MEMS resonators, low-voltage RF-MEMS piezoelectric switches, the first piezoelectric nano-electromechanical digital logic relay and the only demonstration of aerodynamic lift by a millimeter-scale insect-inspired robotic mechanism enabled by piezoelectric MEMS. He earned the 2006 Department of the Army's Research and Development Achievement Award for Technical Excellence, the 2009 ARL Award for Engineering, and the 2010 Hetényi Award by the Society for Experimental Mechanics.

Ryan Q. Rudy received the B.S.E. and M.S.E. degrees in mechanical engineering from the University of Michigan, Ann Arbor, in 2009 and 2010, respectively. Since 2008, he has worked at the U.S. Army Research Laboratory (ARL) as a student intern and visiting researcher, with a focus on ground-mobile robotics and traveling-wave ultrasonic motors. In2010, he became a part of the MEMS and Microfluidics Laboratory at the University of Maryland, College Park, Md., where he is pursuing the Ph.D. degree in mechanical engineering, with the support of the SMART program. His current research interests include millimeter-scale actuators, with a specific focus on traveling wave ultrasonic motors.

Brian M. Sadler is a fellow of the U.S. Army Research Laboratory (ARL), a fellow of the Institute of Electrical and Electronics Engineers (IEEE) and co-chair of the IEEE Robotics and Automation Society Technical Committee on Networked Robotics. He has been an editor for many journals, including the International Journal of Robotics Research, the IEEE Transactions on Signal Processing, IEEE Signal Processing Letters, IEEE JSTSP, IEEE JSAC and the IEEE SP Magazine. In 2006 and 2010, he received Best Paper Awards from the IEEE Signal Processing Society. He has also received several ARL and Army R&D awards, as well as a 2008 Outstanding Invention of the Year Award from the University of Maryland. Currently, he is the government lead for the Autonomous Processing Center within the Micro Autonomous Systems and Technology Collaborative Technology Alliance (MAST CTA). His research interests include autonomous collaborative systems, networking, sensing and information science – he has co-authored more than 300 publications in these areas.

Luz M. Sanchez received her B.A. degree in physics from Hunter College, City University of New York (CUNY), in 2008. She started working at the U.S. Army Research Laboratory (ARL) as a student intern in the summer of 2008 while pursuing her Ph.D. in materials science and engineering at the University of Maryland, College Park. The focus of her research has been the optimization of a piezoelectric material through sol-gel deposition methods for improved device performance.

Gabriel L. Smith received B.S. and M.S. degrees in mechanical engineering from the University of Maryland, College Park, Md., in 1999 and 2002, respectively. He has 17 years of MEMS research experience and has been working on PiezoMEMS at the U.S. Army Research Laboratory (ARL) since 2009. Previously, he was employed with the U.S. Naval Surface Warfare Center and the U.S. Army Armaments Research Development and Engineering Center. He has developed MEMS devices for safe and

arm devices in torpedoes and gun-launched munitions, piezoelectric sensors and actuators for mm-scale robotic systems and piezoelectric traveling-wave ultrasonic motors. Mr. Smith has also fielded MEMS impact switches in Army and Navy systems for target and launch detection. Currently, he holds seven U.S. patents with four patents pending and has authored 16 journal and conference papers on MEMS devices.

Jeffrey N. Twigg received his bachelor's and master's degrees from the Virginia Polytechnic Institute and State University in engineering mechanics. He joined the U.S. Army Research Laboratory (ARL) in 2010 as an intern in the Science Outreach for Army Research program. Currently, he is working with Advanced Resource Technologies, Incorporated, with both the Tactical Network Assurance Branch and the Asset Control and Behavior Branch of the Computation and Information Sciences Directorate of ARL. His work focuses on control strategies for collaborative autonomy; including wireless networking, mapping and exploration.

Paul L. Yu received a B.S. in mathematics, a B.S. in computer engineering, and a Ph.D. in electrical engineering, all at the University of Maryland, College Park. He has been with the U.S. Army Research Laboratory (ARL) since 2006, working in the area of signal processing for wireless networking and autonomy. Most recently, his work focuses on the exploitation of mobility for improved wireless network connectivity in complex propagation environments. In 2008, he received the Outstanding Invention of the Year award and in 2009, the Jimmy Lin Award for Innovation and Invention – both from the University of Maryland. Dr. Yu was also awarded a Best Paper award at the 2008 Army Science Conference.

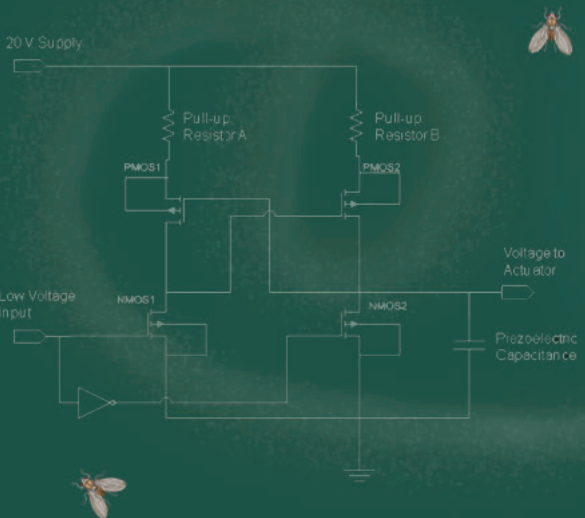

U.S. ARMY RDECOM®